MODICATION OF SMALL MOLECULES AND DELIVERY VEHICLES FOR SUBCELLULAR LOCALIZATION

by

SEAN MARRACHE

(Under the Direction of Shanta Dhar)

ABSTRACT

The mitochondria have long since been known to be of great importance to life. They have roles in heme biosynthesis, energy production, and initiation of apoptosis among many other things. Due to their complex role in everyday life, their dysfunction has been associated with a variety of different diseases such as cancer, diabetes, aging, obesity and several neurodegenerative diseases. Although leaps and bounds have been made towards therapy, many of the general public still lose the battle with these diseases every year. There are several drugs that currently act on restoring mitochondrial function.

However, there still needs to be improvement in that many of the drugs cannot cross the complex structures of the mitochondria. Nanocarriers have recently become more popular for the delivery of therapeutics to specific cells. They have the ability to deliver high amounts of payloads with high effiency without altering the structure of the drug itself. Specific cellular targets, such as target organelles, have not been fully explored. This dissertation will focus on improving the ability for mitochondrial acting therapeutics to reach their desired location through the use of small molecule prodrugs

and nano-carriers. *In vitro* and *in vivo* results will be shown for a variety of different diseases.

INDEX WORDS: Nanomedicine, mitochondria targeting, nanocarrier, drug trafficking, nanotechnology

MODICATION OF SMALL MOLECULES AND DELIVERY VEHICLES FOR SUBCELLULAR LOCALIZATION

by

SEAN MARRACHE

BS, University of Georgia, 2009

A Dissertation Submitted to the Graduate Faculty of The University of Georgia in Partial Fulfillment of the Requirements for the Degree

DOCTOR OF PHILOSOPHY

ATHENS, GEORGIA

2014

© 2014

SEAN MARRACHE

All Rights Reserved

MODIFICATION OF SMALL MOLECULES AND DELIVERY VEHICLES FOR SUBCELLULAR LOCALIZATION

by

SEAN MARRACHE

Major Professor: Shanta Dhar

Committee: Jason Locklin
Robert Phillips
Donald Harn

Electronic Version Approved:

Julie Coffield
Interim Dean of the Graduate School
The University of Georgia
August 2014

DEDICATION

For my fiancé and soon to be wife, Audrey. Thank you for always being there for me. I truly could not have made it through graduate school without you. The constant love and support you have provided me has been a driving force through all of this. I can't wait to spend the rest of our lives together. I love you.

ACKNOWLEDGEMENTS

I would like to take this time to thank the University of Georgia for the funding and support throughout my graduate school career. Without it, this thesis would not have been possible. First and foremore, I would like to thank my principal advisor, Dr. Shanta Dhar. I would not have been nearly as successful without her direction. Her drive and passion for science has been a constant inspiration from day one.

I would also like to thank my advisory committee: Drs. Locklin and Phillips for all the help over the years. They were able to provide me with great advice towards finishing my thesis. I would also like to thank Dr. Harn for his willingness to join my thesis committee this semester. As a collaborator, his advice and ideas have truly allowed me to succeed over the years. I also owe a lot of my success to his post-doc Smanla Tundup. It truly has been a pleasure working with you over the years.

To my animal science collaborators Dr. Franklin West and Emily Wyatt, thank you. It has truly been a pleasure doing working with you and learning new animal techniques over the past few years. I also would like to thank my collaborators in pharmacy, Dr. Raj Govindarajan, Wai Hung, and Hardik Mody. The work on new nano-formulations to deliver cancer therapeutics has been extremely rewarding.

I am also very grateful to have such an amazing research group. Our post-doc, Dr. Rakesh Pathak and my fellow graduate student, Joshua Choi, have made doing research much more enjoyable. I also owe a lot to Dr. Nagesh Kolishetti. His advice and kind words over the past few years have made for a very great place to work.

TABLE OF CONTENTS

Page

ACKNOWLEDGEMENTS v

LIST OF TABLES xi

LIST OF FIGURES xii

CHAPTER

1 INTRODUCTION AND LITERATURE REVIEW 1

Introduction 1

Mitochondria Structure 1

Why the mitochondria? 3

Mitochondria acting therapeutics 6

Mitochondria Targeted Small Molecules 9

Nanoparticles in drug delivery 13

Mitochondria-targeted micelles 16

Mitochondria-targeted dendrimers 16

Liposome based mitochondria targeted nanoparticles 18

Mitochondria-targeted polymeric nanoparticles 21

Mitochondria-targeted metal nanoparticles 22

Objective and outline of this dissertation 24

References 27

2 ENGINEERING OF BLENDED NANOPARTICLE PLATFORM FOR DELIVERY OF MITOCHONDRIA-ACTING THERAPEUTICS 46
Abstract 47
Introduction 48
Experimental 53
Results and discussion 67
Conclusion 83
References 84
3 EX VIVO PROGRAMMING OF DENDRITIC CELLS BY MITOCHONDRIA-TARGETED NANOPARTICLES TO PRODUCE INTERFERON GAMMA FOR CANCER IMMUNOTHERAPY 90
Abstract 91
Introduction 91
Experimental 94
Results and discussion 103
Conclusion 128
References 128
4 DETOURING OF CISPLATIN TO ACCESS MITOCHONDRIAL GENOME FOR OVERCOMING RESISTANCE 135
Abstract 136
Introduction 137
Experimental 138
Results and discussion 150

Conclusion 173

References 174

5 A HIGHLY LIPOPHILIC BLOOD-BRAIN BARRIER PENETRATING MITOCHONDRIA TARGETED THERAPEUTIC NANOPARTICLE FOR THE TREATMENT OF TRAUMATIC BRAIN INJURY 178

Abstract 179

Introduction 180

Experimental 182

Results and discussion 191

Conclusion 208

References 209

6 BIODEGRADABLE SYNTHETIC HIGH DENSITY LIPOPROTEIN NANOPARTICLES FOR ATHEROSCLEROSIS 216

Abstract 217

Introduction 218

Experimental 222

Results and discussion 240

Conclusion 272

References 273

7 THE “ENERGY BLOCKER” INSIDE THE “POWER HOUSE”: MITOCHONDRIA TARGETED DELIVERY OF 3-BROMOPYRUVIC ACID 278

Abstract 279

Introduction 280
Experimental 283
Results and discussion 297
Conclusion 321
References 322
8 MITOCHONDRIA TARGETED MOLECULAR SCAFFOLD FOR EFFICACIOUS DELIVERY OF METABOLIC MODULATOR DICHOLOROACETATE 325
Abstract 326
Introduction 327
Experimental 329
Results and discussion 338
Conclusion 356
References 357
9 CONCLUSION AND FUTURE GOALS 362
Conclusion 362
Future goals 364
APPENDICES
A IMMUNE STIMULATING PHOTOACTIVE HYBRID NANOPARTICLES FOR METASTATIC BREAST CANCER 367
Abstract 368
Introduction 369
Experimental 371

Results and discussion 377
Conclusion 387
References 388
B PHARMACOLOGICAL REVERSAL OF HISTONE METHLATION PRESENSITIZES PANCREATIC CANCER CELLS TO NUCLEOSIDE DRUGS: *IN VITRO* OPTIMIZATION AND NOVEL NANOPARTICLE DELIVERY SYSTEM 394
Abstract 395
Introduction 396
Experimental 398
Results and discussion 402
Conclusion 405
References 406
C THE PRODRUG PLATIN-*A*: SIMULTANEOUS RELEASE OF CISPLATIN AND ASPIRIN 413
Abstract 414
Introduction 414
Experimental 416
Results and discussion 419
References 427

LIST OF TABLES

Page

Table 1.1: NP-Based therapeutics that follow passive targeting 15

Table 1.2: Targeted-NP-Based Therapeutics that follow active targeting.....15

Table 2.1: Examples of Nanocarriers Mitochondrial Delivery.....40

Table 2.2: Size and Zeta Potential Variation from Three Independent NP Synthesis.....60

Table 3.1: Physicochemical properties of the NPs and the loading of ZnPc.....107

Table 4.1: PK Parameters of T-NPs by Using a Two-compartment Model 157

Table 4.2: IC_{50} (μM) Values of Platin-M and NPs. 163

Table 5.1: Characterization of T and NT-NPs used in this study 194

Table 5.2: PK Profiles of T and NT-NPs in Normal Pig 196

Table 5.3: PK Profiles of T and NT-NPs in TBI Pig Model.....200

Table 5.4: Characterization of QD loaded T and NT-NPs used in animal studies 200

Table 6.1: Examples of Known HDL-Mimicking Nanoparticles.....219

Table 6.2: Composition analysis of HDL-mimicking NPs.....244

Table 6.3: PK parameters of TPP-HDL-apoA-I-QD-NPs using two-compartment model 257

Table 6.5: DLS data for varied cholesterol loaded NPs.....260

Table 6.5: Cholesterol and Peptide loading for varied cholesterol NPs 261

Table 6.6: Binding constants for varied cholesterol NPs.....261

Table 6.7: NP characterization of CoQ10 encapsulated NPs 262

Table 7.1: Characterization of AuNPs, data presented here is an average of three independent preparations 304

Table 7.2: IC_{50} with standard deviation calculated from three independent experiments 313

Table 7.3: PK parameters of NPs by using a one-compartmental model 319

Table AII.2: Physiochemical Characterization of NPs 405

LIST OF FIGURES

Page

Figure 1.1: Mitochondria structure 3

Figure 1.2: Diseases associated with mitochondria dysfunction 6

Figure 1.3: Mitochondria targeted based on lipophilic cations.....11

Figure 1.4: Mitchondria-targeting based on nanoformulations 13

Figure 2.1: (A) Synthesis of PLGA-*b*-PEG-OH, PLGA-*b*-PEG-TPP, and QD-conjugated polymer. (B) Construction of targeted and non targeted NPs by blending PLGA-*b*-PEG-OH and PLGA-COOH with PLGA-*b*-PEG-TPP, and mitochondria-acting therapeutics used as payloads 52

Figure 2.2: ^{1}H NMR of PLGA-PEG-OH.....55

Figure 2.3: ^{13}C NMR of PLGA-PEG-OH.....55

Figure 2.4: ^{1}H NMR of PLGA-PEG-TPP.....57

Figure 2.5: ^{13}C NMR of PLGA-PEG-TPP.....57

Figure 2.6: ^{31}P NMR of PLGA-PEG-TPP 58

Figure 2.7: GPC plots of PLGA-COOH, PEG-OH, PLGA-PEG-OH, and PLGA-PEG-TPP.....58

Figure 2.8: Size Distribution (A) and zeta potential (B) of blended NPs with varied size 62

Figure 2.9: Size distribution (A) and zeta potential (B) and of blended NPs with varied zeta potential 63

Figure 2.10: (A) (Left) Size and zeta potential variation in blended NPs from PLGA-*b*-PEG-TPP and PLGA-COOH and (Right) size and zeta potential variation in NPs by blending PLGA-*b*-PEG-TPP with PLGA-*b*-PEG-OH. (B) TEM images of targeted and non targeted blended NPs. All the TEM samples were negatively stained with sterile 2% (w/v) uranyl acetate aqueous solution for 15 min except for the QD-blended NPs. *NPs from 100% PLGA-COOH are unstable and NP diameter varies in between 700 nm to 10 μm based on the batch preparation. 69

Figure 2.11: (A) Subcellular localization of red fluorescent-targeted PLGA-*b*-PEG-TPP/PLGA-*b*-PEG-QD and non targeted PLGA-*b*-PEG-OH/PLGA-*b*-PEG-QD blended NPs. HeLa cells were exposed to targeted NPs (diameter, 79 nm; zeta potential, 27.4 mV) and non targeted NPs (diameter, 79 nm; zeta potential, -26.5 mV) at 10 μM or left untreated for 4 h. (B) Confocal images of time dependent uptake of targeted PLGA-*b*-PEG-TPP/PLGA-*b*-PEG-QD blended NPs and non targeted PLGA-*b*-PEG-OH/PLGA-*b*-PEG-QD blended NPs in HeLa cells. 71

Figure 2.12: DLS and Zeta Potential plots for NPs used for internalization study. (Top – Targeted, Bottom – Non-targeted).....72

Figure 2.13: Time dependent Subcellular localization of red fluorescent-targeted PLGA-*b*-PEG-TPP/PLGA-*b*-PEG-QD and non targeted PLGA-*b*-PEG-OH/PLGA-*b*-PEG-QD blended NPs in HeLa cells. The early endosomes were visualized in green by using the early endosome marker EEA-1. Co-localization with the endosomes are represented by white arrows.....73

Figure 2.14: Stability of targeted PLGA-*b*-PEG-TPP-NPs (5 mg/mL) in 10% FBS-DMEM (left) and 10% FBS-H_2O (right) for 7 days at 4 °C. 74

Figure 2.15: Secretion of IL-6, and TNF-α in the media with charge-varied and size-varied NPs (0.5 mg/mL) after 12 h. 75

Figure 2.16: Mitochondrial and cytosolic distribution of targeted PLGA-*b*-PEG-TPP/PLGA-*b*-PEG-QD blended NPs in HeLa cells by ICP-MS analysis. (A) Effect of size on uptake of NPs; (B) overall cellular uptake of size-varied NPs, (C) effect of zeta potential on cellular trafficking of NPs; and (D) overall cellular uptake of zeta potential-varied NPs. 77

Figure 2.17: Effect on the percent survival of IMR-32 neuroblastoma cells after treatment with targeted-curcumin-NPs, non targeted-curcumin-NPs, and free curcumin against Aβ induced cytotoxicity.....79

Figure 2.18: Cytotoxicity profiles of targeted-LND-NPs, non targeted-LND-NPs, free LND, targeted-α-TOS-NPs, non targeted-α-TOS-NPs, free α-TOS in HeLa cells, empty targeted-NPs, and empty non targeted-NPs in HeLa cells.....80

Figure 2.19: Mouse 3T3-L1 preadipocytes were differentiated into adipocytes in the presence of 1 μM, 4 μM, 25 μM, and 100 μM of targeted-2,4-DNP-NPs, non targeted-2,4-DNP-NPs, and free 2,4-DNP for 7 days.....82

Figure 2.20: Effect of targeted-2,4-DNP-NPs, non targeted-2,4-DNP-NPs, and free 2,4-DNP on adipocyte differentiation.. 83

Figure 3.1: Action of mitochondria-targeted NPs upon light activation inside the mitochondria to produce ROS which causes cell death via apoptosis and necrosis 94

Figure 3.2: Proton NMR of TPP-Pentanoic Acid 97

Figure 3.3: Carbon NMR of TPP-Pentanoic Acid 98

Figure 3.4: Synthesis of T-ZnPc-NPs by following a nanoprecipitation method.....105

Figure 3.5: Size, zeta potential, and ZnPc loading in targeted and non-targeted NPs.....106

Figure 3.5: TEM images of targeted and non-targeted empty and ZnPc-loaded NPs 108

Figure 3.7: Release kinetics of LND from targeted and non-targeted-NPs at 37 °C, pH 7.4 108

Figure 3.8: (a) HeLa and MCF-7 cancer cells respond differently to light activation compared to hMSC. Cells on 96-well plates were incubated for 4 h with T-ZnPc-NP, NT-ZnPc-NP, and free ZnPc. Cells were irradiated with a 660 nm laser (20 mW) for 1 min, media was changed after 12 h, and cells were further incubated for additional 60 h and viability was assessed by the MTT assay. (b) FACS analysis using Annexin V-Alexa Fluor/PI staining for apoptosis detection in MCF-7 cells on treatment with T-ZnPc-NP (1 μM), NT-ZnPc-NP (1 μM), and free ZnPc (1 μM) for 16 h in the dark or irradiation with a 660 nm laser for 1 min after 4 h incubation, followed by incubation in the dark for 12 h. 111

Figure 3.9: FACS analysis using annexin V-Alexa Fluor® 488/PI staining for apoptosis detection in MCF-7 cells.....112

Figure 3.10: Cytokine response from various NP treated and light stimulated MCF-7 cancer cell supernatant.....114

Figure 3.11: BMDCs were purified using anti-CD11c micro-bead column. DCs were incubated with media alone or LPS for 24 h. Expression of CD11c on DCs were tested using a fluorescent anti-CD11c antibody. Cells were acquired and analyzed by flow cytometry.....115

Figure 3.12: Cytokine response from the BMDCs treated with MCF-7 cancer cell supernatant treated with different constructs under dark 115
Figure 3.13: Time dependent PDT-treated MCF-7 cancer cell supernatant induced DC activation 116
Figure 3.14: Cytokine production by BMDCs stimulated with cancer cell supernatants generated by treating MCF-7 cells with different constructs after PDT activation 117
Figure 3.15: LND-NP-treated MCF-7 cancer cell supernatant induced DC activation for 12 h 119
Figure 3.16: Combination of IL-12 and IL-18 is the source of IFN-γ. Purified BMDCs were treated with neutralizing antibodies against IL-12 and/or IL-18 cytokines, followed by incubation with different cancer cell supernatants or with LPS (100 ng/mL) for 48 h 121
Figure 3.17: Various NP treated and light stimulated HeLa cancer cell supernatant induced DC activation after 48 h 123
Figure 3.18: DC maturation assay. MCF-7 cell conditioned media treated with T-ZnPc-NPs followed by PDT stimulation induces expression of CD11c (a), CD86 (b), and CD40 (c) markers on DCs 125
Figure 3.19: CD8 T cell activation assay. DCs exposed to supernatants of MCF-7 cells treated with different conjugates (20 nM with respect to ZnPc for T-ZnPc-NP, NT-ZnPc-NP, and free ZnPc; empty-NPs 0.5 mg/mL with respect to polymer) with or without light activates $CD8^+$ T-cells. MCF-7 cells were incubated with the conjugates 127

Figure 4.1: Schematic figure for mitochondrial delivery of cisplatin prodrug using a targeted NP and the mechanism of action.....138

Figure 4.2: Synthesis of mitochondria targeted Pt(IV) prodrug Platin-M and nanoparticles 151

Figure 4.3: Electrochemistry data of Platin-M 152

Figure 4.4: (A) Distribution of $PLGA_{HMW}$-b-PEG-TPP and $PLGA_{LMW}$-b-PEG-TPP-NPs in mitochondrial compartments of PC3 cells by ICP-MS (top) and IVIS analysis (bottom). (B) Mitochondrial toxicity of Empty-T-NPs and Empty-NT-NPs in PC3 and A2780/CP70 cells by Mito Stress assay. (C) Variation of Cd concentration in plasma with time, tissue distribution, and cumulative excretion profiles following the administration of T-QD-NPs intravenously to male rats 154

Figure 4.5: Effect of Empty T and NT-NPs in H9C2 cardiomyocytes by mito-stress test assay.....156

Figure 4.6: (A) Platin-M percent loading, encapsulation efficiency in T and NT NPs, and TEM images of T-Platin-M and NT-Platin-M-NPs. (B) pH dependent release kinetics of Platin-M from T and NT-NPs in PBS at 37 °C. (C) Distribution of cisplatin, Platin-M, NT-Platin-M-NPs, and T-Platin-M-NPs in cytosolic, nuclear, and mitochondrial fractions of PC3 cells. (D) Comparison of Pt-nDNA and Pt-mtDNA adducts for cisplatin, Platin-M, NT-Platin-M-NP, and T-Platin-M-NPs in PC3 cells. 160

Figure 4.7: Cytotoxicity profiles of cisplatin, Platin-M, NT-Platin-M-NPs, and T-Platin-M-NPs in prostate cancer PC3, neuroblastoma SH-SY5Y, cisplatin-resistant

ovarian cancer A2780/CP70, and human mesenchymal stem cells hMSC cells as determined by the MTT assay.....163

Figure 4.8:A comparison of OCR levels in different cancer cells by Mitostress analyses 164

Figure 4.9: FACS analysis using Annexin V-Alexa Fluor/PI staining for apoptosis detection in SH-SY5Y cells treated with 1 μM cisplatin, 1 μM Platin-M, 1 μM NT-Platin-M-NPs, and 1 μM T-Platin-M-NPs for 12 h at 37 °C 166

Figure 4.10: Citrate synthase activity in SH-SY5Y cells treated with 1 μM cisplatin, 1 μM Platin-M, 1 μM NT-Platin-M-NPs, and 1 μM T-Platin-M-NPs for 12 h at 37 °C 167

Figure 4.11: Mitochondrial bioenergetics in (A) SH-SY5Y and (B) A2780/CP70 cells in response to cisplatin, Platin-M, NT-Platin-M-NPs, and T-Platin-M-NPs 168

Figure 4.12: Effect of cisplatin, Platin-M, and its NPs in PC3 cells by Mito-Stress assay. The cells were treated with Platin-M (10 μM), cisplatin (10 μM), T-Platin-M-NPs (10 μM with respect to Pt), NT-Platin-M-NPs (10 μM with respect to Pt) for 12 h at 37 °C in 5% CO_2 atmosphere.....169

Figure 4.13: Changes in the $\Delta\psi_m$ and mitochondrial mass loss by JC-1 assay 170

Figure 4.14: Pt concentration variation in plasma and organs following the administration of Platin-M, NT-Platin-M-NPs, and T-Platin-M-NPs intravenously to male rats 172

Figure 4.15: A comparison of bioD and excretion profiles of Platin-M, NT-Platin-M-NPs, and T-Platin-M-NPs in male rats 173

Figure 5.1: Design, construction, and characterization of mitochondria-targeted and non-targeted NPs for delivery of antioxidant and anti-inflammatory agents to the brain 194

Figure 5.2: Accumulation of T-NPs in the brain of normal Pig and distribution in brain white matter 197

Figure 5.3: Accumulation of T-NPs in the mitochondria of pig brain tissue. 199

Figure 5.4: Accumulation of T-NPs in the brain of injured Pig. 201

Figure 5.5: MTT assays on NSCs using CoQ10 and its NPs (top) and prednisone and its NPs (bottom).....206

Figure 5.6: Therapeutic Potential of Mitochondria Targeted NPs carrying an Antioxidant and an Anti-inflammatory Agent in NSCs.....207

Figure 6.1: Schematic diagram of the mitochondria-targeted biodegradable HDL mimicking NP platform and various components 221

Figure 6.2: ^{1}H-NMR of stearyl-TPP in $CDCl_3$ 225

Figure 6.3: ^{13}C-NMR of stearyl-TPP in $CDCl_3$ 226

Figure 6.4: ^{31}P-NMR of stearyl-TPP in $CDCl_3$.....226

Figure 6.5: (A) (Left) Size and zeta potential of targeted and non-targeted HDL-mimicking NPs with or without QD and (Right) TEM images of targeted and non-targeted QD-loaded HDL-mimicking NPs. (B) (Left) Toxicity profiles of targeted and non-targeted HDL-mimicking NPs in RAW macrophages and MSC cells as determined by MTT assay and (Right) secretion of IL-6, and TNF-α with targeted and non-targeted NPs (0.5 mg/mL) after 12 h. (C) Binding of NBD-cholesterol to

TPP-HDL-apoA-I-NPs (left). TPP-HDL-NPs (middle) and TPP-PLGA-DSPE-NPs (right) were used as controls 241
Figure 6.6: Size distribution of various NPs 242
Figure 6.7: Zeta potential of various NPs 243
Figure 6.8: (a) In vitro serum stability of TPP-HDL-apoA-I-NPs (2.5 mg/mL) in 10% fetal bovine serum (FBS)-DMEM at 4 °C, room temperature, and at 37 °C. (b) Images of TPP-HDL-apoA-I-NPs (2.5 mg/mL) in 10% FBS-DMEM at 4 °C....245
Figure 6.9: Effect of TPP-HDL-apoA-I-QD-NPs and non-targeted-HDL-apoA-I-QD-NPs on LPS activated RAW 264.7 macrophages (a) and cell viability after treatment with LPS and the NPs (b).....246
Figure 6.10: Temperature and time dependent binding of NBD-cholesterol to TPP-HDL-apoA-I-NPs 248
Figure 6.11: (A) Subcellular localization of TPP-HDL-apoA-I-QD-NPs and non-targeted-HDL-apoA-I-QD-NPs in RAW macrophages. RAW 264.7 cells were exposed to targeted NPs (diameter, 125 nm; zeta potential, 37 mV) and non-targeted NPs (diameter, 189 nm; zeta potential, -29 mV) at 270 μM (with respect to cholesterol) for 4 h 249
Figure 6.12: IVIS of mitochondrial and cytosolic fractions of RAW macrophages after treatment with non-targeted-HDL-apoA-I-QD-NPs with collapse of $\boldsymbol{\Delta\psi_m}$ by addition of FCCP 250
Figure 6.13: (A) Apoptosis detection by HDL-apoA-I-QD-NPs in RAW macrophages by confocal microscopy. Apoptosis was induced by treating macrophages with etoposide. The medium was changed and targeted and non-targeted NPs were

added. Cells were fixed, nuclei were stained with Hoechst, and visualized by confocal microscopy. (B) Flow cytometry patterns of RAW macrophages treated with the targeted and non-targeted-NPs with or without etoposide. Macrophage monolayers were incubated for 3 h with TPP-HDL-apoA-I-QD-NPs (left), non-targeted-HDL-apoA-I-QD-NPs (right). Prior to NP treatment, apoptosis was induced using the above-mentioned conditions. Histograms depict all the acquired events. (C) IVIS and ICP-MS analysis of mitochondrial and cytosolic fractions of healthy and apoptotic RAW macrophages after treatment with targeted (left) and non-targeted NPs (right) 252

Figure 6.14: Apoptosis detection in RAW 264.7 macrophages after treatment with etoposide using Annexin V 254

Figure 6.15: (A) Variation of Cd concentration in ng/mL in plasma with time following the administration of targeted-TPP-HDL-apoA-I-QD-NPs intravenously to rat. (B) Tissue distribution of targeted-TPP-HDL-apoA-I-QD-NPs in male rats. (C) Cumulative 24 h excretion of TPP-HDL-apoA-I-QD-NPs in male rats. Changes in levels of plasma total cholesterol (D) and triglyceride (E) in rats administered with TPP-HDL-apoA-I-QD-NPs 256

Figure 6.16: Mitostress test of HDL-NPs 263

Figure 6.17: AdipoRed RFUs from foam cells with and without treatment with cholesterol NPs 264

Figure 6.18: Confocal Images of pre-treated cholesterol NP foam cells with (40% CO left, 70% CO right) following differentiation 265

Figure 6.19: Confocal Images of therapeutic-treated cholesterol NP foam cells with (40% CO left, 70% CO right) following differentiation 265
Figure 6.20: Foam cell cytokine production 266
Figure 6.21: NBD-Cholesterol binding and release assay for 40% cholesterol (left) and 70% cholesterol (right) 267
Figure 6.22: BioD for (a) 70% HDL NPs and (b) 40% HDL NPs. (c) PK parameters for both NP systems.....268
Figure 6.23: IVIS imaging of isolated pig hearts and aortas treated with 40% HDL NPs (right) and 70% HDL NPs (left). 268
Figure 6.24: In vivo cytokine production for 40% (left) and 70% (right) after injection in piglets.....270
Figure 6.25: In vivo triglyceride reduction after injection of 40% HDL (left) and 70% HDL (right) 271
Figure 6.26: In vivo cholesterol reduction after injection of 40% HDL (left) and 70% HDL (right) 271
Figure 7.1: ^{1}H NMRof TPP-PEG-SH in $CDCl_3$ 298
Figure 7.2: ^{13}C NMRof TPP-PEG-SH in $CDCl_3$ 299
Figure 7.3: ^{31}P NMRof TPP-PEG-SH in $CDCl_3$.....299
Figure 7.4: $^{\mathbf{1}}$H NMR of TPP-$(CH_2)_5$-COOH 300
Figure 7.5: $^{\mathbf{13}}$C NMR of TPP-$(CH_2)_5$-COOH 301
Figure 7.6: Overlay of DLS for (a) hydrodynamic diameter and (b) zeta potential of different NPs 302

Figure 7.7: (A) Characterization of different AuNPs by DLS. (B) TEM of AuNPs. (C) Quantification of 3-BP by GADPH assay. (D) Non-immunogenic behavior of NT and T-AuNPs by ELISA 303

Figure 7.8: Photographs of T-AuNPs, T-3-BP-AuNPs, NT-AuNPs, and NT-3-BP-AuNPs after resuspension in water.....305

Figure 7.9: UV-Vis characterization of T and NT-AuNPs showing the absence of any aggregation with inset showing the TPP peaks from T-AuNPs 305

Figure 7.10: (A) Protease dependent release of 3-BP from T and NT-AuNPs. (B) HK2 binding profile of T-3-BP-AuNPs and NT-3-BP-AuNPs. (C) ICP-MS and (D) cellular TEM Mitochondrial. (E) time-dependent distribution of T-AuNPs and T-3-BP-AuNPs in different mitochondrial compartments of PC3 cells. 308

Figure 7.11: (A) Cells viability in PC3 and DU145 cells after treatment with T-AuNPs, NT-AuNPs, 3-BP, T-3-BP-AuNPs, NT-3-BP-AuNPs. Cell viability was assessed by the MTT assay after treatment with the indicated concentrations of the test articles for 72 h. The data are mean ± SD (n = 3 wells). (B) Cells viability in PC3 cells after treatment with T-AuNPs, NT-AuNPs, 3-BP, T-3-BP-AuNPs, NT-3-BP-AuNPs followed by 660 nm laser radiation for 1 min/well. The data are mean ± SD (n = 3 wells). (C) (Top) Apoptotic patterns induced in PC3 cells upon treatment with T-AuNP (1 mg/mL), NT-AuNP (1 mg/mL), T-3-BP-AuNP (14.1 µg/mL with respect to NP, 10 μM with respect to 3-BP), NT-3-BP-AuNP (13.7 µg/mL with respect to NP, 10 μM with respect to 3-BP), free 3-BP (10 μM) for 6 h at 37 °C in the dark. (Bottom) Apoptosis induced in PC3 cells upon treatment with T-AuNP (1 mg/mL), NT-AuNP (1 mg/mL), T-3-BP-AuNP (14.1 µg/mL

with respect to NP, 10 μM with respect to 3-BP), NT-3-BP-AuNP (13.7 µg/mL with respect to NP, 10 μM with respect to 3-BP), free 3-BP (10 μM) for 4 h at 37 °C, followed by irradiation with 660 nm laser for 1 min, and further incubated for 12 h.....312

Figure 7.12: (A) Cell viability in PC3 cells after treatment with T-AuNPs, NT-AuNPs. (B) Cell viability in MCF-7 cells after treatment with 3-BP, T-3-BP-AuNPs, and NT-3-BP-AuNPs.....314

Figure 7.13: Intracellular (A) and extracellular (B) lactate levels in PC3 cells after treatment with T-AuNP (1 mg/mL), NT-AuNP (1 mg/mL), T-3-BP-AuNP (14.1 µg/mL with respect to NP, 10 μM with respect to 3-BP), NT-3-BP-AuNP (13.7 µg/mL with respect to NP, 10 μM with respect to 3-BP), free 3-BP (10 μM) for 6 h at 37 °C. (C) Changes in intracellular ATP content in PC3 cells after treatment with T-AuNP (1 mg/mL), NT-AuNP (1 mg/mL), T-3-BP-AuNP (14.1 µg/mL with respect to NP, 10 μM with respect to 3-BP), NT-3-BP-AuNP (13.7 µg/mL with respect to NP, 10 μM with respect to 3-BP), free 3-BP (10 μM) for 6 h at 37 °C in 5% CO_2 atmosphere 316

Figure 7.14: Bioenergetics analysis in PC3 cell line 317

Figure 7.15: Variation of Au concentration in μg/L in plasma with time and tissue distribution following the administration of T-AuNPs and NT-AuNPs intravenously to male rats 320

Figure 8.1: (A) Design of MITO-DCA and its possible mechanism of action; (B) synthesis of mitochondria-targeted DCA analogues; (C) ORTEP diagram of MITO-DCA with 50% thermal ellipsoids.....329

Figure 8.2: Changes in the $\Delta\psi_m$ by JC-1 assay.....339

Figure 8.3: Changes in the $\Delta\psi_m$ by the JC-1 assay.....341

Figure 8.4: Reversal of mitochondrial membrane potential by TMRM live cell imaging assay.....342

Figure 8.5: A) Highly glycolytic PC3 and DU145 cells respond differently to MITO-DCA compared to less glycolytic LNCaP cells; MITO-DCA, TPP-DCA, and Na-DCA have no toxicity in MSC cells. Cells on 96-well plates were varied concentrations of MITO-DCA, TPP-DCA, and Na-DCA for 72 h and viability was assessed by the MTT assay. A representative experimental data are shown in the figure and the IC_{50} values were calculated from three independent experiments. (B) FACS analysis using annexin V-alexa fluor/PI staining for apoptosis detection in MSC and PC3 cells on treatment with MITO-DCA (50 μM), TPP-DCA (150 μM), and Na-DCA (150 μM) for 16 h.....344

Figure 8.6: Cytotoxicity of TPP-Tris-$(OH)_3$ in PC3, LNCaP, DU145, and MSC cells as determined by the MTT assay.....346

Figure 8.7: Lactate levels in PC3 cells (left), media (middle) after treatment with 150 μM Na-DCA, 150 μM TPP-DCA, and 50 μM MITO-DCA for 6 h at 37 °C. Changes in intracellular ATP content (right) associated with the lactate fluctuation in the PC3 cells after treatment with 60 μM Na-DCA, 60 μM TPP-DCA, and 20 μM MITO-DCA for 3 h at 37 °C.....347

Figure 8.8: (A) Intracellular lactate levels in LNCaP and MSC cells after treatment with 50 μM TPP-Tris-$(OH)_3$, 150 μM Na-DCA, 150 μM TPP-DCA, and 50 μM MITO-DCA for 6 h at 37 °C. (B) Changes in intracellular ATP content associated

with the lactate fluctuation in the LNCaP and MSC cells after treatment with 60 μM Na-DCA, 60 μM TPP-DCA, and 20 μM MITO-DCA for 3 h at 37 °C 348

Figure 8.9: Intracellular ATP levels in PC3 cells after treatment with TPP-Tris-$(OH)_3$ (50 μM), MITO-DCA (50 μM), TPP-DCA (150 μM), and Na-DCA (150 μM) for 6 h 349

Figure 8.10: (A) Effect of MITO-DCA, TPP-DCA, and Na-DCA on PC3 cell glycolysis. PC3 cells were treated with 10 μM MITO-DCA, 30 μM TPP-DCA, 30 μM Na-DCA for 4 h. ECAR following the addition of glucose represents glycolysis; ECAR following oligomycin shows maximum glycolytic capacity, and ECAR following treatment with 2-DG represents acidification associated with non-glycolytic activity. PC3 cells were subsequently treated with glucose, oligomycin, and 2-DG. (B) Effect of MITO-DCA on OCR in PC3 cells. PC3 cells were treated with 10 μM MITO-DCA, 30 μM TPP-DCA, 30 μM Na-DCA for 4 h. OCR traces were determined using a Seahorse mito stress kit and Seahorse XF24 analyzer 351

Figure 8.11: Effect of Mito-DCA on OCR in PC3 cells. PC3 cells were treated with 10 μM Mito-DCA, 30 μM TPP-DCA, 30 μM Na-DCA for 4 h.....352

Figure 8.12: Lactate reduction by MITO-DCA stimulates anti-tumor immunity 355

Figure A.1: Phagocytosis of tumor antigens by DCs after PDT.....371

Figure A.2: Schematic diagram of the NP platform for combination therapy of metastatic breast cancer.....375

Figure A.3: Characterization of hybrid NP constructs.....379

Figure A.4: Cytotoxicity profiles of ZnPc-Poly-NPs, Au-ZnPc-Poly-NPs, and CpG-ODN-Au-ZnPc-Poly-NPs in 4T1 cells in the dark (left) and after 5 min exposure with a 660 nm LASER (right). Free ZnPc and AuNPs were used as controls 381

Figure A.5: Combination of ZnPc and CpG-ODN in a single NP construct potentiate immune response after PDT. Asterisk represents significant differences between CpG-ODN-Au-ZnPc-Poly-NPs, ZnPc-Poly-NPs, free ZnPc, and a 1:1 combination of free ZnPc and CpG-ODN according to one-way ANOVA with Tukey post hoc test 383

Figure AII.1: Spatiotemporal release of DZNep and gemcitabine using engineered nanoparticles reduced drug dose while potentiating chemosensitivity.....403

Figure AIII.1: Cytotoxic profiles of Platin-*A* in PCa cell lines by the MTT assay.....420

Figure AIII.2: Apoptosis inducing property of Platin-*A* by annexin V-FITC/PI staining of PC3 cells. PC3 cells ($1x10^6$ cells/mL) on day 2 were incubated with aspirin (25 μM), cisplatin (25 μM), an equimolar mixture of cisplatin and aspirin (25 μM), and Platin-*A* (25 μM) for 6 h.....421

Figure AIII.3: COX inhibition properties of Platin-*A*.....423

Figure AIII.4: Reduction of LPS-induced inflammation by Platin-*A* in RAW 264.6 macrophages 426

CHAPTER 1

INTRODUCTION AND LITERATURE REVIEW

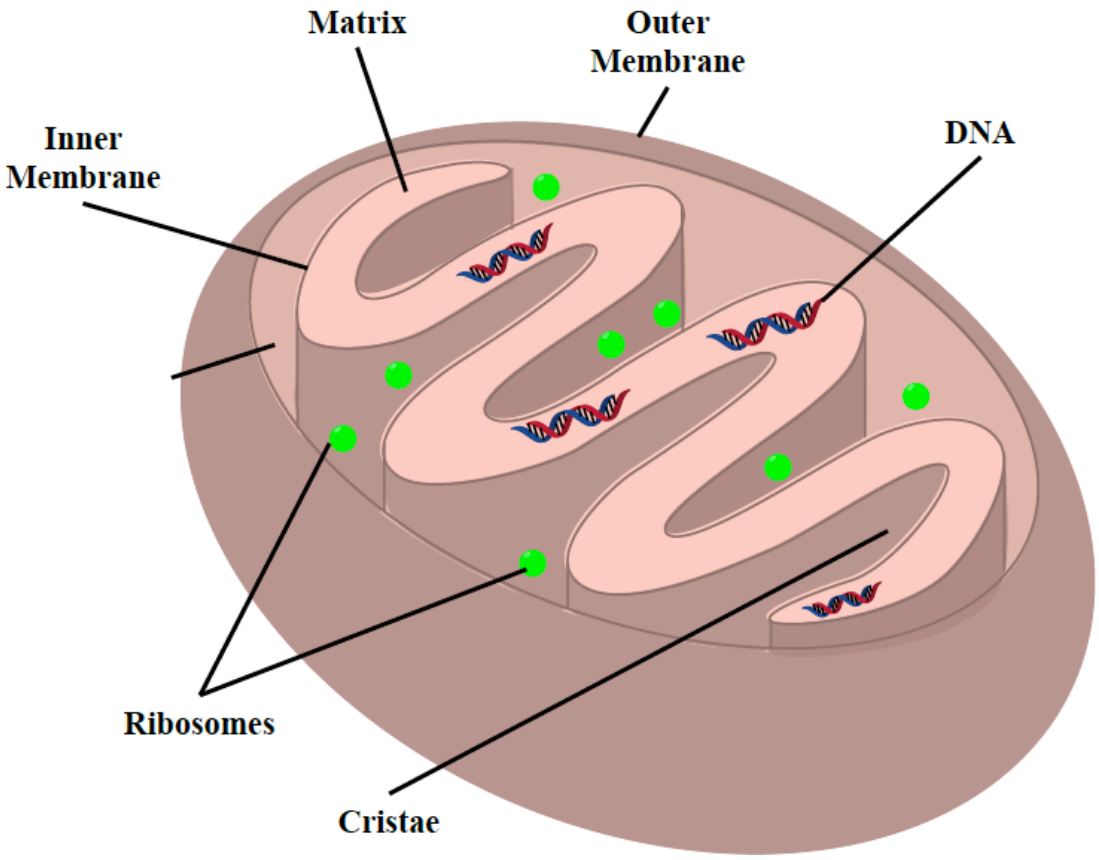
Introduction

The mitochondria are complex organisms that can be found in most eukaryotic cells. Their association with the production of adenosine triphosphate (ATP) makes them essential to life.[1] However, they have not always been an organelle.[2] The introduction of mitochondria into cells occurred over a billion years ago when remnants of bacteria invaded prokaryotic cells.[2, 3] This relationship proved to be synergistic and beneficial for both parties involved in that the remnants of the bacteria were able to survive and the host cells were provided with a new source of energy. The mitochondria's responsibility is not limited to energy production, though. They play crucial roles in a variety of different cellular processes, such as oxygen sensing[4] and initiation of apoptotic pathways.[4, 5] For this reason, mitochondria are considered an ideal drug target for the treatment of a variety of different diseases such as cancer, obesity, aging, and numerous neurodegenerative diseases.

Mitochondria Structure

Mitochondria, or the so-called "cellular powerhouse", are the main site for energy metabolism in cells. Structurally, they are encased in a double-membrane that contains a densely packed matrix that includes multiple copies of its own genome and enzymes of intermediary metabolism.[6-8] The structure was first observed by electron microscope in

the early 1950s separately by Sjostrand and Palade.[9, 10] The outer mitochondrial membrane (OMM) does not offer a barrier to small molecules, which can simply diffuse through pores in the membrane formed by a membrane-spanning protein called porin.[11, 12] Porin is also referred to as the voltage dependent anion channel (VDAC) and is the most abundant protein of the OMM. Proteins can also pass through the OMM via a protein import apparatus. Whereas, the inner mitochondrial membrane (IMM), made up of folded structures and invaginations known as cristae,[13] is much more selective as to what can enter the matrix. The IMM regulates the entry of numerous ions and biomolecules.[14] Due to the unique phospholipid-cardiolipin composition, the mitochondria exhibit high mitochondrial membrane potential[15, 16] ($\Delta\Psi_m$= -160 to -180 mV) which navigate selective transportation of ions and biomolecules across the membrane.[17-19] The IMM has various proteins and selective ion channels, which are involved in the electron transport and ATP synthesis.[20]



Figuure 1.1. Mitochondria Structure

Why the mitochondria?

Mitochondria play pivotal roles in almost every human and animal cell because they provide the majority of cellular energy in the form of ATP through the metabolism of glucose and pyruvate.[21] Within the matrix, the tricarboxylic acid (TCA) and glycolysis cycle reduce nicotinamide adenine dinucleotide (NAD) and flavin adenine dinucleotide (FAD) to NADH and $FADH_2$.[21, 22] These can provide electrons to the electron transport chain (ETC), which produces ATP. This critical role in energy production and metabolism makes mitochondria indispensible, so when it is not functioning properly, problems can arise leading to several diseases including, but not limited to, cancer, obesity, diabetes, and several neurodegenerative disorders.[12, 23-26]

Many neurological disorders such as Alzheimer's disease (AD), Parkinson's disease (PD), and Down syndrome are associated with mitochondrial dysfunction. Specifically, AD is a rapidly increasing epidemic in that ~18 million people worldwide were suffering from AD in the year 2000 alone according to the Delphi consensus study.[27] Dr. R.D. Terry was the first to link mitochondrial dysfunction to AD when he described the mitochondria in brain cells as unusually swollen, watery, and randomly dispersed in the cytoplasm.[28] Compared to healthy brains, the mitochondria are typically densely packed in neuronal cells. Since this discovery, it was observed that there is an involvement of an altered form of amyloid beta (Aβ) peptide aggregating within the mitchondria.[29] This altered form of Aβ was shown to be unusually unfolded and aggregated within the mitochondria.[30] It was proposed that this may be due to malfunctioning mitochondria and an increase in oxidative stress. This is supported by treatment with neuroblastoma cells with hydrogen peroxide (H_2O_2) (200 μM) which lead to an increased concentration of Aβ plaques and aggregates within the mitochondria.[31]

Obesity is a disease that is characterized by a constant imbalance between energy intake and expenditure resulting in the storage of fat.[32] The rapid increase of obesity has lead it to become the most significant contributor to ill health in the developed world.[32] Although, dieting can be effective to prevention and reversal of obesity, a recent poll suggested that more than 90% of individuals who lose weight will eventually gain some if not all of it back.[33] A potential solution to this is through the decoupling of mitochondria. The process of uncoupling essentially causes the ETC to become ineffective leading the cell to work harder to produce the energy needed. This essentially causes a rebalance of the energy intake and output leading to weight loss.[34]

Another disease associated with mitochondrial dysfunction is diabetes. Diabetes has become a worldwide pandemic in that it affects ~160 million individuals, and this number is expected to grow to 370 million individuals by 2030.[35] In general, diabetes is a result of the body's inability to regulate glucose levels with insulin. For type 2 diabetes, the central cause is due to mitochondrial dysfunction leading to increased glucose levels and decreased insulin production.[36] This may be due to type 2 diabetes patients having lower activity of mitochondrial oxidative enzymes.[37] Recently, it was shown using a mouse model that mitochondrial dysfunction can cause impaired insulin production.[38] It is well accepted that mitochondrial dysfunction can cause an increase in reactive oxygen species (ROS). This ROS can often times lead to an inhibition of glucose metabolizing enzymes.[39]

Dysfunctional mitochondria also play a crucial role in the development of cancer. Warburg was the first to demonstrate that even in an oxygen rich environment, cancer cells rely on glycolysis for energy.[40] According to Warburg, a defect in oxidative phosphorylation (OXPHOS) can cause the reliance on aerobic glycolysis in cancer cells. This has since been disproven due to the fact that several cell lines with functioning OXPHOS still rely on glycolysis. The idea of aerobic glycolysis provides cancer cells with several advantages such as growth in adverse microenvironments, generation of substrates for glycosylation reactions and supply of precursors for biosynthetic reactions. Moreover, these metabolism independent functions allow cancer cells to become resistant to apoptosis. This increased glycolytic dependency is for the most part attributable to mitochondrial defects and malfunctions. One of these malfunctions can be mutations in mitochondrial DNA (mtDNA).[26, 41] Unlike nuclear DNA, mtDNA lacks histones, which

makes it more susceptible to ROS and its repair capacity is lowered in comparison to nuclear DNA.[42, 43] It is possible that the highly oxidative stressed environment can lead to an increased rate of mtDNA mutations and a decreased expression of mtDNA-coded polypeptides.[42] Moreover, mtDNA mutations in cancer are considered to be homoplasmic meaning that every cell within a tumor will all have the same DNA mutation. This could in a sense, lead to an inefficient or non-functioning OXPHOS that would in turn drive the cancer cells to an increase in glycolysis.[44-46]



Figure 1.2. Diseases associated with mitochondria dysfunction

Mitochondria Acting Therapeutics

As mentioned above, mitochondrial dysfunction can be implicated as a cause for or a result of a variety of different diseases. It may be possible, however, to treat these

events by developing new therapeutics that can act on these defects for the disease in question. For neurodegenerative diseases, such as AD, the main idea is to target the increased ROS produced.

Curcumin is an aromatic compound that was first isolated from the plant known as turmeric in 1815.[47] Recently, it has been shown that its consumption in elderly people has been associated with greater cognitive functions.[48] As mentioned above, Aβ has been shown to generate a high concentration of ROS in AD patients. By decreasing ROS, they can ultimately limit oxidative damage. Therefore a natural antioxidant like curcumin has been investigated for the prevention and cure of AD.[49-51] Curcumin has been reported to protect PC12 neuroblastomas and human umbilical vein endothelial cells from Aβ related toxicity because of its strong antioxidant properties.[52] Moreover, pretreatment of PC12 cells with 10 μg/mL curcumin reduced Aβ and induced an increase in antioxidant enzymes.[53]

Uncoupling mitochondria for the treatment of obesity has been studied for many years using the potent uncoupler, 2,4-dinitrophenol (2,4-DNP).[34, 54] 2,4-DNP is a lipid soluble weak acid that acts as a protonophore in that it can cross the mitochondrial membrane protonated, lose its proton, and return to the cytosol as an anion. There it can reprotonate and repeat the cycle. By doing so, basal proton conductance is increased and the mitochondria become decoupled. The effect of 2,4-DNP and its derivatives was first observed in 1885.[55] However, due to a limited therapeutic window and negative side effects, its use has since been abandoned.

Alpha-tocopherol (α-TOS) succinate is a redox-inactive vitamin E derivative that has exhibited anti-cancer properties through the induction of apoptosis by generating

ROS.[56-58] The apoptosis is initiated through the blocking of anti-apoptotic proteins B-cell lymphoma 2 (Bcl-2) and Bcl-xl by disrupting their binding to the Bak BH3 peptide.[59] The mitochondria were recently discovered as the molecular target in cancer.[60] Dong *et al.* discovered that α-TOS is a competitive inhibitor of the ubiquinone binding sites in Complex II which thus inhibit succinate dehydrogenase (SDH) activity in the electron transport chain.[60]

Hexokinase (HK) is an enzyme that plays a pivotal role in the ATP generation through glycolysis.[61] Mitochondrial bound HKII also plays an important role in stabilization of mitochondria and suppression of apoptotic death pathways initiated by the mitochondria.[62, 63] For that reason, molecules that inhibit HK have been found to suppress cancer growth.[64] 3-Bromopyruvate (3-BP) is an alkylating agent that has been shown to covalently bind to HK.[65] 3-BP causes cancer cell death through the rapid depletion of ATP and suppresses tumor growth in several animal models.[63, 65]

The TCA cycle, or the Kreb's cycle, is one of the main sources of electrons in the ETC. In cancer, its efficacy is regulated by pyruvate dehydrogenase kinase (PDK) and its ability to transfer pyruvate into the TCA cycle.[66] Due to the fact that the ETC is a main source of ATP, it is a target for many mitochondria acting chemotherapeutics. Dichloroacetate (DCA) is a pyruvate analog that binds to the N-terminal region of PDK.[67] This causes an activation of PDK and an increase in the intra-mitochondrial pyruvate. DCA also increases glucose oxidation and depolarizes the mitochondria which returns the membrane potential to that of non-cancerous cells while not affecting healthy cells.[68] Studies of safety and efficacy of DCA for the treatment of brain cancer are currently in phase II clinical trials.[69, 70]

Although these are all excellent examples of mitochondrial acting therapeutics, much research needs to be done to further improve on their efficacy and negative side effects. Many times, it is not the drug that is not potent enough; it merely cannot reach its target organelle. Most examples presented in this section have shown to be efficient at acting on the mitochondria. However, they would be more efficient if they were further functionalized with mitochondria targeting ligands. There has been an influx of research articles in recent years that take advantage of the uniqueness of the mitochondria membrane.

Mitochondria-targeted Small molecules

Many molecules that enter and disrupt mitochondrial function take advantage of the hydrophobic nature of the membrane. Carbonyl cyanide *m*-chlorophenyl hydrazine (CCCP) has been shown to diffuse across the membrane therefore disrupting the electrochemical potential of the membrane. Under the same purpose, it has been shown that lipophilic cations have the ability to cross both the inner and outer membranes with ease.[71, 72] The positive charge attracts the molecules to the mitochondria while the lipophilic nature allows them to easily pass through the hydrophobic barrier of the lipid bilayer. This was first demonstrated by Skulachev in 1969.[73] Fluorescent lipophilic cations, such as [9-(2-carboxyphenyl)-6-diethylamino-3-xantheylidene]-diethylammonium chloride (rhodamine B) and 5,5',6,6'-tetrachloro-1,1',3,3'-tetraethylbenzimidazoyl-carbocyanine iodide (JC-1), are routinely used to image the mitochondria by fluorescence microscopy.[74-76] At the molecular level, these molecules are able to cross the double membrane of the mitochondria with high efficiency due to

the fact that the positive charge is shielded or delocalized over a large surface area. Mathematically, the accumulation is driven by the Nernst equation:

$$Membrane\ potential\ (mV) = 61.5log_{10}\left\{\frac{[cation]_{in}}{[cation]_{out}}\right\}$$

According to the equation above, for every 61.5 mV increase in membrane potential a ten-fold increase in cation accumulation is witnessed. This ultimately leads to around 100-1000 times greater concentration within the mitochondrial matrix than in the cytoplasm. Furthermore, this equation shows that this not only will allow for easy internalization within the mitochondria but also allows for overall increases in cellular uptake for lipophilic cations.

To expand on this principle, recently, researchers have been using triphenylphosphonium (TPP) cations for mitochondrial targeting. TPP allows for an increase in lipophilicity as well a more delocalized charge compared to a quaternary amine. The beauty of TPP is that functional groups and therapeutics can be merely attached to TPP moieties with relative ease. This allows for drugs to be carried across the matrix and released. The phenyl rings of TPP can also be modified to carry therapeutics to the mitochondria. There are numerous examples to date of the use of such moieties being attached to therapeutics showing a significant enhancement of efficacy.[77] Mike Murphy's lab demonstrated this well by attaching TPP to coenzyme Q10 (CoQ10).[78] They also were able to attach TPP to a vitamin E derivative ($MitoE_2$).[78, 79] Both CoQ10 and vitamin E are antioxidants, so by attaching TPP it allows them to be delivered to the mitochondrial matrix. This allowed the reduction of and further protection from ROS in cells that had been damaged.

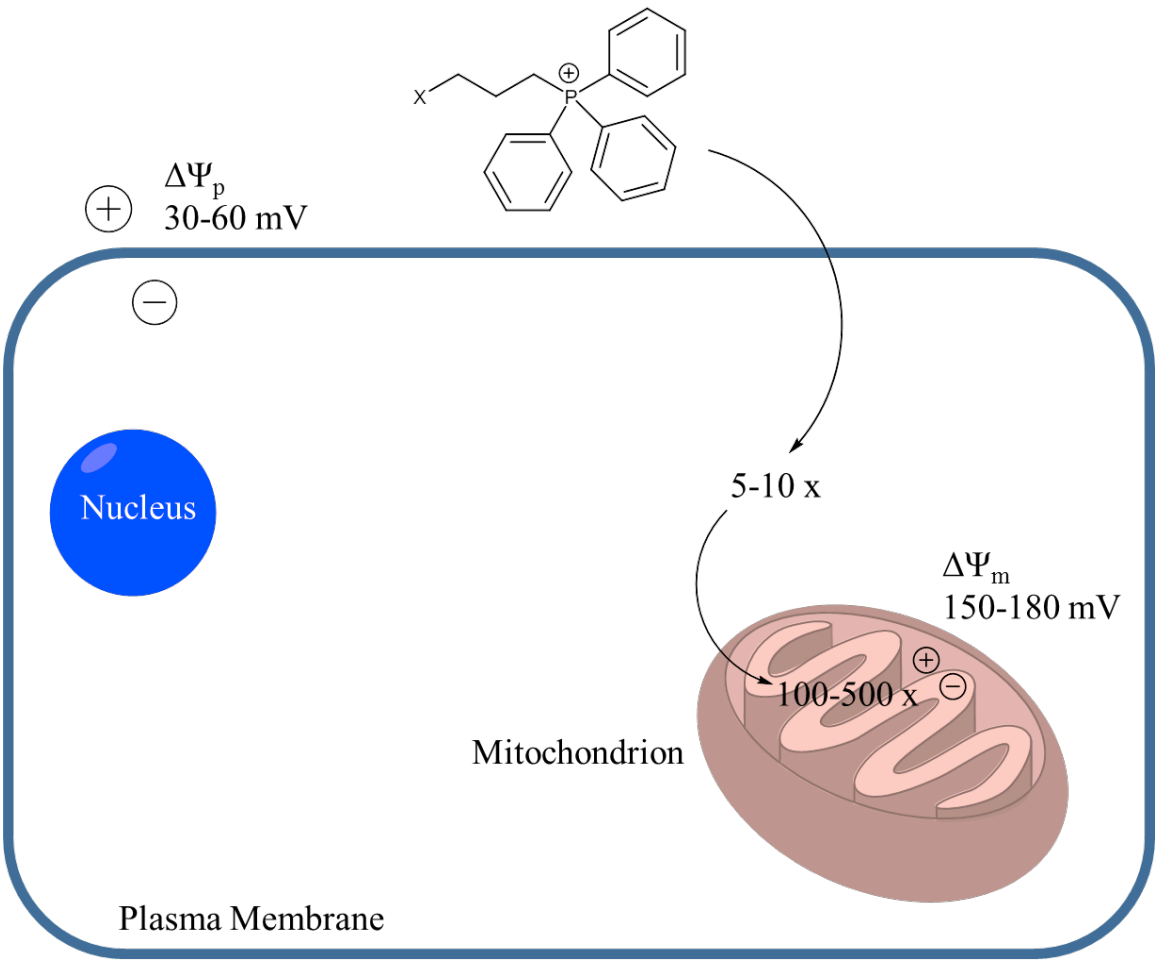


Figure 1.3. Mitochondria-targeting based on lipophilic cations

A different strategy to target the mitochondria is through the use of protein-nucleic acids. Schatz *et al*. showed that mitochondria are capable of importing single or double stranded DNA that was covalently linked to mitochondrial precursor proteins. They were able to show the incorporation of ssDNA and dsDNA into the mitochondria of isolated cells *in vitro*[80].

There also have been several cell-permeable mitochondria targeted peptide sequences covalently attached to antioxidants. One class of these is Szeto-Schiller (SS) peptides. The SS tetrapeptides are a series of mitochondria-targeted antioxidant peptides and typically have similar structures, alternating aromatic and basic residues.

Specifically, SS-02 and SS-31 have been shown to scavenge ROS produced by H_2O_2[81]. The mitochondria targeting properties arise from the basic (amine) units while the ability to cross into the matrix comes from the lipophilicity provided by the aromatic units. Despite having a net positive charge at physiological pH, the peptide crosses into the cytoplasm in an energy dependent fashion, which is opposite to the uptake mechanism of TPP conjugated drugs. Fluorescent analogues of these peptides show similar mitochondria targeting to that of MitoTracker dyes by confocal microscope.[82]

Although mitochondria targeted small molecule therapeutics have shown a vast improvement, there are still significant drawbacks that make them not ideal for the treatment of diseases. For one, many show very poor water-solubility. This leads to less than desirable pharmacokinetic properties. In some cases, drugs begin to lose their efficacy with the attachment of new moieties due to the loss of certain necessary functional groups.[83]

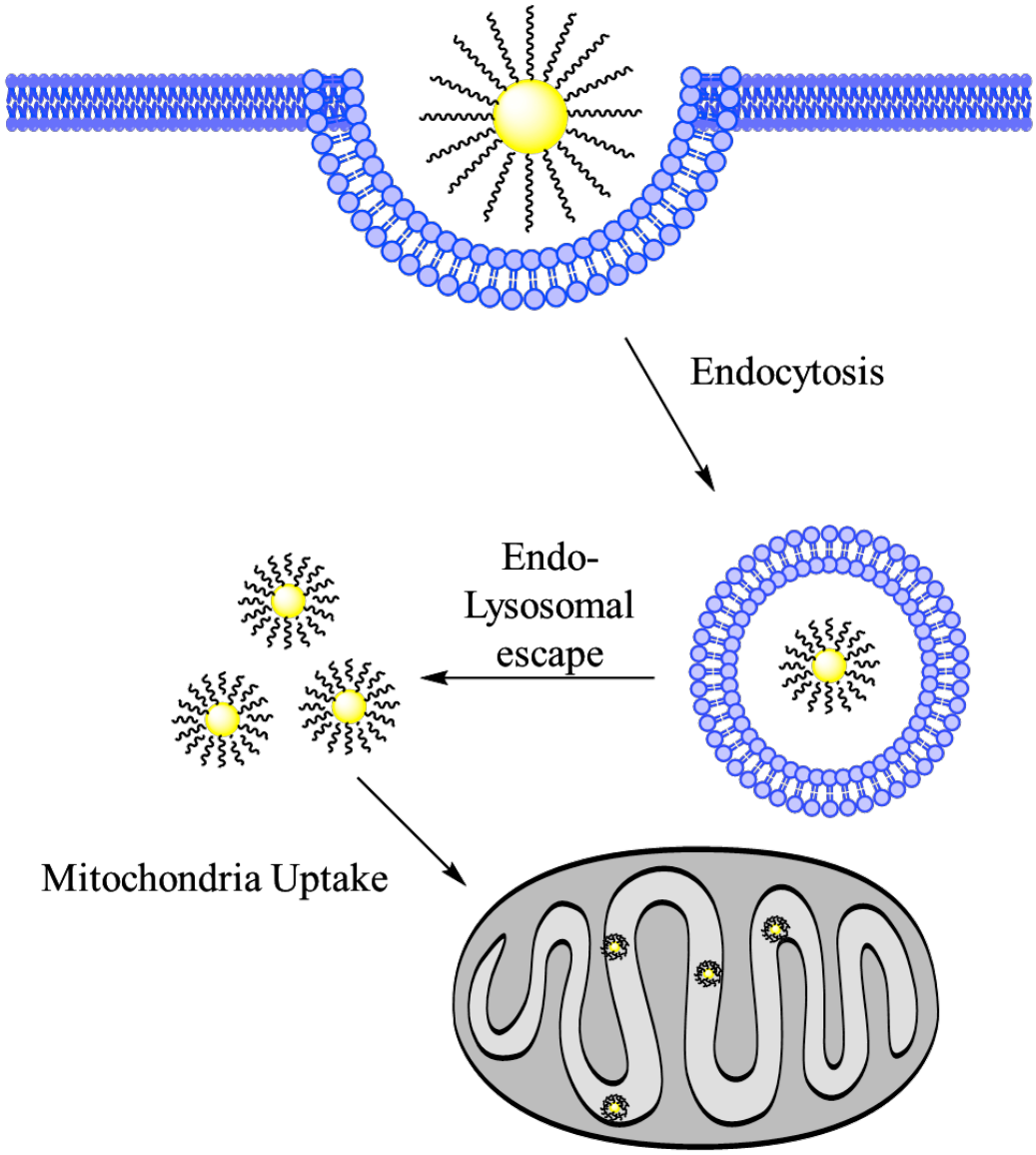


Figure 1.4. Mitchondria-targeting based on nanoformulations

Nanoparticles in Drug Delivery

According to the National Nanotechnology Initiative, nanotechnology is "science, engineering, and technology conducted at the nanoscale, which is about 1 to 100 nanometers." Some scientists have refuted this defined size, seeing the impact of larger-sized (i.e. several hundred nanometers) nanotechnological developments that exhibited similar properties as those sized at 100 nm. However, this quarrel has not prevented the

development of nanocarriers from being pursued. A "nanocarrier" is a term used to describe a nano-sized molecule with the ability to transport another molecule with it. Nanocarrier delivery systems have been essential in the progress of nanomedicine, allowing drugs and other treatment options to be delivered to places in the body that were previously unreachable. Although a small size is important within the realm of nanomedicine, it is more critical for the nanocarrier to be able to accurately and efficiently deliver an adequate drug dosage to the intended site. Hence, the use of nanoparticles (NPs) for drug delivery has been studied and expanded because of the ease in surface modification, drug loading, targeting abilities, and utilization of biodegradable materials.[84]

Among the various nanotechnology-based delivery vehicles, liposomes, polymer-drug conjugates, and polymeric NPs are the most accepted platforms for diagnosis and therapy of different diseases.[85] Extensive research exploited these platforms based on their abilities to improve drug efficacy over free payloads through ameliorated drug encapsulation, increased circulation half-life, sustained and activated payload release. Enhanced permeability and retention (EPR) effect[86, 87] is a passive targeting approach used by most of the liposomal and polymeric NPs to accumulate preferentially at the active site of the targeted disease, whereas active targeting can be achieved through surface modification of the NPs with specific targeting ligands.[88] A variety of therapeutics based on liposomes, polymer-drug conjugates, and polymeric NPs which are either clinically approved or have entered clinical trials are shown in the tables 1.1 and 1.2 below.[89]

Table 1.1. NP-Based therapeutics that follow passive targeting[89]

Trade name	NP Type	Company	Disease	Payload	Current Status / Clinical Trial No.
CRLX101	Cyclodextrin-based polymer	Cerulean Pharma Inc.	Solid tumor of various types including pancreatic cancer, ovarian cancer, and non small cell lung cancer	Camptothecin	Phase II/NCT01380769
Doxil®	PEGylated liposome	Janssen Pharmaceuti-cals	AIDS-related Kaposi's sarcoma, metastatic ovarian cancer, and multiple mye-loma	Doxorubicin	Approved
Genexol-PM	Polymer	Samyang Corporation	Breast cancer	Paclitaxel	Phase III/NCT00876486
CPX-1	Liposome	Celator Pharmaceuticals	Advanced solid tumors in colorectal cancer	Irinotecan- Floxu-ridine	Phase II/NCT00361842
DaunoXome	Liposome	Galen	AIDS-related Kaposi's sarcoma	Daunorubicin	Approved
Myocet	Non-PEGylated liposome	Enzon Pharmaceuticals	Advanced metastatic breast cancer, ovarian cancer	Doxorubicin	Approved in Europe and Canada
LE-SN38	Liposome	NeoPharm	Metastatic colorectal cancer	SN-38	Phase III in USA/NCT00294996
Onco TCS	Liposome	INEX and ENZON	Non-Hodgkin's lymphoma	Vincristine	Approved
SPI-77	Liposome	SEQUUS Pharmaceuticals	Ovarian cancer	Cisplatin	Phase II/NCT00004083
Abraxane	Albumin	Celgene	Metastatic breast cancer	Paclitaxel	Approved
NC6004	Micelle	NanoCarrier	Pancreatic cancer	Cisplatin	Phase I/II /NCT00910741
NK105	Micelle	Nippon Kayaku Co, Ltd.	Breast cancer	Paclitaxel	Phase III/NCT01644890
NK012	Polymer Micelle	Nippon Kayaku Co, Ltd.	Solid tumors, Breast cancer	SN-38	Phase II/NCT00951054

Table 1.2. Targeted-NP-Based Therapeutics that follow active targeting[89]

Trade name	NP Type	Company	Targeting Ligand	Disease	Payload	Current Status	Clinical Trial No.
SGT-53	Liposome	SynerGene Therapeutics, Inc.	Transferrin single-chain antibody fragment	Advanced solid tumors	Gene 53	Phase Ib	NCT00470613
MBP-426	Liposome	Mebiopharm	Transferrin	Solid tumors and esophagus disorders	Oxaliplatin	Phase II	NCT00355888, NCT00964080
SEL-068	Polymeric	Selecta Biosciences	Small molecule	Smoking cessation vaccine	Nicotine antigen T-helper cell peptide, TLR agonist	Phase I	NCT01478893
CALAA-01	Polymeric	Calando	Human Transferrin	Solid tumors	siRNA	Phase Ib	NCT00689065
BIND-014	Polymeric	Bind Biosciences	PSMA peptide	Metastatic cancer	Docetaxel	Phase I	NCT01300533
SGT-94	Liposome	SynerGene Therapeutics, Inc	Anti-transferrin receptor single chain antibody fragment	Solid tumors	RB94 gene	Phase I	NCT01517464

Mitochondria targeted micelles

In the recent past, researchers have investigated the use of lipophilic dequalinium (DQA) cation for the construction of mitochondria targeting liposomal mimic assemblies known as DQAsomes to deliver drugs and genomic materials.[90] These appropriately modified DQAsomes have been used to deliver the plasmid DNA (pDNA) in the form of 'DQAplexes;' a hybrid structure comprised of DQAsome and DNA, selectively to the mitochondria through exhibiting endosomal escape. The utility of DQAsome was extended to deliver the chemotherapeutic drug selectively to the mitochondria. Taxol scaffold derived drug paclitaxel was entrappe in the DQAsomes nanostructures to induce the apoptosis followed by cell death. However, the lack of exact mechanism and versatility of these formulations limits their use as potential drug delivery systems.

Mitochondria targeted dendrimers

Dendrimers are radially emerging hyperbranched structures ranging in size from 2-10 nm.[91] They consist of polymers with regular patterns and repeat units. The core, extent of branching, ease of modification, and size control make dendrimers attractive for drug delivery.[92] The term "dendrimer" is derived from the greek words *dendra* for tree and *meros* for part.[93] Dendrimers can be synthesized from synthetic or natural elements such as sugars or amino acids.[94] They are easily functionalized with tunable and desirable pharmacokinetics and biodistribution. Recently, a dendrimer scaffold was used to deliver potential chemotherapeutic drugs to the mitochondria through modifying its surface with lipohilic cationic moieties, such as rhodamine and TPP cation. Poly(amidoamine) (PAMAM) dendrimer has been extensively used as a scaffold to deliver drugs and genomic materials owing to the presence of amine structures.

Torchilin and coworkers[95] have developed PAMAM based G(5)-D-Ac-TPP (generation 5 dendrimer, NH_2 were acetylated for non-specific binding and further coupled with TPP) mitochondria-targeted drug delivery nanocarrier. These nanocarriers were further labeled with fluorescent dye to monitor the colocalization of the nanocarriers in the mitochondria. Cytotoxicity of these carriers was found to be significantly less which supports future utility of these materials to take therapeutic payload to the mitochondria. However, further investigations were needed to prove the above hypothesis.

A similar approach[96] has been used to deliver enhanced green fluorescent protein (EGFP) and luciferase gene to the HeLa and COS-7 cells through mitochondria targeting TPP bearing PAMAM dendrimers (G5-TPP). These gene transfection dendrimer materials were found to be non-toxic during transfection conditions. The transfection efficacy of G5-TPP was demonstrated to be similar to that of commercial available agents Lipofactamine-2000 and even higher as compared to dendrimer-based gene transfection reagent-SuperFect and unmodified G5 dendrimer. G5-TPP dendrimers scaffolds exhibit efficient DNA packing/unpacking, endosomal escape and finally target the mitochondria. TPP-decorated G5 dendrimers can be used as potential mitochondrial targeted drug and genomic delivery systems.

Theodossiou, et al.,[97] recently developed the lipophilic decyl-TPP coated poly(ethylene imine) (PEI-TPP) hyperbranched polymer based nanoassemblies to deliver encapsulated doxorubicin (DOX), a potent topoisomerase II inhibitor, to the mitochondria. Above-mentioned nano-formulation, viz., PEI-TPP-DOX mainly localized in the mitochondria of the human prostate carcinoma DU145 cell as determined by the

inherent fluorescence of the DOX. The cytocidal nature of the PEI-TPP-DOX was found to be more necrotic type as compared to the slow apoptotic type in case of free DOX.

Liposomes based mitochondria targeted nanoparticles

Among the numerous types of nano-carriers, liposomes have emerged as a promising delivery system *in vitro* and *in vivo*. Since they were first developed in the early 1980s, several formulations have been made commercially or are in the advanced stage of clinical trials. Liposomes are lipid derived biodegradable nanomaterials which utilize their unique structural features to entrap both hydrophobic and hydrophilic drugs. Liposomes are nano- or micro-particles which are essentially bilayer vesicles that have an aqueous core surrounded by a lipid bilayer that can be anywhere from 50 to 5,000 nm in diameter. At the molecular level, a liposome is composed of an amphiphilic lipid that upon hydration with aqueous media self-assembles into the nano-carrier. Although, natural liposomes have the ability to fuse with cell membranes effectively releasing the cargo in the cytoplasm, this is not the case for synthetic lipids.[98] Usually, synthetic lipids are taken up through endocytotic pathways which ultimately lead to their demise due to the fact that many times they are transported out of the cell.[99] Appropriately surface functionalized liposomes with targeted moieties can provide potent therapeutic options for site directed drug delivery.[100] A way to combat this is to have organelle-specific surface attached targeting moieties.[101] which allow the liposome to escape the endosomes and travel to through the cytoplasm to its final destination.

Boddapati and coworkers[102, 103] developed a system that has the ability to undergo edosomal escape and target the mitochondria. To do this, using stearyltriphenylphosphonium (STTP) bromide, a liposome was synthesized via film

rehydration followed by ultrasonication. By encapsulating a rhodamine-PE dye, researchers were able to track the liposomes *in vitro* in BT-20 human breast cancer cells. They found that many of the particles, after a one-hour incubation, were colocalized with mitochondria with the use of a Mitotracker red dye. However, the downside to this system is the size and polydispersity of the liposomes. A smaller, more monodispersed formulation with a longer incubation period may have proven to further colocalize.

Murthy and coworkers[104] utilized the mitochondria targeting characteristic of STTP along with selectively targeting cancer cells. The doxorubicin (DOX) loaded liposomes mitocancerotropic (FA-MTLs) were developed through surface modification with dual targeting motifs, folic acid (FA) for cancer cell targeting and TPP cations for mitochondria targeting. These dual targeting motifs were found to be more potent than the controls through exhibiting efficient delivery of DOX to the mitochondria.

In 2013, D'Souza and coworkers[105] encapsulated paclitaxel in STTP modified liposomes for its delivery to the mitochondria. To further mimic the tumor environment, spheroids of paclitaxel resistant Ovcar-3 cancer cells were devised and cytotoxicity of the STPP+Pxt-liposomes was evaluated. It was found that by targeting paclitaxel to the mitochondria, there was a significant reduction in inhibitory concentration-50 (IC_{50}) values and shows greater drug distributions in spheroids. However, the cell death process is caspase independent and it turns out that the major contribution of cytotoxicity is due to the cell-specific toxicity of STPP.

Wang et al[57] conjugated DQA at the PEG terminal of DSPE-PEG to get DQA-PEG2000-DSPE as mitochondria targeting phospholipid motif. Liposomes constructed using this targeting motif are able to deliver resveratrol to the mitochondria and to induce

apoptosis in cisplatin resistance cancer cells. In addition, mitochondria targeting resveratrol liposomes exhibit enhanced therapeutic efficacy of co-treated vinorelbine liposomes on the cisplatin resistance A549/cDDP cell lines.

Torchilin and coworkers[106] modified the 1,2-distrearoyl-*sn*-glycero-3-phosphoethanolamine-*N*-[amino(polyethylene glycol)], or DSPE-PEG, with TPP to incorporate in liposomes for targeting mitochondria. Upon self-assembly, the liposomes formed were of similar size to the STTP version, however, advantageously the empty liposomes were found to be less toxic. The liposomes, when loaded with paclitaxel, were also found to have similar mitochondrial uptake properties as well as cytotoxicity profiles. The system was also tested *in vivo* in a 4T1 murine mammary carcinoma xenograft. After 26 days, the average tumor volumes were ~1/3rd the size of the free paclitaxel treated groups.

In similar way Lu and coworkers[107] synthesized D-α-tocopheryl succinate polyethylene glycol 1000 succinate-triphenylphosphonium conjugate (TPGS1000-TPP) as a targeting ligand for liposomal delivery of paclitaxel. The TPGS1000-TPP modified liposomes exhibit long circulation time in blood with rapid elimination by RES system. The incorporation of TPP and TPGS1000 provides efficient delivery of paclitaxel in the mitochondria of drug-resistant cancer cells and induces apoptosis by releasing cytochrome C, and initiating a cascade of caspases -9 and -3 reactions.

Theodossiou and coworkers[108] used TPP conjugated biodegradable oligo(L-lysine) to deliver D-Luciferin, a substrate of the firefly enzyme Luciferase, to the mitochondria Delivery of D-Luciferase was aimed to provide bioluminescence activated destruction (BLADe) to cancer cells and in situ, measurement of ATP changes in the

mitochondria. The observed intensity of chemiluminiscence was less as compared to that of free D-Luciferin and this only demonstrates a proof of example for the above properties.

Mitochondria-targeted Polymeric NPs

Polymeric NPs are generally synthesized from biocompatible and biodegradable polymers.[109] When composed of hydrophobic and hydrophilic blocks, these polymers can be used to encapsulate both water-soluble and water-insoluble therapeutics, through emulsion or nanoprecipitation, respectively. Polymeric NPs have the ability to overcome many of the drawbacks associated with liposomes in that they possess higher stability and a more controlled release.[110,111] The hydrophobic block is generally composed of a biocompatible and biodegradable polyester such as poly(lactic acid) (PLA), poly(glycolic acid) (PGA), their copolymer poly(lactic-*co*-glycolic acid) (PLGA), or polycaprolactone (PCL). The most widely used hydrophilic block is polyethylene glycol (PEG) in that it is FDA approved and biocompatible. While the hydrophobic blocks typically provide added stability, PEG allows for longer retention time within the body. PEGylation also has the unique characteristic of allowing for further functionalization for the attachment of drugs or targeting moieties. These desirable qualities along with the ability to encapsulate numerous drugs efficiently while keeping the size at a minimum makes polymeric NPs a prime candidate for mitochondria targeting.

One of the first examples of this came from the Kakkar group[112] in 2011. They were able to modify the linker between PCL-PEG block copolymer with TPP. This allowed them to take into account the properties of a typical PCL-PEG NP while introducing a mitochondria targeting ligand. They were able to then encapsulate and

direct CoQ10 to the mitochondria exerting beneficial antioxidant stress. Confocal imaging showed a small amout of colocalization with mitotracker red. However, the small amount of colocalization could be attributed to the fact that the mitochondria targeting ligand is being somewhat masked due to the fact that it is at the conjuncture between the hydrophobic and hydrophilic blocks. Although, NMR analysis of the NPs showed presence of aromatic peaks from TPP, one has to wonder if some of the charge is being buried in the hydrophobic core, which would limit the system's potential.

Metal Nanoparticles

Metal-based NPs provide unique characteristics and advantages to other types of nanoparticles in the field of nanomedicine.[113] They often times are composed of gold (AuNPs), iron oxide (IONPs), platinum oxide (PtONPs), and titanium dioxide (TiO_2NPs).[114] These NPs offer a high surface area to volume ratio, facile synthesis, and ease of surface functionalization. They also present highly tunable optical properties, which can be easily tuned to their desirable wavelengths according to their shape, size (1 to 100 nm), and composition. The shape can vary from nanoparticles, nanoshells, and nanorods. Any of these can be easily functionalized to allow attachment of biocompatible polymers to increase *in vivo* circulation times, cell-specific targeting peptides, and antibodies, and organelle targeting moieties.

AuNPs are one of the most popular metal based NPs in that they can be synthesized easily with a variety of different sizes (from <10 nm to 100 nm) while remaining relatively monodispersed.[115] There have been several different methods published to produce AuNPs.[116-119] However, most involve a gold salt, such as gold hydrochlorate, and a reducing agent. Differing the stirring speed, reducing agent, and

stabilizing reagents can help to optimize the size and stability. Another intriguing property is the ability to control their overall geometry. Several different geometries have been reported from nanorods, core-shell nanoparticles, nanostars, and nanocubes.[120] Recently, it was shown that size plays the utmost importance when it comes to mitochondrial entry of gold nanoparticles.[121] Without targeting ligands, only AuNPs of a diameter 3 nm or less were able to cross into the matrix via VDAC. To bypass this barrier, Wang et al. were able to synthesize a mitochondria-targeted gold nanorod formulation that was able to induce apoptosis in cancer cells but leave healthy bronchial epithelial and stem cells unharmed.[122] The serum protein-coated showed a remarkable ability to escape A549 lung cancer cell lysosomes. However, the particles were not able to escape lysosomes of healthy cells.

The use of small molecule and protein-based fluorophores has continued to have its limitations in their use in molecular and cellular biology as well as molecular diagnostics.[123, 124] These limitations include narrow excitation wavelengths, broad emission spectra, spectral cross-talk and poor water-solubility and pharmacokinetic properties makes quantification in relative amounts difficult.[125] The development of semiconducting nanocrystals, or quantum dots, has shown vast improvements by introducing fluorophores with spectrally resolved emissions and narrow, symmetric emissions that can be excited at single wavelengths.[124, 126] The increased water solubility over conventional organic dyes have been widely used in biological applications in recent years.[127-130] Yamamoto and co-workers took this to the next level by attaching a mitochondrial targeted peptide sequence to the surface of a quantum dot. These quantum dots exhibited strong mitochondrial localization in living cells.[131] A similar study brought

this technology to the next level by attaching a pro-apoptotic trigger. After 18 hours incubation with HeLa cells, severe morphological changes were observed indicating efficient apoptosis.[132]

Objectives and Outline of this Dissertation

Although there has been an influx of literature in recent years regarding mitochondria-targeted small molecules and NPs, mitochondria targeting is still in its infancy. The bulk of this dissertation will describe the research efforts made to improve upon an already expanding field. The objectives of this dissertation are as followed: (1) to design novel, new mitochondria targeted NPs and small molecules and (2) evaluate their efficacy in a variety of diseases by *in vitro* and *in vivo* methods. This dissertation is organized in eight chapters with three appendices.

Chapter 2 describes the development of a mitochondria-targeted, biodegradable, and biocompatible polymeric drug delivery vehicle. A library of NPs was synthesized by a nanoprecipitation technique. A quantum dot (QD) was used to track the NPs *in vitro.* Their overall mitochondria targeting efficiency was analyzed by fluorescence microscopy and inductively coupled plasma mass spectrometry (ICP-MS). As a proof of concept, the NPs were loaded with a variety of different mitochondria-acting therapeutics. Their efficacy was tested in cancer, obesity, and AD.

Chapter 3 investigates the use of the polymeric delivery vehicle described in Chapter 2 in photodynamic therapy (PDT). The mitochondria targeted and non-targeted NPs were loaded with a photosensitizer, zinc phthalocyanine. The efficiency at inducing apoptosis in breast and cervical cancer was explored, as well as the delivery vehicle's ability to induce a potent immune response.

Chapter 4 describes the development of a novel, new cisplatin produg and its ability to overcome cancer resistance. Cisplatin was functionalized with a mitochondria-targeting moiety via strain promoted azide alkyne click chemistry. The free drug as well as a NP formulation was used to redirect cisplatin to the mitochondria to attack mitochondrial DNA. Its cytotoxicity was tested in prostate, brain, and cisplatin-resistant ovarian cancer *in vitro*. The biodistribution and pharmacokinetic properties were also tested *in vivo*.

Chapter 5 discusses the use of the same mitochondria-targeted polymeric delivery vehicle in its use in treating the symptoms of traumatic brain injury. The NPs were loaded with an antioxidant and an anti-inflammatory agent in order to show their efficiency at reducing inflammation and oxidative stress in neural stem cells. As a proof-of-concept, the NPs were tracked *in vivo* to determine their ability to cross the blood-brain-barrier (BBB) in healthy and traumatic brain injury (TBI) induced pig models. The NPs showed that they were remarkably able to cross the blood-brain-barrier with high efficiency.

Chapter 6 shows the development of a synthetic, mitochondria-targeted, high-density lipoprotein mimicking NP. The NP was investigated for its ability to detect apoptosis in macrophages. It also was tested for its ability to bind to free cholesterol using a fluorescent 22-(*N*-(7-nitrobenz-2-oxa-1,3-diazol-4-yl)amino)-23,24-bisnor-5-Cholen-3β-Ol. The system proved to be efficient at lowering overall cholesterol and triglyceride content *in vivo* in a rat model.

Chapter 7 describes the development of a mitochondria-targeted AuNP that is used for combined chemo- and photothermal therapy in prostate cancer. The AuNPs were coated with a biocompatible PEG unit that can be easily functionalized with 3-BP, a

mitochondria-acting chemotherapeutic agent. By targeting to the mitochondria, this system showed markedly enhanced ability to inhibit glycolysis in prostate cancer. It also showed the ability to release 3-BP while also showing enhanced cytotoxic effects upon laser irradiation.

Chapter 8 describes the development of a mitochondria-targeted prodrug of the mitochondrial kinase inhibitor, DCA. The prodrug, named Mito-DCA, was shown to significantly reduce lactic acid production in cancer cells, and not normal cells. By targeting the mitochondria, Mito-DCA was able to not only inhibit cancer cell growth, but also the ability to induce a potent immune response.

Finally, chapter 9 summarizes the work performed from these different projects and discusses the goals of future studies.

Appendix I describes the synthesis and biological activity of a hybrid immune boosting nanoparticle system used in photodynamic therapy. Zinc phthalocyanine was encapsulated in a biodegradable and biocompatible PLGA-PEG-NH_2 nanoparticle. The nanoparticle was then coated with a immune boosting gold nanoparticle for enhanced anti-tumor immunity. The hybrid nanoparticle system showed enhanced cytotoxicity and dendritic cell activation.

Appendix II decribes the synthesis of a unique nanoparticle for enhanced treatment with DZNep and gemcitabine. After many *in vitro* tests, it was shown that priming pancreatic cancer cells with DZNep before treatment with gemcitabine proved to have enhanced cytotoxic effects. A unique nanoparticle formulation was then employed having controlled release profiles of DZNep and gemcitabine.

Appendix III describes the use of a novel, new prodrug of cisplatin and aspirin, called Platin-*A*. This prodrug showed similar cytotoxic effects to cisplatin in prostate cancer but also had the remarkable ability to induce a potent anti-inflammatory response.

References:

1. Vander Heiden MG, L. J., Swanson KD, Sharfi H, Heffron GJ, Evidence for an alternative glycolytic pathway in rapidly proliferating cells. *Science* **2010,** *329*, 1492-1499.
2. Michelakis, P. D. a. E. D., Mitochondria in Vascular Health and Disease. *Annu. Rev. Physiol.* **2013,** *75*, 95-126.
3. Gray, M. W., Mitochondrial evolution. *Cold Spring Harb. Perspect. Biol.* **2012,** *4*.
4. MR, D., Contributions of mitochondria to animal physiology: from homeostatic sensor to calcium signalling and cell death. *J. Physiol.* **1999,** *516*, 1-17.
5. Zamzami N, K. G., The mitochondrion in apoptosis: how Pandora's box opens. *Nat. Rev. Mol. Cell. Biol.* **2001,** *2*, 67-71.
6. GM., C., *The Cell: A Molecular Approach*. 2nd Edition ed.; Sinauer Associates: Sunderland (MA), 2000.
7. Sherratt, H. S., Mitochondria: structure and function. *Rev. Neurol. (Paris)* **1991,** *147*, 417-430.
8. Picard, M.; Taivassalo, T.; Gouspillou, G.; Hepple, R. T., Mitochondria: isolation, structure and function. *J. Physiol.* **2011,** *589*, 4413-4421.
9. Sjöstrand, F. S., The Ultrastructure of Cells as Revealed by the Electron Microscope. *Int. Rev. Cytol.* **1956,** *5*, 455-533.
10. Palade, G. E., The fine structure of mitochondria. *Anat. Rec.* **1952,** *114*, 427-451.

11. Mathupala, S. P.; Ko, Y. H.; Pedersen, P. L., Hexokinase II: Cancer's double-edged sword acting as both facilitator and gatekeeper of malignancy when bound to mitochondria. *Oncogene* **2006,** *25*, 4777-4786.

12. Yamada, Y.; Harashima, H., Mitochondrial drug delivery systems for macromolecule and their therapeutic application to mitochondrial diseases. *Adv. Drug Delivery Rev.* **2008,** *60*, 1439-1462.

13. John, G. B.; Shang, Y.; Li, L.; Renken, C.; Mannella, C. A.; Selker, J. M.; Rangell, L.; Bennett, M. J.; Zha, J., The mitochondrial inner membrane protein mitofilin controls cristae morphology. *Mol. Biol. Cell* **2005,** *16*, 1543-1554.

14. Crompton, M., The mitochondrial permeability transition pore and its role in cell death. *Biochem. J.* **1999,** *341*, 233-249.

15. Gottlieb, E.; Armour, S. M.; Harris, M. H.; Thompson, C. B., Mitochondrial membrane potential regulates matrix configuration and cytochrome c release during apoptosis. *Cell Death Differ.* **2003,** *10*, 709-717.

16. Chen, L. B., Mitochondrial Membrane Potential in Living Cells. *Annu. Rev. Cell Biol.* **1988,** *4*, 155-181.

17. Indran, I. R.; Tufo, G.; Pervaiz, S.; Brenner, C., Recent advances in apoptosis, mitochondria and drug resistance in cancer cells. *BBA-Bioenergetics* **2011,** *1807*, 735-745.

18. Ly, J. D.; Grubb, D. R.; Lawen, A., The mitochondrial membrane potential (deltapsi(m)) in apoptosis; an update. *Apoptosis* **2003,** *8*, 115-128.

19. Koya, R. C.; Fujita, H.; Shimizu, S.; Ohtsu, M.; Takimoto, M.; Tsujimoto, Y.; Kuzumaki, N., Gelsolin Inhibits Apoptosis by Blocking Mitochondrial Membrane

Potential Loss and Cytochrome c Release. *J. Biol. Chem.* **2000,** *275*, 15343-15349.

20. Alberts B, J. A., Lewis J, et al., *Molecular Biology of the Cell. 4th edition*. Garland Science: New York, 2002.

21. Pathania, D.; Millard, M.; Neamati, N., Opportunities in discovery and delivery of anticancer drugs targeting mitochondria and cancer cell metabolism. *Adv Drug Deliv Rev* **2009,** *61*, 1250-1275.

22. DeBerardinis, R. J.; Lum, J. J.; Hatzivassiliou, G.; Thompson, C. B., The biology of cancer: metabolic reprogramming fuels cell growth and proliferation. *Cell Metab.* **2008,** *7*, 11-20.

23. Fulda, S.; Galluzzi, L.; Kroemer, G., Targeting mitochondria for cancer therapy. *Nat. Rev. Drug Discov.* **2010,** *9*, 447-464.

24. Davis, R. E.; Williams, M., Mitochondrial Function and Dysfunction: An Update. *J. Pharmacol. Exp. Ther.* **2012,** *342*, 598-607.

25. Biasutto, L.; Dong, L.-F.; Zoratti, M.; Neuzil, J., Mitochondrially targeted anti-cancer agents. *Mitochondrion* **2010,** *10*, 670-681.

26. Chatterjee, A.; Mambo, E.; Sidransky, D., Mitochondrial DNA mutations in human cancer. *Oncogene* **2006,** *25*, 4663-4674.

27. Ferri, C. P.; Prince, M.; Brayne, C.; Brodaty, H.; Fratiglioni, L.; Ganguli, M.; Hall, K.; Hasegawa, K.; Hendrie, H.; Huang, Y.; Jorm, A.; Mathers, C.; Menezes, P. R.; Rimmer, E.; Scazufca, M., Global prevalence of dementia: a Delphi consensus study. *Lancet* **2005,** *366*, 2112-2117.

28. Terry, R. D., The fine structure of neurofibrillary tangles in Alzheimer's disease. *J. Neuropathol. Exp. Neurol.* **1963,** *22*, 629-642.

29. Harris, M. E.; Hensley, K.; Butterfield, D. A.; Leedle, R. A.; Carney, J. M., Direct evidence of oxidative injury produced by the Alzheimer's beta-amyloid peptide (1-40) in cultured hippocampal neurons. *Exp. Neurol.* **1995,** *131*, 193-202.

30. Levy, E.; Carman, M. D.; Fernandez-Madrid, I. J.; Power, M. D.; Lieberburg, I.; van Duinen, S. G.; Bots, G. T.; Luyendijk, W.; Frangione, B., Mutation of the Alzheimer's disease amyloid gene in hereditary cerebral hemorrhage, Dutch type. *Science* **1990,** *248*, 1124-1126.

31. Misonou, H.; Morishima-Kawashima, M.; Ihara, Y., Oxidative stress induces intracellular accumulation of amyloid beta-protein (Abeta) in human neuroblastoma cells. *Biochemistry (Mosc.)* **2000,** *39*, 6951-6959.

32. Kopelman, P. G., Obesity as a medical problem. *Nature* **2000,** *404*, 635-643.

33. Wadden, T. A., Treatment of Obesity by Moderate and Severe Caloric Restriction: Results of Clinical Research Trials. *Ann. Intern. Med.* **1993,** *119*, 688-693.

34. Harper, J. A.; Dickinson, K.; Brand, M. D., Mitochondrial uncoupling as a target for drug development for the treatment of obesity. *Obes. Rev.* **2001,** *2*, 255-265.

35. Wild, S.; Roglic, G.; Green, A.; Sicree, R.; King, H., Global prevalence of diabetes: estimates for the year 2000 and projections for 2030. *Diabetes Care* **2004,** *27*, 1047-1053.

36. Lowell, B. B.; Shulman, G. I., Mitochondrial Dysfunction and Type 2 Diabetes. *Science* **2005,** *307*, 384-387.

37. Ritov, V. B.; Menshikova, E. V.; He, J.; Ferrell, R. E.; Goodpaster, B. H.; Kelley, D. E., Deficiency of subsarcolemmal mitochondria in obesity and type 2 diabetes. *Diabetes* **2005,** *54*, 8-14.

38. Silva, J. P.; Kohler, M.; Graff, C.; Oldfors, A.; Magnuson, M. A.; Berggren, P. O.; Larsson, N. G., Impaired insulin secretion and beta-cell loss in tissue-specific knockout mice with mitochondrial diabetes. *Nat. Genet.* **2000,** *26*, 336-340.

39. Anastasiou, D.; Poulogiannis, G.; Asara, J. M.; Boxer, M. B.; Jiang, J. K.; Shen, M.; Bellinger, G.; Sasaki, A. T.; Locasale, J. W.; Auld, D. S.; Thomas, C. J.; Vander Heiden, M. G.; Cantley, L. C., Inhibition of pyruvate kinase M2 by reactive oxygen species contributes to cellular antioxidant responses. *Science* **2011,** *334*, 1278-1283.

40. Warburg, O., On the origin of cancer cells. *Science* **1956,** *123*, 309-314.

41. Carew, J. S.; Huang, P., Mitochondrial defects in cancer. *Mol. Cancer* **2002,** *1*, 9.

42. Penta, J. S.; Johnson, F. M.; Wachsman, J. T.; Copeland, W. C., Mitochondrial DNA in human malignancy. *Mutat. Res.* **2001,** *488*, 119-133.

43. Croteau, D. L.; Bohr, V. A., Repair of Oxidative Damage to Nuclear and Mitochondrial DNA in Mammalian Cells. *J. Biol. Chem.* **1997,** *272*, 25409-25412.

44. Gasparre, G.; Porcelli, A. M.; Bonora, E.; Pennisi, L. F.; Toller, M.; Iommarini, L.; Ghelli, A.; Moretti, M.; Betts, C. M.; Martinelli, G. N.; Ceroni, A. R.; Curcio, F.; Carelli, V.; Rugolo, M.; Tallini, G.; Romeo, G., Disruptive mitochondrial DNA mutations in complex I subunits are markers of oncocytic phenotype in thyroid tumors. *Proc. Natl. Acad. Sci. U. S. A.* **2007,** *104*, 9001-9006.

45. Gasparre, G.; Hervouet, E.; de Laplanche, E.; Demont, J.; Pennisi, L. F.; Colombel, M.; Mège-Lechevallier, F.; Scoazec, J.-Y.; Bonora, E.; Smeets, R.; Smeitink, J.; Lazar, V.; Lespinasse, J.; Giraud, S.; Godinot, C.; Romeo, G.; Simonnet, H., Clonal expansion of mutated mitochondrial DNA is associated with tumor formation and complex I deficiency in the benign renal oncocytoma. *Hum. Mol. Genet.* **2008,** *17*, 986-995.

46. Bonora, E.; Porcelli, A. M.; Gasparre, G.; Biondi, A.; Ghelli, A.; Carelli, V.; Baracca, A.; Tallini, G.; Martinuzzi, A.; Lenaz, G.; Rugolo, M.; Romeo, G., Defective oxidative phosphorylation in thyroid oncocytic carcinoma is associated with pathogenic mitochondrial DNA mutations affecting complexes I and III. *Cancer Res.* **2006,** *66*, 6087-6096.

47. Ringman, J. M.; Frautschy, S. A.; Cole, G. M.; Masterman, D. L.; Cummings, J. L., A Potential Role of the Curry Spice Curcumin in Alzheimer's Disease. *Curr. Alzheimer Res* **2005,** *2*, 131-136.

48. Ng, T.-P.; Chiam, P.-C.; Lee, T.; Chua, H.-C.; Lim, L.; Kua, E.-H., Curry Consumption and Cognitive Function in the Elderly. *Am. J. Epidemiol.* **2006,** *164*, 898-906.

49. Pratico, D.; Delanty, N., Oxidative injury in diseases of the central nervous system: focus on Alzheimer's disease. *Am. J. Med.* **2000,** *109*, 577-585.

50. Smith, M. A.; Rottkamp, C. A.; Nunomura, A.; Raina, A. K.; Perry, G., Oxidative stress in Alzheimer's disease. *Biochim. Biophys. Acta* **2000,** *1502*, 139-144.

51. Varadarajan, S.; Yatin, S.; Aksenova, M.; Butterfield, D. A., Review: Alzheimer's amyloid beta-peptide-associated free radical oxidative stress and neurotoxicity. *J. Struct. Biol.* **2000,** *130*, 184-208.

52. Kim, D. S. H. L.; Park, S.-Y.; Kim, J.-Y., Curcuminoids from Curcuma longa L. (Zingiberaceae) that protect PC12 rat pheochromocytoma and normal human umbilical vein endothelial cells from β A(1–42) insult. *Neurosci. Lett.* **2001,** *303*, 57-61.

53. Park, S.-Y.; Kim, H.-S.; Cho, E.-K.; Kwon, B.-Y.; Phark, S.; Hwang, K.-W.; Sul, D., Curcumin protected PC12 cells against beta-amyloid-induced toxicity through the inhibition of oxidative damage and tau hyperphosphorylation. *Food Chem. Toxicol.* **2008,** *46*, 2881-2887.

54. Tainter, M. L.; Cutting, W. C.; Stockton, A. B., Use of Dinitrophenol in Nutritional Disorders *. *Am J Public Health Nation Health* **1934,** *24*, 1045-1053.

55. Cazeneuze, P.; Lepine, R., Sur les effets produits par l'ingestion et l'infusion intra-veineuse de trois colorants jaunes, derives de la houille. *Compt Rend Soc. Biol.* **1885,** *101*, 1167-1169.

56. Stapelberg, M.; Gellert, N.; Swettenham, E.; Tomasetti, M.; Witting, P. K.; Procopio, A.; Neuzil, J., α-Tocopheryl Succinate Inhibits Malignant Mesothelioma by Disrupting the Fibroblast Growth Factor Autocrine Loop: Mechanism and the role of oxidative stress. *J. Biol. Chem.* **2005,** *280*, 25369-25376.

57. Wang, X.-X.; Li, Y.-B.; Yao, H.-J.; Ju, R.-J.; Zhang, Y.; Li, R.-J.; Yu, Y.; Zhang, L.; Lu, W.-L., The use of mitochondrial targeting resveratrol liposomes modified

with a dequalinium polyethylene glycol-distearoylphosphatidyl ethanolamine conjugate to induce apoptosis in resistant lung cancer cells. *Biomaterials* **2011,** *32*, 5673-5687.

58. Weber, T.; Dalen, H.; Andera, L.; Nègre-Salvayre, A.; Augé, N.; Sticha, M.; Lloret, A.; Terman, A.; Witting, P. K.; Higuchi, M.; Plasilova, M.; Zivny, J.; Gellert, N.; Weber, C.; Neuzil, J., Mitochondria Play a Central Role in Apoptosis Induced by α-Tocopheryl Succinate, an Agent with Antineoplastic Activity: Comparison with Receptor-Mediated Pro-Apoptotic Signaling†. *Biochemistry (Mosc.)* **2003,** *42*, 4277-4291.

59. Shiau, C.-W.; Huang, J.-W.; Wang, D.-S.; Weng, J.-R.; Yang, C.-C.; Lin, C.-H.; Li, C.; Chen, C.-S., α-Tocopheryl Succinate Induces Apoptosis in Prostate Cancer Cells in Part through Inhibition of Bcl-xL/Bcl-2 Function. *J. Biol. Chem.* **2006,** *281*, 11819-11825.

60. Dong, L.-F.; Low, P.; Dyason, J. C.; Wang, X.-F.; Prochazka, L.; Witting, P. K.; Freeman, R.; Swettenham, E.; Valis, K.; Liu, J.; Zobalova, R.; Turanek, J.; Spitz, D. R.; Domann, F. E.; Scheffler, I. E.; Ralph, S. J.; Neuzil, J., α-Tocopheryl succinate induces apoptosis by targeting ubiquinone-binding sites in mitochondrial respiratory complex II. *Oncogene* **2008,** *27*, 4324-4335.

61. Pedersen, P. L., Voltage dependent anion channels (VDACs): a brief introduction with a focus on the outer mitochondrial compartment's roles together with hexokinase-2 in the "Warburg effect" in cancer. *J. Bioenerg. Biomembr.* **2008,** *40*, 123-126.

62. Neuzil, J.; Dong, L.-F.; Rohlena, J.; Truksa, J.; Ralph, S. J., Classification of mitocans, anti-cancer drugs acting on mitochondria. *Mitochondrion* **2013,** *13*, 199-208.

63. Mathupala, S. P.; Ko, Y. H.; Pedersen, P. L., Hexokinase II: cancer's double-edged sword acting as both facilitator and gatekeeper of malignancy when bound to mitochondria. *Oncogene* **2006,** *25*, 4777-4786.

64. Simons, A. L.; Ahmad, I. M.; Mattson, D. M.; Dornfeld, K. J.; Spitz, D. R., 2-Deoxy-D-glucose combined with cisplatin enhances cytotoxicity via metabolic oxidative stress in human head and neck cancer cells. *Cancer Res.* **2007,** *67*, 3364-3370.

65. Chen, Z.; Zhang, H.; Lu, W.; Huang, P., Role of mitochondria-associated hexokinase II in cancer cell death induced by 3-bromopyruvate. *Biochim. Biophys. Acta* **2009,** *1787*, 553-560.

66. McFate, T.; Mohyeldin, A.; Lu, H.; Thakar, J.; Henriques, J.; Halim, N. D.; Wu, H.; Schell, M. J.; Tsang, T. M.; Teahan, O.; Zhou, S.; Califano, J. A.; Jeoung, N. H.; Harris, R. A.; Verma, A., Pyruvate dehydrogenase complex activity controls metabolic and malignant phenotype in cancer cells. *J. Biol. Chem.* **2008,** *283*, 22700-22708.

67. Pastorino, J. G.; Hoek, J. B.; Shulga, N., Activation of glycogen synthase kinase 3beta disrupts the binding of hexokinase II to mitochondria by phosphorylating voltage-dependent anion channel and potentiates chemotherapy-induced cytotoxicity. *Cancer Res.* **2005,** *65*, 10545-10554.

68. Bonnet, S.; Archer, S. L.; Allalunis-Turner, J.; Haromy, A.; Beaulieu, C.; Thompson, R.; Lee, C. T.; Lopaschuk, G. D.; Puttagunta, L.; Bonnet, S.; Harry, G.; Hashimoto, K.; Porter, C. J.; Andrade, M. A.; Thebaud, B.; Michelakis, E. D., A mitochondria-K+ channel axis is suppressed in cancer and its normalization promotes apoptosis and inhibits cancer growth. *Cancer Cell* **2007,** *11*, 37-51.

69. Roche, T. E.; Hiromasa, Y., Pyruvate dehydrogenase kinase regulatory mechanisms and inhibition in treating diabetes, heart ischemia, and cancer. *Cell. Mol. Life Sci.* **2007,** *64*, 830-849.

70. Lu, C. W.; Lin, S. C.; Chen, K. F.; Lai, Y. Y.; Tsai, S. J., Induction of pyruvate dehydrogenase kinase-3 by hypoxia-inducible factor-1 promotes metabolic switch and drug resistance. *J. Biol. Chem.* **2008,** *283*, 28106-28114.

71. M.F. Ross, G. F. K., F.H. Blaikie, A.M. James, H.M. Cochemé, A. Filipovska, T. Da Ros, T.R. Hurd, R.A.J. Smith, and M.P. Murphy, Lipophilic Triphenylphosphonium Cations as Tools in Mitochondrial Bioenergetics and Free Radical Biology. *Biochemistry (Moscow)* **2005,** *70*, 273-283.

72. Liberman, E.; Topaly, V.; Tsofina, L.; Jasaitis, A.; Skulachev, V., Mechanism of coupling of oxidative phosphorylation and the membrane potential of mitochondria. *Nature* **1969**. *222,* 1076-1078.

73. Grinius, L. L.; Jasaitis, A. A.; Kadziauskas, Y. P.; Liberman, E. A.; Skulachev, V. P.; Topali, V. P.; Tsofina, L. M.; Vladimirova, M. A., Conversion of biomembrane-produced energy into electric form. I. Submitochondrial particles. *BBA-Bioenergetics* **1970,** *216*, 1-12.

74. De Proost, I.; Pintelon, I.; Brouns, I.; Kroese, A. B.; Riccardi, D.; Kemp, P. J.; Timmermans, J. P.; Adriaensen, D., Functional live cell imaging of the pulmonary neuroepithelial body microenvironment. *Am. J. Respir. Cell Mol. Biol.* **2008,** *39*, 180-189.

75. Liu, T.; Hannafon, B.; Gill, L.; Kelly, W.; Benbrook, D., Flex-Hets differentially induce apoptosis in cancer over normal cells by directly targeting mitochondria. *Mol. Cancer Ther.* **2007,** *6*, 1814-1822.

76. Reungpatthanaphong, P.; Dechsupa, S.; Meesungnoen, J.; Loetchutinat, C.; Mankhetkorn, S., Rhodamine B as a mitochondrial probe for measurement and monitoring of mitochondrial membrane potential in drug-sensitive and -resistant cells. *J. Biochem. Biophys. Methods* **2003,** *57*, 1-16.

77. Wang F, O. M., Huang P., Small mitochondria-targeting molecules as anticancer agents. *Mol. Aspects. Med.* **2010,** *31*, 75-92.

78. Saretzki, G.; Murphy, M. P.; von Zglinicki, T., MitoQ counteracts telomere shortening and elongates lifespan of fibroblasts under mild oxidative stress. *Aging Cell* **2003,** *2*, 141-143.

79. Covey, M. V.; Murphy, M. P.; Hobbs, C. E.; Smith, R. A. J.; Oorschot, D. E., Effect of the mitochondrial antioxidant, Mito Vitamin E, on hypoxic–ischemic striatal injury in neonatal rats: A dose–response and stereological study. *Exp. Neurol.* **2006,** *199*, 513-519.

80. Schatz, G.; Haslbrunner, E.; Tuppy, H., Deoxyribonucleic acid associated with yeast mitochondria. *Biochem. Biophys. Res. Commun.* **1964,** *15*, 127-132.

81. Thomas, D. A.; Stauffer, C.; Zhao, K.; Yang, H.; Sharma, V. K.; Szeto, H. H.; Suthanthiran, M., Mitochondrial targeting with antioxidant peptide SS-31 prevents mitochondrial depolarization, reduces islet cell apoptosis, increases islet cell yield, and improves posttransplantation function. *J. Am. Soc. Nephrol.* **2007,** *18*, 213-222.

82. Zhao, K.; Zhao, G. M.; Wu, D.; Soong, Y.; Birk, A. V.; Schiller, P. W.; Szeto, H. H., Cell-permeable peptide antioxidants targeted to inner mitochondrial membrane inhibit mitochondrial swelling, oxidative cell death, and reperfusion injury. *J. Biol. Chem.* **2004,** *279*, 34682-34690.

83. Susan Chalmers , S. T. C., Caroline Quin, Tracy A. Prime, Andrew M. James, Andrew G. Cairns, Michael P. Murphy, John G. McCarron , and Richard C. Hartley Selective Uncoupling of Individual Mitochondria within a Cell Using a Mitochondria-Targeted Photoactivated Protonophore. *J. Am. Chem. Soc.* **2012,** *134*, 758-761.

84. Panyam, J.; Labhasetwar, V., Biodegradable nanoparticles for drug and gene delivery to cells and tissue. *Adv. Drug Delivery Rev.* **2003,** *55*, 329-347.

85. Kamaly, N.; Xiao, Z.; Valencia, P. M.; Radovic-Moreno, A. F.; Farokhzad, O. C., Targeted polymeric therapeutic nanoparticles: design, development and clinical translation. *Chem. Soc. Rev.* **2012,** *41*, 2971-3010.

86. Maeda, H., Tumor-Selective Delivery of Macromolecular Drugs via the EPR Effect: Background and Future Prospects. *Bioconjugate Chem.* **2010,** *21*, 797-802.

87. Matsumura, Y.; Maeda, H., A new concept for macromolecular therapeutics in cancer chemotherapy: mechanism of tumoritropic accumulation of proteins and the antitumor agent smancs. *Cancer Res.* **1986,** *46*, 6387-6392.

88. Leserman, L. D.; Barbet, J.; Kourilsky, F.; Weinstein, J. N., Targeting to cells of fluorescent liposomes covalently coupled with monoclonal antibody or protein A. *Nature* **1980,** *288*, 602-604.

89. Marrache, S.; Pathak, R. K.; Darley, K. L.; Choi, J. H.; Zaver, D.; Kolishetti, N.; Dhar, S., Nanocarriers for tracking and treating diseases. *Curr. Med. Chem.* **2013,** *20*, 3500-3514.

90. Weissig, V., From Serendipity to Mitochondria-Targeted Nanocarriers. *Pharm. Res.* **2011,** *28*, 2657-2668.

91. Chou, L. Y.; Ming, K.; Chan, W. C., Strategies for the intracellular delivery of nanoparticles. *Chem Soc Rev* **2011,** *40*, 233-245.

92. Faraji, A. H.; Wipf, P., Nanoparticles in cellular drug delivery. *Bioorg Med Chem* **2009,** *17*, 2950-2962.

93. Patel, J.; Garala, K.; Basu, B.; Raval, M.; Dharamsi, A., Solubility of aceclofenac in polyamidoamine dendrimer solutions. *Int J Pharm Investig* **2011,** *1*, 135-138.

94. Wang, A. Z.; Langer, R.; Farokhzad, O. C., Nanoparticle delivery of cancer drugs. *Annu Rev Med* **2012,** *63*, 185-198.

95. Biswas, S.; Dodwadkar, N. S.; Piroyan, A.; Torchilin, V. P., Surface conjugation of triphenylphosphonium to target poly(amidoamine) dendrimers to mitochondria. *Biomaterials* **2012,** *33*, 4773-4782.

96. Wang, X.; Shao, N.; Zhang, Q.; Cheng, Y., Mitochondrial targeting dendrimer allows efficient and safe gene delivery. *J. Mater. Chem. B* **2014,** *2*, 2546-2553.

97. Theodossiou, T.; Sideratou, Z.; Katsarou, M.; Tsiourvas, D., Mitochondrial Delivery of Doxorubicin by Triphenylphosphonium-Functionalized Hyperbranched Nanocarriers Results in Rapid and Severe Cytotoxicity. *Pharm. Res.* **2013,** *30*, 2832-2842.

98. Kakudo, T.; Chaki, S.; Nakase, I.; Akaji, K.; Kawakami, T.; Maruyama, K.; Harashima, H., Transferrin-modified liposomes equipped with a pH-sensitive fusogenic peptide: an artificial viral-like delivery system. *Biochemistry (Mosc.)* **2004,** *43*, 5618-5628.

99. Huth, U.; Wieschollek, A.; Garini, Y.; Schubert, R.; Peschka-Suss, R., Fourier transformed spectral bio-imaging for studying the intracellular fate of liposomes. *Cytometry* **2004,** *57A*, 10-21.

100. Yamada, Y.; Akita, H.; Kogure, K.; Kamiya, H.; Harashima, H., Mitochondrial drug delivery and mitochondrial disease therapy – An approach to liposome-based delivery targeted to mitochondria. *Mitochondrion* **2007,** *7*, 63-71.

101. Yamada, Y.; Akita, H.; Kamiya, H.; Kogure, K.; Yamamoto, T.; Shinohara, Y.; Yamashita, K.; Kobayashi, H.; Kikuchi, H.; Harashima, H., MITO-Porter: A liposome-based carrier system for delivery of macromolecules into mitochondria via membrane fusion. *BBA-Biomembranes* **2008,** *1778*, 423-432.

102. Boddapati, S. V.; D'Souza, G. G. M.; Erdogan, S.; Torchilin, V. P.; Weissig, V., Organelle-Targeted Nanocarriers: Specific Delivery of Liposomal Ceramide to

Mitochondria Enhances Its Cytotoxicity in Vitro and in Vivo. *Nano Lett.* **2008,** *8*, 2559-2563.

103. Boddapati, S. V.; Tongcharoensirikul, P.; Hanson, R. N.; D'Souza, G. G. M.; Torchilin, V. P.; Weissig, V., Mitochondriotropic Liposomes. *J. Liposome Res.* **2005,** *15*, 49-58.

104. Malhi, S. S.; Budhiraja, A.; Arora, S.; Chaudhari, K. R.; Nepali, K.; Kumar, R.; Sohi, H.; Murthy, R. S. R., Intracellular delivery of redox cycler-doxorubicin to the mitochondria of cancer cell by folate receptor targeted mitocancerotropic liposomes. *Int. J. Pharm.* **2012,** *432*, 63-74.

105. Solomon, M. A.; Shah, A. A.; D'Souza, G. G. M., In Vitro assessment of the utility of stearyl triphenyl phosphonium modified liposomes in overcoming the resistance of ovarian carcinoma Ovcar-3 cells to paclitaxel. *Mitochondrion* **2013,** *13*, 464-472.

106. Biswas, S.; Dodwadkar, N. S.; Deshpande, P. P.; Torchilin, V. P., Liposomes loaded with paclitaxel and modified with novel triphenylphosphonium-PEG-PE conjugate possess low toxicity, target mitochondria and demonstrate enhanced antitumor effects in vitro and in vivo. *J. Controlled Release* **2012,** *159*, 393-402.

107. Zhou, J.; Zhao, W.-Y.; Ma, X.; Ju, R.-J.; Li, X.-Y.; Li, N.; Sun, M.-G.; Shi, J.-F.; Zhang, C.-X.; Lu, W.-L., The anticancer efficacy of paclitaxel liposomes modified with mitochondrial targeting conjugate in resistant lung cancer. *Biomaterials* **2013,** *34*, 3626-3638.

108. Theodossiou, T. A.; Sideratou, Z.; Tsiourvas, D.; Paleos, C. M., A novel mitotropic oligolysine nanocarrier: Targeted delivery of covalently bound D-Luciferin to cell mitochondria. *Mitochondrion* **2011,** *11*, 982-986.

109. Soppimath, K. S.; Aminabhavi, T. M.; Kulkarni, A. R.; Rudzinski, W. E., Biodegradable polymeric nanoparticles as drug delivery devices. *J. Controlled Release* **2001,** *70*, 1-20.

110. Kolishetti, N.; Dhar, S.; Valencia, P. M.; Lin, L. Q.; Karnik, R.; Lippard, S. J.; Langer, R.; Farokhzad, O. C., Engineering of self-assembled nanoparticle platform for precisely controlled combination drug therapy. *Proc Natl Acad Sci USA* **2010,** *107*, 17939-17944.

111. Langer, R.; Folkman, J., Polymers for the sustained release of proteins and other macromolecules. *Nature* **1976,** *263*, 797-800.

112. Sharma, A.; Soliman, G. M.; Al-Hajaj, N.; Sharma, R.; Maysinger, D.; Kakkar, A., Design and Evaluation of Multifunctional Nanocarriers for Selective Delivery of Coenzyme Q10 to Mitochondria. *Biomacromolecules* **2011,** *13*, 239-252.

113. Conde, J.; Doria, G.; Baptista, P., Noble Metal Nanoparticles Applications in Cancer.*Drug Deliv.* **2012,** *2012*, 12.

114. Liao, H.; Nehl, C. L.; Hafner, J. H., Biomedical applications of plasmon resonant metal nanoparticles. *Nanomedicine (Lond)* **2006,** *1*, 201-208.

115. Link, S.; El-Sayed, M. A., Size and Temperature Dependence of the Plasmon Absorption of Colloidal Gold Nanoparticles. *J. Phys. Chem. B,* **1999,** *103*, 4212-4217.

116. Zhang, C. X.; Zhang, Y.; Wang, X.; Tang, Z. M.; Lu, Z. H., Hyper-Rayleigh scattering of protein-modified gold nanoparticles. *Anal. Biochem.* **2003,** *320*, 136-140.

117. Turkevich, J.; Stevenson, P. C.; Hillier, J., A study of the nucleation and growth processes in the synthesis of colloidal gold. *Discuss. Faraday Soc.* **1951,** *11*, 55-75.

118. Kimling, J.; Maier, M.; Okenve, B.; Kotaidis, V.; Ballot, H.; Plech, A., Turkevich Method for Gold Nanoparticle Synthesis Revisited. *The Journal of Physical Chemistry B* **2006,** *110*, 15700-15707.

119. Prevo, B. G.; Esakoff, S. A.; Mikhailovsky, A.; Zasadzinski, J. A., Scalable routes to gold nanoshells with tunable sizes and response to near-infrared pulsed-laser irradiation. *Small* **2008,** *4*, 1183-1195.

120. Sau, T. K.; Murphy, C. J., Room Temperature, High-Yield Synthesis of Multiple Shapes of Gold Nanoparticles in Aqueous Solution. *J. Am. Chem. Soc.* **2004,** *126*, 8648-8649.

121. Salnikov, V.; Lukyanenko, Y. O.; Frederick, C. A.; Lederer, W. J.; Lukyanenko, V., Probing the outer mitochondrial membrane in cardiac mitochondria with nanoparticles. *Biophys. J.* **2007,** *92*, 1058-1071.

122. Wang, L.; Liu, Y.; Li, W.; Jiang, X.; Ji, Y.; Wu, X.; Xu, L.; Qiu, Y.; Zhao, K.; Wei, T.; Li, Y.; Zhao, Y.; Chen, C., Selective Targeting of Gold Nanorods at the Mitochondria of Cancer Cells: Implications for Cancer Therapy. *Nano Lett.* **2010,** *11*, 772-780.

123. Bruchez, M., Jr.; Moronne, M.; Gin, P.; Weiss, S.; Alivisatos, A. P., Semiconductor nanocrystals as fluorescent biological labels. *Science* **1998,** *281*, 2013-2016.

124. Waggoner, A., Covalent labeling of proteins and nucleic acids with fluorophores. *Methods Enzymol.* **1995,** *246*, 362-373.

125. Schrock, E.; du Manoir, S.; Veldman, T.; Schoell, B.; Wienberg, J.; Ferguson-Smith, M. A.; Ning, Y.; Ledbetter, D. H.; Bar-Am, I.; Soenksen, D.; Garini, Y.; Ried, T., Multicolor spectral karyotyping of human chromosomes. *Science* **1996,** *273*, 494-497.

126. Roederer, M.; Kantor, A. B.; Parks, D. R.; Herzenberg, L. A., Cy7PE and Cy7APC: Bright new probes for immunofluorescence. *Cytometry* **1996,** *24*, 191-197.

127. Miltenyi, S.; Muller, W.; Weichel, W.; Radbruch, A., High gradient magnetic cell separation with MACS. *Cytometry* **1990,** *11*, 231-238.

128. Elghanian, R.; Storhoff, J. J.; Mucic, R. C.; Letsinger, R. L.; Mirkin, C. A., Selective colorimetric detection of polynucleotides based on the distance-dependent optical properties of gold nanoparticles. *Science* **1997,** *277*, 1078-1081.

129. Alivisatos, A. P.; Johnsson, K. P.; Peng, X.; Wilson, T. E.; Loweth, C. J.; Bruchez, M. P., Jr.; Schultz, P. G., Organization of 'nanocrystal molecules' using DNA. *Nature* **1996,** *382*, 609-611.

130. Beverloo, H. B.; van Schadewijk, A.; van Gelderen-Boele, S.; Tanke, H. J., Inorganic phosphors as new luminescent labels for immunocytochemistry and time-resolved microscopy. *Cytometry* **1990,** *11*, 784-792.

131. Hoshino, A.; Fujioka, K.; Oku, T.; Nakamura, S.; Suga, M.; Yamaguchi, Y.; Suzuki, K.; Yasuhara, M.; Yamamoto, K., Quantum dots targeted to the assigned organelle in living cells. *Microbiol. Immunol.* **2004,** *48*, 985-994.

132. Rozenzhak, S. M.; Kadakia, M. P.; Caserta, T. M.; Westbrook, T. R.; Stone, M. O.; Naik, R. R., Cellular internalization and targeting of semiconductor quantum dots. *Chem. Commun. (Camb.)* **2005**, 2217-2219.

CHAPTER 2

ENGINEERING OF BLENDED NANOPARTICLE PLATFORM FOR DELIVERY OF MITOCHONDRIA-ACTING THERAPEUTICS[1]

[1]Reprinted with the permission of Marrache, S. and Dhar, S. *Proc. Natl. Acad. Sci. USA*, 109, 16288-16293. Copyright 2012, United States National Academy of Sciences

Abstract

Mitochondrial dysfunctions cause numerous human disorders. A platform technology based on biodegradable polymers for carrying bioactive molecules to the mitochondrial matrix could be of enormous potential benefit in treating mitochondrial diseases. Here, we report a rationally designed mitochondria-targeted polymeric nanoparticle (NP) system and its optimization for efficient delivery of various mitochondria-acting therapeutics by blending a targeted poly(D,L-lactic-co-glycolic acid)-block (PLGA-b)-poly(ethylene glycol) (PEG)-triphenylphosphonium (TPP) polymer (PLGA-b- PEG-TPP) with either nontargeted PLGA-b-PEG-OH or PLGA-COOH. An optimized formulation was identified through in vitro screening of a library of charge- and size-varied NPs, and mitochondrial uptake was studied by qualitative and quantitative investigations of cytosolic and mitochondrial fractions of cells treated with blended NPs composed of PLGA-b-PEG-TPP and a triblock copolymer containing a fluorescent quantum dot, PLGA-b-PEG-QD. The versatility of this platform was demonstrated by studying various mitochondria-acting therapeutics for different applications, including the mitochondria-targeting chemotherapeutics lonidamine and α-tocopheryl succinate for cancer, the mitochondrial antioxidant curcumin for Alzheimer's disease, and the mitochondrial un- coupler 2,4-dinitrophenol for obesity. These biomolecules were loaded into blended NPs with high loading efficiencies. Considering efficacy, the targeted PLGA-b-PEG-TPP NP provides a remarkable improvement in the drug therapeutic index for cancer, Alzheimer's disease, and obesity compared with the nontargeted construct or the therapeutics in their free form. This work represents the

potential of a single, programmable NP platform for the diagnosis and targeted delivery of therapeutics for mitochondrial dysfunction-related diseases.

Introduction

Mitochondrial dysfunction is a key player in a variety of human disorders, including cancer, neurodegenerative and neuromuscular diseases, obesity and diabetes.[1-3] One of the most challenging problems in the development of drugs to treat mitochondrial dysfunction is not to develop drugs but to distribute them to the mitochondria of cells.[2] Drugs ranging from chemotherapeutics for cancer to antioxidants for Alzheimer's disease (AD), and uncoupler of oxidative phosphorylation for obesity act on the mitochondria of cells, however, clinical trials with the mitochondria acting therapeutics have failed to show benefits in humans due to the logistics of their safe delivery to the mitochondria in sufficient amounts and the toxicity associated at high doses.

The potential of nanoparticles (NPs) to improve any therapy lies in their ability to deliver payloads directly to the cells of interest and simultaneously enhancing the stability and pharmacokinetics, however, an equally important consideration is whether the same NP can get the therapeutic payload to their intended target inside the cells. Delivery of payloads using biodegradable and the Food and Drug Administration (FDA) approved poly(lactic-*co*-glycolic acid) (PLGA) based NPs to the target tissue is well defined and characterized,[4-6] but the intracellular barriers which delivery vehicles have to overcome in order to reach its subcellular target site, are less well characterized. Several NP-based therapeutics are in clinical use for treating non-mitochondrial diseases,[4] but NPs for mitochondrial dysfunction associated diseases are still in their infancy.[7] Development of technologies for targeted delivery of known mitochondria-acting

therapeutics to the site of mitochondria will potentially launch new therapeutic approaches for the treatment of mitochondria-related diseases.[8] Till date, there are only a handful of metal oxide or liposomal based carriers, which are known to deliver payloads to the mitochondria of cells (Table 2.1)[9-17] and no example demonstrates optimization and application of the FDA approved, biodegradable PLGA based NP system in delivering known mitochondria acting therapeutics to their precise destination.

Table 2.1. Examples of Nanocarriers Mitochondrial Delivery

Nanocarrier	**Size (nm)**	**Disease**	**Action**	**References**
STPP-functionalized liposomes	55	Cancer	Apoptosis	Boddapati et al. 2008. Organelle targeted nanocarriers: specific delivery of liposomal ceramide to mitochondria enhances its cytotoxicity in vitro and in vivo. Nano Lett. 8, 2559–2563.
STPP functionalized liposomes	105	Cancer	Apoptosis	Patel et al. 2010. Mitochondria-targeted liposomes improve the apoptotic and cytotoxic action of sclareol. J. Liposome Res. 20, 244–249.
Chitosan functionalized Au nanoparticles	6–16	Oxidative stress	Antioxidant	Esumi et al. 2003. Antioxidant-potentiality of gold-chitosan nanocomposites. Colloids Surf. B Biointerfaces 32, 117–123.
PAMAM functionalized Au nanoparticles	3.6	Oxidative stress	Antioxidant	Esumi et al. 2004. Antioxidant action by gold-PAMAM dendrimer nanocomposites. Langmuir 20, 2536–2538.
CTAB functionalized Au nanorods	55 × 13	Cancer	Apoptosis	Wang et al. 2011. Selective targeting of gold nanorods at the mitochondria of cancer cells: implications for cancer therapy. Nano Lett. 11, 772–780.

Oligonucleotide functionalized TiO_2 nanoparticles	3–5	Mitochondrial DNA diseases	Gene delivery	Paunesku et al. 2007. Intracellular distribution of TiO2-DNA oligonucleotide nanoconjugates directed to nucleolus and mitochondria indicates sequence specificity. Nano Lett. 7, 596–601.
Pectin functionalized Pt nanoparticles	5	Diseases with NADH dehydrogenase deficiency	Antioxidant	Hikosaka et al. 2008. Platinum nanoparticles have an activity similar to mitochondrial NADH:ubiquinone oxidoreductase. Colloids Surf. B Biointerfaces 66, 195–200.
Au/Pt bimetallic nanoparticles	5	Oxidative stress	Antioxidant	Kajita et al. 2007. Platinum nanoparticle is a useful scavenger of superoxide anion and hydrogen peroxide. Free Radic. Res. 41, 615–626.
PCL-PEG Polymeric nanoparticles	40	Oxidative stress	Antioxidant	Sharma et al. 2012. Design and Evaluation of Multifunctional Nanocarriers for Selective Delivery of Coenzyme Q10 to Mitochondria. Biomacromolecules 13, 239−252
Abbreviations: stearyl triphenyl phosphonium (STPP), polyamidoamine (PAMAM), and cetytrimethylamonium bromide (CTAB), polycaprolactone (PCL)				

In this report, we describe an engineering approach in designing and execution of a polymer blending technology[18] to fine tune size and surface charge of the resultant NPs to provide an optimized PLGA based NP platform for mitochondria-targeted delivery of therapeutics. Incorporation of polyethylene glycol (PEG) based polymer on the surface of PLGA-NPs results in long blood circulation.[19] We synthesized a PLGA-*b*-PEG copolymer possessing a single terminal lipophilic triphenylphosphonium (TPP) cation, which is known to cross into the mitochondrial matrix space,[20] to determine how the

attached cation, variation of NP size and charge affect intracellular trafficking of blended NPs formed by mixing PLGA-*b*-PEG-TPP either with PLGA-*b*-PEG-OH or PLGA-COOH (Fig. 2.1A and 2.1B). To demonstrate wide application of our engineered NPs, we used a variety of mitochondria-acting therapeutics,[8] which are used in Alzheimer's disease (AD),[21] obesity,[22] and cancer chemotherapy[23] as payloads. We chose curcumin as an inhibitor of amyloid *β*-protein (A*β)* for AD,[24, 25] a mitochondrial decoupler 2,4-dinitrophenol (2,4-DNP) as an anti-obesity drug,[21] and lonidamine (LND), which inhibits mitochondrial glycolysis [26] and *α*-tocopheryl succinate (*α*-TOS), a tumor-selective drug for cancer [27] (Fig. 2.1B).

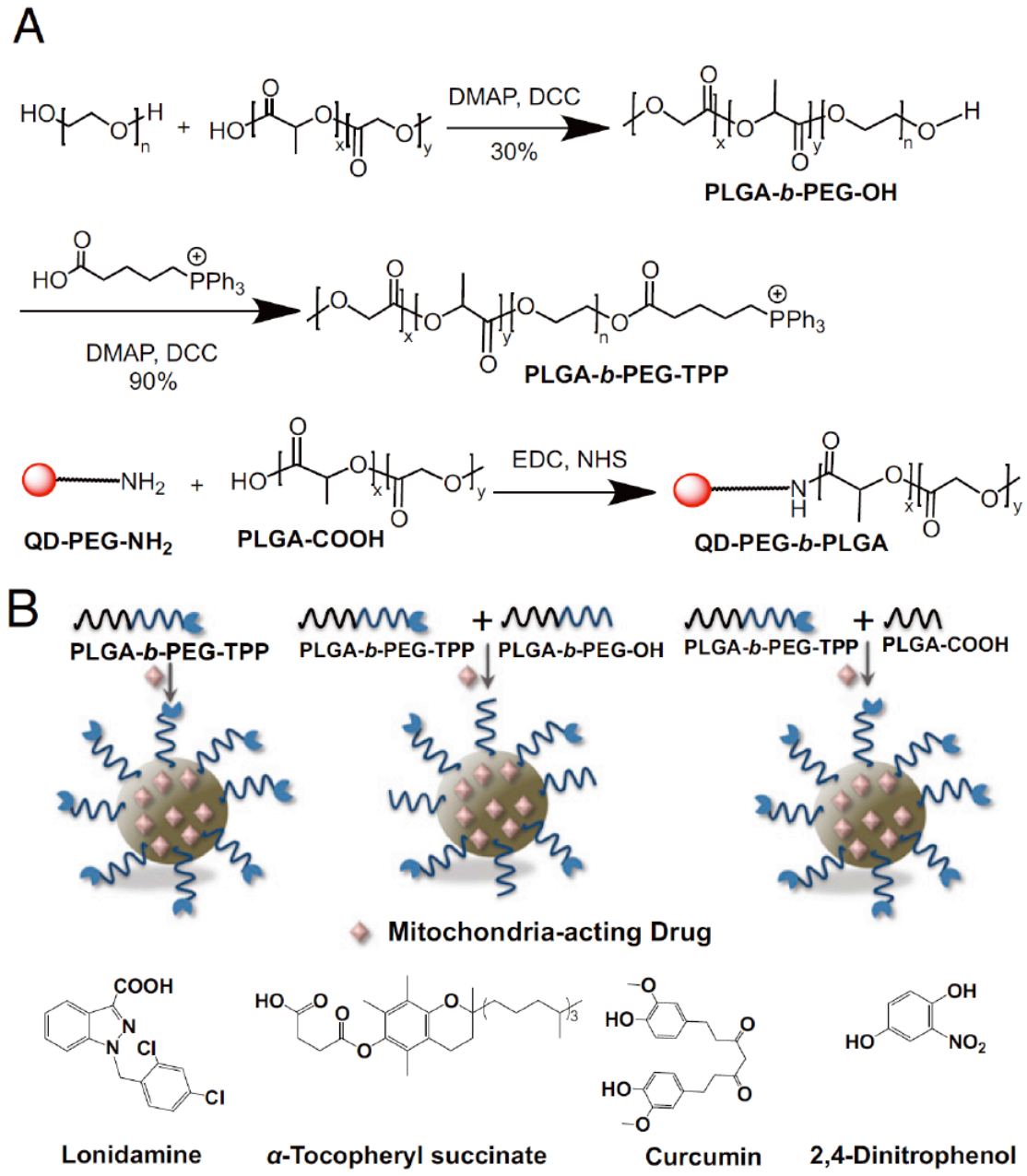


Figure 2.1. (A) Synthesis of PLGA-b-PEG-OH, PLGA-b-PEG-TPP, and QD-conjugated polymer. (B) Construction of targeted and non targeted NPs by blending PLGA-*b*-PEG-OH and PLGA-COOH with PLGA-*b*-PEG-TPP, and mitochondria-acting therapeutics used as payloads.

Methods and Materials

Materials.

All chemicals were received and used without further purification unless otherwise noted. PLGA-COOH of inherent viscosity of 0.18 dL/g was purchased from Lactel. HO-PEG-OH (MW 3350), 4-dimethylaminopyridine (DMAP), N,N'-dicyclohexylcarbodiimide (DCC), 2,4-DNP, curcumin, D-α-tocopherol succinate, LND, dexamethasone (Dex), 3-isobutyl-1-methylxanthine (IBMX), and MTT were purchased from Sigma-Aldrich. Qdot 705 ITK amino PEG quantum dots, mitotracker green, and CellLight™ lysosomes-GFP were purchased from Invitrogen. Bicinchoninic acid (BCA) protein assay and the mitochondria isolation kits were purchased from Thermo Scientific. AdipoRed™ adipogenesis assay reagent was purchased from Lonza. Amyloid β-protein fragment 25-35 was purchased from Sigma-Aldrich. Dynamic light scattering (DLS) measurements were carried out using a Malvern Zetasizer Nano ZS system. ^{1}H, ^{13}C, and ^{31}P NMR spectra were recorded on a 400 MHz Varian NMR spectrometer. Gel permeation chromatographic (GPC) analyses were performed on Shimadzu LC20-AD prominence liquid chromatographer equipped with a RI detector. Optical measurements were carried out on a NanoDrop 2000 spectrophotometer. HPLC analyses were made on an Agilent 1200 series instrument. TEM images were taken in a Tecnai 20 FEM microscope. Confocal images were recorded in a Nikon A1 confocal microscope. ICP-MS studies were performed on a VG PlasmaQuad 3 ICP mass spectrometer. Early endosomal marker, rabbit monoclonal EEA-1, was obtained from Abcam. The secondary antibody for EEA-1, Alexa Fluor 488 goat anti-rabbit antibody, was purchased from Invitrogen.

Cell Line and Cell Culture.

Human cervical cancer HeLa and the adherent human neuroblastoma IMR-32 cell lines were procured from the ATCC. 3T3-L1 fibroblast cells were a generous gift from Prof. Cliff A. Baile, Center for Animal & Dairy Science, University of Georgia. HeLa, IMR-32, and 3T3-L1 cells were grown at 37 °C in 5% CO_2 in DMEM medium supplemented with 10% fetal bovine serum and 1% penicillin/streptomycin. Cells were passed every 3 to 4 days and restarted from frozen stocks upon reaching pass number 20.

Synthesis of PLGA-*b*-PEG-OH.

HO-PEG-OH (0.75 g, 0.23 mmol), PLGA-COOH (0.50 g, 0.1 mmol), and DMAP (0.01 g, 0.08 mmol) were dissolved in 7 mL dry CH_2Cl_2. A 2 mL CH_2Cl_2 solution of DCC (0.02 g, 0.1 mmol) was added drop-wise to the reaction mixture at 0 °C with stirring. The mixture was warmed to room temperature and stirred overnight. Insoluble dicyclohexylurea ((DCU) was filtered and the mixture was precipitated from a 50 mL 50:50 diethyl ether and methanol. The resulting solid was centrifuged at 5000 rpm for 15 min at 4 °C. As a final purification, a methanolic solution of PLGA-*b*-PEG-OH was repeatedly precipitated and washed with cold diethyl ether and isolated as a white solid in 30% (0.2 g) yield. ^{1}H NMR ($CHCl_3$-*d*) (Figure 2.2): δ 5.2 [m, 37H (O*CH*CH_3C(O)], 4.8 [m, 74H (O*CH*$_2$C(O))], 3.6 [s, 102H (O*CH*$_2$)], 1.6 [m, 115H (*CH*$_3$CH)]. ^{13}C NMR ($CHCl_3$-*d*) (Figure 2.3): δ 169.4, 166.3, 70.5, 69.1, 60.8, 16.66. GPC (Figure 2.4): M_n=6,900 g/mol, M_w=9,200 g/mol, M_z=12,300 g/mol, PDI = 1.33.

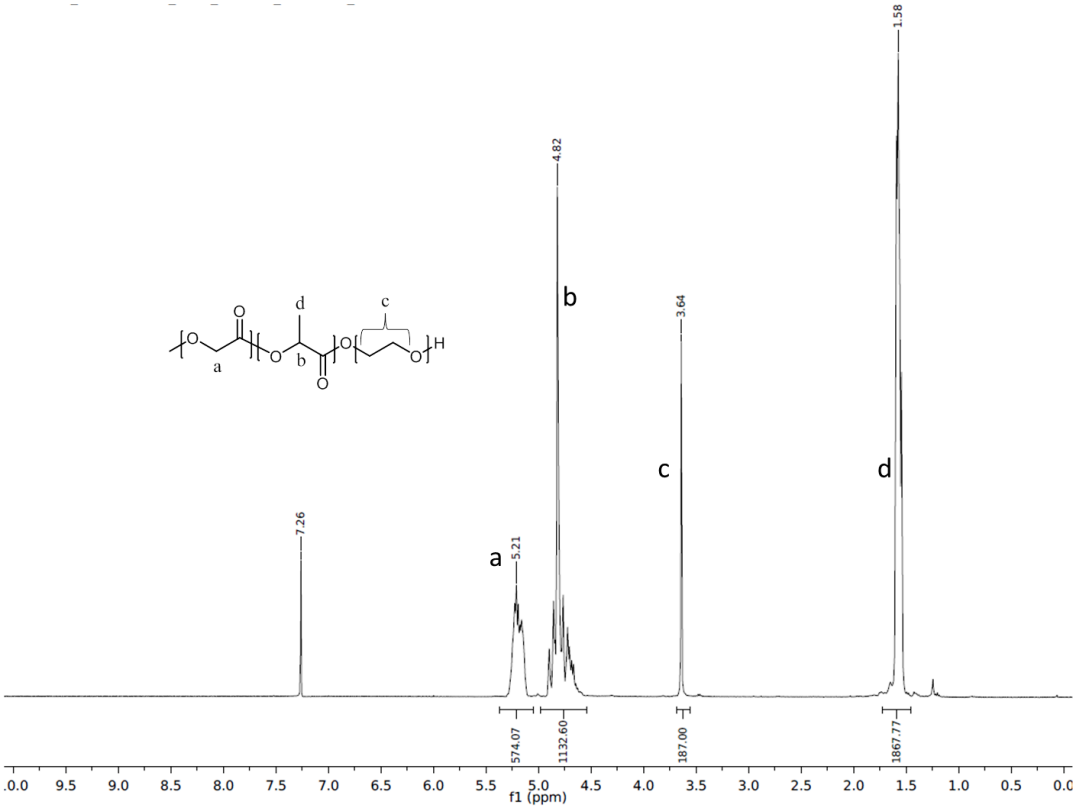


Figure 2.2. ^{1}H NMR of PLGA-PEG-OH

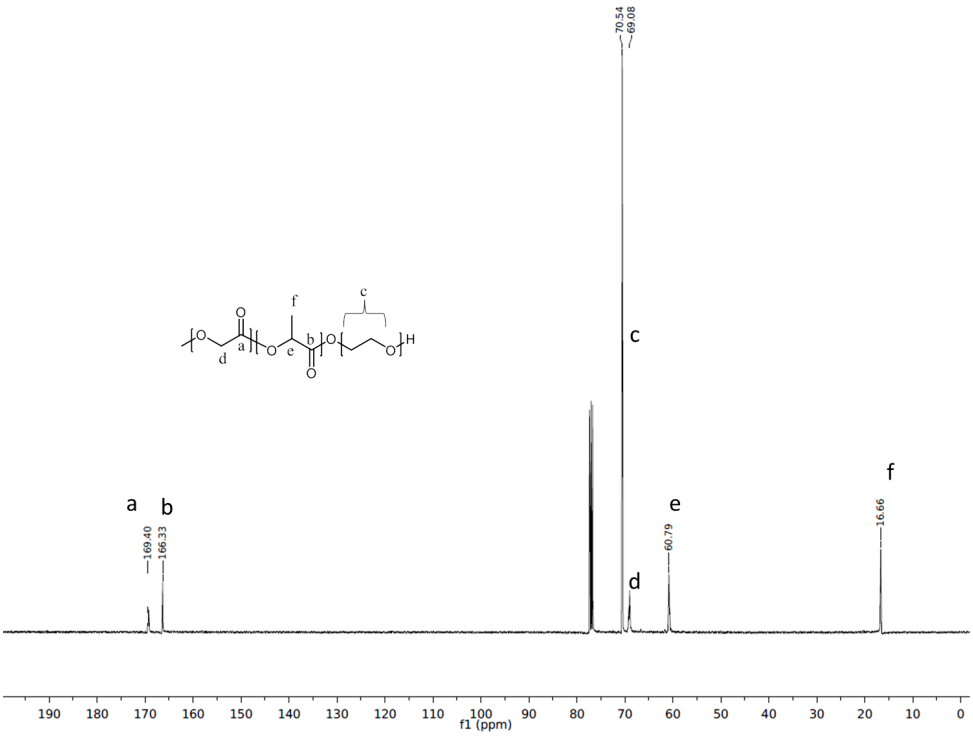


Figure 2.3. ^{13}C NMR of PLGA-PEG-OH

Synthesis of PLGA-PEG-TPP

PLGA-*b*-PEG-OH (0.29 g, 0.03 mmol), 5-carboxypentyl)triphenylphosphonium cation[28] (0.11 g, 0.29 mmol), and DMAP (0.007 g, 0.06 mmol) were dissolved in 3 mL dry CH_2Cl_2. DCC (0.06 g, 0.29 mmol) was dissolved in CH_2Cl_2 (1 mL) and added drop-wise to the reaction mixture 0° C with stirring. The mixture was stirred over night at room temperature. DCU formed was filtered off. To the resulting mixture, 50 mL cold diethyl ether was added to precipitate the polymer. The solid was centrifuged at 5000 rpm for 15 min at 4 °C. The solvent was removed and the solid was lyophilized. The polymer was isolated as a white solid in 99% (0.3 g) yield. ^{1}H NMR ($CHCl_3$-*d*) (Figure 2.4): δ 7.9-7.6 [m, 15H (Ar)], 5.2 [m, 37H (O*CH*CH_3C(O)], 4.8 [m, 73H (O*CH*$_2$C(O))], 3.6 [s, 102H (O*CH*$_2$)], 1.6 [m, 112H, (*CH*$_3$CH)]. ^{13}C NMR ($CHCl_3$-*d*) (Figure 2.5): δ 169.3, 166.3, 135.0, 133.8, 130.3, 118.8, 117.9, 70.5, 69.0, 60.8, 16.7. IR: *v* cm^{-1} 3029 (C-H sp^2), 2944 (C-H sp^3), 2200-2000 (C-H Ar), 1741 (C=O). ^{31}P NMR ($CHCl_3$-*d*) (Figure 2.7): δ 24.62.

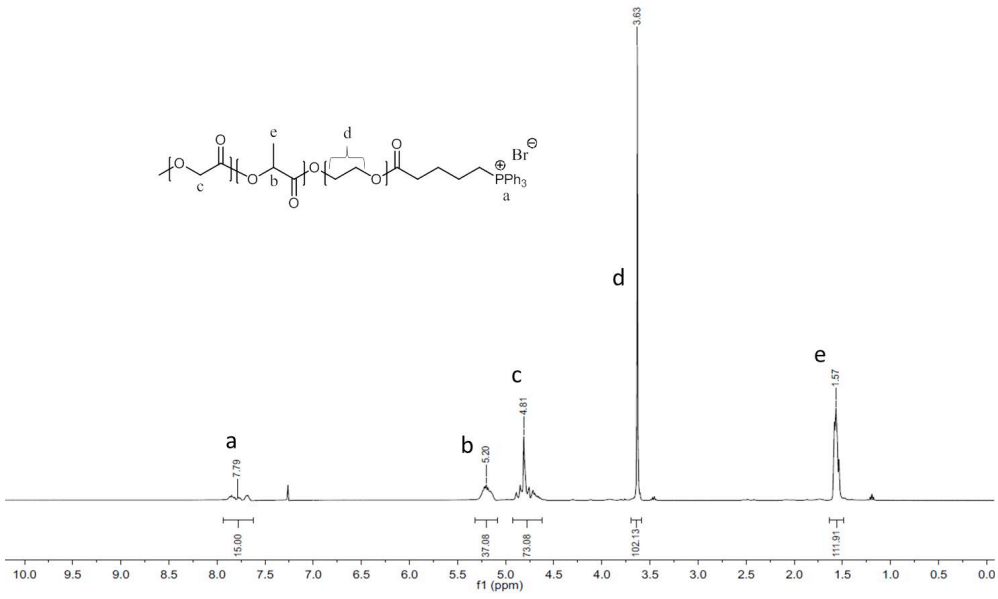


Figure 2.4. ^{1}H NMR of PLGA-PEG-TPP

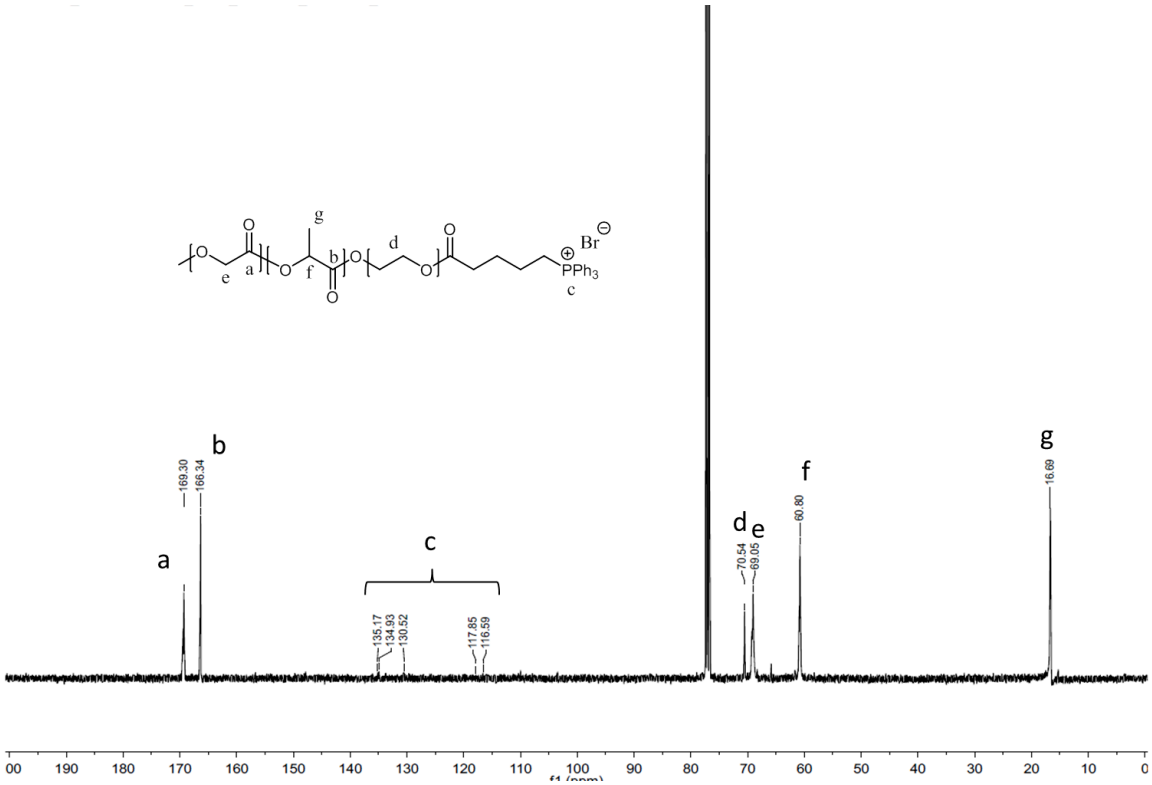


Figure 2.5. ^{13}C NMR of PLGA-PEG-TPP

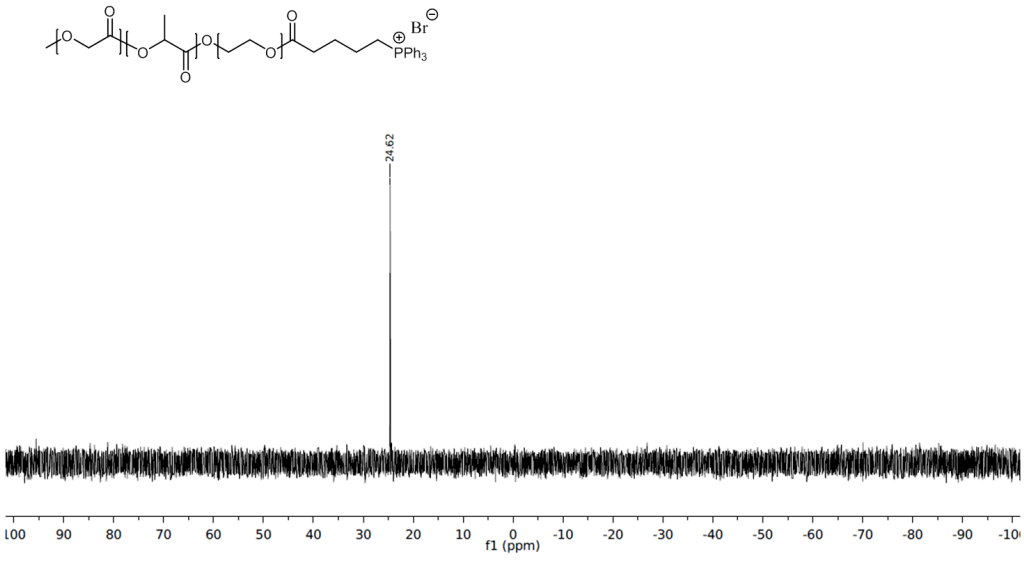


Figure 2.6. ^{31}P NMR of PLGA-PEG-TPP

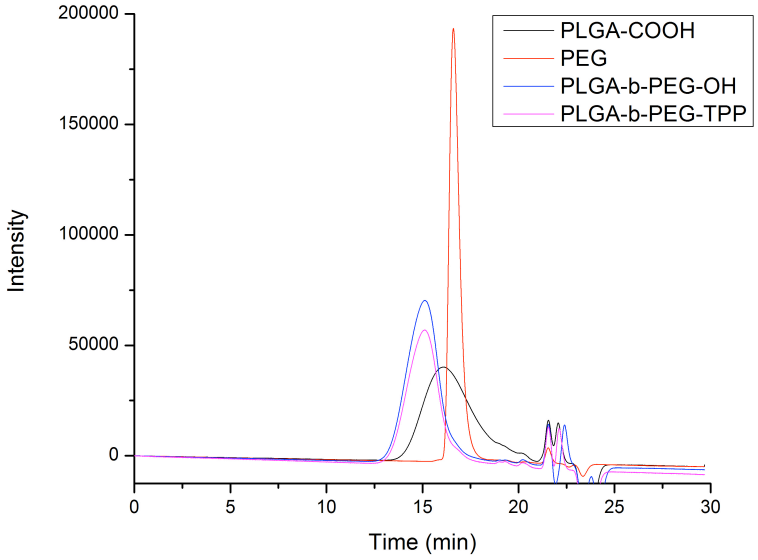


Figure 2.7. GPC plots of PLGA-COOH, PEG-OH, PLGA-PEG-OH, and PLGA-PEG-TPP

Synthesis of PLGA-*b*-PEG-QD.

PLGA-COOH (1.0 mg, 0.15 μmol), EDC (12.4 mg, 80 μmol), NHS (9 mg, 80 μmol) were dissolved in *N,N*-dimethylformamide (3 mL). A 250 μL solution of 8 μM QD-PEG-NH_2 was added. The mixture was stirred at room temperature for 24 h. This solution was filtered through a 100 kDa cutoff amicon filter. The resulting solid was removed from the Amicon filter with the help of nanopure H_2O, lyophilized overnight, and resuspended in DMF. PLGA-*b*-PEG-QDs were characterized using DLS, which gave hydrodynamic diameter of 10.1 ± 0.1 nm, PDI of 0.3.

Synthesis of Targeted and Non Targeted NPs.

NPs were synthesized by the nanoprecipitation method.[18, 29] Briefly, PLGA-*b*-PEG-OH or PLGA-*b*-PEG-TPP in *N,N*-dimethylformamide (DMF) to a final polymer concentration of 5 mg/mL was added drop-wise to nanopure water with constant stirring.

The NPs were stirred for 2 h. Organic solvent was removed by washing three times using an Amicon filtration membrane of 100 kDa cut-off. The NPs were resuspended in nanopure water to a concentration of 5 mg/mL and stored at 4 °C until further use. DLS measurements were carried to determine NP size, PDI, and zeta potential. PLGA-*b*-PEG-TPP-NPs with tunable sizes were synthesized by blending predefined ratios of PLGA-COOH (0, 10, 20, 35, 50, 70, and 90%) with PLGA-*b*-PEG-TPP following the nanoprecipitation method (Table 2.2, Fig. 2.8). Surface charges of PLGA-*b*-PEG-TPP-NPs were varied by blending predefined ratios of PLGA-*b*-PEG-TPP (0, 15, 35, 50, 65, 80, 90, and 100%) with PLGA-*b*-PEG-OH following the above mentioned nanoprecipitation method (Table 2.2, Fig. 2.9). QD-blended-NPs were synthesized following the above mentioned nanoprecipitation method by using PLGA-*b*-PEG-OH or PLGA-*b*-PEG-TPP in DMF with PLGA-*b*-PEG-QD (8 μM solution in DMF) to a final polymer concentration of 5 mg/mL. DLS measurements were carried to determine size, PDI, and zeta potential. All NPs were characterized using TEM. For the synthesis of therapeutics loaded NPs, PLGA-*b*-PEG-OH or PLGA-*b*-PEG-TPP in (50 mg/mL in DMF) was mixed with a predefined amount of therapeutics (10 mg/mL in DMF) and diluted with acetonitrile to a final polymer concentration of 5 mg/mL, this mixture was added drop-wise to nanopure water with constant stirring following the nanoprecipitation method, DLS measurements were carried to determine size, PDI, and zeta potential, drug loading and EE were determined by dissolving the polymeric core and quantifying the amount of the therapeutics in the NPs using HPLC.

Table 2.2. Size and Zeta Potential Variation from Three Independent NP Synthesis

	Diameter (nm)	PDI	Zeta Potential (mV)
100% PLGA-*b*-PEG-TPP NPs			
Experiment 1	84.9 ± 0.1	0.187	34.5 ± 0.6
Experiment 2	84.4 ± 0.8	0.186	32.2 ± 1.6
Experiment 3	71.9 ± 1.4	0.299	30.7 ± 2.6
90% PLGA-*b*-PEG-TPP/10% PLGA-*b*-PEG-OH NPs			
Experiment 1	84.0 ± 0.3	0.192	26.0 ± 0.5
Experiment 2	79.8 ± 1.3	0.181	27.1 ± 2.6
Experiment 3	79.1 ± 0.4	0.216	22.0 ± 1.3
80% PLGA-*b*-PEG-TPP/20% PLGA-*b*-PEG-OH NPs			
Experiment 1	83.9 ± 0.3	0.197	24.3 ± 0.9
Experiment 2	79.9 ± 0.6	0.169	22.6 ± 4.2
Experiment 3	79.4 ± 0.6	0.159	18.9 ± 1.2
65% PLGA-*b*-PEG-TPP/35% PLGA-*b*-PEG-OH			
Experiment 1	84.0 ± 0.3	0.198	22.5 ± 0.7
Experiment 2	79.4 ± 0.2	0.187	13.7 ± 0.8
Experiment 3	79.0 ± 1.5	0.199	12.4 ± 0.9
50% PLGA-*b*-PEG-TPP/50% PLGA-*b*-PEG-OH NPs			
Experiment 1	83.6 ± 0.5	0.209	7.1 ± 0.4
Experiment 2	79.6 ± 0.9	0.174	3.6 ± 0.7
Experiment 3	79.1 ± 1.1	0.237	3.6 ± 0.7
35% PLGA-*b*-PEG-TPP/65% PLGA-*b*-PEG-OH NPs			
Experiment 1	83.5 ± 0.6	0.193	1.3 ± 0.8
Experiment 2	68.9 ± 0.4	0.377	-1.2 ± 1.4
Experiment 3	65.1 ± 0.8	0.211	-0.5 ± 1.0
15% PLGA-*b*-PEG-TPP/85% PLGA-*b*-PEG-OH NPs			
Experiment 1	83.4 ± 0.7	0.195	-12.0 ± 2.9
Experiment 2	79.5 ± 0.5	0.177	-30.3 ± 0.6
Experiment 3	78.4 ± 1.7	0.232	-24.4 ± 0.8
PLGA-*b*-PEG-OH NPs			
Experiment 1	72.5 ± 0.5	0.214	-23.7 ± 0.9
Experiment 2	79.9 ± 0.5	0.191	-31.9 ± 2.4
Experiment 3	79.4 ± 0.2	0.402	-31.0 ± 0.6
90% PLGA-*b*-PEG-TPP/10% PLGA-COOH NPs			
Experiment 1	102.6 ± 1.7	0.289	30.4 ± 0.7
Experiment 2	106.7 ± 1.9	0.251	28.2 ± 1.5
Experiment 3	105.8 ± 1.6	0.291	32.1 ± 4.1
80% PLGA-*b*-PEG-TPP/20% PLGA-COOH NPs			
Experiment 1	171.0 ± 9.6	0.317	30.9 ± 0.8
Experiment 2	171.6 ± 1.9	0.286	30.6 ± 1.1
Experiment 3	176.9 ± 1.1	0.214	33.4 ± 2.2
65% PLGA-*b*-PEG-TPP/35% PLGA-COOH NPs			
Experiment 1	188.3 ± 5.7	0.270	30.9 ± 1.4

Experiment 2	189.9 ± 2.4	0.262	29.1 ± 0.5
Experiment 3	196.7 ± 4.0	0.267	32.6 ± 2.9
50% PLGA-*b*-PEG-TPP/50% PLGA-COOH NPs			
Experiment 1	212.4 ± 1.3	0.268	30.4 ± 2.8
Experiment 2	219.6 ± 4.6	0.222	27.2 ± 2.5
Experiment 3	217.2 ± 2.6	0.228	31.4 ± 4.1
35% PLGA-*b*-PEG-TPP/65% PLGA-COOH NPs			
Experiment 1	320.5 ± 0.3	0.106	30.9 ± 1.6
Experiment 2	321.2 ± 3.2	0.317	29.3 ± 2.0
Experiment 3	334.7 ± 2.1	0.334	31.9 ± 4.4
10% PLGA-*b*-PEG-TPP/90% PLGA-*b*-PEG-OH NPs			
Experiment 1	409.4 ± 2.3	0.356	31.7 ± 1.7
Experiment 2	413.7 ± 2.0	0.125	29.9 ± 2.0
Experiment 3	412.6 ± 0.7	0.108	28.1 ± 1.4

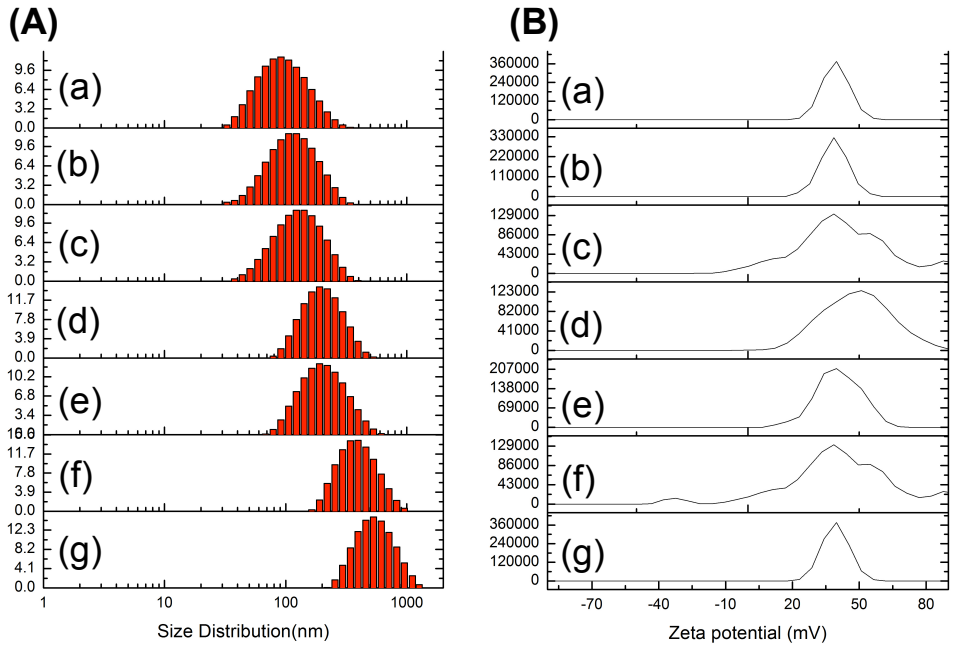


Fig. 2.8. Size Distribution (A) and zeta potential (B) of blended NPs with varied size: (a) 100% PLGA-*b*-PEG-TPP NPs; (b) 90% PLGA-*b*-PEG-TPP/10% PLGA-COOH NPs; (c) 80% PLGA-*b*-PEG-TPP/20% PLGA-COOH NPs; (d) 65% PLGA-*b*-PEG-TPP/35% PLGA-COOH NPs; (e) 50% PLGA-*b*-PEG-TPP/50% PLGA-COOH NPs; (f) 35% PLGA-*b*-PEG-TPP/65% PLGA-COOH NPs; and (g) 10% PLGA-*b*-PEG-TPP/90% PLGA-COOH NPs.

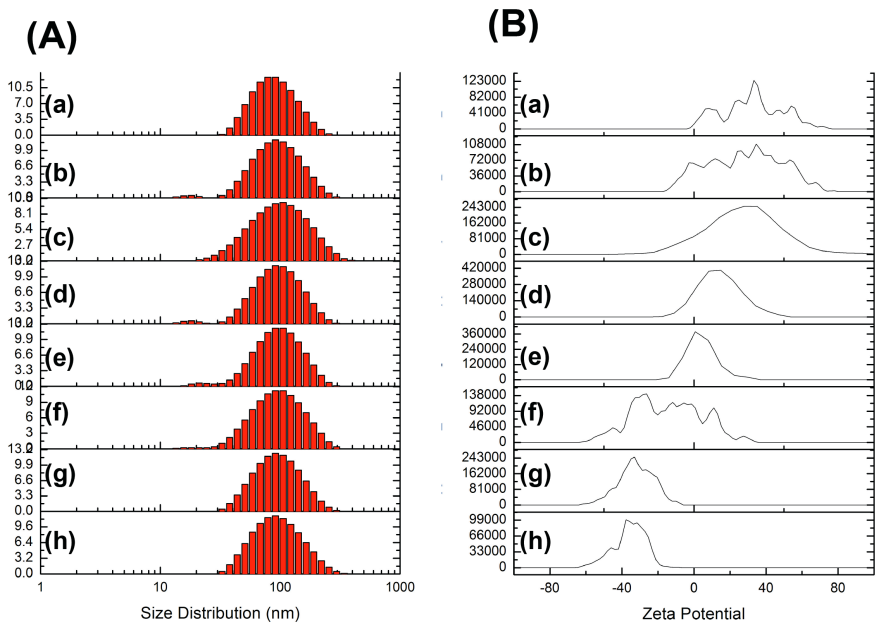


Fig. 2.9. Size distribution (A) and zeta potential (B) and of blended NPs with varied zeta potential: (a) 100% PLGA-*b*-PEG-TPP NPs; (b) 90% PLGA-*b*-PEG-TPP/10% PLGA-*b*-PEG-OH NPs; (c) 80% PLGA-*b*-PEG-TPP/20% PLGA-*b*-PEG-OH NPs; (d) 65% PLGA-*b*-PEG-TPP/35% PLGA-*b*-PEG-OH NPs; (e) 50% PLGA-*b*-PEG-TPP/50% PLGA-*b*-PEG-OH NPs; (f) 35% PLGA-*b*-PEG-TPP/65% PLGA-*b*-PEG-OH NPs; and (g) 15% PLGA-*b*-PEG-TPP/85% PLGA-*b*-PEG-OH NPs; (h) 100% PLGA-*b*-PEG-OH NPs.

Fluorescence Imaging.

HeLa cells were seeded on microscope coverslips (1.0 cm) at a density of 6 x 10^7 cells/mL and grown overnight in DMEM. The medium was changed and fluorescent targeted and non targeted NPs were added to a final NP concentration of 0.5 mg/mL. The cells were incubated for 4 h at 37 °C in 5% CO_2. MitoTracker Green (100 nM) in DMSO and media was added and incubated for 45 min at 37 °C. The medium was removed and the cells were fixed using cold methanol for 30 min. The coverslips were then rinsed with PBS, water, and mounted on slides using mounting media. Images were collected at 320

ms for the FITC and Cy5 channels. In order to determine NP accumulation in the lysosomes of cells, HeLa cells were seeded on microscope coverslips (1.0 cm) at a density of 6 x 10^7 cells/mL and grown overnight in DMEM. The medium was changed and CellLight® Lysosome-GFP *BacMam* 2.0 was added at a concentration of 1.0 μL/10,000 cells and incubated for 24 h at 37 °C under 5% CO_2. The media was replaced and the NPs were added and allowed to internalize for varying times (1 h, 4 h, and 6 h). The medium was removed and the cells were fixed using cold methanol for 30 min. The coverslips were rinsed with PBS, water, and mounted on slides using mounting media [20 mM Tris (pH 8.0), 0.5% N-propyl gallate, and 70% glycerol] . Images were collected at 320 ms for the FITC and Cy5 channels. Images were further analyzed with ImageJ.

Quantification of NPs in the Intracellular Compartments.

QD-blended NPs (10 μM) with varied size and zeta potentials were internalized in HeLa cells (1.5x10^7 cells) for 12 h. After internalization, the mitochondria and the cytosol were isolated using a mitochondria isolation kit for mammalian cells. Cells were isolated by trypsonization and centrifuged (1,800 RPM, 4 °C, 3 min) and washed 3x with 1X PBS. The resulting cell pellet was resuspended in reagent A (800 μL) and incubated on ice for 2 min. To this, reagent B (10 μL) was added and the solution was incubated on ice for 5 min, vortexing the solution every min. This was diluted with reagent C (800 μL) and the solution was centrifuged (700 x g, 4 °C, 10 min). The supernatant was collected and centrifuged (12,000 x g, 4 °C, 15 min). again. The supernatant was collected as the cytosolic fraction and the mitochondrial pellet was resuspended in reagent C (500 μL). The mitochondria were purified by centrifuging (12,000 x g, 4 °C, 5 min). The cytosolic and mitochondrial fractions were then analyzed for Cd concentration from the QD by

inductively coupled plasma mass spectrometry (ICP-MS). A Bicinchoninic acid (BCA) assay was performed on the isolated mitochondrial and cytosolic fractions in order to calculate the amount of Cd/μg of protein isolated.

Assessment of Immune Response by ELISA.

Mouse RAW 264.7 macrophages were plated at a density of 10,000 cells/mL and allowed to grow overnight. Cells were treated with NPs (0.5 mg/mL) and incubated for 12 h. As controls, RAW cells were left untreated or incubated with 0.125 mg/mL of lipopolysaccharide (LPS). An ELISA assay was performed against the cytokines IL-6 and TNF-α according to the manufacture's protocol. Briefly, the cell lysate was incubated in antibody-coated plates for 2 h at RT, incubated with the cytokine-biotin conjugate and streptavidin working solution. The stabilized chromagen was added to each well followed by a stop solution and the absorbance was recorded at 450 nm.

MTT Assay.

The cytotoxic behavior of all the NPs loaded with lonidamine (LND) and alpha-tocopherol succinate (α-TOS), was evaluated using the MTT assay against HeLa cells. Cells (2000 cells/well) were seeded on a 96-well plate in 200 μL of DMEM medium and incubated for 24 h. The cells were treated with empty NPs, targeted and non targeted NPs containing the chemotherapeutics, and the free drug at varying concentrations (with respect to LND or α-TOS) and incubated for 12 h at 37 °C. The medium was changed, and the cells were incubated for additional 60 h. The cells were then treated with 20 μL of MTT (5 mg/mL in PBS) for 5 h. The medium was removed, the cells were lysed with 100 μL of DMSO, and the absorbance of the purple formazan was recorded at 550 nm. Each well was performed in triplicate. All experiments were repeated three times. Cytotoxicity

data (where appropriate) was fitted to a sigmoidal curve and a three parameters logistic model used to calculate the IC_{50}. The IC_{50} values were reported at ±99% confidence intervals. This analysis was performed with Graph Pad Prism (San Diego, U.S.A). For protective activity against neuroblastoma, IMR-32 cells were treated with 20 μM Aβ with/without different concentrations of targeted or non targeted NPs containing curcumin or free curcumin (with respect to curcumin), incubated for 12 h at 37 °C, and MTT assay was performed.

Adipogenesis Assay.

In order to induce adipogenesis, 3T3-L1 preadipocytes were plated on a 96 well plate at a density of 5000 cells per well. The cells were grown to confluence. The anti-adipogenesis properties of targeted and non targeted NPs loaded with 2,4-DNP and free 2,4-DNP was evaluated by internalizing the NPs on day 1 of the adipogenesis assay. Also on day 1, cells were induced to differentiate in a differentiation DMEM media containing 10% FBS and supplemented with 0.5 mM 3-isobutyl-1-methylxanthine (IBMX), 0.5 μM dexamethasone (Dex), 20 nM insulin. On day 3, the induction media was replaced with insulin media containing DMEM, 10% FBS, and 20 nM insulin. After 6 days of treatment, cells were analyzed for triglyceride accumulation using the AdipoRed™ assay. AdipoRed was added to the cells and incubated for 10 min at room temperature. The cells were washed 3 times and resuspended with 1X PBS. The fluorescence was read on the plate reader at the excitation of 485 nm and an emission of 572 nm.

Endocytosis of Targeted and non targeted-QD-blended NPs.

HeLa cells were seeded on microscope coverslips (1.0 cm) at a confluence of 1×10^6 cells per coverslip and grown overnight in a humidified incubator with 5% CO_2 at

37 °C in DMEM. The medium was changed and suspensions targeted and non targeted QD-blended NPs (0.5 mg/mL with respect to NP) were added. The cells were incubated for 1.0, 2.0, and 4.0 h at 37 °C. The medium was removed and the cells were fixed using 4% paraformaldehyde at room temperature. The cells were washed three times with PBS (pH 7.4). The cells were then permeabilized with 0.1% Triton-X 100 in PBS for 10 min followed by five washes using PBS. The cells were then blocked with blocking buffer (PBS, 0.1% goat serum, 0.075% glycine) for 1 h at room temperature. The cells were incubated for 1 h at 37 °C with the early endosomal marker, rabbit polyclonal EEA-1, in a humidified box. After two washes with PBS, the cells were blocked with blocking buffer for 30 min min at RT and then incubated with the secondary Alexa Fluor® 488 goat anti-rabbit antibody for 1 h at 37 °C. After five washes with blocking buffer, the cells were incubated with Hoescht 33258 for 10 min at room temperature. After five washes with PBS and three washes with water, cells were mounted on microscope slides using the mounting solution [20 mM Tris (pH 8.0), 0.5% N-propyl gallate, and 70% glycerol] for imaging. Images were collected at 320 msec for DAPI, FITC, and TRITC channels.

Statistics.

All data were expressed as mean ± S.D (standard deviation). Differences between targeted, non targeted, and free drugs were assessed by the one-way analysis of variance (ANOVA). $P < 0.05$ was considered as the statistical significance level.

Results and Discussion

Development of Targeted Blended NPs.

Advances in understanding the importance of size, shape, and surface charge of

PLGA-based NPs for mitochondrial uptake have the potential of creating new opportunities for the development of targeted delivery vehicles for mitochondrial dysfunction related diseases. We blended a mitochondria targeting functionalized polymer PLGA-*b*-PEG-TPP with PLGA-COOH or with PLGA-*b*-PEG-OH to vary the size and surface charge of the resultant NPs to study the effect of these properties on the mitochondrial uptake to find an optimized formulation. The likelihood of variation in NP properties increases with the number of processing steps required for synthesis. We anticipated that by incorporating the TPP targeting moiety in the polymer before NP synthesis, we would minimize such variability. To deliver therapeutics inside the mitochondria with high efficiency, we synthesized a biodegradable polymer with a terminal -OH group (PLGA-*b*-PEG-OH) to enable the conjugation of TPP to obtain PLGA-*b*-PEG-TPP (Fig. 2.1A). The conjugation of the targeting ligand affected the key properties of the NPs, which include zeta potential, size, cellular uptake, and intracellular trafficking. Synthesis of the blended NPs was carried out by the nanoprecipitation method [18, 29] (Fig. 2.1B). Targeted and non targeted blended NPs with reproducible diameter and surface charges were obtained in over 3 independent nanoprecipitation experiments (Table 2.2).

Optimization of NP Size and Charge for Mitochondrial Uptake.

To optimize the application of PLGA-based NPs as mitochondrial targeted delivery vehicles, a representative and comprehensive study addressing the effect of size and surface charge on the mitochondrial uptake is highly in demand. To achieve this goal, a crucial prerequisite is to fabricate NPs, which will hold different size or surface charge but identical other properties. We blended varied amounts of PLGA-COOH with PLGA-

b-PEG-TPP to construct a library of NPs with varying size and constant surface charge. By using the blending technology, we were able to tune NP size from ~80 to ~410 nm (Fig. 2.9A, Fig. 2.8, Table 2.2), keeping the number of TPP moiety constant as evident from the constant surface charge (Fig. 2.9A). To explore the effect of surface charge on the mitochondrial uptake, we blended predefined amounts of PLGA-*b*-PEG-OH with PLGA-*b*-PEG-TPP. The surface charge was successfully altered without changing the main scaffold and NP size (Fig. 2.9A, Fig. 2.8, Table 2.2). These NP libraries exhibited homogenous populations of similar shape (TEM images, Fig. 2.9B) and enabled us to explore the effect of NP size and charge on the mitochondrial uptake.

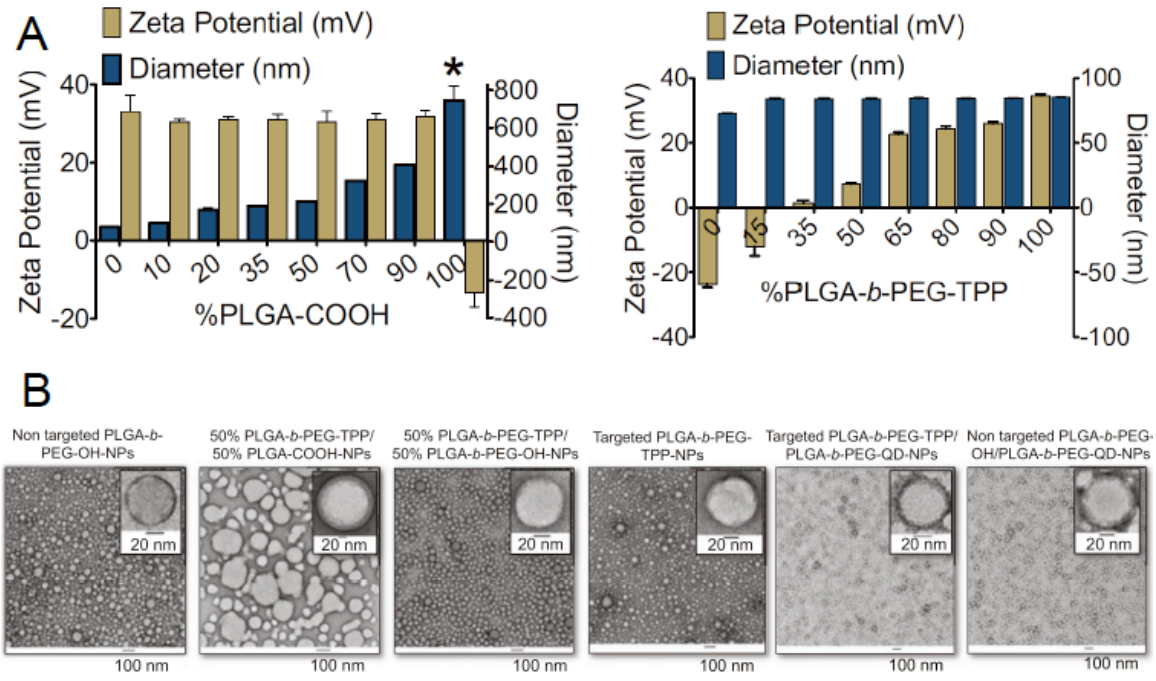


Figure 2.10. (A) (Left) Size and zeta potential variation in blended NPs from PLGA-*b*-PEG-TPP and PLGA-COOH and (Right) size and zeta potential variation in NPs by blending PLGA-*b*-PEG-TPP with PLGA-*b*-PEG-OH. (B) TEM images of targeted and non targeted blended NPs. All the TEM samples were negatively stained with sterile 2% (w/v) uranyl acetate aqueous solution for 15 min except for the QD-blended NPs. *NPs

from 100% PLGA-COOH are unstable and NP diameter varies in between 700 nm to 10 μm based on the batch preparation.

Mitochondria Targeting Properties.

Cellular uptake profile of any NP system reflects its efficiency and bioavailability. Besides the quantitative evaluation of cellular uptake, subcellular location is of crucial importance to assess the effectiveness of the current NP platform. A robust fluorescent reporter quantum dot (QD) was used to investigate the distribution of the targeted and non targeted NPs in human cervical cancer HeLa cells. We used a QD-conjugated amine-terminated PEG, NH_2-PEG-QD, to track the NPs in the intracellular compartments. PLGA-COOH was conjugated to NH_2-PEG-QD to give a tri-block copolymer PLGA-*b*-PEG-QD (Fig. 2.1A). We monitored the internalization of the targeted and non targeted NPs by blending PLGA-*b*-PEG-QD with PLGA-*b*-PEG-TPP and PLGA-*b*-PEG-OH, respectively. Confocal microscopy analysis of the treated cells indicated significantly higher uptake of targeted NPs in the mitochondria of cells compared to the non targeted NPs (Fig. 2.8A). Comparison of fluorescence intensities indicated that the overall uptake of the positively charged targeted NPs was significantly higher; in contrast the cells took up a smaller number of non targeted NPs. Quantitative analysis using ImageJ **"**Colocalization finder**"** plugin revealed a high co-localization of the targeted NPs with the MitoTracker® Green in the mitochondria of cells (Pearson's correlation coefficient, ρ = 0.53). With the non targeted NPs, the red signals of the NPs and the mitochondrial staining differ in position as underlined by a decreased ρ-value (ρ = 0.03).

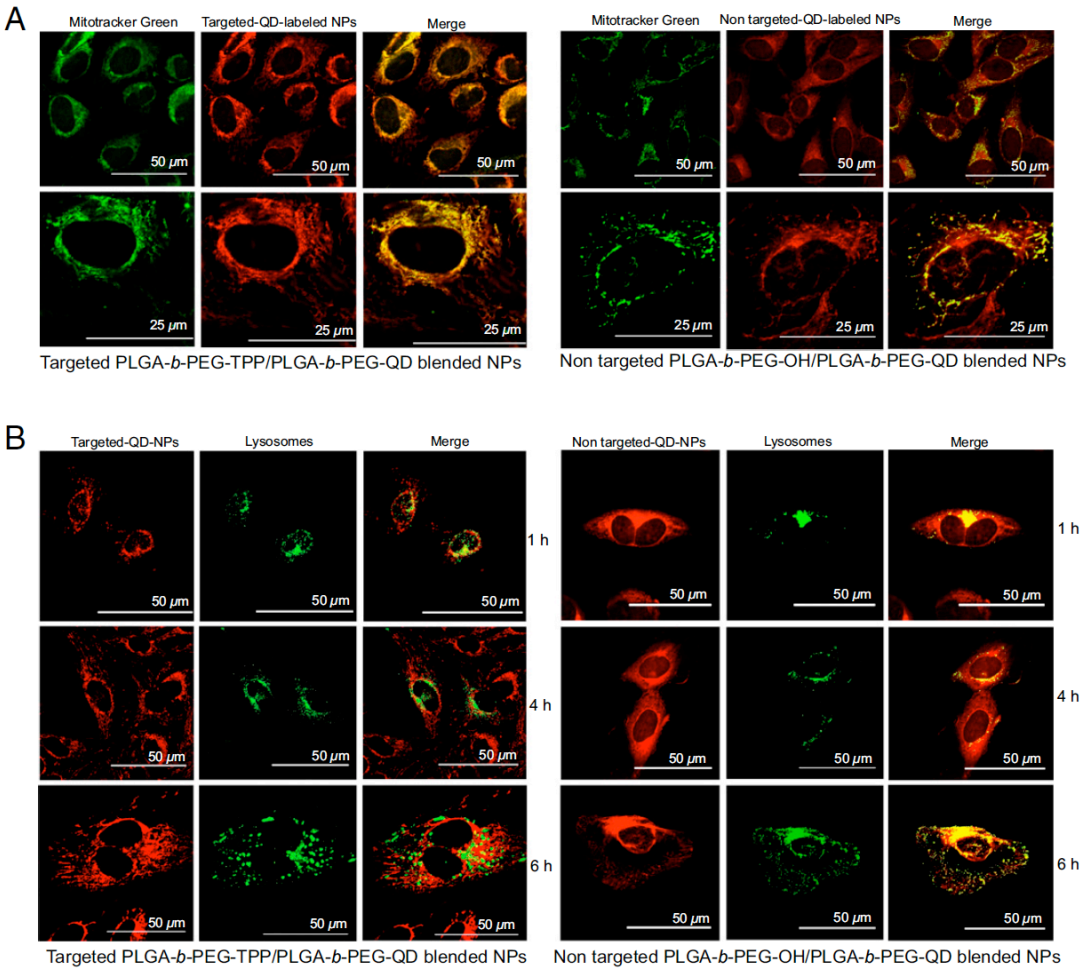


Figure 2.11 (A) Subcellular localization of red fluorescent-targeted PLGA-*b*-PEG-TPP/PLGA-*b*-PEG-QD and non targeted PLGA-*b*-PEG-OH/PLGA-*b*-PEG-QD blended NPs. HeLa cells were exposed to targeted NPs (diameter, 79 nm; zeta potential, 27.4 mV) and non targeted NPs (diameter, 79 nm; zeta potential, -26.5 mV) at 10 μM or left untreated for 4 h. They were subsequently stained with the mitochondrial marker MitoTracker® Green, fixed, and observed with wide field fluorescence microscopy. The merged images and also at higher magnification, show effective overlap of mitochondrial staining (green) and targeted NPs (red), no significant overlap was observed with non targeted NPs. (B) Confocal images of time dependent uptake of targeted PLGA-*b*-PEG-TPP/PLGA-*b*-PEG-QD blended NPs and non targeted PLGA-*b*-PEG-OH/PLGA-*b*-PEG-

QD blended NPs in HeLa cells. Lysosomes were stained with CellLight™ lysosomes-GFP *BacMam* 2.0 (green).

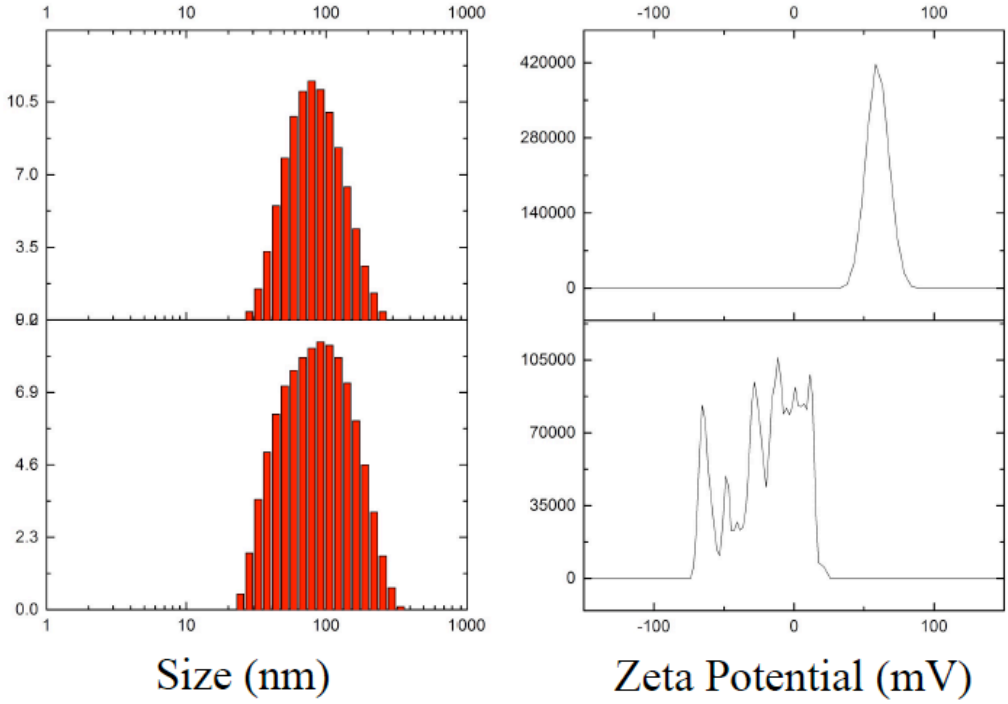


Figure 2.12. DLS and Zeta Potential plots for NPs used for internalization study. (Top – Targeted, Bottom – Non-targeted)

Endosomal and Lysosomal Escape Properties.

Several competing pathways exist in the uptake and intracellular trafficking of NPs. Use of NPs to target mitochondria is often limited by the fact that the NPs are taken up by endosomal pathway and endosomes serve as a barrier to mitochondrial trafficking. We carried out a time-dependent uptake study using early endosome marker EAA-1 to investigate the fusogenic character necessary for efficient endosomal escape of the targeted NPs. The details of immunofluorescence procedure are described in the supporting information. For the targeted NPs, co-localization with the endosomes was observed in the initial 1 h, the co-localization decreased by 2 h (Fig. 2.13), and as the

time progressed, the targeted NPs showed complete endosomal escape and localized in the mitochondria of cells (Fig. 2.11A), however, a significant amount of co-localization with the early endosomes was observed with the non targeted NPs even after 4 h (Fig. 2.13).

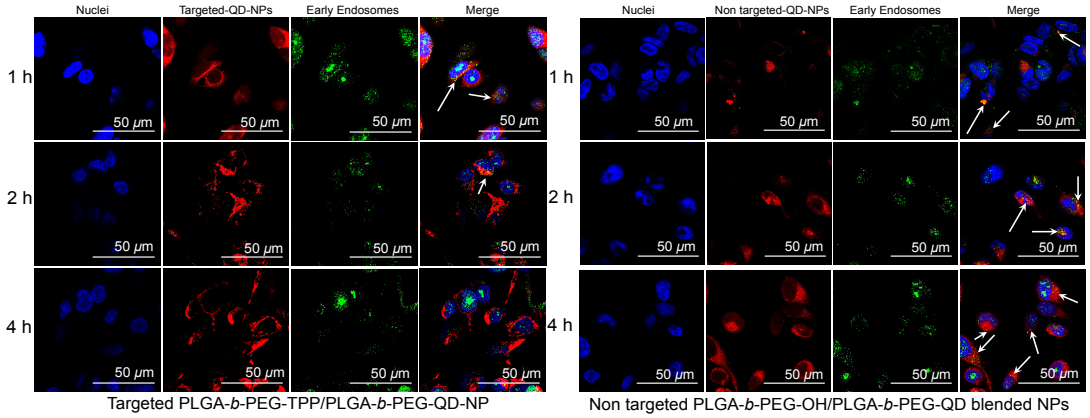


Fig. 2.13. Time dependent Subcellular localization of red fluorescent-targeted PLGA-*b*-PEG-TPP/PLGA-*b*-PEG-QD and non targeted PLGA-*b*-PEG-OH/PLGA-*b*-PEG-QD blended NPs in HeLa cells. The early endosomes were visualized in green by using the early endosome marker EEA-1. Co-localization with the endosomes are represented by white arrows.

The high efficiency of endosomal escape of the targeted NPs can be attributed to their high buffering capacity by acting as 'proton sponges',[30] proton absorbance by buffering positively charged PEG prevents acidification of endosomal vesicles, thereby increasing the ATPase-mediated influx of protons and counter ions which lead to osmotic swelling, endosomal membrane rupture, and the eventual leakage of the NPs into the cytosol and making them accessible for mitochondrial uptake.

To further support our observation that our NPs possess a high endosomal escape property and that a portion of the targeted NPs are not engaged in their trafficking to

lysosomes, we studied a time-dependent co-localization of the NPs with lysosomes (Fig. 2.11B). For the targeted NPs, co-localization with the lysosome decreased over time suggesting lysosomal escape ability whereas the non targeted NPs were distributed in the lysosomes and in the cytoplasm.

Stability and Immunological Effect of the Optimized NP Platform.

A variety of positively charged NPs show interactions with serum proteins which causes aggregation due to the surface adsorption of negatively charged proteins. Serum proteins showed no effect on the size and polydispersity index (PDI) of our targeted NPs upon incubation with 10% FBS in DMEM or 10% FBS in H_2O (Fig. 2.14) for 7 days. This was further supported by the observation that zeta potential of the targeted NPs were changed minimally following the contact with 10% FBS in DMEM or H_2O for 7 days and no visible aggregation of particles was observed (Fig. 2.14). These results suggest that the excellent stability of the targeted NPs in serum renders them suitable for in vivo application.

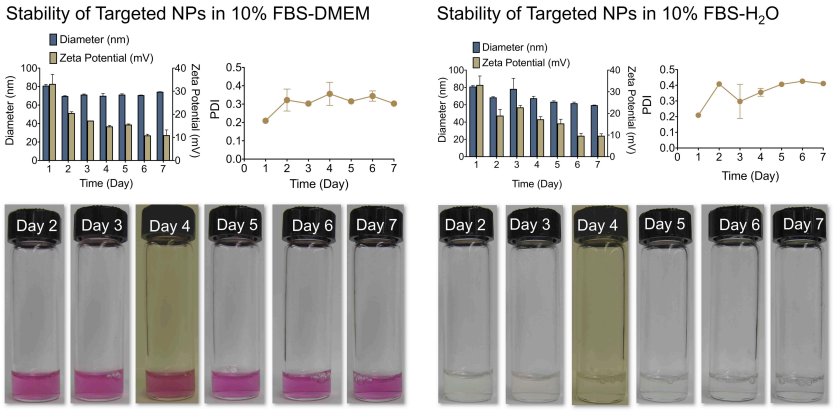


Fig. 2.14. Stability of targeted PLGA-*b*-PEG-TPP-NPs (5 mg/mL) in 10% FBS-DMEM (left) and 10% FBS-H_2O (right) for 7 days at 4 °C.

This engineered NP platform can be used to transport therapeutics for in vivo application only if they do not trigger any immune response. Immune cells in bloodstream and in tissues have a propensity to engulf and eliminate positively charged NPs. Immune responses from the size and charge varied-NPs were measured in terms of the production of pro-inflammatory cytokines interleukin 6 (IL-6) and tumor necrosis factor α (TNF-α) in RAW 264.7 macrophages using an enzyme-linked immunosorbent assay (ELISA). Lipopolysaccharide (LPS) was used as a control. For the charge-varied NPs, we did not observe any pronounced immune response. However, NPs of diameter >200 nm showed TNF-α production (Fig. 2.15). This study confirmed that NPs of suitable size and charge would be non-immunogenic during systemic in vivo studies.

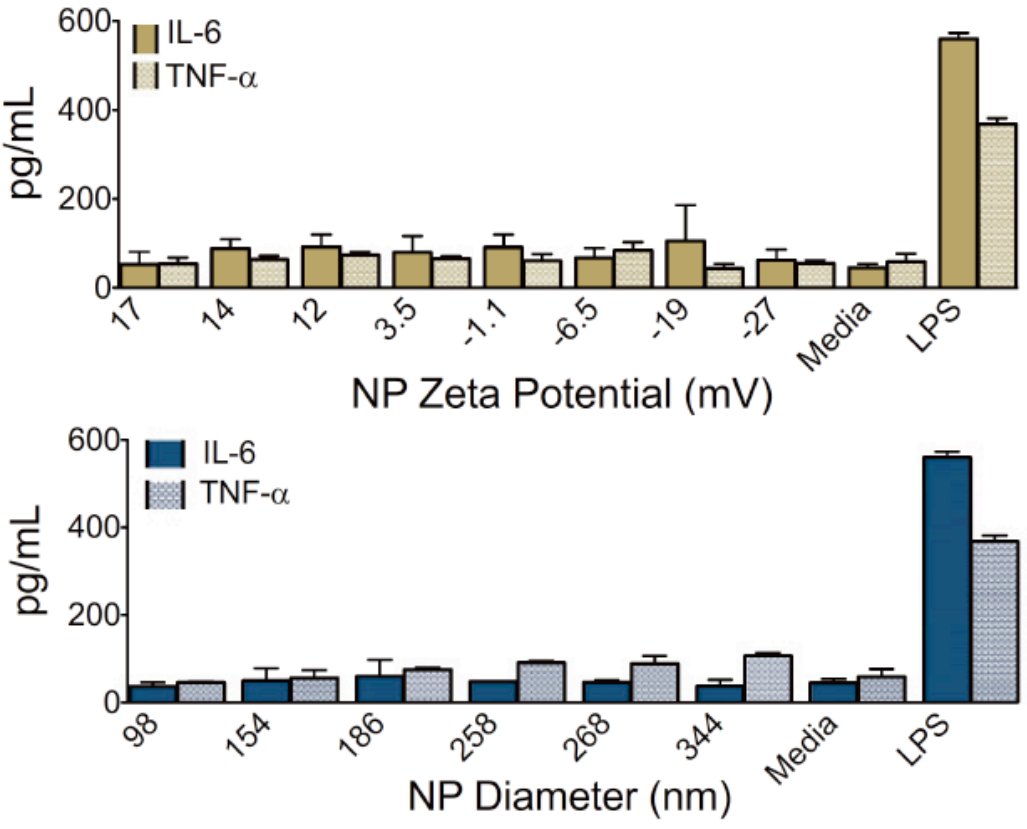


Figure 2.15. Secretion of IL-6, and TNF-α in the media with charge-varied and size-varied NPs (0.5 mg/mL) after 12 h.

Quantification of Targeted NPs in Subcellular Compartments.

On the tour to cross the mitochondrial membranes, NPs are transported across the outer membrane through the general import pore. We anticipated that the complicated structure of the tubular, vesicular or flat cristae and their small connections to the inner mitochondrial membrane might impose constraints on NP mobility and make their diffusion a very complicated size dependent process. The inner membrane potential ($\Delta\Psi_m$), which is negative on the inside, plays a major function in import by exerting an electrophoretic effect on the positively charged species and NPs with a high positive charge are expected to be imported at a lower $\Delta\Psi_m$ than NPs with a lower positive charge. Therefore, we investigated a comparative evaluation of the effect of NP size and charge in crossing the mitochondrial inner membrane (Fig. 2.16A-2.16D) using a model cell line HeLa. We treated HeLa cells with targeted PLGA-*b*-PEG-TPP/PLGA-*b*-PEG-QD blended NPs of different sizes but similar zeta potential. A quantitative investigation using inductively coupled plasma mass spectrometry (ICP-MS) was conducted to estimate the amount of cadmium (Cd) from the QDs internalized by the cells. The mitochondrial uptake of NPs between 80 and 330 nm followed a trend, with maximum uptake occurring at a NP size range of 80-100 nm. Fig. 2.16A shows a histogram of amounts of NPs in the cytosolic and mitochondrial fractions versus NP size. It also indicates that the overall cellular uptake of the NPs is heavily dependent upon particle size (Fig. 2.16B). The effect of NP surface charge on the cellular and mitochondrial uptake (Fig. 2.16C) using a library of NPs with varied surface charge but similar hydrodynamic diameter demonstrated that the negatively charged NPs have no mitochondrial uptake and very little overall cellular uptake was observed (Fig. 2.16D).

Cellular uptake increases as the surface charge reaches to 1.3 mV and remains constant until the surface charge reaches ~22 mV with an increased mitochondrial uptake. We see another jump in the cellular uptake as the surface charge increases to ~34 mV and it saturates. The mitochondrial uptake increases significantly as we move to the more positively charged NPs. This systematic investigation of the effect of NP diameter and surface charge can be very useful in designing optimized NP platforms for mitochondrial trafficking.

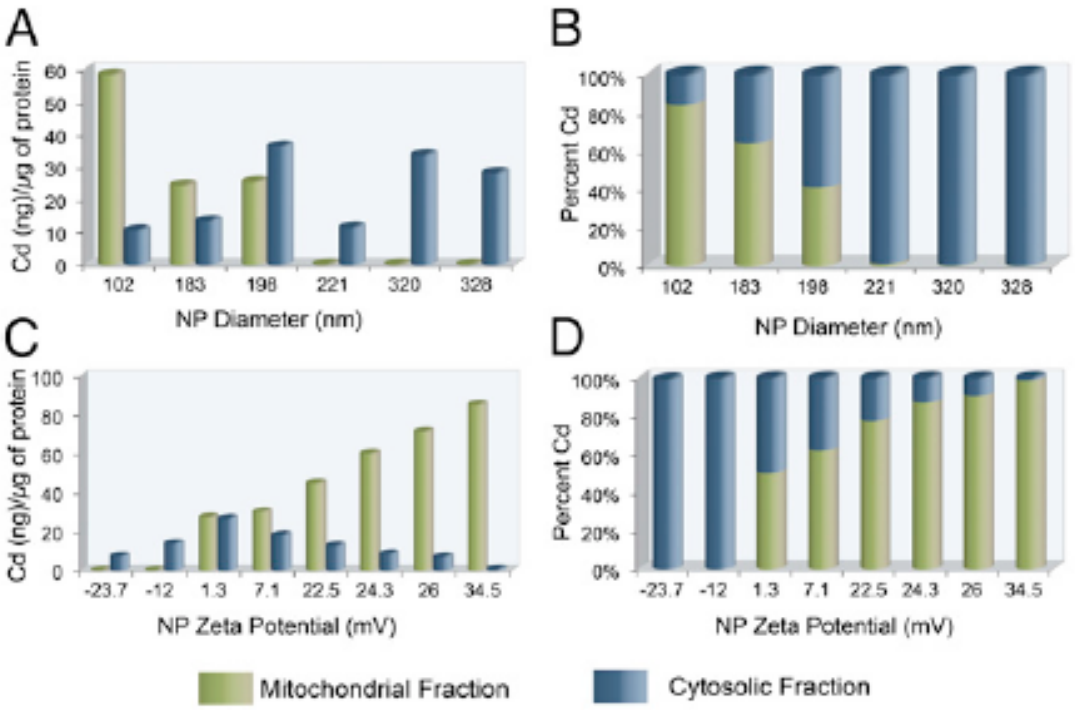


Figure 2.16. Mitochondrial and cytosolic distribution of targeted PLGA-*b*-PEG-TPP/PLGA-*b*-PEG-QD blended NPs in HeLa cells by ICP-MS analysis. (A) Effect of size on uptake of NPs; (B) overall cellular uptake of size-varied NPs, (C) effect of zeta potential on cellular trafficking of NPs; and (D) overall cellular uptake of zeta potential-varied NPs.

Delivery of Therapeutics to Dysfunctional Mitochondria.

As a proof-of-concept demonstration of versatility of this system, we studied delivery of mitochondria acting therapeutics for the management of neurodegeneration, obesity, and cancer. Targeted and non targeted NPs loaded with therapeutics were synthesized with high loading and encapsulation efficiency (EE) using the nanoprecipitation method.

Application in Neurodegenerative Diseases.

Amyloid-like plaques define the neuropathology of AD. Aggregation of the Aβ peptide form amyloid-like lesions and thus reduction of amyloid burden by preventing Aβ represents an attractive approach to improve the therapeutic arsenal for AD. Curcumin is known to inhibit Aβ and the associated mitochondrial oxidative stress; however, its low bioavailability and photodegradation are the major concerns. With such issues in mind, we formulated targeted curcumin loaded NPs to provide photo stability and enhance mitochondrial uptake. In vitro survival assay on human neuroblastoma IMR-32 cells treated with 20 μM Aβ using the [3-(4,5-dimethylthiazole-2-yl)-2,5-diphenyltetrazolium bromide] or MTT assay showed enhanced neuroprotection with the targeted-curcumin-NPs compared to the non targeted-curcumin-NPs or free curcumin (Fig. 2.17) against Aβ which accounts for its targeted delivery to the mitochondria of cells.

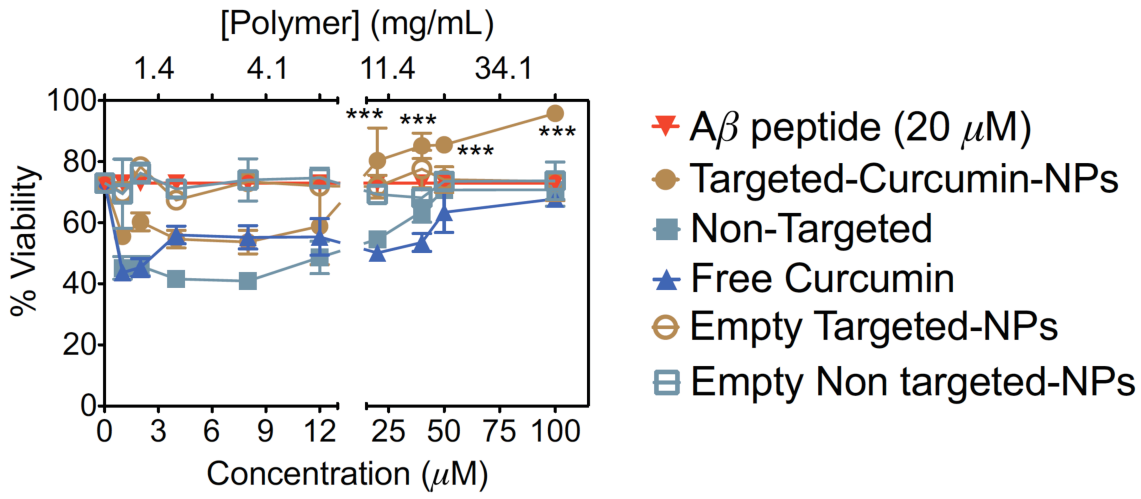


Figure 2.17. Effect on the percent survival of IMR-32 neuroblastoma cells after treatment with targeted-curcumin-NPs, non targeted-curcumin-NPs, and free curcumin against Aβ induced cytotoxicity. Asterisk represents significant differences between targeted-curcumin-NPs, non targeted-curcumin-NPs, and free curcumin according to one-way ANOVA with Tukey post hoc test, $p < 0.001$.

Application in Cancer Chemotherapy.

Mitochondria have emerged as a novel target for cancer treatment and it is possible that targeting mitochondria may provide the means for achieving the long sought after universal cancer treatment. Mitochondria acting LND and α-TOS were selected to demonstrate the applicability of our system in cancer. Selectivity and efficiency of LND or α-TOS against cancer cells depend on their ability to target the mitochondria of cells. To determine the efficacy of our targeted NPs in delivering LND or α-TOS, MTT assays were conducted in HeLa cells. The IC_{50} values with targeted-LND-NPs was ~5 and 108 times less than that for non targeted NPs and the free form, respectively (Fig. 2.18). A higher cytotoxic effect was observed with targeted-α-TOS-NPs (IC_{50}; 75±2 nM) compared to the non targeted-α-TOS-NPs (IC_{50}; 230±4 nM) or free α-TOS (IC_{50}; 381±5

nM) (Fig. 2.18). Preferential localization in the target organelle accounts for the enhanced cytotoxicity of both LND and *α*-TOS encapsulated in the targeted NPs. The finding that the empty PLGA-*b*-PEG-TPP-NPs did not show any cytotoxic effect even at high concentrations rules out the contribution of the delivery system and/or high zeta potentials towards any cellular toxicity (Fig. 2.18).

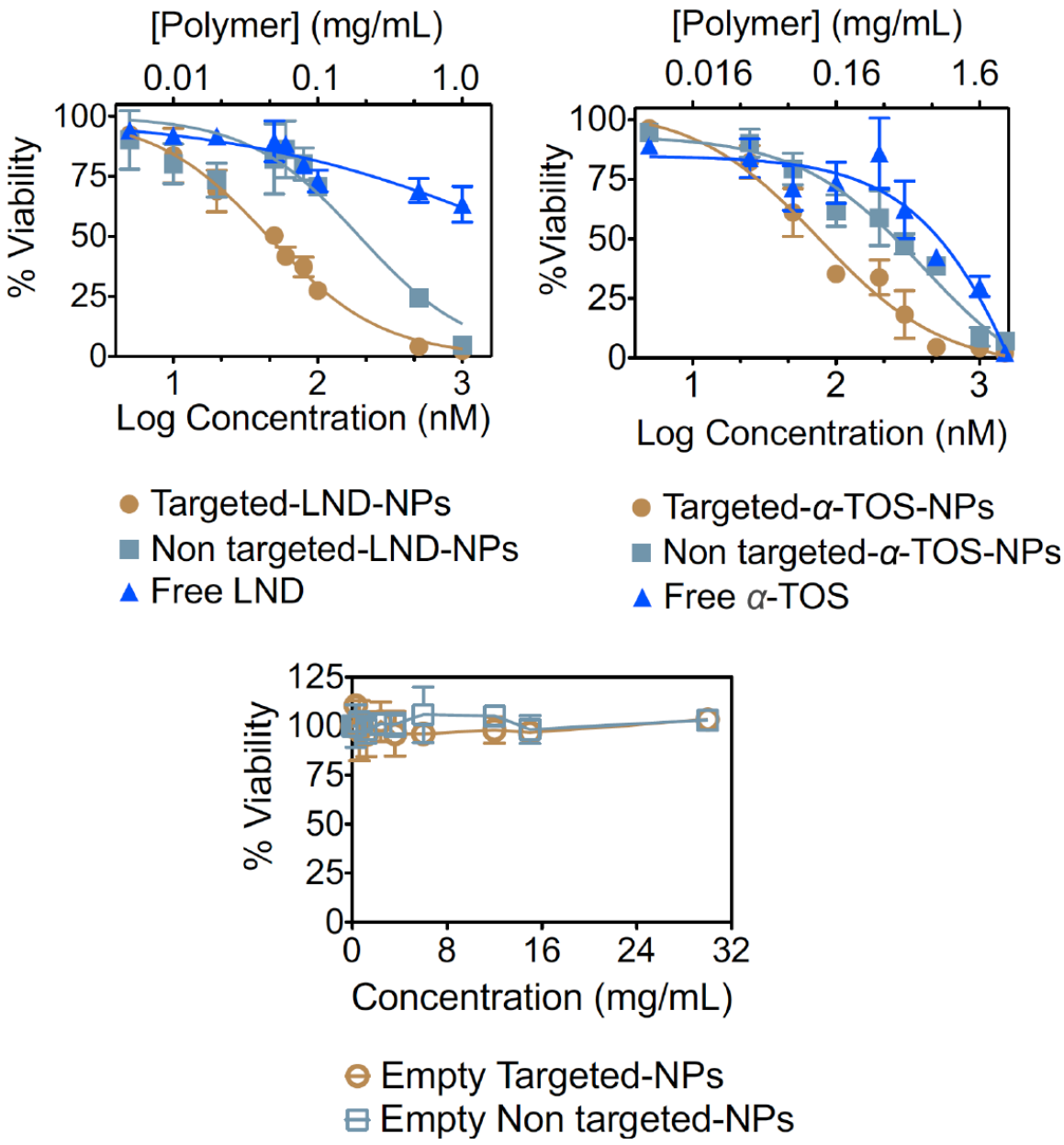


Figure 2.18. Cytotoxicity profiles of targeted-LND-NPs, non targeted-LND-NPs, free

LND, targeted-α-TOS-NPs, non targeted-α-TOS-NPs, free α-TOS in HeLa cells, empty targeted-NPs, and empty non targeted-NPs in HeLa cells.

Possible Application in Obesity.

Obesity has become a global health problem due to its association with various metabolic disorders such as type 2 diabetes, cardiovascular diseases, and certain types of cancer. Due to the undesirable side-effects associated with the currently available anti-obesity medications and limited efficacy, much attention has been focused on developing delivery vehicles that can directly deliver the drugs to the subcellular site to modulate energy metabolism. The notable success of the mitochondrial uncoupler 2,4-DNP as a treatment for human obesity showed that the beneficial effect of uncoupling on energy expenditure is not overwhelmed by compensatory increases in caloric intake. However, the narrow therapeutic window of 2,4-DNP led to the abandonment of its use. A recent study showed that 2,4-DNP linked to TPP in a covalent manner is ineffective at uncoupling.[31] Concern over the narrow therapeutic window and failure of covalently-linked uncoupler indicate that mitochondria-targeted NPs can be promising to direct this uncoupler to the mitochondria of cells. To examine whether encapsulation of 2,4-DNP in the targeted NPs can suppress the induced differentiation of 3T3-L1 pre-adipocytes at a low dosage which is not enough to exert cytotoxicity, 3T3-L1 cells were exposed continuously to 1, 4, 25, and 100 μM targeted-2,4-DNP-NPs (Fig. 2.19, Fig. 2.20) during the differentiation period for 7 days, and then the cell viability and intracellular lipid accumulation were determined, non targeted-2,4-DNP-NPs and free 2,4-DNP were used as controls.

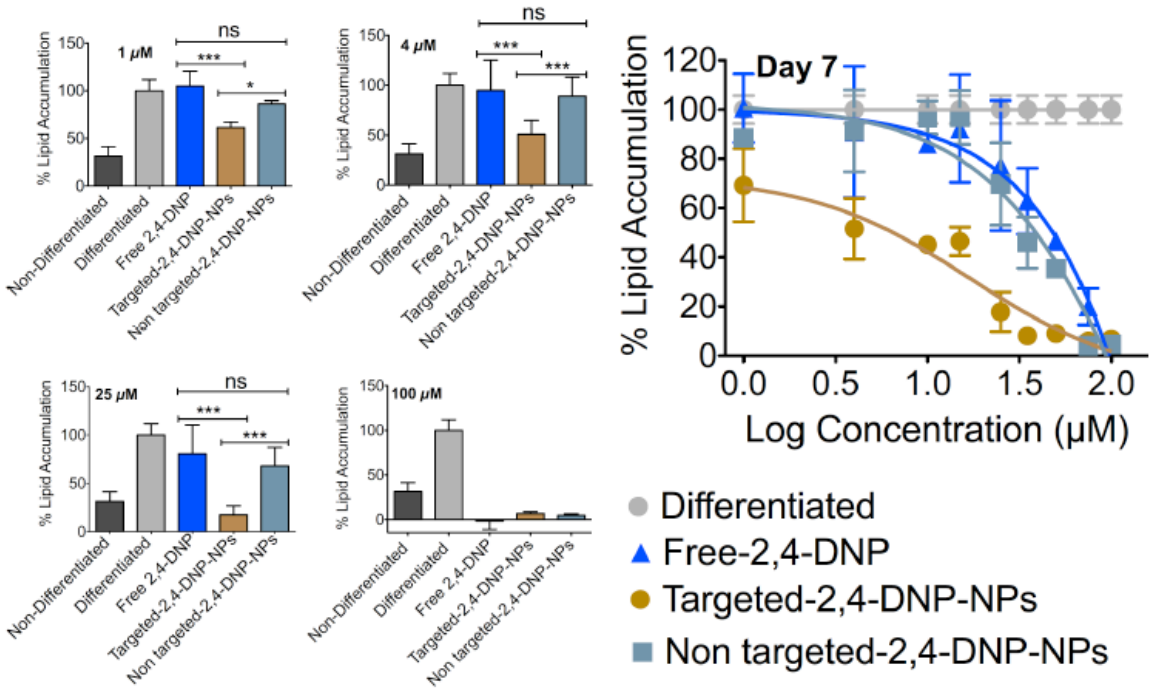


Figure 2.19. Mouse 3T3-L1 preadipocytes were differentiated into adipocytes in the presence of 1 μM, 4 μM, 25 μM, and 100 μM of targeted-2,4-DNP-NPs, non targeted-2,4-DNP-NPs, and free 2,4-DNP for 7 days. Non differentiated cells and completely differentiated cells were used as controls. Intracellular lipids were stained with AdipoRed and percent lipid accumulation was calculated. Inhibition of adipocyte differentiation is shown for day 7. Statistical analyses were performed using one-way ANOVA with Tukey post hoc test. Single and triple asterisks indicate a P value < 0.05 and < 0.001, respectively. Similar results were obtained from two independent experiments. "ns": non significant.

As shown in Fig. 2.20, the presence of 1, 4, or 100 μM targeted-2,4-DNP-NPs during the differentiation period for 7 did not influence the cell viability but showed significant reduction in the lipid accumulation compared to the non targeted-2,4-DNP-NPs or free 2,4-DNP. Free 2,4-DNP at a concentration of 100 μM showed cellular toxicity. These results indicated that 2,4-DNP in the targeted NPs could suppress the

adipocytic differentiation of 3T3-L1 cells at a low concentration (1 or 4 μM) and do not exert a cytotoxic effect on the cells. This is the first report to demonstrate that 2,4-DNP can be delivered to the mitochondria of cells using a targeted polymeric NP system to reduce lipid accumulation at a lower dose compared to the free form for possible application in the management of obesity.

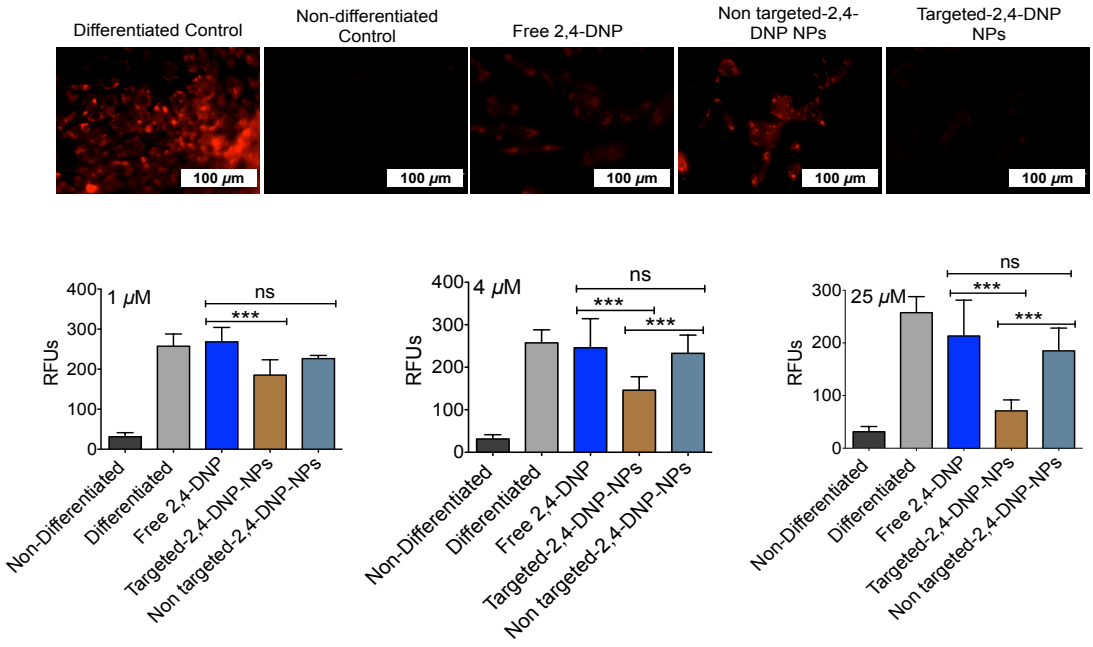


Fig. 2.20. Effect of targeted-2,4-DNP-NPs, non targeted-2,4-DNP-NPs, and free 2,4-DNP on adipocyte differentiation. Top: fluorescence images after 7 days, the cells were stained with Oil-red-O to visualize the degree of lipid accumulation. Bottom: quantification of stained cells using relative fluorescence intensity at different concentrations.

Summary

In this proof-of-concept study, for the first time, we demonstrated that a suitably engineered mitochondria-targeted biodegradable PLGA-based NP delivery system can enter the mitochondria of cells with high efficacy by fine tuning NP surface charge and

size. Not all types of NPs have the ability to enter mitochondria because they cannot cross the complex double membrane due to restrictions in programming surface charge and size. No report thus far indicates the relation between NP size and charge for efficient import to the mitochondria. This rationalized study addressing the effects of surface charge and diameter on the intracellular trafficking of PLGA-based NPs provided us with a generalized approach to design biodegradable nanocarriers for their application in mitochondrial delivery. These targeted NPs can be used in a variety of mitochondrial dysfunction related disorders including AD, obesity, and cancer. This work highlights several exceptionally promising research directions and provides a platform for diverse applications of PLGA based NPs which can be integrated in the near future for imaging and therapy of mitochondrial dysfunction related diseases.

Acknowledgments.

This work was supported by a start-up grant from the National Institutes of Health (P30 GM 092378) and by the Office of the Vice President for Research, UGA to S.D. We thank Dr. Nagesh Kolishetti for helpful discussions. We thank Dr. Srujana Rayalam for assistance with the adipogenesis study. We thank the CVM Cytometry Core Facility for technical assistance with the confocal microscopy analysis.

References

1. Duchen, M. R., Mitochondria in health and disease: perspectives on a new mitochondrial biology. *Mol. Aspects Med.* **2004,** *25*, 365-451.
2. Fulda, S.; Galluzzi, L.; Kroemer, G., Targeting mitochondria for cancer therapy. *Nat. Rev. Drug Discov.* **2010,** *9*, 447-64.

3. Galluzzi, L.; Morselli, E.; Kepp, O.; Vitale, I.; Rigoni, A.; Vacchelli, E.; Michaud, M.; Zischka, H.; Castedo, M.; Kroemer, G., Mitochondrial gateways to cancer. *Mol. Aspects Med.* **2010,** *31*, 1-20.

4. Peer, D.; Karp, J. M.; Hong, S.; Farokhzad, O. C.; Margalit, R.; Langer, R., Nanocarriers as an emerging platform for cancer therapy. *Nat. Nanotechnol.* **2007,** *2*, 751-760.

5. Dhar, S.; Gu, F. X.; Langer, R.; Farokhzad, O. C.; Lippard, S. J., Targeted delivery of cisplatin to prostate cancer cells by aptamer functionalized Pt(IV) prodrug-PLGA-PEG nanoparticles. *Proc. Natl. Acad. Sci. USA* **2008,** *105*, 17356-17361.

6. Hrkach, J.; Von Hoff, D.; Ali, M. M.; Andrianova, E.; Auer, J.; Campbell, T.; De Witt, D.; Figa, M.; Figueiredo, M.; Horhota, A.; Low, S.; McDonnell, K.; Peeke, E.; Retnarajan, B.; Sabnis, A.; Schnipper, E.; Song, J. J.; Song, Y. H.; Summa, J.; Tompsett, D.; Troiano, G.; Hoven, T. V.; Wright, J.; LoRusso, P.; Kantoff, P. W.; Bander, N. H.; Sweeney, C.; Farokhzad, O. C.; Langer, R.; Zale, S., Preclinical development and clinical translation of a PSMA-targeted docetaxel nanoparticle with a differentiated pharmacological profile. *Sci Transl Med* **2012,** *4*, 128ra39-128ra39.

7. Agemy, L.; Friedmann-Morvinski, D.; Kotamraju, V. R.; Roth, L.; Sugahara, K. N.; Girard, O. M.; Mattrey, R. F.; Verma, I. M.; Ruoslahti, E., Targeted nanoparticle enhanced proapoptotic peptide as potential therapy for glioblastoma. *Proc Natl Acad Sci U S A* **2011,** *108*, 17450-17455.

8. Weissig, V.; D'Souza, G. G. M., Mitochondria-targeted drug delivery. *Targeted Deliver. Small Macromol. Drugs* **2010**, 255-273.

9. Boddapati, S. V.; D'Souza, G. G. M.; Erdogan, S.; Torchilin, V. P.; Weissig, V., Organelle-targeted nanocarriers: Specific delivery of liposomal ceramide to mitochondria enhances its cytotoxicity in vitro and in vivo. *Nano Lett.* **2008,** *8*, 2559-2563.

10. Patel, N. R.; Hatziantoniou, S.; Georgopoulos, A.; Demetzos, C.; Torchilin, V. P.; Weissig, V.; D'Souza, G. G. M., Mitochondria-targeted liposomes improve the apoptotic and cytotoxic action of sclareol. *J. Liposome Res.* **2010,** *20*, 244-249.

11. Esumi, K.; Takei, N.; Yoshimura, T., Antioxidant-potentiality of gold-chitosan nanocomposites. *Colloid Surface B* **2003,** *32*, 117-123.

12. Esumi, K.; Houdatsu, H.; Yoshimura, T., Antioxidant action by gold-PAMAM dendrimer nanocomposites. *Langmuir* **2004,** *20*, 2536-2538.

13. Wang, L. M.; Liu, Y.; Li, W.; Jiang, X. M.; Ji, Y. L.; Wu, X. C.; Xu, L. G.; Qiu, Y.; Zhao, K.; Wei, T. T.; Li, Y. F.; Zhao, Y. L.; Chen, C. Y., Selective targeting of gold nanorods at the mitochondria of cancer cells: Implications for cancer therapy. *Nano Lett.* **2011,** *11*, 772-780.

14. Paunesku, T.; Vogt, S.; Lai, B.; Maser, J.; Stojicevic, N.; Thurn, K. T.; Osipo, C.; Liu, H.; Legnini, D.; Wang, Z.; Lee, C.; Woloschak, G. E., Intracellular distribution of TiO2-DNA oligonucleotide nanoconjugates directed to nucleolus and mitochondria indicates sequence specificity. *Nano Lett.* **2007,** *7*, 596-601.

15. Hikosaka, K.; Kim, J.; Kajita, M.; Kanayama, A.; Miyamoto, Y., Platinum nanoparticles have an activity similar to mitochondrial NADH : Ubiquinone oxidoreductase. *Colloid Surface B* **2008,** *66*, 195-200.

16. Kajita, M.; Hikosaka, K.; Iitsuka, M.; Kanayama, A.; Toshima, N.; Miyamoto, Y., Platinum nanoparticle is a useful scavenger of superoxide anion and hydrogen peroxide. *Free Radical Res.* **2007,** *41*, 615-626.

17. Sharma, A.; Soliman, G. M.; Al-Hajaj, N.; Sharma, R.; Maysinger, D.; Kakkar, A., Design and evaluation of multifunctional nanocarriers for selective delivery of coenzyme Q10 to mitochondria. *Biomacromolecules* **2012,** *13*, 239-252.

18. Kolishetti, N.; Dhar, S.; Valencia, P. M.; Lin, L. Q.; Karnik, R.; Lippard, S. J.; Langer, R.; Farokhzad, O. C., Engineering of self-assembled nanoparticle platform for precisely controlled combination drug therapy. *Proc. Natl. Acad. Sci. USA* **2010,** *107*, 17939-17944.

19. Beletsi, A.; Panagi, Z.; Avgoustakis, K., Biodistribution properties of nanoparticles based on mixtures of PLGA with PLGA-PEG diblock copolymers. *Int. J. Pharma.* **2005,** *298*, 233-41.

20. Smith, R. A.; Porteous, C. M.; Gane, A. M.; Murphy, M. P., Delivery of bioactive molecules to mitochondria in vivo. *Proc. Natl. Acad. Sci. USA* **2003,** *100*, 5407-12.

21. Blaikie, F. H.; Brown, S. E.; Samuelsson, L. M.; Brand, M. D.; Smith, R. A. J.; Murphy, M. P., Targeting dinitrophenol to mitochondria: Limitations to the development of a self-limiting mitochondrial protonophore. *Bioscience Rep.* **2006,** *26*, 231-243.

22. Liu, J. K.; Shen, W. L.; Zhao, B. L.; Wang, Y.; Wertz, K.; Weber, P.; Zhang, P. F., Targeting mitochondrial biogenesis for preventing and treating insulin resistance in diabetes and obesity: Hope from natural mitochondrial nutrients. *Adv. Drug Deliver. Rev.* **2009,** *61*, 1343-1352.

23. Wang, F.; Ogasawara, M. A.; Huang, P., Small mitochondria-targeting molecules as anti-cancer agents. *Mol. Aspects Med.* **2010,** *31*, 75-92.

24. Mulik, R. S.; Monkkonen, J.; Juvonen, R. O.; Mahadik, K. R.; Paradkar, A. R., ApoE3 mediated poly(butyl) cyanoacrylate nanoparticles containing curcumin: Study of enhanced activity of curcumin against beta amyloid induced cytotoxicity using in vitro cell culture model. *Mol. Pharmaceutics* **2010,** *7*, 815-825.

25. Ono, K.; Hasegawa, K.; Naiki, H.; Yamada, M., Curcumin has potent anti-amyloidogenic effects for Alzheimer's beta-amyloid fibrils in vitro. *J. Neurosci. Res.* **2004,** *75*, 742-750.

26. Floridi, A.; Paggi, M. G.; Marcante, M. L.; Silvestrini, B.; Caputo, A.; Demartino, C., Lonidamine, a selective inhibitor of aerobic glycolysis of murine tumor-cells. *J. Natl. Cancer I.* **1981,** *66*, 497-499.

27. Neuzil, J.; Dyason, J. C.; Freeman, R.; Dong, L. F.; Prochazka, L.; Wang, X. F.; Scheffler, I.; Ralph, S. J., Mitocans as anti-cancer agents targeting mitochondria: lessons from studies with vitamin E analogues, inhibitors of complex II. *J. Bioenerg. Biomembr.* **2007,** *39*, 65-72.

28. Deroose, F. D.; Clercq, P. J. D., Novel Enatioselective Syntheses of (+)-Biotin. . *J. Org. Chem.*. **1995,** *60*, 321-330.

29. Dhar, S.; Kolishetti, N.; Lippard, S. J.; Farokhzad, O. C., Targeted delivery of a cisplatin prodrug for safer and more effective prostate cancer therapy in vivo. *Proc. Natl. Acad. Sci. USA* **2011,** *108*, 1850-5.

30. Sonawane, N. D.; Szoka, F. C.; Verkman, A. S., Chloride accumulation and swelling in endosomes enhances DNA transfer by polyamine-DNA polyplexes. *J. Biol. Chem.* **2003,** *278*, 44826-44831.

31. Chalmers, S.; Caldwell, S. T.; Quin, C.; Prime, T. A.; James, A. M.; Cairns, A. G.; Murphy, M. P.; McCarron, J. G.; Hartley, R. C., Selective uncoupling of individual mitochondria within a cell using a mitochondria-targeted photoactivated protonophore. *J. Am. Chem. Soc.* **2012,** *134* (2), 758-761.

CHAPTER 3

EX VIVO PROGRAMMING OF DENDRITIC CELLS BY MITOCHONDRIA-TARGETED NANOPARTICLES TO PRODUCE INTERFERON-GAMMA FOR CANCER IMMUNOTHERAPY[1]

[1]Reprinted with the permission of Marrache, S.; Tundup, S.; Harn, D.A.; and Dhar, S. *ACS Nano*, 7, 7392-7402. Copyright 2013, American Chemical Society

Abstract

One of the limitations for clinical applications of dendritic cell (DC)-based cancer immunotherapy is the low potency in generating tumor antigen specific T cell responses. We examined the immunotherapeutic potential of a mitochondria-targeted nanoparticle (NP) based on a biodegradable polymer and zinc phthalocyanine (ZnPc) photosensitizer (T-ZnPc-NPs). Here, we report that tumor antigens generated from treatment of breast cancer cells with T-ZnPc-NPs upon light stimulation activate DCs to produce high levels of interferon-gamma, an important cytokine considered as a product of T and natural killer cells. The remarkable ex vivo DC stimulation ability of this tumor cell supernatant is a result of an interleukin (IL)-12/IL-18 autocrine effect. These findings contribute to the understanding of how in situ light activation amplifies the host immune responses when NPs deliver the photosensitizer to the mitochondria and open up the possibility of using mitochondria-targeted-NP-treated, light-activated cancer cell supernatants as possible vaccines.

Introduction

Host's dysfunctional immune system assists tumors to evade immunosurveillance.[1] However, the immune system when properly stimulated can cause eradication of cancer cells.[2] Tumor immunity involves a team play of cytokines and effector cells. One cytokine that plays a central role in coordinating tumor immune responses is interferon-gamma (IFN-γ). Immature dendritic cells (iDCs) secrete cytokines to initiate and enhance both innate and acquired immunity, detect and capture antigens, undergo a maturation process, and prime immune responses by activating naïve T cells. Use of DCs for clinical cancer immunotherapy can be extremely attractive.[3, 4] DCs are

professional antigen presenting cells (APCs), which possess the entire array of antigen-presenting and co-stimulatory molecules. One of the major limitations for clinical application of DCs is the low potency in generating tumor antigen specific $CD8^+$ T cell responses *in vivo*.[5, 6] Infectious agents activate DCs to secret interleukin (IL)-12, which subsequently induces IFN-γ production by natural killer (NK) cells and directs T helper cell type 1 (Th1) development. We hypothesized that *ex vivo* engineering of DCs to produce IFN-γ for increased T-cell activity and development of a Th1-type immune response can serve as an alternative therapeutic modality for metastatic cancer. Photodynamic therapy (PDT), an anti-tumor therapeutic modality that has approval for the treatment of oncological diseases, involves administration of a photosensitizer (PS) followed by illumination of the tumor with a long wavelength (600-800 nm) light. PDT produces reactive oxygen species (ROS) resulting vascular shutdown, cancer cell apoptosis, and the induction of a host immune response.[7, 8] Preclinical and clinical techniques of this method of cancer treatment are still being optimized to address that PDT sometimes fails to eradicate the targeted tumor and to enhance its immune boosting properties. We speculated that these failures may in part arise from inhomogeneous delivery of PS within the tumor, in particular the inability to reach its target organelle, the mitochondria of cells, and the inability to produce short-lived singlet oxygen ($^1O_2$) in the mitochondria of tumor cells. Those PS that accumulate inside the mitochondria induce apoptosis upon photo-irradiation, whereas those that bind to the non-mitochondrial compartments kill cells less efficiently by a non-apoptotic mechanism. Photodynamically induced mitochondrial apoptosis induces signal transduction pathways, which participate in the development of immune responses. Thus, we conjectured that exposing DCs *ex*

vivo to tumor cell supernatant generated from mitochondria-targeted light activated cancer cells may unravel the unknown pathways, which can be used to improve DC-based cancer immunotherapy. Thus we ask whether targeting mitochondria with an engineered biodegradable nanoparticle (NP) containing a mitochondria acting PS such as zinc phthalocyanine (ZnPc),[9] induction of mitochondrial apoptosis after light stimulation, and activation of DCs *ex vivo* with cancer cell antigens can induce immunity. Polymeric NPs of poly(lactide-*co*-glycolide)-*b*-polyethyleneglycol (PLGA-*b*-PEG) block copolymers are especially promising as drug delivery vehicles.[10-16] We recently constructed a targeted functionalized polymer using PLGA-*b*-PEG and a lipophilic triphenyl phosphonium (TPP) cation[17] for mitochondria-targeted delivery of payloads.[18] Targeted-NPs from PLGA-*b*-PEG-TPP takes the advantage of substantial negative mitochondrial inner membrane potential ($\Delta\psi_m$) to deliver cargos into the mitochondria.[18] By using such an engineered vehicle to target the intracellular organelle mitochondria, we observed that treatment of DCs with breast cancer cell supernatant activated with mitochondria-targeted PDT shows significant secretion of IFN-γ. To best of our knowledge this is the first report, which demonstrates the ability of mitochondria-targeted system to stimulate murine bone marrow derived DCs (BMDCs) *ex vivo* to secret IFN-$\boldsymbol{\gamma}$**,** the most versatile player of immune activation. By highlighting the importance of mitochondria targeted PDT of breast cancer and subsequent cytokine secretion by BMDCs receiving stimulation with mitochondria targeted PDT treated cancer cell, our data provide a model considering *ex vivo* manipulation of DC function for clinical applications. In this report, we discuss *ex vivo* IFN-γ production pathways from DCs

upon stimulation with mitochondria-targeted-PDT-activated breast tumor cell antigens (Figure 3.1).

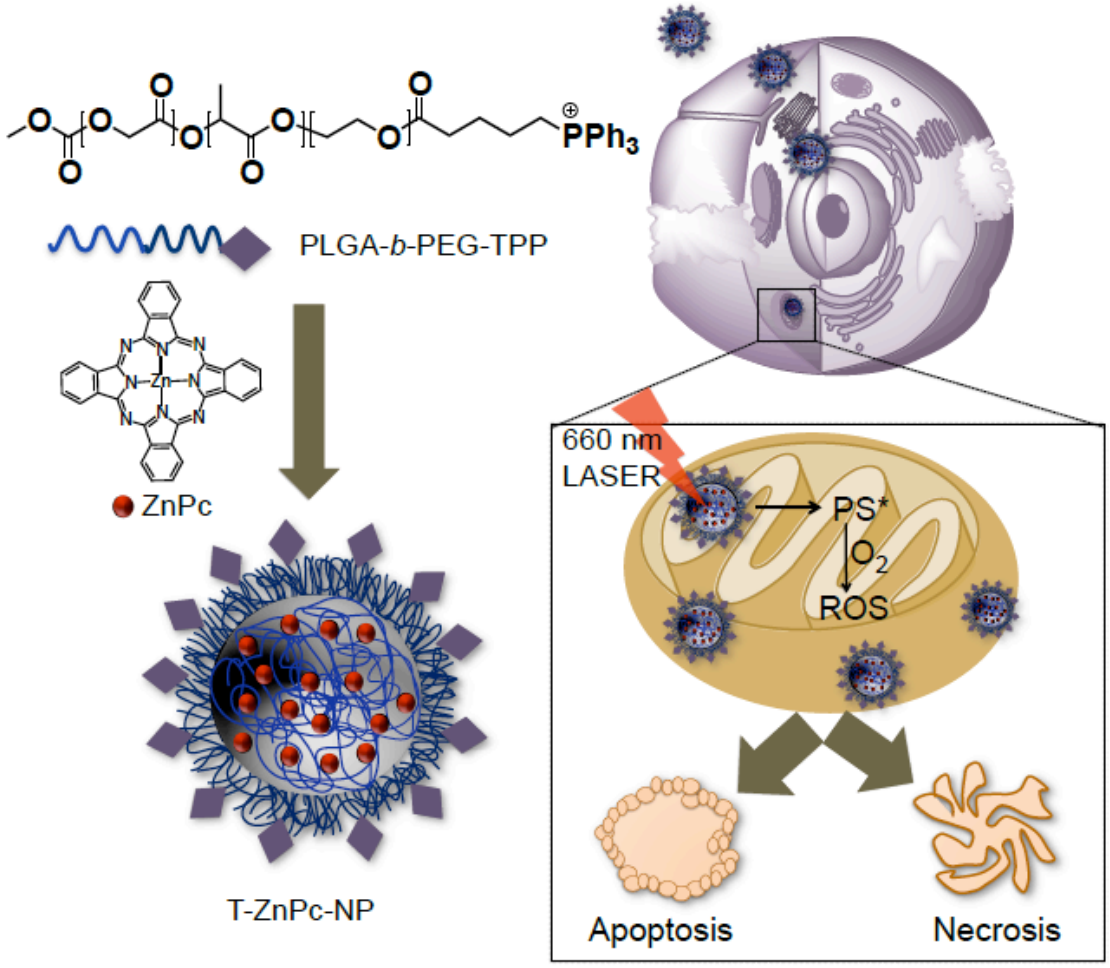


Figure 3.1. Action of mitochondria-targeted NPs upon light activation inside the mitochondria to produce ROS which causes cell death via apoptosis and necrosis

EXPERIMENTAL SECTION

Materials and Instrumentations

All chemicals were received and used without further purification unless otherwise noted. PLGA-COOH of inherent viscosity of 0.18 dL/g was purchased from Lactel. HO-PEG-OH (MW 3350), 4-dimethylaminopyridine (DMAP), N,N'-

dicyclohexylcarbodiimide (DCC), Zinc phthalocyanine (ZnPc), lonidamine (LND), and 3-(4,5-dimethylthiazol-2-yl)-2,5-diphenyltetrazolium bromide (MTT) were purchased from Sigma-Aldrich. PLGA-b-PEG-OH, and PLGA-b-PEG-TPP[2] were synthesized according to the literature methods. Granulocyte-macrophage colony-stimulating factor (GM-CSF) was purchased from R&D systems. Cytokines were tested using BD OptEIA mouse enzyme-linked immunosorbent assay (ELISA) kits.

Distilled water was purified by passage through a Millipore Milli-Q Biocel water purification system (18.2 MΩ) containing a 0.22 μm filter. Dynamic light scattering (DLS) measurements were carried out using a Malvern Zetasizer Nano ZS system. ^{1}H, ^{13}C, and ^{32}P NMR spectra were recorded on a 400 MHz Varian NMR spectrometer. Gel permeation chromatographic (GPC) analyses were performed on Shimadzu LC20-AD prominence liquid chromatographer equipped with a RI detector, molecular weights were calculated using a conventional calibration curve constructed from narrow polystyrene standards. Optical measurements were carried out on a NanoDrop 2000 spectrophotometer. HPLC analyses were made on an Agilent 1200 series instrument equipped with a multi-wavelength UV-visible and a fluorescence detector. LASER irradiation was performed using a Melles Griot 660 nm 56 ICS series diode laser equipped with a fiber optic cable in a dark environment. TEM images were taken in a Tecnai 20 FEM microscope. Flow cytometry studies were performed on a BD LSR II flow cytometer equipped with digital acquisition using FACSDiva v6. Plate reader analysis was performed on a Bio-Tek Synergy HT microplate reader.

Cell line and Cell Culture.

Human cervical cancer HeLa, human breast adenocarcinoma MCF-7, and primary hMSC were procured from the American type culture collection (ATCC). HeLa and MCF-7 cells were grown at 37 °C in 5% CO_2 in Dulbecco's Modified Eagle Medium (DMEM) medium supplemented with 10% fetal bovine serum (FBS) and 1% penicillin/streptomycin. MSC cells were grown in MSC basal medium supplemented with MSC growth kit-low serum components and 2% FBS. Cells were passed every 3 to 4 days and restarted from frozen stocks upon reaching pass number 20 for MCF-7, HeLa and 3 for MSC.

Animals.

Animals were obtained from Jackson Laboratory and handled in accordance with "The guide for the Care and Use of Laboratory Animals" of American Association for Accreditation of Laboratory Animal Care (AAALAC), Animal Welfare Act (AWA), and other applicable federal and state guidelines. All animal work presented here was approved by Institutional Animal Care and Use Committee (IACUC) of University of Georgia (UGA).

Generation of Immature BMDCs.

BMDCs were isolated by Dr. Smanla Tundup from the department of Infectious diseases following the protocol mentioned below. BMDCs were isolated from 6-8 weeks old C57BL/6 mice. Mice were euthanized and bone marrows were isolated by flushing mouse femurs in Roswell Park Memorial Institute medium (RPMI) 1640. The harvested cells were centrifuged at 1250 rpm for 10 min and the resulting pellet was resuspended in ice-cold 2 mL of buffer to lyse erythrocytes. The cells were counted, resuspended and transferred to petri dishes at the final concentration of 1.5×10^6 cells/mL. To this culture

granulocyte-macrophage colony-stimulating factor (GM-CSF) (20 ng/mL) was added to generate BMDCs. Media was changed on days 2 and 4. On day 6 cells were processed further to obtain pure DC population by subjecting cells to MACS bead purification using anti-CD11c antibody as per manufacturer's instructions. DC purity was tested by incubating BMDCs with LPS (100 ng/mL) and measured the surface expression of CD11c. DCs were found to be >90% pure.

Synthesis of triphenylphosphoniumpentanoic acid (TPP)

5-bromo-pentanoic acid (0.94 g, 5.2 mmol) and triphenyl phosphine (1.5 g, 5.4 mmol) were dissolve in acetonitrile (25 mL) and heated to a reflux under nitrogen for 24 h. The solution was cooled to room temperature and concentrated under reduced pressure. The resulting solid was washed with hexanes (2 x 15 mL) and diethyl ether (2 x 20 mL). The resulting solid was filtered off and dried under vacuum to produce a 95.7% yield.

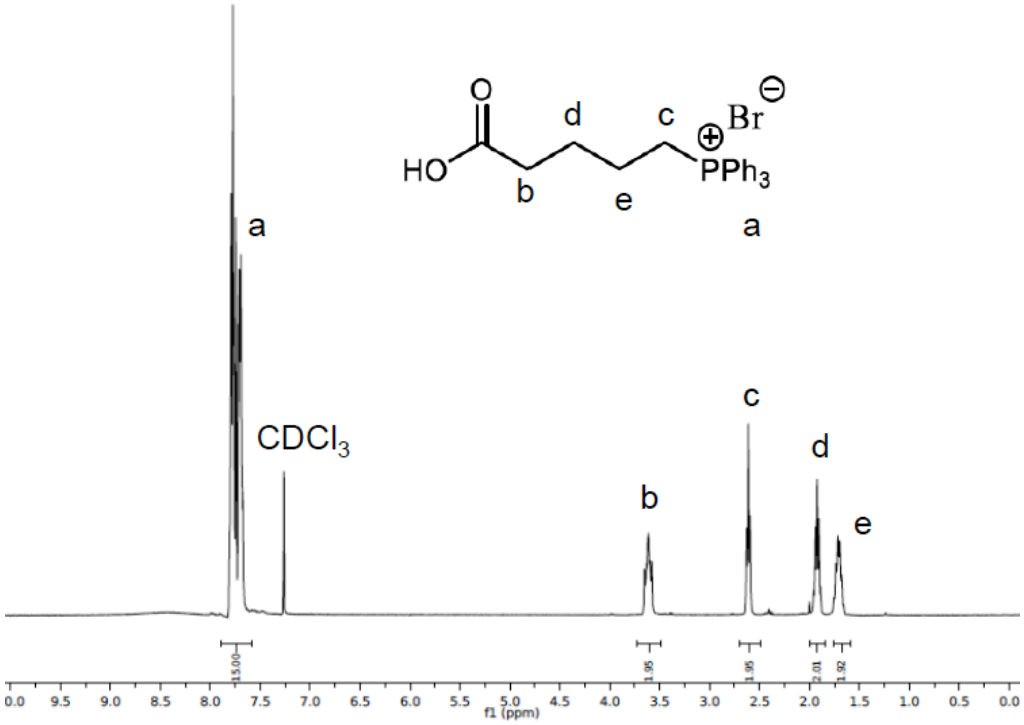


Figure 3.2. Proton NMR of TPP-Pentanoic Acid

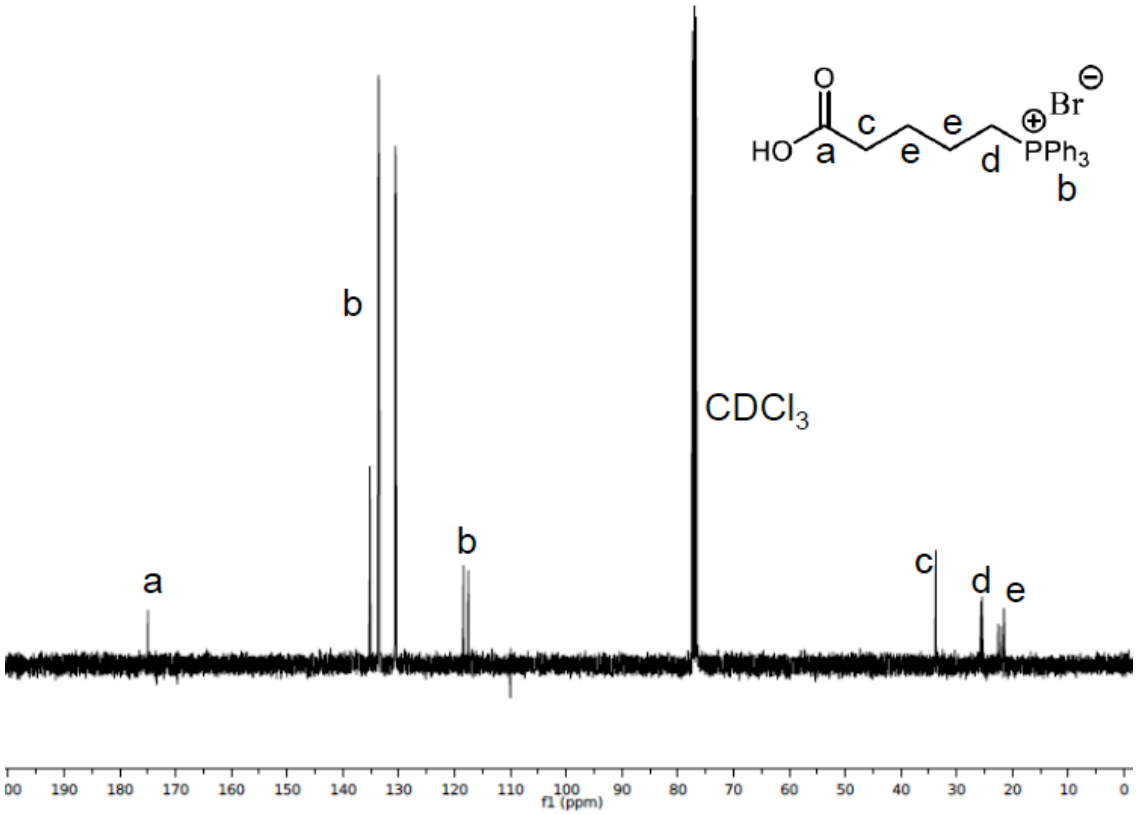


Figure 3.3. Carbon NMR of TPP-Pentanoic Acid

Synthesis of Empty targeted and Non targeted-NPs.

Empty NPs were synthesized by the nanoprecipitation method.[4,5] Briefly, PLGA-*b*-PEG-OH or PLGA-*b*-PEG-TPP in N,N-dimethylformamide (DMF) to a final polymer concentration of 5 mg/mL was added drop-wise to nanopure water with constant stirring. The NPs were stirred for 2 h. Organic solvent was removed by washing three times using an amicon filtration membrane of 100 kDa cut-off. The NPs were resuspended in nanopure water and stored at 4 °C until further use. DLS measurements were carried to determine size, polydispersity index (PDI), and zeta potential of the NPs. NPs were characterized using TEM at an acceleration voltage of 200 kV. The TEM samples were prepared by depositing 8 μL of the NPs (5 mg/mL) onto a 200-mesh carbon-coated

copper grid. Samples were blotted away after 15 min and grids were negatively stained with sterile 2% (w/v) uranyl acetate aqueous solution for 15 min.

Synthesis of ZnPc or LND-encapsulated NPs.

NPs were synthesized by the nanoprecipitation method. Briefly, PLGA-*b*-PEG-OH or PLGA-*b*-PEG-TPP in (50 mg/mL in DMF) was mixed with a 30% feed of ZnPc (10 mg/mL in DMF) and diluted with DMF to a final polymer concentration of 5 mg/mL. This mixture was added drop-wise to nanopure water with constant stirring. The NPs were stirred for 2 h at room temperature. Organic solvent was removed by washing three times using a 100 kDa cut-off Amicon filtration membrane. The NPs were resuspended in nanopure water and stored at 4 °C until further use. DLS measurements were carried to determine size, PDI, and zeta potential. NPs were characterized using TEM at an acceleration voltage of 200 kV. The TEM samples were prepared by depositing 8 μL of the NPs (5 mg/mL) onto a 200-mesh carbon-coated copper grid. Samples were blotted away after 15 min and grids were negatively stained with sterile 2% (w/v) uranyl acetate aqueous solution for 15 min. ZnPc loading and EE were determined by dissolving the polymeric core with 0.1 M aqueous NaOH and quantifying the amount of ZnPc in the NPs using HPLC (wavelength used: 670 nm).

For LND-encapsulated NPs, PLGA-*b*-PEG-OH or PLGA-*b*-PEG-TPP in (50 mg/mL in DMF) was mixed with a predefined amount of LND (10 mg/mL in DMSO) and diluted with DMF to a final polymer concentration of 5 mg/mL. This mixture was added drop-wise to nanopure water with constant stirring. The NPs were stirred for 2 h at room temperature. Organic solvent was removed by washing three times using a 100 kDa cut-off Amicon filtration membrane. The NPs were resuspended in nanopure water and

stored at 4 °C until further use. DLS measurements were carried to determine size, PDI, and zeta potential. LND loading and EE were determined by dissolving the polymeric core with 0.1 M aqueous NaOH and quantifying the amount of LND in the NPs using HPLC (wavelength used: 297 nm).

Determination of ZnPc and LND Loading and Encapsulation Efficiency.

Loading and EE of ZnPc and LND in NPs were calculated by dissolving the polymeric core by mixing equal portions of the NP solution and 0.1 M NaOH, followed by dilution with a 50:50 water:acetonitrile mixture, and subsequent HPLC analysis. Drug loading is defined as the mass fraction of drug in the NPs, whereas EE is the fraction of initial drug that is encapsulated in the NPs.

Cytotoxicity Assay.

The cytotoxic behavior of all the NPs was evaluated using the MTT assay against MCF-7, HeLa, and MSC cells. Cells (2000 cells/well) were seeded on a 96-well plate in 100 μL of DMEM medium and incubated for 24 h. The cells were treated with NPs at varying concentrations (with respect to ZnPc) and incubated for 4 h at 37 °C. The cells were then irradiated with 660 nm LASER (power 20.0 mV) light with a fiber optics for 1 min per well. Irradiated cells were incubated for 12 h at 37 °C, followed by a media change for all cells, and the cells were incubated for additional 60 h. The cells were then treated with 20 μL of MTT (5 mg/mL in PBS) for 5 h. The medium was removed, the cells were lysed with 100 μL of DMSO, and the absorbance of the purple formazan was recorded at 550 nm using a Bio-Tek Synergy HT microplate reader. Each well was performed in triplicate. All experiments were repeated three times. Cytotoxicity was expressed as mean percentage increase relative to the unexposed control ± SD. Control

values were set at 0% cytotoxicity or 100% cell viability. Cytotoxicity data (where appropriate) was fitted to a sigmoidal curve and a three parameters logistic model used to calculate the IC_{50}, which is the concentration of chemotherapeutics causing 50% inhibition in comparison to untreated controls. The mean IC_{50} is the concentration of agent that reduces cell growth by 50% under the experimental conditions and is the average from at least three independent measurements that were reproducible and statistically significant. The IC_{50} values were reported at ±99% confidence intervals. This analysis was performed with GraphPad Prism (San Diego, U.S.A).

Apoptosis Detection.

MCF-7 cells were seeded at a density of 1 x 10^6 on each well of a six well plate and allowed to grow overnight. Cells were treated with 1 μM ZnPc, 0.5 mg/mL empty NPs, 1 μM targeted and non-targeted ZnPc encapsulated NPs and incubated for 4 h, then irradiated with a 660 nm laser (1 min/well). As a control, the same formulations were added without light irradiation. The cells were further incubated at 37 °C overnight followed by trypsinization. To account for the cells that might have detatched due to apoptosis, the cell media was saved and centrifuged with the trypsinized cells centrifuged at 1,800 RPM for 3 min. The cells were repeatedly washed and centrifuged at 1,800 RPM for 3 min and the supernatants were discarded. Cell density was determined and cells were resuspended in annexin-binding buffer to ~1 × 10^6 cells/mL preparing a sufficient volume to have 100 μL per assay. To 100 μL of cell suspension, 5 μL alexa fluor® 488 annexin V and 1 μL 100 µg/mL PI working solution were added, incubated for 15 min at room temperature. After the incubation period, 400 μL annexin-binding buffer was added

to each sample, samples were gently mixed keeping the samples on ice and the samples were analyzed on the flow cytometer immediately.

Anti-tumor Immunity Study.

MCF-7 or HeLa cells were plated at the concentration of 0.5 x 10^6 cells/mL in six well plates and allowed to grow for 12 h. On the next day, the cells were incubated with 20 nM ZnPc, 0.5 mg/mL empty NPs, 20 nM with respect to ZnPc targeted and non-targeted ZnPc encapsulated NPs for 4 h, and irradiated with 660 nm light for 1 min per well. As a control, the same doses were incubated without light irradiation. Cells were left in the culture for overnight at 37°C and PDT supernatants were added to freshly prepared BMDCs (0.5 x 10^6 cells/mL) DCs were incubated with supernatants at 37 °C in time dependent manner (12 h, 24 h, and 48 h) for MCF-7 cells and 48 h for HeLa cells. Additionally LPS alone (100 ng/mL) was added to the DC cultures. The DCs were centrifuged at 1,800 RPM for 3 min and ELISA assays were performed on the supernatants against the cytokines IL-2, IL-4, IL-6, IL-10, IL-12, IL-18, TNF-α, and IFN-γ according to manufacturer's protocol. Briefly, antibody coated plates were blocked with 10% FBS in PBS for 1 h at room temperature followed by washings. Afterwards, DC supernatants were incubated on the plates for 1 h at room temperature. This was immediately followed by washings and sequential incubations with the cytokine-biotin conjugate and streptavidin working solution. Finally, the substrate reagent containing 3,3',5,5' tetramethylbenzidine (100 μL) was added to each well, incubated for 30 min, the reaction was stopped by adding 50 μL stop solution containing 0.1 M H_2SO_4. The absorbance was recorded at 450 nm using a BioTek Synergy HT well plate reader.

Neutralization of IL-12 and IL-18.

Purified BMDCs were treated with neutralizing antibodies against IL-12 (5 μg/mL) and/or IL-18 (1 μg/mL) cytokines for 18 h, followed by incubation with different NP treated and PDT activated MCF-7 cancer cell supernatants for 48 h. MCF-7 (0.5 x 10^6 cells/mL) were incubated with T-ZnPc-NP (20 nM), NT-ZnPc-NP (20 nM), or free ZnPc (20 nM) for 4 h, activated by PDT for 1 min as described before. Supernatants from the BMDCs were analyzed by ELISA to evaluate the levels of IL-12, IL-18, IFN-γ. BMDCs were also harvested by Dr. Smanla Tundup to stain for surface marker CD11c followed by intracellular staining of IFN-γ. Cells were acquired on flow cytometer and data were analyzed on FlowJo software. Production of IFN-γ was analyzed in $CD11c^+$ gated population.

DC Maturation and T-cell Activation Assays.

These experiments were performed by Dr. Smanla Tundup. For DC maturation assay, cancer cell lysates obtained after treatment of MCF-7 cells with different conjugates followed by PDT were incubated with BMDCs for 24 h at 37 °C. Cells were harvested and stained with antibodies against surface markers CD11c, CD86, and MHCII for 1 h on ice. Cells were washed in stain buffer and acquired on BD LSRII flow cytometer. Data obtained were analyzed using FlowJo software. To study $CD8^+$ T-cell activation, BMDCs, incubated with cancer cell lysates were treated with different conjugates followed by PDT as described above, were further incubated with $CD8^+$ T cells purified from splenocytes of naïve C57BL/6 mice using MACS bead negative selection method for 72 h. Cells were harvested by Dr. Smanla Tundup and $CD8^+$ T-cell activation was studied by staining the cells with antibodies against CD8 and CD25 surface markers. Cells were then acquired on flow cytometer.

RESULTS AND DISCUSSION

Construction of Mitochondria-Targeted NP for DC Activation.

The use of mitochondria-targeted NPs for ZnPc delivery is obvious due to the fact that ZnPc acts on the mitochondria of cells and upon photo-activation generates short-lived $^1O_2$ as the cytotoxic agent to show its photodynamic activity.[19, 20] The second-generation ZnPc photosensitizer has strong photo-toxicity in the therapeutic window of 600-800 nm; however, the hydrophobic characteristic hinders its systemic administration and restricts its possible translation to the clinic. The active species involved in the ZnPc-based PDT, $^1O_2$ has a short lifetime of <0.04 μs in biological systems and restricts its reactivity to within a radius of about 0.2 μm from its point of generation.[19, 20] Our recently developed mitochondria-targeted biodegradable polymer, PLGA-*b*-PEG-TPP[18] has the ability to encapsulate hydrophobic compounds such as ZnPc with very high efficiency. Using a nanoprecipitation method,[21, 22] we were able to load high amounts of ZnPc in the polymeric core to construct targeted T-ZnPc-NPs (Figure 3.4).

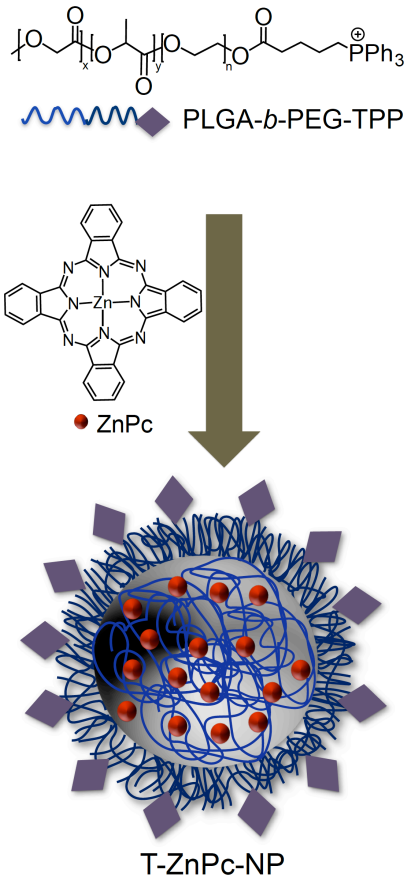


Figure 3.4. Synthesis of T-ZnPc-NPs by following a nanoprecipitation method

The polymer PLGA-*b*-PEG-OH without a cationic TPP moiety allowed us to construct a non-targeted NT-ZnPc-NP that served as a control to probe the advantages of delivering ZnPc inside the mitochondria of cells. Dynamic light scattering (DLS) measurements revealed that the mean diameter of the mitochondria targeted NPs, T-ZnPc-NPs to be ~65 to 75 nm and are positively charged (~24 to 34 mV) (Figure 3.5, Table 3.1). The size of the NT-ZnPc-NPs was found to be ~70 nm and are negatively charged (~-25 to -30 mV) (Figure 3.5c, Table 3.1). ZnPc loading and the encapsulation efficiency (EE) were optimized by varying the weight percentage of ZnPc to polymer (% w/w).

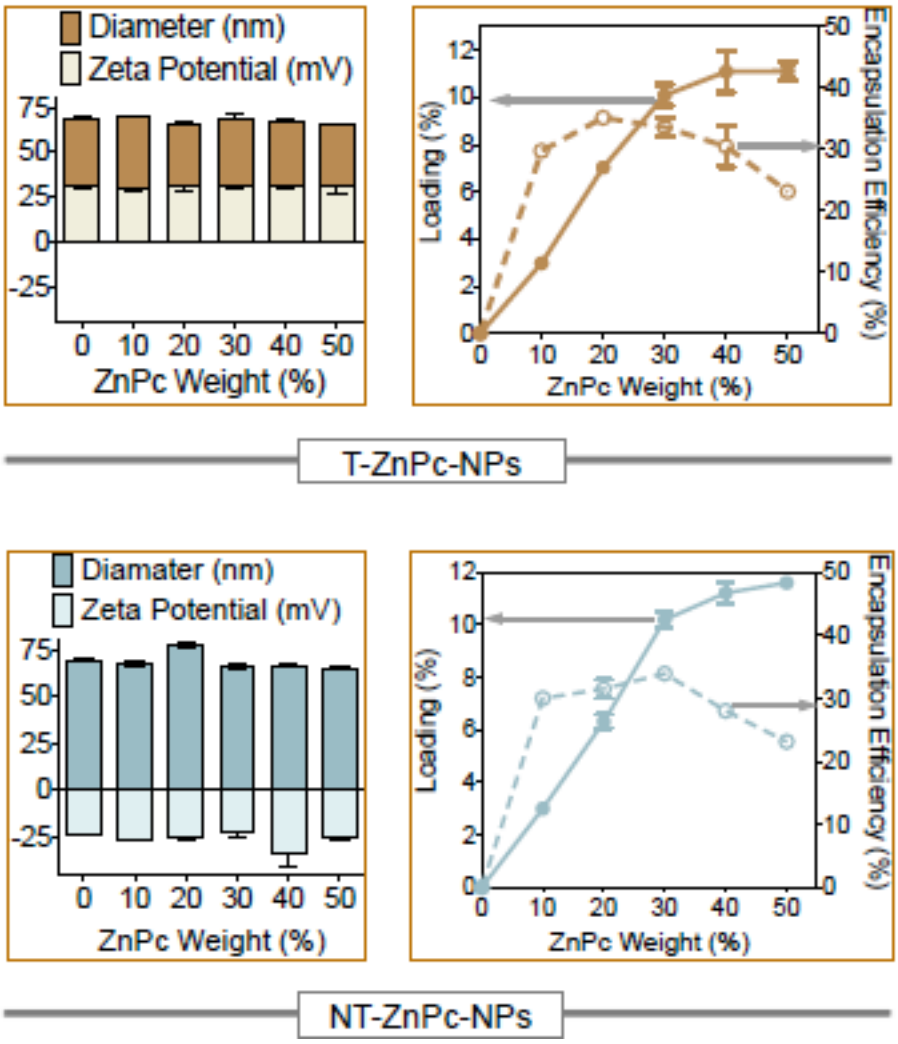


Figure 3.5. Size, zeta potential, and ZnPc loading in targeted and non-targeted NPs

Table 3.1. Physicochemical properties of the NPs and the loading of ZnPc

Nanoparticle	Size (nm)	PDI	Zeta potential (mV)
T-ZnPc-NP	81.7 ± 1.3	0.224	29.6 ± 3.3
NT-ZnPc-NP	80.3 ± 2.6	0.253	-31.5 ± 0.5
T-LND-NP	81.6 ± 1.3	0.272	23.7 ± 0.2
NT-LND-NP	85.8 ± 5.2	0.262	-28.1 ± 1.8
Empty-T-NP	84.0 ± 1.9	0.271	31.6 ± 2.3
Empty-NT-NP	87.6 ± 0.8	0.306	-33.4 ± 0.7

For both T-ZnPc-NPs and NT-ZnPc-NPs, %loading increased as the percent feed was raised and then saturated as the feed reached 40%. For all studies, we used ~10% ZnPc loaded NPs. Transmission electron microscopy (TEM) images of the NPs showed homogenous populations (Figure 3.6). To compare the immune activation properties of PDT with chemotherapeutics, we encapsulated a mitochondria-targeting cancer chemotherapeutic lonidamine (LND)[23] in the targeted and non-targeted polymers to construct T-LND-NPs and NT-LND-NPs.[18] We studied LND release kinetics from the NPs, a necessary property to show anti-cancer property by inhibiting mitochondria-bound hexokinase. The amount of LND released from the NPs under physiological conditions shows an initial 19% burst release followed by a period of controlled release reaching a value of 60% after 4 h and most LND was released in 8 h (Figure 3.7).

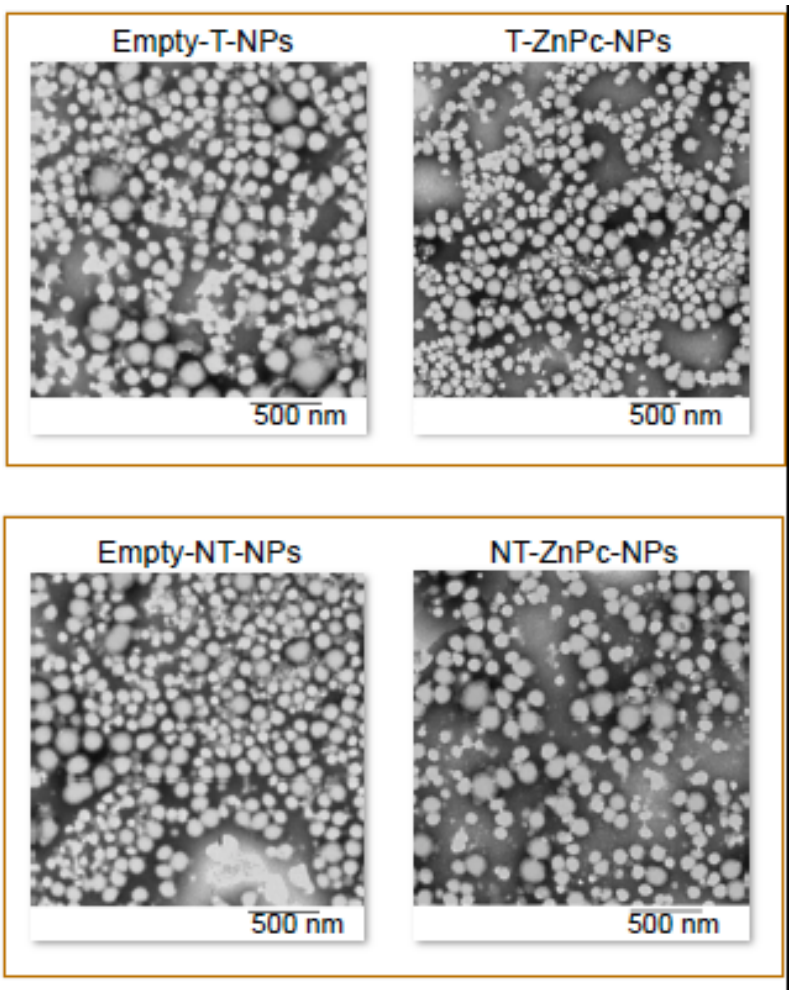


Figure 3.6. TEM images of targeted and non-targeted empty and ZnPc-loaded NPs**.**

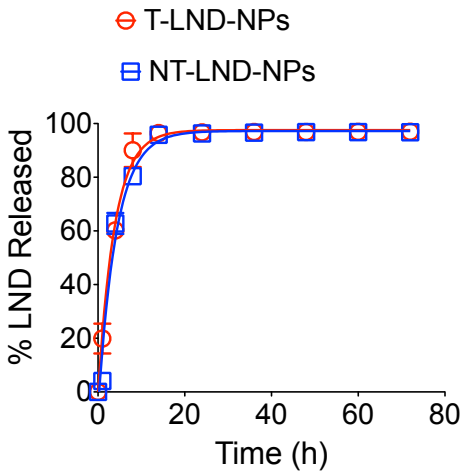


Fig. 3.7. Release kinetics of LND from targeted and non-targeted-NPs at 37 °C, pH 7.4.

Mitochondria Targeted Light Activation of Cancer Cells.

The photodynamic activities of T-ZnPc-NPs, NT-ZnPc-NPs, and free ZnPc were investigated against human breast cancer MCF-7 and cervical cancer HeLa cells. We used hMSCs as non-cancerous controls for their ability to differentiate into other cell types, and to partake in the anatomy and physiology of remote organs. None of these constructs showed any toxicity in the dark (Figure S3). Four hours following incubations with different constructs, cells were stimulated with a 660 nm laser light for 1 min and viability was determined following the 3-(4,5-dimethylthiazol-2-yl)-2,5-diphenyltetrazolium bromide (MTT) assay. A higher phototoxic effect was observed with T-ZnPc-NPs in HeLa and MCF-7 cells ($IC_{50\text{-}HeLa}$: 96±19 nM, $IC_{50\text{-}MCF\text{-}7}$: 49±12 nM) than NT-ZnPc-NPs ($IC_{50\text{-}HeLa}$: 222±59 nM, $IC_{50\text{-}MCF\text{-}7}$: 349±125 nM) and free ZnPc ($IC_{50\text{-}HeLa}$: 570±51 nM, $IC_{50\text{-}MCF\text{-}7}$: 406±129 nM) (Figure 3.8a). Control cells incubated with empty-T-NPs and empty-NT-NPs did not show any cell death after illumination. When hMSCs were exposed to T-ZnPc-NPs, NT-ZnPc-NPs, and free ZnPc and stimulated with laser, viability was higher for the cells treated with T-ZnPc-NPs ($IC_{50\text{-}hMSC}$: 36 μM) compared to those treated with NT-ZnPc-NPs ($IC_{50\text{-}hMSC}$: 31 μM) or free ZnPc ($IC_{50\text{-}hMSC}$: 6.5 μM) (Figure 3.8a). An interesting observation was T-ZnPc-NP or NT-ZnPc-NP had limited toxicity in hMSC cells, however, free ZnPc significantly decreased hMSC cell viability. We believe that the greater uptake of T-ZnPc-NPs by the cancer cells with elevated $\Delta\psi_m$ is responsible for their enhanced efficiency compared to the non-malignant hMSCs with normal $\Delta\psi_m$.[24, 25] Our results suggest that T-ZnPc-NPs with nanomolar IC_{50} in cancer cells may not have an adverse effect on hMSC cells and potentially other normal cell types in the body as well.

Mitochondria Targeted NPs Provide Unique Mixture of Apoptotic Necrotic Cells.

Immature DCs have unique properties of phagocytosis, processing, and presentation of tumor-associated antigens (TAA) from apoptotic cancer cells for inducing potent immune responses.[26] However, optimal presentation of TAA requires not only phagocytosis of apoptotic tumor cells by iDCs, but also activation and maturation of iDCs *via* exposure to the necrotic tumor cells. Therefore, a unique combination of apoptotic and necrotic tumor cells is needed for the tumor associated DCs to induce potent immune response. PDT-induced apoptosis can proceed through different pathways involving either an extrinsic cytoplasmic or an intrinsic mitochondrial pathway.[27] Intracellular localization of the PS coincides with the primary site of photo-damage because the active species $^1O_2$ has a short lifetime and very limited diffusion in biological systems indicating that primary molecular targets of PDT process must reside within few nanometers from the PS. Thus, PS localizing in the mitochondria promote apoptosis, but PDT with PS residing either in the non-mitochondrial compartments, can either delay or block the apoptotic program predisposing the cells to necrosis. To explore the ability of T-ZnPc-NPs to induce apoptosis upon PDT, we exposed breast cancer MCF-7 cells to T-ZnPc-NPs and compared the apoptosis ability with that of NT-ZnPc-NPs and free ZnPc by annexin-V-propidium iodide (PI) assay.

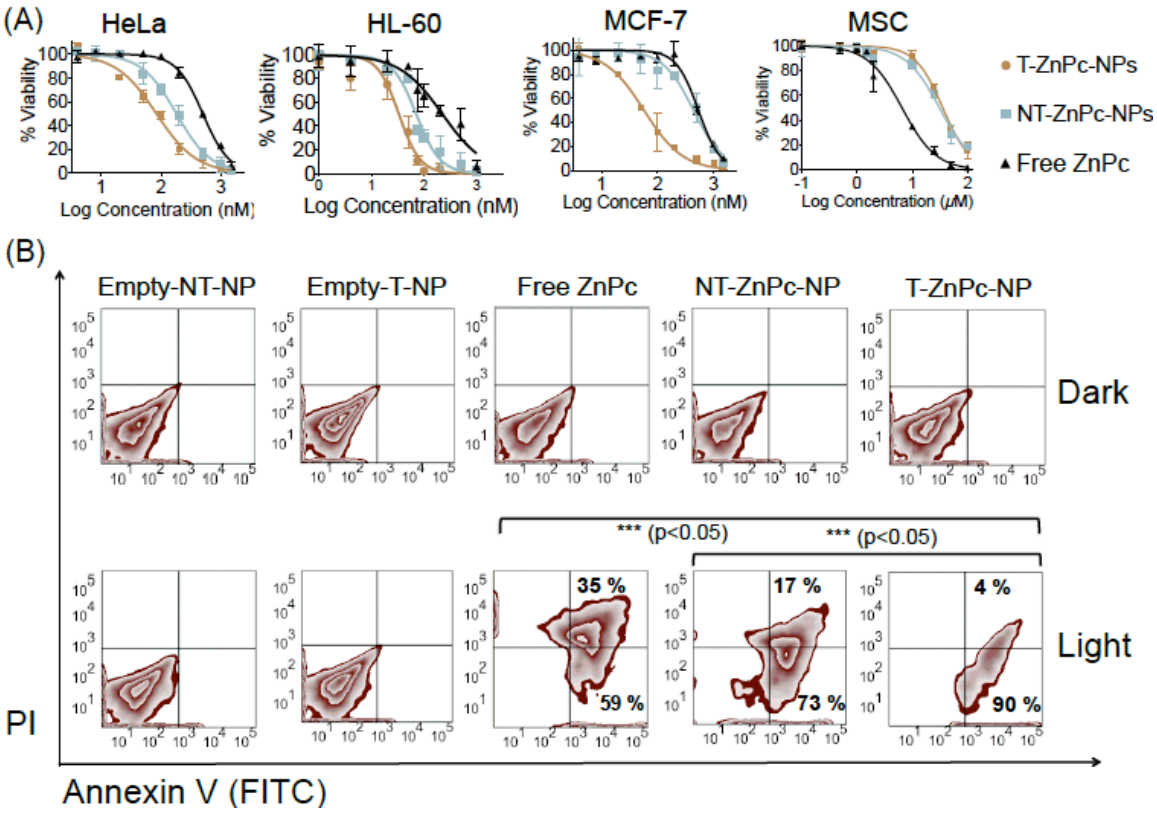


Figure 3.8. (a) HeLa and MCF-7 cancer cells respond differently to light activation compared to hMSC. Cells on 96-well plates were incubated for 4 h with T-ZnPc-NP, NT-ZnPc-NP, and free ZnPc. Cells were irradiated with a 660 nm laser (20 mW) for 1 min, media was changed after 12 h, and cells were further incubated for additional 60 h and viability was assessed by the MTT assay. (b) FACS analysis using Annexin V-Alexa Fluor/PI staining for apoptosis detection in MCF-7 cells on treatment with T-ZnPc-NP (1 μM), NT-ZnPc-NP (1 μM), and free ZnPc (1 μM) for 16 h in the dark or irradiation with a 660 nm laser for 1 min after 4 h incubation, followed by incubation in the dark for 12 h. Cells in the lower right quadrant indicate Annexin-positive/PI negative, early apoptotic cells. The cells in the upper right quadrant indicate Annexin-positive/PI positive, late apoptotic or necrotic cells.

T-ZnPc-NPs strongly induced the early stage of apoptosis, in contrast, the empty-T-NPs, empty-NT-NPs, and the dark controls did not increase the total number of apoptotic cells (Figure 3.8b, Figure 3.9). NT-ZnPc-NPs showed less apoptotic efficacy compared with the targeted-NPs. Free ZnPc induced late apoptosis or necrosis to a higher extent, compared with the T-ZnPc-NPs and NT-ZnPc-NPs. Increased apoptotic activity of T-ZnPc-NPs may possibly be due to the unique ability of the targeted NPs to deliver ZnPc inside the mitochondria, thereby triggering mitochondrial mediated cell death cascade/sequence. Apoptotic cancer cells, as a result of PDT, release antigens, which interact with and internalized by DCs resulting into their activation, maturation, antigen presentation, and initiation of a robust adaptive immune response against cancer cells.

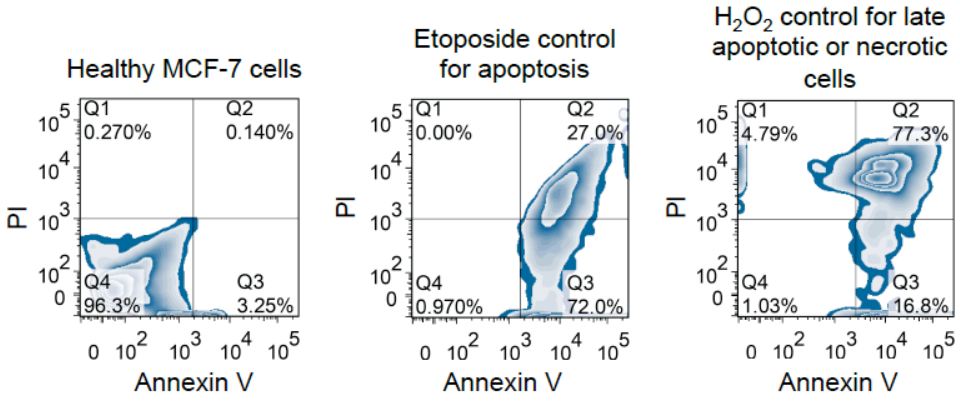


Figure 3.9. FACS analysis using annexin V-Alexa Fluor® 488/PI staining for apoptosis detection in MCF-7 cells. Cells in the lower right quadrant indicate Annexin-positive/PI negative, early apoptotic cells. The cells in the upper right quadrant indicate Annexin positive/PI positive, late apoptotic or necrotic cells. As positive controls, etoposide (100 μM, incubation time: 12 h) and H_2O_2 (1 mM, incubation time: 45 min) treated cells were used to determine the early apoptotic and late apoptotic population.

Mitochondria-targeted NP Activated Light Stimulated Breast Cancer Antigens Drive *Ex Vivo* IFN-γ-secretion from BMDCs.

Several studies demonstrated activation of the host immune response by PDT following unknown mechanisms.[28] Secretion of IFN-γ by human T and NK cells in the adaptive immune responses against pathogens is well established[29, 30], but *ex vivo* generation of IFN-γ by DCs is still controversial.[31] We next assessed the activation of BMDCs by cancer cell antigens generated by treating MCF-7 cells with different constructs followed by light stimulation using an enzyme-linked immunosorbent assay (ELISA).[9] Treatment of MCF-7 cells with different constructs and light stimulation did not increase any cytokine levels (Figure 3.10). Cytokine production by monocytes or macrophages is not always reproducible as a consequence of purity of the isolated BMDC population, a small numbers of NK or T cells contaminating macrophage cultures could mislead many cytokine production.

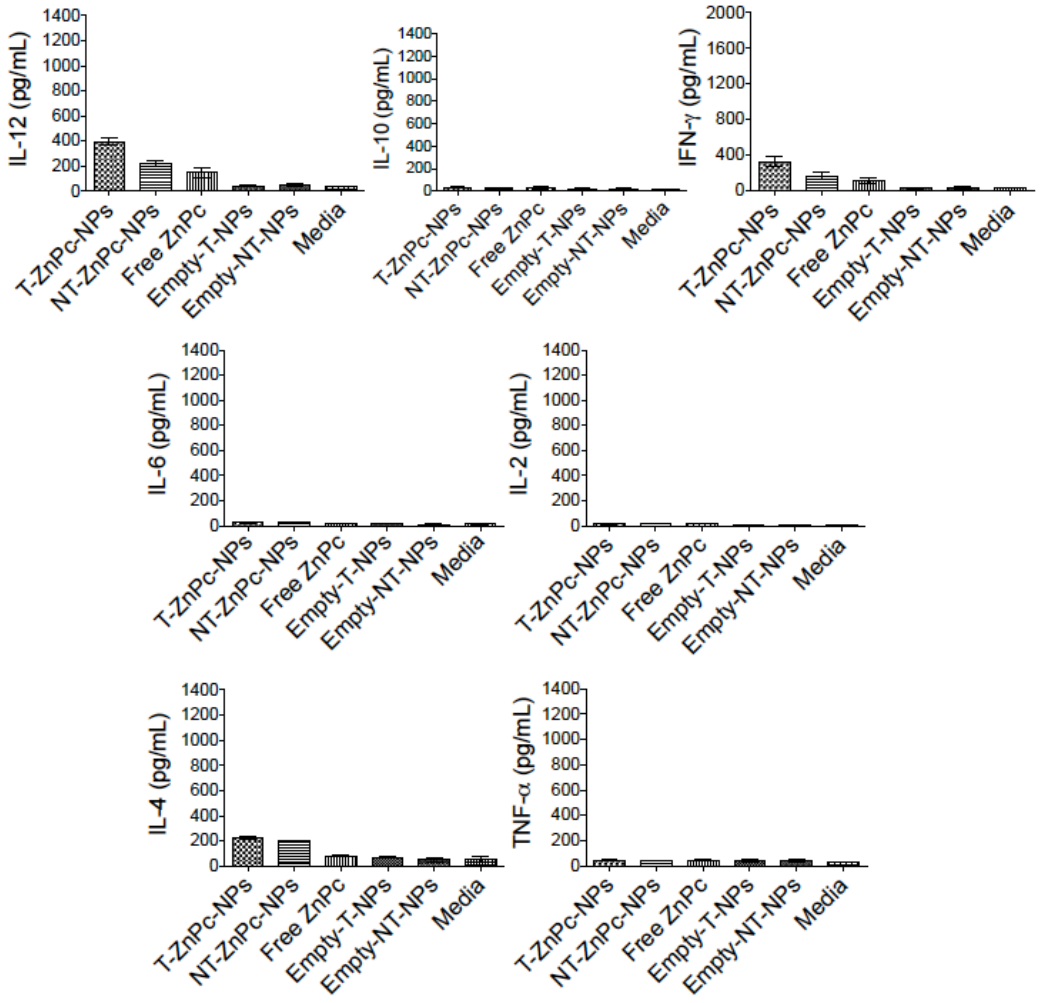


Figure 3.10. Cytokine response from various NP treated and light stimulated MCF-7 cancer cell supernatant.

These experiments were performed by Dr. Smanla Tundup. Therefore, we purified BMDCs isolated from C57BL/6 mice using anti-CD11c micro-bead column (Figure 3.9). Control experiments by treating MCF-7 cells with different NPs followed by incubation of BMDCs with cancer cell supernatants in the dark did not show any induction of cytokine secretion (Figure 3.10). BMDCs activated with cancer cell supernatants from T-ZnPc-NP treated and PDT activated MCF-7 cells led to significant induction of pro-inflammatory cytokine secretion which included IL-12, IL-18, and TNF-

α as well as production of anti-inflammatory cytokines such as IL-4 and IL-10 (Figure 3.13) in a time dependent manner (Figure 3.12) compared to BMDCs stimulated with supernatants of NT-ZnPc-NP or ZnPc treated and light activated cancer cells.

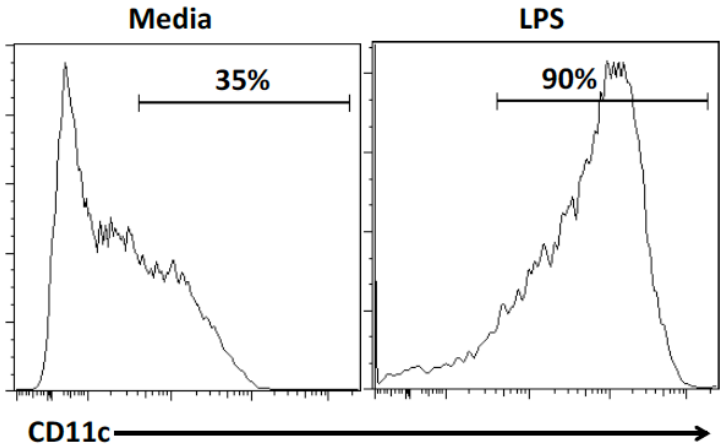


Figure 3.11. BMDCs were purified using anti-CD11c micro-bead column. DCs were incubated with media alone or LPS for 24 h. Expression of CD11c on DCs were tested using a fluorescent anti-CD11c antibody. Cells were acquired and analyzed by flow cytometry.

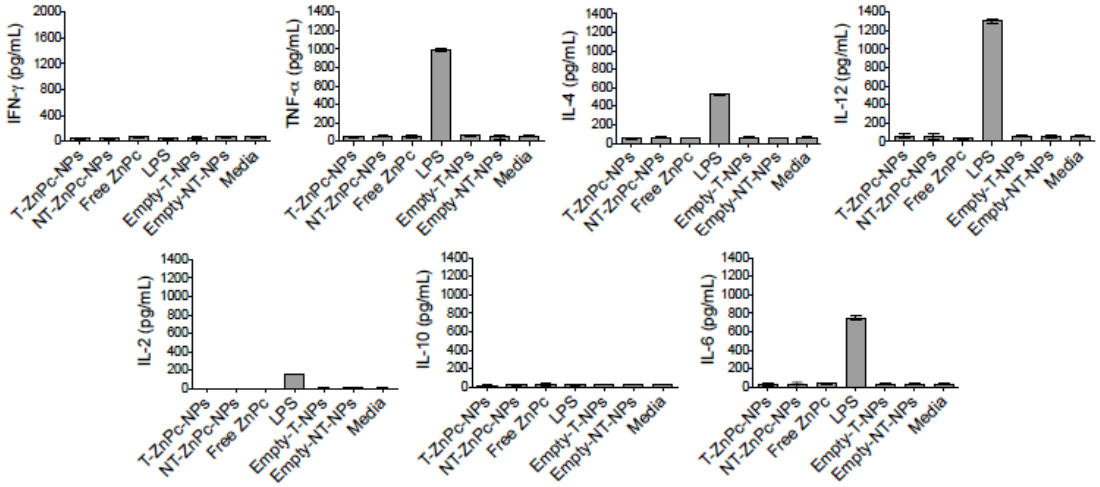


Figure 3.12. Cytokine response from the BMDCs treated with MCF-7 cancer cell supernatant treated with different constructs under dark.

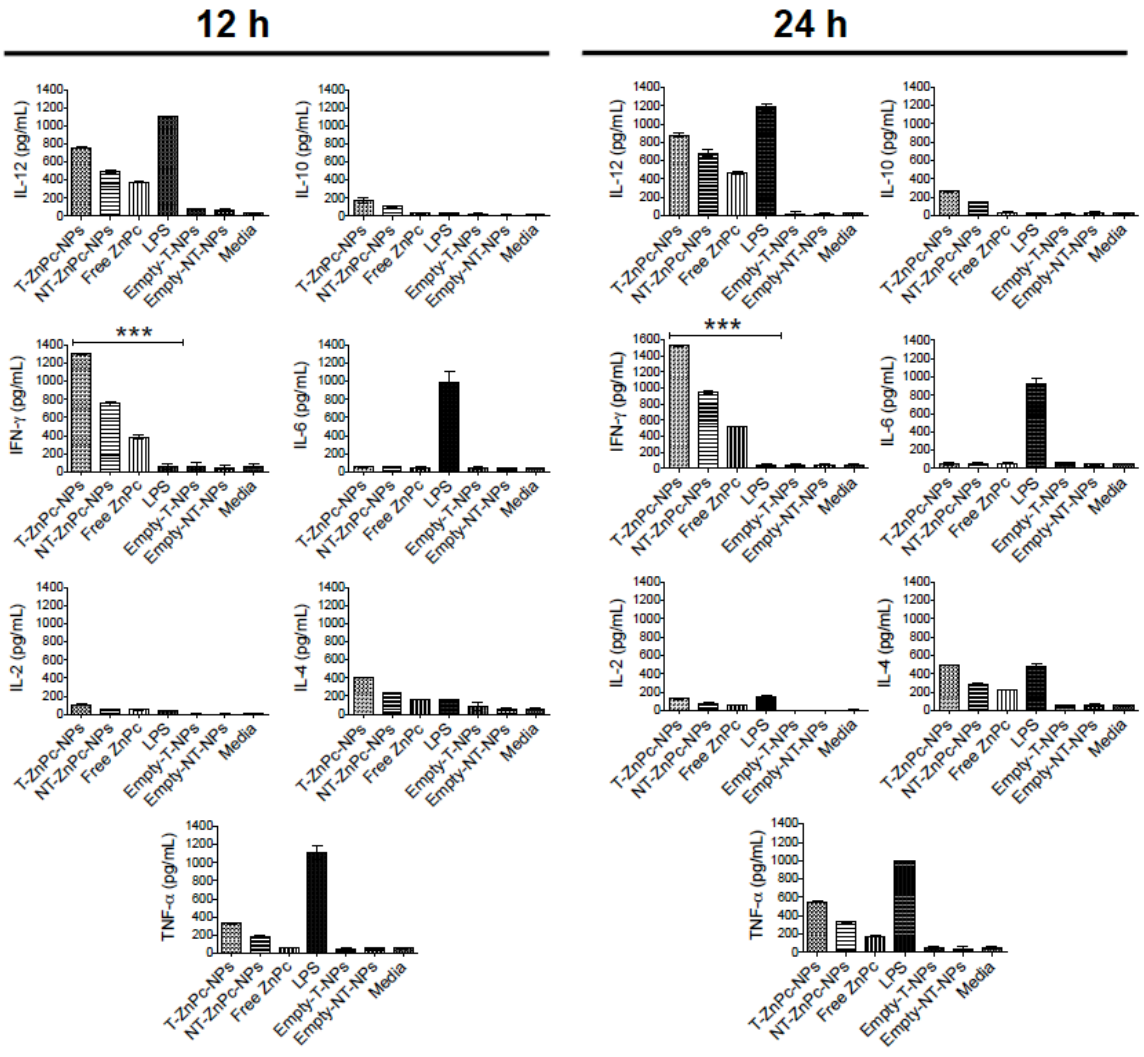


Figure 3.13. Time dependent PDT-treated MCF-7 cancer cell supernatant induced DC activation.

Most importantly under these settings, BMDCs stimulated with cancer cell supernatants from T-ZnPc-NP treated and light activated MCF-7 cells produced IFN-γ to a greater extent compared to BMDCs which were treated with cancer cell supernatants generated with NT-ZnPc-NP or free ZnPC followed by PDT activation (Figure 3.13). Whereas, BMDCs stimulated with T-ZnPc-NP treated PDT activated cancer cell supernatant generated a marked IL-18 and IFN-γ response, in contrast the bacterial

lipopolysaccharide (LPS) stimulus did not induce these two-cytokines secretion from BMDCs.

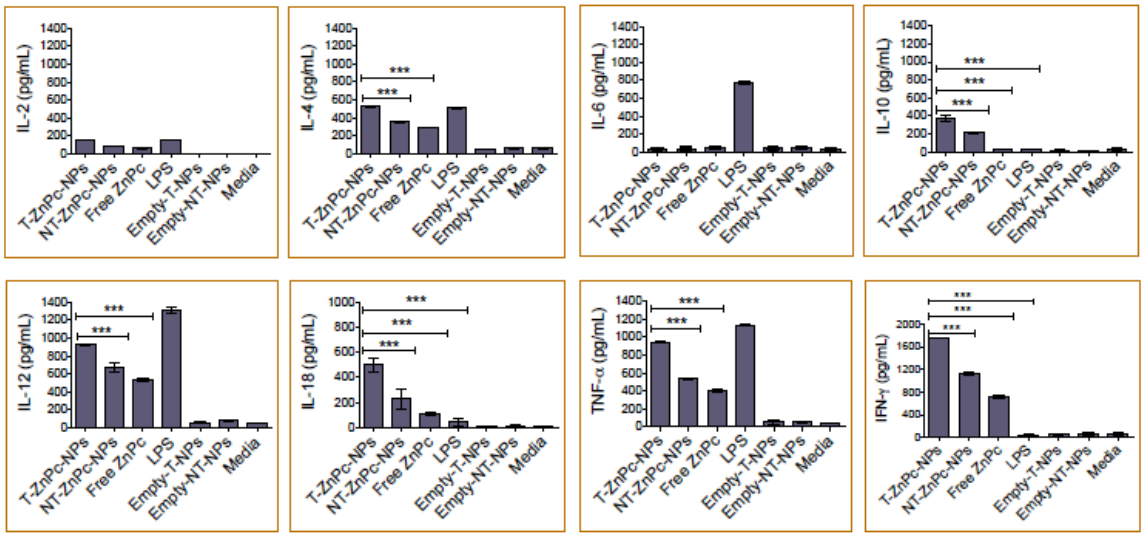


Figure 3.14. Cytokine production by BMDCs stimulated with cancer cell supernatants generated by treating MCF-7 cells with different constructs after PDT activation. Highly purified DCs were cultured at 0.5 x 10^6 cells/mL in the presence of a range of stimuli: MCF-7 cancer cells (0.5 x 10^6 cells/mL) treated with T-ZnPc-NP (20 nM with respect to ZnPc), NT-ZnPc-NP (20 nM with respect to ZnPc), ZnPc (20 nM), empty-T-NP (0.5 mg/mL with respect to polymer), empty-NT-NP (0.5 mg/mL with respect to polymer) for 4 h followed by photo-stimulation with 660 nm laser light for 1 min and further incubation in the dark for 12 h or stimulation with LPS (100 ng/mL). After 48 h, DC culture supernatants were harvested and assayed by ELISA. Data shown are based upon triplicate cultures of pooled cells sorted from 3 mice and are representative of four separate experiments. All data were expressed as mean ± S.D (standard deviation). A one-way ANOVA with a post-hoc Tukey test was used to identify significant differences among the groups with a *P* value <0.001.

Treatment of MCF-7 cells with T-LND-NPs, NT-LND-NPs, and free LND and stimulation of BMDCs with the LND-treated MCF-7 cancer cell supernatants did not show any immune-stimulatory cytokine production (Fig. 3.12) further supporting that localization of mitochondria acting PS using a NP system causes potent immune response, however similar strategies by directing mitochondria-acting chemotherapeutic such as LND using a delivery vehicle do not show any immune stimulation.[32, 33] However, it should be noted that some chemotherapeutic agents act on the immune system to trigger a direct antitumor immune response.[34, 35] Thus mitochondria targeted PDT-generated lysates provide a unique immune stimulation than chemotherapy. To investigate cancer cell specificity of IFN-γ production, we carried out experiments using cervical cancer HeLa cells (Figure 3.15). We observed that BMDCs stimulated with cell supernatants from HeLa cells treated with T-ZnPc-NPs, NT-ZnPc-NPs, and free ZnPc followed by PDT showed very similar cytokine secretion prolife except for IL-18 and IFN-γ. This indicates that IFN-γ production by the activated BMDCs is dependent of the cancer cell type.

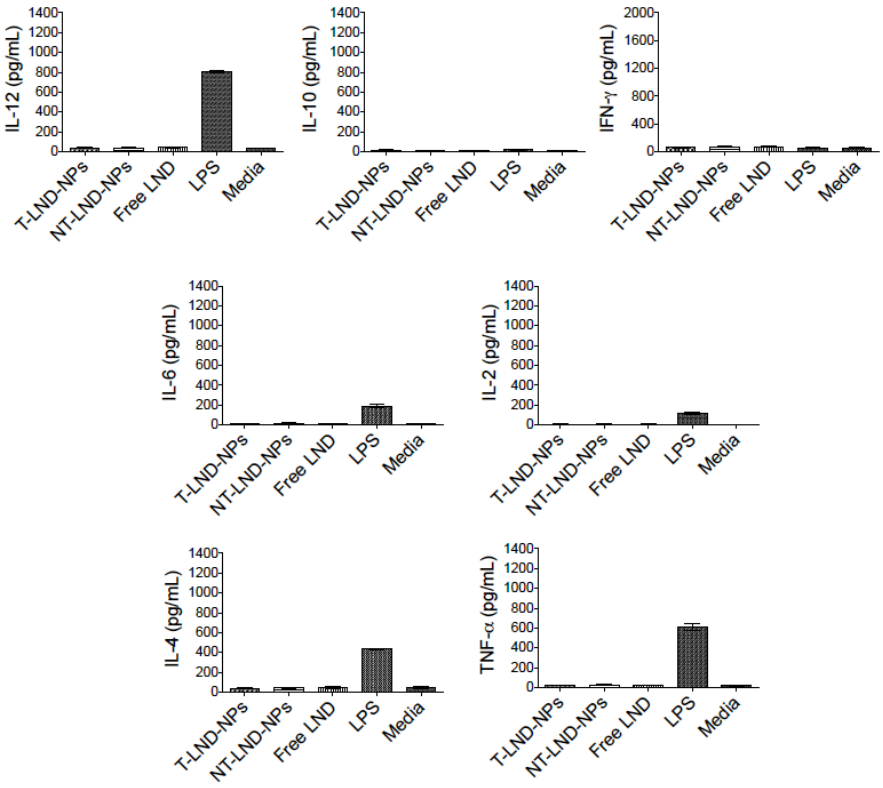


Figure 3.15. LND-NP-treated MCF-7 cancer cell supernatant induced DC activation for 12 h.

IL-12 and IL-18 Neutralization Abrogates T-ZnPc-NP Treated and Light Stimulated Cancer Cell Induced IFN-γ Production by BMDCs.

A potential mechanism behind the remarkable immune response from the T-ZnPc-NP treated MCF-7 vaccine lies in the ability of this tumor cell lysates to stimulate IFN-γ production from DCs by an unique combinatory secretion of IL-12 and IL-18. There are few reports demonstrating that a combination of IL-12 and IL-18 induces IFN-γ production in human DCs.[36, 37] IL-12 secretion is a measure of functional DC maturation and IL-18 is identified as an IFN-γ inducing factor. The regulation of IL-18 secretion by the interaction of human DCs with T cells is known but IL-18 secretion by mouse DCs are sparse.[38] Neutralization of either of IL-12 or IL-18 using neutralization

antibodies completely eliminated the induction of IFN-γ secretion by the DCs activated with T-ZnPc-NP treated and PDT stimulated MCF-7 tumor cell supernatant compared to the BMDCs incubated with respective isotype controls (Figure 3.16). These data indicate that the IFN-γ secretion from DCs pulsed with T-ZnPc-NP treated PDT stimulated MCF-7 cancer cells was triggered by an autocrine effect of IL-12 and IL-18 (Figure 3.16). Our results showed that only breast cancer MCF-7 cell conditioned media generated by treating with T-ZnPc-NPs upon photo stimulation triggered the release of IL-18 from the BMDCs and cervical cancer HeLa cells upon similar stimulation failed to produce IFN-γ. Moreover, we found that IL-18 secretion varied strongly according to the use of the NP delivery vehicle, mitochondria targeted delivery showed highest IL-18 secretion, and the extent of IL-18 secretion from the NT-ZnPc-NPs or free ZnPc were less. These findings suggested that the extent at which PDT triggers the secretion of IL-18 in the DCs depends on the mechanism of apoptosis. Because the pattern of IL-18 secretion induced by the different NP stimulated BMDCs resembled the pattern of IFN-γ from these BMDCs, we sought to identify the molecular mechanisms that might link IL-18 secretion, apoptosis, and IFN-γ production.

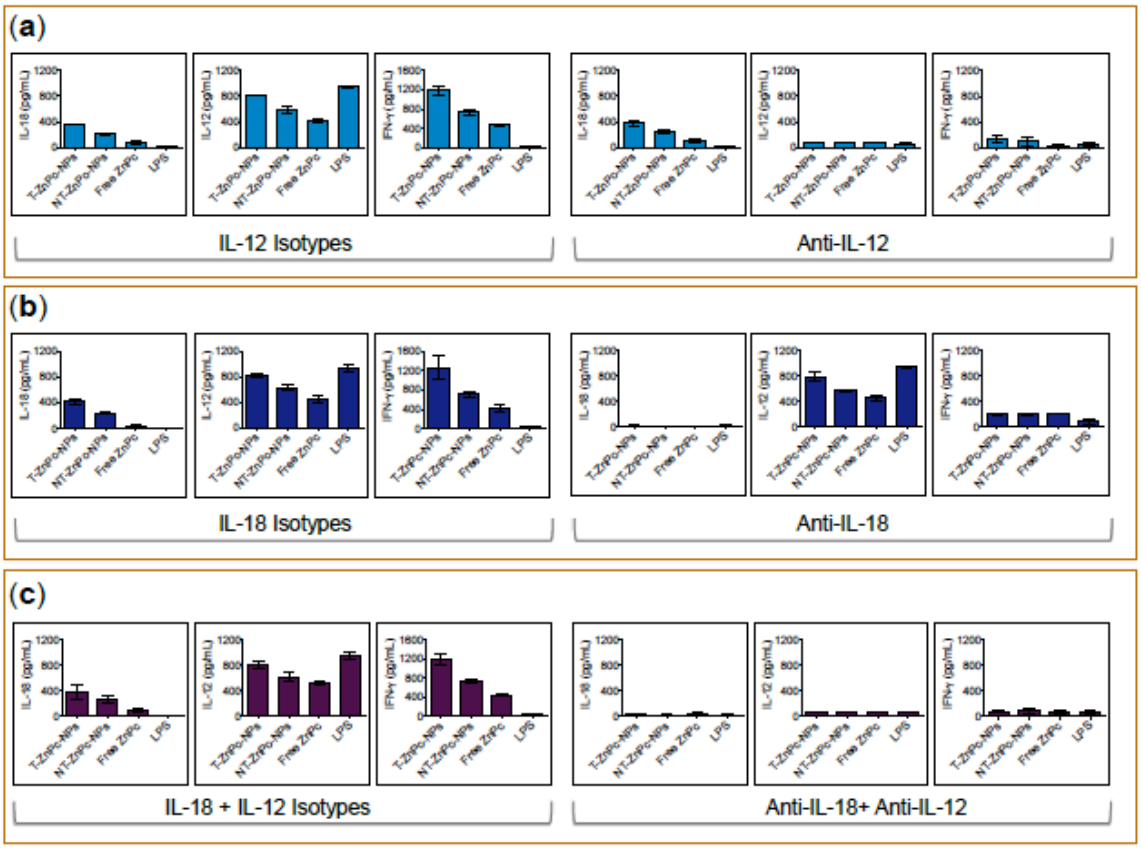


Figure 3.16. Combination of IL-12 and IL-18 is the source of IFN-γ. Purified BMDCs were treated with neutralizing antibodies against IL-12 and/or IL-18 cytokines, followed by incubation with different cancer cell supernatants or with LPS (100 ng/mL) for 48 h. MCF-7 cancer cells were incubated with T-ZnPc-NP (20 nM with respect to ZnPc), NT-ZnPc-NP (20 nM with respect to ZnPc), ZnPc (20 nM) for 4 h followed by photo-stimulation with 660 nm laser light for 1 min and further incubation in the dark for 12 h. BMDCs were then harvested for ELISA.

The secretion of IL-18 by DCs appeared to be a specific, caspase-1-mediated apoptosis effect and a slow release of pro-IL-18 from the apoptotic cancer cells is required for DC activation to release IL-18.[39] This underlines the important role of caspase-1 in the activation of IL-18 and IFN-γ. Caspase-3 plays a central role in key

apoptotic events. MCF-7 breast cancer cells lack caspase-3 protein,[40] yet they remain apoptosis responsive in our studies suggesting an alternative mechanism. We believe that the mitochondria-targeted PDT in MCF-7 cells involved release of cytochrome c, a reduction in the $\Delta\psi_m$, and activation of different aspects of the caspase cascade,[41] the possibility existed that caspase-1 might substitute for caspase-3. Thus caspase-1 activation by the T-ZnPc-NPs upon light stimulation leads to the production of IL-18 from the BMDCs and the subsequent activation by the unique combination of IL-12 and IL-18 might be responsible for the *ex vivo* induction of BMDCs to produce IFN-γ. This is further supported by the observation that the HeLa cells with caspase-3 undergo a normal apoptotic pathway upon treatment with T-ZnPc-NPs and do not secrete IL-18 and IFN-γ (Fig. 3.17). The precise mechanisms why T-ZnPc-NP treated and PDT stimulated breast cancer cells activate BMDCs to give rise to IFN-γ warrants further investigation.

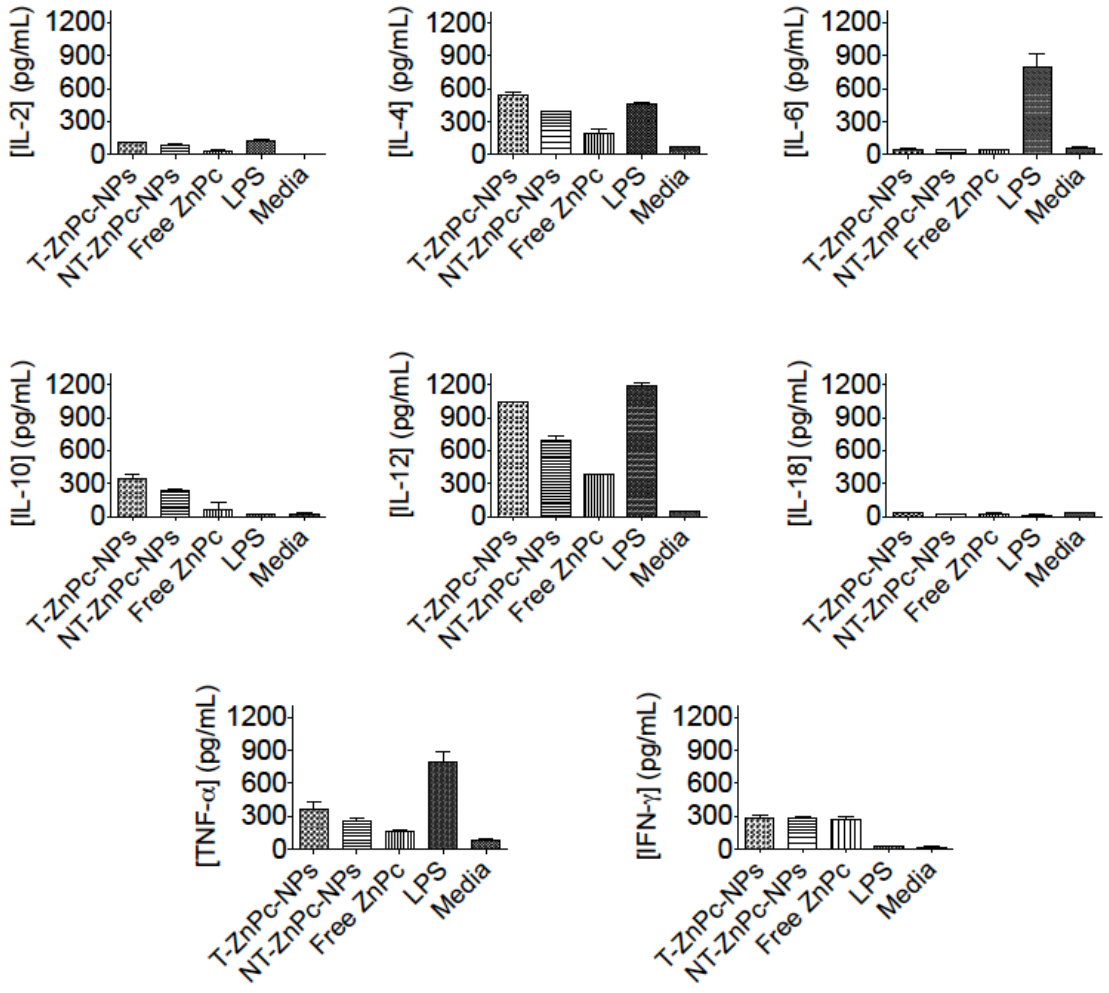


Figure 3.17. Various NP treated and light stimulated HeLa cancer cell supernatant induced DC activation after 48 h.

Mitochondria-targeted NP Treated, Light Activated MCF-7 Cells Induce DC Maturation.

Maturation and activation of DCs is a prerequisite for up-regulation of co-stimulatory molecules, enhancement of their APC function, and expression of chemokine receptors for migration to nodal T-cell areas.[42] DCs undergo a number of phenotypical and functional changes and DC-based therapy in humans demonstrated that DC maturation is a requirement for the induction of immunity.[43, 44] In general, DC maturation

involves a redistribution of major histocompatibility complex (MHC) from intracellular endocytic compartments to the DC surface, down-regulation of antigen internalization, an increase in the surface expression of co-stimulatory markers, secretion of chemokines, cytokines and proteases, and surface expression of adhesion molecules and chemokine receptors.

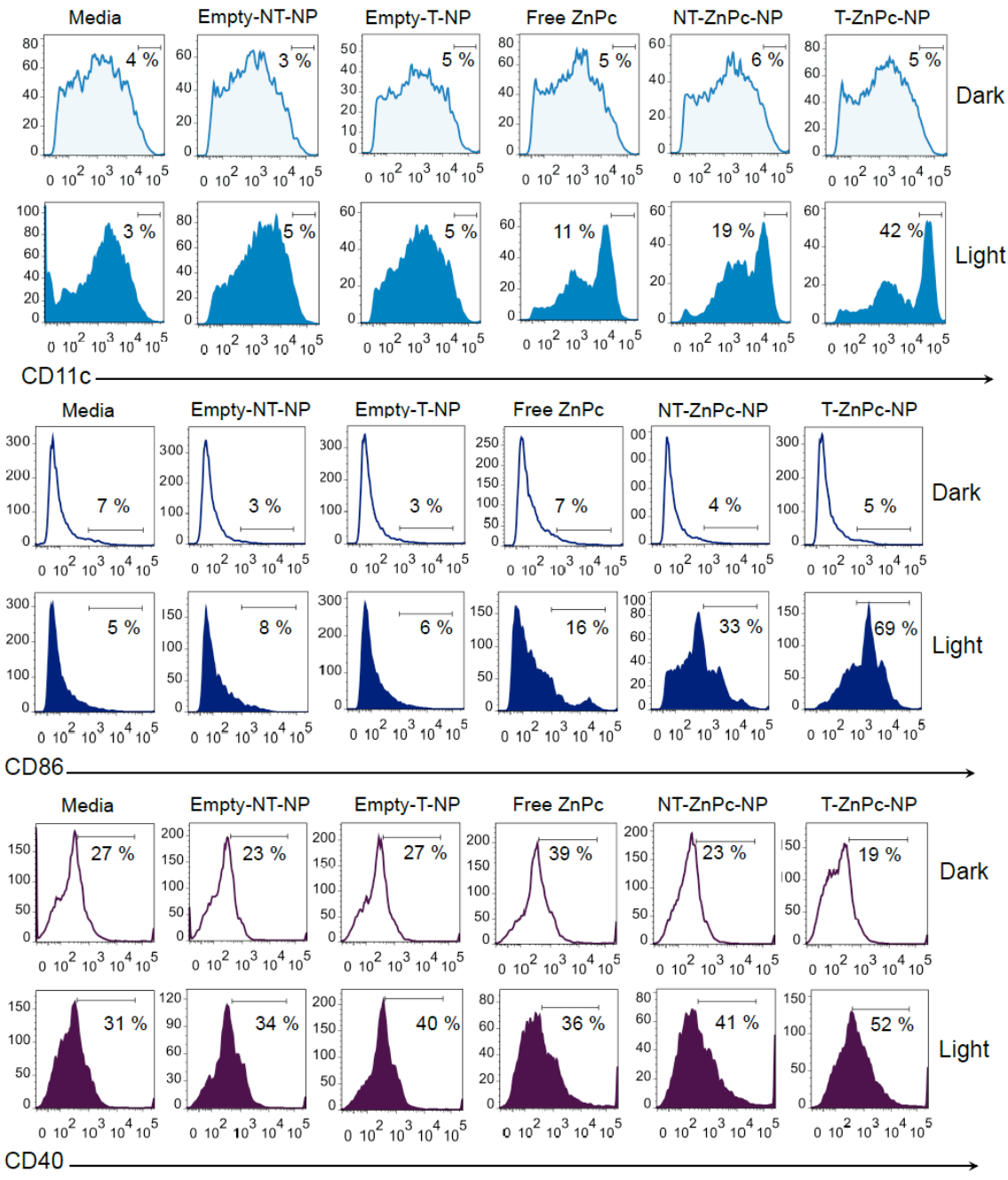


Figure 3.18. DC maturation assay. MCF-7 cell conditioned media treated with T-ZnPc-NPs followed by PDT stimulation induces expression of CD11c (a), CD86 (b), and CD40 (c) markers on DCs.

Proper DC maturation by the PDT antigens is an integral part of PDT-based vaccine development. We studied the ability of the T-ZnPc-NP treated PDT stimulated MCF-7 cancer cell supernatant induced maturation of BMDCs by performing phenotypic analysis using flow cytometry (Figure 3.18). BMDCs incubated with T-ZnPc-NP treated PDT stimulated MCF-7 cell supernatant induced significant increase in the expression of CD11c on BMDCs compared to PDT treated MCF-7 supernatants which were treated with NT-ZnPc-NP or free ZnPc or DCs incubated with PDT stimulated MCF-7 cells alone (Figure 3.16a). Expression of CD86 and CD40 surface markers on BMDCs were significantly increased when BMDCs were incubated with MCF-7 cell supernatants treated with T-ZnPc-NPs after light stimulation compared to PDT treated cell supernatants generated from NT-ZnPc-NPs (Figures 3.18c and d) or free ZnPc.

$CD8^+$ T-cell Activation.

The inaugural step of T-cell immunity involves interaction of naïve T cells with mature DCs.[45] iDCs are stimulators of T-cells and $CD8^+$ T-cells play a crucial role in providing full strength adaptive immune response against cancer. Our observation that T-ZnPc-NP treated light stimulated MCF-7 cell supernatant is efficient in driving DC maturation led us hypothesized that BMDCs activated with this lysate will show effective $CD8^+$ T cell activation. To probe this, $CD8^+$ T-cells were incubated with BMDCs pre-exposed to the cancer cell supernatants treated with NPs and pulsed with laser. CD25 was significantly up-regulated on the $CD8^+$ T-cells which were co-cultured with the BMDCs stimulated with T-ZnPc-NP treated light activated cancer cell media. In comparison, $CD8^+$ T-cells incubated with BMDCs exposed to MCF-7 cancer cell supernatants that received NT-ZnPc-NP or free ZnPc showed significantly reduced T cell activation

(Figure 3.19). This remarkable ability of BMDCs stimulated with T-ZnPc-NP treated light activated tumor cell supernatant to show high surface expression of CD25 markers indicated that this mitochondria-targeted PS containing NP has the opportunity to be explored further for possible vaccine application.

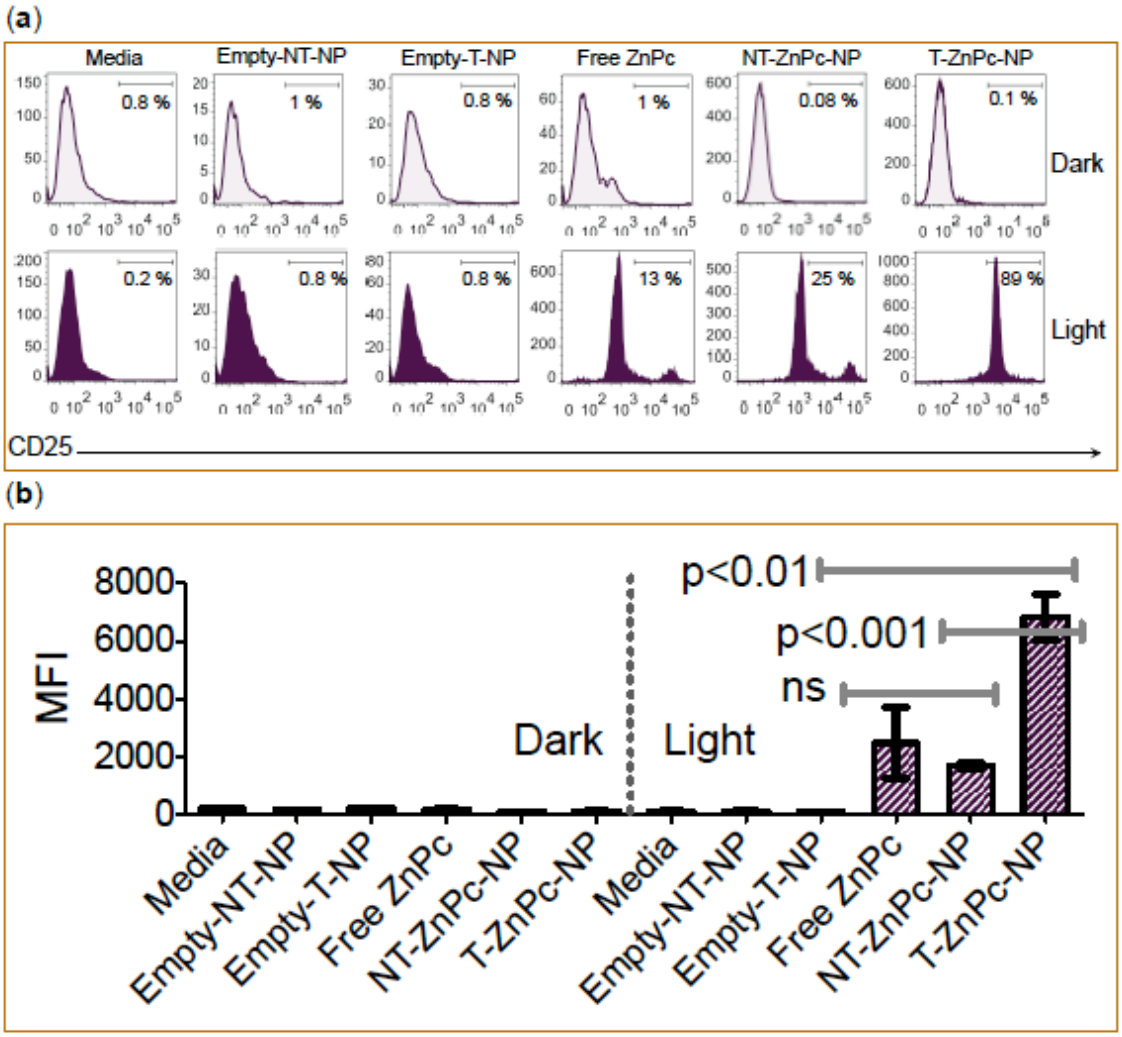


Figure 3.19. CD8 T cell activation assay. DCs exposed to supernatants of MCF-7 cells treated with different conjugates (20 nM with respect to ZnPc for T-ZnPc-NP, NT-ZnPc-NP, and free ZnPc; empty-NPs 0.5 mg/mL with respect to polymer) with or without light activates $CD8^+$ T-cells. MCF-7 cells were incubated with the conjugates. Cancer cell

supernatants were incubated with BMDCs. Activated BMDCs were incubated with $CD8^+$ T-cells enriched from spleens of C57BL/6 mice. Cells were harvested to measure T-cell activation by staining with antibodies against CD8 and CD25 (a) and median fluorescence intensities (MFIs) of CD25 was calculated using FlowJo software (b).

CONCLUSIONS

In conclusion, we demonstrate an exceptional potency of mitochondria-targeted NP-based light activated breast cancer cell antigens to uniquely stimulate DCs for cancer immunotherapy. A major advantage of activating DCs *ex vivo* to produce IFN-γ is that these activated DCs can be produced in bulk quantities, *ex vivo* culture conditions can be carefully controlled, and DC quality can be checked before the cells are administered to the patient. Our findings encourage the use of mitochondria-targeted NP delivery systems to deliver mitochondria acting PS for generation of tumor cell antigens to activate DCs *ex vivo* for potential interactive innate/acquired immune response with relevance and impact in health and disease.

ACKNOWLEDGMENT

This work was supported by a start-up grant from the National Institutes of Health (P30 GM 092378) to UGA and by the Office of the Vice President for Research, UGA to S.D., a grant from the National Institutes of Health (NIH AI056484) to D.H. We thank Dr. Nagesh Kolishetti for helpful discussions and critical reading of the manuscript.

REFERENCES

1. Swann, J. B.; Smyth, M. J., Immune surveillance of tumors. *J. Clin. Invest.* **2007,** *117* (5), 1137-1146.

2. Mellman, I.; Coukos, G.; Dranoff, G., Cancer immunotherapy comes of age. *Nature* **2011,** *480* (7378), 480-489.

3. Tacken, P. J.; de Vries, I. J. M.; Torensma, R.; Figdor, C. G., Dendritic-cell immunotherapy: from ex vivo loading to in vivo targeting. *Nat. Rev. Immunol.* **2007,** *7* (10), 790-802.

4. Timmerman, J. M.; Levy, R., Dendritic cell vaccines for cancer immunotherapy. *Annu. Rev. Med.* **1999,** *50*, 507-529.

5. Chang, D. H.; Dhodapkar, M. V., Dendritic cells and immunotherapy for cancer. *Int. J. Hematol.* **2003,** *77* (5), 439-443.

6. Nestle, F. O.; Farkas, A.; Conrad, C., Dendritic-cell-based therapeutic vaccination against cancer. *Curr. Opin. Immunol.* **2005,** *17* (2), 163-169.

7. Garg, A. D.; Nowis, D.; Golab, J.; Agostinis, P., Photodynamic therapy: illuminating the road from cell death towards anti-tumour immunity. *Apoptosis* **2010,** *15* (9), 1050-71.

8. Castano, A. P.; Mroz, P.; Hamblin, M. R., Photodynamic therapy and anti-tumour immunity. *Nat. Rev. Cancer* **2006,** *6* (7), 535-45.

9. Marrache, S.; Choi, J. H.; Tundup, S.; Zaver, D.; Harn, D. A.; Dhar, S., Immune stimulating photoactive hybrid nanoparticles for metastatic breast cancer. *Integr. Biol.* **2013,** *5* (1), 215-223.

10. Farokhzad, O. C.; Jon, S. Y.; Khademhosseini, A.; Tran, T. N. T.; LaVan, D. A.; Langer, R., Nanoparticle-aptamer bioconjugates: A new approach for targeting prostate cancer cells. *Cancer Res.* **2004,** *64* (21), 7668-7672.

11. Farokhzad, O. C.; Cheng, J.; Teply, B. A.; Sherifi, I.; Jon, S.; Kantoff, P. W.; Richie, J. P.; Langer, R., Targeted nanoparticle-aptamer bioconjugates for cancer chemotherapy in vivo. *Proc. Natl. Acad. Sci. USA* **2006,** *103* (16), 6315-20.

12. Soppimath, K. S.; Aminabhavi, T. M.; Kulkarni, A. R.; Rudzinski, W. E., Biodegradable polymeric nanoparticles as drug delivery devices. *J. Control. Release* **2001,** *70* (1-2), 1-20.

13. Gu, F.; Zhang, L.; Teply, B. A.; Mann, N.; Wang, A.; Radovic-Moreno, A. F.; Langer, R.; Farokhzad, O. C., Precise engineering of targeted nanoparticles by using self-assembled biointegrated block copolymers. *Proc. Natl. Acad. Sci. USA* **2008,** *105* (7), 2586-91.

14. Dhar, S.; Kolishetti, N.; Lippard, S. J.; Farokhzad, O. C., Targeted delivery of a cisplatin prodrug for safer and more effective prostate cancer therapy in vivo. *Proc. Natl. Acad. Sci. USA* **2011,** *108* (5), 1850-1855.

15. Marrache, S.; Dhar, S., Biodegradable synthetic high-density lipoprotein nanoparticles for atherosclerosis. *Proc. Natl. Acad. Sci. USA* **2013,** *110* (23), 9445-9450.

16. Marrache, S.; Pathak, R. K.; Darley, K. L.; Zaver, D.; Choi, J. H.; Kolishetti, N.; Dhar, S., Nanocarriers as Therapeutic Platforms for Tracking and Treating Diseases. *Curr. Med. Chem.* **2013**.

17. Smith, R. A. J.; Porteous, C. M.; Gane, A. M.; Murphy, M. P., Delivery of bioactive molecules to mitochondria in vivo. *Proc. Natl. Acad. Sci. USA* **2003,** *100* (9), 5407-5412.

18. Marrache, S.; Dhar, S., Engineering of blended nanoparticle platform for delivery of mitochondria-acting therapeutics. *Proc. Natl. Acad. Sci. USA* **2012,** *109* (40), 16288-16293.

19. Redmond, R. W.; Kochevar, I. E., Spatially resolved cellular responses to singlet oxygen. *Photochem. Photobiol.* **2006,** *82* (5), 1178-86.

20. Skovsen, E.; Snyder, J. W.; Lambert, J. D.; Ogilby, P. R., Lifetime and diffusion of singlet oxygen in a cell. *J. Phys. Chem. B* **2005,** *109* (18), 8570-3.

21. Dhar, S.; Gu, F. X.; Langer, R.; Farokhzad, O. C.; Lippard, S. J., Targeted delivery of cisplatin to prostate cancer cells by aptamer functionalized Pt(IV) prodrug-PLGA-PEG nanoparticles. *Proc. Natl. Acad. Sci. USA* **2008,** *105* (45), 17356-61.

22. Kolishetti, N.; Dhar, S.; Valencia, P. M.; Lin, L. Q.; Karnik, R.; Lippard, S. J.; Langer, R.; Farokhzad, O. C., Engineering of self-assembled nanoparticle platform for precisely controlled combination drug therapy. *Proc. Natl. Acad. Sci. USA* **2010,** *107* (42), 17939-44.

23. Floridi, A.; Paggi, M. G.; Marcante, M. L.; Silvestrini, B.; Caputo, A.; Demartino, C., Lonidamine, a selective inhibitor of aerobic glycolysis of murine tumor-cells. *J. Natl. Cancer I.* **1981,** *66* (3), 497-499.

24. Davis, S.; Weiss, M. J.; Wong, J. R.; Lampidis, T. J.; Chen, L. B., Mitochondrial and plasma membrane potentials cause unusual accumulation and retention of rhodamine 123 by human breast adenocarcinoma-derived MCF-7 cells. *J. Biol. Chem.* **1985,** *260* (25), 13844-50.

25. Chen, L. B., Mitochondrial membrane potential in living cells. *Annu. Rev. Cell. Biol.* **1988,** *4*, 155-81.

26. Steinman, R. M.; Inaba, K.; Turley, S.; Pierre, P.; Mellman, I., Antigen capture, processing, and presentation by dendritic cells: recent cell biological studies. *Hum. Immunol.* **1999,** *60* (7), 562-7.

27. Buytaert, E.; Dewaele, M.; Agostinis, P., Molecular effectors of multiple cell death pathways initiated by photodynamic therapy. *BBA-Rev. Cancer* **2007,** *1776* (1), 86-107.

28. Mroz, P.; Hashmi, J. T.; Huang, Y. Y.; Lange, N.; Hamblin, M. R., Stimulation of anti-tumor immunity by photodynamic therapy. *Expert Rev. Clin. Immunol.* **2011,** *7* (1), 75-91.

29. Papadakis, K. A.; Prehn, J. L.; Landers, C.; Han, Q. W.; Luo, X.; Cha, S. C.; Wei, P.; Targan, S. R., TL1A synergizes with IL-12 and IL-18 to enhance IFN-gamma production in human T cells and NK cells. *J. Immunol.* **2004,** *172* (11), 7002-7007.

30. Tominaga, K.; Yoshimoto, T.; Torigoe, K.; Kurimoto, M.; Matsui, K.; Hada, T.; Okamura, H.; Nakanishi, K., IL-12 synergizes with IL-18 or IL-1 beta for IFN-gamma production from human T cells. *Int. Immunol.* **2000,** *12* (2), 151-160.

31. Fricke, I.; Mitchell, D.; Mittelstadt, J.; Lehan, N.; Heine, H.; Goldmann, T.; Bohle, A.; Brandau, S., Mycobacteria induce IFN-gamma production in human dendritic cells via triggering of TLR2. *J. Immunol.* **2006,** *176* (9), 5173-5182.

32. Oliver, R. T. D.; Nouri, A. M. E., T-cell immune-response to cancer in humans and Its relevance for immunodiagnosis and therapy. *Cancer Surv.* **1992,** *13*, 173-204.

33. Mokyr, M. B.; Dray, S., Interplay between the toxic effects of anticancer drugs and host antitumor immunity in cancer-therapy. *Cancer Invest.* **1987,** *5* (1), 31-38.

34. Menard, C.; Martin, F.; Apetoh, L.; Bouyer, F.; Ghiringhelli, F., Cancer chemotherapy: not only a direct cytotoxic effect, but also an adjuvant for antitumor immunity. *Cancer Immunol. Immunother.* **2008,** *57* (11), 1579-87.

35. Mattarollo, S. R.; Loi, S.; Duret, H.; Ma, Y.; Zitvogel, L.; Smyth, M. J., Pivotal role of innate and adaptive immunity in anthracycline chemotherapy of established tumors. *Cancer Res* **2011,** *71* (14), 4809-20.

36. Robinson, C. M.; O'Dee, D.; Hamilton, T.; Nau, G. J., Cytokines involved in interferon-gamma production by human macrophages. *J. Innate. Immun.* **2010,** *2* (1), 56-65.

37. Darwich, L.; Coma, G.; Pena, R.; Bellido, R.; Blanco, E. J.; Este, J. A.; Borras, F. E.; Clotet, B.; Ruiz, L.; Rosell, A.; Andreo, F.; Parkhouse, R. M.; Bofill, M., Secretion of interferon-gamma by human macrophages demonstrated at the single-cell level after costimulation with interleukin (IL)-12 plus IL-18. *Immunology* **2009,** *126* (3), 386-93.

38. Gardella, S.; Andrei, C.; Costigliolo, S.; Poggi, A.; Zocchi, M. R.; Rubartelli, A., Interleukin-18 synthesis and secretion by dendritic cells are modulated by interaction with antigen-specific T cells. *J. Leukocyte Biol.* **1999,** *66* (2), 237-241.

39. Dreher, D.; Kok, M.; Obregon, C.; Kiama, S. G.; Gehr, P.; Nicod, L. P., Salmonella virulence factor SipB induces activation and release of IL-18 in human dendritic cells. *J. Leukoc. Biol.* **2002,** *72* (4), 743-51.

40. Mooney, L. M.; Al-Sakkaf, K. A.; Brown, B. L.; Dobson, P. R., Apoptotic mechanisms in T47D and MCF-7 human breast cancer cells. *Br. J. Cancer* **2002,** *87* (8), 909-17.

41. Benjamin, C. W.; Hiebsch, R. R.; Jones, D. A., Caspase activation in MCF7 cells responding to etoposide treatment. *Mol. Pharmacol.* **1998,** *53* (3), 446-50.

42. Banchereau, J.; Briere, F.; Caux, C.; Davoust, J.; Lebecque, S.; Liu, Y. T.; Pulendran, B.; Palucka, K., Immunobiology of dendritic cells. *Annu. Rev. Immunol.* **2000,** *18*, 767-811.

43. de Vries, I. J. M.; Lesterhuis, W. J.; Scharenborg, N. M.; Engelen, L. P. H.; Ruiter, D. J.; Gerritsen, M. J. P.; Croockewit, S.; Britten, C. M.; Torensma, R.; Adema, G. J.; Figdor, C. G.; Punt, C. J. A., Maturation of dendritic cells is a prerequisite for inducing immune responses in advanced melanoma patients. *Clin. Cancer Res.* **2003,** *9* (14), 5091-5100.

44. Dhodapkar, M. V.; Steinman, R. M.; Krasovsky, J.; Munz, C.; Bhardwaj, N., Antigen-specific inhibition of effector T cell function in humans after injection of immature dendritic cells. *J. Exp. Med.* **2001,** *193* (2), 233-238.

45. Lanzavecchia, A.; Sallusto, F., Regulation of T cell immunity by dendritic cells. *Cell* **2001,** *106* (3), 263-266.

CHAPTER 4

DETOURING OF CISPLATIN TO ACCESS MITOCHONDRIAL GENOME FOR OVERCOMING RESISTANCE[1]

[1] Reprinted with the permission of Marrache, S.; Pathak, R.K.; and Dhar, S. *Proc. Natl. Acad. Sci. USA*, 2014, doi: 10.1073/pnas.1405244111. Copyright 2014, United States National Academy of Sciences

Abstract

Chemo-resistance of cisplatin therapy is related to extensive repair of cisplatin-modified DNA in the nucleus by the nucleotide excision repair (NER). Delivering cisplatin to the mitochondria to attack mitochondrial genome lacking NER machinery can lead to a rationally designed therapy for metastatic, chemo-resistant cancers and might overcome the problems associated with conventional cisplatin treatment. An engineered hydrophobic mitochondria-targeted cisplatin prodrug, Platin-M was constructed using a strain promoted alkyne azide cycloaddition chemistry. Efficient delivery of Platin-M using a biocompatible polymeric nanoparticle (NP) based on biodegradable poly(lactic-*co*-glycolic acid)-block-polyethyleneglycol functionalized with a terminal triphenylphosphonium cation which has remarkable activity to target mitochondria of cells resulted in controlled release of cisplatin from Platin-M locally inside the mitochondrial matrix to attack mitochondrial DNA (mtDNA) and exhibited otherwise resistant advance cancer sensitive to cisplatin-based chemotherapy. Identification of an optimized targeted-NP formulation with brain-penetrating properties allowed for delivery of Platin-M inside the mitochondria of neuroblastoma cells resulting in ~18 times more activity than cisplatin. The remarkable activity of Platin-M and its targeted-NP in cisplatin resistant cells was correlated with the hyperpolarization of mitochondria in these cells and mitochondrial bioenergetics studies in the resistance cells further supported this hypothesis. This unique dual targeting approach to controlled mitochondrial delivery of cisplatin in the form of a prodrug to attack the mitochondrial genome lacking NER machinery and in vivo distribution of the delivery vehicle in the brain suggested previously undescribed routes for cisplatin-based therapy.

Introduction

The cellular powerhouse, mitochondria are implicated in the process of carcinogenesis because of their vital role in energy production and apoptosis. Mitochondria are the key players in generating the cellular energy through oxidative phosphorylation (OXPHOS) that produces reactive oxygen species (ROS) as by-products. Mitochondrial DNA (mtDNA) plays significant roles in cell death and metastatic competence. The close proximity of mtDNA to the ROS production site makes this genome vulnerable to oxidative damage. Mitochondrial dysfunction and associated mtDNA depletion possibly reversibly control epigenetic changes in the nucleus that contributes to cancer development.[1] Thus targeting mtDNA could lead to novel and effective therapies for aggressive cancers. Cisplatin, a Food and Drug Administration approved chemotherapeutic agent, is most extensively characterized as a DNA-damaging agent and the cytotoxicity of cisplatin is attributed to the ability to form interstrand and intrastrand nuclear DNA (nDNA) cross-links.[2] The nucleotide excision repair (NER) pathway plays major roles in repairing cisplatin-nDNA adducts [3]. Resistance to cisplatin can result from several mechanisms, including decreased uptake and accelerated DNA repair by NER machinery. Limited studies have examined cisplatin activity on mtDNA of cancer cells [4]. The lack of NER in the mitochondria and enhanced mtDNA mutation in aggressive cancer gives a strong rationale in directing cisplatin inside the mitochondrial matrix to provide an effective therapeutic option. However, the most important step to attack mtDNA by cisplatin requires a mitochondria-targeted drug and even better an optimal drug delivery system that is able to reach the innermost mitochondrial space, the mitochondrial matrix, where the mtDNA is located. We recently developed a

biocompatible polymeric nanoparticle (NP) based on biodegradable poly(lactic-*co*-glycolic acid) (PLGA)-block (*b*)-polyethyleneglycol (PEG) functionalized with a terminal triphenylphosphonium (TPP) cation which has remarkable activity to target mitochondria of cells due to its high lipophilic properties, presence of delocalized positive charge, and appropriate size range [5, 6]. Here, we describe construction of a hydrophobic mitochondria targeted cisplatin prodrug, Platin-M, using strain promoted alkyne azide cycloaddition (SPAAC) chemistry and its delivery using PLGA-*b*-PEG-TPP NPs to release cisplatin locally inside the mitochondrial matrix to attack mtDNA for overcoming resistance associated with conventional cisplatin-based chemotherapy (Fig. 4.1).

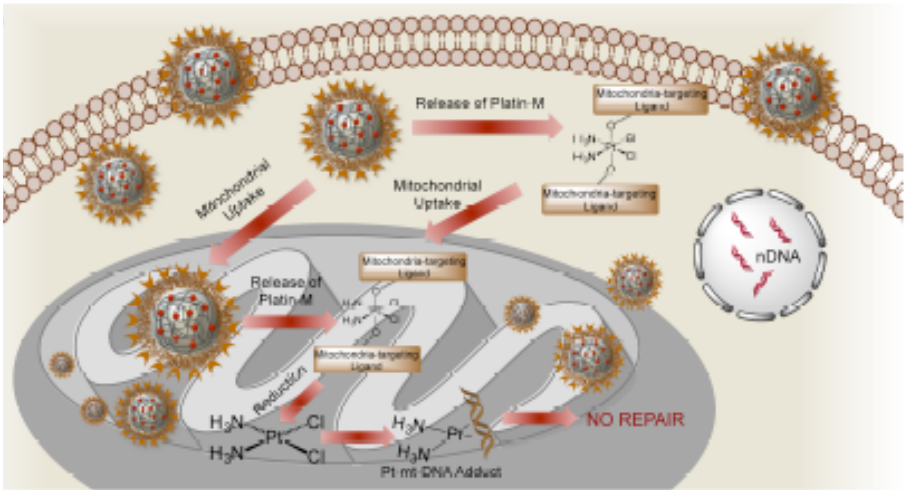


Figure 4.1. Schematic figure for mitochondrial delivery of cisplatin prodrug using a targeted NP and the mechanism of action.

Materials and Methods

Synthesis of Platin-M:

Platin-M was synthesized and characterized by Dr. Rakesh K. Pathak and the details can be found in *Proc. Natl. Acad. Sci. USA*, 2014, doi: 10.1073/pnas.1405244111

Platin-M Ability to Form Micelles

Platin-M was dissolved in DMF to a final concentration of 1.5 mg/mL. This solution was added drop wise slowly into vigorously stirring nanopure water (10 mL) and stirred at room temperature for 3 h. This solution was then filtered and washed 3 times via centrifugation using Amicon centrifugal filters with a MW cutoff of 100 kDa in order to ensure removal of organic solvent. Finally, the micelles were resuspended in nanopure water (1 mL) and filtered through a 0.2 μm filter. The resulting suspension was characterized by DLS.

Synthesis of $PLGA_{LMW}$-b-PEG-OH and $PLGA_{LMW}$-b-PEG-TPP:

These two polymers were synthesized following methods previously reported by us [5]. Spectral Data for $PLGA_{LMW}$-*b*-PEG-OH: ^{1}H NMR ($CDCl_3$, 400 MHz): δ 5.22 [m, 37 H (O*CH*CH_3C(O)], 4.81 [m, 74 H (O*CH*$_2$C(O)], 3.63 [s, 102 H (O*CH*$_2$)], 1.57 [m, 115 H (*CH*$_3$CH)] ppm. ^{13}C NMR ($CDCl_3$, 100 MHz): δ 169.40, 166.33, 70.54, 69.08, 60.79, 16.66 ppm. Spectral Data for $PLGA_{LMW}$-*b*-PEG-TPP: ^{1}H NMR ($CDCl_3$, 400 MHz): δ 7.8-7.3 [m 15 H (PPh_3), 5.20 [m, 37 H (O*CH*CH_3C(O)], 4.81 [m, 73 H (O*CH*$_2$C(O)], 3.63 [s, 102 H (O*CH*$_2$)], 1.57 [m, 112 H (*CH*$_3$CH)] ppm. ^{13}C NMR ($CDCl_3$, 100 MHz): *δ* 169.27, 166.32, 134.90, 133.84, 130.33, 118.79, 117.93, 70.54, 69.00, 60.80, 16.67 ppm. ^{31}P NMR ($CDCl_3$, 100 MHz): *δ* 24.62 ppm. GPC: M_n=14,420 g/mol, M_w=17,030 g/mol, M_z=20,320 g/mol, PDI = 1.18.

Synthesis of $PLGA_{HMW}$-b-PEG-OH

HO-PEG-OH (3.75 g, 1.1 mmol), PLGA-COOH (inherent viscosity of 0.55-0.75, 5.0 g, 0.38 mmol), and DMAP (0.045 g, 0.38 mmol) were dissolved in dry CH_2Cl_2 (50 mL). The reaction mixture was cooled to 0 °C while stirring. DCC (0.2 g, 1.1 mmol) was

dissolved in CH_2Cl_2 (3 mL) and added drop wise to the polymer solution. The mixture was then warmed to room temperature and stirred overnight. Afterwards, DCU was filtered out and the resulting mixture was precipitated in a 50:50 mixture of cold diethyl ether:methanol (200 mL), repeatedly. The resulting solid was centrifuged at 5000 rpm for 10 min. The resulting solid was lyophilized to produce the polymer with a 41% yield. Final product was analyzed by NMR and GPC. ^{1}H NMR ($CDCl_3$, 400 MHz): δ 5.21 [m, 574 H (O*CH*CH_3C(O)], 4.82 [m, 1132 H (O*CH*$_2$C(O)], 3.64 [s, 187 H (O*CH*$_2$)], 1.58 [m, 1868 H (*CH*$_3$CH)] ppm. ^{13}C NMR ($CDCl_3$, 100 MHz): δ 169.30, 166.33, 70.55, 68.96, 68.93, 60.80, 16.69 ppm. GPC: M_n=47,280 g/mol, M_w=68,210 g/mol, M_z=92,900 g/mol, PDI = 1.36.

Synthesis of PLGA$_{HMW}$-b-PEG-TPP

PLGA$_{HMW}$-*b*-PEG-OH (1 g, 0.02 mmol), TPP-$(CH_2)_4$-COOH (0.045 g, 0.12 mmol), and DMAP (0.010 g, 0.08 mmol) were dissolved in CH_2Cl_2 for 30 min at 0 °C. A solution of DCC (12 mg, 0.06 mmol) was added drop wise. The solution was slowly returned to room temperature and stirred for 12 h. The resulting DCU was removed *via* gravity filtration. CH_2Cl_2 was removed *in vacuo* and the resulting polymer was dissolved in a 50:50 mixture of CH_2Cl_2/CH_3OH and precipitated with cold diethyl ether. The resulting solid was isolated by centrifugation (5000 rpm, 10 min, 4 °C) This process was repeated 4 times in order to remove the residual TPP-$(CH_2)_4$-COOH. Finally, the resulting polymer was lyophilized to produce the targeted polymer with a 59% yield. ^{1}H NMR ($CDCl_3$, 400 MHz): δ 7.6-7.7 [m, 15 H, (PPh_3)], 5.21 [m, 615 H (O*CH*CH_3C(O)], 4.82 [m, 1203 H (O*CH*$_2$C(O)], 3.64 [s, 187 H (O*CH*$_2$)], 1.57 [m, 2002 H (*CH*$_3$CH)] ppm. ^{13}C NMR ($CDCl_3$, 100 MHz): δ 169.30, 166.34, 135.17, 134.93, 130.52, 117.85, 116.59,

70.54, 69.05, 60.80, 16.69 ppm. ^{31}P NMR ($CDCl_3$, 100 MHz): δ 24.37 ppm. GPC: M_n=54,510 g/mol, M_w= 73,510 g/mol, M_z=94,380 g/mol, PDI = 1.35.

Preparation of Platin-M Encapsulated PLGA-b-PEG Polymeric Nanoparticles (NPs)

Platin-M encapsulated targeted NPs (T-Platin-M-NP) and non-targeted (NT-Platin-M-NP) NPs were prepared by a nanoprecipitation method. Briefly, PLGA-*b*-PEG-TPP [5] or PLGA-PEG-OH were dissolved in DMF (50 mg/mL). Varying amounts of Platin-M (10 mg/mL in DMF) were added to the PLGA-*b*-PEG-TPP or PLGA-*b*-PEG-OH solution to a final polymer solution of 5 mg/mL. This was added drop-wise slowly into vigorously stirring nanopure water (10 mL) and stirred at room temperature for 2 h. This solution was then filtered and washed through centrifugal filters with a MW cutoff of 100 kDa 3 times in order to ensure the removal of all organic solvent. Finally, the NPs were resuspended in nanopure water (1 mL) and filtered through a 0.2 μm filter. The NPs were characterized by DLS for size and zeta potential and Platin-M content was analyzed by ICP-MS.

Preparation of PLGA-PEG-QD Encapsulated PLGA-b-PEG-TPP-NPs

$PLGA_{LMW}$-*b*-PEG-TPP-NPs and $PLGA_{HMW}$-*b*-PEG-TPP-NPs containing PLGA-PEG-QD [5] were synthesized using nanoprecipitation method. A mixture of $PLGA_{LMW}$-*b*-PEG-TPP or $PLGA_{HMW}$-*b*-PEG-TPP (5 mg/mL in DMF) and PLGA-PEG-QD (10 μL, 8 μM in DMF) was added drop wise to vigorously stirring water. The NPs were stirred for 2 h. Organic solvent was removed by 3 washes using centrifugal filters with a 100 kDa cut-off. NPs were resuspended in nanopure water.

Release Kinetics of Platin-M from NPs

In order to understand the rate at which Platin-M was released from the NP core, release kinetics of T-Platin-M-NPs and NT-Platin-M-NPs were studied. The NPs (T or NT) were synthesized according to the method above. The resulting NPs were subjected to dialysis using Slide-A-Lyzer Mini dialysis devices with a 100 kDa MW cutoff of in 1X PBS at physiological conditions (pH 7.4 and 6.0, 37 °C). PBS was changed every 12 h. At different time points, the dialysis bag was removed and the amount of Platin-M remaining in the polymeric core was analyzed by ICP-MS.

Cellular Fractionation of Cells Treated with Platin-M-NPs, Platin-M, and Cisplatin

Platin-M, T-Platin-M-NPs, NT-Platin-M-NPs, and cisplatin (1 μM with respect to Pt) were added in PC3 cells ($1.0x10^6$ cells/mL in 15 mL) for 12 h. After internalization, the mitochondria and the cytosol were isolated using a mitochondria isolation kit for mammalian cells. Cells were isolated by trypsinization and washed 3x with 1X PBS. Reagent A supplemented with protease inhibitors (10 mg/mL) was added followed by incubation on ice for 2 min. Reagent B was added and incubated on ice for 5 min with gentle vortexing every min. Following this, reagent C was added and the cells were centrifuged (700x*g* at 4 °C for 10 min). The resulting pellet yielded the nuclei and cellular debris. The supernatant, containing the cytosolic and mitochondrial fractions, was removed and further centrifuged (12,000x*g* at 4 °C for 15 min). The resulting supernatant contained the cytosolic fraction and the pellet contained the impure mitochondrial fraction. This was further purified by washing with reagent C and centrifuging at 12,000 x*g* at 4 °C for 5 min. The isolated nucleus and cellular debris were further fractionated in order to obtain a pure nuclear fraction. The pellet was resuspended in 600 μL of a modified Tris.HCl buffer (10 mM Tris.HCl, pH 7.0, 10 mM NaCl, 3 mM

$MgCl_2$, 30 mM sucrose). This was incubated on ice for 10 min and centrifuged (3000 rpm, 4 °C). The resulting pellet was resuspended in 1 mL of pre-chilled $CaCl_2$ buffer (10 mM Tris.HCl of pH 7.0, 10 mM NaCl, 3 mM $MgCl_2$, 30 mM sucrose, 10 mM $CaCl_2$). This was repeatedly centrifuged and washed with the $CaCl_2$ buffer and the supernatant was discarded each time. The pellet was further purified by resuspending in a buffer containing 20 mM Tris-HCl of pH 7.9, 20% glycerol, 0.1 M KCl, and 0.2 mM EDTA and centrifuging at 14,000 rpm for 30 min at 4 °C. The resulting pellet yielded the purified nuclear fraction and was resuspended in H_2O. The amount of protein in each fraction was analyzed by a BCA assay and the Pt content of each fraction was quantified by ICP-MS.

Mitochondrial Sub-fractionation

QD blended $PLGA_{HMW}$-*b*-PEG-TPP or $PLGA_{LMW}$-*b*-PEG-TPP NPs (0.5 mg/mL with respect to NP) were internalized in PC3 cells ($1.0x10^6$ cells/mL in 30 mL) for 6 h. After internalization, the mitochondria and the cytosol were isolated using a mitochondria isolation kit for mammalian cells. These fractions were further sub-fractionated. The freshly isolated PC3 mitochondria in PBS (1x) were incubated with protease inhibitor (0.125 mg/mL) and 0.6 % digitonin for 10 min on ice. Immediately after incubation, the mitochondria were centrifuged at 10,000xg for 10 min at 4 °C. The supernatant (SN-I) contained the outer mitochondrial membrane (OMM) fraction and the intermembrane space (IMS). The pellet was resuspended in 150 mmol/L KCl, protease inhibitor (0.125 mg/mL) and incubated on ice for 10 min. This was centrifuged at 10,000xg for 10 min at 4 °C. The supernatant, which contained the mitochondrial matrix, was collected. To this, 50 μL of 1x cell lysis buffer (30 mM Tris-HCl, 0.1 mM EDTA, 20 % w/v sucrose) was added. This was subsequently sonicated and centrifuged at 10,000xg for 15 min at 4 °C.

The supernatant (SN-II) containing the purified inner mitochondrial membrane (IMM) fraction and matrix was collected. SN-I and SN-II were centrifuged at 105,000xg for 60 min. The pellet from SN-I contained the OMM fraction and the supernatant contained the IMS. The pellet from SN-II was resuspended in PBS containing Lubrol WX (0.5 mg/mL), 37 % sucrose and incubated for 15 min on ice. This was once again centrifuged at 105,000 g for 60 min at 4 °C. The pellet containing the IMM fraction and the supernatant containing the matrix were collected. The collected fractions were analyzed for Cd concentration by ICP-MS. A BCA assay was performed on all the fractions in order to calculate the Cd (ng)/protein (pg). The collected fractions were imaged on a Xenogen IVIS® Lumina system with 570 excitation wavelength and a Cy5.5 emission channel with an exposure time of 0.5 s.

Cell Mito Stress Analysis

Different parameters of respiration: basal respiration, coupling efficiency, and spare respiratory capacity were investigated by using Seahorse XF-24 cell Mito Stress Test Kit. Prior to the assay, XF sensor cartridges were hydrated. To each well of an XF utility plate, 1 mL of Seahorse Bioscience calibrant was added and the XF sensor cartridges were placed on top of the utility plate, and kept at 37 °C incubator without CO_2 for a minimum of 12 h. PC3, A2780-CP70, SH-SY5Y, and H9C2 cells were cultured in XF24-well cell culture microplates (Seahorse Bioscience) at a density of 2.5×10^4 cells/well (except for H9C2, cell density of this cell line: 5×10^4 cells/well) (0.32 cm^2) in 200 μL growth medium and then incubated for 24 h at 37 °C in 5% CO_2 atmosphere. The cells were treated with Platin-M (10 μM), cisplatin (10 μM), DBCO-TPP (10 μM), empty-T-NPs, empty-NT-NPs, T-Platin-M-NPs, NT-Platin-M-NPs (10 μM with respect

to Pt; ~0.5 mg/mL for empty NPs) for 12 h at 37 °C in 5% CO_2 atmosphere. After 12 h, all but 50 μL of the culture medium was removed from each well and the cells were rinsed two times with 500 μL of XF stress test glycolysis optimization medium pre-warmed to 37 °C and finally 450 μL of glucose depleted optimization medium was added to each well and the plate was placed at 37 °C without CO_2 for 1 h prior to assay. Different parameters of respiration were calculated by subtracting the average respiration rates before and after the addition of the electron transport inhibitors oligomycin (1.0 μM), trifluorocarbonylcyanide phenylhydrazone or FCCP (1.0 μM), an ionophore that is a mobile ion carrier, and a mixture of antimycin-A (1.0 μM) which is a complex III inhibitor and rotenone (1.0 μM), a mitochondrial inhibitor that prevents the transfer of electrons from the Fe-S center in Complex I to ubiquinone. The parameters calculated included: basal respiration (baseline respiration minus antimycin-A post injection respiration), ATP turnover (baseline respiration minus oligomycin post injection respiration), maximal respiratory capacity (FCCP stimulated respiration minus antimycin-A post injection respiration) and reserve respiratory capacity (FCCP stimulated respiration minus baseline respiration). Test articles on each well had four replicates.

In Vivo Biodistribution (bioD) and Pharmacokinetics (PK)

BioD and PK properties were determined using male Sprague Dawley rats weighing around ~300 g. These experiments were carried out at a Contract Research Organization, VivoPath. Three rats per group, had T-QD-NPs injected *via* tail vein with ~1 mL of T-NPs (23 mg/kg with respect to NPs, 81 μg/kg with respect to Cd) or saline. In a separate experiment, two rats per group had Platin-M (~0.5 mL, 95.8±0.7 μg Pt),

NT-Platin-M-NPs (~0.5 mL, 98.0±7.2 μg Pt), and T-Platin-M-NPs (~0.14 mL, 25.7±2.1 μg Pt) injected *via* tail vein or saline. At varying time intervals, blood samples were collected in heparinized tubes and centrifuged in order to collect blood plasma. The percentage of QD or Pt was calculated by taking into consideration that blood constitutes 7% of body weight and plasma constitutes 55% of blood volume [9]. The amount of Cd from the QD or Pt from Platin-M was calculated in the blood plasma by ICP-MS. After 24 h, the animals were sacrificed and the vital organs were collected. The collective urine and feces were also collected over a 24 h period for T-QD-NPs. For Platin-M, NT-Platin-M-NPs, and T-Platin-M-NPs, urine samples (~100 μL) were collected at 24 h directly from the bladder and collective feces were collected over 24 h. The overall bioD was calculated by analyzing the amount of Cd or Pt in each organ as well as the feces and urine by ICP-MS. Before analysis, the organs and feces were dissolved with PerkinElmer solvable (Product number: 6NE9100) for 24 h with gentle heating and shaking. The calculations for AUC, C_{max}, T_{max}, and C_L (t=0) were performed in the GraphPad Prism (Version 5.01). PK parameters were determined by fitting the data using a two-compartmental or one compartmental model equation. These calculations were performed by Walter Lunsmann from VivoPath.

Quantification of mtDNA-Pt and nDNA-Pt Adducts

The mitochondria and nuclei were isolated according to the protocols mentioned before. These fractions were further fractionated in order to isolate mitochondrial and nuclear DNA, respectively. For mitochondrial DNA (mtDNA), the freshly isolated mitochondria were re-suspended in 35 μL of mitochondrial lysis buffer. To this, 5 μL of the enzyme mix was added. This was incubated at 50 °C in water bath until the solution

turned clear (~1 h). To this, 100 μL of absolute ethanol was added and the resulting solution was incubated for 10 min at -20 °C. The solution was then centrifuged at 14000 rpm for 5 min at room temperature. The resulting pellet was then purified by washing with 70% ethanol in nanopure H_2O. The resulting purified mtDNA was resuspended in tris-EDTA (TE) buffer. The resulting solution was quantified for the amount and purity of DNA by UV-Vis spectroscopy (260/280 nm) and the amount of Pt by ICP-MS. For nuclear DNA (nDNA), the freshly isolated nuclei were re-suspended in 40 μL of cell lysis buffer. To this, 5 μL of the enzyme mix was added. This was incubated in a 50 °C water bath until the solution turned clear (~1 h). To this, 100 μL of absolute ethanol was added and the resulting solution was incubated for 10 min at -20 °C. The solution was then centrifuged at 14000 rpm for 5 min at room temperature. The resulting pellet was then purified by washing with 70% ethanol in nanopure H_2O. Reprecipitation with 70% ethanol in nanopure H_2O was performed until the ratio of the absorbances at 260 and 280 nm was ≥1.75 and ≤2.1. The resulting purified nDNA was resuspended in TE buffer. The resulting solution was quantified for the amount of DNA by UV-Vis spectroscopy (260/280 nm) and the amount of Pt by ICP-MS.

Citrate Synthase Assay

SH-SY5Y cells were seeded at a density of $1x10^6$ cells/mL on each well of a six well plate and allowed to grow overnight. Cells were treated with 1.0 μM cisplatin, 1.0 μM Platin-M, 1.0 μM NT-Platin-M-NPs, and 1.0 μM T-Platin-M-NPs for 12 h at 37 °C. The cells were trypsinized and washed 3x with PBS. The isolated cell pellet was then solubilized using 500 μL of the extraction buffer and incubated on ice for 20 min. The cells were then centrifuged at 16,000xg at 4 °C for 20 min. The samples (100 μL) were

then added to the pre-coated microplate strips, sealed, and incubated for 3 h at room temperature. The wells were aspirated and washed 3x with wash buffer. Activity buffer (100 μL) was then added to each well and the plate was transferred to the microplate reader. The plate was read every minute for 20 sec intervals for 10 min at a wavelength of 412 nm.

Cytotoxicity of Platin-M and Platin-M-NPs

The cytotoxicity of Platin-M, T-Platin-M-NPs, NT-Platin-M-NPs, and cisplatin was tested in PC3, A2780/CP70, SH-SY-5Y, and MSC by MTT assay (Fig. S20, Table S4). PC3 cells (2000 cells/well), A2780/CP70 cells (2000 cells/well), SH-SY-5Y (2000 cells/well), and MSC (2000 cells/well) were plated on a 96 well plate and allowed to grow overnight. The media was changed and increasing concentrations of each formulation was added. For T-Platin-M-NPs, NT-Platin-M-NPs, the media was changed after 12 h and further incubated for an additional 60 h. The free drugs were incubated for 72 h without further media changes. After the given incubation time, MTT was added (5 mg/mL, 20 μL/well) and incubated for 5 h in order for MTT to be reduced to purple formazan. The media was removed and the cells were lysed with 100 μL of DMSO. In order to homogenize the formazan solution, the plates were subjected to 10 min of gentle shaking and the absorbance was read at 550 nm with a background reading at 800 nm with a plate reader. Cytotoxicity was expressed as mean percentage increase relative to the unexposed control ± SD. Control values were set at 0% cytotoxicity or 100% cell viability. Cytotoxicity data (where appropriate) was fitted to a sigmoidal curve and a three parameters logistic model used to calculate the IC_{50}, which is the concentration of chemotherapeutics causing 50% inhibition in comparison to untreated controls. The mean

IC_{50} is the concentration of agent that reduces cell growth by 50% under the experimental conditions and is the average from at least three independent measurements that were reproducible and statistically significant. The IC_{50} values were reported at ±99% confidence intervals. These analyses were performed with GraphPad Prism (San Diego, U.S.A).

Cellular Apoptosis Detection by Flow Cytometry

SH-SY5Y cells were seeded at a density of $1x10^6$ cells/mL on each well of a six well plate and allowed to grow overnight. Cells were treated with 1.0 μM cisplatin, 1.0 μM Platin-M, 1.0 μM NT-Platin-M-NPs, and 1.0 μM T-Platin-M-NPs for 12 h at 37 °C. As positive controls, etoposide (100 μM, incubation time: 12 h) for apoptosis and H_2O_2 (1 mM, incubation time: 45 min) for necrosis were used. The cells were trypsinized, repeatedly washed with cold PBS, and centrifuged at 1800 rpm for 3 min, and the supernatants were discarded (Note: During trypsinization, media was centrifuged and to isolate the floating cells). Cell density was determined and cells were resuspended in 1X Annexin-binding buffer to ~1×10^6 cells/mL preparing a sufficient volume to have 100 μL per assay. To 100 μL of cell suspension, 5 μL Alexa Fluor® 488 Annexin V and 1 μL (100 μg/mL) PI working solution were added, and incubated for 15 min at room temperature. After the incubation period, 400 μL 1X Annexin-binding buffer was added to each sample, samples were gently mixed keeping the samples on ice and the samples were analyzed on the flow cytometer immediately.

Flow Cytometric Analyses of Mitochondrial Function and Mitochondrial Mass by JC-1 Assay

To evaluate the integrity of mitochondrial functions, we used the cationic dye JC-1 assay. SH-SY5Y cells were cultured on a six well plate at a density of $1x10^6$ cells/mL and allowed to grow overnight at 37 °C. Cells were treated with 1.0 μM cisplatin, 1.0 μM Platin-M, 1.0 μM NT-Platin-M-NPs, and 1.0 μM T-Platin-M-NPs for 12 h at 37 °C. A solution of JC-1 reagent (10 μg/mL in RPMI) was added and incubated for 10 min at 37 °C. The cells were washed 3 times with PBS and trypsinized. The cells were isolated and washed 3x by centrifugation with PBS (1,800 rpm for 3 min at 4 °C). The resulting cell pellet was resuspended in 100 μL PBS and analyzed by flow cytometry using 488 nm and 633 nm excitations with 530 nm and 660 nm bandpass filters.

Animals.

Animals were obtained from Harlan Laboratory and handled in accordance with ‘‘The Guide for the Care and Use of Laboratory Animals’’ of American Association for Accreditation of Laboratory Animal Care (AAALAC), Animal Welfare Act (AWA), and other applicable federal and state guidelines. All animal work presented here was approved by Institutional Animal Care and Use Committee (IACUC) of University of Georgia.

Statistics

All data were expressed as mean ± S.D (standard deviation). Statistical analysis were performed using GraphPad Prism® software v. 5.00. Comparisons between two values were performed using an unpaired Student t test. A one-way ANOVA with a post-hoc Tukey test was used to identify significant differences among the groups.

Results and Discussion

Construction of Mitochondria-Targeted Cisplatin Prodrug

A mitochondria-targeted Pt(IV)-prodrug of cisplatin, Platin-M, was designed by introducing two mitochondria targeting delocalized lipophilic TPP cations in the axial positions (Fig. 1*A*). Recently, a Pt(II) compound, mtPt with a mitochondria targeting peptide for attacking mtDNA was reported [10]. Pt(IV) prodrugs are advantageous over the Pt(II) counterparts because of their greater stability and local activation which allow a greater proportion of the active drug at the target site(s) [11]. Mitochondrial functions including respiration are greatly reduced in cancer cells and tumor microenvironments differ greatly from that of normal tissues. Mitochondrial membrane potential ($\Delta\Psi_m$) in most cancer cells is greater compared to that of normal cells [12].

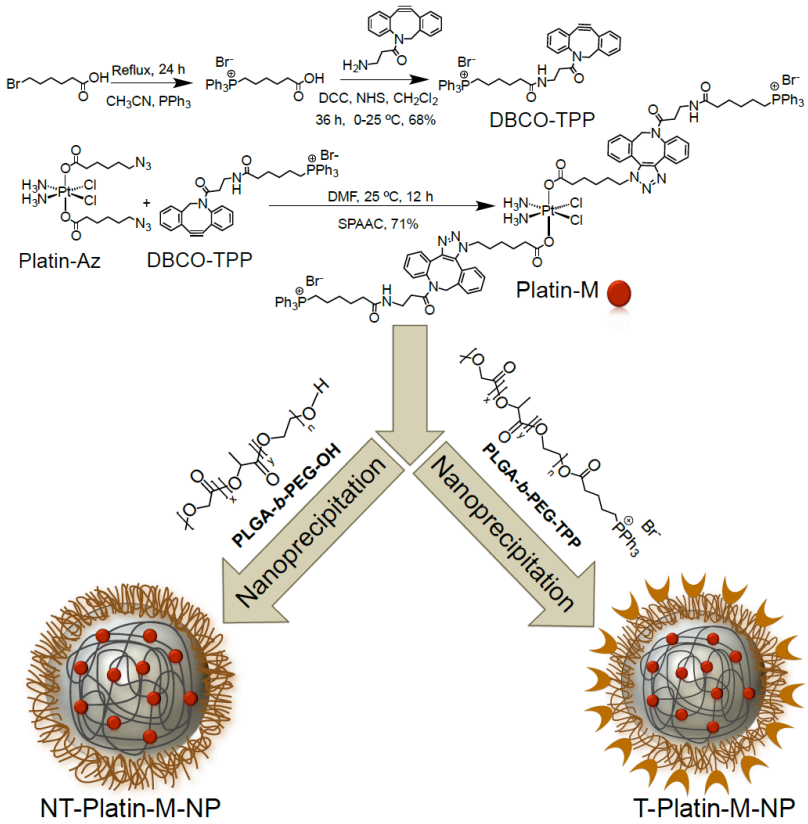


Fig 4.2. Synthesis of mitochondria targeted Pt(IV) prodrug Platin-M and nanoparticles

Therefore, TPP cation containing Platin-M will take advantage of the substantial negative $\Delta\Psi_m$ across the inner mitochondrial membrane (IMM) to efficiently accumulate inside the matrix (Fig. 4.1). Conventional coupling reaction with TPP ligands was found to be problematic due to reduction of Pt(IV). We recently developed a copper(I) free cycloaddition approach to introduce numerous functionalities on to Pt(IV) with high efficiency.[13] A TPP moiety was introduced on azadibenzocyclooctyne (DBCO) derivative to result DBCO-TPP (Fig. 4.2). A SPAAC reaction between an azide-Pt(IV) precursor Platin-Az [13] and DBCO-TPP resulted Platin-M with high efficiency (Fig. 4.2). Feasible cellular reduction of Pt(IV) prodrug is required to release active cisplatin. Electrochemical studies performed at two different biologically relevant pH values of 7.4 and 6.4 demonstrated that Platin-M will release active cisplatin in the cellular environment.

Development of Mitochondria-targeted NP for Platin-M

Small molecules, in particular Pt-based therapeutics show poor biodistribution (bioD) and pharmacokinetic (PK) properties, rapid clearance, and inactivation by biological nucleophiles before reaching the cellular targets. We anticipated that Platin-M would face similar challenges if administered in its pristine form. Self-assembled polymeric NPs composed of biodegradable PLGA-*b*-PEG block copolymer hold promise as carriers for small molecules [14]. However, the NP system that can deliver Platin-M successfully to the mitochondria of cells can be challenging. We recently developed an engineered NP from a triblock copolymer PLGA-*b*-PEG-TPP and identified an optimized targeted formulation for mitochondria delivery of small molecules [5, 6]. We anticipated that engineering of NPs from PLGA-*b*-PEG-TPP polymers of different molecular weight

would allow us to have a control over NP distribution in different mitochondrial compartments, outer mitochondrial membrane (OMM), IMM, the intermembrane space (IMS), and matrix and control the release kinetics of Platin-M from these NPs.

Thus, we constructed two triblock copolymers $PLGA_{LMW}$-*b*-PEG-TPP and $PLGA_{HMW}$-*b*-PEG-TPP based on a low molecular weight and a high molecular weight PLGA-COOH, respectively. To understand the distribution properties of the NPs in different mitochondrial compartments, we fractionated mitochondria isolated from prostate cancer (PCa) PC3 cells treated with NPs from $PLGA_{HMW}$-*b*-PEG-TPP and $PLGA_{LMW}$-*b*-PEG-TPP into OMM, IMM, IMS, and mitochondrial matrix. We incorporated 10% of PLGA-*b*-PEG-quantum dot (QD) [5] in both NPs, the NPs from $PLGA_{LMW}$-*b*-PEG-TPP had hydrodynamic diameter of 51.3±0.8 nm and zeta potential of 44.0±1.2 mV and the NPs from $PLGA_{HMW}$-*b*-PEG-TPP were 143.2±3.2 nm in size with zeta potential of 28.1±0.7 mV. Cd quantification by inductively coupled plasma mass spectrometry (ICP-MS) and imaging using an *in vivo* imaging system (IVIS) of cytosolic, IMM, OMM, IMS, and mitochondrial matrix indicated that the NPs from $PLGA_{LMW}$-*b*-PEG-TPP distributed most efficiently in the mitochondrial matrix, the NPs from $PLGA_{HMW}$-*b*-PEG-TPP accumulated mainly in the OMM (Fig. 4.3A). We used the NPs based on $PLGA_{LMW}$-*b*-PEG-TPP for efficient delivery of Platin-M inside the mitochondria for further studies.

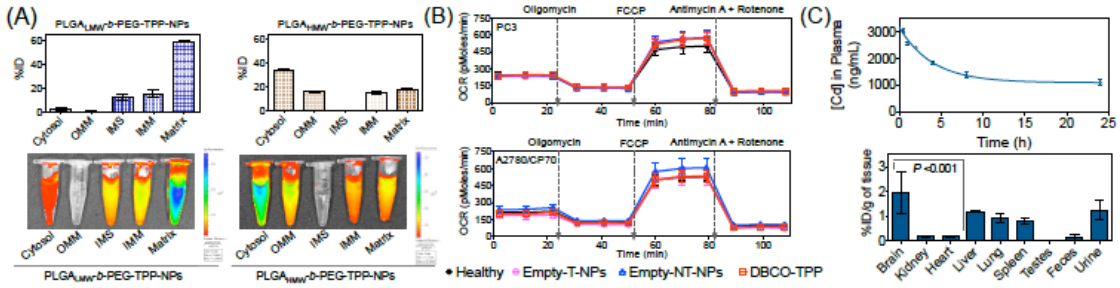


Figure 4.3. (A) Distribution of $PLGA_{HMW}$-b-PEG-TPP and $PLGA_{LMW}$-b-PEG-TPP-NPs in mitochondrial compartments of PC3 cells by ICP-MS (top) and IVIS analysis (bottom). (B) Mitochondrial toxicity of Empty-T-NPs and Empty-NT-NPs in PC3 and A2780/CP70 cells by Mito Stress assay. (C) Variation of Cd concentration in plasma with time, tissue distribution, and cumulative excretion profiles following the administration of T-QD-NPs intravenously to male rats.

Mitochondrial Toxicity of Mitochondria Targeted NPs (T-NPs)

Preclinical mitochondrial toxicology tests can have high predictive value. Thus we studied whether empty $PLGA_{LMW}$-*b*-PEG-TPP-NPs (Empty-T-NPs) containing TPP molecules exhibit any deleterious effects after entering mitochondria. TPP-based small molecules were described to disrupt $\Delta\Psi_m$, uncouple OXPHOS, and inhibit mitochondrial respiration [15]. We examined Empty-T-NP, empty non targeted $PLGA_{LMW}$-*b*-PEG-OH-NPs (Empty-NT-NPs), and DBCO-TPP induced changes in mitochondrial respiration in PC3 and cisplatin resistant ovarian cancer A2780/CP70 cells as a measure of mitochondrial toxicity (Fig. 4.3B). Oxygen consumption rate (OCR) of cells is an important indicator of normal mitochondrial functions. Mitochondrial bioenergetics in PC3 and A2780/CP70 cells treated with Empty-T-NPs (0.5 mg/mL), Empty-NT-NPs (0.5 mg/mL), and DBCO-TPP (10 μM) for 12 h were assessed using XF24 extracellular flux analyzer. The effects of metabolic modulators oligomycin, carbonyl cyanide 4-

(trifluoromethoxy)phenylhydrazone (FCCP), antimycin A, and rotenone allowed determination of multiple parameters of mitochondrial functions (Fig. 4.4B). Empty-T-NPs, Empty-NT-NPs, and DBCO-TPP did not show any changes in the basal OCR and the OCR linked to ATP production in the treated cells. Several parameters linked to mitochondrial respiration; spare respiratory capacity, coupling efficiency, basal respiration, electron transport chain (ETC) accelerator response, and ATP coupler response were calculated from the OCR (pMoles/min) vs. Time (min) traces (Fig. 4.3B). The ATP synthase inhibitor oligomycin was injected to evaluate mitochondrial coupling upon accumulation of T-NPs inside the mitochondria. When proton flux through the ATP synthase is inhibited, phosphorylating respiration stops and residual oxygen consumption is primarily due to proton leak across the IMM. Oligomycin decreased OCR to the same level in healthy and Empty-T-NPs, Empty-NT-NPs, and DBCO-TPP treated cells (Fig. 4.3B) indicating that the mitochondria remain coupled. Next, we injected FCCP, a H^+ ionophore and uncoupler of oxidative phosphorylation, to examine maximal respiratory capacity. FCCP dissipates the proton gradient across the IMM and uncouple electron transport from oxidative phosphorylation, thus, in the presence of FCCP, OCR increases to the maximum extent supported by the ETC and substrate supply. Stimulation of respiration by FCCP in healthy cells and Empty-T-NPs, Empty-NT-NPs, and DBCO-TPP treated cells were similar indicating that bioenergetic functions are well preserved in the presence of T-NPs. Inhibition of mitochondrial flux by addition of rotenone, a complex I inhibitor and antimycin A, a complex III inhibitor in healthy, Empty-T-NP, Empty-NT-NP, and DBCO-TPP treated cells indicated similar levels of mitochondrial and non-mitochondrial respiration. Collectively, these data suggested that several TPP containing

T-NPs enter mitochondrial matrix efficiently, however these NPs do not cause any mitochondrial function inhibition or toxicity. Heart cells contain hyperpolarized mitochondria; we therefore, studied toxicity of mitochondria accumulating Empty-T-NPs in myogenic H9C2 cardiomyocytes derived from embryonic rat heart ventricle (Fig. 4.4).

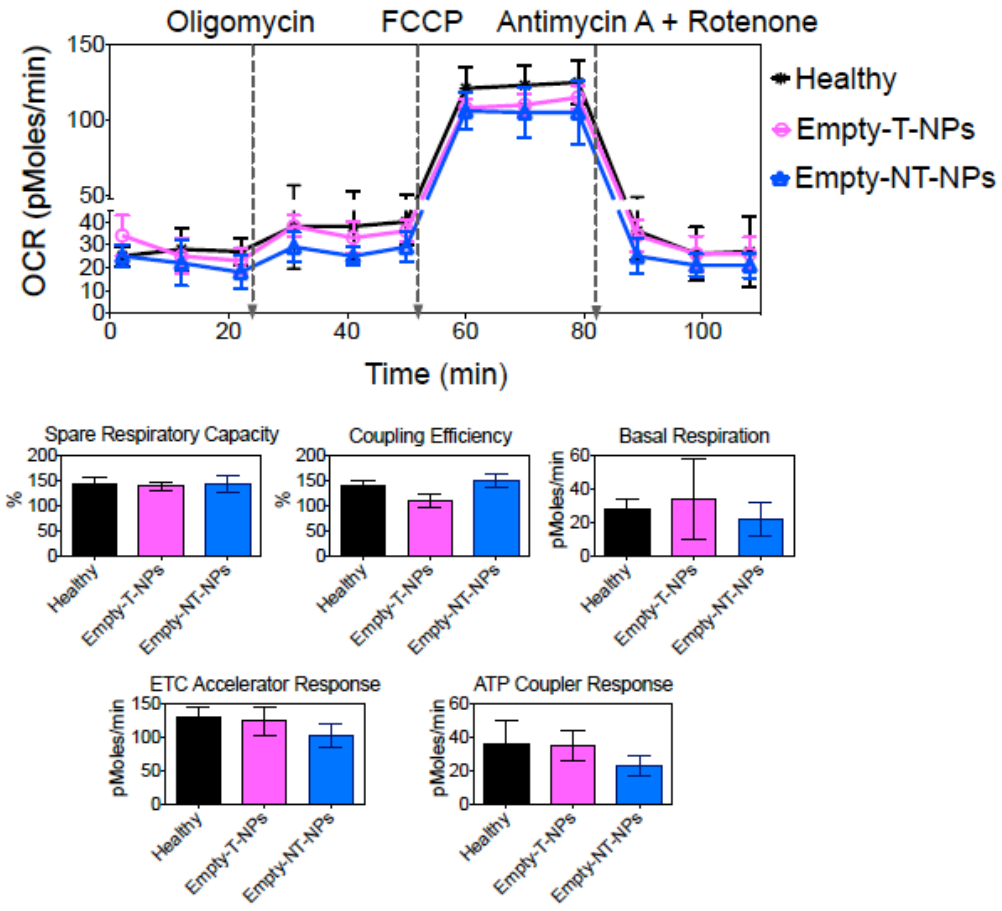


Fig. 4.4. Effect of Empty T and NT-NPs in H9C2 cardiomyocytes by mito-stress test assay

Mito stress assay using mitochondrial inhibitors as described before on H9C2 cells after treatment with 0.5 mg/mL Empty-T-NPs and Empty-NT-NPs for 12 h demonstrated no significant effects on basal OCR levels in these cells (Fig. 4.4). The basal OCR levels in cardiomyocytes were low compared to other cells indicating

significant mitochondrial hyperpolarization. These properties make the T-NPs suitable for delivery of therapeutics inside the mitochondria.

Long Circulating T-NPs Distribute in the Brain

For potential *in vivo* translation of T-NPs in delivering Platin-M; bioD, excretion, and PK properties are the most critical parameters. We injected T-QD-NPs into Sprague Dawley rats by a single dose intravenous injection. Blood samples at predetermined time points up to 24 h post injection, organs after 24 h, and cumulative urine, feces over 24 h were collected and analyzed for Cd by ICP-MS. Calculation of PK parameters by a two-compartment intravenous input model revealed a plasma elimination half life ($t_{1/2}$) from the central compartment of 2.4 h followed by a very high $t_{1/2}$ value in the periphery compartment of ~214 h (Fig. 4.3*C,* Table 4.1).

Table 4.1. PK Parameters of T-NPs by Using a Two-compartment Model*

		Central Compartment (Initial Phase, t = 0)			**Periphery Compartment (Terminal Phase, t = 24 h)**	
$AUC_{[0\text{-}24\ h]}$ (h.ng/mL)	C_{max} (ng/mL)	V_d (mL/kg)	C_L (mL/h.kg)	$t_{1/2}$ (h)	V_d (mL/kg)	C_L (mL/h.kg)
34784± 2117	3237± 128	25.2 ± 0.9	4.7 ± 0.8	2.4 ± 0.8	8.4 ± 0.9	0.05 ± 0.07

Least-square fit to model. $C = a \times \exp[(-k_1 \times t) + b \times \exp(-k_2 \times t)]$. AUC, area under curve; C_{max}, Peak plasma concentration; C_L, total body clearance; $t_{1/2}$, plasma half-life; V_d, volume of distribution. *Model used to extrapolate concentrations at t = 0.

The total body clearance (C_L) of T-NPs was ~4.7 mL/h.kg in the central compartment and 0.05 mL/h.kg in the terminal phase (Table 4.1). The high $t_{1/2}$ and a small C_L values indicated long circulating properties of T-NPs. The significantly higher area under curve (AUC) of 34784±2117 h.ng/mL further supported the long circulation property of T-NPs. A peak plasma concentration (C_{max}) of 3237±128 ng/mL indicated

efficient distribution of T-NPs into bloodstream. A large volume of distribution (V_d) in the central compartment suggested that initially T-NPs distribute extensively into body tissues, however a reduced V_d in the terminal compartment supported that due to their unique composition with sterically hindered surface covered with –TPP moieties, these NPs exhibited decreased protein binding. All these parameters together supported that T-NP will be an excellent candidate for mitochondrial delivery of Platin-M.

Distribution of T-NPs in the major tissues, including spleen, liver, lungs, brain, heart, kidneys, and testes at 24 h post-dose indicated maximum NP accumulation in the brain (Fig. 4.3*C*). The dichotomy between the brain capillary endothelium forming the blood-brain-barrier (BBB) and endothelia in peripheral prevent passage of larger NPs with hydrophilic anionic surface. Pass from blood to brain of circulating NPs may only happen by transcellular mechanisms, which require a highly lipophilic NP with suitable size and charge. Brain endothelial cell surface and basement membrane components bearing highly anionic charges from sulfated proteoglycans are different from non-brain endothelium and would allow the adsorptive-mediated transcytosis of cationic NPs [16]. Thus the small size and highly lipophilic surface of T-NPs helped their distribution in the brain. Furthermore, high mitochondrial density in cerebral endothelial cells than in peripheral endothelia further assisted these T-NPs to accumulate in the brain efficiently [17, 18]. The distinctive properties of brain endothelium, high lipophilicity, and mitochondria targeting properties of T-NPs provided selective targeting of these NPs to the brain. In many instances, positively charged NPs accumulate in the liver and the spleen by phagocytic cells present in the mononuclear phagocyte system (MPS) located primarily in these organs. T-NPs in spite of positively charged surface, showed a high brain-to-

spleen ratio of ~2.4 and a moderate brain-to-liver ratio of ~1.6 (Fig. 4.3C). T-NPs demonstrated a high brain-to-kidney ratio of ~10 and a brain-to-lung distribution ratio of ~2.2. Retention of T-NPs was extremely low in the heart with a brain-to-heart ratio of 11 indicating that although the heart cells have hyperpolarized mitochondria; the lipophilic properties of the T-NPs help preferential distribution in the brain. These highly positively charged NPs demonstrated hepatobiliary excretion.

Mitochondria-targeted NP Formulation of Platin-M

The rationale behind incorporation of Platin-M into a mitochondria-targeted delivery system such as T-NPs was to efficiently encapsulate hydrophobic Platin-M to increase its blood circulation, upon uptake by cancer cells with hyperpolarized $\Delta\Psi_m$, these NPs will deliver Platin-M with high accuracy and efficiency inside the mitochondrial matrix. However, any Platin-M released from the NPs prior reaching mitochondria will take advantage of the TPP moieties present on Platin-M for mitochondrial uptake. Thus, this dual targeted system expected to show effective mitochondrial accumulation. We constructed T-Platin-M-NPs by entrapping Platin-M inside $PLGA_{LMW}$-*b*-PEG-TPP polymer. As a single targeted control, we used Platin-M entrapped inside $PLGA_{LMW}$-*b*-PEG-OH to construct NT-Platin-M-NPs. We used a nanoprecipitation method [5] for entrapping Platin-M in these polymers and the NPs were characterized by dynamic light scattering (DLS) to give the size, polydispersity index (PDI), and zeta potential of each preparation (Fig. 4.5A).

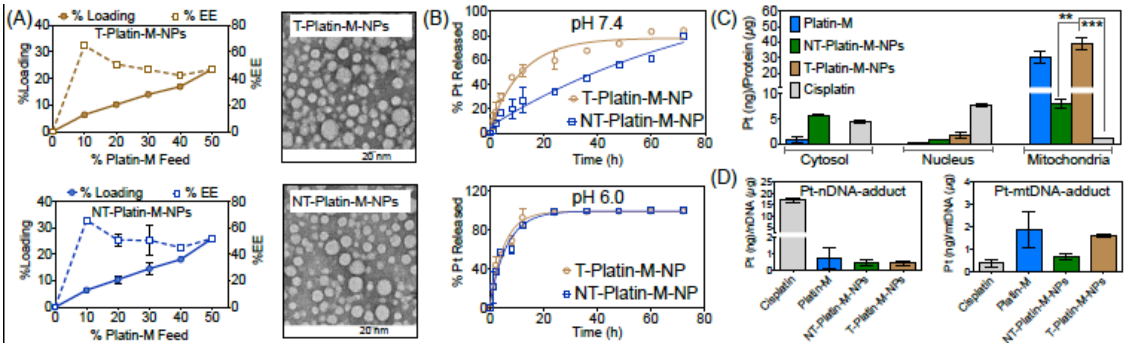


Figure 4.5. (A) Platin-M percent loading, encapsulation efficiency in T and NT NPs, and TEM images of T-Platin-M and NT-Platin-M-NPs. (B) pH dependent release kinetics of Platin-M from T and NT-NPs in PBS at 37 °C. (C) Distribution of cisplatin, Platin-M, NT-Platin-M-NPs, and T-Platin-M-NPs in cytosolic, nuclear, and mitochondrial fractions of PC3 cells. (D) Comparison of Pt-nDNA and Pt-mtDNA adducts for cisplatin, Platin-M, NT-Platin-M-NP, and T-Platin-M-NPs in PC3 cells. ***, P<0.001; **, P=0.001-0.01.

T-Platin-M-NPs and NT-Platin-M-NPs showed sizes in the range of 50-55 nm. T-Platin-M-NPs exhibited a highly positive zeta potential between 28 to 37 mV. NT-Platin-M-NPs showed a negative zeta potential between -22 to -34 mV. Morphology of T-Platin-M and NT-Platin-M-NPs was investigated using transmission electron microscopy (TEM) (Fig. 4.6A). Loading efficiencies of Platin-M at various added weight-percentage values of Pt(IV) to polymer indicated that Platin-M can be entrapped in these NPs with a very high loading and encapsulation efficiency (EE) (Fig. 4.5A). Percent loading of Platin-M varied between 6 to 27% based on %feed with respect to feed of the polymer (Fig. 4.5A). Given the amphiphilic character of Platin-M with two cationic TPP head groups and lipophilic DBCO moieties, we questioned whether high loading of Platin-M is due to the formation of self-micelles. Nanoprecipitation of an organic solution of Platin-M into water resulted in unstable macroparticles (Size: 941.6 ± 589.5 nm; PDI: 0.799;

Zeta Potential: -5.38 ± 1.66 mV) leaving out such a possibility. To the best of our knowledge, Platin-M showed the highest loading efficiency among the known Pt(IV) complexes in a PLGA-PEG-based NP system [19, 20]. Release kinetics of Platin-M from T and NT-NPs under physiological pH 7.4 in phosphate buffered saline (PBS) at 37 °C demonstrated sustained release over a longer period of 72 h (Fig. 4.5B). A comparison of release kinetics of T and NT-NPs demonstrated that Platin-M released from NT-NPs at a slower rate (Fig. 4.5B). Positively charged Platin-M released from NT-NPs might get adsorb on the negatively charged NP surface and this non-covalent interaction might be responsible for slower release kinetics of Platin-M from NT-NPs. Platin-M was found to be released at a much faster rate at pH 6.0 compared to pH 7.4 (Fig. 4.5B). The pH-dependent release is possibly due to accelerated degradation of PLGA backbone and reduction of Platin-M at acidic pH.

Mitochondrial Accumulation of Platin-M and NPs

Analysis of mitochondrial, cytosolic, and nuclear fractions isolated from PC3 cells treated with cisplatin, Platin-M, NT-Platin-M-NPs, and T-Platin-M-NPs showed that Pt concentration in the mitochondrial protein was 30-times higher than in the nuclear protein fractions for Platin-M or its T-NP formulation compared to cisplatin (Fig. 4.5C). Overall uptake of cisplatin was much lower than Platin-M or its NP formulations. The non-targeted system showed only ~8 times greater accumulation of Platin-M in the mitochondrial fraction compared to cisplatin, a significant of portion of NT-Platin-M-NPs was found in the cytosolic fractions, and the overall uptake was much lower than Platin-M or its T-NPs. (Fig. 4.6C). This further supported our hypothesis that dual targeting will enhance mitochondrial delivery efficiency of Platin-M. Further

quantification and comparison of Pt bound to nDNA and mtDNA from the treated PC3 cells indicated that cisplatin released from Platin-M and T-Platin-M-NPs exhibited binding with mtDNA (Fig. 4.5D). Cisplatin adduct level in the nDNA was much higher than cisplatin-mtDNA adducts. Platin-M showed marginally higher mtDNA adduct compared to T-Platin-M-NP system. This might be due to the fact that for T-NP system, Platin-M needs to be released from the NPs prior to reduction to cisplatin and subsequent mtDNA interaction and all Platin-M might not have released from the NPs during the course of this experiment; mtDNA isolation was carried out after 12 h and we expect that only ~50% of Platin-M will be released from T-NPs during this time period (Fig. 4.5B). NT-Platin-M-NPs showed reduced levels of mtDNA and nDNA adduct formation. This may be due to the slow release of Platin-M from the NT-NPs, only ~26% of Platin-M is expected to be released in 12 h period of time (Fig. 4.5B).

Efficacy of Platin-M and NPs in Neuroblastoma and Cisplatin Resistant Cells

In vitro cytotoxicity of Platin-M, T-Platin-M-NPs, and NT-Platin-M-NPs was assessed by the 3-(4,5-dimethylthiazol-2-yl)-2,5-diphenyltetrazolium bromide or MTT assay on PC3, human neuroblastoma SH-SY5Y, and cisplatin resistant A2780/CP70 ovarian cancer cell lines (Table 4.2, Fig. 4.6). The rationale behind the use of androgen independent PC3 cell line was the inherent resistance of these cells to cisplatin therapy due to enhanced repair of Pt-nDNA adducts by the NER, poor targeting. Furthermore, androgen-independent PCa with reduced normal mtDNA acquire a more progressive phenotype by inducing mutations to nDNA. Thus targeting mtDNA could lead to effective therapies for aggressive androgen independent PCa. The human neuroblastoma SH-SY5Y cell line displays several characteristics of neurons and neuronal cells typically

require an increased number of mitochondria since most neuronal ATP is generated through OXPHOS. Distribution of the T-NPs in the brain and increased number of mitochondria prompted us to use SH-SY5Y cells in our studies.

Table 4.2. IC_{50} (μM) Values of Platin-M and NPs.			
	PC3	**SH-SY5Y**	**A2780/CP70**
Cisplatin	13.1±0.1	19±4.7	12.0±2.8
Platin-M	7.3±0.8	3.4±0.5	0.74±0.05
NT-Platin-M-NPs	3.1±0.1	2.7±0.6	2.2±0.7
T-Platin-M-NPs	0.19±0.01	1.1±0.2	0.14±0.04

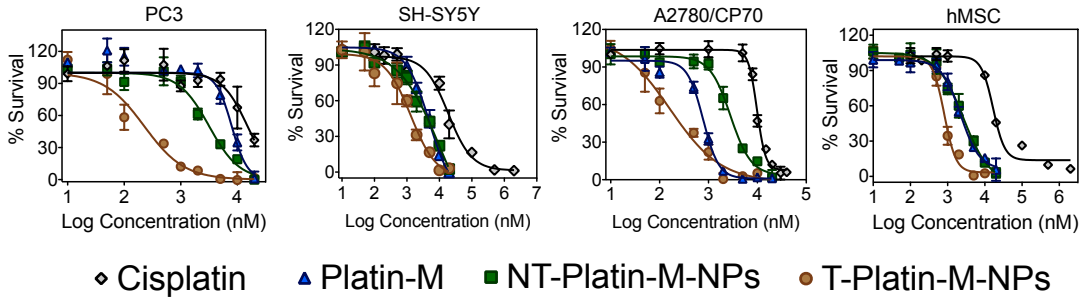


Fig. 4.6. Cytotoxicity profiles of cisplatin, Platin-M, NT-Platin-M-NPs, and T-Platin-M-NPs in prostate cancer PC3, neuroblastoma SH-SY5Y, cisplatin-resistant ovarian cancer A2780/CP70, and human mesenchymal stem cells hMSC cells as determined by the MTT assay.

To understand the ability of Platin-M and its T-NPs to overcome resistance, we used cisplatin resistant A2780/CP70 cells with hyperpolarized mitochondria and efficient cisplatin-nDNA repair machinery. In all the cell lines, Platin-M and its NPs showed significantly enhanced efficiency compared to cisplatin. In the resistant cells, Platin-M activity was ~16 times better than cisplatin. Incorporation of Platin-M in T-NPs further enhanced this activity, the potency of T-Platin-M-NPs was ~85 times better than cisplatin in the resistance cells. Incorporation of Platin-M in a non-targeted NP system showed only an increase of ~6 times compared to cisplatin in the resistance cells. These

differences in activities between Platin-M and its mitochondria targeted and non targeted NP formulations can be correlated to the differences in $\Delta\Psi_m$ values of A2780/CP70, PC3, and SH-SY5Y cells. A simple OCR study on these cells using Mito Stress assay supported this hypothesis (Fig. 4.7). Cisplatin resistant A2780/CP70 cells showed low basal OCR due to the hyperpolarized $\Delta\Psi_m$ compared to the other two cell lines. This hyperpolarization assisted Platin-M to accumulate into the matrix efficiently. Incorporation of Platin-M inside a mitochondria-targeted NP system with multiple –TPP molecules on the NP surface increased the accumulation further demonstrating an enhanced activity in the resistant cells.

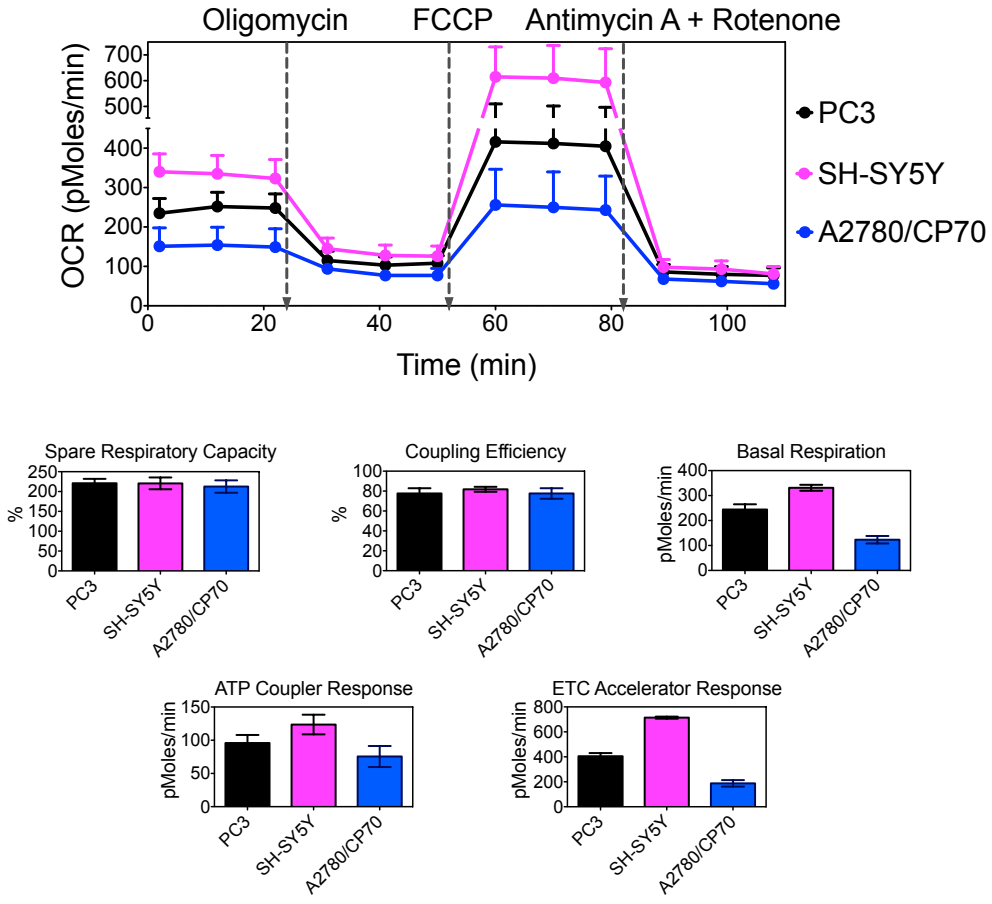


Fig. 4.7. A comparison of OCR levels in different cancer cells by Mitostress analyses.

However, NT-Platin-M was not able to accumulate in the hyperpolarized resistant cells and high glutathione levels in the resistant cells [21] facilitated reduction of released Platin-M to generate cisplatin in the cytosol and hence NT-Platin-M-NPs showed less activity compared to Platin-M and T-Platin-M-NPs in resistant cells. These observations further supported our rationale of using dual targeting approach for effective delivery of cisplatin inside the mitochondrial matrix. Neuroblastoma accounts for ~15% of all childhood cancer deaths [22]. Cisplatin is widely used to treat patients with high-risk neuroblastoma. Thus the distribution of T-NPs in the brain prompted us to explore the use of Platin-M and its NPs for possible use in neuroblastoma. Platin-M activity in neoroblastoma SH-SY5Y cell line was 5.5 times higher compared to cisplatin. Upon encapsulation of Platin-M in T-NPs demonstrated a response which was ~17 times greater than the effects shown by cisplatin (Table 4.2, Fig. 4.6). NT-Platin-M-NPs also showed enhanced activity over cisplatin. The increased efficiency of Platin-M and its T-NPs over cisplatin might be due to the increased number of mitochondria present in the SH-SY5Y cells. This was further supported by our data that these neuroblastoma cells showed higher OCR levels due to the presence of increased number of mitochondria (Fig. 4.7). Toxicity of Platin-M and its NPs in human mesenchymal stem cells (hMSCs) was investigated to understand the effect of these formulations in non-cancerous cells. Toxicity of Platin-M in hMSCs was found to be ~3 times less than in the resistance cells. Incorporation of Platin-M inside the T-NPs reduced the toxicity further, T-Platin-M-NPs showed ~5.5 times less toxicity in stem cells compared to the resistant cells (Table 4.2, Fig. 4.6). This remarkable ability of Platin-M and its T-NP formulation to overcome cisplatin resistance will play significant roles in the success of this technology. The cell

death phenotype analysis in SH-SY5Y cells upon treatment with Platin-M and its NPs was carried out by Alexa Fluor® 488-Annexin-V-propidium iodide (PI) staining (Fig. 4.8). 12 hour post treatment with cisplatin, Platin-M, NT-Platin-M-NPs, and T-Platin-M-NPs, cells were stained with Annexin-V and PI, and analyzed by flow cytometry. Early apoptotic cells characterized by a high Annexin-V signal in the absence of PI staining was observed only in Platin-M and T-Platin-M-NP treated cells under the experimental conditions. The pivotal role of mitochondria in initiating apoptotic cell decay might be responsible for more apoptotic population with Platin-M and T-Platin-M-NPs since both of these formulations accumulate inside the mitochondria in significant amounts.

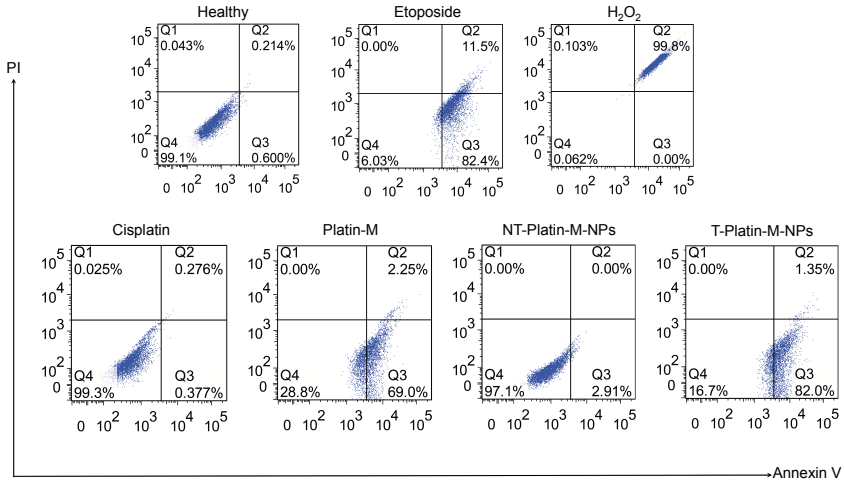


Fig. 4.8. FACS analysis using Annexin V-Alexa Fluor/PI staining for apoptosis detection in SH-SY5Y cells treated with 1 μM cisplatin, 1 μM Platin-M, 1 μM NT-Platin-M-NPs, and 1 μM T-Platin-M-NPs for 12 h at 37 °C. As positive controls, etoposide (100 μM, incubation time: 12 h) for apoptosis and H_2O_2 (1 mM, incubation time: 45 min) for necrosis were used. Cells in the lower right quadrant indicate Annexin V-positive/PI negative, early apoptotic cells. The cells in the upper right quadrant indicate Annexin V-positive/PI positive, late apoptotic or necrotic cells.

Given the substantial Pt adduct formation with mtDNA, cell death, and cellular apoptosis after treatment with Platin-M or its T-NPs, we performed citrate synthase activity to assess whether these activities translate into functional impairment of the ETC activity (Fig. 4.9). Citrate synthase activity as a mitochondrial marker in SH-SY5Y cells treated with 1 μM cisplatin, 1 μM Platin-M, 1 μM NT-Platin-M-NPs, and 1 μM T-Platin-M-NPs for 12 h at 37 °C was studied. A diminished citrate synthase activity was observed with Platin-M and T-Platin-M-NP treated cells confirming disruption of ETC activity.

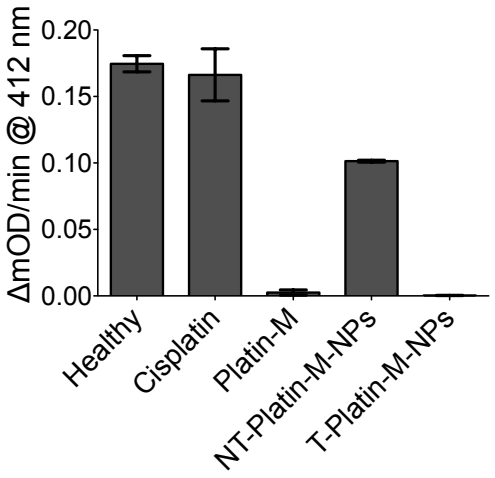


Fig. 4.9. Citrate synthase activity in SH-SY5Y cells treated with 1 μM cisplatin, 1 μM Platin-M, 1 μM NT-Platin-M-NPs, and 1 μM T-Platin-M-NPs for 12 h at 37 °C.

Mitochondrial Bioenergetics

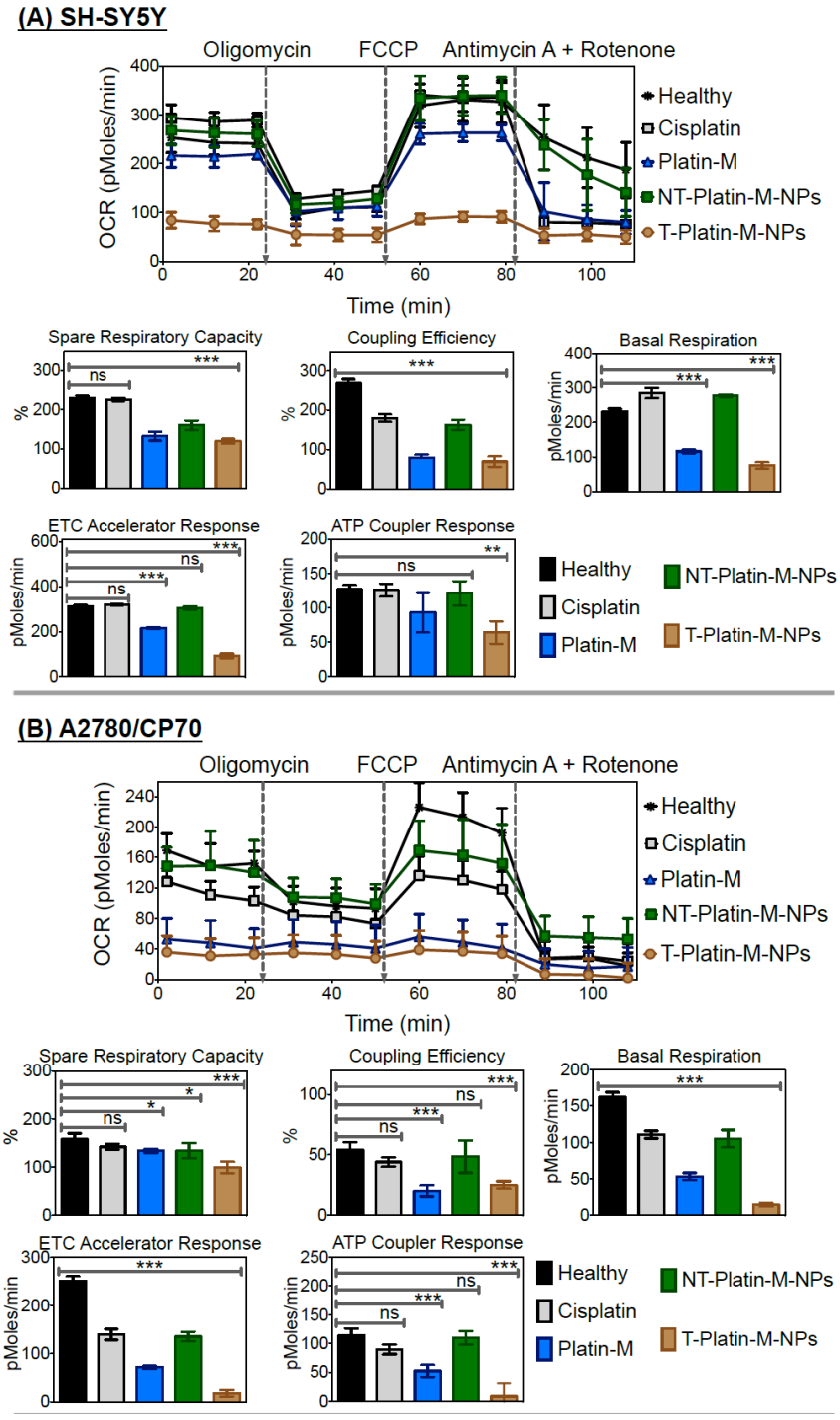


Figure 4.10. Mitochondrial bioenergetics in (A) SH-SY5Y and (B) A2780/CP70 cells in response to cisplatin, Platin-M, NT-Platin-M-NPs, and T-Platin-M-NPs. ***, P<0.001; **, P=0.001-0.01; *, P=0.01-0.05; non significant (ns), P>0.05.

We next investigated whether accumulation of Platin-M inside the mitochondrial matrix of PC3, A2780/CP70, and SH-SY5Y cells altered mitochondrial respiration by measuring OCRs as a way of assessing OXPHOS (Fig. 4.10, Fig. 4.11). PC3, A2780/CP70, and SH-SY5Y cells were treated with cisplatin, Platin-M, NT-Platin-M-NPs, and T-Platin-M-NPs, for 12 h. The basal OCR levels of Platin-M or T-Platin-M-NP treated cells were found to be significantly less than control cells, indicating a loss in total mitochondrial mass.

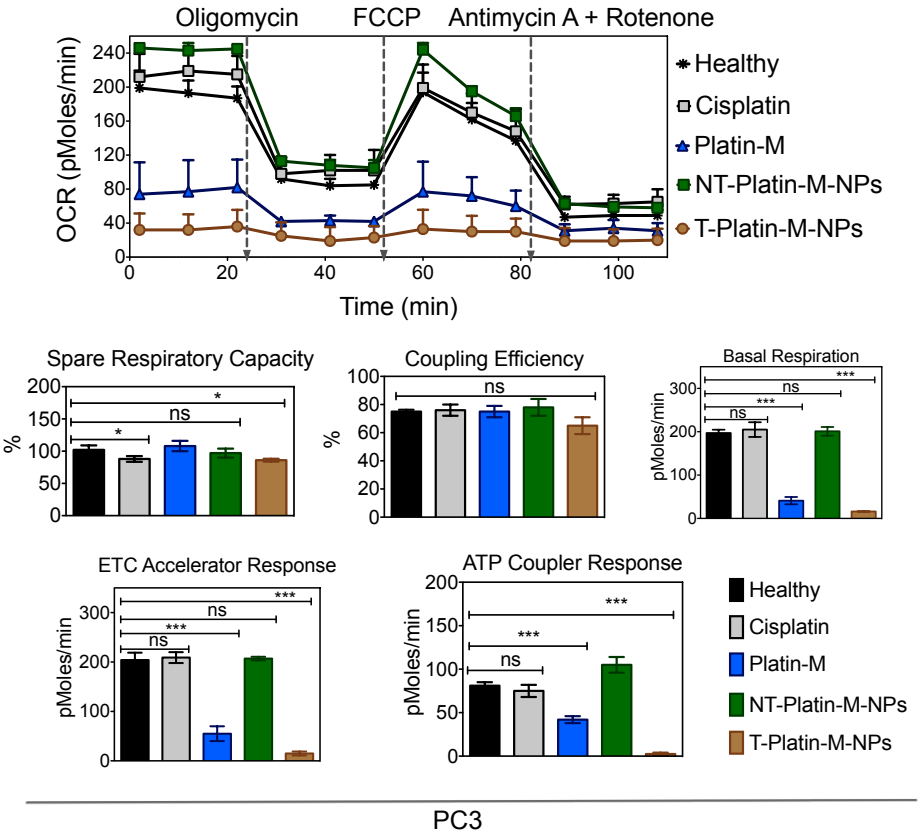


Fig. 4.11. Effect of cisplatin, Platin-M, and its NPs in PC3 cells by Mito-Stress assay. The cells were treated with Platin-M (10 μM), cisplatin (10 μM), T-Platin-M-NPs (10 μM with respect to Pt), NT-Platin-M-NPs (10 μM with respect to Pt) for 12 h at 37 °C in 5%

CO_2 atmosphere. ***, P<0.001; **, P=0.001-0.01; *, P=0.01-0.05; non significant (ns), P>0.05.

To support that the reduced OCR upon treatment with T-Platin-M-NPs is due to total mitochondrial mass, we decided to use 5,5′,6,6′-tetrachloro-1,1′,3,3′-tetraethylbenzimidazolylcarbocyanine iodide or JC-1 red/green fluorescence measurements in SH-SY5Y cells, which would allow careful discrimination between a shift in fluorescence due to reduced potential in the total cell population and reduced JC-1 red/green fluorescence due to cell death (Fig. 4.12). Our results from flow cytometry analyses confirmed the loss of $\Delta\Psi_m$ and mitochondrial mass in T-Platin-M-NP treated cells in a greater extent compared to Platin-M, NT-Platin-M-NPs, and cisplatin treated cells (Fig. 4.12).

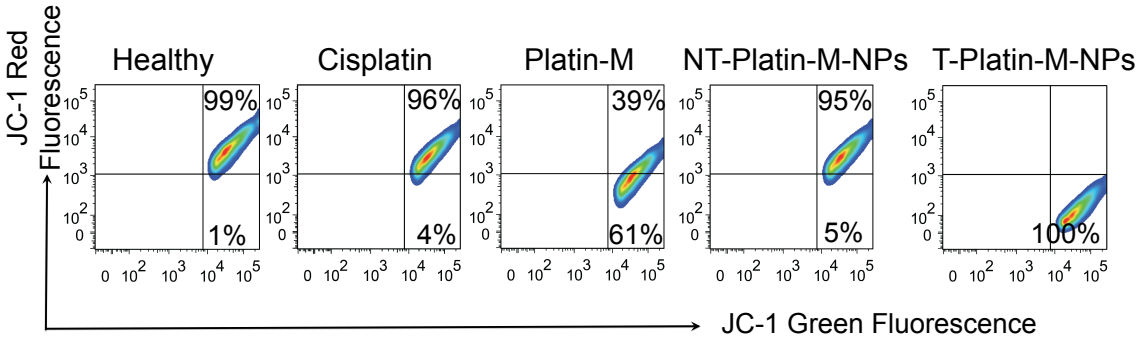


Fig. 4.12. Changes in the $\Delta\psi_m$ and mitochondrial mass loss by JC-1 assay.

The ATP synthase inhibitor oligomycin was injected to evaluate mitochondrial coupling upon accumulation of Platin-M inside the mitochondria in these cells. Addition of oligomycin showed that the levels of ATP-linked respiration were attenuated in control cells or cells treated with cisplatin, NT-Platin-M-NPs; Platin-M treated cells showed less reduction, and T-Platn-M-NPs did not show any significant changes. Stimulation of mitochondrial respiration with FCCP after oligomycin was comparable for cisplatin, NT-

Platin-M-NPs and control cells, but Platin-M and T-Platin-M-NPs showed no enhancement in OCR levels. Finally, injection of a combination of mitochondrial complex III inhibitor antimycin A and mitochondrial complex I inhibitor rotenone significantly inhibited the OCR due to the formation of mitochondrial ROS and non-mitochondrial O_2 consumption. Overall, Platin-M and T-Platin-M-NPs showed inhibition of mitochondrial respiration in A2780/CP70 and SH-SY5Y cells to a greater extent compared to PC3 cells. This mitochondrial respiration programming by Platin-M and T-Platin-M-NPs indicated enormous potential of the current technology in the treatment of chemo-resistance tumor with inherently hyperpolarized mitochondria and of neuroblastoma with increased number of mitochondria. Effects of cisplatin, Platin-M, NT-Platin-M-NPs, and T-Platin-M-NPs on hyperpolarized H9C2 cardiomyocytes under identical conditions showed similar trends as observed with other cell lines (Fig. 4.4).

Distribution of T-Platin-M-NPs in the Brain.

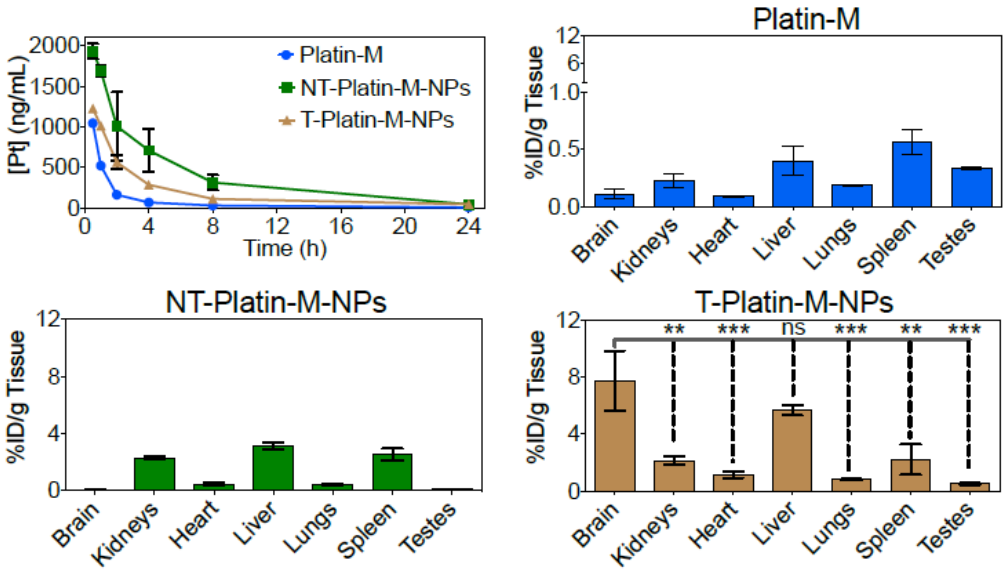


Figure 4.13. Pt concentration variation in plasma and organs following the administration of Platin-M, NT-Platin-M-NPs, and T-Platin-M-NPs intravenously to male rats. ***, P<0.001; **, P=0.001-0.01; non significant (ns), P>0.05.

We next assessed whether the brain-penetrating T-NPs could deliver Platin-M to the brain by crossing the BBB in *in vivo* settings. We administered Platin-M, NT-Platin-M-NPs, and T-Platin-M-NPs to male rats by intravenous injection. The serum Pt concentrations from T-Platin-M-NPs and NT-Platin-M-NPs indicated long circulatory properties compared to Platin-M delivered without any delivery system (Fig. 4.13). Pt remaining in systemic circulation 1 h post administration from T-Platin-M-NPs was significantly higher than from Platin-M (Fig. 4.13). The high $t_{1/2,}$ significantly higher AUC, and a large V_d of T-Platin-M-NPs supported that T-NP is an excellent candidate for mitochondrial delivery of Platin-M. Similar to Empty-T-NPs, Pt distribution was significantly higher in the brain compared to kidneys, heart, lungs, and spleen when T-Platin-M-NP was used (Fig. 4.13).

Platin-M from NT-Platin-M-NPs was mostly distributed in the spleen, liver, and kidneys and a significant amount of Pt from these samples was found in urine collected at 24 h directly from the animal bladders (Fig. 4.13). The significant differences in bioD patterns between Platin-M, NT-Platin-M-NPs, and T-Platin-M-NPs further supported the rationale for using a dual targeting system for delivery of Platin-M. The bioD data indicated that both liver and kidney are involved in Pt elimination (Fig. 4.13) of these NPs. A comparison of T-QD-NPs (Fig. 4.3C) and T-Platin-M-NPs (Fig. 4.13) bioD profiles showed very similar distribution pattern further confirming that Platin-M is associated with the NPs throughout the study. Plasma Pt levels coupled with unique distribution pattern which involved significant Pt accumulation in the brain demonstrated that T-Platin-M-NPs have the potential to demonstrate significant clinical impact.

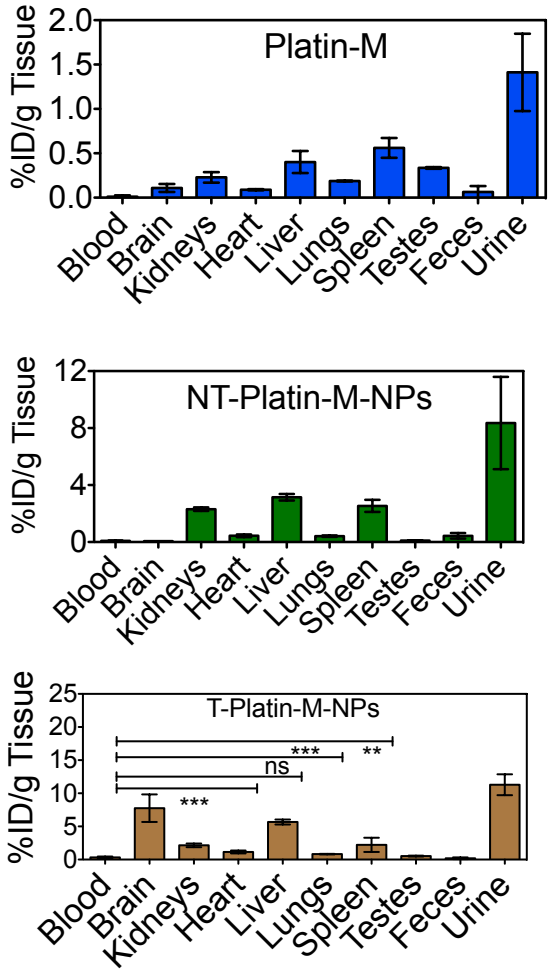


Fig. 4.14. A comparison of bioD and excretion profiles of Platin-M, NT-Platin-M-NPs, and T-Platin-M-NPs in male rats. ***, P<0.001; **, P=0.001-0.01; *, P=0.01-0.05; non significant (ns), P>0.05.

Conclusion

Here, we outlined a strategy for precise mitochondrial delivery of cisplatin for chemo-resistance aggressive cancers-from construction of a mitochondria targeted cisplatin prodrug to its formulation in a targeted delivery vehicle-that can be implemented in cisplatin resistance settings and in cancers of central nervous system. These studies represent an initial development of previously undescribed routes for cisplatin-based

therapy. Since most late stage cancers are resistant to cisplatin treatment because of the development of chemo-resistance, therefore, delivery of cisplatin inside the mitochondrial matrix to attack mtDNA lacking NER using a mitochondria targeted Pt(IV) prodrug and a targeted NP, as outlined here, can be extremely beneficial in providing a new therapeutic strategy to tackle otherwise resistant advanced cancers.

References:

1. Smiraglia, D. J.; Kulawiec, M.; Bistulfi, G. L.; Gupta, S. G.; Singh, K. K., A novel role for mitochondria in regulating epigenetic modification in the nucleus. *Cancer Biol Ther* **2008,** *7* (8), 1182-90.
2. Jamieson, E. R.; Lippard, S. J., Structure, Recognition, and Processing of Cisplatin-DNA Adducts. *Chem Rev* **1999,** *99* (9), 2467-98.
3. Damia, G.; Imperatori, L.; Stefanini, M.; D'Incalci, M., Sensitivity of CHO mutant cell lines with specific defects in nucleotide excision repair to different anti-cancer agents. *Int J Cancer* **1996,** *66* (6), 779-83.
4. Yang, Z.; Schumaker, L. M.; Egorin, M. J.; Zuhowski, E. G.; Guo, Z.; Cullen, K. J., Cisplatin preferentially binds mitochondrial DNA and voltage-dependent anion channel protein in the mitochondrial membrane of head and neck squamous cell carcinoma: possible role in apoptosis. *Clin Cancer Res* **2006,** *12* (19), 5817-25.
5. Marrache, S.; Dhar, S., Engineering of blended nanoparticle platform for delivery of mitochondria-acting therapeutics. *Proc Natl Acad Sci USA* **2012,** *109* (40), 16288-16293.

6. Marrache, S.; Tundup, S.; Harn, D. A.; Dhar, S., Ex vivo programming of dendritic cells by mitochondria-targeted nanoparticles to produce interferon-gamma for cancer immunotherapy. *ACS Nano* **2013,** *7* (8), 7392-402.

8. Pathak, R. K.; McNitt, C. D.; Popik, V. V.; Dhar, S., A versatile bioorthogonal copper-free click chemistry platform to functionalize cisplatin prodrugs. *Chem Eur J* **2014,** *20*, 6861-6865.

9. Lee, H. B.; Blaufox, M. D., Blood volume in the rat. *J Nucl Med* **1985,** *26* (1), 72-6.

10. Wisnovsky, S. P.; Wilson, J. J.; Radford, R. J.; Pereira, M. P.; Chan, M. R.; Laposa, R. R.; Lippard, S. J.; Kelley, S. O., Targeting mitochondrial DNA with a platinum-based anticancer agent. *Chem Biol* **2013,** *20* (11), 1323-8.

11. Pathak, R. K.; Marrache, S.; Choi, J. H.; Berding, T. B.; Dhar, S., The prodrug platin-A: simultaneous release of cisplatin and aspirin. *Angew Chem Int Ed* **2014,** *53* (7), 1963-1967.

12. Summerhayes, I. C.; Lampidis, T. J.; Bernal, S. D.; Nadakavukaren, J. J.; Nadakavukaren, K. K.; Shepherd, E. L.; Chen, L. B., Unusual retention of rhodamine 123 by mitochondria in muscle and carcinoma cells. *Proc Natl Acad Sci USA* **1982,** *79* (17), 5292-6.

14. Peer, D.; Karp, J. M.; Hong, S.; Farokhzad, O. C.; Margalit, R.; Langer, R., Nanocarriers as an emerging platform for cancer therapy. *Nat Nanotechnol* **2007,** *2* (12), 751-60.

15. Reily, C.; Mitchell, T.; Chacko, B. K.; Benavides, G.; Murphy, M. P.; Darley-Usmar, V., Mitochondrially targeted compounds and their impact on cellular bioenergetics. *Redox Biol* **2013,** *1* (1), 86-93.

16. dos Santos, W. L.; Rahman, J.; Klein, N.; Male, D. K., Control of lymphocyte adhesion to brain and aortic endothelium: ICAM-1, VCAM-1 and negative charge. *J Neuroimmunol* **1996,** *66* (1-2), 125-34.

17. Oldendorf, W. H.; Cornford, M. E.; Brown, W. J., The large apparent work capability of the blood-brain barrier: a study of the mitochondrial content of capillary endothelial cells in brain and other tissues of the rat. *Ann Neurol* **1977,** *1* (5), 409-17.

18. Herve, F.; Ghinea, N.; Scherrmann, J. M., CNS delivery via adsorptive transcytosis. *AAPS J* **2008,** *10* (3), 455-72.

19. Dhar, S.; Gu, F. X.; Langer, R.; Farokhzad, O. C.; Lippard, S. J., Targeted delivery of cisplatin to prostate cancer cells by aptamer functionalized Pt(IV) prodrug-PLGA-PEG nanoparticles. *Proc Natl Acad Sci USA* **2008,** *105* (45), 17356-61.

20. Kolishetti, N.; Dhar, S.; Valencia, P. M.; Lin, L. Q.; Karnik, R.; Lippard, S. J.; Langer, R.; Farokhzad, O. C., Engineering of self-assembled nanoparticle platform for precisely controlled combination drug therapy. *Proc Natl Acad Sci USA* **2010,** *107* (42), 17939-44.

21. Godwin, A. K.; Meister, A.; O'Dwyer, P. J.; Huang, C. S.; Hamilton, T. C.; Anderson, M. E., High resistance to cisplatin in human ovarian cancer cell lines is

associated with marked increase of glutathione synthesis. *Proc Natl Acad Sci USA* **1992,** *89* (7), 3070-4.

22. Maris, J. M.; Matthay, K. K., Molecular biology of neuroblastoma. *J Clin Oncol* **1999,** *17* (7), 2264-79.

CHAPTER 5

A HIGHLY LIPOPHILIC BLOOD-BRAIN-BARRIER PENETRATING MITOCHONDRIA TARGETED THERAPEUTIC NANOPARTICLE FOR THE TREATMENT OF TRAUMATIC BRAIN INJURY

[1]Marrache, S.; Wyatt, E.L.; West, F.D.; Dhar, S., Submitted for publication

Abstract

Traumatic brain injury (TBI) is one of the leading causes of death and long-term disability in both civilian life and the battlefield worldwide. Beyond the primary injury caused by the initial insult, a cascaded of events rapidly occur including the production of free radicals and heightened immune response which result in considerable secondary injury to brain tissue. Significant efforts made by the medical and research communities to develop neuroprotective therapeutics that will limit secondary injury led to numerous clinical trials. Despite years of research and advancements, there are no neuroprotective treatment options that exist with improved neurological outcomes. One potential option to improve efficacy is the use of a nanoparticle (NP) delivery system that is of optimized size, charge, lipophilicity, and targeting properties to cross the blood-brain barrier (BBB) and can reach specific intracellular targets to deliver neuroprotectant payloads. In this study, we examined for the first time the therapeutic potential of a highly lipophilic BBB penetrating biodegradable mitochondria targeted nanoparticle (NP) containing an antioxidant and an anti-inflammatory cocktail therapy in a piglet model of TBI. The targeted NP was found to distribute in the lipophilic white matter of normal pig brain. Evaluation of the targeted NP in a piglet model of TBI demonstrates favorable pharmacokinetics and unique distribution in the injured brain. The targeted NP system was further engineered to carry a mitochondria-acting antioxidant coenzyme Q_{10} and an anti-inflammatory agent prednisone. Therapeutic potential of the targeted NP containing cocktail therapy in neural stem cells demonstrated unique abilities to provide therapeutic effects against the cascade of events which rapidly occur after TBI including the

production of free radicals and heightened immune response which result in considerable secondary injury to brain tissue.

Introduction

Traumatic brain injury (TBI) is a "silent epidemic" as one of the leading causes of death and long-term disability among persons in the United States[1]. More than 1.7 million individuals suffer a TBI annually with approximately 50,000 patient deaths and 80,500 patients with long-term disabilities[2]. The life quality of TBI survivors is often significantly reduced with victims suffering from learning and memory problems, challenges with language, decision making, problem solving, motor function and afflicted with chronic fatigue, depression and emotional instability. The catastrophic nature of TBI is heightened by the fact that children less than five years old are the demographic that suffer the highest incidence of TBI-related hospitalizations and deaths[1, 3]. The sequel of TBI is initiated by a primary injury to the brain that is rapidly followed by a cascade of secondary events including oxidative and inflammatory insults that further exacerbate tissue loss and damage and ultimately brain function [4, 5]. It is this secondary injury cascade that has become a prime target for therapeutic intervention.

The TBI secondary injury cascade has proven to be a complex series of mechanisms and events that lead to the destruction of brain tissue at the cellular level with two major components being the formation of free radicals and immune response. After initial trauma to the brain, a series of catabolic processes lead to an increase in intracellular concentration of free radicals including reactive oxygen species (ROS) [4]. Increased ROS production leads to peroxidation of cellular structures, cleavage of DNA, and disruption of the mitochondrial electron transport chain (ETC). Simultaneously, a

mounting immune response further heightens secondary injury. Microglia and infiltrating macrophages secrete inflammatory cytokines and chemokines such as tumor necrosis factor-alpha (TNF-α) and interleukin-8 (IL-8) that lead to increased levels of cellular apoptosis [4, 6]. TNF-α signals through its cognate receptors TNFR1 and TNFR2 to induce cell death *via* caspase-8-mediated apoptosis.[7] The cell ultimately fragments into apoptotic cell bodies that are engulfed by neighboring cells [5]. The expression of these inflammatory cytokines and chemokines are shown to be significantly upregulated in both human brains and serum samples post-TBI and are used as biomarkers to assess the extent of head trauma[8, 9].

Neuroprotectants that inhibit secondary injury cascades have led to a number of phase II and III clinical trials[2, 10]. However, despite promising data in preclinical rodent animal models and early phase randomized and double blinded trials, no neuroprotective treatment option exists that leads to improved neurological outcomes. One potential option to improve efficacy is to improve therapeutic delivery through approaches that are better able to cross the blood-brain barrier (BBB), better target cells, and cellular compartments of interest. Only a handful of small lipophilic molecules, including therapeutic antioxidants and anti-inflammatory agents that could ameliorate secondary injury, can freely diffuse across the lipid membranes of the BBB [11, 12]. However, increasing the lipophilicity of a small molecule-based drug to enhance BBB penetration can have undesirable effects, which include reduced overall solubility, and bioavailability, increased plasma protein interactions, and increased uptake by the cells of the mononuclear phagocyte system (MPS). Delivery of neuroprotectants to the brain can potentially be achieved by using biodegradable nanoparticles (NPs) engineered to achieve

three crucial milestones: (1) optimize size charge, lipophilicity, and targeting properties to cross the BBB into the brain, (2) reach specific intracellular targets and demonstrate controlled release of the payload at the target, and (3) performing its ameliorative function there. This would enable effective and robust delivery of neuroprotectants to injured cells and stem cellular degradation and tissue damage. High mitochondrial density in cerebral endothelial cells than in peripheral endothelia[13, 14] provide a strategy to target brain by constructing a highly lipophilic mitochondria targeted NP system with suitable size and charge.

Most studies have focused on rodent models for the development of neuroprotectants, but in part this has likely contributed to the limited translatability of therapeutic findings developed in the rodent to human patients. To enhance the therapeutic potential, efforts have been made to work in models more similar to humans such as the pig[9, 15]. Compared to the rodent, the piglet brain has greater anatomical and physiological similarities to humans with comparable gray-white matter composition, brain size, and both having gyrencephalic brains unlike rodents[16],[17-19] This suggests that the pig TBI model may be more advantageous for neural injury as outcomes are likely to be more predictive of what would occur in a human brain.

In this study, we examined the therapeutic potential of a highly lipophilic BBB penetrating biodegradable mitochondria targeted nanoparticle (NP) containing an antioxidant and an anti-inflammatory cocktail therapy in a piglet model of TBI.

Materials and Methods.

Animals.

American Landrace piglets (4 weeks old) were obtained from the University of Georgia Swine Farm and handled in accordance with ‘‘The Guide for the Care and Use of Laboratory Animals’’ of American Association for Accreditation of Laboratory Animal Care (AAALAC), Animal Welfare Act (AWA), and other applicable federal and state guidelines. All animal work presented here was approved by Institutional Animal Care and Use Committee (IACUC) of University of Georgia.

Materials and Instrumentations.

All chemicals were received and used without further purification unless otherwise noted. Dimethylaminopyridine (DMAP), KCl, N-hydroxysuccinimide (NHS), triethylamine, 5-bromopentanoic acid, N,N'-dicyclohexylcarbodiimide (DCC), hydrogen peroxide solution (30 wt.% in H_2O), (3-(4,5-dimethylthiazol-2-yl)-2,5-diphenyltetrazolium bromide (MTT), CoQ_{10} (Product number C9538) were purchased from Sigma-Aldrich. Prednisone, carboxy terminated (dL/g, 0.15 to 0.25) was procured from Lactel and OH-PEG-OH of molecular weight 3350 was purchased from Sigma Aldrich. Triphenyphosphine (TPP) was purchased from Sigma Aldrich. Bicinchoninic acid (BCA) protein assay kit (Pierce 23227) was purchased from Thermo Scientific. Sodium chloride, magnesium chloride, sucrose, potassium chloride, and ethylyenediaminetetraacetic acid (EDTA) were purchased from J.T. Baker. Slide-A-Lyzer MINI Dialysis Units (catalog number 69572) were purchased from Thermo Scientific. Human induced pluripotent neural stem cells (NSC) were purchased from GlobalStem. Matrigel was purchased from BD Bioscience. Accutase was purchased from

Innovative Cell Technologies. NSC expansion media reagents were purchased from Life Technologies with the exception of basic fibroblast growth factor (bFGF), which was purchased from R&D Systems. 2'7'-Dichlorofluorescin diacetate (DCF-DA) for reactive oxygen species detection was purchased from Sigma Aldrich. Swine specific enzyme-linked immunosorbent assay (ELISA) kits were purchased from Life Technologies and absorbance was read on a FlexStation Plate Reader from Molecular Devices.

Distilled water was purified by passage through a Millipore Milli-Q Biocel water purification system (18.2 MΩ) containing a 0.22 μm filter. ^{1}H, ^{13}C spectra were recorded on a 400 MHz; ^{31}P NMR spectra were recorded on a 500 MHz Varian NMR spectrometer. Cells were counted using Countess® Automated cell counter procured from Invitrogen. Dynamic light scattering (DLS) measurements were carried out using a Malvern Zetasizer Nano ZS system. Optical measurements were carried out on a NanoDrop 2000 spectrophotometer. Transmission electron microscopy (TEM) images were acquired using a Philips/FEI Technai 20 microscope. Inductively coupled plasma mass spectrometry (ICP-MS) studies were performed on a VG PlasmaQuad 3 ICP mass spectrometer. Plate reader analyses were performed on a Bio-Tek Synergy HT microplate reader. Gel permeation chromatographic (GPC) analyses were performed on Shimadzu LC20-AD prominence liquid chromatographer equipped with a refractive index detector and Waters columns; molecular weights were calculated using a conventional calibration curve constructed from narrow polystyrene standards using tetrahydrofuran (THF) as an eluent at a temperature of 40 °C. Antioxidative stress assays were carried out using a Seahorse XF24 analyzer (Seahorse Biosciences, North Billerica, MA, USA).

Fluorescence imaging of brain samples was carried out on a Xenogen IVIS® Lumina system.

Cell Culture.

Human induced pluripotent stem cell-derived neural stem cells (HIP™ hNSC BC1, GlobalStem®, Rockville, MD) used for the *in vitro* portion of this study. NSCs were maintained on matrigel-coated tissue culture dishes in neural stem cell media composed of neural basal medium, 2% B-27 supplement, 1% non-essential amino acids, 2 mM L-alanine/L-glutamine, 1% penicillin/streptomycin, and 20 ng/mL bFGF. The media was changed every other day. When NSCs reached confluence (approximately every 4 to 5 days), cells were enzymatically passaged using Accutase and removed from the dish using a cell scrapper. Cells were split at a 1:4 ratio. To prepare NSCs for MTT and ROS Reduction assays, NSCs were plated in matrigel-coated 96-well dishes at a ratio of 40,000 cells per well in neural stem cell media.

Synthesis of PLGA-*b*-PEG-OH and PLGA-*b*-PEG-TPP.

The non-targeted PLGA-b-PEG-OH and targeted PLGA-b-PEG-TPP were synthesized and characterized by following methods previously reported by us. [20]

Synthesis of PLGA-PEG-QD.

Conjugation of PLGA to PEG-QD was carried out using a slight modification based on our previously reported method.[20] PLGA-COOH of an inherent viscosity of 0.15-0.25 (1 mg, ~0.16 μmol) was dissolved in 2 mL DMF. To activate the carboxyl moiety for conjugation, EDC (10 mg, 52 μmol) and NHS (10 mg, 86.9 μmol) were added, and the mixture was stirred at room temperature for 5 h. To this, QDot® 705 ITK Amino (PEG) quantum dots (250 μL, 2 nMol) slowly dropwise to ensure no precipitation

of PLGA. The reaction mixture was stirred overnight at RT. The QDots were isolated and washed by repeated centrifugations (14,000 RPM, 1 hr). The final QDot pellet was resuspended in 250 µL and kept at 4℃ until further use.

T and NT-QD NP Construction.

NPs were synthesized by nanoprecipitation method. Briefly, PLGA-*b*-PEG-OH or PLGA-*b*-PEG-TPP in (50 mg/mL in DMF) was mixed with a predefined amount of prednisone (10 mg/mL in DMF) and diluted with DMF to a final polymer concentration of 5 mg/mL. This was mixed with PLGA-PEG-QDs (10 µL, 8 µM solution in DMF). This mixture was added drop-wise to nanopure water with constant stirring. The NPs were stirred for 2 h at room temperature. Organic solvent was removed by washing three times using a 100 kDa cut-off amicon filtration membrane. The NPs were resuspended in nanopure water and stored at 4 °C until further use. DLS measurements were carried to determine size, PDI, and zeta potential.

T and NT-Prednisone-NP Synthesis

NPs were synthesized by the nanoprecipitation method. Briefly, PLGA-*b*-PEG-OH or PLGA-*b*-PEG-TPP in (50 mg/mL in DMF) was mixed with a predefined amount of prednisone (10 mg/mL in DMF) and diluted with DMF to a final polymer concentration of 5 mg/mL. This mixture was added drop-wise to nanopure water with constant stirring. The NPs were stirred for 2 h at room temperature. Organic solvent was removed by washing three times using a 100 kDa cut-off amicon filtration membrane. The NPs were resuspended in nanopure water and stored at 4 °C until further use. DLS measurements were carried to determine size, PDI, and zeta potential. Prednisone loading

and EE were determined by dissolving the polymeric core and quantifying the amount of Prednisone in the NPs using HPLC (wavelength used: 261 nm).

Synthesis of T and NT-CoQ10-NPs.

NPs were synthesized by the nanoprecipitation method. Briefly, PLGA-*b*-PEG-OH or PLGA-*b*-PEG-TPP in (50 mg/mL in DMF) was mixed with a predefined amount of CoQ10 (10 mg/mL in DMF) and diluted with DMF to a final polymer concentration of 5 mg/mL. This mixture was added drop-wise to nanopure water with constant stirring. The NPs were stirred for 2 h at room temperature. Organic solvent was removed by washing three times using a 100 kDa cut-off amicon filtration membrane. The NPs were resuspended in nanopure water and stored at 4 °C until further use. DLS measurements were carried to determine size, PDI, and zeta potential. CoQ10 loading and EE were determined by dissolving the polymeric core and quantifying the amount of CoQ10 in the NPs using HPLC (wavelength used: 329 nm).

Release of Prednisone and CoQ10 from T and NT-NPs.

The release kinetics analyzed for CoQ10 and Prednisone encapsulated NPs by subjecting them to dialysis against 1x PBS (pH 7, 37℃). The NPs were added to a Slide-a-lyzer mini dialysis unit (100 µL) and placed in the PBS bath with gentle shaking. At various time points, a dialysis unit was removed. The amount of remain drug was determined by dissolving the polymeric core and quantifying the amount of Prednisone or CoQ10 in the NPs using HPLC.

Antioxidative Properties of T and NT NPs or free CoQ10 by Seahorse Analyzer.

CoQ10 (T-NP, NT-NP, or free) was tested for its ability to reduce oxidative stress in iPS-NPs. The cells were plated at a concentration of 50,000 cells/well on each well of

Seahorse XF24 well plate and allowed to grow overnight. The media was changed and the cells were washed and the media was replaced with seahorse basal media. The cells were monitored for changes in oxygen consumption rate (OCR) with respect to time. A basal reading was acquired for 45 min and then hydrogen peroxide was injected. The OCR was monitored for 90 min and CoQ10 (targeted, non-targeted, or free) was injected. The OCR levels were then further measured for 4.5 hours. As a control, cells were also monitored with no treatment or only treatment of hydrogen peroxide.

Anti-inflammatory Properties of NPs in Stem Cells.

NSCs were plated on each well of a 12-well plate at a density of $1x10^7$ per well and allowed to grow overnight. LPS (100 ng/mL) was added to the NSCs and incubated for 36 h. T-CoQ_{10}-NPs, NT-CoQ_{10}-NPs, T-Pred-NPs, NT-Pred-NPs, T-CoQ_{10}-NPs + T-Pred-NPs, NT-Pred-NPs + NT-CoQ_{10}-NPs, free CoQ_{10}, free prednisone, or free prednisone + free CoQ_{10} (1 μM each) was then added to the cells and incubated for 12 h. ELISA was performed on the supernatants against the cytokines interleukin (IL)-6, IL-10, IL-4, IL-12, and TNF-α according to the methods reported by us.[21, 22] Briefly, antibody coated plates were blocked with 10% FBS in PBS for 1 h at room temperature followed by 3 washes. NSC supernatants were incubated on the plates for 2 h at room temperature. This was immediately followed by washings and sequential incubations with the cytokine-biotin conjugate and streptavidin working solution. Finally, the substrate reagent containing 3,3',5,5'-tetramethylbenzidine (100 μL) was added to each well, incubated for 15 min, the reaction was stopped by adding 50 μL H_2SO_4 (0.1 M). The absorbance was recorded at 450 nm using a BioTek Synergy HT well plate reader.

Cytotoxicity of CoQ_{10} and Prednisone NPs in NSCs.

The cytotoxic behavior of all the NPs was evaluated by using the MTT assay against NSCs. Cells (40,000 cells/well) were seeded on a 96-well plate in 100 μL of NSC basal complete medium and incubated for 24 h. The cells were treated with NPs at varying concentrations (with respect to prednisone and CoQ_{10}) and incubated at 37 °C. The medium was changed after 12 h, and the cells were incubated for an additional 60 h. The cells were then treated with 20 μL of MTT (5 mg/mL in PBS) for 5 h. The medium was removed and the cells were lysed with 100 μL of DMSO and the absorbance of the purple formazan was recorded at 550 nm using a Bio-Tek Synergy HT microplate reader. Each well was performed in triplicate and a background reading was recorded at 800 nm.

BioD and PK of NPs in Pig.

American Landrace piglets (4 weeks old, 3 per group) were anesthetized using isofluorane. T-QD-NPs (2.5mg/kg with respect to NP and 0.46 mg/kg with respect to Cd), NT-QD-NPs (2.5 mg/kg with respect to NP and 0.62 mg/kg with respect to Cd), and saline were administered *via* intravenous catheter placed into an ear vein. Blood samples were collected in heparinized tubes at 0, 2, 4, 6, 8, and 24 h post-injection and stored at 4 °C until use. Blood samples were centrifuged at 2000 rpm for 20 minutes at 4 °C in order to collect serum. The percentage of QD from NPs was calculated by taking into consideration that blood constitutes 3.5% of body weight and serum constitutes 55% of blood volume for pig.[23] The amount of Cd from the QD was calculated in the blood plasma by ICP-MS. After 24 h post-surgery, piglets were deeply anesthetized using 5% vaporized isoflurane with oxygen utilizing a surgical mask and then euthanized via CO_2 inhalation. After euthanasia, the piglets were decapitated and the brain was removed and

stored at -80 °C. For bioD studies, the heart, lungs, kidneys, liver, and spleen were removed and stored at -80 °C. The overall bioD was calculated by analyzing the amount of Cd in each organ by ICP-MS. The brain samples were also imaged by IVIS using Cy5.5 filter (emission, excitation) with an exposure time of 1 sec. Brains were then sectioned into 5 mm coronal sections and imaged by IVIS. Before analysis, the organs were dissolved with nitric acid for 24 h with gentle heating and shaking. The calculations for AUC, C_{max}, T_{max}, and C_L (t=0) were performed in the GraphPad Prism (Version 5.01). PK parameters were determined by fitting the data using a two-compartmental model equation.

Induction of TBI in Pig.

Induction and characterization of TBI was performed by Emily L. Wyatt from the Department of Food and Dairy Sciences.

BioD and PK of NPs in TBI Pig Model.

American Landrace piglets (4 weeks old, 2 per group) were anesthetized using isofluorane and the TBI was induced. After 5 h, T-QD-NPs (2.33 mg/kg with respect to NP and 0.889 mg/kg with respect to Cd), NT-QD-NPs (1.5 mL suspension, 2.33 mg/kg with respect to NP and 1.05 mg/kg with respect to Cd), and saline were administered *via* intravenous catheter placed into an ear vein and nanoparticle solution was administered. Blood samples were collected in heparinized tubes at 0, 2, 4, 6, 8, and 24 h post-injection *via* orbital sinus bleed and stored at 4 °C until use. Blood samples were centrifuged at 2000 rpm for 20 minutes at 4 °C in order to collect serum. The percentage of QD from NPs was calculated by taking into consideration that blood constitutes 6.5% of body weight and serum constitutes 55% of blood volume for pig.[23] The amount of Cd from the

QD was calculated in the blood plasma by ICP-MS. After 24 h post-surgery, piglets were deeply anesthetized using 5% vaporized isoflurane with oxygen utilizing a surgical mask and then euthanized via CO_2 inhalation. After euthanasia, the piglets were decapitated and the brain was removed and stored at -80 °C. The injured area of the brain was sectioned into 5 mm coronal sections for analysis. For bioD studies, the heart, lungs, kidneys, liver, and spleen were removed and stored at -80 °C. The overall bioD was calculated by analyzing the amount of Cd in each organ by ICP-MS. The brain samples were also imaged by IVIS using Cy5.5 filter (emission, excitation) with an exposure time of 1 sec. Brains were then sectioned into 5 mm coronal sections and imaged by IVIS. Before analysis, the organs and feces were dissolved with PerkinElmer solvable (Product number: 6NE9100) for 24 h with gentle heating and shaking. The calculations for AUC, C_{max}, T_{max}, and C_L (t=0) were performed in the GraphPad Prism (Version 5.01). PK parameters were determined by fitting the data using a two-compartmental model equation.

Statistics.

All data were expressed as mean ± S.D (standard deviation). Statistical analysis were performed using GraphPad Prism® software v. 5.00. Comparisons between two values were performed using an unpaired Student t test. A one-way ANOVA with a post-hoc Tukey test was used to identify significant differences among the groups.

Results and Discussion

Mitochondria targeted lipophilic NPs for TBI.

One consideration in developing a NP system in delivering a combination of an antioxidant and an anti-inflammatory agent is the ability of the NP to cross BBB.

Furthermore, the intracellular location of oxidative stress is the mitochondria of cells and the target organelle of most antioxidants is mitochondria of cells. Moreover, a combination of roles in pro-inflammatory signaling and abilities of pro-inflammatory mediators to alter mitochondrial function increase mitochondrial oxidative stress, promoting a vicious inflammatory cycle. Strategies aimed at controlling excessive oxidative and inflammatory stress within mitochondria may represent both preventive and therapeutic interventions in inflammation. Thus, the NP system for delivery of antioxidant and anti-inflammatory agents in brain tissue needs to have both BBB and mitochondria targeting properties. The BBB is formed by endothelial cells in the brain lining the cerebral vasculature that form tight junctions that are 50-100 times tighter than peripheral microvessels.[11] In addition, astrocytic endfeet form "rosette"-like structures around the brain capillary surface and communicate to the endothelial cells to regulate blood flow and nutrient supply.[12] The BBB is an important mechanism in protecting the brain from fluctuations in plasma composition and in maintaining homeostasis in the brain microenvironment. These tight junctions restrict hydrophilic solutes from diffusing out of the brain capillaries, so penetration of the BBB is effectively confined to transcellular mechanisms. Thus, pass from blood to brain of circulating NPs may only happen by transcellular mechanisms, which require a highly lipophilic NP with suitable size and charge. Brain endothelial cell surface and basement membrane components bearing highly anionic charges from sulfated proteoglycans are different from non-brain endothelium and would allow the adsorptive-mediated transcytosis of cationic NPs [24]. The small size and highly lipophilic surface of NPs can help their distribution in the brain. Furthermore, high mitochondrial density in cerebral endothelial cells than in

peripheral endothelia[13, 14] provide a strategy to target brain by constructing a highly lipophilic mitochondria targeted NP system with suitable size. We recently developed a biocompatible polymeric NP based on biodegradable poly(lactic-*co*-glycolic acid) (PLGA)-block (*b*)-polyethyleneglycol (PEG) functionalized with a terminal triphenylphosphonium (TPP) cation which has efficient with brain-penetrating properties and remarkable activity to target mitochondria of cells due to its high lipophilic properties, presence of delocalized positive charge, and appropriate size range [20, 22]. The TPP cation in PLGA-*b*-PEG-TPP polymer takes advantage of the substantial negative $\Delta\Psi_m$ across the inner mitochondrial membrane (IMM) to efficiently accumulate inside the matrix. In rodent model, an optimized formulation of targeted NPs (T-NPs) derived from PLGA-*b*-PEG-TPP polymer was found to accumulate in the brain efficiently upon intravenous administration.[25] This optimized formulation was also found to accumulate in the mitochondria matrix. We therefore, used this particular NP formulation to encapsulate a mitochondria-acting antioxidant coenzyme Q10 (CoQ_{10}) to develop T-CoQ_{10}-NPs (Fig. 5.1A). The non-targeted polymer PLGA-*b*-PEG-OH devoid of a mitochondria targeting lipophilic TPP moiety was used to generate control NP formulation NT-CoQ_{10}-NPs. For anti-inflammatory effects, prednisone, a synthetic corticosteroid drug was used and T-Prednisone-NPs and NT-Prednisone-NPs were formulated (Fig. 5.1B, Table 5.1). The targeted polymer PLGA-b-PEG-TPP and the non-targeted control PLGA-b-PEG-OH were synthesized and characterized following methods previously described by us[20]. The NPs were characterized by dynamic light scattering (DLS) to give the size, polydispersity index (PDI), and zeta potential of each preparation (Fig. 5.1B, Table 5.1).

Table 5.1. Characterization of T and NT-NPs used in this study					
	$Z_{Average}$ (nm)	Zeta Potential (mV)	Polydispersity index (PDI)	%Loading	%EE
T-Empty-NPs	52.6 ± 1.3	34.1 ± 0.7	0.256	-	-
NT-Empty-NPs	52.7 ± 0.6	-25.1 ± 1.5	0.244	-	-
T-Pred-NP	55.8 ± 2.6	27.3 ± 3.6	0.133	18.4 ± 0.8	61.6 ± 2.5
NT-Pred-NP	53.5 ± 1.4	-17.4 ± 2.1	0.199	18.8 ± 1.7	62.6 ± 5.7
T-CoQ_{10}-NP	67.1 ± 1.2	52.4 ± 3.1	0.148	24.9 ± 2.6	83.7 ± 8.7
NT-CoQ_{10}-NP	65.3 ± 0.6	-16.3 ± 0.5	0.132	23.5 ± 2.1	78.8 ± 6.9

Loading efficiencies of CoQ_{10} and prednisone at various added weight-percentage values of these drugs to polymer indicated that both CoQ_{10} and prednisone can be entrapped in these NPs with a very high loading and encapsulation efficiency (EE) (Fig. 5.1B, Table 5.1). Morphology of these NPs was investigated using transmission electron microscopy (TEM) (Fig. 5.1C, Table 5.1).

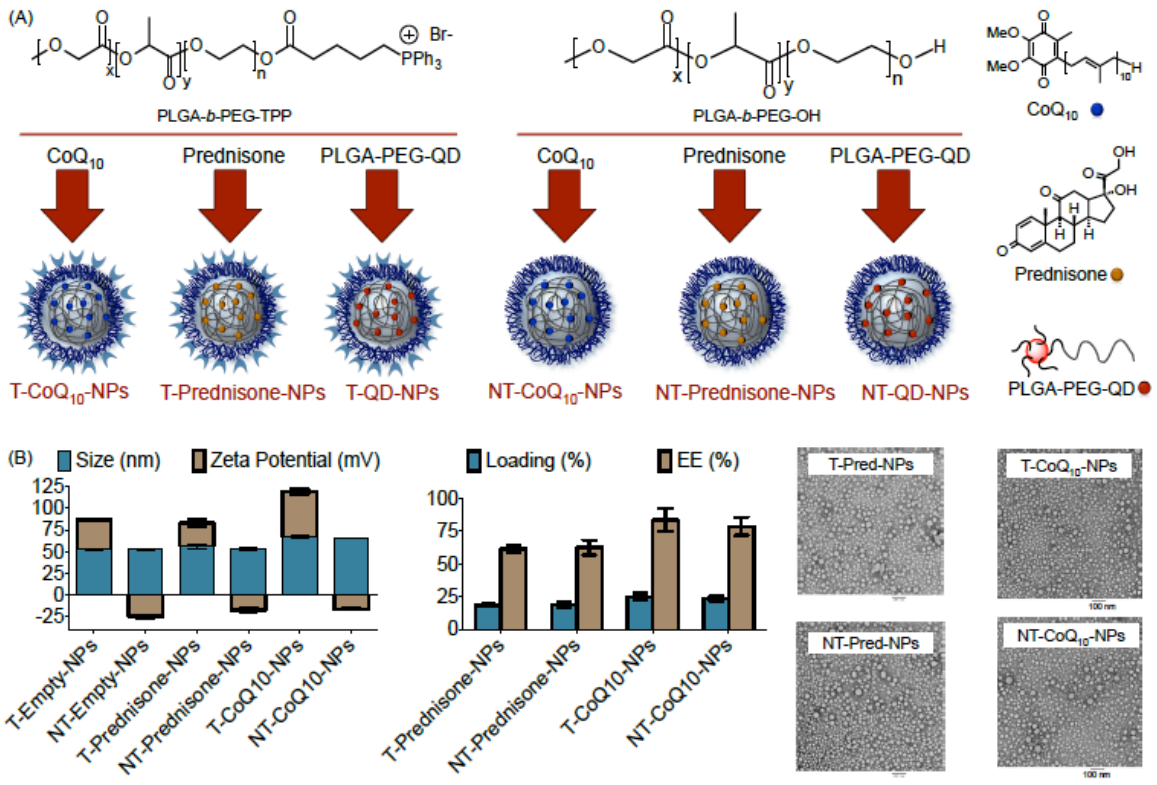


Figure 5.1. Design, construction, and characterization of mitochondria-targeted and non-targeted NPs for delivery of antioxidant and anti-inflammatory agents to the brain. (A) Structure of polymers and payloads used and visual representation of targeted and non-targeted NPs. (B) Size, zeta potential, loading, EE, and TEM of targeted and non-targeted NPs containing CoQ10 and Prednisone.

Distribution of T-NPs in the lipophilic white matter of Brain

We recently determined brain accumulating properties of T-NPs using rat model[25]. Since rodent brains are much smaller than human brains, it is difficult to assess whether the brain penetrating properties T-NPs obtained in the rat is relevant to treatment of TBI in human. We therefore extended our analysis to larger brains and studied bioD and PK profiles of T-NPs in piglet. We administered brain-penetrating T-NPs (2.5 mg/kg with respect to total NP and 0.46 μg/kg with respect to Cd) via ear vein of 4 week old

male piglets (n=3). NT-QD-NPs (2.5 mg/kg with respect to total NP and 0.62 μg/kg with respect to Cd) and saline were used as control groups and each group had n=3 animals. Blood samples were collected at predetermined time points after i.v. NP administration and amount of Cd present in the plasma were determined by inductively coupled plasma-mass spectroscopy (ICP-MS) (Fig. 5.2A). The plasma Cd profiles from T and NT-QD-NPs were used to evaluate PK parameters (Table 5.2) Peak plasma concentration (C_{max}) was calculated directly from the time-concentration curves for QD. The fitted parameters did not differ significantly between the pigs treated with T-QD-NPs versus NT-QD-NPs (Table 5.2).

Table 5.2. PK Profiles of T and NT-NPs in Normal Pig

	T-NPs	NT-NPs
$AUC_{[0\text{-}24\ h]}$ (ng/mL)	12,250 ± 715	12,617 ± 654
C_{max} (ng/mL)	3,666 ± 158	3,586 ± 410
V_d (mL/kg)	126.2 ± 5.3	174.7 ± 20.7
C_L (mL/h)	188.9 ± 11.1	246.2 ± 13.0
$t_{1/2}$ (h)	2.32 ± 0.08	2.45 ± 017

The elimination half-life ($t_{1/2}$) was 2.3 h for T-QD-NPs that is in close agreement with the half-life previously observed in a rat model. A similar $t_{1/2}$ of 2.5 h was observed demonstating that the positively charged TPP moieties do not have any effect on the clearance of the T-NPs. High area under curve (AUC) values for blood concentrations were observed for T-QD-NPs and NT-QD-NPs. A smaller volume of distritibution (V_d) was observed in the pigs receiving both T-QD-NPs and NT-QD-NPs (Table 5.2) Animals

were sacrificed after 24 h and bioD was studied by quantifying Cd in the different organ samples (Fig. 5.2A). The brains samples were analyzed by performing fluorescence microscopy using in vivo imaging system (IVIS) (Fig. 5.2B). Significant distribution of T-NPs was observed in brain tissue, so such distribution was noted with the NT-NPs (Fig. 5.2B). NT-QD-NPs were mostly distributed in the liver.

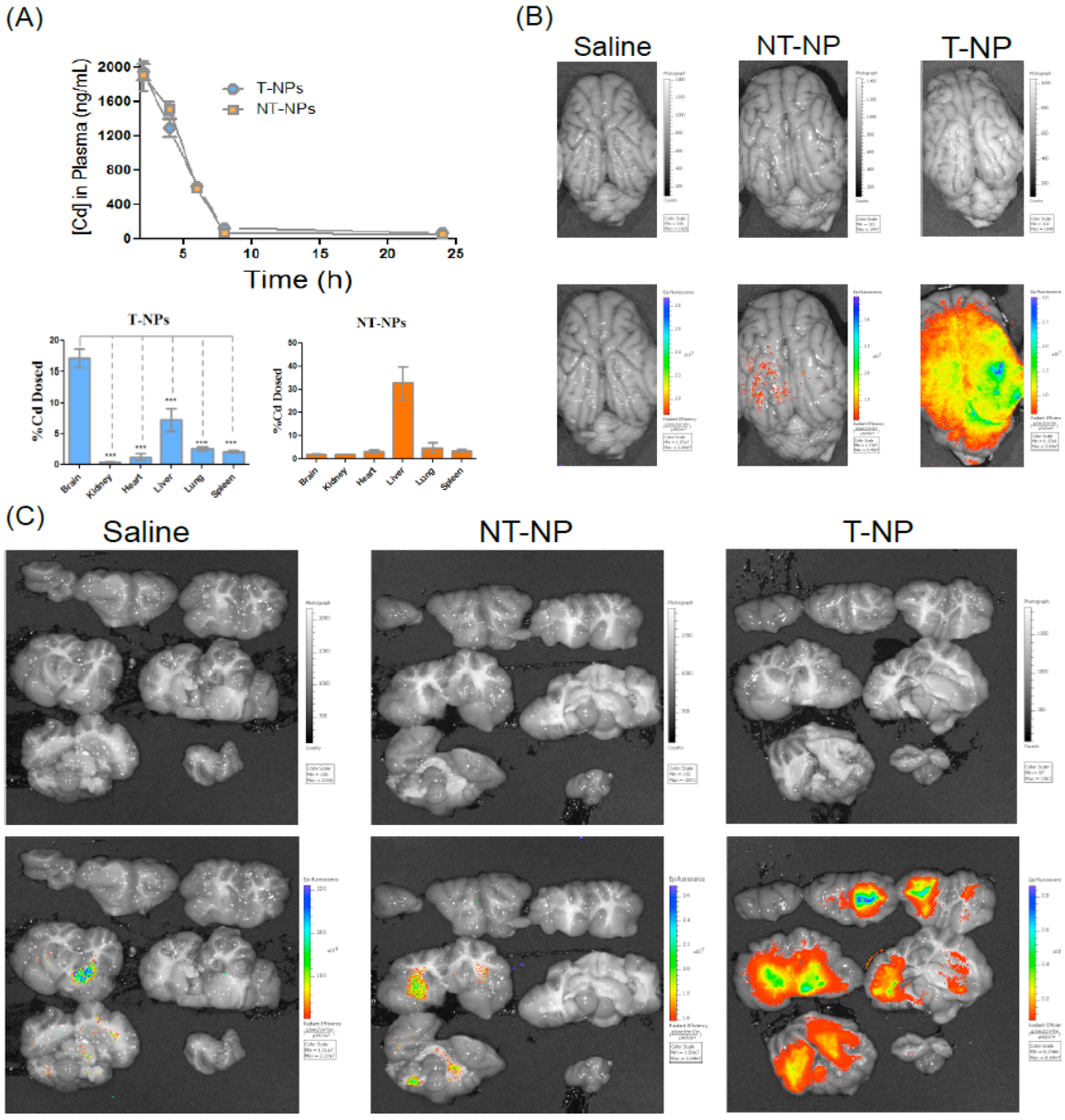


Figure 5.2. Accumulation of T-NPs in the brain of normal Pig and distribution in brain white matter**.** American Landrace piglets (4 weeks old, n=3) were anesthetized using

isofluorane and T-QD-NPs (2.5 mg/kg with respect to NP and 0.46 mg/kg with respect to Cd) and NT-QD-NPs (2.5 mg/kg with respect to NPs and 0.62 mg/kg with respect to Cd) was administered *via* ear vein IV. (A) Plasma circulation and different organ distribution of T and NT-NPs by ICP-MS in pig model. (B) 24 h post injection brain accumulation using IVIS, top: Normal photograph and bottom: Fluorescence image. (C) Distribution of T-NPs in the white matter of the brain by performing IVIS analyses of the vertically cut slices of whole brain. top: Normal photograph showing the white and grey matter and bottom: Fluorescence image.

The brain is not a homogenous organ and the phospholipid pattern varies in its different regions resulting different lipophilicity profiles. Total lipid content in the white matter is twice as high as in the grey matter. The white matter with a higher total lipid content have higher levels of cerebrosides and sulfatides and lower percentages of phosphatidylcholine and phosphatidylinositol. Since the T-NPs are highly lipophilic, we therefore studied the relative distribution of these NPs in different regions of the brain (Fig. 5.2C). IVIS analyses of vertically cut slices of whole brain indicated distribution of the T-NPs in the lipophilic white matter to a greater extent (Fig. 5.2C). Inflammation and injury are often diffuse in the white matter, therefore the current T-NPs which selectively accumulate in the white matter of the brain can be extremely beneficial in delivering neuroprotectants after TBI.[26] Taken together, these data demonstrated that our brain-penetrating T-NPs have PK profile, distribution pattern, and in particular accumulation in brain white are clinically relevant and might show therapeutic potentials when developed further.

Accumulation of T-Ns in the Mitochondria of Brain Tissue

Because the T-QD-NP formulations showed significant accumulation in the brains and higher accumularion was observed in the lipophilic white matter, we subjected brain tissue samples from white and grey matter to additional confocal imaging (Fig 5.3). Both grey and white matter samples from pig brains treated with T and NT-NPs were isolated, samples were fixed, mitochondria were stained with MitoTracker green, and the samples were sectioned for imaging. Confocal imagin of these samples illustrated significant association of T-QD-NPs in the mitochondria of brain cells present in the white and grey matter. Mitochondrial association of T-QD-NPs were higher in the white matter compared to that in the grey matter. The NT-QD-NPs were not detected in the brain tissue samples (Fig. 5.3B), however no T-QD-NPs were found in the liver cells (Fig 5.3A).

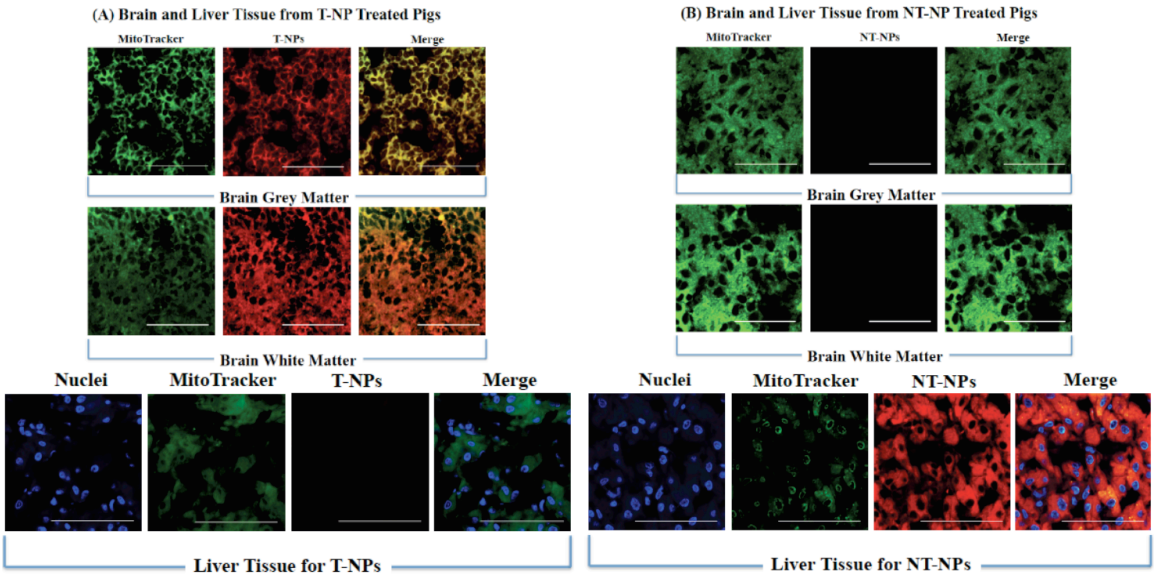


Figure 5.3. Accumulation of T-NPs in the mitochondria of pig brain tissue. Grey and white matter samples were isolated from each brain. Brain and liver samples were fixed in 4% paraformaldehyde for 5 h before being cryoprotected in 30% sucrose. Samples

were then embedded in Optimal cutting temperature (OCT) compound and cryosectioned at 5 μm. The sections were then stained with MitoTracker green for mitochondria labeling and ProLong® Gold mountant with DAPI for nuclear stain. Scale bar: 25μm.

Table 5.3. PK Profiles of T and NT-NPs in TBI Pig Model		
	T-NPs	**NT-NPs**
$AUC_{[0\text{-}24\ h]}$ (ng/mL)	43,449 ± 742	32,137 ± 5,315
C_{max} (ng/mL)	4,143 ± 1,228	4,324 ± 678
V_d (mL/kg)	226.0 ± 67.0	246.0 ± 38.6
C_L (mL/h)	85.3 ± 15.8	156.8 ± 35.2
$t_{1/2}$ (h)	9.60 ± 4.51	5.68 ± 2.13
Least-squares fit to model: $C = a*\exp[-k_1*t) + b*\exp(-k_2*t)$		

Distribution of T-NPs traumatic brain injured pig.

Table 5.4. Characterization of QD loaded T and NT-NPs used in animal studies				
	$Z_{Average}$ (nm)	Zeta Potential (mV)	PDI	QD Content
PK and bioD in Normal Pig				
NT-QD-NP	53.0 ± 0.3	-13.7 ± 1.1	0.183 ± 0.010	0.150 mg Cd/mg Polymer
T-QD-NP	50.5 ± 0.8	42.4 ± 1.9	0.447 ± 0.027	0.127 mg Cd/mg Polymer
PK and bioD in TBI Pig				
NT-QD-NP	49.3 ± 1.5	-16.0 ± 1.3	0.169 ± 0.025	0.124 mg Cd/mg Polymer
T-QD-NP	60.5 ± 7.5	43.4 ± 2.0	0.295 ± 0.089	0.092 mg Cd/mg Polymer

We next assessed the bioD and PK profile of T-NPs and NT-NPs in TBI pig model. NP size and zeta potential of the NPs used in this study are represented in Table 5.4. Consistent with our previous work in rats and current work in normal piglet, the T-NPs demonstrated favorable PK and bioD profiles. A penetrating TBI was generated 5h prior to intravenous NP injection. T-NPs (2.33 mg/kg with respect to total NP and 0.889 mg/kg with respect to Cd) and NT-NPs (2.33 mg/kg with respect to total NP and 1.05 mg/kg with respect to Cd) were administered by ear vein injection. Blood samples were collected at predetermined time points of 2, 4, 8, and 24 h post injection and major organ samples were collected at 24 h (Fig. 5.5 and Table 5.3). Plasma circulation properties of T and NT-NPs are presented in Fig. 5.5A and the PK parameters calculated using a two compartment intravenous input model presented in Table 5.3.

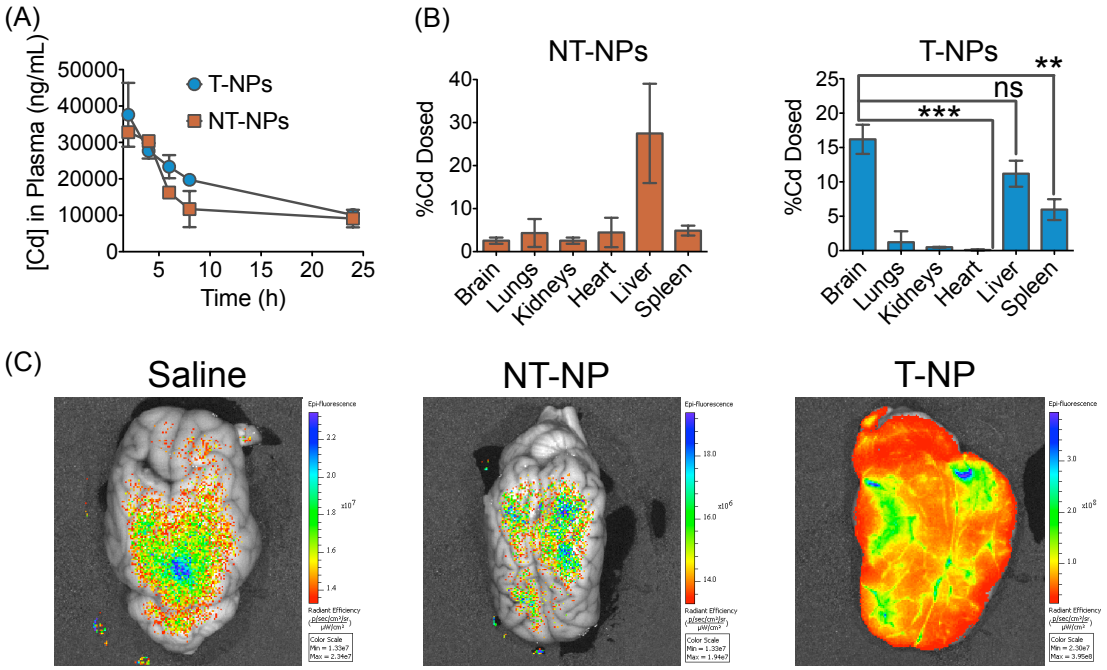


Figure 5.4. Accumulation of T-NPs in the brain of injured Pig. American Landrace piglets (5 weeks old) were anesthetized using isofluorane and the TBI was induced. After 5 h, NPs (T-NPs (2.33 mg/kg with respect to total NP and 0.889 mg/kg with respect to Cd

and NT-NPs 2.33 mg/kg with respect to total NP and 1.05 mg/kg with respect to Cd) was administered via ear vein IV. (A) Plasma circulation of T and NT-NPs in TBI pig model. Brain accumulation was followed by ICP-MS (B) and (C) IVIS 24 h post injection.

T and NT-NP time-plasma concentration profiles are shown in Fig. 5A. In contrast to our studies in normal pigs, the PK parameters for T- and NT-NPs differ significantly when evaluated in injured pigs. There was a significant difference between the plasma $t_{1/2}$ values of T-QD-NPs compared to NT-QD-NP treatments. Notable in these results are increase in the AUC for T-NPs over the non-targeted formulation. This coupled with the observation that the T-NPs have a greater mean residence time in plasma ($t_{1/2}$: 9.6 h compared to $t_{1/2}$ of NT-NPs: 5.7 h), is a confirmation of unique features of TPP containing mitochondria-targeted NPs that allow it to circulate for longer time in the plasma.

Organ distribution profiles that a major fraction of T-QD-NPs in the brain and most of NT-QD-NPs were found in the liver (Fig 5.5B). The preferential distribution of the T-NPs in the brain was further confirmed by performing IVIS on the injured brain samples (Fig 5.5C). The T-NPs were present in the brain at much higher levels that NT-NPs, consistent with the *in vivo* imaging studies in normal pig. The PK and distribution profiles of T-NPs demonstrated that mitochondria targetin NPs can be extremely beneficial in delivering neuroprotectants after traumatic brain injury.

Reduction of inflammation and oxidative stress in neural stem cells (NSCs).

Transplantation of NSCs can provide a promising therapy after TBI. However, the efficacy of such NSC transplantation is limited because of massive grafted-cell death and insufficient tissue repair. Stem cells in the nervous are NSCs that can renew and

differentiate to differentiated progenitor cells for generation of lineages of neurons and glia. We therefore, used NSCs to study the therapeutic potential of BBB penetrating T-NPs containing prednisone and CoQ_{10}.

Oxidative stress induced by the production of ROS including free radicals and peroxides is one of the major mechanisms, which leads to neuronal destruction and is closely related to apoptosis and necrosis in these cells during TBI. Mitochondria are well known to be a major source of ROS production. CoQ_{10} is endogenously synthesized in mammalian mitochondria, acts as both antioxidant and pro-oxidant, and is involved in shuttling electrons from complexes I or II and a number of other electron donors, including electron transfer factor, which moves electrons from fatty acid beta oxidation. CoQ_{10} is found in all cell and organelle membranes, where it can participate in redox shuttling. However, defects in CoQ_{10} biosynthesis can be found during TBI. Therefore, exogenous CoQ_{10} administration to brain during TBI can represent an attractive strategy to reduce local oxidative stress. However, CoQ_{10} is insoluble in water, powder formulations have very poor intestinal absorption, and no BBB penetrating properties. Improved bioavailability, controlled release (Fig. 5.7A), brain accumulation, and efficient mitochondrial distribution of CoQ10 using T-CoQ10-NPs can be extremely beneficial for TBI treatment. We induced oxidative stress in NSCs by bolus doses of hydrogen peroxide (H_2O_2) and studied the effect of mitochondria targeting T-CoQ_{10}-NPs on mitochondrial respiration of these adherent NSCs under the oxidative stress induced by H_2O_2 using a Seahorse Bioscience XF24 Extracellular Flux (Fig. 5.7B). As controls, free CoQ_{10} and NT-CoQ_{10}-NPs were used using same conditions (Fig. 5.7B). CoQ_{10} accepts electron in the IMM from mitochondrial complexes I and II and transfers these electrons to complex

III and also increases expression of proteins with an antioxidant effect by inhibiting ROS production. NSCs were exposed to H_2O_2. Then, NSCs were treated with CoQ_{10} (1 μM), NT-CoQ_{10}-NPs (1 μM with respect to), and T-CoQ_{10}-NPs (1 μM with respect to CoQ_{10}) under hypoxia and oxygen consumption rates (OCRs) of these cells were measured. Addition of H_2O_2 to the NSCs, decreased OCRs in these cells significantly, OCR value decreased from ~40 pMoles/min to ~-530 pMoles/min. Subsequent addition of T-CoQ_{10}-NPs to NSCs under oxidative stress demonstrated remarkable effect on reversal of the oxidative stress as early as at 167 min and the respiration rates in these cells reached the levels of healthy cells at 267 min. In comparison, NT-CoQ_{10}-NPs and free CoQ_{10} showed less efficiency in oxidative stress reduction at 330 min and the respiration in these cells reached significant levels only after 400 min and the OCR levels were less than those observed in healthy cells. Taken together these results demonstrated a decreased bioenergetics in intact neural cells by the oxidant, H_2O_2 and mitochondrial delivery of CoQ_{10} in the form of T-CoQ_{10}-NPs demonstrated remarkable efficiency in reducing the oxidative stress.

Immunosuppressant corticoid based rugs such as prednisone can exert biphasic effects on neuronal mitochondrial dynamics. A low level of prednisone and chronic high levels can attenuate various aspects of mitochondrial function[37]. We, therefore, hypothesized that by delivering prednisone in a controlled release fashion using T-Prednisone-NPs as evident by the release kinetics showed in Fig. 5.7A to the mitochondria of NSCs, we can potentially observe effects related to mitochondrial oxidation, membrane potential, and calcium holding capacity. Cytokines like TNF-α and IL-6 secreted by cells link their inflammatory responses. TNF-α levels are one of the

most important predictors of cerebral inflammation. We therefore used lipopolysaccharide (LPS) stimulated TNF-α and IL-6 secreting NSCs to understand the anti-inflammatory effects of Prednisone-NPs and CoQ_{10}-NPs in an *in vitro* model (Fig. 5.7C). When LPS stimulated NSCs were treated with Prednisone, T-Pred-NPs, NT-Pred-NPs, T-CoQ_{10}-NPs, NT-CoQ_{10}-NPs or any combination of the T and NT-NPs, TNF-α secretion induced by LPS stimulation was significantly reduced to >95% (P<0.001 versus NSC + LPS, n=3 wells per group). IL-6 is up-regulated during TBI. IL-6 levels in cerebrospinal fluid (CSF) can be significantly higher than plasma levels in patients who had suffered TBI[38]. An IL-6 polymorphism can be associated with fatal outcome in patients with severe TBI[39]. As expected, IL-6 was up-regulated in NSCs after treatment with LPS. The T and NT NPs containing prednisone reduced the levels of IL-6 in the LPS stimulated NSCs. The addition of T or NT-CoQ10 NPs further to prednisone NP further increased the efficiency of IL-6 reduction. To exclude the possibility that the decrease in these cytokine levels was simply due to the cytotoxicity of prednisone or CoQ10 NPs, viability of NSCs was evaluated in the presence of prednisone or CoQ10 , T-pred-NPs, NT-Pred-NPs, T-CoQ10-NPs, and NT-CoQ10 NPs using the (3-(4,5-dimethylthiazol-2-yl)-2,5-diphenyltetrazolium bromide) (MTT) assay (Fig 5.6).

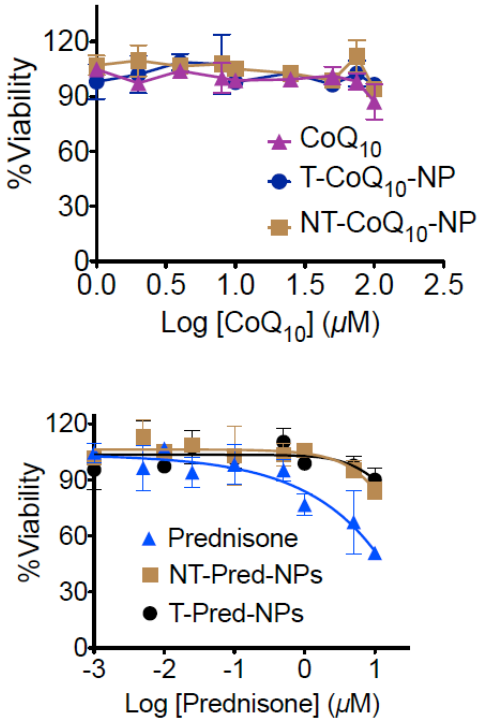


Figure 5.5. MTT assays on NSCs using CoQ10 and its NPs (top) and prednisone and its NPs (bottom)

The concentrations for prednisone or CoQ_{10} used in the anti-inflammatory studies did not show any cytotoxic effects in the treated NSCs ruling out the possibility of IL-6 or TNF-α reduction through cell death. These results demonstrating the reduction of a pro-inflammatory cytokine such as TNF-α and IL-6 which is involved in the pathogenesis of TBI further supported our hypothesis that preconditioning of injured area with BBB penetrating NPs containing a combination of prednisone and CoQ_{10} before NSC transplantation may enhance the repair efficacy and accelerate amelioration of TBI after transplantation.

IL-10 is primarily an anti-inflammatory cytokine with potent inhibitory effects on several pro-inflammatory mediators such as IL-1β and TNF, IL-1α, granulocyte-macrophage colony stimulating factor (GM-CSF), IL-6, IL-8, IL-12, and IL-18

production. The anti-inflammatory properties of IL-10 after TBI are well established, however the IL-10 expression profile following TBI in animals is not well understood. On e of the initial studies suggested that IL-10 in the brain increases rapidly during the first 4 h following TBI and remains elevated for at least 20 h thereafter.[40] A recent study suggested that TBI-induced decrease in brain levels of anti-inflammatory cytokine IL-10[41] and in diffuse brain injured rats, no change in IL-10 was observed over 4 days post-injury.[42] These together suggested that IL-10 may play a role in a delayed phase after TBI. In our experiments we found that IL-10 was elevated in NSCs when the cells were treated with CoQ_{10} or prednisone and their NPs. A combined administration of T-CoQ_{10}-NP and T-Pred-NP was more effective in inducing IL-10 compared to the other formulations (Fig. 5.7)

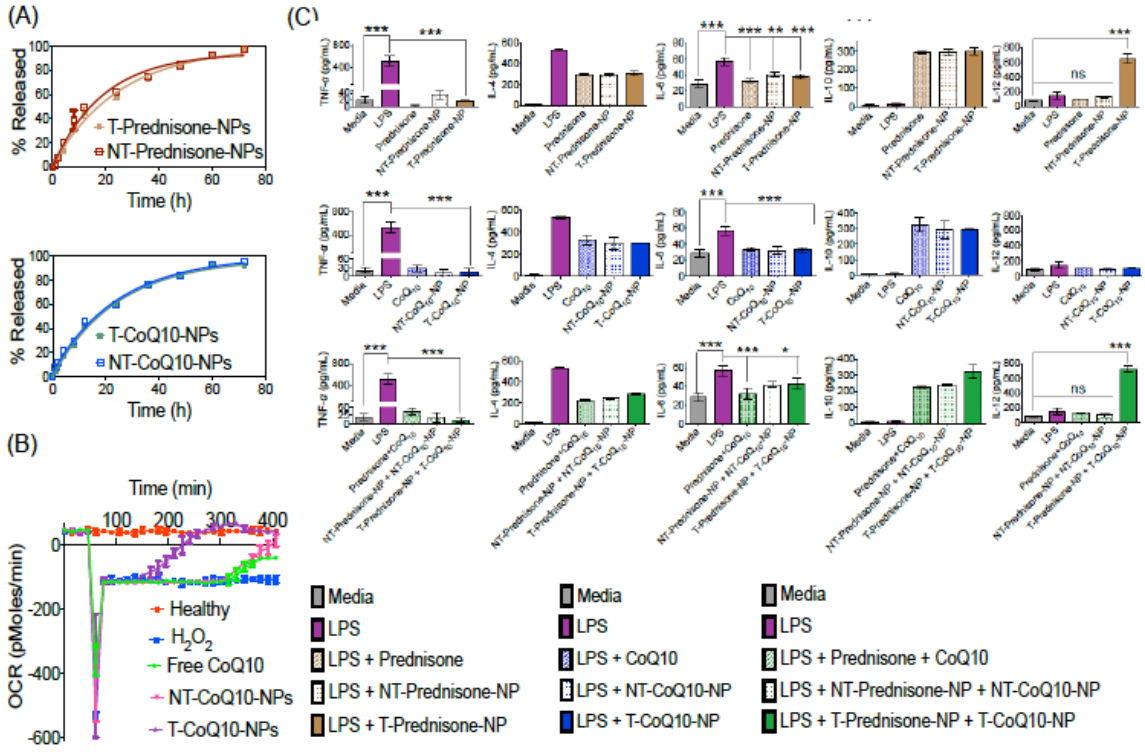


Figure 5.6. Therapeutic Potential of Mitochondria Targeted NPs carrying an Antioxidant and an Anti-inflammatory Agent in NSCs. (A) Release kinetics of anti-inflammatory

prednisone and antioxidant CoQ10 from mitochondria targeted T-NPs and non targeted NT-NPs. (B) Antioxidative properties of T-CoQ_{10}-NPs in hiPS cells using Seahorse analyzer. (C) Anti-inflammatory properties of mitochondria targeted NPs using ELISA.

IL-4 plays major roles as a negative regulator of pro-inflammatory cytokine production by both brain cells and T lymphocytes. Differentiation of antigen-stimulated naïve T cells into Th2 cells produces anti-inflammatory IL-4, IL-10, and IL-13. However, IL-4 induced inhibition of generation of Th1 cells, which produce pro-inflammation cytokines such as IL-1 and IFN-γ, also contribute to IL-4 roles in inflammation. Thus, we studied IL-4 response from NSCs upon treatment with prednisone and CoQ10 and their NPs in the presence of LPS (Fig. 5.6). All test articles showed a decreased IL-4 response when compared to LPS induced production of this cytokine (Fig. 5.6). IL-12 on spontaneous immune responses are unknown. In our studies LPS treated NSCs that were stimulated with mitochondria targeted T-Pred-NPs or a combination of T-Pred-NPs and T-CoQ_{10}-NPs showed significant increase in the IL-12 levels (Fig. 5.6). The exact mechanism why only mitochondria targeted therapy produces IL-12 from the NSCs warrants further investigation. These results indicated that a combination of T-Pred-NP and T-CoQ_{10}-NP treatment have the potential to improve outcome after TBI by inducing reductions in pro-inflammatory cytokines synthesis and stimulating production of anti-inflammatory cytokines.

Conclusion

In conclusion, this study provides a nanomedicine platform for combined neuroprotectant-stem cell therapy for TBI. The mitochondria targeted highly lipophilic NPs can locally deliver a combination of an anti-inflammatory and an antioxidant reagent

in a controlled release fashion and the subsequent application of NSCs has the potential to repair the damaged tissue. This methodology can be described as an ideal therapeutic strategy, which potentially would not only suppress inflammation and oxidative stress but also promote regeneration and repair. The distribution of the T-NPs in the lipophilic white matter of the brain which is rich in inflammation and oxidative stress during injury and the delivery of mitochondria acting antioxidant such as CoQ_{10} and an anti-inflammatory reagent such as prednisone to the white matter using the T-NPs in a controlled release way provides an important means to deliver therapeutic doses locally and simultaneously to reduce the problem of systemic toxicity common to intravenously administered therapeutic agents with limited ability to cross the BBB with poor PK properties. Although this BBB penetrating biodegradable mitochondria targeted NPs were evaluated for possible use in TBI, this technology can be tailored for plethora of central nervous system (CNS) diseases such as neurodegenerative disorders like Parkinson disease or Huntington disease, diseases with localized cerebral dysfunction, such as stroke. The targeted NPs are simple in composition which will be extremely beneficial for clinical translation and constructed from a well characterized biodegradable targeting moiety appended polymer and have the potential to encapsulate variety of hydrophobic drugs, negatively charged nucleic acids, we foresee that this BBB penetrating mitochondria targeting NP platform will have significant clinical impact.

Acknowledgments.

This work was supported in part by the Center of Metalloenzyme Studies center grant from the National Institutes of Health (P30GM092378) as a start-up fund to S.D., by the Office of the Vice President for Research, UGA to S.D. and by the University of

Georgia Research Foundation to F.D.W. We thank Dr. Nagesh Kolishetti for helpful discussions. We thank Vivian Lau, Holly Kinder, and Lisa Reno for surgical expertise and support; Robert Strickland, Kelly Parham, and Richard Utley for animal assistance; Elizabeth Howerth for her aid in pathological assessment. We thank Prof. Rick Tarleton for the Seahorse analyzer. We thank Walter J. Lunsmann for assistance with PK parameter calculations.

References

1. Coronado, V. G.; Xu, L.; Basavaraju, S. V.; McGuire, L. C.; Wald, M. M.; Faul, M. D.; Guzman, B. R.; Hemphill, J. D., Surveillance for traumatic brain injury-related deaths--United States, 1997-2007. *MMWR Surveill. Summ.* **2011,** *60*, 1-32.
2. McConeghy, K. W.; Hatton, J.; Hughes, L.; Cook, A. M., A review of neuroprotection pharmacology and therapies in patients with acute traumatic brain injury. *CNS Drugs* **2012,** *26*, 613-636.
3. Bowman, S. M.; Bird, T. M.; Aitken, M. E.; Tilford, J. M., Trends in hospitalizations associated with pediatric traumatic brain injuries. *Pediatrics* **2008,** *122*, 988-993.
4. Werner, C.; Engelhard, K., Pathophysiology of traumatic brain injury. *Br. J. Anaesth.* **2007,** *99*, 4-9.
5. Yakovlev, A. G.; Faden, A. I., Caspase-dependent apoptotic pathways in CNS injury. *Mol. Neurobiol.* **2001,** *24*, 131-144.
6. Ziebell, J. M.; Morganti-Kossmann, M. C., Involvement of pro- and anti-inflammatory cytokines and chemokines in the pathophysiology of traumatic brain injury. *Neurotherapeutics* **2010,** *7*, 22-30.

7. Guadagno, J.; Xu, X.; Karajgikar, M.; Brown, A.; Cregan, S. P., Microglia-derived TNFalpha induces apoptosis in neural precursor cells via transcriptional activation of the Bcl-2 family member Puma. *Cell Death Dis.* **2013,** *4*, e538.

8. Frugier, T.; Morganti-Kossmann, M. C.; O'Reilly, D.; McLean, C. A., In situ detection of inflammatory mediators in post mortem human brain tissue after traumatic injury. *J. Neurotrauma* **2010,** *27*, 497-507.

9. Sullivan, S.; Friess, S. H.; Ralston, J.; Smith, C.; Propert, K. J.; Rapp, P. E.; Margulies, S. S., Behavioral deficits and axonal injury persistence after rotational head injury are direction dependent. *J. Neurotrauma* **2013,** *30*, 538-545.

10. Maas, A. I.; Roozenbeek, B.; Manley, G. T., Clinical trials in traumatic brain injury: past experience and current developments. *Neurotherapeutics* **2010,** *7*, 115-126.

11. Abbott, N. J., Astrocyte-endothelial interactions and blood-brain barrier permeability. *J. Anat.* **2002,** *200*, 629-638.

12. Wolburg, H.; Noell, S.; Mack, A.; Wolburg-Buchholz, K.; Fallier-Becker, P., Brain endothelial cells and the glio-vascular complex. *Cell Tissue Res.* **2009,** *335*, 75-96.

13. Oldendorf, W. H.; Cornford, M. E.; Brown, W. J., The large apparent work capability of the blood-brain barrier: a study of the mitochondrial content of capillary endothelial cells in brain and other tissues of the rat. *Ann. Neurol.* **1977,** *1*, 409-417.

14. Herve, F.; Ghinea, N.; Scherrmann, J. M., CNS delivery via adsorptive transcytosis. *AAPS J.* **2008,** *10*, 455-472.

15. Missios, S.; Harris, B. T.; Dodge, C. P.; Simoni, M. K.; Costine, B. A.; Lee, Y. L.; Quebada, P. B.; Hillier, S. C.; Adams, L. B.; Duhaime, A. C., Scaled cortical impact in immature swine: effect of age and gender on lesion volume. *J. Neurotrauma* **2009,** *26*, 1943-1951.

16. Zhang, K.; Sejnowski, T. J., A universal scaling law between gray matter and white matter of cerebral cortex. *Proc. Natl. Acad. Sci. U. S. A.* **2000,** *97*, 5621-5626.

17. Watanabe, H.; Andersen, F.; Simonsen, C. Z.; Evans, S. M.; Gjedde, A.; Cumming, P., MR-based statistical atlas of the Gottingen minipig brain. *Neuroimage* **2001,** *14*, 1089-1096.

18. Lind, N. M.; Moustgaard, A.; Jelsing, J.; Vajta, G.; Cumming, P.; Hansen, A. K., The use of pigs in neuroscience: modeling brain disorders. *Neurosci. Biobehav. Rev.* **2007,** *31*, 728-751.

19. Tanaka, Y.; Imai, H.; Konno, K.; Miyagishima, T.; Kubota, C.; Puentes, S.; Aoki, T.; Hata, H.; Takata, K.; Yoshimoto, Y.; Saito, N., Experimental model of lacunar infarction in the gyrencephalic brain of the miniature pig: neurological assessment and histological, immunohistochemical, and physiological evaluation of dynamic corticospinal tract deformation. *Stroke* **2008,** *39*, 205-212.

20. Marrache, S.; Dhar, S., Engineering of blended nanoparticle platform for delivery of mitochondria-acting therapeutics. *Proc. Natl. Acad. Sci. U. S. A.* **2012,** *109*, 16288-16293.

21. Marrache, S.; Choi, J. H.; Tundup, S.; Zaver, D.; Harn, D. A.; Dhar, S., Immune stimulating photoactive hybrid nanoparticles for metastatic breast cancer. *Integr. Biol.* **2013,** *5*, 215-223.

22. Marrache, S.; Tundup, S.; Harn, D. A.; Dhar, S., Ex vivo programming of dendritic cells by mitochondria-targeted nanoparticles to produce interferon-gamma for cancer immunotherapy. *ACS Nano* **2013,** *7*, 7392-7402.

23. Wolfensohn, S.; Lloyd, M., *Handbook of Laboratory Animal Management and Welfare*. 3 ed.; Wiley-Blackwell: 2003.

24. dos Santos, W. L.; Rahman, J.; Klein, N.; Male, D. K., Control of lymphocyte adhesion to brain and aortic endothelium: ICAM-1, VCAM-1 and negative charge. *J. Neuroimmunol.* **1996,** *66*, 125-134.

25. Marrache, S.; Pathak, R. K.; Dhar, S., Detouring of cisplatin to access mitochondrial genome for overcoming resistance *Proc. Natl. Acad. Sci. U. S. A.* **2014,** *In press*.

26. Kinnunen, K. M.; Greenwood, R.; Powell, J. H.; Leech, R.; Hawkins, P. C.; Bonnelle, V.; Patel, M. C.; Counsell, S. J.; Sharp, D. J., White matter damage and cognitive impairment after traumatic brain injury. *Brain* **2010**.

27. Kumar, A.; Loane, D. J., Neuroinflammation after traumatic brain injury: opportunities for therapeutic intervention. *Brain Behav. Immun.* **2012,** *26*, 1191-1201.

28. Loane, D. J.; Faden, A. I., Neuroprotection for traumatic brain injury: translational challenges and emerging therapeutic strategies. *Trends Pharmacol. Sci.* **2010,** *31*, 596-604.

29. Narayan, R. K.; Michel, M. E.; Ansell, B.; Baethmann, A.; Biegon, A.; Bracken, M. B.; Bullock, M. R.; Choi, S. C.; Clifton, G. L.; Contant, C. F.; Coplin, W. M.; Dietrich, W. D.; Ghajar, J.; Grady, S. M.; Grossman, R. G.; Hall, E. D.; Heetderks, W.; Hovda, D. A.; Jallo, J.; Katz, R. L.; Knoller, N.; Kochanek, P. M.; Maas, A. I.; Majde, J.; Marion, D. W.; Marmarou, A.; Marshall, L. F.; McIntosh, T. K.; Miller, E.; Mohberg, N.; Muizelaar, J. P.; Pitts, L. H.; Quinn, P.; Riesenfeld, G.; Robertson, C. S.; Strauss, K. I.; Teasdale, G.; Temkin, N.; Tuma, R.; Wade, C.; Walker, M. D.; Weinrich, M.; Whyte, J.; Wilberger, J.; Young, A. B.; Yurkewicz, L., Clinical trials in head injury. *J. Neurotrauma* **2002,** *19*, 503-557.

30. Perez-Pinzon, M. A.; Steinberg, G. K., CGS 19755 (Selfotel): A Novel Neuroprotective Agent Against CNS Injury. *CNS Drug Rev.* **1996,** *2*, 257-268.

31. Duhaime, A. C.; Hunter, J. V.; Grate, L. L.; Kim, A.; Golden, J.; Demidenko, E.; Harris, C., Magnetic resonance imaging studies of age-dependent responses to scaled focal brain injury in the piglet. *J. Neurosurg.* **2003,** *99*, 542-548.

32. Kuluz, J. W.; Prado, R.; He, D.; Zhao, W.; Dietrich, W. D.; Watson, B., New pediatric model of ischemic stroke in infant piglets by photothrombosis: acute changes in cerebral blood flow, microvasculature, and early histopathology. *Stroke* **2007,** *38*, 1932-1937.

33. Quinzii, C. M.; Hirano, M., Coenzyme Q and mitochondrial disease. *Dev Disabil Res Rev* **2010,** *16*, 183-188.

34. Raslan, A.; Bhardwaj, A., Medical management of cerebral edema. *Neurosurg. Focus* **2007,** *22*, E12.

35. Ransohoff, R. M.; Brown, M. A., Innate immunity in the central nervous system. *J. Clin. Invest.* **2012,** *122*, 1164-1171.

36. Summers, B. A. C., J.F.; de Lahunta, A, *Veterinary Neuropathology*. 1 ed.; Mosby: 1994; p 527.

37. Du, J.; Wang, Y.; Hunter, R.; Wei, Y.; Blumenthal, R.; Falke, C.; Khairova, R.; Zhou, R.; Yuan, P.; Machado-Vieira, R.; McEwen, B. S.; Manji, H. K., Dynamic regulation of mitochondrial function by glucocorticoids. *Proc. Natl. Acad. Sci. U. S. A.* **2009,** *106*, 3543-3548.

38. Kossmann, T.; Hans, V. H.; Imhof, H. G.; Stocker, R.; Grob, P.; Trentz, O.; Morganti-Kossmann, C., Intrathecal and serum interleukin-6 and the acute-phase response in patients with severe traumatic brain injuries. *Shock* **1995,** *4*, 311-317.

39. Dalla Libera, A. L.; Regner, A.; de Paoli, J.; Centenaro, L.; Martins, T. T.; Simon, D., IL-6 polymorphism associated with fatal outcome in patients with severe traumatic brain injury. *Brain Inj.* **2011,** *25*, 365-369.

40. Knoblach, S. M.; Faden, A. I., Interleukin-10 improves outcome and alters proinflammatory cytokine expression after experimental traumatic brain injury. *Exp. Neurol.* **1998,** *153*, 143-151.

41. Lee, H. F.; Lee, T. S.; Kou, Y. R., Anti-inflammatory and neuroprotective effects of triptolide on traumatic brain injury in rats. *Respir. Physiol. Neurobiol.* **2012,** *182*, 1-8.

42. Yan, E. B.; Hellewell, S. C.; Bellander, B. M.; Agyapomaa, D. A.; Morganti-Kossmann, M. C., Post-traumatic hypoxia exacerbates neurological deficit,

neuroinflammation and cerebral metabolism in rats with diffuse traumatic brain injury. *J. Neuroinflammation* **2011,** *8*, 147.

CHAPTER 6

BIODEGRADABLE SYNTHETIC HIGH DENSITY LIPOPROTEIN NANOPARTICLES FOR ATHEROSCLEROSIS[1]

[1]Part of this chapter is reprinted with the permission of Marrache, S. and Dhar, S. *Proc. Natl. Acad. Sci. USA*, 110, 9445-9450. Copyright 2013, United States National Academy of Sciences

Abstract

Atherosclerosis remains one of the most common causes of death in the United States and throughout the world because of lack of early detection. Macrophage apoptosis is a major contributor to the instability of atherosclerotic lesions. Development of an apoptosis targeted high-density lipoprotein (HDL)-mimicking nanoparticle (NP) to carry contrast agents for early detection of vulnerable plaques and the initiation of preventative therapies that exploit the vascular protective effects of HDL can be attractive candidate for atherosclerosis. Here we report the construction of a synthetic, biodegradable HDL-NP platform for detection of vulnerable plaques by targeting the collapse of mitochondrial membrane potential ($\Delta\Psi_m$) that occurs during apoptosis. This HDL mimic contains a core of biodegradable poly(lactic-*co*-glycolic acid), cholesteryl oleate, and a phospholipid bilayer coat which is decorated with triphenylphosphonium (TPP) cations for detection of $\Delta\Psi_m$ collapse. The lipid layer provides the surface for adsorption of apolipoprotein (apo) A-I mimetic 4F peptide and the core contains diagnostically active quantum dots (QDs) for optical imaging. In vitro uptake, detection of apoptosis, and cholesterol binding studies indicated promising detection ability and therapeutic potential of TPP-HDL-apoA-I-QD-NPs. In vitro studies indicated potential of these NPs in reverse cholesterol transport. In vivo biodistribution and pharmacokinetics indicated favorable tissue distribution, controlled PK parameters, and significant triglyceride reduction for intravenously injected TPP-HDL-apoA-I-QD-NPs in rats. These HDL-NPs demonstrate excellent biocompatibility, stability, non-toxic and non-immunogenic properties, which prove to be promising for future translation in early plaque diagnosis and might find applications to prevent vulnerable plaque progression.

Introduction

Despite advances in both primary and secondary prevention, atherosclerosis [1] remains one of the leading causes of morbidity and mortality in the western world because of lack of early detection and targeted therapy. In general, atherosclerosis is a result of excess cholesterol circulating in the bloodstream. At the cellular level, atherosclerotic plaque formation is caused by cholesterol consumption and foam cell formation by macrophages situated within the intimal layers of the arteries [2]. The term "vulnerable plaque" designates a plaque at high risk of disruption leading to thrombosis. Identification of vulnerable plaques before the thrombus formation is essential to enable the development of treatment modalities. One intriguing possibility for the development of image-guided therapies of coronary heart diseases (CHDs) is through high-density lipoproteins (HDLs), because of its function in the reverse cholesterol transport (RCT) pathway [3, 4]. Along with apolipoprotein (apo) E, which promotes cholesterol efflux from foam cells, apoA-I containing HDL facilitate the transport of cholesterol from lesions. Development of targeted HDL-nanoparticles (NPs) to carry contrast agents for early detection of vulnerable plaques [5] and the initiation of preventative therapies that exploit the vascular protective effects of HDL could reduce the morbidity and mortality of thromboembolism [6]. It is hypothesized that apoptosis of macrophages and of smooth muscle cells (SMCs) play an important role in plaque rupture [7]. A unique approach for the noninvasive detection of apoptosis in SMCs and macrophages could be developed by targeting the collapse of mitochondrial membrane potential ($\Delta\Psi_m$), a hallmark of the initiating phase of apoptosis [8]. Thus a completely synthetic biodegradable $\Delta\Psi_m$ targeting HDL mimicking NP platform containing contrast agents could be of enormous benefits to

patients with CHD. Surprisingly, all the reports on using HDL-NP for imaging atherosclerosis are based on reconstituted HDL (rHDL) [9-11] (Table 6.1). Particles based on rHDL use lipoproteins and apoA-I extracted from human plasma. Potential problem in using rHDL NPs includes batch-to-batch variability when lipoproteins are isolated from donor plasma and scale-up challenges. A completely synthetic targeted HDL-mimicking NP platform that can navigate through the interstitial space protecting its contrast agent to the mitochondria of apoptotic macrophages in vulnerable plaque would result in potential early detection of atherosclerotic plaques.

Table 6.1. Examples of Known HDL-Mimicking Nanoparticles.

HDL mimicking composition	**Type**	**Disease**	**Reference**
Gold-core-reconstituted HDL	Gold-core-reconstituted HDL	Lymphoma	*Proc Natl Acad Sci U S A*, **2013**, 110, 2511-2516
HDL-mimicking peptide-lipid nanoparticles	Liposomal formulation	Cancer	*Small*, **2010**, *6*, 430-437
High-density lipoprotein-mimicking peptide lipid nanoparticles	Liposomal formulation	Cancer	*Nanomedicine*, **2012**, *7*, 1813-1825
HDL-Mimicking Nanoparticles	Liposomal formulation	Cancer	*Small*, **2011**, *7*, 568–573
Gold-core-reconstituted HDL	Gold core with reconstituted HDL	None	*J Am Chem Soc*, **2009**, *131*, 1384–1385
Gold-core-reconstituted HDL	Gold core with reconstituted HDL	Nucleic acid delivery	*Nano Lett*, **2011**, *11*, 1208–1214

Gd-DTPA-DMPE with reconstituted HDL	Lipid based NPs with reconstituted HDL	Atherosclerosis	*Bioconjugate Chem*, **2009**, *20*, 937–943
QD, IO, Au core with reconstituted HDL	Reconstituted HDL nanoparticles with incorporation of gold, iron oxide, or quantum dot nanocrystals	Atherosclerosis	*Nano Lett*, **2008**, *8*, 3715–3723
Iron oxide core HDL nanoparticle	Iron oxide, lipids, and reconstituted HDL	Atherosclerosis	*Biomaterials,* **2011**, *32*, 206-213
Recombinant HDL-like nanoparticles	Reconstituted HDL with Gd-DTPA-DMPE	Atherosclerosis	*J Am Chem Soc*, **2004**, *126*, 16316–16317

There are a handful of HDL-mimicking liposomes and metal-based carriers for targeted delivery of siRNA, therapeutics, or contrast agents for cancer therapy [12-16] (Table 6.1). However, no example thus far demonstrates the use of the Food and Drug Administration (FDA) approved biodegradable poly(lactic-*co*-glycolic acid) (PLGA) based synthetic HDL NPs. In this report, we present a proof-of-concept demonstration of such a technology. We developed a fluorescent HDL-mimicking polymer lipid NP platform (Fig. 6.1) consisting of a HDL resembling hydrophobic core of PLGA and cholesteryl oleate (CO). The polymer-cholesterol matrix incorporated diagnostically active quantum dot (QD) conjugated polymer PLGA-block (*b*)-polyethylene glycol (PEG), PLGA-*b*-PEG-QD for optical imaging. This core is surrounded by a 1,2-distearoyl-*sn*-glycero-3-phosphoethanolamine (DSPE)-COOH lipid layer embedded with cholesterol and apoA-I mimetic 4F peptide with a FAEKFKEAVKDYFAKFWD

sequence [13], and a triphenyl phosphonium (TPP) containing cationic stearyl-TPP ligand for targeting the collapse of $\Delta\psi_m$ during apoptotic events. Lipophilic TPP cations are known to accumulate several hundred-fold by mitochondria within cells and can be used to direct a wide range of probe or therapeutic molecules to mitochondria [17]. Here we report our preliminary results demonstrating the ability to construct such a biodegradable HDL mimic, in vitro and in vivo execution of this platform for detection and therapy of vulnerable plaques.

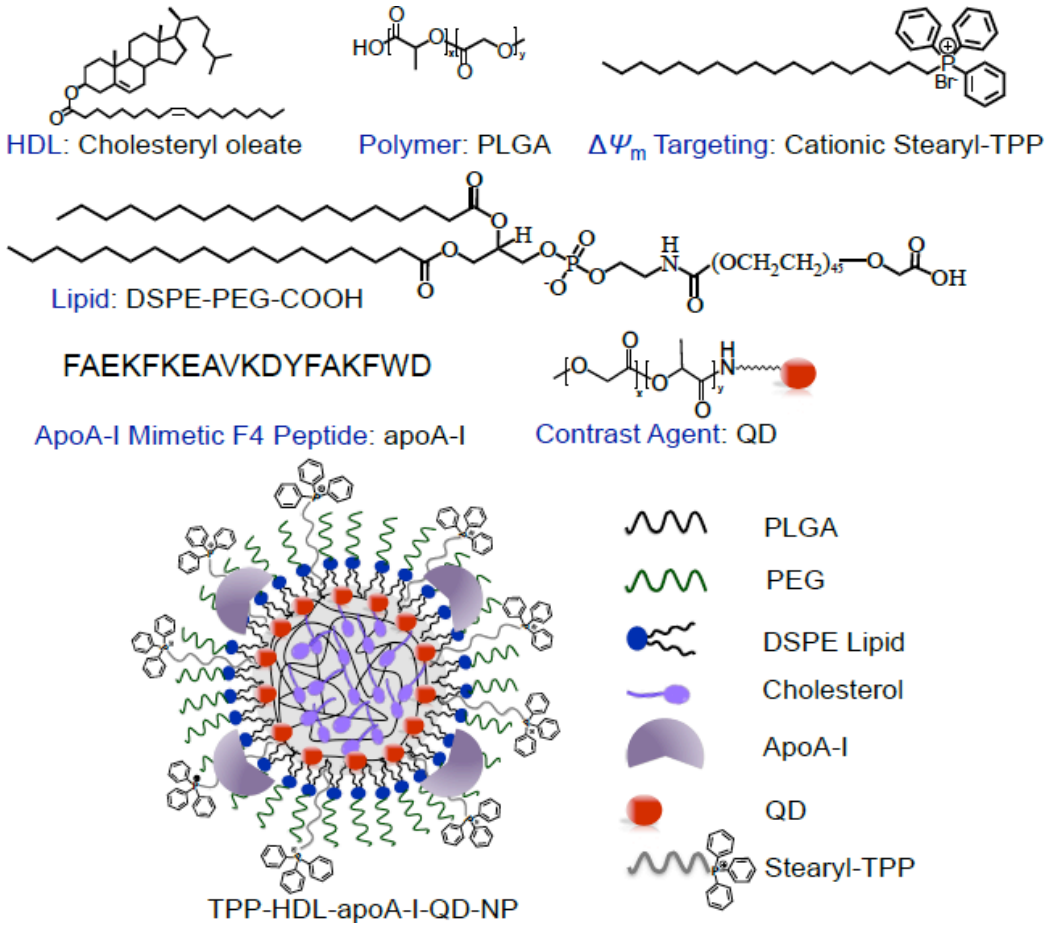


Figure 6.1. Schematic diagram of the mitochondria-targeted biodegradable HDL mimicking NP platform and various components.

Materials and Methods

All chemicals were received and used without further purification unless otherwise noted. PLGA-COOH of inherent viscosity of 0.15-0.25 dL/g was purchased from Lactel. Cholesteryl oleate (CO), N,N'-dicyclohexylcarbodiimide (DCC), and (3-(4,5-Dimethylthiazol-2-yl)-2,5-diphenyltetrazolium bromide (MTT), carbonyl cyanide-*p*-(trifluoromethoxy)phenylhydrazone (FCCP), and digitonin were purchased from Sigma-Aldrich. Sucrose used in the mitochondrial subfractionation experiment was purchased from J. T. Baker. Lubrol WX was procured from MP Biomedicals. Qdot 705 ITK amino PEG quantum dots, mitotracker green, and 25-{N-[(7-nitrobenz-2-oxa-1,3-diazol-4-yl)-methyl]amino}-27-norcholesterol (NBD-cholesterol) were purchased from Invitrogen. The apoA-I mimetic peptide 4F (Ac-FAEKFKEAVKDYFAKFWD-COOH) was custom synthesized by RS Synthesis and characterized by MALDI and HPLC. Solvable™, used for solubilizing tissue samples, was purchased from PerkinElmer. DSPE-PEG-COOH was purchased from Avanti Polar Lipids, Inc. AdipoRed was purchased from Lonza. The AmplexRed Assay kit for cholesterol quantification was purchased from Invitrogen. Mitochondria isolation kit for mammalian cells was acquired from Thermo Scientific (product #89874). Pierce® Bicinchoninic acid (BCA) protein assay kit was purchased from Thermo Scientific. Ultra pure lipopolysaccharide (LPS) from *E.coli* was obtained from InvivoGen. Dynamic light scattering (DLS) measurements were carried out using a Malvern Zetasizer Nano ZS system. ^{1}H and ^{13}C spectra were recorded on a 400 MHz Varian NMR spectrometer. ^{31}P NMR was recorded on a 500 MHz Varian NMR spectrometer. Optical measurements were carried out on a NanoDrop 2000 spectrophotometer. TEM images were taken in a Tecnai 20 FEM microscope. Confocal

images were recorded in a Nikon A1 confocal microscope. Inductively coupled plasma mass spectrometry (ICP-MS) studies were performed on a VG PlasmaQuad 3 ICP mass spectrometer. Cytokines were tested using BD OptEIA mouse enzyme-linked immunosorbent assay (ELISA) kits. Flow cytometry studies were performed on a BD LSR II flow cytometer equipped with digital acquisition using FACSDiva v6. Plate reader analysis was performed on a Bio-Tek Synergy HT microplate reader. Optical imaging of tissue samples and cellular components was carried out on a Xenogen IVIS® Lumina system.

Cell Line and Cell Culture.

Human adipose-derived MSC and mouse monocyte/macrophage RAW 264.7 cells were procured from the ATCC. MSC cells were grown in MSC basal medium in low serum (2% FBS) conditions and supplemented with rh EGF and L-alanyl-L-glutamine. RAW 264.7 cells were grown in DMEM medium supplemented with 10% FBS and 1% penicillin/streptomycin at 37 °C in 5% CO_2. Cells were passed every 3 to 4 days and restarted from frozen stocks upon reaching pass number 4 for MSC and 20 for RAW cells.

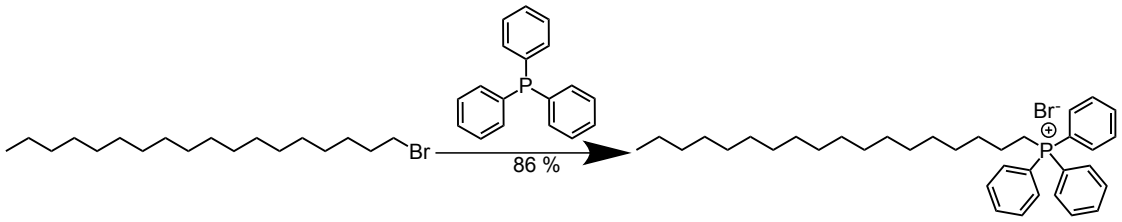
Animals.

Animals were obtained from Harlan Laboratory and handled in accordance with ‘‘The Guide for the Care and Use of Laboratory Animals’’ of American Association for Accreditation of Laboratory Animal Care (AAALAC), Animal Welfare Act (AWA), and other applicable federal and state guidelines. All animal work presented here was approved by Institutional Animal Care and Use Committee (IACUC) of University of Georgia.

Methods

Synthesis of Polymers and Nanoparticles

Synthesis of Stearyl-TPP.



Stearyl bromide (1.0 g, 3.0 mmol) and triphenylphosphine (0.83 g, 3.2 mmol) were dissolved in acetonitrile (25 mL). The resulting solution was heated to a reflux under argon for overnight. The reaction was cooled to room temperature and concentrated under reduced pressure. The resulting oil was washed with hexanes (2 x 20 mL) and diethyl ether (2 x 15 mL) and dried to produce a white solid in an 86% yield (melting point = 62-64 °C. ^{1}H NMR ($CHCl_3$-*d*): δ 7.97-7.53 [m, 15 H], 3.93-3.75 [m, 2H], 1.71-1.53 [m, 4H], 1.20-1.06 [m, 28H], 0.91-0.83 [m, 3H]. ^{13}C NMR ($CHCl_3$-*d*): δ 135.1, 134.0, 133.9, 130.7, 130.6, 32.1, 29.0, 29.4, 22.9. ^{31}P NMR ($CHCl_3$-*d*): δ 24.

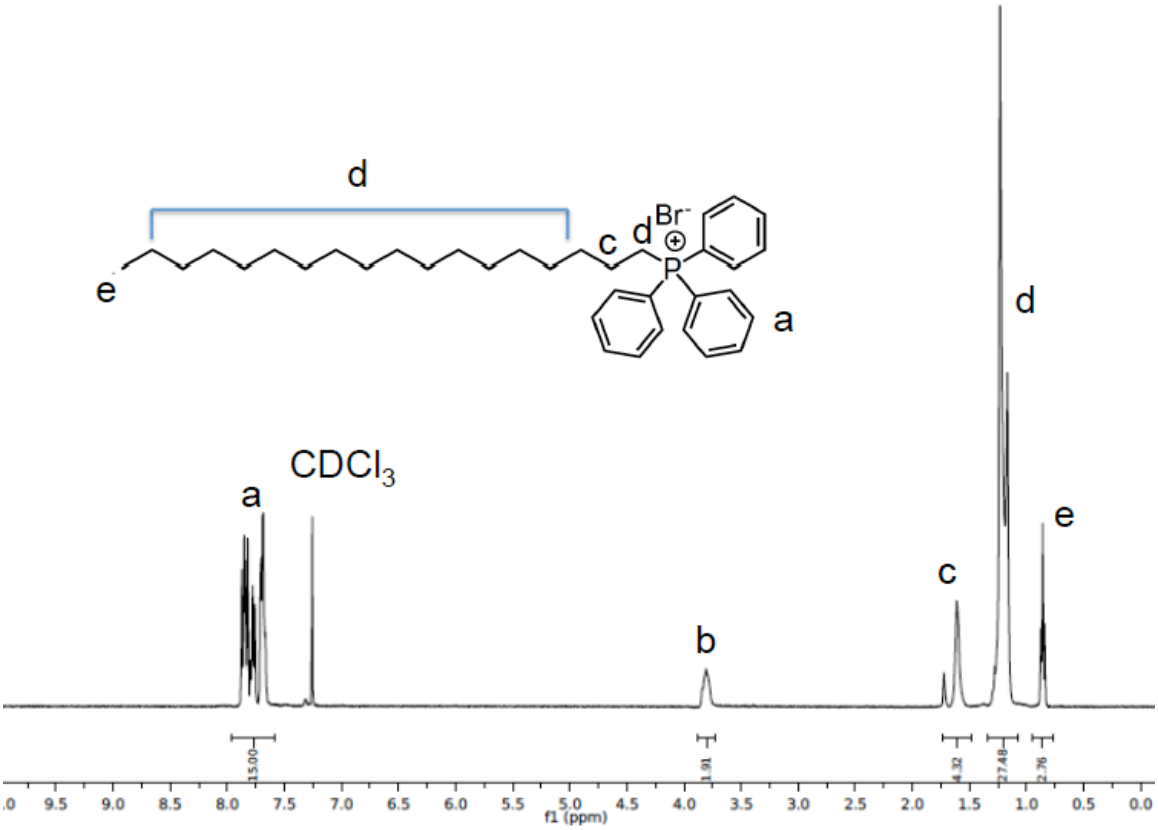


Fig. 6.2. ^{1}H-NMR of stearyl-TPP in $CDCl_3$.

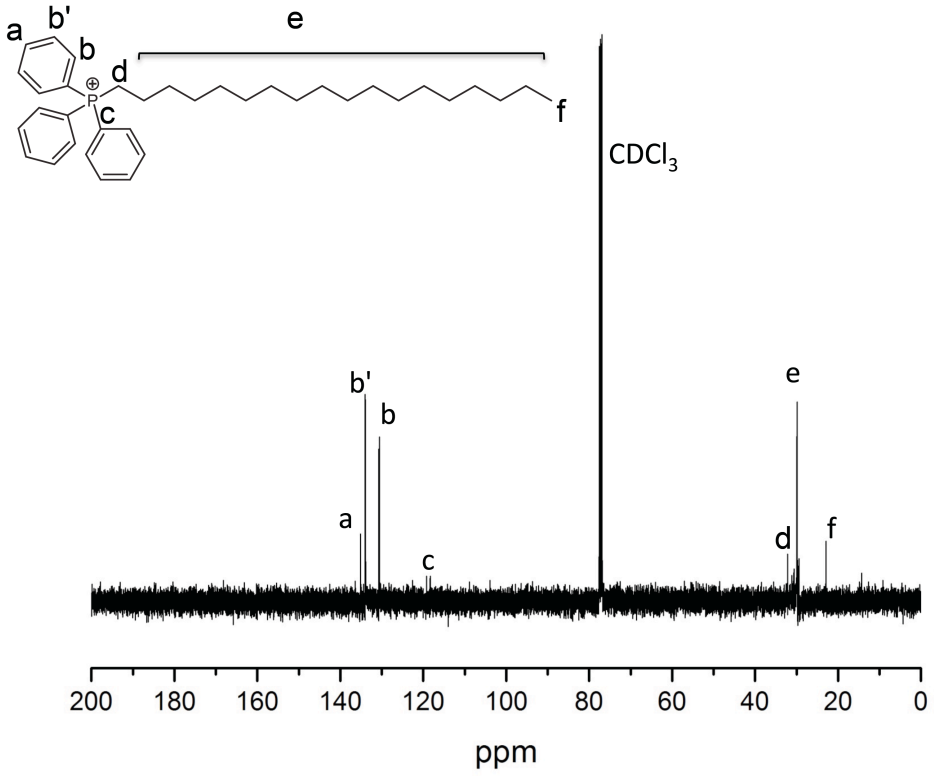


Fig. 6.3. ^{13}C-NMR of stearyl-TPP in $CDCl_3$.

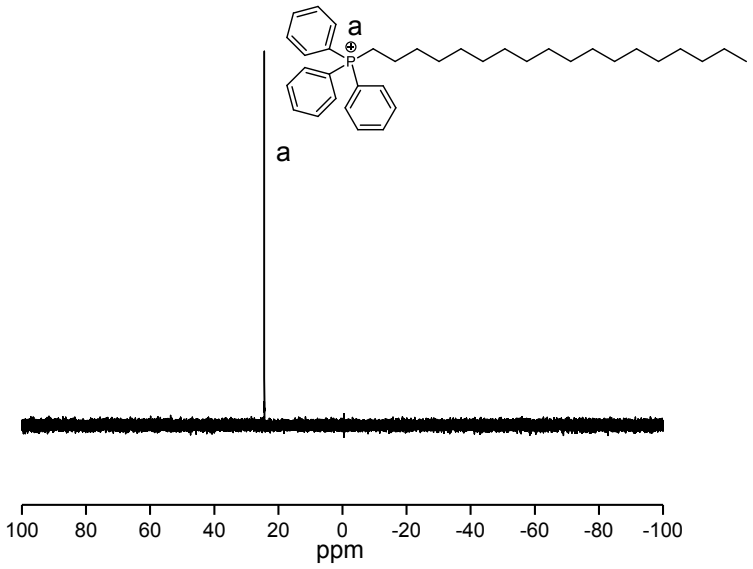


Fig. 6.4. ^{31}P-NMR of stearyl-TPP in $CDCl_3$.

Synthesis of PLGA-b-PEG-QD.

Synthesis of PLGA-*b*-PEG-QD was performed as previously described [18].

Synthesis of HDL-Mimicking NPs.

Targeted hybrid NPs were prepared via self-assembly of PLGA, PLGA-*b*-PEG-QD, CO, stearyl-TPP, DSPE-PEG-COOH and apoA-I mimetic 4F peptide through a modified nanoprecipitation. PLGA-COOH (25 μL, 25 mg/mL in CH_3CN), PLGA-*b*-PEG-QD (20 μL, 8 μM in DMF), CO (75 μL, 25 mg/mL in DMSO) were mixed. Stearyl-TPP (5 mg/mL) and DSPE-PEG-COOH (1 mg/mL, 100 μL) with a weight ratio of 16% to the PLGA polymer were dissolved in 4 % ethanol aqueous solution. The lipid solution was heated to 65 °C to ensure all lipids are in the non assembled state. The PLGA/CO/QD solution was added into the preheated lipid solution drop-wise under vigorous stirring. The mixed solution was vortexed vigorously for 3 min followed by vigorous stirring for 2 h at room temperature. The remaining organic solvent and free molecules were removed by washing the NP solution three times using an Amicon Ultra-4 centrifugal filter with a molecular weight cutoff of 100,000 Da. To prepare non-targeted NPs, PVA (5 mg/mL in 4% aqueous ethanol, 100 μL) was used instead of stearyl-TPP during the modified nanoprecipitation process. The resultant NPs were incubated with apoA-I mimetic peptide (1 mg/mL, 0.5 mL) at 4 °C for 14 h [19] and was further purified and washed three times using Amicon Ultra-4 centrifugal filter with a molecular weight cutoff of 100,000 Da. NP size (diameter, nm), PDI, and surface charge (zeta potential, mV) were obtained from three independent measurements with a Zetasizer Nano-ZS DLS detector QD loading in the NPs was quantified by ICP-MS and apoA-I loading was determined by following tryptophan absorbance at 280 nm. The amount of cholesterol was determined

by an AmplexRed assay. Briefly, NP suspensions (50 μL) were incubated with a working solution (50 μL) composed of AmplexRed (300 μM), horseradish peroxidase (HRP) (0.2 U/mL), cholesterol oxidase (2 U/mL), and cholesterol esterase (0.2 U/mL) for 30 min at 37 °C in the dark. After 30 min, fluorescence was measured using a plate reader with an excitation of 560 nm and an emission of 590 nm. Relative fluorescence units (RFUs) were converted to amount of cholesterol by plotting against a standard curve of a cholesterol reference standard.

Reproducibility of construction of targeted and non-targeted HDL-mimicking NPs was confirmed by multiple independent nanoprecipitation experiments.

Synthesis of TPP-PLGA-DSPE-NPs for Cholesterol Binding experiment.

Targeted hybrid NPs were prepared via self-assembly of PLGA-COOH, stearyl-TPP, and DSPE-PEG-COOH through a double-step modified nanoprecipitation method. PLGA (100 μL, 25 mg/mL in CH_3CN was mixed with acetonitrile (900 μL). Stearyl-TPP (5 mg/mL) and DSPE-PEG-COOH (1 mg/mL, 100 μL) with a weight ratio of 16 % to the PLGA polymer were dissolved in 4 % ethanol aqueous solution. The lipid solution was heated to 65 °C to ensure all lipids are in the non-assembled state. The PLGA-COOH solution was added into the preheated lipid solution drop-wise under vigorous stirring. The mixed solution was vortexed vigorously for 3 min followed by vigorous stirring for 2 h at room temperature. The remaining organic solvent and free molecules were removed by washing the NP solution three times using an Amicon Ultra-4 centrifugal filter with a molecular weight cutoff of 100,000 Da.

Quantification of apoA-I in NPs.

To measure the protein loading on the NPs, apoA-I standard curve was created by measuring the tryptophan absorbance at 280 nm at various concentration of the peptide. HDL-NPs were synthesized using the procedure described above. NPs were treated with NaOH (0.1 mM) in order to dissolve the PLGA-COOH core and liberate apoA-I. Absorbance was measured at 280 nm and apoA-I content in the NPs was calculated using the apoA-I standard curve. The standard curve was prepared by dissolving the apoA-I peptide in nanopure water at concentrations of 0.01, 0.02, 0.03, 0.04, and 0.04 mg/mL and measuring the absorbance at 280 nm.

NP Stability in 10% FBS-Medium.

TPP-HDL-apoA-I-NPs (2.5 mg/mL) suspension in 10% FBS-DMEM media was stored at 4 °C, room temperature, and 37 °C for 7 days. Size, PDI (not shown), and zeta potential were measured everyday. Cholesterol binding ability of the targeted NPs was checked everyday using NBD-cholesterol following a protocol as mentioned below.

Cholesterol Binding Experiments.

Cholesterol binding to TPP-HDL-apoA-I-NPs, TPP-HDL-NPs, and TPP-PLGA-DSPE-NPs were determined by adding 5 μL of varying concentrations (0.2, 0.1, 0.05, 0.025, and 0.0125 mg/mL) of NBD-cholesterol in DMF to 0.5 mg/mL of 995 μL of NPs in water. The solutions were vortexed and incubated for ~20 min. Fluorescence of the solutions were followed by exciting at 473 nm and emission from 560 nm.

Assessment of Immune Response by ELISA.

RAW 264.7 macrophages were plated at a density of 2,000 cells/well and grown overnight. Cells were treated with NPs (0.5 mg/mL) and incubated for 12 h. As controls,

RAW cells were left untreated or treated with 100 ng/mL of LPS. An ELISA assay was performed against the cytokines IL-6 and TNF-α. Briefly, the cell supernatant was incubated in antibody-coated plates for 2 h at room temperature, incubated with the cytokine-biotin conjugate and streptavidin working solution. The stabilized chromagen (3,3′,5,5′-tetramethylbenzidine) was added to each well followed by a stop solution (0.1 M HCl) and the absorbance was recorded at 450 nm. By following similar procedure, cytokine production in LPS-activated RAW macrophages was studied. Briefly, RAW 264.7 macrophages (2,000 cells per well) were grown overnight in RPMI media. These cells were treated with LPS (100 ng/mL) for 24 h. QD containing targeted and non-targeted NPs were added to the LPS activated macrophages at a concentration of 0.5 mg/mL with respect to total NP construct and incubated for 12 h at 37 °C. ELISA was performed on these macrophages following similar procedure as mentioned above. Cell viability was simultaneously measured on these LPS activated and/or NP treated cells following the MTT assay as mentioned below.

MTT Assay.

The cytotoxic behavior of all the NPs was evaluated using the MTT assay against RAW 264.7 and MSC cells. Cells (2,000 cells/well) were seeded on a 96-well plate in 200 μL of DMEM medium for RAW cells and 200 μL of MSC basal medium for MSC cells and incubated for 24 h. The cells were treated with targeted and non-targeted NPs at varying concentrations (with respect to the total NP construct) and incubated for 12 h at 37 °C. The medium was changed, and the cells were incubated for additional 60 h. The cells were then treated with 20 μL of MTT (5 mg/mL in PBS) for 5 h. The medium was removed, the cells were lysed with 100 μL of DMSO, and the absorbance of the purple

formazan was recorded at 550 nm. Each well was performed in triplicate. All experiments were repeated three times. Cytotoxicity data were plotted with Graph Pad Prism (San Diego, U.S.A).

Mitochondrial Uptake Study by Confocal Microscopy.

RAW 264.7 cells were seeded on microscope coverslips (1.0 cm) at a density of $6x10^6$ cells/mL and grown overnight in DMEM. The medium was changed and fluorescent targeted and non-targeted HDL-mimicking NPs were added to a concentration of 0.5 mg/mL (with respect to total NP). The cells were incubated for 4 h at 37 °C in 5% CO_2. MitoTracker Green (500 nM) was added and incubated for 45 min at 37 °C. The medium was removed, cells were rinsed with PBS (3x) and phenol red free media was added. Live cell imaging was performed by collecting images using FITC and Cy5 channels (exposure time: 320 ms for both the channels).

Apoptosis Detection by Confocal Microscopy.

RAW 264.7 cells were seeded on microscope coverslips (1.0 cm) at a density of 6×10^6 cells/mL and grown overnight in DMEM. In order to induce apoptosis, etoposide (200 μM) was added and the cells were incubated for 3 h. The medium was changed and fluorescent targeted and non-targeted NPs were added to a NP concentration of 0.5 mg/mL (with respect to the total NP construct). The cells were incubated for 3 h at 37 °C in 5 % CO_2. The medium was removed and the cells were fixed using cold methanol for 30 min. Cells were permeabilized with 0.1 % Triton-x 100 for 30 min at room temperature followed by washing with PBS (3x). Cells were then stained with Hoescht (250 μg/L) for 15 min at room temperature. The coverslips were then rinsed with PBS (3x), water (5x), and mounted on slides using mounting media. Images were collected at

320 ms for DAPI and Cy5 channels with 320 ms exposure time.

Apoptosis Detection by Flow Cytometry.

RAW 264.7 macrophages ($1x10^6$ cells) were plated on each well of a 6-well plate and allowed to grow overnight. The media was changed and the cells were incubated with etoposide (200 μM) for 3 h. The cells were then washed 3 times with fresh media. TPP-HDL-apoA-I-NPs or non-targeted-HDL-apoA-I-NPs (0.5 mg/mL with respect to the total NP construct) were added and allowed to internalize for 3 h. The cells were washed with fresh media (3x), removed from the plate surface by gentle scraping followed by repeated centrifugation and wash cycles. Finally, the cells were analyzed on the flow cytometer on a FITC channel. As a control, an Annexin V assay was done on RAW macrophages. Briefly, RAW Macrophages were plated on each well of a 6-well plate at a density of $5x10^5$ cells/mL and allowed to grow overnight. The media was replaced and the etoposide (200 μM) was added. The cells were then incubated for 3 h followed by washing with fresh media (3x). The cells were removed from the plate surface by gentle scraping followed by repeated centrifugation and wash cycles with 1x PBS. The cells were resuspended in 1X annexin-binding buffer at a concentration of $1x10^6$ cells/mL. Annexin V (5 μL) was added to each tube and the cells were incubated for 15 min. Cells were analyzed immediately on the flow cytometer on an FITC channel.

Isolation of Mitochondrial and cytosolic fractions of apoptotic and non apoptotic cells.

Targeted TPP-HDL-apoA-I-NPs or non-targeted-HDL-apoA-I-NPs (0.5 mg/mL with respect to the total NP formulation) were internalized in RAW macrophages ($1.0x10^6$ cells/mL in 30 mL) for 12 h. After internalization, the mitochondrial and the

cytosolic fractions were isolated using a mitochondria isolation kit for mammalian cells.[18] Briefly, cells were isolated by scraping and washed with 1X PBS. Reagent A with protease inhibitors (10 mg/mL) was added followed by incubation on ice for 2 min. Reagent B was added followed by vortexing and incubation on ice. After 5 min of incubation, reagent C was added, and the cells were centrifuged (700 ×*g* at 4 °C). The pellet containing nuclei and cellular debris was discarded and the supernatant was centrifuged (12,000 ×*g* at 4 °C). The supernatant containing the cytosolic fraction was removed and the pellet composed of mitochondria was washed with reagent C. The pure mitochondria were isolated by centrifugation (12,000 ×*g* at 4 °C).

Imaging Intracellular Fractions of Apoptotic and Healthy Cells by IVIS.

Targeted TPP-HDL-apoA-I-NPs or non-targeted-HDL-apoA-I-NPs (0.5 mg/mL with respect to the total NP formulation) were internalized in RAW macrophages (1.0×10^6 cells/mL in 30 mL) for 12 h. After internalization, the mitochondrial and the cytosolic fractions were isolated using a mitochondria isolation kit for mammalian cells.[18] For apoptotic cells, cells were treated with 200 μM etoposide for 3 h prior to NP treatment. In the $\Delta\psi_m$ blocking experiments, cells were exposed to a protonophore FCCP (50 μM) for 1 h before they were treated with NPs. The cytosolic and mitochondrial fractions were analyzed for Cd concentration from the QD by ICP-MS. A Bicinchoninic (BCA) assay was performed on the isolated mitochondrial and cytosolic fractions. Each sample or standard curve solution (25 μL) was pipetted in to a 96 well plate. To this, the working reagent (200 μL) was added and the plate was covered and incubated at 37 °C with gentle shaking for 30 min. The plate was cooled to RT and the absorbance was

measured at 562 nm. In order to calculate the Cd (ng)/protein (*p*g) isolated, the values were plotted against a standard and also submitted to ICP-MS. The mitochondrial and cytosolic fractions were imaged on a Xenogen IVIS® Lumina system on a Cy5.5 channel with an exposure time of 0.5 s.

Mitochondrial Sub-fractionation.

TPP-HDL-apoA-I-NPs or (0.5 mg/mL with respect to NP) were internalized in RAW 264.7 macrophages (1.0 x 10^6 cells/mL in 30 mL) for 12 h. After internalization, the mitochondria and the cytosol were isolated using a mitochondria isolation kit for mammalian cells as described above. These fractions were further sub-fractionated using a modified literature reported protocol [20, 21]. The freshly isolated RAW macrophage mitochondria in PBS (1x) were incubated with protease inhibitor (0.125 mg/mL) and 0.6 % digitonin for 10 min on ice. Immediately after incubation, the mitochondria were centrifuged at 10,000 g for 10 min at 4 °C. The supernatant (SN-I) contained the OMM fraction and the interstitial membrane space. The pellet was resuspended in 150 mmol/L KCl, protease inhibitor (0.125 mg/mL) and incubated on ice for 10 min. This was centrifuged at 10,000 g for 10 min at 4 °C. The supernatant, which contained the mitochondrial matrix, was collected. To this, 50 μL of 1x cell lysis buffer (30 mM Tris-HCl, 0.1 mM EDTA, 20 % w/v sucrose) was added. This was subsequently sonicated and centrifuged at 10,000 g for 15 min at 4 °C. The supernatant (SN-II) was collected, containing the purified IMM fraction and matrix. SN-I and SN-II were centrifuged at 105,000 g for 60 min. The pellet from SN-I contained the OMM fraction and the supernatant contained the interstitial membrane space. The pellet from SN-II was resuspended in PBS containing Lubrol WX (0.5 mg/mL), 37 % sucrose and incubated for

15 min on ice. This was once again centrifuged at 105,000 g for 60 min at 4 °C. The pellet was collected containing the IMM fraction and the supernatant contained the matrix. The collected fractions were analyzed for Cd concentration by ICP-MS. A BCA assay was performed on all the fractions in order to calculate the Cd (ng)/protein (pg). The collected fractions were imaged on a Xenogen IVIS® Lumina system on a Cy5.5 channel with an exposure time of 0.5 s.

BioD, PK, and Two-compartment model for PK parameters.

These studies were carried out at a Contract Research Organization (CRO) VivoPath-delivering *in vivo* proof-of-concept, 55 Union Street, Worcester, MA 01608. BioD and PK properties of HDL-apoA-I-QD-NPs were determined using male Sprague Dawley rats weighing ~300 g. The animals, two per group, were injected in the tail vein with ~900 μL of HDL-apoA-I-QD-NPs (80 $\mu g \cdot kg^{-1}$ with respect to QD) or saline. At predetermined time intervals, blood samples were collected in pre-weighed heparinized tubes and centrifuged to get the plasma. The percentage of QD was calculated by taking into consideration that blood constitutes 7% of body weight and plasma constitutes 55% of blood volume [22]. The QD content plasma were determined by ICP-MS. Collective urine and feces samples were accumulated over 24 h and stored frozen until analyzed by ICP-MS. Tissue samples and feces, however, required prior digestion in 1 mL of solvable for 250 mg of tissue for 24 h. Gentle heating (40 °C) was required to complete the digestion. The calculations for AUC, C_{max}, T_{max} and $C_L(t=0)$ were performed in the GraphPad Prism (version 5.01). PK parameters were determined by fitting the data using a two-compartment model equation:

$$C = A*\exp[-k_1*t] + B*\exp[-k_2*t]$$

Where C: Plasma concentration at time t

A: 1st compartment constant which is the portion of the initial concentration, $C_{(t=0)}$, allocated to the first compartment

k_1: Decay constant from the first compartment

B: 2nd compartment constant

k_2: Decay constant from the second compartment

C_L and V_d for all other times (after t=0) were calculated using a "Stepwise Newtonian iteration" algorithm in Microsoft Excel, version 2010 to solve the partial differential equation in time for any time after t=0. These calculations were carried out by Walter Lunsmann from Vivo Path.

Blood Plasma Cholesterol and Triglyceride Quantification.

Cholesterol content in blood plasma was quantified by an AmplexRed assay by following manufacturers' procedure. Briefly, plasma samples (50 μL) from various time points were incubated with a working solution (50 μL) composed of AmplexRed (300 μM), horseradish peroxidase (HRP) (0.2 U/mL), cholesterol oxidase (2 U/mL) and cholesterol esterase (0.2 U/mL) for 30 min at 37 °C in the dark. After 30 min, fluorescence was measured using a plate reader with an excitation of 560 nm and an emission of 590 nm. Arbitrary fluorescence units (AFUs) were converted to amount of cholesterol by plotting against a standard curve. Plasma sample triglyceride content was analyzed by an AdipoRed fluorescent assay. Briefly, to each plasma sample (100 μL) in a 96-well plate, AdipoRed reagent (5 μL) was added. The well plates were gently shaken to ensure uniform mixing and incubated in the dark for 10-12 min. The fluorescence was then measured on the plate reader using an excitation of 485 nm and emission of 535 nm.

Synthesis of cholesterol nanoparticles (NPs) with varied cholesterol loading.

Targeted hybrid NPs were prepared via self-assembly of PLGA, cholesteryl oleate (CO), stearyl-TPP, DSPE-PEG-COOH and apoA-I mimetic 4F peptide through a modified nanoprecipitation. PLGA-COOH (10 to 90 μL, 25 mg/mL in CH_3CN), CO (90 to 10 μL, 25 mg/mL in DMSO) were mixed so that the total volume of PLGA and CO was 100 μL. Stearyl-TPP (5 mg/mL, 100 μL) and DSPE-PEG-COOH (1 mg/mL, 100 μL) with a weight ratio of 16% to the PLGA polymer were dissolved in 4 % ethanol aqueous solution. The lipid solution was heated to 65 °C to ensure all lipids are in the non-assembled state. The PLGA/CO solution was added into the preheated lipid solution drop-wise under vigorous stirring. The mixed solution was vortexed vigorously for 3 min followed by vigorous stirring for 2 h at room temperature. The remaining organic solvent and free molecules were removed by washing the NP solution three times using an Amicon Ultra-4 centrifugal filter with a molecular weight cutoff of 100,000 Da.

Synthesis of CoQ10 encapsulated NPs

Targeted hybrid NPs were prepared via self-assembly of PLGA, cholesteryl oleate (CO), stearyl-TPP, DSPE-PEG-COOH and apoA-I mimetic 4F peptide through a modified nanoprecipitation. PLGA-COOH (60 μL, 25 mg/mL in CH_3CN), CO (40, 25 mg/mL in DMSO) were mixed along with varying concentrations of ATV (5 mg/mL in DMSO). Stearyl-TPP (5 mg/mL, 100 μL) and DSPE-PEG-COOH (1 mg/mL, 100 μL) with a weight ratio of 16% to the PLGA polymer were dissolved in 4 % ethanol aqueous solution. The lipid solution was heated to 65 °C to ensure all lipids are in the non-assembled state. The PLGA/CO/ATV solution was added into the preheated lipid solution drop-wise under vigorous stirring. The mixed solution was vortexed vigorously

for 3 min followed by vigorous stirring for 2 h at room temperature. The remaining organic solvent and free molecules were removed by washing the NP solution three times using an Amicon Ultra-4 centrifugal filter with a molecular weight cutoff of 100,000 Da. The CoQ10 loading was determined by HPLC (wavelength: 275 nm)

Mitostress test of CoQ10 encapsulated NPs using Seahorse XF24 analyzer

Mitochondrial function and the four key parameters of mitochondrial function, basal respiration, ATP turnover, proton leak, and maximal respiration, were measured using a MitoStress test on the Seahorse XF24 analyzer. Briefly, RAW macrophages were plated on a XF24 microplate at a density of 50,000 cells per well and incubated at 37ºC and 5% CO_2. After 24 h, the media was changed and NPs were added and incubated for 4 h. After 4 h, the media was changed to the seahorse XF base media by removing all but 50 μL from each well and repeatedly adding and removing 500 μL of XF media. The plate was then incubated at 37ºC at 0% CO_2 for 1 h. The plate was placed in the XF24 analyzer and a basal respiration level was measured. After 20 min, ATP production with the addition of oligomycin (1 μM), an ATP coupler. Maximal respiration was then measured with the addition of FCCP (1 μM), an electron transport accelerator. Lastly, the spare respiration capacity was measure with the addition of Antimycin A and Rotenone (1 μM each), two potent mitochondrial inhibitors.

Foam Cell Formation and prevention with RAW macrophages.

RAW macrophages were plated on a 24 well plate at a density of 2.0 x 10^6/well in DMEM (10% FBS, 1% PS) and allowed to grow overnight. The media was removed and a lipid depleted DMEM (10% lipid depleted FBS, 1% PS) media was added and the cells were grown for an additional 24 hr. For preventative treatment, T-HDL-NPs (30% CO,

0.1 mg/mL or 0.5 mg/mL) were added and allowed to internalize for 6 hours. The media was changed and fresh DMEM was added supplemented with oxidized low density lipoprotein (Ox-LDL) (100 μg/mL). The cells were further incubated for 12 hr. For therapeutic foam cell treatment, after 24 hr treatment with lipid deprived media, the media was replaced with DMEM supplement with Ox-LDL (100 μg/mL) and the cells were incubated for 12 hr. After which, the media was removed and T-HDL-NPs (40% or 70% CO) were added and allowed to internalize for 24 hours. The media was removed for both cases, and washed with 1x PBS (3x). To image the foam cell formation, AdipoRed in PBS was added to each well and incubated for 10 min. The AdipoRed was removed and the cells were washed with 1x PBS (5x). The plates were then either read on the plate reader for the relative fluorescent units or image via fluorescent microscope.

Inflammation Prevention in foam Cells.

RAW macrophages were plated on a 24 well plate at a density of 2.0 x 10^6/well in DMEM (10% FBS, 1% PS) and allowed to grow overnight. The media was removed and a lipid depleted DMEM (10% lipid depleted FBS, 1% PS) media was added and the cells were grown for an additional 24 hr. For preventative treatment, T-HDL-NPs (40% or 70% CO) were added and allowed to internalize for 6 hours. The media was changed and fresh DMEM was added supplemented with oxidized low density lipoprotein (Ox-LDL) (100 μg/mL). The cells were further incubated for 12 hr. For therapeutic foam cell treatment, after 24 hr treatment with lipid deprived media, the media was replaced with DMEM supplement with Ox-LDL (100 μg/mL) and the cells were incubated for 12 hr. After which, the media was removed and T-HDL-NPs (30% CO, 0.1 mg/mL or 0.5 mg/mL) were added and allowed to internalize for 24 hours. The media was removed for

both cases, and washed with 1x PBS (3x). The supernatants were then analyzed for the secretion of pro-inflammatory cytokines interleukin (IL) 6 and tumor necrosis factor (TNF) α and the anti-inflammatory cytokine IL-10.

Statistics.

All data were expressed as mean ± S.D (standard deviation). Statistical analysis were performed using GraphPad Prism® software v. 5.00 (GraphPad Software, Inc., CA). Comparisons between two values were performed using an unpaired Student t test. A one-way ANOVA with a post-hoc Tukey test was used to identify significant differences among the groups.

Results and Discussion

Development of Synthetic HDL-Mimicking NPs.

Given the clinical success of polymeric NPs and liposomes, we hypothesized that a biodegradable polymer lipid hybrid NP will have the unique advantages and strengths of polymeric NPs and liposomes. Clinical uses of PLGA, PEG, and lipids in FDA approved products motivated us to use these components to engineer a completely synthetic HDL-mimicking polymer lipid hybrid NPs with the ability of high contrast agent loading for utilization of cardioprotective action of HDL. A HDL-mimicking hybrid NP with a cholesterol and PLGA core was synthesized via self-assembly of PLGA, PLGA-*b*-PEG-QD, CO, cationic stearyl-TPP (Fig. 6.2-6.4), DSPE-PEG-COOH, and apoA-I mimetic peptide through a two-step modified nanoprecipitation method. For the non-targeted NPs, polyvinyl alcohol (PVA) was used instead of stearyl-TPP.

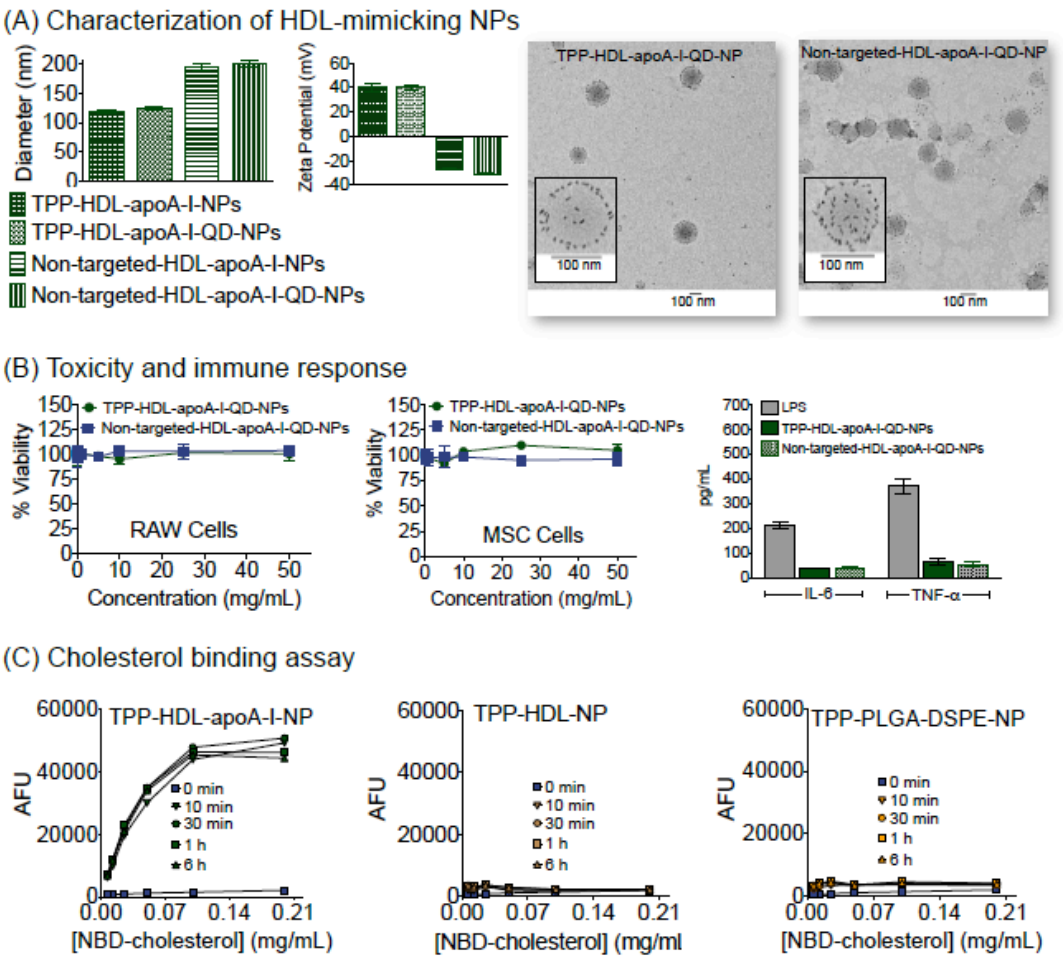


Figure 6.5. (A) (Left) Size and zeta potential of targeted and non-targeted HDL-mimicking NPs with or without QD and (Right) TEM images of targeted and non-targeted QD-loaded HDL-mimicking NPs. (B) (Left) Toxicity profiles of targeted and non-targeted HDL-mimicking NPs in RAW macrophages and MSC cells as determined by MTT assay and (Right) secretion of IL-6, and TNF-α with targeted and non-targeted NPs (0.5 mg/mL) after 12 h. (C) Binding of NBD-cholesterol to TPP-HDL-apoA-I-NPs (left). TPP-HDL-NPs (middle) and TPP-PLGA-DSPE-NPs (right) were used as controls.

Dynamic light scattering (DLS) revealed the size of the mitochondria targeted NPs, TPP-HDL-apoA-I-QD-NPs to be ~123±3 nm and are mono dispersed (Fig. 6.5-6.6). This small size of the targeted NPs will facilitate extravasation in areas with enhanced

endothelial permeability, such as atherosclerotic lesions. The size of non-targeted-HDL-apoA-I-QD-NPs by DLS was found to be ~191±7 nm. The hydrodynamic radius of the targeted NPs determined by DLS agrees with the transmission electron microscopy (TEM) results, however, for the non-targeted NPs, the hydrodynamic radius determined by DLS is almost twice the TEM size.

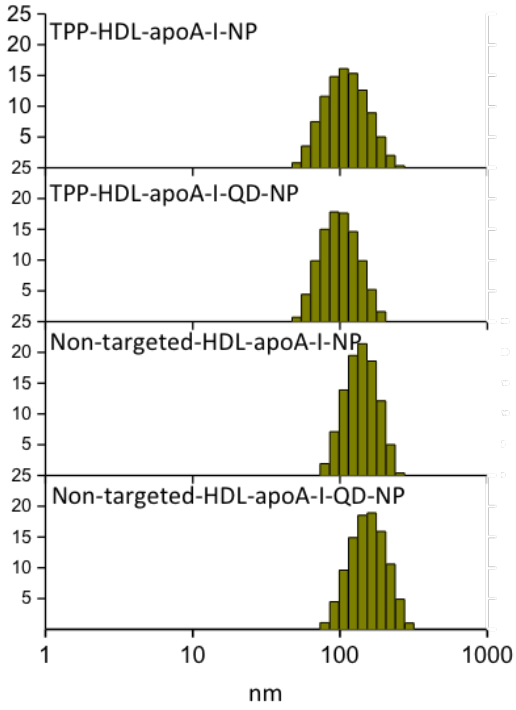


Fig. 6.6. Size distribution of various NPs.

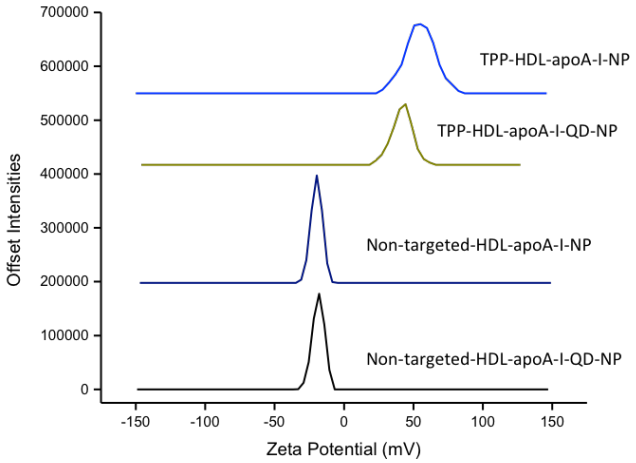


Fig. 6.7. Zeta potential of various NPs.

We believe that this is due to the difference in sizes of the lipid layers between targeted and non-targeted NPs and the location of the QDs within the core. The stearyl-TPP in the targeted NPs has a molecular weight of ~500, whereas PVA in the non-targeted NPs has an average molecular weight range of 10,000-26,000. The QDs are located at the interface between the core and lipid layer. Therefore, by the unstained TEM images as reported here, the particles appear to be of same size for the targeted NPs. For the non-targeted NPs, DLS takes into account the larger lipid layer rendering them larger compared to TEM size. Zeta potential measurements showed that the mitochondria targeted NPs are highly positively charged (~39 mV) (Fig. 6.5, Fig 6.7). Our recent study indicated that a NP size of <160 nm and zeta potential of ~30 mV is an optimized formulation for mitochondria targeting [18]. The non-targeted NP surface is negatively charged (~-28 mV). Composition analysis of the targeted NPs by inductively coupled plasma mass spectrometry (ICP-MS) for QD indicated 70% QD encapsulation efficiency (EE) and the non-targeted NPs showed moderately higher EE of ~80%. A major challenge of atherosclerosis imaging is the design of imaging probes to achieve sufficient

target-to-background levels for visualization and high loading of the contrast agent to boost the signal at the target. A high QD loading as observed in our NPs might face less challenge when executed in vivo. Spectroscopic analysis of targeted and non-targeted NPs for quantification of apoA-I by examining tryptophan absorbance at 280 nm showed that the percent loading varies between 1.7-2%. Cholesterol analysis of NPs using Amplex Red assay demonstrated ~58% cholesterol loading (Table 6.2). An interesting observation was that cholesterol and apoA-I loadings do not change significantly with formulation which might be of indicative that this synthetic HDL tries to attain a specific cholesteryl ester (CE):apoA-I ratio as seen in native HDL particles [23].

Table 6.2. Composition analysis of HDL-mimicking NPs.

Test article	QD	CE		ApoA-I		CE/apoA-I
	%EE	%Loading	%EE	%Loading	%EE	
TPP-HDL-apoA-I-QD-NPs	70	58±0.2	46±0.3	1.9±0.1	9.5±0.4	33
Non-targeted-HDL-apoA-I-QD-NPs	83	58±0.2	47±0.3	1.7±1.3	8.7±1.8	34
TPP-HDL-apoA-I- NPs	-	58±0.2	47±0.3	2.0±0.2	9.8±0.9	32
Non-targeted-HDL-apoA-I-NPs	-	59±0.6	48±1.2	1.8±0.1	8.8±0.6	36
EE: Encapsulation efficiency; CE: Cholesteryl ester						

Stability, Toxicity, and Immunogenic Properties of HDL-Mimicking NPs.

In addition to the size, charge, and contrast agent loading, serum stability and immunological effects of these new NPs are expected to affect the in vivo biodistribution (bioD), pharmacokinetic (PK) parameters, and overall utility of this system. In vitro serum stability of the NPs was investigated by storing a 2.5 mg/mL NP suspension in 10% fetal bovine serum (FBS)-Dulbecco's modified eagle medium (DMEM) at 4 °C,

room temperature (RT), and 37 °C and monitoring the changes in particle size and surface charge. Serum proteins showed no significant effect on the size, polydispersity index (PDI), and surface charge of the targeted NPs over a period of 7 days at all the three temperatures (Fig. 6.8).

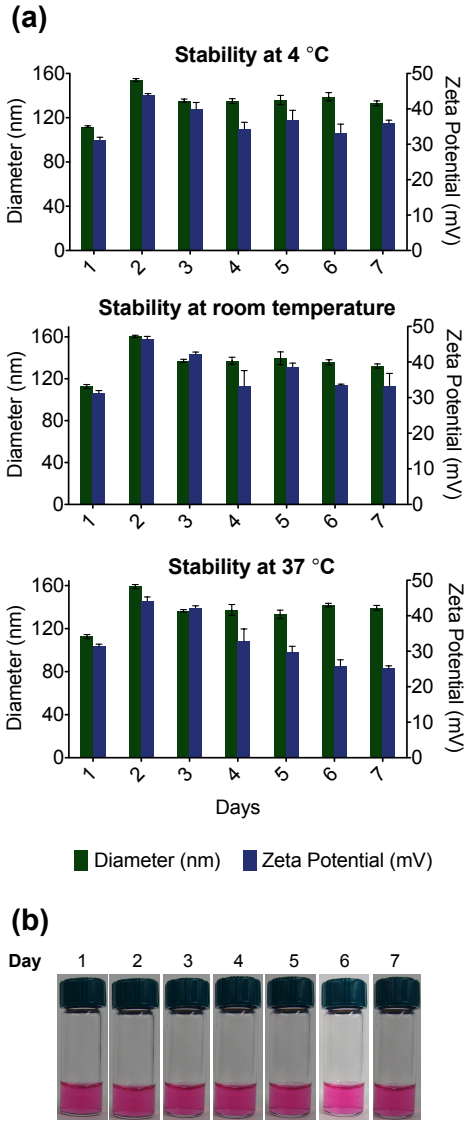


Fig. 6.8. (a) In vitro serum stability of TPP-HDL-apoA-I-NPs (2.5 mg/mL) in 10% fetal bovine serum (FBS)-DMEM at 4 °C, room temperature, and at 37 °C. (b) Images of TPP-HDL-apoA-I-NPs (2.5 mg/mL) in 10% FBS-DMEM at 4 °C.

These results are indicative of an excellent stability of the targeted NPs under biologically relevant conditions. For in vivo studies, especially when positively charged NPs are injected at multiple time points, the potential exists for an immunogenic reaction that could adversely affect the binding of the NPs to the intended target or, even worse, be unsafe. Innate immunity plays an important role in the first-line immune response. We focused on macrophage-associated immune responses from the targeted and non-targeted-HDL-NPs by measuring the production of cytokines interleukin 6 (IL-6) and tumor necrosis factor α (TNF-α) using an enzyme-linked immunosorbent assay (ELISA). Lipopolysaccharide (LPS) was used as a positive control. Incubation of RAW 264.7 macrophages with targeted and non-targeted-HDL-NPs (0.5 mg/mL) did not show secretion of IL-6 and TNF-α (Fig. 6.5B). After seeing that these NPs have no pro-inflammatory effect on naïve macrophages, the ability of the targeted and non-targeted NPs to modulate cytokine production in LPS-activated RAW macrophages was assessed. When exposed to an optimal concentration of LPS (100 ng/mL) for 24 h, macrophages produce enhanced amounts of IL-6 and TNF-α (Fig. 6.9).

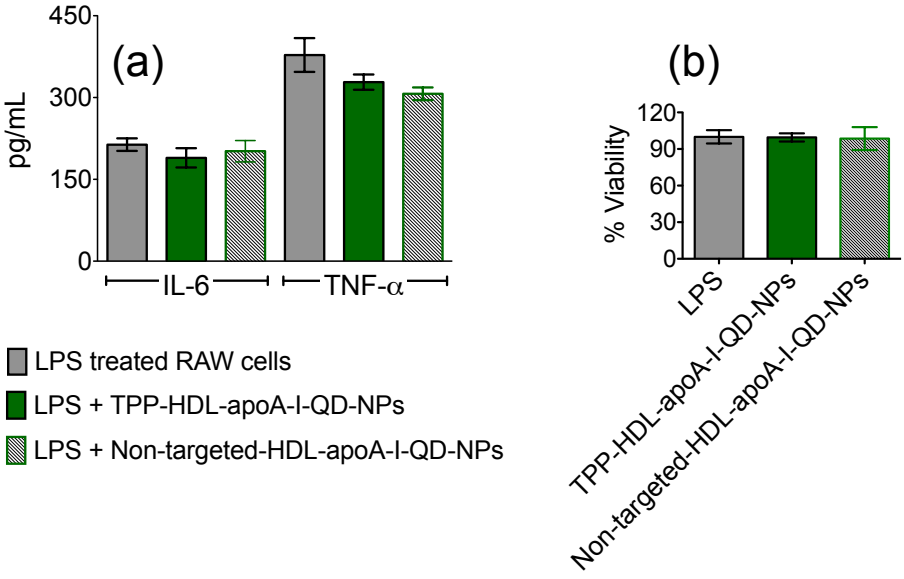


Fig. 6.9. Effect of TPP-HDL-apoA-I-QD-NPs and non-targeted-HDL-apoA-I-QD-NPs on LPS activated RAW 264.7 macrophages (a) and cell viability after treatment with LPS and the NPs (b).

Treatment of these LPS-activated macrophages with targeted or non-targeted-NPs (0.5 mg/mL with respect to total NP) for 12 h did not show any additional amounts of IL-6 and TNF-α, a slight decreased production of both the cytokines was observed in the presence of these NPs (Fig. 6.9). This further confirms that these NPs have no effect on naïve and M1-polarized macrophages. Targeted and non-targeted-HDL-NP induced cytotoxicity was assessed by the 3-(4,5-dimethylthiazol-2-yl)-2,5-diphenyltetrazolium bromide (MTT) assay in RAW macrophages and primary human mesenchymal stem cells (MSCs). MSCs represent an interesting target cell type regarding nanotoxicology and especially nanogenotoxicology since they actively proliferate and repeatedly expand in contrast to other primary cells, although they are not immortalized. Directly following 72 h incubation with NPs at various concentrations showed no particle related cytotoxicity and morphological transformation even at 50 mg/mL concentration compared to that of

untreated cells (Fig. 6.5B). This indicates the use of biodegradable components in this HDL-mimicking NPs result in a biocompatible, non-toxic, and non-immunogenic formulation.

In Vitro Cholesterol Binding Properties.

A fluorescent sterol, NBD-cholesterol or 22-(*N*-(7-nitrobenz-2-oxa-1,3-diazo-4-yl)-amino)-23,24-bisnor-5-cholen-3β-ol was used to examine the HDL-mimicking NP mediated cholesterol uptake to explore the therapeutic potential. The weak fluorescence of NBD-cholesterol in polar environment was enhanced by the presence of non-polar TPP-HDL-apoA-I-NP matrix (Fig. 6.5C). Similar formulation without any apoA-I, TPP-HDL-NPs, did not show any cholesterol binding. Control polymer lipid hybrid NPs prepared from PLGA-COOH, DSPE-PEG-COOH, and stearyl-TPP; PLGA-DSPE-NPs, which lack HDL-apoA-I mimicking core, did not show any cholesterol binding. We also explored time and temperature dependent cholesterol binding abilities of the targeted NPs. Storage of targeted-NPs at 4 °C, RT, and 37 °C in 10% FBS-DMEM and examination of NBD-cholesterol binding for 7-days at all the three temperatures indicated enhanced cholesterol binding with the NPs which were kept at RT or at 37 °C compared to those at 4 °C (Fig. 6.10).

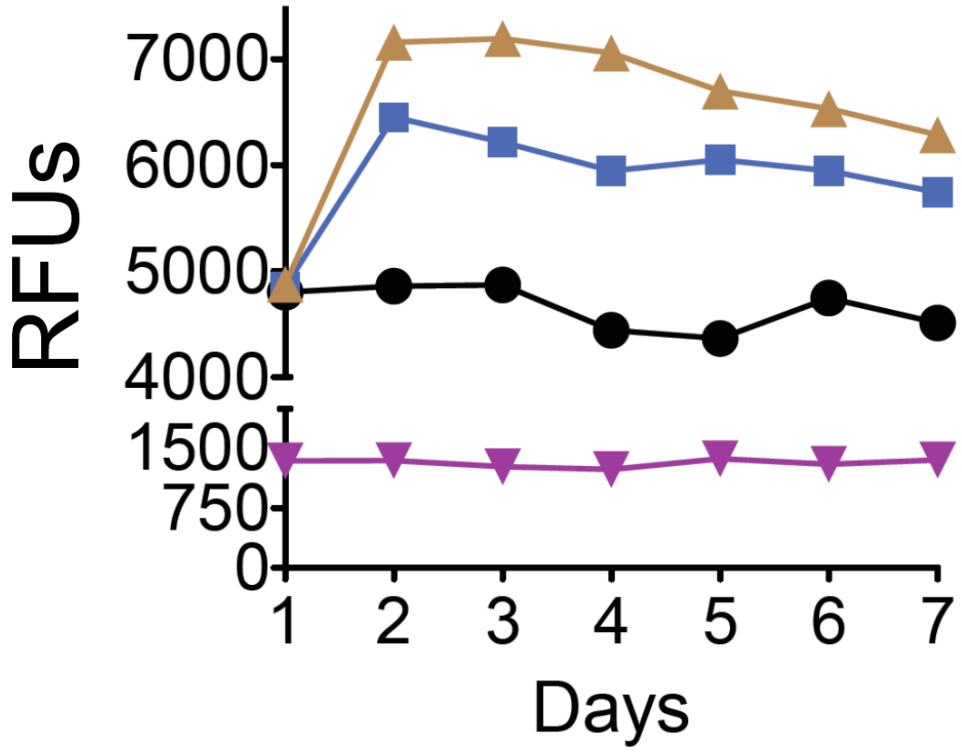


Fig. 6.10. Temperature and time dependent binding of NBD-cholesterol to TPP-HDL-apoA-I-NPs.

We think this is due to increased NP swelling at higher temperatures. A decreased cholesterol-binding trend with time indicates biodegradable nature of these NPs. These preliminary experiments are indicative that cholesterol can bind to TPP-HDL-apoA-I-NPs for potential participation in the RCT pathway.

$\Delta\psi_m$-Targeted TPP-HDL-apoA-I-QD-NPs Located in the Mitochondria.

Significant cell association and mitochondrial internalization of the targeted TPP-HDL-apoA-I-QD-NPs by healthy RAW 264.7 was noted (Fig. 6.11A). Only limited non-specific cytosolic uptake was observed for the non-targeted-HDL-apoA-I-QD-NPs (Fig. 3A). To find out whether the uptake of the targeted-NPs is indeed a $\Delta\psi_m$-driven process, studies were performed in the presence of a mild uncoupler carbonylcyanide-*p*-(trifluoromethoxy)phenylhydrazone (FCCP) (Fig. 6.11B). Uptake of TPP-HDL-apoA-I-

QD-NPs were completely blocked by the presence of FCCP, which abolishes the $\Delta\psi_m$ of the inner mitochondrial membrane (IMM), as shown by in vivo imaging system (IVIS) analyses of the mitochondrial and cytosolic fractions of the NP treated cells in the absence or presence of the uncoupler FCCP (Fig. 6.11B).

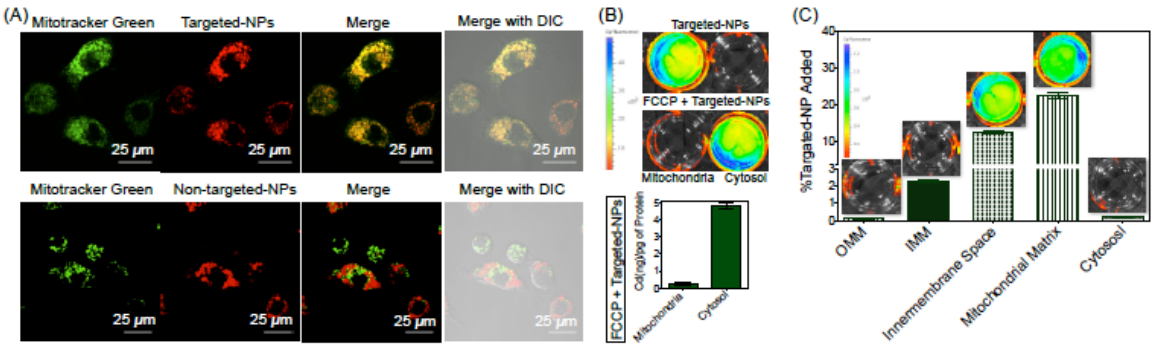


Figure 6.11. (A) Subcellular localization of TPP-HDL-apoA-I-QD-NPs and non-targeted-HDL-apoA-I-QD-NPs in RAW macrophages. RAW 264.7 cells were exposed to targeted NPs (diameter, 125 nm; zeta potential, 37 mV) and non-targeted NPs (diameter, 189 nm; zeta potential, -29 mV) at 270 μM (with respect to cholesterol) for 4 h. They were stained with the mitochondrial marker MitoTracker® Green, and live cell imaging was performed. The merged images show effective association of the targeted-NPs (red) with the mitochondria (green) and no significant association was observed with non-targeted NPs. (B) IVIS of mitochondrial and cytosolic fractions of RAW macrophages after treatment with targeted TPP-HDL-apoA-I-QD-NPs with or without collapse of $\boldsymbol{\Delta\psi_m}$ by addition of FCCP. QD content in the mitochondrial and cytosolic fractions of FCCP-blocked cells by ICP-MS. (c) Quantification of targeted-NPs in the mitochondrial sub-fractions by ICP-MS and IVIS.

The mitochondrial uncoupler FCCP had no effect on the uptake profile of non-targeted NPs (Fig. 6.12). This data was further confirmed by determining the QD content

of the mitochondrial and cytosolic fractions of the FCCP treated macrophages, which showed no significant accumulation of the targeted-NPs in the mitochondria of $\Delta\psi_{m}$-blocked macrophages. Taken together, these data support our claim that the TPP-HDL-apoA-I-NPs takes the advantage of the substantial negative $\boldsymbol{\Delta\psi_{m}}$ maintained across the IMM at crossing the hydrophobic membranes and preferentially associate with the mitochondrial network.

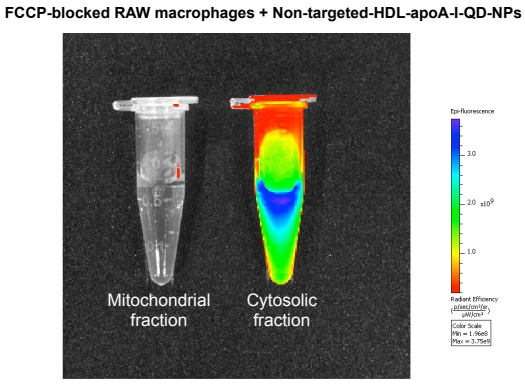


Fig. 6.12. IVIS of mitochondrial and cytosolic fractions of RAW macrophages after treatment with non-targeted-HDL-apoA-I-QD-NPs with collapse of $\boldsymbol{\Delta\psi_{m}}$ by addition of FCCP.

To further determine the localization of the targeted HDL-apoA-I-NPs within these organelles, targeted NP treated RAW macrophage mitochondrial fractions were lysed and further fractionated into outer mitochondrial membrane (OMM), IMM, innermembrane space, and mitochondrial matrix. These fractions were examined by IVIS analyses and ICP-MS (Fig. 6.11C). Within the mitochondria, TPP-HDL-apoA-I-QD-NPs were localized mainly in the mitochondrial matrix and the innermembrane space as demonstrated by IVIS analyses (Fig. 6.11C). This observation was further supported by quantitative ICP-MS of targeted-NP treated mitochondrial sub-fractions. Cd quantification of mitochondrial compartments demonstrated that targeted-NPs were

mainly found in the mitochondrial matrix (22.7±0.9%) and the innermembrane space (12.6±0.4%), only trace amounts of these NPs were detected in the IMM (2.3±0.1%), or the OMM (0.1±0.04%). In our study, isolation of mitochondrial compartments and analyses using IVIS and ICP-MS provided us concrete evidence that our targeted HDL-NPs reside inside the mitochondrial matrix. Our data also suggest that these targeted-NPs are imported to the matrix by an $\Delta\psi_m$-mediated mechanism that is active only in healthy cells with active mitochondria. These targeted NPs will take the advantage of collapse of $\Delta\psi_m$ during apoptotic events of macrophages for selective detection of vulnerable plaques.

Apoptosis Sensing in Macrophages.

Apoptosis sensing ability of this platform was investigated in apoptotic RAW macrophages by fluorescence microscopy, flow cytometry, IVIS, and ICP-MS. The permanent collapse of the $\Delta\psi_m$ plays a key role in apoptosis. Because of its apparent simplicity, we carried out a qualitative fluorescence monitoring of $\Delta\psi_m$ collapse for monitoring apoptotic event using macrophages. During apoptosis, changes in the $\Delta\psi_m$ occur due to the opening of the mitochondrial permeability transition pore. The electrochemical proton gradient across the IMM in viable cells favors inward movement of TPP-HDL-apoA-I-QD-NPs into the mitochondrial matrix (Fig. 6.11). Apoptotic macrophages treated with this NP showed a significant decrease in NP accumulation due to the lost gradient early on induction of apoptosis (Fig. 6.13A) compared to the healthy cells. Therefore, these NPs manifest signal reduction on induction of the macrophage death process, in contrast to the non-targeted NPs, which do not show any significant difference between viable and apoptotic cells (Fig. 6.13A).

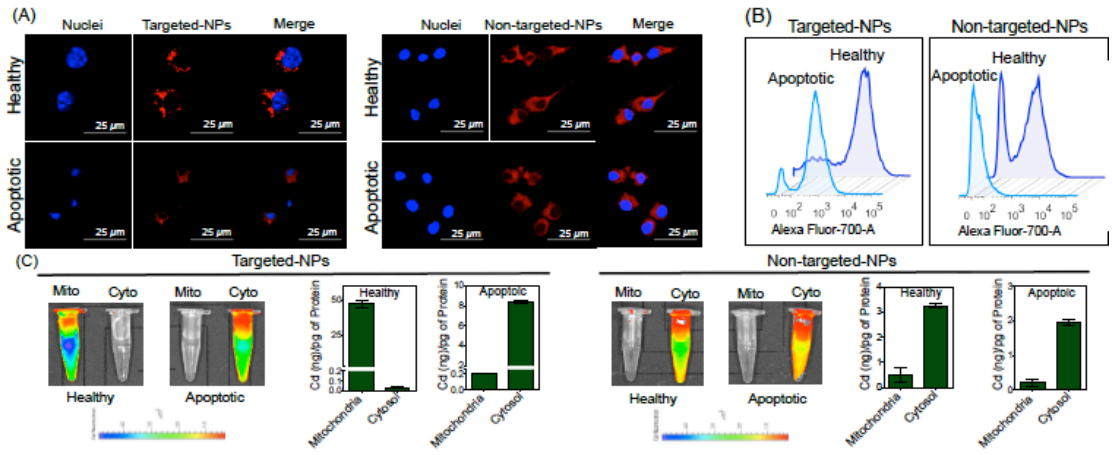


Figure 6.13. (A) Apoptosis detection by HDL-apoA-I-QD-NPs in RAW macrophages by confocal microscopy. Apoptosis was induced by treating macrophages with etoposide. The medium was changed and targeted and non-targeted NPs were added. Cells were fixed, nuclei were stained with Hoechst, and visualized by confocal microscopy. (B) Flow cytometry patterns of RAW macrophages treated with the targeted and non-targeted-NPs with or without etoposide. Macrophage monolayers were incubated for 3 h with TPP-HDL-apoA-I-QD-NPs (left), non-targeted-HDL-apoA-I-QD-NPs (right). Prior to NP treatment, apoptosis was induced using the above-mentioned conditions. Histograms depict all the acquired events. (C) IVIS and ICP-MS analysis of mitochondrial and cytosolic fractions of healthy and apoptotic RAW macrophages after treatment with targeted (left) and non-targeted NPs (right).

Qualitative detection of apoptotic macrophages using our targeted NPs was further supported quantitatively by carrying out flow cytometry. Annexin V, which is used for noninvasive apoptosis detection in myocardial infarction and inflammatory myocardial diseases [24], was used as a control. By using low concentration of TPP-HDL-apoA-I-QD-NPs, significant detection of apoptotic macrophages was observed (Fig. 6.13B) which was comparable to annexin V (Fig. 6.14). In the flow cytometric profiles,

apoptotic cells were recognized by the targeted-NPs on the basis of well-established light scatter characteristics. These apoptotic cells after treatment with targeted-NPs showed a diminished staining. In contrast, the non-targeted construct did not show any sensing property under the same conditions (Fig. 6.13B). The electrochemical proton gradient across the IMM in viable cells favors association of the targeted NPs with the mitochondria. This gradient is lost with an overall reduction in the concentration of the targeted-NPs in the apoptotic cells. Non-targeted NPs, in contrast, did not exhibit resolution between apoptotic and non-apoptotic cells. Thus, these data support the hypothesis that mitochondrial demise step can be used as an indicator to use the targeted HDL-NPs to differentiate between vulnerable and stable plaques.

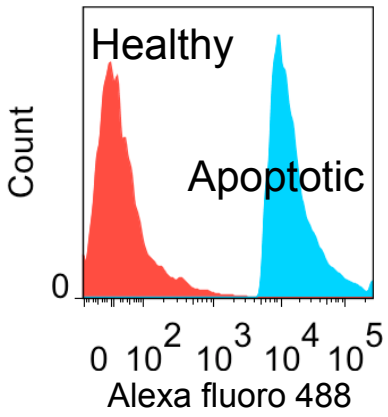


Fig. 6.14. Apoptosis detection in RAW 264.7 macrophages after treatment with etoposide using Annexin V.

To confirm the apoptosis sensing property further, we fractionated the NP treated apoptotic and healthy cells to mitochondrial and cytosolic fractions and conducted IVIS (Fig. 6.13C). We expected in the healthy cells with respiration-active mitochondria, the targeted-TPP-HDL-apoA-I-QD-NPs will localize in the mitochondria, whereas the non-targeted NPs will accumulate in the cytosols. In apoptotic cells, upon collapse of $\Delta\psi_m$,

the targeted-NPs will get expelled out to the cytosols with an overall reduced uptake. Upon apoptosis, we observed loss of fluorescence in the mitochondrial fractions with the targeted-TPP-HDL-apoA-I-QD-NPs, whereas, the non-targeted NPs did not show any difference between healthy and apoptotic cells (Fig. 6.13C). Quantifying Cd by ICP-MS in the mitochondrial and cytosolic fractions further supported that the targeted HDL-NPs have superior ability to sense apoptosis in macrophages (Fig. 6.13C). Compared with the transient nature of PS externalization used by labeled annexin V to detect apoptosis associated with unstable human carotid plaques [25], loss of $\Delta\psi_m$ used by our targeted-NPs is an ongoing process [26] and hence allows detection not limited to a specific time window. The potential toxic effects of QDs should be considered for possible in vivo translation of this technology [27]. However, we want to emphasize that the biodegradable polymer conjugated PLGA-*b*-PEG-QDs as used in our studies can be better suited for in vivo studies. For polymer-conjugated QDs, chemical and enzymatic degradation of the QD core will be less compared to the traditional QDs. Polymer-conjugated QDs embedded in the NP core will have the potential to show in vivo clearance by slow infiltration and excretion. With QD toxicity issues and the limitations of optical imaging in the clinic, we think that this highly sensitive HDL-based NP could provide a platform for preclinical drug screening and therapy monitoring. In future, we plan to use a complementary magnetic resonance imaging (MRI) by incorporating iron oxide for in vivo imaging and use ex-vivo QD imaging to complement the MRI results.

BioD and PK of Targeted-TPP-HDL-apoA-I-NPs.

Favorable BioD, excretion, and PK properties are important for a newly developed NP platform for its in vivo application. To determine the PK, bioD, and

excretion profiles, we injected TPP-HDL-apoA-I-QD-NPs into Sprague Dawley rats by a single dose intravenous injection; blood samples at predetermined time points up to 24 h post injection, organs after 24 h, and cumulative urine, feces over 24 h were collected. Analyses of the plasma samples for Cd by ICP-MS and calculation of PK parameters by a two-compartment intravenous input model revealed a plasma elimination half life ($t_{1/2}$) from the central compartment of ~36 min (Fig. 6.15, Table 6.1).

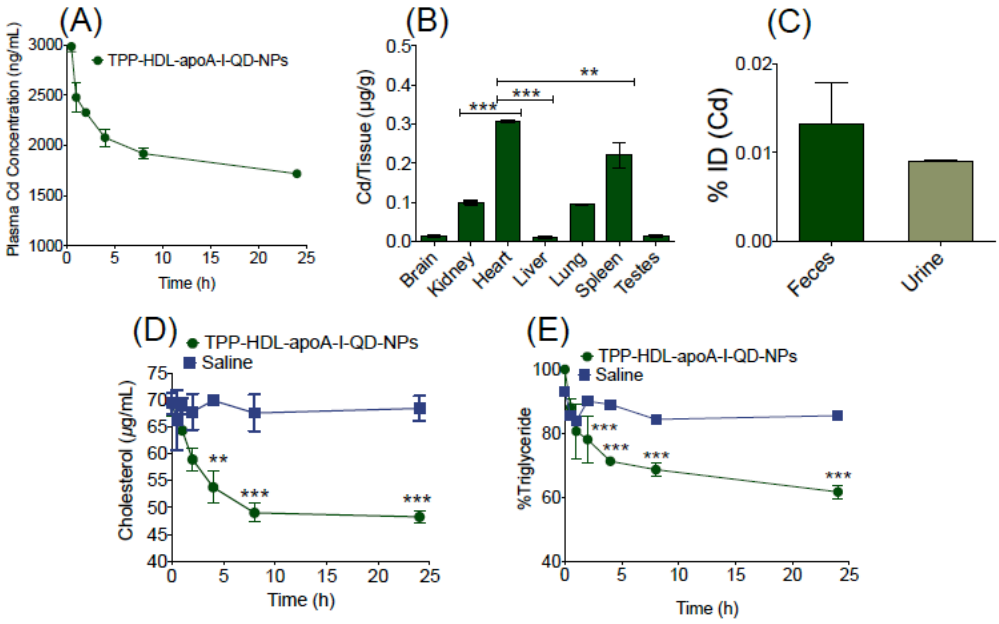


Figure 6.15. (A) Variation of Cd concentration in ng/mL in plasma with time following the administration of targeted-TPP-HDL-apoA-I-QD-NPs intravenously to rat. (B) Tissue distribution of targeted-TPP-HDL-apoA-I-QD-NPs in male rats. (C) Cumulative 24 h excretion of TPP-HDL-apoA-I-QD-NPs in male rats. Changes in levels of plasma total cholesterol (D) and triglyceride (E) in rats administered with TPP-HDL-apoA-I-QD-NPs. Statistical analyses were performed using one-way ANOVA with Tukey post hoc test. ** and *** indicate a *P* value < 0.001 and < 0.0001, respectively.

This initial phase is followed by a slower decline, a very high $t_{1/2}$ value in the periphery compartment of ~72 h was observed (Table 6.1). Such a slow clearance of this engineered NP indicates that this platform has the potential to serve as an excellent delivery system. The total body clearance (C_L) of the targeted-HDL-mimicking-NPs was 0.03 mL/h. The longer terminal phase $t_{1/2}$ and a smaller C_L of the targeted NPs indicate that the engineered HDL-mimicking NPs could stay in the body for a longer period of time (Table 1). Based on the very high area under curve (AUC) of 47196 ng/mL and peak plasma concentration (C_{max}) of 3676 ng/mL produced by the HDL-mimicking-NPs indicate that these NPs are delivered into the bloodstream very effectively (Table 6.3). The extraordinary PK properties of our HDL-NP mimic various attractive features of native HDL such as long circulation, $t_{1/2}$ ranging from 10 to 12 h in rodents and 5 days in humans due to the presence of unique combination of apoA-I, lipid, and favorable surface properties [28]. A smaller volume of distribution (V_d) was observed in the rats receiving the targeted-NPs (Table 6.3). It is possible that upon intravenous administration these NPs, due to their unique composition, may hinder the distribution in the body or rapid conversion to metabolites. This increases the initial concentration of the NPs and results in decreased V_d making this platform an excellent delivery system.

Table 6.3. PK parameters of TPP-HDL-apoA-I-QD-NPs using two-compartment model.

$AUC_{[0\text{-}24\ h]}$ (ng/mL) [2]	**C_{max} (ng/mL) [2]**	**Central Compartment (Initial Phase, t = 0)**			**Periphery Compartment (Terminal Phase, t = 24 h)**		
		V_d (mL/kg)	**C_L, t = 0 (mL/h)**	**$t_{1/2}$ (h)**	**V_d (mL/kg)**	**C_L, terminal (mL/h)**	**$t_{1/2}$ (h)**
47196	3676	21.5	3.5	0.6	9.9	0.03	71.7
[1] Least-square fit to model: $C = a*\exp[(-k_1*t) + b*\exp(-k_2*t)]$; [2] Model used to extrapolate concentrations at t = 0; AUC: Area under curve; C_{max}: Peak plasma concentration; C_L: Total body clearance; $t_{1/2}$: Plasma half-life; V_d: Volume of distribution							

The excretion profiles for the HDL mimicking NPs via urine and feces were studied by measuring Cd levels from QDs (Fig. 6.15). At 24 h post injection, cumulative NPs recovered in urine represented only 0.009% and feces represented only 0.013% of the administered dose (Fig. 6.15).

The concentration of the targeted HDL-mimicking-NPs was monitored in major tissues, including spleen, liver, lungs, brain, heart, kidney, and testes at 24 h post-dose (Fig. 6.15). The total recovery in organs accounted for ~4.8% of the total dose administered with highest accumulation in the heart (Fig. 6.15). Quantitative ICP-MS results indicated that 1.5% of the injected dose of our engineered NPs was distributed in the heart after 24 h. In general, positively charged NPs accumulate in the liver and the spleen due to the positive zeta potential which favors uptake by phagocytic cells of the reticuloendothelial system mainly present in these organs. The targeted HDL-mimicking NPs in spite of positively charged surface showed a very high heart-to-liver ratio of 29 and a moderate heart-to-spleen ratio of ~1.5 (Fig. 6.15). The targeted NPs also showed high heart-to-kidney ratio of ~3. The absence of TPP-HDL-apoA-I-QD-NPs in the lungs as indicated by the high heart-to-lung ratio of ~3.5 reflects a satisfactory colloidal stability of these NPs despite the presence of negatively charged serum proteins, which are well known for inducing the agglomeration of positively charged NPs. Such a colloidal stability can probably be originated due to the steric hindrance caused by the TPP moieties on the surface of the NPs. We believe that NP accumulation in the heart is due high NP concentration (57% of the injected dose) in the circulatory system, which increases the possibility that the NPs accumulate in the heart. Significant accumulation of

the targeted-HDL-mimicking NPs in the heart indicates that these NPs have the potential for further development for imaging and therapy of CHD.

In Vivo Lipid Dynamics by TPP-HDL-apoA-I-NPs.

Studies have shown an inverse correlation between plasma HDL concentrations and atherosclerotic cardiovascular risk [29]. HDL, its major lipoprotein, and apoA-I play key roles in RCT from atherosclerotic plaques to the liver. Cholesterol in the nascent discoidal HDL is esterified by lecithin-cholesterol acyltransferase to form cholesteryl esters, which occupies the core of HDL thus producing a steady gradient of free cholesterol and enabling HDL to accept cholesterol from various donors. We speculated that the HDL-mimicking NPs with a CE core would be able to mimic the RCT action of natural HDL. In our study, targeted TPP-HDL-apoA-I-QD-NPs significantly reduced the serum total cholesterol and triglyceride compared to the saline control (Figs. 6.15D and 6.15E). TPP-HDL-apoA-I-QD-NPs in low dose (80 $\mu g \cdot kg^{-1}$ with respect to QD) for 24 h tended to decrease total cholesterol levels by 30% (P <0.0001) (Fig. 6.15D) and triglyceride levels by 24% (P <0.0001) (Fig. 6.10E) compared to the saline group. These effects are likely to be related to the binding of cholesterol to TPP-HDL-apoA-I-NPs as seen in our in vitro cholesterol binding experiments (Fig. 6.5C). It is important to note that these data demonstrate potential utility of this engineered HDL-mimicking NP as a therapeutic platform for atherosclerosis. Given the simplicity of the system, biodegradability, and the scope of easy manipulation, this platform has the potential for further development to improve the lipid profile for dyslipidemic patients.

Rationale for varying cholesterol content in the core.

Above is a proof-of-concept completely synthetic HDL-mimic composed of a Food and Drug Administration (FDA) approved polymeric core.[30] The particle was composed of a cholesterol ester held together by the polymeric core and coated with lipids in order to increase blood circulation. One of the lipids was tagged with a mitochondrial targeting ligand in order to sense plaque collapse at a very early stage by encapsulating a previously synthesized polymer-quantum dot conjugate.[18] Not only was the particle non-toxic and non-immunogenic, it appeared behave much like natural HDL (n-HDL) in that it was able to bind to free cholesterol *in vitro* and also lower cholesterol levels *in vivo* in male Sprague Dawley rats.[30] This follow up report displays an engineers' approach to the synthesis of similar particles with varied cholesterol to lipid ratio in order to enhance the therapeutic effects by making the completely synthetic particles more "HDL-like." As a proof-of-concept, the particles were loaded with therapeutic doses of Atorvastatin (ATV) or coenzyme Q10 (CoQ10) in order to not only potentially boost the therapeutic ability of said nanoparticles but to also show the attractiveness in using a completely synthetic formulation. Herein, the synthesis and HDL mimicking properties will be discussed as well as in vivo biodistribution properties in a pig model.

Synthesis of cholesterol nanoparticles (NPs) with varied cholesterol loading.

NPs with varying amounts of cholesterol were synthesized. A general trend was observed with the size of the nanoparticles. As less cholesterol and more PLGA was incorporated in the core, the size was increased (Table 6.4), with exception to the 90% cholesterol formulation. This is most likely, we believe, due to the lack of stability and sufficient hydrophobic core with the NPs causing aggregation.

Table 6.4. DLS data for varied cholesterol loaded NPs

Nanoparticle	Size	PDI	Zeta
10% Chol	173.0 ± 0.9	0.177 ± 0.02	42.1 ± 7.5
20% Chol	166.0 ± 6.4	0.262 ± 0.04	41.3 ± 2.2
30% Chol	158.7 ± 3.4	0.200 ± 0.03	48.7 ± 2.2
40% Chol	150.9 ± 2.2	0.153 ± 0.08	45.4 ± 1.7
50% Chol	145.9 ± 2.1	0.158 ± 0.01	56.6 ± 3.3
60% Chol	144.4 ± 3.6	0.151 ± 0.03	46.6 ± 2.5
70% Chol	137.6 ± 2.1	0.121 ± 0.01	47.2 ± 7.2
80% Chol	131.5 ± 1.5	0.128 ± 0.04	29.0 ± 3.1
90% Chol	183.9 ± 9.6	0.140 ± 0.08	31.8 ± 9.9

It appears that the lower amount of cholesterol incorporated, the higher the efficiency as can be seen in the table below. However, this is the inverse to what was observed for the ApoA-1 peptide loading. More cholesterol within the NP core leads to higher binding of peptide. This produces a lipid ratio that is somewhat random. It was seen that the highest ratio was produced at a 40% cholesterol formulation.

Table 6.5. Cholesterol and Peptide loading for varied cholesterol NPs.

Nanoparticle (%Chol)	Cholesterol Loading	Cholesterol EE	Peptide Loading	Peptide EE	Lipid Ratio
10	10.2±0.2	102±2.8	0.56±0.03	2.82±0.15	64.9±5.1
20	20.1±0.9	98±2.8	0.73±0.002	3.81±0.22	93.6±0.03
30	26.1±0.2	81.9±1.3	0.90±0.06	4.49±0.29	97.8±5.4
40	34.5±0.2	78.8±1.1	1.1±0.06	5.54±0.29	101.4±4.6
50	41.2±0.03	69.9±0.007	1.44±0.06	7.21±0.30	86.3±3.7
60	47.3±0.2	59.7±0.9	1.84±0.03	9.20±0.14	69.4±0.5
70	55.7±1.7	53.8±3.7	2.17±0.14	10.84±0.77	61.6±0.05
80	66.4±0.9	49.4±2.1	2.87±0.16	14.37±0.81	48.8±0.7
90	84.4±0.6	35.3±4.4	3.36±0.13	16.76±0.66	57.5±4.8

NBD Cholesterol Binding Study.

The nanoparticles synthesized above with varying amounts of cholesterol were then subjected to a cholesterol binding assay. Using GraphPad Prism software, the curves produced were used to calculate the binding constants at the 6 hr incubation time. It appears that the max binding occurs at 20% cholesterol with a steady decrease as the amount of cholesterol increases. This appears to be somewhat in relation to the lipid ratios calculated above. As the ratio decreases with increasing cholesterol, the binding constant decreases. For this reason, 40% and 70% cholesterol NPs were used for the remainder of this study.

Table 6.6. Binding constants for varied cholesterol NPs.

Nanoparticle (%Chol)	Binding Constant (mg/mL NBD)
10	11.7±0.7
20	14.9±0.04
30	10.78±1.51
40	7.88±1.89
50	3.61±0.9
60	5.5±1.5
70	3.9±0.08
80	1.71 ±1.29
90	0.87±0.97

Synthesis of CoQ10 encapsulated NPs

CoQ10 was encapsulated in 40% CO NPs in order to be able to deliver a molecule that will prevent and relieve oxidative stress. The nanoparticle size was no affected by the incorporation of CoQ10 and a high loading of CoQ10 was observed.

Table 6.7. NP characterization of CoQ10 encapsulated NPs.

Size	148.0 ± 0.9 nm
Zeta	38.6 ± 1.5 mV
PDI	0.115 ± 0.012
CO Loading	33.4%
ApoA1 Loading	1.4%
CoQ10 Loading	13.4%
CoQ10 EE	44.7%

Mitostress test of CoQ10 encapsulated NPs using Seahorse XF24 analyzer.

To observe whether or not cholesterol NPs affected overall mitochondrial health, a MitoStress test was performed using the Seahorse XF24 analyzer. It appears with increasing amounts of the cholesterol NPs, overall, the RAW macrophages are not responding well to the MitoStress test chemicals indicating that the mitochondria has lost some functionality. However, with the addition of CoQ10 (blue line), it almost fully reduces the amount of oxidative stress thereby restoring mitochondrial function to almost healthy levels (red line) when compared to 0.5 mg/mL (teal line) and 0.25 mg/mL (pink line) without the addition of CoQ10.

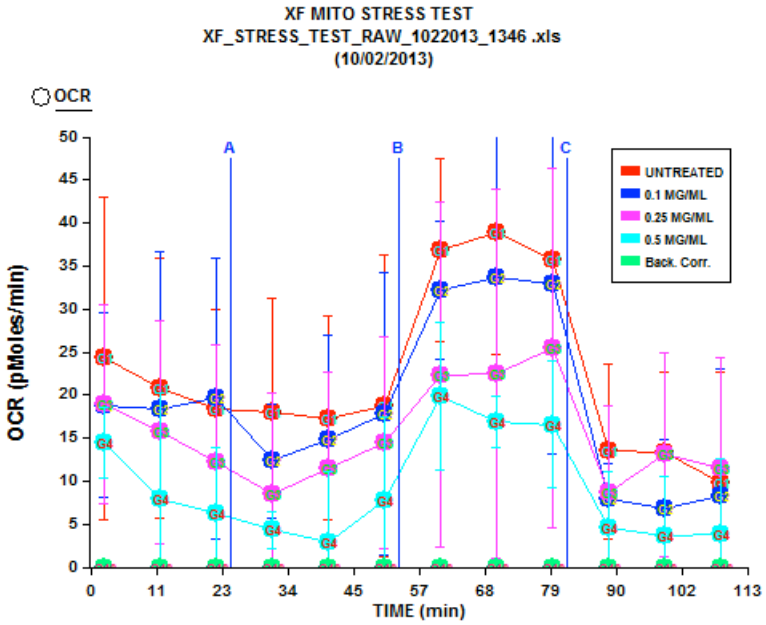


Figure 6.16. Mitostress test of HDL-NPs

Foam Cell Formation and prevention with RAW macrophages.

Foam cells were derived from RAW macrophages through the starvation of lipids followed by the treatment with Ox-LDL. As one can see by the bar diagram below, with only 24 hr treatment with 40% and 70% cholesterol NPs, almost complete foam cell formation is prevented for both preventative and therapeutic treatment. The confocal images below are not a solid proof of the prevention or even formation of foam cells. The beauty of AdipoRed is that it only shows fluorescence in the presence of a hydrophobic environment much like that of a lipid droplet formed from the addition of Ox-LDL. The non-cholesterol treated cells display this well. The differentiated cells show significantly more fluorescence when compared to the non-differentiated cells. However, the cells that were treated with cholesterol NPs, whether it was pretreatment or therapeutic treatment did not show enough for the researchers to make a definitive statement about the

effectiveness even though they show similar fluorescence to that of a non-differentiated RAW macrophage.

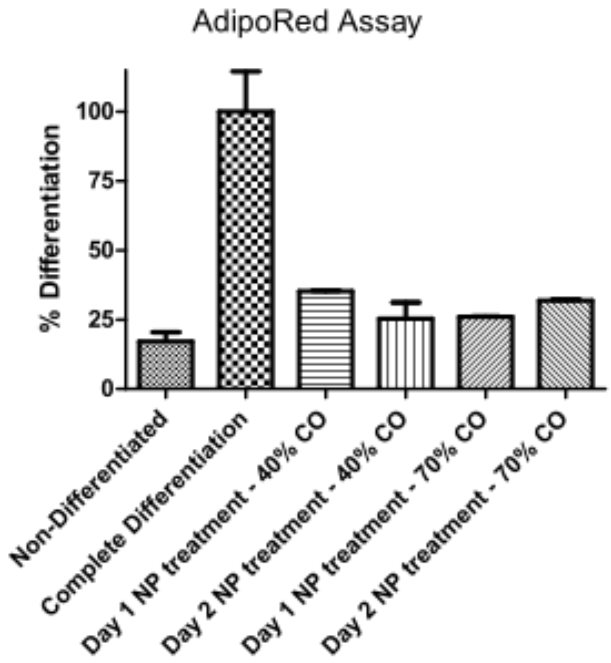


Figure 6.17. AdipoRed RFUs from foam cells with and without treatment with cholesterol NPs

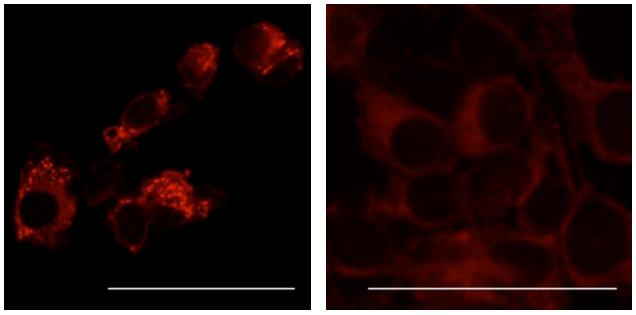


Figure 6.18. Confocal Images of non-cholesterol NP treated RAW cells with (left) and without (right) differentiation

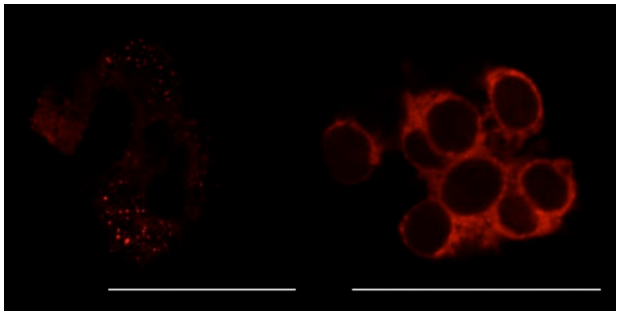


Figure 6.19. Confocal Images of pre-treated cholesterol NP foam cells with (40% CO left, 70% CO right) following differentiation

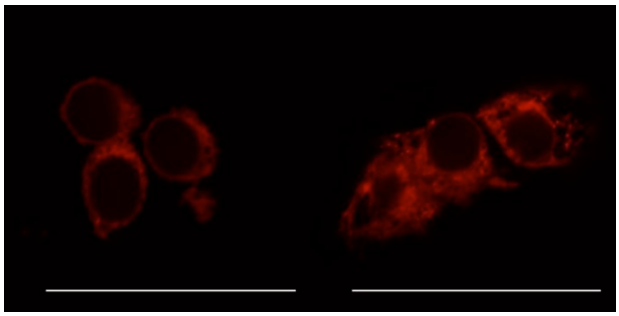


Figure 6.20. Confocal Images of therapeutic-treated cholesterol NP foam cells with (40% CO left, 70% CO right) following differentiation

Inflammation Prevention in foam Cells.

One of the marquis characteristics of plaques and foams cells is the presence of an inflammatory response. To observe how this differed with treatment with Cholesterol NPs, an ELISA assay was run on therapeutically treated and pre-treated RAW macrophage derived foam cells. When comparing differentiated to non-differentiated foam cells, there is a significant difference in the proinflammatory cytokines (IL-6 and TNF-α) with no significant difference in the anti-inflammatory IL-10. However, there appears to significant reduction in IL-6 with the addition of cholesterol NP during pre- and therapeutic treatment. However, there does not seem to be a significant reduction or

induction of TNF-α or IL-10, respectively, with exception to 70% cholesterol therapeutic treatment.

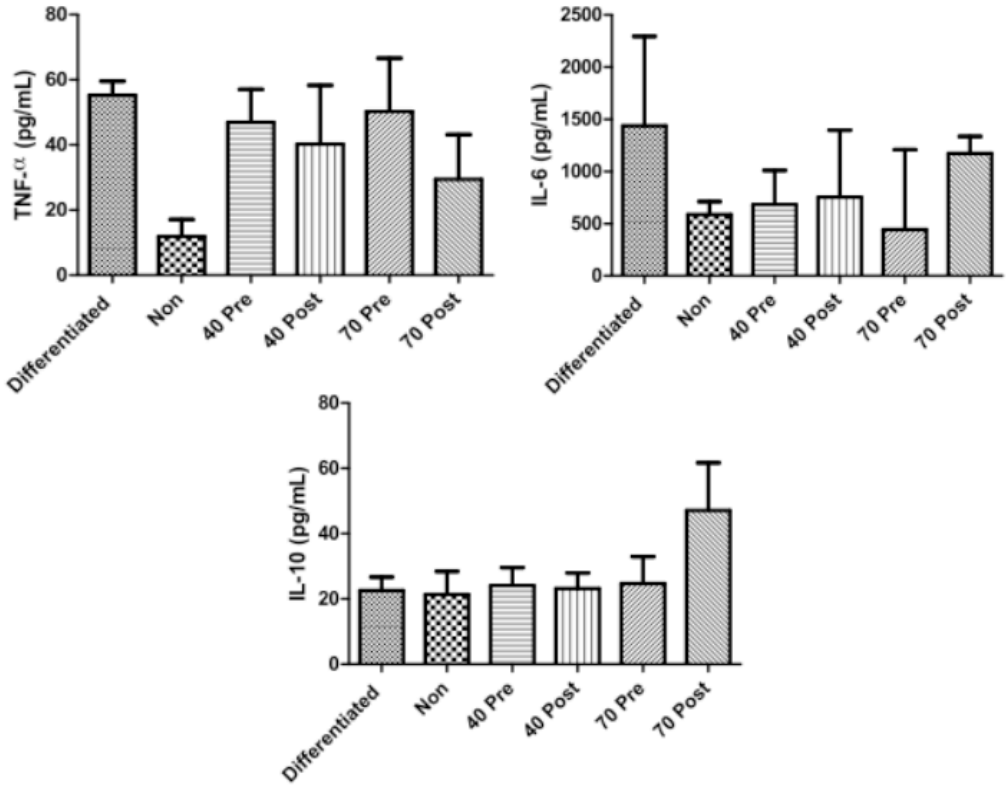


Figure 6.21. Foam cell cytokine production

Cholesterol Binding and release study.

In order to determine whether or not the entrapped NBD cholesterol could be released for excretion, a release study following a binding assay was performed. The release kinetics for each NP differed greatly. It appears that 40% HDL NPs had a much slower and sustained release whereas 70% HDL had a much faster release. This will be interesting to see upon injection *in vivo* how the overall cholesterol reduction differs.

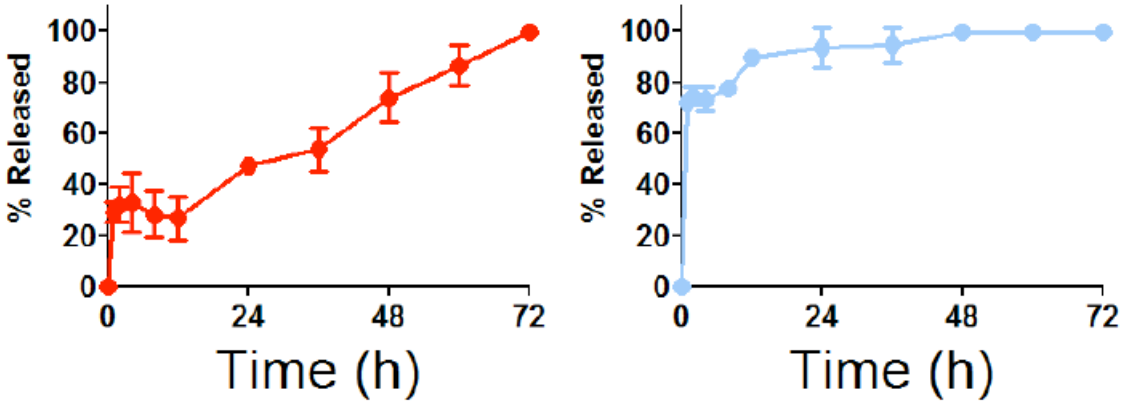


Figure 6.22. NBD-Cholesterol binding and release assay for 40% cholesterol (left) and 70% cholesterol (right)

In vivo biodistribution in pigs.

Although favorable biodistribution was observed in rodents, it was important to see if there would be a difference in bioD and PK parameters in a large animal model and with the new NP formulations. For that reason, 40% and 70% cholesterol NPs were injected into 4-week-old piglets. After organ isolation, it appeared that the NPs had similar bioD. The majority of the NPs were found to be in the heart and aorta. However, upon closer evaluation, the distribution within the heart and aorta differed greatly. The 40% HDL NPs appeared to have a greater distribution within the aorta whereas the 70% HDL NPs were distributed mostly in the heart (Fig. 6.23 a-b). IVIS imaging of the hearts and aortas further confirmed this qualitatively(Fig. 6.24). For the use in plaque reduction and imaging, a NP formulation that could target the aorta could be much more beneficial. Conversely to their difference in bioD in the heart and aorta, the NPs had very similar PK parameters (Fig. 6.23c)

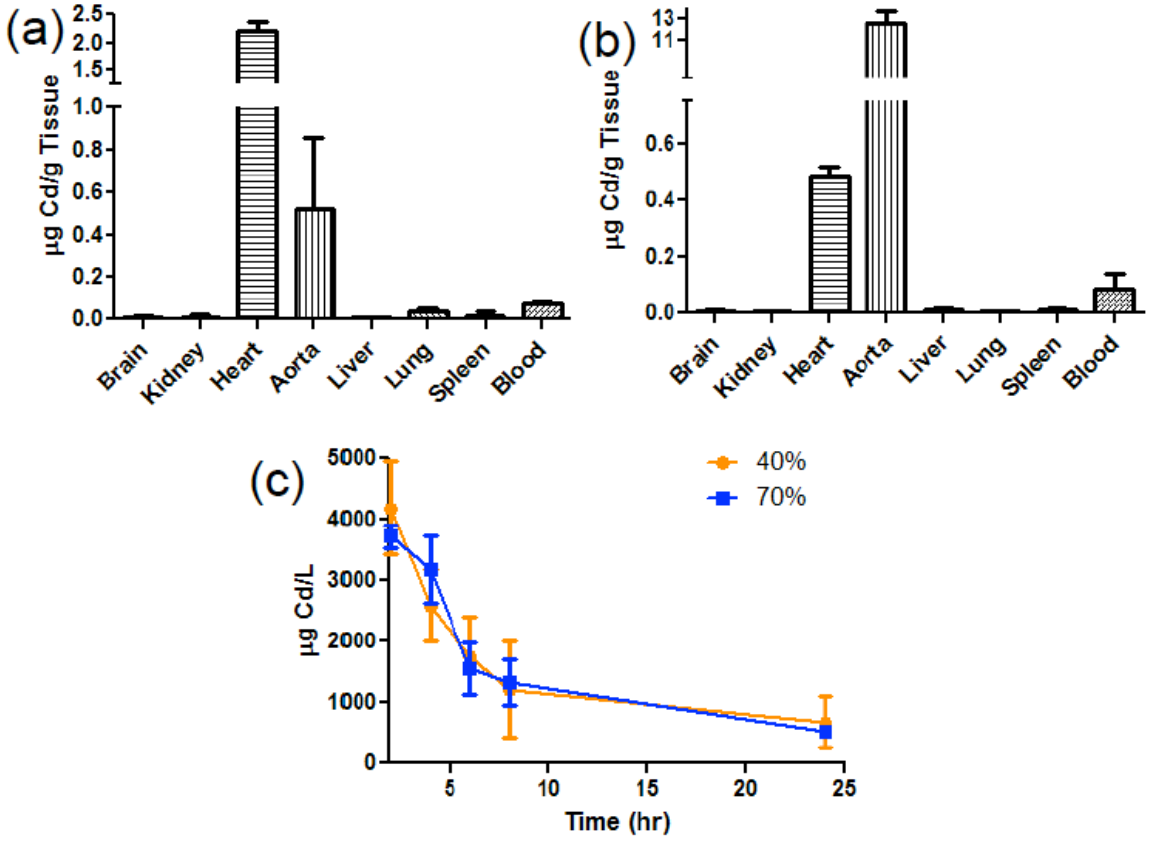


Figure 6.23. BioD for (a) 70% HDL NPs and (b) 40% HDL NPs. (c) PK parameters for both NP systems

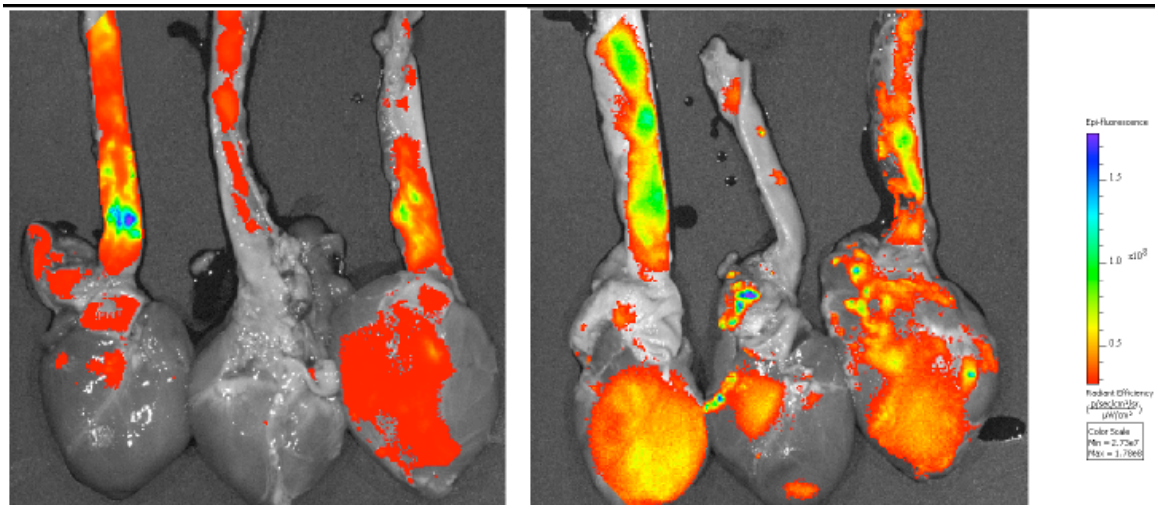


Figure 6.24. IVIS imaging of isolated pig hearts and aortas treated with 40% HDL NPs (right) and 70% HDL NPs (left).

***In vivo* cytokine reduction in pigs.**

With the plasma samples isolated from piglets treated with 40% and 70% HDL NPs, an ELISA was run in order to determine the cytokine production of TNF-α, IL-6, and IL-10. This would show the *in vivo* anti-inflammatory potential of each system. Both systems have the ability to counter act a pro-inflammatory response noticed by the significant decrease in both TNF-α and IL-6. However, the anti-inflammatory properties differed greatly between the two systems. 70% HDL proved to have a much more significant and faster reduction than its 40% counter-part. 40% HDL seemed to have a much slower reduction with the overall levels not ever reaching the lower potential of 70% HDL. The induction of IL-10 also proved to be significantly different between the two systems. While 70% HDL does not appear to have the therapeutic potential to induce IL-10 production, 40% HDL is able to produce significant increases over the first 4 hours post injection. These levels, however, reduce to normal levels after 4 hours, which could correlate to the secretion of the NPs from the body.

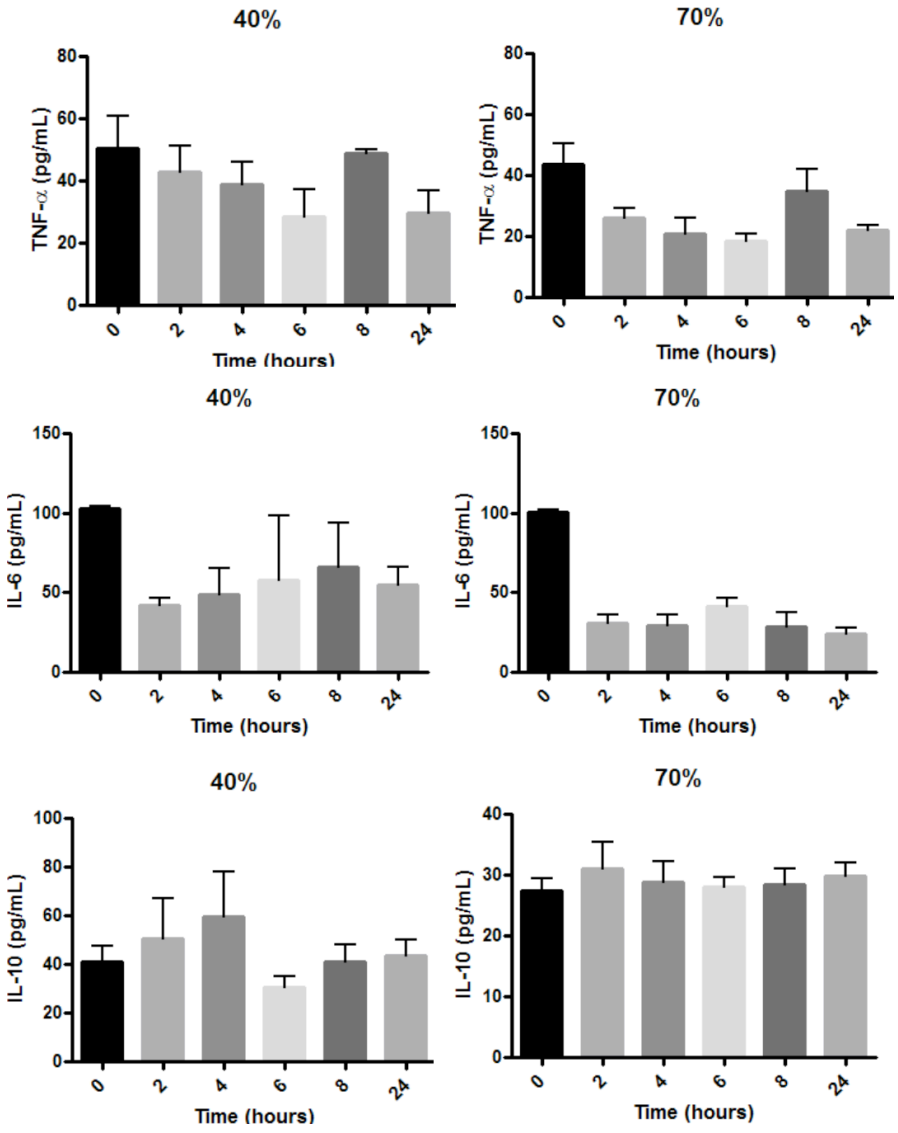


Figure 6.25. In vivo cytokine production for 40% (left) and 70% (right) after injection in piglets

***In vivo* cholesterol and triglyceride reduction in pigs.**

The potential for these systems to be a therapeutic model for atherosclerosis therapy lies in their ability to reduce cholesterol and triglyceride levels *in vivo*. Much like the cytokine reduction, 40% and 70% HDL had much different reduction profiles. 70% HDL provided a fast reduction in cholesterol and triglyceride content, but after 4 hours, the cholesterol and triglyceride levels begin to rise back to normal levels. On the other

hand, 40% HDL had a much slower sustained reduction of cholesterol and triglycerides with the levels not returning to that of untreated piglets.

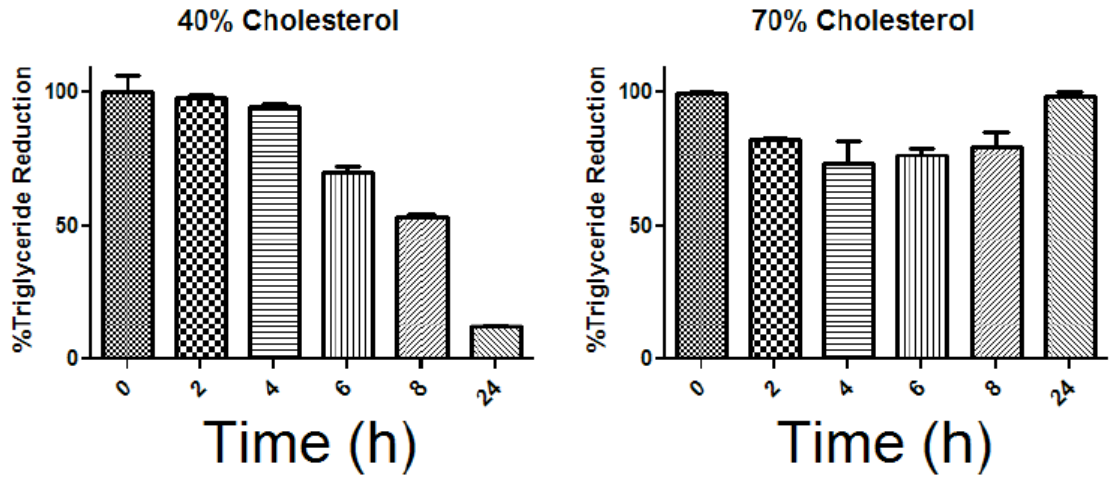


Figure 6.26. In vivo triglyceride reduction after injection of 40% HDL (left) and 70% HDL (right)

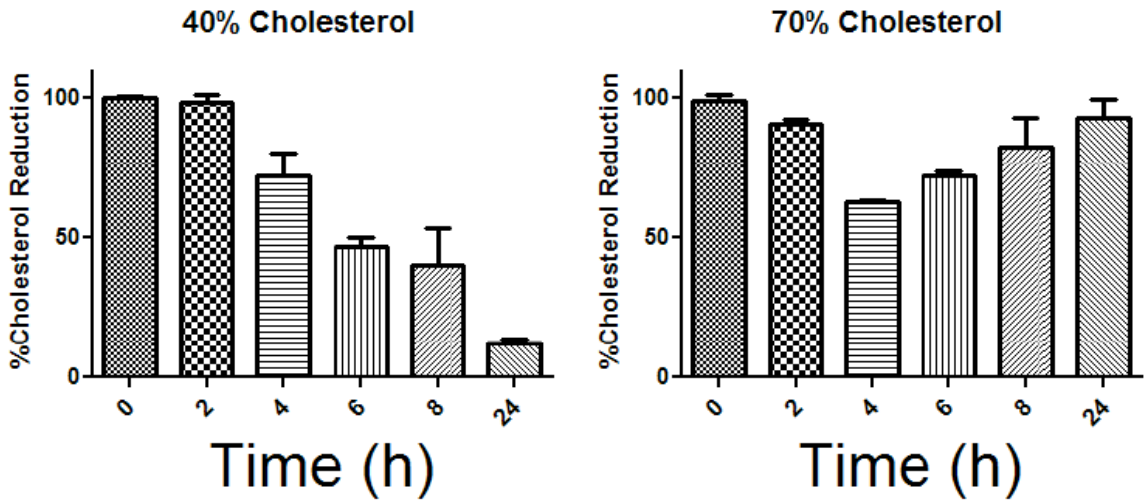


Figure 6.27. In vivo cholesterol reduction after injection of 40% HDL (left) and 70% HDL (right)

Potential for 40% and 70% HDL in an atherosclerotic model.

The bioD and PK parameters of 40% and 70% HDL proved to be beneficial for the potential treatment and imaging of an atherosclerotic pig or rodent model. With the

differences between the cytokine production and cholesterol and triglyceride reduction, it will be interesting to see how these models differ in an atherosclerotic model. 70% HDL seems to have a greater potential to reduce over pro-inflammatory cytokines, whereas 40% HDL appears to have a greater potential in overall cholesterol and triglyceride reduction. One potential strategy to take advantage of both attributes is to co-administer them. This would potentially allow for the 70% HDL to reduce the anti-inflammatory responses produced during atherosclerosis, while 40% HDL will have the ability to remove excess cholesterol from the body. This would allow the systems to work synergistically to reduce the adverse side effects while also protecting the body from further damage.

Conclusion

A proof-of-concept demonstration of a biodegradable polymer lipid hybrid synthetic-HDL-mimicking NP was established for imaging and therapy of vulnerable plaques. We demonstrated that the mitochondria targeted-NPs can sense apoptosis with high resolution over the non-targeted NPs. These NPs closely mimic endogenous HDL in cholesterol binding properties. In addition, we observed the avid uptake of the targeted HDL-NPs by the mitochondria of macrophages. In vivo applicability of the targeted-HDL-NPs for imaging and therapy of atherosclerosis was demonstrated by establishing that this system is non-toxic, shows promising PK parameters and favorable bioD, and has the ability to reduce lipid levels. This is the first report of a mitochondria-targeted biodegradable PLGA-based HDL-mimicking NPs in the literature. Understanding of this biodegradable HDL-NP mimic could lead to the development of candidates that can detect vulnerable plaque early and enhance atheroprotection by increasing levels of HDL

and/or enhancing its functionality. Although additional studies will follow to address the applicability of this platform for imaging and therapy of CHD, this proof-of-concept study demonstrates the feasibility, flexibility, and ease with which the composition of this platform can be manipulated/modified to make them well suited for the creation of artificial HDL-based biodegradable NPs for imaging and therapy of atherosclerosis.

Acknowledgments.

This work was supported by a start-up grant from the National Institutes of Health (P30GM092378) and by the Office of the Vice President for Research, UGA to S.D. We thank Dr. Nagesh Kolishetti for helpful discussions. We thank Walter J. Lunsmann and Dr. Angel Padilla for assistance with PK parameter calculations and IVIS, respectively.

References

1. Sanz, J.; Fayad, Z. A., Imaging of atherosclerotic cardiovascular disease. *Nature* **2008,** *451*, 953-957.
2. Ross, R., The Pathogenesis of Atherosclerosis - a Perspective for the 1990s. *Nature* **1993,** *362*, 801-809.
3. van der Velde, A. E., Reverse cholesterol transport: From classical view to new insights. *World J Gastroentero* **2010,** *16*, 5908-5915.
4. Ross, R.; Glomset, J. A., Atherosclerosis and arterial smooth-muscle cell. *Science* **1973,** *180*, 1332-1339.
5. Desai, M. Y.; Schoenhagen, P., Emergence of targeted molecular imaging in atherosclerotic cardiovascular disease. *Expert Rev. Cardiovasc. Ther.* **2009,** *7*, 197-203.

6. Group, T. B. S., Secondary prevention by raising HDL cholesterol and reducing triglycerides in patients with coronary artery disease: the Bezafibrate Infarction Prevention (BIP) study. *Circulation* **2000,** *102*, 21-27.

7. Kruth, H. S., Macrophage foam cells and atherosclerosis. *Front. Biosci.* **2001,** *6*, D429-455.

8. Petit, P. X.; Lecoeur, H.; Zorn, E.; Dauguet, C.; Mignotte, B.; Gougeon, M. L., Alterations in mitochondrial structure and function are early events of dexamethasone-induced thymocyte apoptosis. *J Cell Biol* **1995,** *130*, 157-167.

9. Frias, J. C.; Williams, K. J.; Fisher, E. A.; Fayad, Z. A., Recombinant HDL-like nanoparticles: A specific contrast agent for MRI of atherosclerotic plaques. *J Am Chem Soc* **2004,** *126*, 16316-16317.

10. Skajaa, T.; Cormode, D. P.; Falk, E.; Mulder, W. J.; Fisher, E. A.; Fayad, Z. A., High-density lipoprotein-based contrast agents for multimodal imaging of atherosclerosis. *Arterioscler. Thromb. Vasc. Biol.* **2010,** *30*, 169-176.

11. Frias, J. C.; Ma, Y.; Williams, K. J.; Fayad, Z. A.; Fisher, E. A., Properties of a versatile nanoparticle platform contrast agent to image and characterize atherosclerotic plaques by magnetic resonance imaging. *Nano letters* **2006,** *6*, 2220-2224.

12. Yang, M.; Jin, H. L.; Chen, J. A.; Ding, L. L.; Ng, K. K.; Lin, Q. Y.; Lovell, J. F.; Zhang, Z. H.; Zheng, G., Efficient cytosolic delivery of siRNA using HDL-mimicking nanoparticles. *Small* **2011,** *7*, 568-573.

13. Zhang, Z.; Chen, J.; Ding, L.; Jin, H.; Lovell, J. F.; Corbin, I. R.; Cao, W.; Lo, P. C.; Yang, M.; Tsao, M. S.; Luo, Q.; Zheng, G., HDL-mimicking peptide-lipid nanoparticles with improved tumor targeting. *Small* **2010,** *6*, 430-437.

14. McMahon, K. M.; Mutharasan, R. K.; Tripathy, S.; Veliceasa, D.; Bobeica, M.; Shumaker, D. K.; Luthi, A. J.; Helfand, B. T.; Ardehali, H.; Mirkin, C. A.; Volpert, O.; Thaxton, C. S., Biomimetic high density lipoprotein nanoparticles for nucleic acid delivery. *Nano letters* **2011,** *11*, 1208-1214.

15. Thaxton, C. S.; Daniel, W. L.; Giljohann, D. A.; Thomas, A. D.; Mirkin, C. A., Templated spherical high density lipoprotein nanoparticles. *J Am Chem Soc* **2009,** *131*, 1384-1385.

16. Yang, S.; Damiano, M. G.; Zhang, H.; Tripathy, S.; Luthi, A. J.; Rink, J. S.; Ugolkov, A. V.; A, T. K. S.; Dave, S. S.; Gordon, L. I.; Thaxton, C. S., Biomimetic, synthetic HDL nanostructures for lymphoma. *Proc. Natl. Acad. Sci. USA* **2013,** *110*, 2511-2516.

17. Smith, R. A.; Porteous, C. M.; Gane, A. M.; Murphy, M. P., Delivery of bioactive molecules to mitochondria in vivo. *Proc. Natl. Acad. Sci. USA* **2003,** *100*, 5407-5412.

18. Marrache, S.; Dhar, S., Engineering of blended nanoparticle platform for delivery of mitochondria-acting therapeutics. *Proc Natl Acad Sci USA* **2012,** *109*, 16288-16293.

19. Sempf, K.; Array, T.; Gelperina, S.; Schorge, T.; Meyer, B.; Karas, M.; Kreuter, J., Adsorption of plasma proteins on uncoated PLGA nanoparticles. *Eur. J. Pharm. Biopharm. e.V* **2013**.

20. Rodriguez-Sinovas, A.; Boengler, K.; Cabestrero, A.; Gres, P.; Morente, M.; Ruiz-Meana, M.; Konietzka, I.; Miro, E.; Totzeck, A.; Heusch, G.; Schulz, R.; Garcia-Dorado, D., Translocation of connexin 43 to the inner mitochondrial membrane of cardiomyocytes through the heat shock protein 90-dependent TOM pathway and its importance for cardioprotection. *Circ. Res.* **2006,** *99*, 93-101.

21. Benga, G.; Hodarnau, A.; Tilinca, R.; Porutiu, D.; Dancea, S.; Pop, V.; Wrigglesworth, J., Fractionation of human liver mitochondria: enzymic and morphological characterization of the inner and outer membranes as compared to rat liver mitochondria. *J. Cell Sci.* **1979,** *35*, 417-429.

22. Lee, H. B.; Blaufox, M. D., Blood-volume in the rat. *J Nucl Med* **1985,** *26*, 72-76.

23. Kontush, A.; Chapman, M. J., Functionally defective high-density lipoprotein: A new therapeutic target at the crossroads of dyslipidemia, inflammation, and atherosclerosis. *Pharmacol Rev* **2006,** *58*, 342-374.

24. Flotats, A.; Carrio, I., Non-invasive in vivo imaging of myocardial apoptosis and necrosis. *Eur J Nucl Med Mol I* **2003,** *30*, 615-630.

25. Kietselaer, B. L. J. H.; Reutelingsperger, C. P. M.; Heidendal, G. A. K.; Daemen, M. J. A. P.; Mess, W. H.; Hofstra, L.; Narula, J., Noninvasive detection of plaque instability with use of radiolabeled annexin A5 in patients with carotid-artery atherosclerosis. *New Engl J Med* **2004,** *350*, 1472-1473.

26. Green, D. R.; Kroemer, G., The pathophysiology of mitochondrial cell death. *Science* **2004,** *305*, 626-629.

27. Fitzpatrick, J. A.; Andreko, S. K.; Ernst, L. A.; Waggoner, A. S.; Ballou, B.; Bruchez, M. P., Long-term persistence and spectral blue shifting of quantum dots in vivo. *Nano letters* **2009,** *9*, 2736-2741.

28. Daerr, W. H.; Pethke, W.; Windler, E. T. E.; Greten, H., Biotinyl-high-density lipoproteins as a probe for the determination of high-density-lipoprotein turnover in humans. *Biochim Biophys Acta* **1990,** *1043*, 311-317.

29. Boden, W. E., High-density lipoprotein cholesterol as an independent risk factor in cardiovascular disease: Assessing the data from Framingham to the Veterans Affairs high-density lipoprotein intervention trial. *Am J Cardiol* **2000,** *86*, 19L-22L.

30. Marrache, S.; Dhar, S., Biodegradable synthetic high-density lipoprotein nanoparticles for atherosclerosis. *Proc. Natl. Acad. Sci. USA*. **2013,** *110*, 9445-9450.

CHAPTER 7

THE "ENERGY BLOCKER" INSIDE THE "POWER HOUSE": MITOCHONDRIA TARGETED DELIVERY OF 3-BROMOPYRUVATE[1]

[1]Marrache, S.; Dhar, S., *Submitted for publication*

ABSTRACT

A key hallmark of many aggressive cancers is accelerated glucose metabolism. The enzymes that catalyze the first step of glucose metabolism are hexokinases. Hexokinase 2 (HK2) is expressed at high level in cancer cells, but only in a limited number of normal adult tissues. Cancer cell mitochondrial alterations and metabolic reprogramming using the energy blocker, 3-bromopyruvate (3-BP) that inhibits HK2 could provide tumor-specific anticancer agents. However, the unique structural and functional characteristics of mitochondria prohibit selective subcellular targeting of 3-BP to modulate the function of this organelle for therapeutic gain. A mitochondria targeted gold nanoparticle (T-3-BP-AuNP) decorated with 3-BP and delocalized lipophilic triphenylphosphonium (TPP) cations to target the mitochondrial membrane potential ($\Delta\psi_m$) was developed for delivery of 3-BP to cancer cell mitochondria by taking advantage of higher $\Delta\psi_m$ in cancer cell mitochondria compared to normal cells. This construct showed remarkable anticancer activity in prostate cancer cells compared to non-targeted construct NT-3-BP-AuNP and free 3-BP. The anticancer activity of T-3-BP-AuNP was further enhanced upon laser irradiation by exciting the surface plasmon resonance band of AuNP and thereby utilizing a combination of 3-BP chemotherapeutic and AuNP photothermal effects. T-3-BP-AuNPs showed markedly enhanced ability to alter cancer cell metabolism by inhibiting glycolysis as well as demolishing mitochondrial oxidative phosphorylation in prostate cancer cells. Our findings demonstrated that concerted chemo-photothermal treatment of glycolytic cancer cells with a single NP capable of targeting mitochondria mediating simultaneous local release

of a glycolytic inhibitor and photothermal ablation may have promise as a new anticancer therapy.

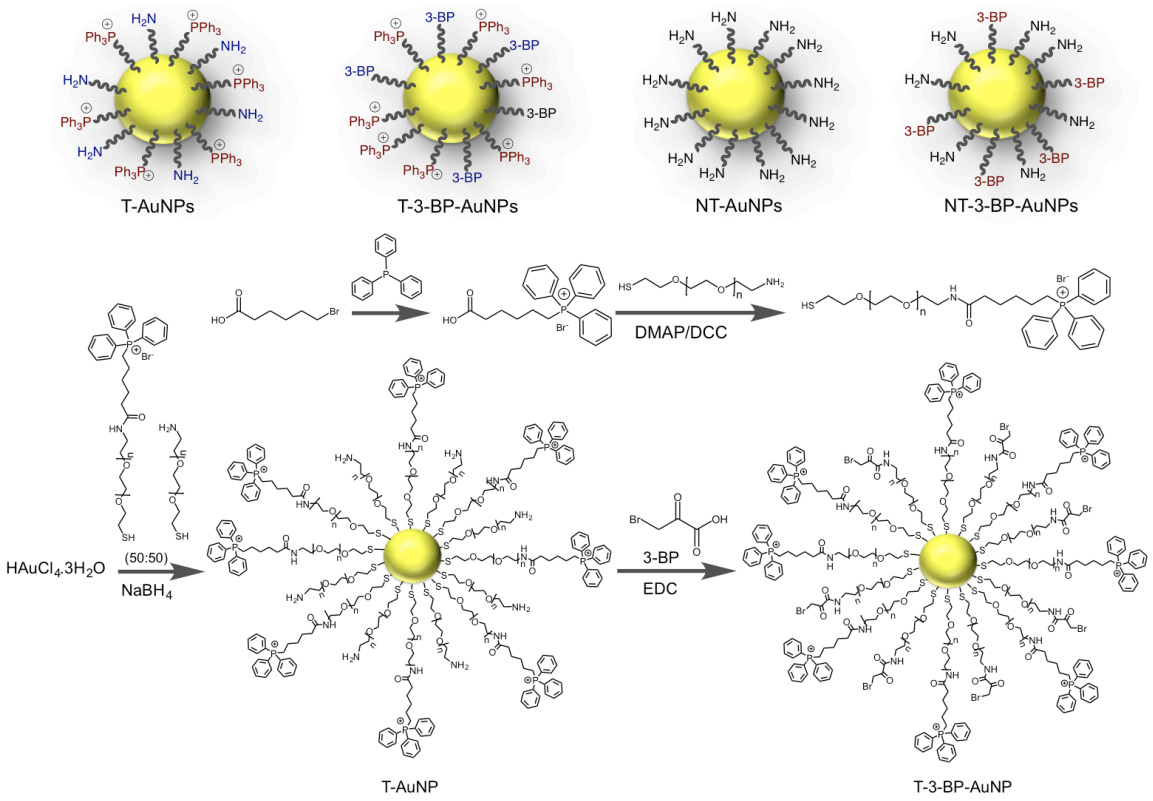
Introduction

The majority of cancers use aerobic glycolysis, which is accompanied by high rates of glucose consumption and lactate production, even when oxygen is available for oxidative phosphorylation (OXPHOS).[1-3] Hexokinase (HK) is a key enzyme involved in the first step of glycolysis pathway in transferring a phosphate group from adenosine triphosphate (ATP) to glucose to produce glucose-6-phosphate. There are four different isoforms HK2-4 in mammalian cells which show overall structural similarity but differ in their expression, subcellular localizations, and catalytic properties.[4] HK 1 and 2 with abilities to bind to mitochondria through their interaction with voltage dependent anion channel (VDAC) play significant roles in the mitochondria homeostasis.[5] The high glycolytic environment of aggressive cancers requires an up-regulation of the key glycolytic enzyme and significantly increased HK2 protein level is found in cancer cells. Approximately 80% of HK2 are associated with mitochondria though their interaction with VDAC in cancer cells. Mitochondria-bound HK2 can acquire the required ATP for glucose phosphorylation to accelerate the glycolytic rate and stimulate the tricarboxylic acid (TCA) cycle in the mitochondria. Interactions of VDAC and HK2 on the outer mitochondrial membrane (OMM) not only increase mitochondrial energy metabolism, but also down-regulate the apoptotic pathway by suppressing cytochrome c release. Increased association of HK2 with the mitochondria in cancer cells *via* VDAC, which has privileged access to mitochondrial ATP and regulates the opening of the mitochondrial permeability transition (MTP) pore, causes resistance to apoptosis for cancer cells. This

significant translocation of HK2 from cytoplasm to the OMM in cancer cells combined with its important roles in glycolytic pathway makes HK2 an attractive target for anticancer therapeutic modality development.[6] A brominated derivative of pyruvic acid, 3-bromopyruvate (3-BP) is an antitumoral alkylating agent that selectively kills cancer cells, leaving normal cells unharmed by inhibiting HK2.[7] 3-BP has the ability to suppress the glycolytic capacity of tumor by abolishing the activity of mitochondrial-bound HK2 and inhibiting mitochondrial respiration.[8] 3-BP also participates in the inhibition of mitochondrial succinate dehydrogenase, mitochondrial phosphate carrier (PIC), and adenine nucleotide carrier (ANC).

The characteristic alterations of mitochondrial function in cancer, association of HK2 to the OMM *via* VDAC, the ability of 3-BP in inhibition of HK2, and subsequent apoptosis of cancer cells led to many studies to evaluate the therapeutic potential of 3-BP. However, 3-BP showed limited clinical potential caused by non-specificity such as interaction with HK1 or other metabolic proteins and systemic toxicity. A recent study suggested that the cytotoxic effect of 3-BP is not a result of its inhibitory effects on glycolysis but rather its highly alkylating nature that is responsible for its activity.[9] Once inside cells, 3-BP has several non-glycolytic targets, such as V-ATPases, sarcoplasmic reticulum Ca^{2+}-ATPases, carbonic anhydrases, and histone deacetylases. A family of proton-coupled monocarboxylate transporters (MCTs) are involved in the transport of monocarboxylic acids such as lactate, pyruvate, butyrate, and acetate across the plasma membrane. Although these transporters are up-regulated in cancer cells to compensate the increased lactic acid production and consequent efflux by the cell, we hypothesized that 3-BP will face tremendous challenge for its uptake by the MCTs in cancer cells. To

circumvent this, mitochondria-targeted local delivery strategies can be extremely important to enhance overall treatment efficacy and to reduce toxic effects of 3-BP. A variety of targeted-nanoparticles (NPs) have the ability to take the current medicine to the next level by precise delivery, improving the pharmacokinetic (PK) and biodistribution (bioD) of small molecule based drugs. One of the most studied nanostructures in medicine is gold NPs (AuNPs) which can be constructed in different sizes, shapes, and have the ability to be decorated with drug molecules and targeting moieties. Furthermore, when AuNPs are illuminated with light of wavelengths of 650-900 nm, the photons will be strongly absorbed or scattered, the absorbed light can be transformed into heat, a process known as the photothermal effect causing an increase in temperature. The heat generated from the photothermal effect can be used to destroy cancer cells directly. With these properties in mind, we hypothesized that the use of a mitochondria-targeted AuNP delivery system for 3-BP will allow us to deliver this HK2 inhibitor specifically to mitochondria and subsequent laser irradiation will further enhance the therapeutic efficacy of the engineered construct by photothermal effect. In this article, we highlight the findings related to remarkable increase in anti-tumor activity of 3-BP by mitochondrial delivery using a triphenylphosphonium (TPP) cation modified AuNP (T-3-BP-AuNP), efficient inhibition of glycolysis, and subsequent changes in the mitochondrial bioenergetics (Scheme 7.1).



Scheme 7.1. Engineered AuNP and control NPs used in the mitochondria-targeted delivery of 3-BP. Synthesis of mitochondria-targeted TPP-modified PEG ligand, T-AuNP, and conjugation of 3-BP.

Materials and Methods.

All chemicals were received and used without further purification unless otherwise noted. Dicyclohexylcarbodiimide (DCC), 5-bromopentanoic acid, 4-dimethylaminopyridine (DMAP), $NaBH_4$, and (3-(4,5-dimethylthiazol-2-yl)-2,5-diphenyltetrazolium bromide (MTT), adenosine 5'-triphosphate (ATP) disodium salt hydrate, gold(III) chloride trihydrate ($HAuCl_4.3H_2O$), 30% hydrogen peroxide (H_2O_2), and etoposide were purchased from Sigma-Aldrich. 3-Bromopyruvic acid (3-BP) hydrate was purchased from Acros Organics. SH-polyethyleneglycol-NH_2 (SH-PEG-NH_2) of molecular weight of 3500 was obtained from JenKem Technology, USA. Potassium

iodide (KI), Ethyl(dimethylaminopropyl) carbodiimide (EDC) and *N*-hydroxysuccinimide (NHS) were procured from Sigma-Aldrich. Spectra/Por® Dialysis membranes with a molecular weight cutoff of 5000 Da were purchased from Spectrum® Labs. Alexa Fluor® 488 Annexin V/Dead cell apoptosis kit was purchased from Invitrogen. Lactate assay kit was obtained from BioVision, CA, USA. CellTiter-Glo® luminescent cell viability assay kit from Promega was used to quantify cellular ATP content. The Ambion® KDalert™ Glyceraldehyde 3-phosphate dehydrogenase (GAPDH) assay kit was purchased from Life Technologies. Interleukin (IL)-6 and tumor necrosis factor (TNF)-α cytokines were tested using BD OptEIA mouse enzyme-linked immunosorbent assay (ELISA) kits. Ultra pure lipopolysaccharide (LPS) was purchased from Invivogen, CA, USA. Bicinchoninic acid (BCA) protein assay kit (Pierce 23227) was purchased from Thermo Scientific. Human hexokinase 2 (HK2) was procured from Sigma-Aldrich. Protease from *Streptomyces griseus* was purchased from Sigma-Aldrich. The mitochondrial isolation kit for mammalian cells was purchased from Thermo Scientific.

Distilled water was purified by passage through a Millipore Milli-Q Biocel water purification system (18.2 MΩ) containing a 0.22 μm filter. ^{1}H, ^{13}C spectra were recorded on a 400 MHz Varian NMR spectrometer. ^{31}P NMR spectrum was recorded on a 500 MHz Varian NMR spectrometer using phosphoric acid as a standard. Dynamic light scattering (DLS) measurements were carried out using a Malvern Zetasizer Nano ZS system. Transmission electron microscopy (TEM) images were taken in a Tecnai 20 FEM microscope. Laser irradiation was performed using a Melles Griot 660 nm 56 ICS series diode laser equipped with a fiber optic cable in a dark environment. Optical

measurements were carried out on a NanoDrop 2000 spectrophotometer. Flow cytometry studies were performed on a BD LSRII flow cytometer equipped with digital acquisition using FACSDiva v6. Plate reader analysis was performed on a Bio-Tek Synergy HT microplate reader. Bioenergetic assays were carried out using a Seahorse XF24 analyzer (Seahorse Biosciences, North Billerica, MA, USA).

Cell Line and Cell Culture.

Human prostate cancer PC3, DU145 cells and RAW 264.7 macrophages were procured from the American type culture collection (ATCC). DU145 cells were grown at 37 °C in 5% CO_2 in Eagle's minimum essential medium (EMEM) supplemented with 10% fetal bovine serum (FBS) and 1% penicillin/streptomycin. PC3 cells were grown in Roswell Park Memorial Institute (RPMI) 1640 medium supplemented with supplemented with supplemented with 10% FBS and 1% penicillin/streptomycin. RAW 264.7 macrophages were cultured in RPMI media supplemented with 10% FBS and 1% penicillin/streptomycin. Cells were passed every 3 to 4 days and restarted from frozen stocks upon reaching pass number 20.

Synthesis of TPP-$(CH_2)_5$-COOH.

6-Bromohexanoic acid (0.5 g, 2.6 mmol) and triphenylphosphine (0.7 g, 2.7 mmol) were dissolved in acetonitrile (15 mL). The resulting mixture was heated to a reflux under nitrogen flow for 24 h. The solution was cooled to room temperature and concentrated under reduced pressure. The resulting viscous oil was washed with hexanes (2 x 15 mL) and diethyl ether (3 x 15 mL) to produce a white solid (0.85 g, 87% yield). ^{1}H NMR ($CDCl_3$): δ 7.8-7.6 [m, 15], 3.52 [t, 2H], 2.3 [t, 2H], 1.61 [m, 6H] ppm. ^{13}C

NMR ($CDCl_3$): δ 175, 135.2, 133.4, 130.2, 118.5, 34.3, 29.5, 23.9, 22.8, 22.4, 22.1 ppm. ^{31}P NMR ($CDCl_3$): δ 24.39 ppm.

Synthesis of SH-PEG-TPP.

SH-PEG-NH_2 (0.2 g, 0.0571 mmol), TPP-$(CH_2)_5$-COOH (0.043 g, 0.1142 mmol), and 4-dimethylaminopyridine (DMAP) (0.014 g, 0.1142 mmol) were dissolved in 7 mL CH_2Cl_2, cooled to 0 °C while spinning, and a solution of dicyclohexylcarbodiimide (DCC) (0.024 g, 0.1142 mmol) in 1 mL CH_2Cl_2 was added. The mixture was warmed to room temperature and stirred overnight. The reaction by-product, dicyclohexylurea (DCU) precipitated was filtered off and the filtrate was precipitated in chilled diethyl ether. The resulting solid was centrifuged at 5000 revolutions per minute (rpm) for 15 min. The supernatant was decanted off and the resulting solid was lyophilized to result white solid. Yield: 50 % (0.11 g). ^1H NMR ($CDCl_3$): δ 7.82-7.57 [m, 15], 3.81 [m, 2H], 3.71 [m, 2H], 3.64 [m, 414], 2.88 [m, 2H], 1.73 [m, 2H] ppm. ^{13}C NMR ($CDCl_3$): δ 207.15, 131.51, 131.48, 129.99, 129.9, 126.95, 126.83, 66.9 ppm. ^{31}P NMR ($CDCl_3$): δ 24.63 ppm.

Synthesis of T and NT-AuNPs.

For T-AuNP synthesis, a solution of SH-PEG-TPP (0.1 g, 0.25 mmol) and SH-PEG-NH_2 (0.1 g, 0.25 mmol) were prepared in 15 mL H_2O and gold(III) chloride trihydrate ($HAuCl_4 \cdot 3H_2O$) (0.05 g, 0.12 mmol) was added. This mixture was vigorously stirred for 10 min until all of the gold salt was dissolved. The reduction was carried out by adding drop wise a freshly prepared aqueous solution of sodium borohydride (0.05 g, 1.2 mmol in 3 mL H_2O) with vigorous stirring and 15 mL of deionized (DI) water was then added to the mixture. After 24 h, the solution was dialyzed using a Spectra/Por®

dialysis membrane of MW cutoff of 5,000 Da against H_2O for 12 h. The water was changed every hour. The NPs were further purified by differential centrifugation at 7,000 RPMs for 30 min. After centrifugation the supernatant was kept and the pellet was discarded to obtain monodispersed T-Au-NPs. The non-targeted NPs, NT-Au-NPs were prepared following the same synthetic method as mentioned for T-AuNPs using SH-PEG-NH_2 (0.2 g, 0.5 mmol) and $HAuCl_4.3H_2O$ (0.05 g, 0.12 mmol).

Synthesis of T-3-BP-AuNPs and NT-3-BP-AuNPs.

3-BP was conjugated to the surface of the T-AuNP and NT-AuNP surface by EDC/NHS coupling. 3-BP (30 mg, 0.18 mmol), *N*-hydroxysuccinimide (NHS) (39 mg, 0.12 mmol), and ethyl(dimethylaminopropyl) carbodiimide (EDC) (30 mg, 0.18 mmol) were dissolved in H_2O (5 mL). 3-BP was allowed to activate for 6 h at 25 °C. To this, T-AuNPs or NT-AuNPs (10 mg/mL, 5 mL) was added and stirred overnight at 25 °C. NPs were purified by dialysis (MW cutoff of 2,000 Da) against water for 8 h changing the water every hour. NPs were lyophilized and resuspended in nanopure water.

Determination of 3-BP Loading by GADPH Assay.

The activity of 3-BP on GAPDH was used to determine 3-BP loading on AuNPs using a KDalert™ GAPDH assay kit. GAPDH was treated with predetermined concentration of 3-BP to generate a standard curve (Figure S6). AuNPs (100 μL, 10 mg/mL) were treated with 1.0 mM potassium iodide (KI) to dissolve the gold core and then 10 μL of the NPs were then added to GADPH enzyme (10 μL, 0.133 U/mL) and subjected to the activity assay. The NP/GADPH enzyme suspension (10 μL) was then added to the KDalert™ master mix (90 μL) in a 96 well plate. The mixture was then

gently shaken to ensure full mixing and the fluorescence was measured (emission: 560 nm, excitation: 590 nm).

Immune Response from NPs in RAW 264.7 Macrophages by ELISA.

RAW 264.7 macrophages were plated at a concentration of 50,000 cells/mL in 96 well plates and allowed to grow for 12 h. The cells were incubated with T-AuNP (10 mg/mL), NT-AuNP (10 mg/mL) for 24 h at 37 °C. Additionally, LPS alone (100 ng/mL) was added to the macrophage culture to serve as a control. ELISA was performed on the supernatants against the pro-inflammatory cytokines IL-6 and TNF-α. Antibody coated plates were prepared by treating ELISA compatible thermo scientific Nunc 96-well plates with the antibody for 12 h at 4 °C and then blocked with 10% FBS in PBS for 1 h at room temperature followed by 5 washings with the washing buffer (1X PBS with 0.05% v/v Tween® 20). Macrophage supernatants (100 μL) were incubated to the plates and incubated for 2 h at room temperature, followed by 5 washes with the washing buffer and sequential incubations with the cytokine-biotin conjugate and streptavidin working solution. The substrate reagent containing 3,3',5,5' tetramethylbenzidine (100 μL) was then added to each well, incubated for 15 min, and the reaction was stopped by adding 50 μL stop solution containing 0.1 M H_2SO_4. The absorbance was recorded at 450 nm using a BioTek Synergy HT well plate reader.

Release of 3-BP from T-3BP-AuNP and NT-3-BP-AuNP.

The ability of 3-BP to be cleaved from the NP surface was tested by using proteases from *Streptomyces griseus* type XIV. T-3-BP-AuNP and NT-3-BP-AuNPs (10 mg/mL with respect to AuNP and 1.4 mM with respect to 3-BP) were treated with 0.5 mg/mL of protease in water for up to 6 h at 37 °C with gentle shaking. At a

predetermined time point, the NPs were isolated by repeated centrifugations and resusensions in nanopure water while discarding the supernatant each time at 12,000 rpms for 30 min. The resulting pellet was resuspended in 100 μL water and the amount of 3-BP was quantified by KDalert™ GADPH assay described above.

HK2 Binding Assay.

HK2 binding ability of T and NT 3-BP loaded AuNPs was tested by using human HK2 recombinant of molecular mass 104.1 kDa expressed in *Escherichia coli*. T-3-BP-AuNP and NT-3-BP-AuNPs (10 mg/mL with respect to AuNP and 1.4 mM with respect to 3-BP) were treated with 10 UG/mL of HK2 in water for 1 h at 37 °C. HK2 bound NPs were then centrifuged at 12000 RPM for 30 min and supernatants were discarded to remove unbound HK2. This process was repeated 3 times and finally the NP pellet obtained was resuspended in water. BCA assay directly on the HK2-bound to AuNP did not show any signal. Therefore, the Au core was dissolved using 1 mM KI and BCA assay was performed to quantify the amount of HK2 bound to 3-BP. A standard curve was constructed using BSA. For protease mediated cleavage of HK2-loaded AuNPs, these NPs were treated with proteases for 12 hand subsequently BCA assay was performed.

Quantification of AuNPs in the Mitochondrial Compartments.

PC3 cells were grown at a density of 5×10^5/mL in 30 mL RPMI media overnight in T-150 flask. The media was changed and T-AuNPs or NT-AuNPs were added (1 mg/mL) and incubated for 12 h. The media was changed and the cells were rinsed with 1x phosphate buffered saline (PBS) (3x). The cells were isolated by trypsinization and centrifuged for 3 min at 1,800 RPMs. The final cell suspension was resuspended in

reagent A from the mitochondria isolation kit for mammalian cells and incubated on ice for 2 min. After 2 min, reagent B (10 μL) was added and incubated on ice for 5 min, vortexing each min. These cells were treated with reagent C and the cells were centrifuged at 700×g for 10 min. The resulting supernatant was collected containing the mitochondrial and cytosolic fractions. This was further centrifuged at 12,000×g for 15 min at 4 °C to yield a mitochondrial pellet and the cytosolic supernatant. The resulting pellet was further purified with a washing and centrifugation at 12,000×g for 5 min to yield the mitochondrial fraction. These fractions were analyzed for the amount of gold by ICP-MS and the amount of protein recovered by BCA assay. To evaluate the exact location of the T-AuNPs and T-3-BP-AuNPs within the mitochondria, the mitochondria were further fractionated. PC3 cells were grown at a density of $5x10^5$/mL in 30 mL RPMI media overnight in T-150 flask. The media was changed and T-AuNPs or T-3-BP-AuNPs were added (1 mg/mL) and incubated for either 4 or 12 h. After the given time, the cells were trypsinized and repeatedly washed with PBS at 1,800 RPM for 3 min. The mitochondria were isolated as described above. This was further subfractionated into the OMM, the intermembrane space, the IMM, and the matrix. The freshly isolated PC3 mitochondria in PBS (1x) were incubated with protease inhibitor (0.125 mg/mL) and 0.6% digitonin for 10 min on ice. Immediately after incubation, the mitochondria were centrifuged at 10,000xg for 10 min at 4 °C. The supernatant (SN-I) contained the OMM fraction and the interstitial membrane space. The pellet was resuspended in 150 mmol/L KCl, protease inhibitor (0.125 mg/mL) and incubated on ice for 10 min. This was centrifuged at 10,000 xG for 10 min at 4 ^{0}C. The supernatant, which contained the mitochondrial matrix, was collected. To this, 50 µL of 1x cell lysis buffer (30 mM Tris-

HCl, 0.1 mM EDTA, 20 % w/v sucrose) was added. This was subsequently sonicated and centrifuged at 10,000 g for 15 min at 4 °C. The supernatant (SN-II) was collected, containing the purified IMM fraction and matrix. SN-I and SN-II were centrifuged at 105,000xg for 60 min. The pellet from SN-I contained the OMM fraction and the supernatant contained the interstitial membrane space. The pellet from SN-II was resuspended in PBS containing Lubrol WX (0.5 mg/mL), 37 % sucrose and incubated for 15 min on ice. This was once again centrifuged at 105,000xg for 60 min at 4 °C. The pellet was collected containing the IMM fraction and the supernatant contained the matrix. The collected fractions were analyzed for Au concentration by ICP-MS. A BCA assay was performed on all the fractions in order to calculate the Cd (ng)/protein (pg).

Cellular TEM Studies.

PC3 cells were plated on a 6-well plate at a density of 0.5 x 10^6 and allowed to attach and grow over night. The media was changed, AuNPs were added (T-AuNPs and NT-AuNPs, 1 mg/mL), and the cells were incubated for 12 h at 37 °C. The cells were washed 3x with 1X PBS to remove AuNPs that had not internalized. The cells were trypsinized followed by 3 washes by centrifugation (4 °C, 1,800 rpm, 3 min). These cells were then fixed with 1% glutaraldehyde for 1 h at room temperature followed by 3 washes with 1X PBS. Fixation was followed by a counter fixation with 1% osmium tetroxide for 1 h at room temperature. The residual osmium tetroxide was removed by repeated washing with PBS and water. The cells were then transitioned into 100% ethanol in a series of incubation (10 min per incubation, RT) increasing the ethanol percentage by 25 each time. Once in 100% ethanol, the cells were transitioned to 100% propylene oxide increasing by 50% each incubation (30 min/incubation, RT). To ensure

the residual ethanol was removed, the cells were then washed with 100% propylene oxide (3 times, room temperature, 10 min/wash). The cells were then infiltrated with EmBed 812 resin by slowly increasing the amount of resin in propylene oxide by 25% each incubation (1 h/incubation, RT). The samples in fresh 100% resin were placed in an oven at 60 °C overnight in order to polymerize the resin. The hardened blocks were then trimmed and sectioned on an ultramicrotome to a thickness of ~50 nm. The sections were collected on a copper grid and imaged on a JEM-1210 Transmission Electron Microscope equipped with a XR41C bottom-mount CCD camera.

MTT Assay and Data Analysis.

Cytotoxicity profiles of T-AuNPs, NT-AuNPs, T-3-BP-AuNPs, NT-3-BP-AuNPs, and 3-BP were studied using the MTT assay against prostate cancer PC3 and DU145 cell lines. Cells (2000 cells/well) were seeded on a 96-well plate in 100 μL of desired medium and incubated for 24 h. The cells were then treated with different constructs at varying concentrations and incubated for 12 h at 37 °C and the media was changed. The cells were further incubated for additional 60 h at 37 °C under 5% CO_2. For photothermal MTT studies, after 4 h treatment of cells with NPs, the cells were irradiated with 660 nm laser (power 20.0 mV) light with a fiber optics for 1 min per well and the irradiated cells were incubated for 12 h at 37 °C, followed by a media change and further incubation for 60 h. The cells were then treated with 20 μL of MTT (5 mg/mL in PBS) for 5 h. The medium was removed, the cells were lysed with 100 μL of DMSO, and the absorbance of the purple formazan was recorded at 550 nm using a Bio-Tek Synergy HT microplate reader and background absorbance was measured at 800 nm. Each well was performed in triplicate and each experiment was repeated three times. Cytotoxicity was expressed as

mean percentage increase relative to the unexposed control ± standard deviation (SD). Control values were set at 0% cytotoxicity or 100% cell viability. Cytotoxicity data (where appropriate) was fitted to a sigmoidal curve and a three parameters logistic model used to calculate the IC_{50}, which is the concentration of chemotherapeutics causing 50% inhibition in comparison to untreated controls. The mean IC_{50} is the concentration of agent that reduces cell growth by 50% under the experimental conditions and is the average from at least three independent measurements that were reproducible and statistically significant. The IC_{50} values were reported at ±95% confidence intervals (check your confidence level when you fit the data in Prism and correct accordingly). This analysis was performed with GraphPad Prism (San Diego, U.S.A).

Apoptosis Detection by Flow Cytometry.

PC3 cells were plated at a density of 1×10^6 cells/mL and allowed to grow for 14 h. Media was changed and cells were treated with T-AuNP (1 mg/mL), NT-AuNP (1 mg/mL), T-3-BP-AuNP (14.1 μg/mL with respect to NP, 10 μM with respect to 3-BP), NT-3-BP-AuNP (13.7 μg/mL with respect to NP, 10 μM with respect to 3-BP), free 3-BP (10 μM or 1 mM) for 6 h at 37 °C. As positive controls, etoposide (100 μM, incubation time: 12 h) for apoptosis and H_2O_2 (1 mM, incubation time: 45 min) for necrosis were used. For apoptosis detection after laser treatment, cells were treated with T-AuNP (1 mg/mL), NT-AuNP (1 mg/mL), T-3-BP-AuNP (14.1 μg/mL with respect to NP, 10 μM with respect to 3-BP), NT-3-BP-AuNP (13.7 μg/mL with respect to NP, 10 μM with respect to 3-BP), free 3-BP (10 μM) for 4 h at 37 °C, irradiated with laser of 660 nm for 1 min, and further incubated for 12 h. Cells were trypsinized, washed 3 times with cold 1x PBS, and centrifuged at 1800 rpm for 3 min, and the supernatants were discarded. Cells

were counted and resuspended in 1X annexin-binding buffer at a density of ~1 × 10^6 cells/mL preparing a sufficient volume to have 100 μL per assay. To 100 μL of cell suspension, 5 μL Alexa Fluor® 488 annexin V and 1 μL 100 µg/mL PI working solution were added, incubated for 15 min at room temperature, followed by addition of 400 μL 1X annexin-binding buffer, gently mixing in ice, and the samples were analyzed on the flow cytometer immediately.

Lactate Determination.

PC3 cells were seeded at a density of 1×10^6 cells/mL and allowed to grow for 12 h at 37 °C under 5% CO_2. Cells were treated with T-AuNP (1 mg/mL), NT-AuNP (1 mg/mL), T-3-BP-AuNP (14.1 µg/mL with respect to NP, 10 μM with respect to 3-BP), NT-3-BP-AuNP (13.7 µg/mL with respect to NP, 10 μM with respect to 3-BP), free 3-BP (10 μM) for 6 h at 37 °C. After 6 h, the media was removed and the cells were homogenized. The lysate and the media supernatant were added to the enzyme and substrate working reagent mixture and incubated for 30 min. Lactate concentration was measured using Bio-Tek Synergy HT microplate reader at 450 nm and comparing to a standard curve.

CellTiter-Glo® Luminescent ATP Quantification.

PC3 cells were seeded at a density of 1×10^6 cells/mL in a 12 well plate and allowed to grow for 12 h at 37 °C under 5% CO_2. Cells were treated with T-AuNP (1 mg/mL), NT-AuNP (1 mg/mL), T-3-BP-AuNP (14.1 µg/mL with respect to NP, 10 μM with respect to 3-BP), NT-3-BP-AuNP (13.7 µg/mL with respect to NP, 10 μM with respect to 3-BP), free 3-BP (10 μM) for 6 h at 37 °C in 5% CO_2 atmosphere. Control wells containing medium without cells were used to obtain background luminescence

value. Plates were then equilibrated at room temperature for ~30 min. A volume of CellTiter-Glo reagent equal to the volume of cell culture medium present in each well was added, this mixtures were mixed for 2 min in a shaker to induce cell lysis. The plates were incubated at room temperature for additional 10 min to stabilize luminescent signal. Luminescence was recorded using a plate reader. ATP quantification was carried out from a standard curve using ATP disodium salt hydrate.

Bioenergetic Assay.

Prior to the assay, XF sensor cartridges were hydrated. To each well of an XF utility plate, 1 mL of Seahorse Bioscience calibrant was added and the XF sensor cartridges were placed on top of the utility plate, and kept at 37 °C incubator without CO_2 for a minimum of 12 h. PC3 cells were cultured in XF24-well cell culture microplates (Seahorse Bioscience) at a density of 5×10^4 cells/well (0.32 cm^2) in 200 μL growth medium and then incubated for 24 h at 37 °C in 5% CO_2 atmosphere. The three key parameters of glycolytic function: glycolysis, glycolytic capacity, and glycolytic reserve were assessed using a Seahorse XF glycolysis stress kit. After the cells were attached, an additional 100 μL growth medium was added and the cells were incubated for 24 h at 37 °C in 5% CO_2 atmosphere. The cells were treated with T-3-BP-AuNP (10 μM with respect to 3-BP), NT-3-BP-AuNP (10 μM with respect to 3-BP), and 3-BP (10 μM) for 6 h at 37 °C in 5% CO_2 atmosphere. After 6 h, all but 50 μL of the culture medium was removed from each well and the cells were rinsed two times with 600 μL of XF stress test glycolysis optimization medium pre-warmed to 37 °C and finally 610 μL of glucose depleted optimization medium was added to each well and the plate was placed at 37 °C without CO_2 for 1 h prior to assay. The OCR and the ECAR were measured

simultaneously for 16 min to establish a baseline rate. Glycolysis, glycolytic capacity, and glycolytic reserve were calculated by subtracting the average rates before and after the addition of glucose (10 mM), ATP synthase inhibitor oligomycin (1.0 μM), and 2-deoxy-D-glucose (2-DG) (100 mM). These three compounds were injected consecutively with specific time gap and ECAR values were measured after each injection. Different parameters of respiration: basal respiration, coupling efficiency, and spare respiratory capacity were investigated by using Seahorse XF-24 cell Mito Stress Test Kit. PC3 cells were plated and treated with different constructs as mentioned above. After 6 h incubation with the constructs, the media was changed as above with the optimization media supplemented with sodium pyruvate, L-glutamine, and D-glucose to a final volume of 500 µL. Different parameters of respiration were calculated by subtracting the average respiration rates before and after the addition of the electron transport inhibitors oligomycin (1.0 μM), FCCP (1.0 μM), an ionophore that is a mobile ion carrier, and a mixture of antimycin-A (1.0 μM) which is a complex III inhibitor and rotenone (1.0 μM), a mitochondrial inhibitor that prevents the transfer of electrons from the Fe-S center in Complex I to ubiquinone. The parameters calculated included: basal respiration (baseline respiration minus antimycin-A post injection respiration), ATP turnover (baseline respiration minus oligomycin post injection respiration), maximal respiratory capacity (FCCP stimulated respiration minus antimycin-A post injection respiration) and reserve respiratory capacity (FCCP stimulated respiration minus baseline respiration). Test articles on each well had five replicates.

In Vivo BioD and PK of AuNPs.

BioD and PK properties of T-AuNP and NT-AuNP were determined using male Sprague Dawley rats weighing around ~300 g. Two rats per group, had T-AuNPs and NT-AuNPs (for T-AuNPs: 16 mg/kg with respect to total NP, 2.7 μg/kg with respect to Au; NT-AuNPs: 8.3 mg/kg with respect to total NP, 2.7 μg/kg with respect to Au) or saline. At varying time intervals, blood samples were collected in herparinized tubes and centrifuged in order to collect blood plasma. The percentage of Au was calculated by taking into consideration that blood constitutes 7% of body weight and plasma constitutes 55% of blood volume.[10] The amount of Au from the AuNPs was calculated in the blood plasma by ICP-MS. After 24 h, the animals were sacrificed and the vital organs were collected. The collective urine and feces were also collected over a 24 h period. The overall bioD was calculated by analyzing the amount of Au in each organ as well as the feces and urine by ICP-MS. Before analysis, the liver samples were dissolved in PerkinElmer solvable (product number: 6NE9100). Other organs and feces were dissolved in concentrated HNO_3 for 24 h with gentle heating and shaking. The calculations for AUC, C_{max}, T_{max}, and C_L (t=0) were performed in the GraphPad Prism (version 5.01). PK parameters were determined by fitting the data using one-compartmental model equation.

RESULTS AND DISCUSSION

AuNPs for Targeted Delivery of 3-BP.

AuNPs are widely used in delivery of therapeutics due to their unique surface chemistry, tunable size, shape, and optical properties.[11-14] However, one of the important issues in clinical translation of AuNPs is their toxicological effect. A recent study

demonstrated that unmodified citrate coated AuNPs can cause inhibition of cell proliferation in a concentration and size dependent manner.[15] Therefore, it is very important to design a biocompatible surface functionalized AuNP for delivery of 3-BP inside the mitochondria. Poly(ethylene glycol) (PEG) is extensively used to protect surfaces from nonspecific interactions with biomolecules.[16] To deliver 3-BP inside the mitochondria, we constructed AuNPs with surface covered lipophilic cationic –TPP moieties attached to PEG (Figures 7.1-3).

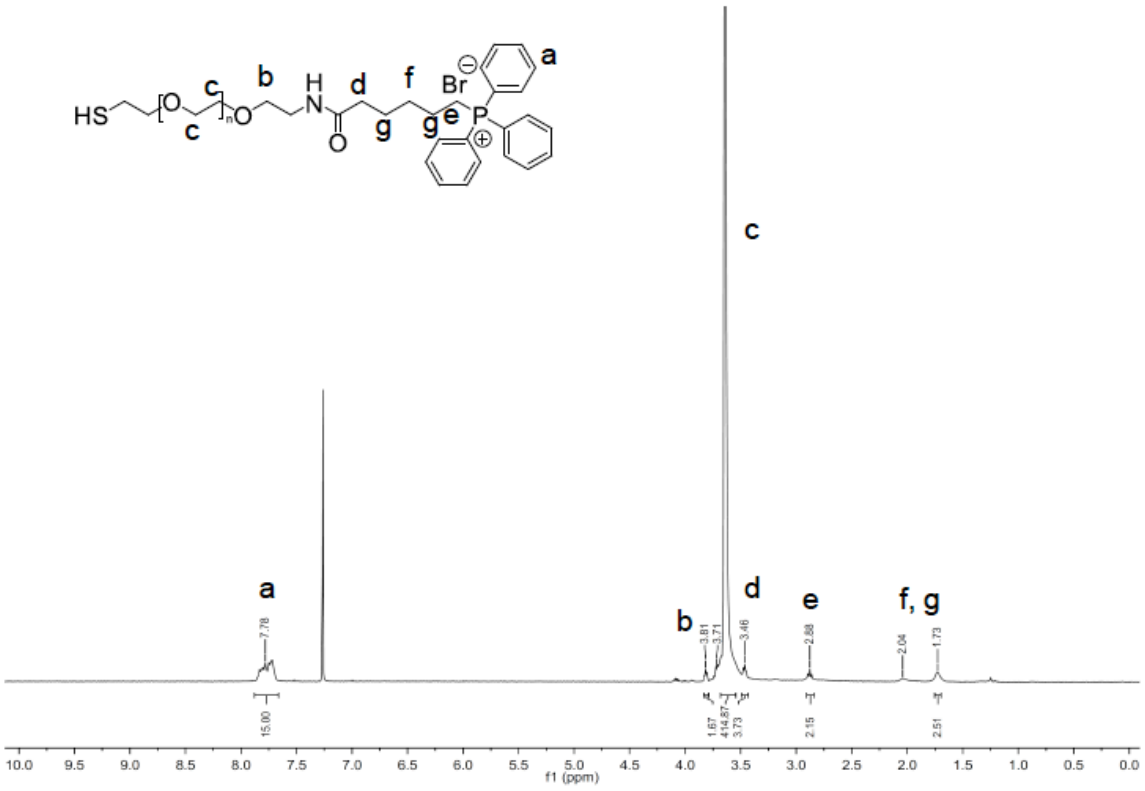


Figure 7.1. ^{1}H NMR of TPP-PEG-SH in $CDCl_3$

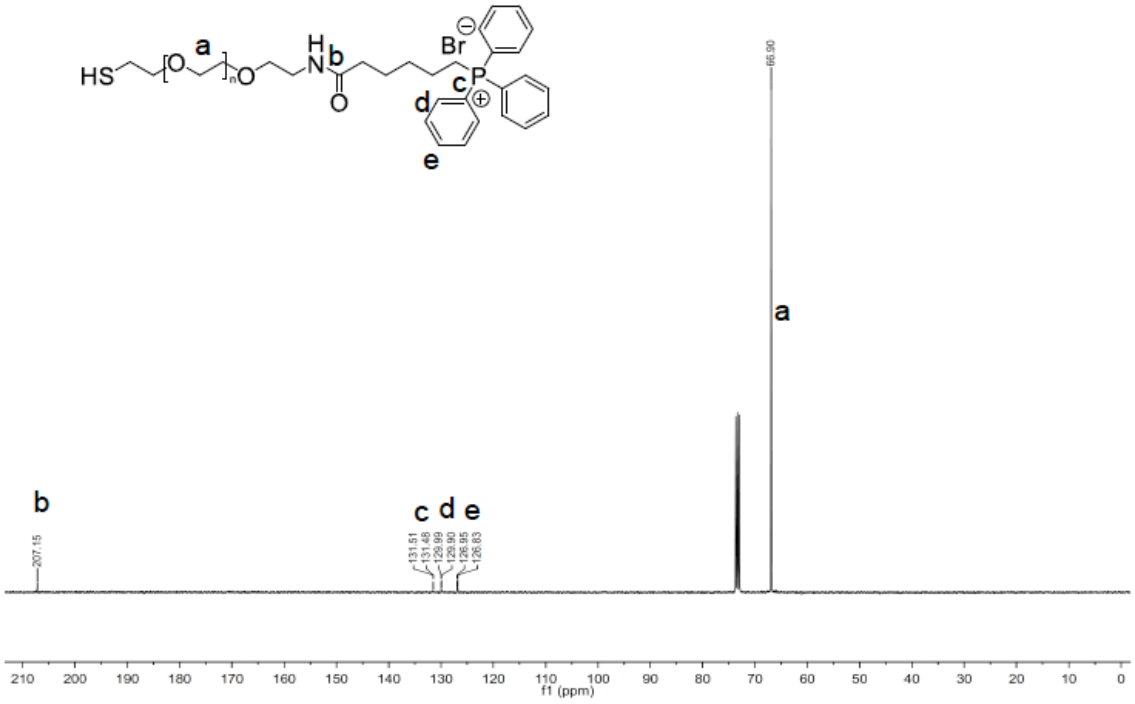


Figure 7.2. ^{13}C NMR of TPP-PEG-SH in $CDCl_3$

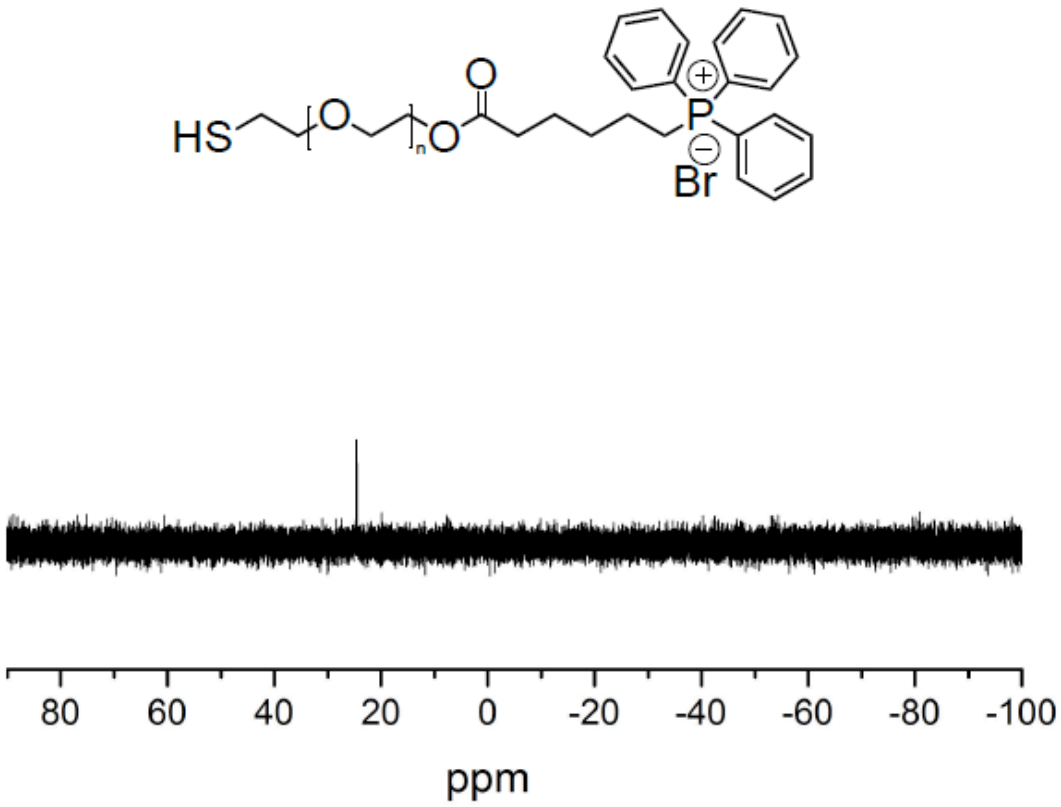


Figure 7.3. ^{31}P NMR of TPP-PEG-SH in $CDCl_3$

The lipophilic TPP cations easily permeate lipid bilayers driven by the plasma membrane potential (-30–60 mV negative inside) to enter cytoplasm and then concentrated several hundred-fold into mitochondria by the large mitochondrial membrane potential ($\Delta\psi_m$) (-150-180 mV negative inside) maintained across the inner mitochondrial membrane (IMM). To construct T-AuNPs, we synthesized TPP-PEG-SH by reacting NH_2-PEG-SH with TPP-$(CH_2)_5$-COOH (Scheme 7.1, Figure 7.4-7.5).

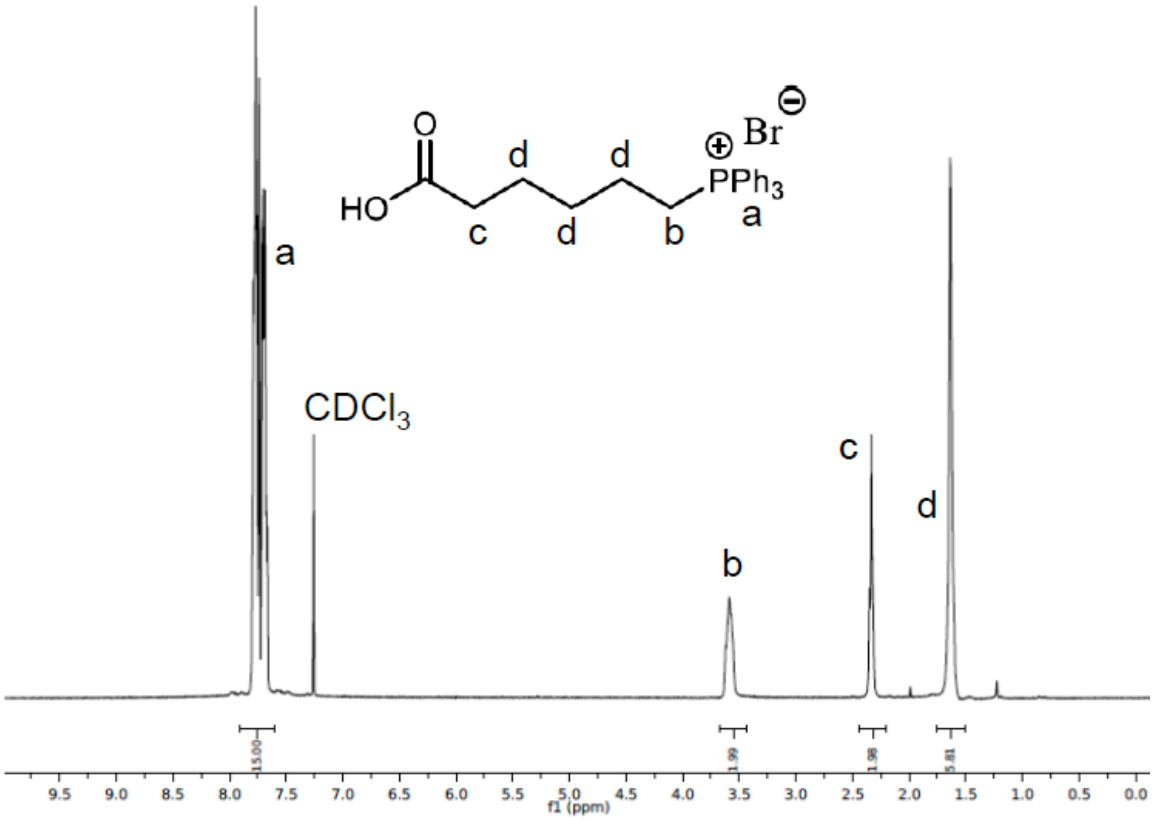


Figure 7.4. ^{1}H NMR of TPP-$(CH_2)_5$-COOH

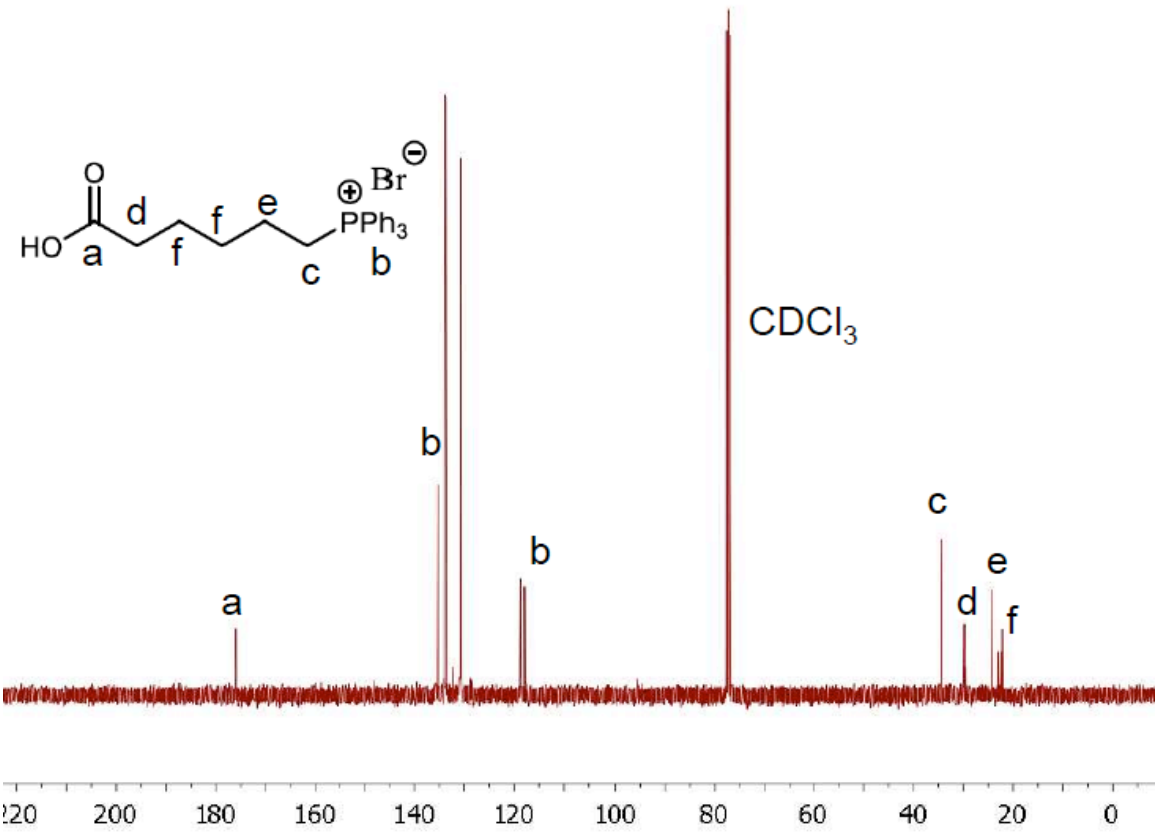


Figure 7.5. ^{13}C NMR of TPP-$(CH_2)_5$-COOH

The –TPP group in TPP-PEG-SH allowed for mitochondria targeting and the –SH group allowed for easy manipulation of AuNP surface. T-AuNPs were synthesized through the reduction of $HAuCl_4 \cdot 3H_2O$ and simultaneous stabilization with a mixture of NH_2-PEG-SH and TPP-PEG-SH. The amine groups from T-AuNPs were used to conjugate 3-BP using a standard amide coupling reaction to result T-3-BP-AuNPs (Scheme 7.1).

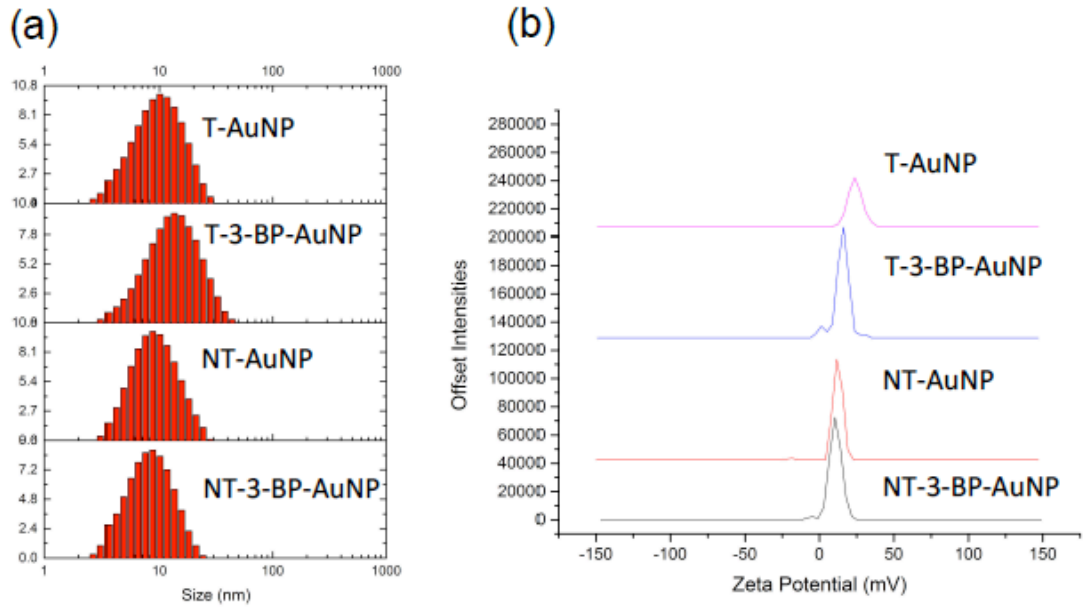


Figure 7.6. Overlay of DLS for (a) hydrodynamic diameter and (b) zeta potential of different NPs.

To investigate the advantages of delivering 3-BP inside mitochondria, we constructed non-targeted system, NT-AuNPs as control. NT-AuNPs were constructed from $HAuCl_4 \cdot 3H_2O$ using NH_2-PEG-SH and the amine groups were used to conjugate 3-BP to generated NT-3-BP-AuNPs. AuNPs were characterized by dynamic light scattering (DLS), zeta potential measurements, and by TEM (Figures 7.7A, 7.7B, Figure 7.6, and Table 7.1).

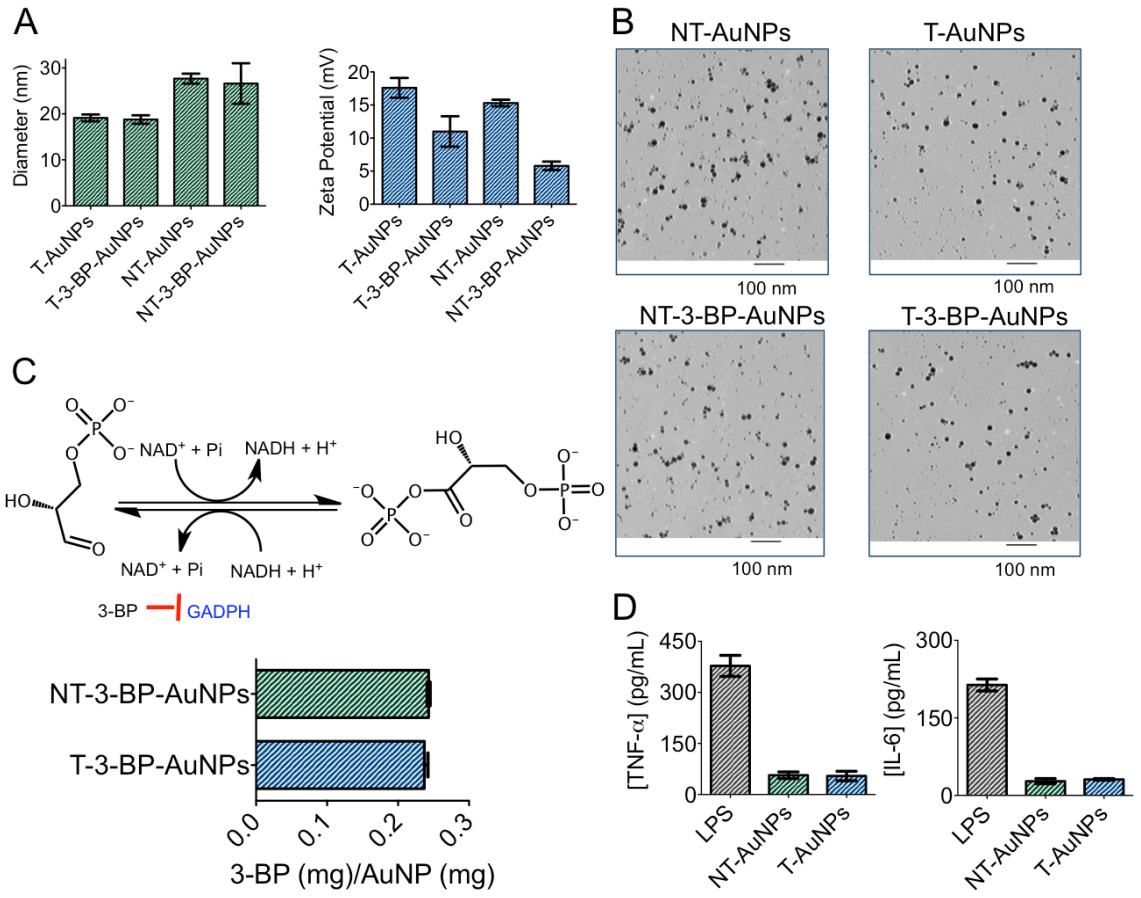


Figure 7.7. (A) Characterization of different AuNPs by DLS. (B) TEM of AuNPs. (C) Quantification of 3-BP by GADPH assay. (D) Non-immunogenic behavior of NT and T-AuNPs by ELISA.

The intensity-weighted average or the Z average of these NPs were mostly between 20 to 30 nm and were narrowly distributed. In our previous studies, we demonstrated that positively charged NPs of suitable size have the ability to enter mitochondria of cells, whereas negatively charged particles or NPs which are not highly positively charged or larger in size mostly distribute in the cytosols.[17, 18] Zeta potential measurements indicated that T-AuNP surface is positively charged and conjugation of 3-BP on the surface does not change the surface charge. Non-targeted NPs showed positive zeta potential and conjugation of 3-BP diminished the positive charge by ~10 mV.

Table 7.1 Characterization of AuNPs, data presented here is an average of three independent preparations

NP System	Z-Average (nm)	Number Average Diameter (nm)	PDI	Zeta Potential (mV)	% 3-BP Loading	% Coupling Efficiency 3-BP
T-AuNP	19.1 ± 0.8	3.1 ± 0.8	0.38	17.6 ± 1.5	-	-
T-3-BP-AuNP	18.8 ± 0.9	4.3 ± 0.7	0.31	11.0 ± 2.3	23.7 ± 0.5	7.9 ± 0.2
NT-AuNP	27.7 ± 1.1	2.9 ± 0.2	0.39	15.3 ± 0.5	-	-
NT-3-BP-AuNP	26.6 ± 4.4	3.1 ± 0.9	0.19	5.8 ± 0.7	24.3 ± 0.2	8.1 ± 0.1

The small sizes and high positively charged surface coated with highly lipophilic cationic TPP moieties in T-3-BP-AuNPs will play significant roles in their navigation to the mitochondria. The morphology of these NPs was mostly spherical as demonstrated by TEM, with few NPs were found to be of irregular shapes (Figure 7.7C). To demonstrate the versatility in biomedical applications, the dispersion stability these AuNPs was evaluated by freeze drying the NPs and assessing the formation of aggregates and change in color upon making aqueous suspension at a concentration of 10 mg/mL. No visible aggregation or changes in the color was observed (Figure 7.8) and the resuspended NPs demonstrated similar sizes and zeta potential.

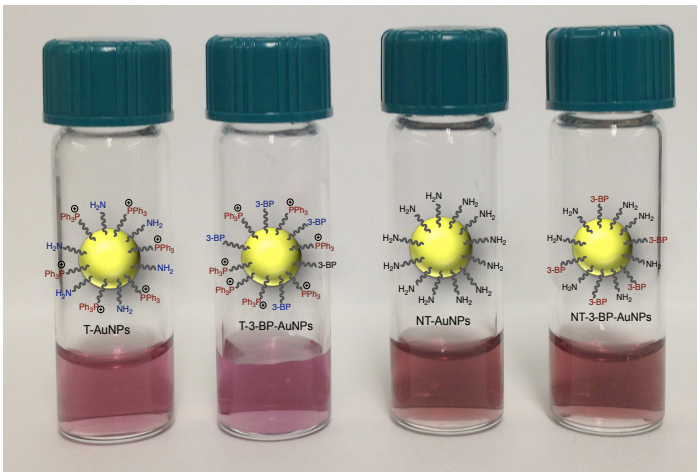


Figure 7.8. Photographs of T-AuNPs, T-3-BP-AuNPs, NT-AuNPs, and NT-3-BP-AuNPs after resuspension in water.

The T and NT-AuNPs showed strong absorption band at 540 and 523 nm, respectively those correspond to excitation of surface plasmon band (Figure 7.9). Upon conjugation of 3-BP on the surface of both T and NT-AuNPs, no broadening or red shift of the surface plasmon band was observed indicating that no aggregation of the AuNPs occurred during surface modification.

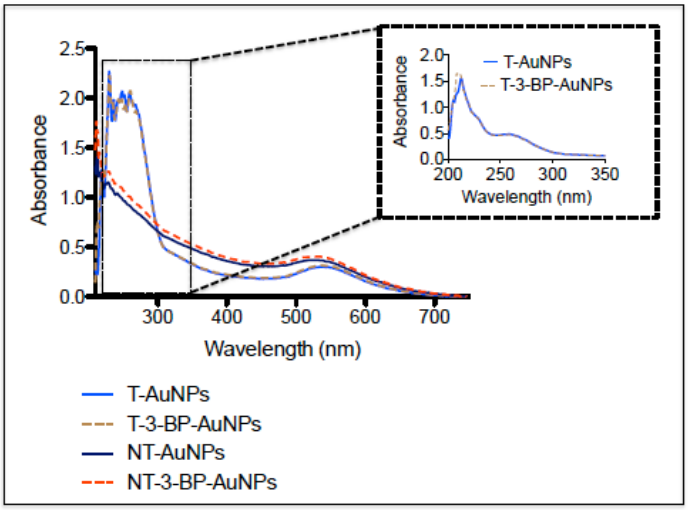


Figure 7.9. UV-Vis characterization of T and NT-AuNPs showing the absence of any aggregation with inset showing the TPP peaks from T-AuNPs.

It is challenging to quantify 3-BP in AuNPs using conventional analytical methods. We therefore devised an enzyme inhibition assay to quantify coupling efficiency of 3-BP on NP surface based on the fact that glyceraldehyde-3-phosphate dehydrogenase (GAPDH) is an intracellular target of 3-BP (Figure 7.6C). Pyruvylation of GADPH by 3-BP causes inhibition of the enzymatic function. The enzyme activity of GAPDH can be determined using a KDalert™ GAPDH assay kit. Generation of a standard curve by treating GAPDH with known concentrations of 3-BP, dissolution of Au core of T and NT-3-BP-AuNPs with KI, and subsequent treatment with GADPH allowed us to quantify amount of 3-BP present on the NP surface (Figure 7.6B). Similar coupling efficiencies of 3-BP on the surface of T and NT-AuNPs were noted (~8%).

Macrophages are one of the principal immune effector cells, hence the immunological response of RAW264.7 macrophage cells when exposed to T and NT-AuNPs was studied by following the production of pro-inflammatory cytokines tumor necrosis factor alfa (TNF-α) and interleukine-6 (IL-6) (Figure 7.9D) using enzyme-linked immunosorbent assay (ELISA). Neither the control cells nor the cells treated with T and NT-AuNPs showed any secretion of either TNF-α or IL-6. Although both the cytokines were detected in the cells treated with bacterial lipopolysaccharide (LPS) as control (Figure 7.1D). These results indicated that the AuNPs do not elicit immunological response and do not induce production of pro-inflammatory cytokines even at high concentrations.

Protease Dependent Release of 3-BP from AuNPs.

3-BP can be a multitasking agent if it can be delivered to cancer cell, its mitochondria, and released at the target sites. For inhibition of cytosolic glycolysis, 3-BP

directly alkylates HK2 by reacting with the –SH groups from Cys 158 and Cys 606 which are present in the enzyme active sites. 3-BP has the ability to block mitochondrial OXPHOS. The terminal step of OXPHOS in making ATP in the mitochondria requires an ATP synthase (F(0)F(1)) comprised of two motors, PIC and ANC which carry phosphate and adenine nucleotide for ATP synthesis, respectively. 3-BP alkylates PIC and ANC that results in halting the final step of OXPHOS. Conformational changes associated with VDAC bound HK2 leads to its direct dissociation from the mitochondria that promotes mitochondrial injury provoked by pro-apoptotic proteins. Specific release of apoptosis-inducing factor (AIF), cytochrome c from the mitochondria to cytosol leads to eventual cell death. For successful execution of these processes, 3-BP needs to be released from the AuNPs at the target sites. In T-3-BP-AuNPs and NT-3-BP-AuNPs, 3-BP was conjugated to the AuNP surface *via* amide bonds in order to take advantage of the cellular proteases to catalyze the hydrolysis of these linkages to release 3-BP. Moreover, various proteases within mitochondria regulate mitochondrial biogenesis to ensure complete degradation of excess or damaged proteins. To test 3-BP release profile from the AuNPs in presence of proteases, T-3-BP-AuNP and NT-3-BP-AuNP were treated with proteases from *Streptomyces griseus* type XIV at 37 °C and the concentration of 3-BP released was followed using the GADPH assay (Figure 7.10).

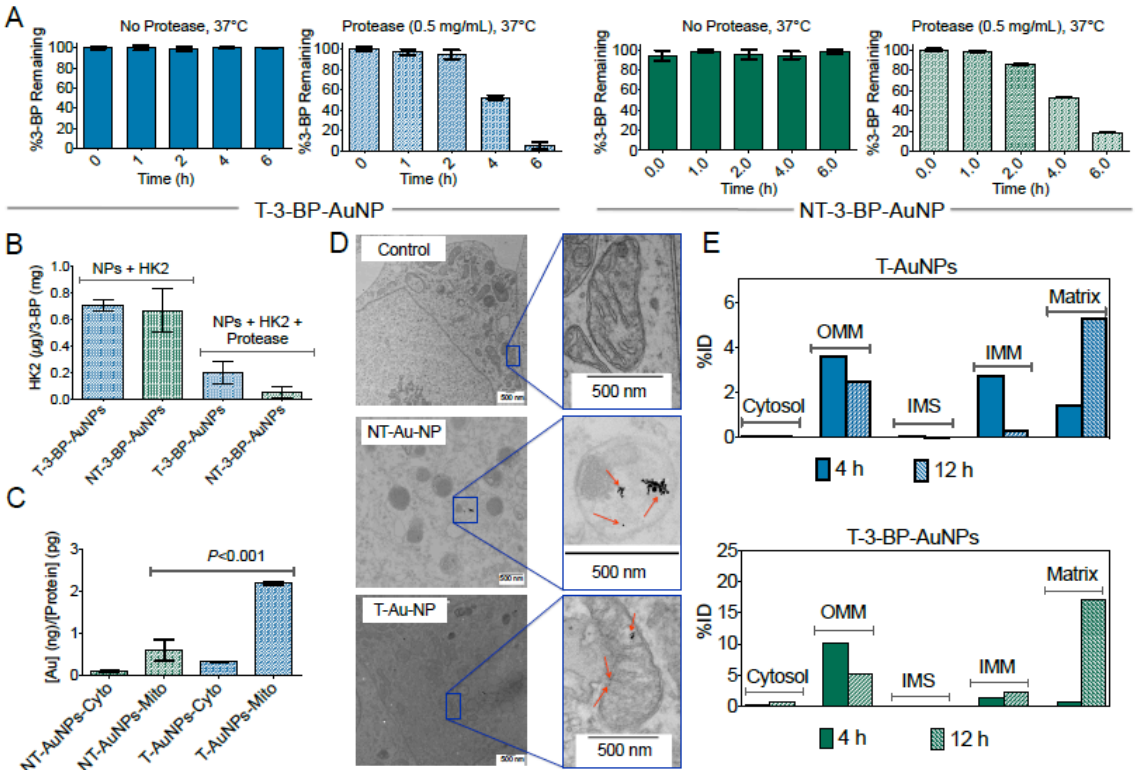


Figure 7.10. (A) Protease dependent release of 3-BP from T and NT-AuNPs. (B) HK2 binding profile of T-3-BP-AuNPs and NT-3-BP-AuNPs. (C) ICP-MS and (D) cellular TEM Mitochondrial. (E) time-dependent distribution of T-AuNPs and T-3-BP-AuNPs in different mitochondrial compartments of PC3 cells. Cyto: Cytosolic fraction; Mito: Mitochondrial fraction. The data are presented as percent-injected dose (%ID).

In the absence of protease, no release of 3-BP from T-AuNP or NT-AuNP was observed under these conditions. In the presence of 0.5 mg/mL protease, ~50% of 3-BP was released from both T and NT-AuNPs in 4 h and complete release of 3-BP was observed after 6 h. Thus, based on the available data on protease-induced release of 3-BP from these NPs in a time dependent manner, we believe that some 3-BP will be released in the cytosol by the cytosolic proteases (Figure 7.10A). T-3-BP-NPs that will enter mitochondria will take advantage of high concentration of proteases in the mitochondrial matrix for 3-BP release.

HK2 Binding Affinity of Released 3-BP from T- and NT-AuNPs.

The ability of 3-BPs from T-3-BP-AuNPs and NT-3-BP-AuNPs to covalently modify HK2 was tested using human HK2 recombinant of molecular mass 104.1 kDa expressed in *Escherichia coli*. Incubation of HK2 with T-3-BP-AuNPs and NT-3-BP-AuNPs, quantification of 3-BP-bound HK2 using the bicinchoninic acid (BCA) assay after dissolving the Au core with potassium iodide (KI) indicated that 3-BP from both T and NT-AuNPs has the ability to covalently bind to HK2 (Figure 7.10B). Incubation of HK2 bound AuNPs with protease and subsequent protein quantification by BCA assay showed less protein concentration further confirming that 3-BP from AuNPs has the ability to inhibit HK2 (Figure 7.11B).

Intracellular Location of T-3-BP-AuNPs.

3-BP has several intracellular targets, thus the distribution of the T-AuNPs is the key factor in determining the efficacy of 3-BP. Where T-AuNPs or NT-AuNPs are located is essential information for understanding intracellular compartmentation of 3-BP. We first investigated distribution of NT and T-AuNPs in the mitochondria and cytosol in prostate cancer (PCa) PC3 cells. Treatment of these cells with the NPs for 12 h, isolation of mitochondrial (mito) and cytosolic (cyto) fractions, and quantification of gold by inductively coupled plasma mass spectrometry (ICP-MS) indicated that the overall uptake of T-AuNPs is higher than that of NT-AuNPs (Figure 7.10C). Most of T-AuNPs are associated with the mitochondria. Only a small fraction of NT-AuNPs were associated with the mitochondria which might be attributed from the positively charged amine groups on the surface of these NPs. Highly lipophilic cationic –TPP groups are responsible for greater association of T-AuNPs with the mitochondria. We next assessed

the exact location of T-AuNPs and T-3-BP-AuNPs inside the mitochondria and investigated the time dependency of the mitochondrial compartmentalization (Fig. 7.10D). PC3 cells were treated with T-AuNPs and T-3-BP-AuNPs for two time points, 4 h and 12 h, and mitochondrial sufractions, OMM, IMM, intermembrane space, and matrix were isolated from the treated cells at both the time points, and gold was quantified in these fractions by ICP-MS (Figure 7.10E). T-AuNPs and T-3-BP-AuNPs show very similar patterns in their mitochondrial distribution; however, the overall concentrations of T-3-BP-AuNPs were higher in the mitochondrial compartments compared to the T-AuNPs without ant 3-BP. At early stage after 4 h incubation both T-AuNPs and T-3-BP-AuNPs were found in the OMM and at 12 h, almost all T-AuNPs and T-3-BP-AuNPs were located inside the matrix. These observations indicated that the T-3-BP-AuNPs distributed in the OMM will be able to modify HK2 bound to VDAC. Complete localization of the T-3-BP-AuNPs at 12 h might also be due to opening of the VDACs upon deactivation of HK2 by 3-BPs. Intra-mitochondrial distribution patterns of T-3-BP-AuNPs in a time dependent manner indicated that 3-BP delivered by T-AuNPs will be able to attack all of its intracellular targets for maximum efficacy.

Anti-proliferative Effects of T-3-BP-AuNPs.

We determined the effect of these AuNPs on the proliferation of two different PCa cell lines-PC3 and DU145 cells by the 3-(4,5-dimethylthiazol-2-yl)-2,5-diphenyltetrazolium bromide (MTT) assay. The widely used PCa cell lines PC3 and DU145 show differences in their metabolic phenotype. Both DU145 and PC3 lines have higher rates of lactate production, however these cell lines differed in glycolytic rate. PC3 cells show higher mRNA levels for all glycolytic enzymes studied. The glycolytic

reliance of PC3 and DU145 cells is believed to be due to OXPHOS insufficiency and the reduced reliance on OXPHOS is due to a mitochondrial dysfunction. T-3-BP-AuNPs exhibited the highest efficacy at 72 h in inhibiting the proliferation of both PC3 and DU145 cells, NT-3-BP-AuNPs demonstrated significantly reduced inhibition compared to the T-3-BP-AuNPs, free 3-BP showed only a modest inhibition whereas no inhibition was observed with T-AuNPs and NT-AuNPs without 3-BP (Figure 7.11A, Table 7.1). Moreover, T-3-BP-AuNPs demonstrated an enhanced cytotoxic activity when combined with a 660 nm laser irradiation than NT-3-BP-AuNPs or free 3-BP plus laser treatment. It was very interesting to note that T-AuNPs without any 3-BP showed an enhanced cytotoxicity under laser irradiation, whereas the NT-AuNPs did not show any significant toxicity in presence of photo-irradiation (Figure 7.11B, Table 7.1). These findings suggested that the higher accumulation of T-AuNPs inside mitochondria might be responsible for its toxicity under photo-irradiation by inducing local mitochondrial toxicity. These results together support that T-AuNP is highly effective for selective delivery of 3-BP and T-3-BP-AuNPs demonstrated interaction between chemotherapy and photothermal effect.

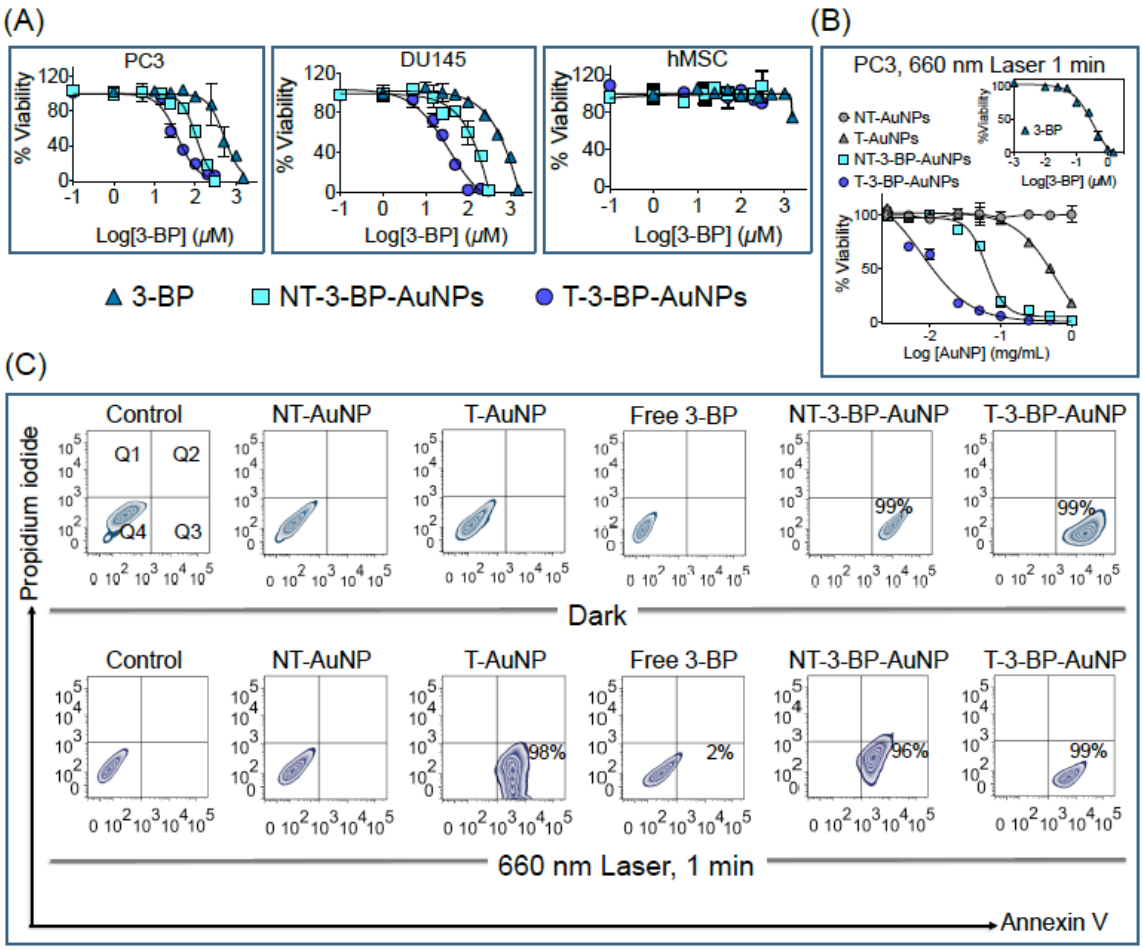


Figure 7.11. (A) Cells viability in PC3 and DU145 cells after treatment with T-AuNPs, NT-AuNPs, 3-BP, T-3-BP-AuNPs, NT-3-BP-AuNPs. Cell viability was assessed by the MTT assay after treatment with the indicated concentrations of the test articles for 72 h. The data are mean ± SD (n = 3 wells). (B) Cells viability in PC3 cells after treatment with T-AuNPs, NT-AuNPs, 3-BP, T-3-BP-AuNPs, NT-3-BP-AuNPs followed by 660 nm laser radiation for 1 min/well. The data are mean ± SD (n = 3 wells). (C) (Top) Apoptotic patterns induced in PC3 cells upon treatment with T-AuNP (1 mg/mL), NT-AuNP (1 mg/mL), T-3-BP-AuNP (14.1 µg/mL with respect to NP, 10 μM with respect to 3-BP), NT-3-BP-AuNP (13.7 µg/mL with respect to NP, 10 μM with respect to 3-BP), free 3-BP (10 μM) for 6 h at 37 °C in the dark. (Bottom) Apoptosis induced in PC3 cells upon

treatment with T-AuNP (1 mg/mL), NT-AuNP (1 mg/mL), T-3-BP-AuNP (14.1 µg/mL with respect to NP, 10 μM with respect to 3-BP), NT-3-BP-AuNP (13.7 µg/mL with respect to NP, 10 μM with respect to 3-BP), free 3-BP (10 μM) for 4 h at 37 °C, followed by irradiation with 660 nm laser for 1 min, and further incubated for 12 h. Annexin V-PI assay results are presented in quadrants as analyzed by flow cytometry. The *x*-axis represents Alexa Fluor® 488 annexin V and the *y*-axis represents PI. Living cells accumulate in Q4 (Annexin V and PI negative), cells undergoing apoptosis accumulate in Q3 (Annexin V positive and PI negative), cells in end-stage apoptosis or necrotic stage accumulate in Q2 (Annexin V and PI positive).

Induction of apoptosis is an important mechanism whereby 3-BP can suppress tumorigenesis. Several studies demonstrated that 3-BP can induce apoptosis in variety types of cancer cells.[19, 20] The pro-apoptotic effect of T-3-BP-AuNPs, NT-3-BP-AuNPs, and free 3-BP was studied in PC3 cells using Alexa Fluor® 488 annexin V-propidium iodide (PI) assay by flow cytometry both in the dark and in presence of 660 nm laser irradiation for 1 min (Figure 7.11C). Treatment of PC3 cells with T- and NT-3-BP-AuNPs showed increased percentage of apoptotic cells from 0% in control group to 99%. No necrotic cell population was noted in the T and NT-3-BP-AuNP cells. Free 3-BP under same conditions with a concentration of 10 μM was unable to show any apoptotic activity, however at a much higher concentration of 1 mM, significant apoptosis was observed in 3-BP treated PC3 cells (Figure 7.12).

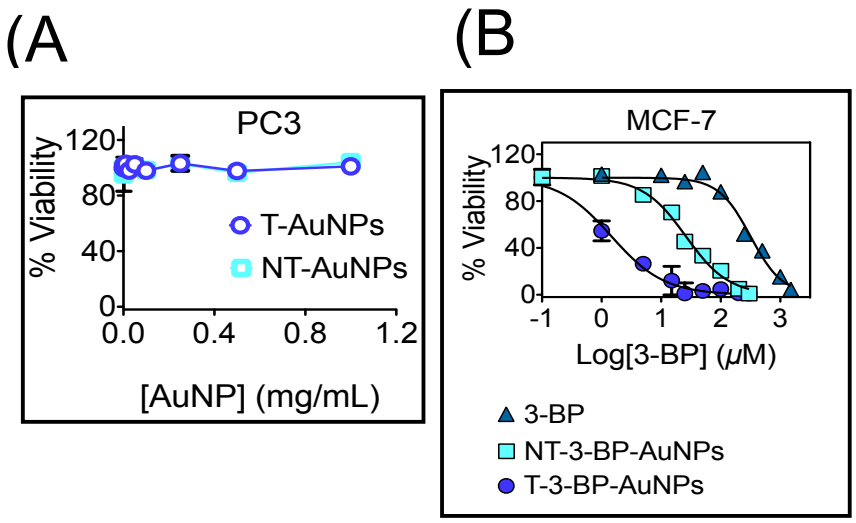


Figure 7.12. (A) Cell viability in PC3 cells after treatment with T-AuNPs, NT-AuNPs. (B) Cell viability in MCF-7 cells after treatment with 3-BP, T-3-BP-AuNPs, and NT-3-BP-AuNPs. Cell viability was assessed by the MTT assay after treatment with the indicated concentrations of the test articles for 72 h. The data are mean ± SD (n = 3 wells).

Under photo-irradiation with a 660 nm laser for 1 min, T-AuNPs with the ability to accumulate in the mitochondria showed apoptotic activity. The apoptosis inducing properties of T-3-BP-AuNPs and NT-3-BP-AuNPs were found to be very similar (Figure 7.12C). Our data thus suggest that 3-BP can promote apoptosis at a much lower concentration when delivered with a mitochondria-targeted delivery system and use of AuNPs as delivery system further enhances its activity by utilizing photothermal activity of gold nanocrystals.

Table 7.2. IC_{50} with standard deviation calculated from three independent experiments

	PC3[a] (μM)	DU145[a] (μM)	MCF-7[a] (μM)	PC3 + Laser[b] (μg/mL)
T-AuNPs	N/A	N/A	N/A	550±90
NT-AuNPs	N/A	N/A	N/A	N/A
3-BP	271±9	541±37	274±36	N/A
T-3-BP-AuNPs	13±3	28±8	1.4±0.4	10±3
NT-3-BP-AuNPs	45±6	109±7	29±4	60±3

[a]With respect to 3-BP; [b]With respect to AuNP

Lactate Reduction and ATP Depletion.

The final product of glycolysis is lactate. Hence, we quantified intracellular and extracellular lactate levels in PC3 cell lines treated with 3-BP, T-3-BP-AuNPs, NT-3-BP-AuNPs; the NPs without 3-BP, T-AuNP and NT-AuNPs were used as controls. Extracellular lactate levels were found to be much higher than those observed in the cells (Figures 7.13A and 7.13B). Our results showed that the levels of both intracellular and extracellular lactate declined with treatment with free 3-BP, T-3-BP-AuNPs, and NT-3-BP-AuNPs. This decrease was more significant in cells which were treated with T-3-BP-AuNPs compared to the cells treated with either 3-BP or 3-BP conjugated to NT-AuNPs (Figures 7.13A and 7.13B). Treatment with T-3-BP-AuNPs, NT-3-BP-AuNPs, and 3-BP showed a decrease in the level of ATP in PC3 cells (Figure 7.13C). The PC3 cells were found to be much more sensitive to T-3-BP-AuNPs than free 3-BP or NT-3-BP-AuNPs as inferred from the intracellular ATP levels at 6 h (Figure 7.13C). The present data showed T-3-BP-AuNPs has the ability to show depletion of ATP and reduction in lactate levels at lower 3-BP concentrations compared to free 3-BP or NT-3-BP-AuNPs. These

observations further supports the importance of delivering 3-BP to the mitochondria can be beneficial in modulation of its efficacy.

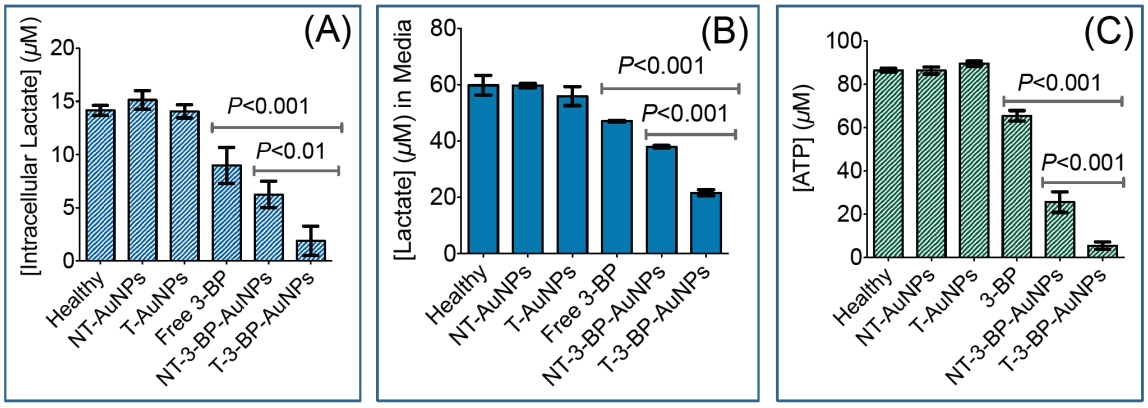


Figure 7.13. Intracellular (A) and extracellular (B) lactate levels in PC3 cells after treatment with T-AuNP (1 mg/mL), NT-AuNP (1 mg/mL), T-3-BP-AuNP (14.1 µg/mL with respect to NP, 10 μM with respect to 3-BP), NT-3-BP-AuNP (13.7 µg/mL with respect to NP, 10 μM with respect to 3-BP), free 3-BP (10 μM) for 6 h at 37 °C. (C) Changes in intracellular ATP content in PC3 cells after treatment with T-AuNP (1 mg/mL), NT-AuNP (1 mg/mL), T-3-BP-AuNP (14.1 µg/mL with respect to NP, 10 μM with respect to 3-BP), NT-3-BP-AuNP (13.7 µg/mL with respect to NP, 10 μM with respect to 3-BP), free 3-BP (10 μM) for 6 h at 37 °C in 5% CO_2 atmosphere. Results are represented as mean ± SD (n=3). Statistical analyses were performed by using one-way ANOVA with Tukey post hoc test.

Perturbation of Bioenergetic Functions of PC3 Cells by T-3-BP-AuNPs.

We performed real-time measurements of extracellular acidification rate (ECAR), an indicator of glycolysis and oxygen consumption rate (OCR) which is a marker of OXPHOS in PC3 cells after treatment with T-3-BP-AuNPs, NT-3-BP-AuNPs, and free 3-BP using a Seahorse XF24 extracellular flux analyzer (Figure 7.14). After measuring the

basal rates of OCR and ECAR in the treated cells, pharmacologic inhibitors of glycolysis and the mitochondrial respiratory chain were injected. Glycolytic parameters were calculated by monitoring changes in ECAR in response to sequential addition of D-glucose to assess glycolysis, oligomycin to measure maximal glycolytic capacity, and 2-deoxy-D-glucose (2-DG) as a measure of glycolytic reserve capacity (Figures 7.8A and 7.8B). Administration of excess of glucose to T-3-BP-AuNP treated PC3 cells in glucose-depleted medium showed only modest increase in the ECAR levels indicating remarkable activity of T-3-BP-AuNPs in glycolysis inhibition. Under similar conditions, 3-BP delivered by NT-AuNPs showed less efficiency in glycolysis inhibition and free 3-BP at this low concentration of 10 μM did not show any glycolysis inhibitory effect (Figure 7.14A).

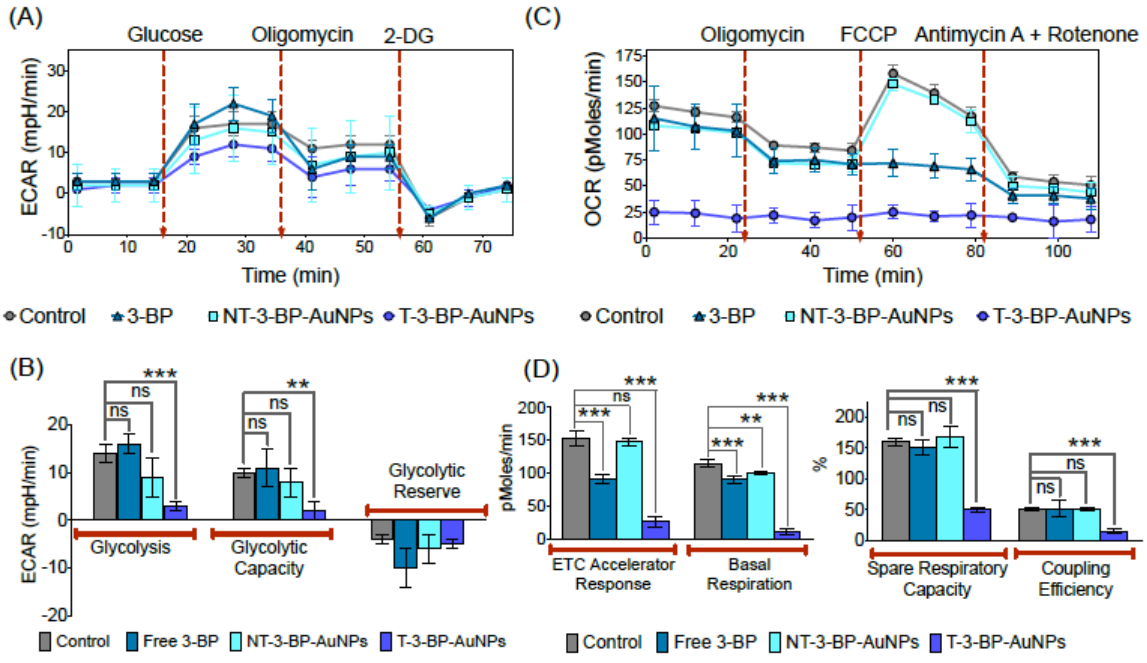


Figure 7.14. Bioenergetics analysis in PC3 cell line. (A) A representative graph of ECAR output from XF24 analyzer of control, T-3-BP-AuNP, NT-3-BP-AuNP, and free 3-BP treated PC3 cells and its response to glucose, oligomycin, and 2-DG and (B) comparison

of glycolysis, glycolytic capacity, and glycolytic reserve in the treated cells. (C) A representative graph of OCR output from XF24 analyzer of control, T-3-BP-AuNP, NT-3-BP-AuNP, and free 3-BP treated PC3 cells and its response to oligomycin, FCCP, antimycin A/rotenone and comparison of (D) spare respiratory capacity, coupling efficiency, and (E) ETC accelerator response and basal respiration in the treated cells.

Significant inhibition of glycolysis by T-3-BP-AuNPs in PC3 cells was further supported by sequential administration oligomycin and 2-DG, the cells treated with T-3-BP-AuNPs did not show any significant changes in the ECAR levels. These data demonstrated remarkable ability of 3-BP at a low concentration of 10 μM in inhibition of glycolysis only when delivered with a mitochondria-targeted delivery system. We next assessed the effects of T-3-BP-AuNPs on the mitochondrial OXPHOS pathway and compared the results when 3-BP was either delivered with a NT-AuNP or in the free form (Figures 7.14C-E). By following the changes in the OCR values (Figure 7.9C) in response to oligomycin to give maximal glycolytic capacity, carbonyl cyanide 4-trifluoromethoxy-phenylhydrazone (FCCP), an uncoupling agent that allows maximum electron transport and therefore a measure of maximum OXPHOS respiration capacity and a combination of mitochondrial complex III inhibitor antimycin A and mitochondrial complex I inhibitor rotenone that allow precise measurement of mitochondrial uncoupling, spare respiratory capacity, coupling efficiency, ETC accelerator response, and basal respiration (Figures 7.14D and 7.14E) were measured. Significant decrease in the OCR in the PC3 cells that were treated with T-3-BP-AuNPs was noted. We believe that the origin of this reduction is due to the ability of T-3-BP-AuNPs to target mitochondria-bound HK2 leading to loss of the mitochondrial integrity. Free 3-BP

however has no preference for mitochondrial and cytosolic HK2. NT-3-BP-AuNPs showed preference for cytosolic HK2 as shown by their ability to reduce glycolysis and induce apoptosis, however, NT-3-BP-AuNPs did not affect the overall mitochondrial integrity. T-3-BP-AuNPs suppressed basal levels of OXPHOS and affected the ability of cancer cells to upregulate OXPHOS in response to agents such as FCCP that uncouple the mitochondrial proton gradient from ATP production. The effect of T-3-BP-AuNPs on OXPHOS, at a low 3-BP concentration of 100 μM is an important finding because other non-mitochondrial effects of free 3-BP may account for its cytotoxic effect at least at high doses. We believe that T-3-BP-AuNPs do not exert its effects *via* a single molecular target within the mitochondrial respiratory chain, but through several collective disruptions that leads to impairment of OXPHOS.

Table 7.3. PK parameters of NPs by using a one-compartmental model

	T-AuNPs	**NT-AuNPs**
Route of Administration	IV	IV
Dose Level, μg/animal	797.8 ± 4.9	818 ± 35
Dose Level, mg/kg	2.7	2.7
AUC $_{[0\text{-}24\ h]}$, ng.h/mL/mg/kg	401,918 ± 22,581	25,094 ± 3,313
C_{max}, ng/mL	176,770 ± 831	6,250 ± 721
V_d, L/kg	738.8 ± 12.5	25.1 ± 0.8
C_L [t=0], L/h.kg	119.9 ± 10.0	02.0 ± 0.0
$t_{1/2}$ (h)	4.3 ± 0.3	8.8 ± 0.2

AUC, area under curve; C_{max}, Peak plasma concentration; C_L, total body clearance; $t_{1/2}$, plasma half-life; V_d, volume of distribution.

***In Vivo* bioD and PK properties of T-Au-NPs**

In order to obtain insight into the bioD, PK, and excretion profiles of T-AuNPs and NT-AuNPs, accumulation, we investigated the biokinetics after intravenous injection of T-AuNPs and NT-AuNPs in Sprague Dawley rats. Blood samples at predetermined time points up to 24 h post injection, organs after 24 h were and analyzed for Au by ICP-MS (Figure 7.15). PK parameters calculations revealed a plasma elimination half life ($t_{1/2}$) of ~4.3 h for T-AuNPs and ~ 8.8 h for NT-AuNPs (Table 7.3, Figure 7.15). These half lives indicated that both the NPs will be in circulation for prolonged time. The small C_L and high AUC further supported long circulating properties of these NPs. The variation of T and NT-AuNPs in the spleen, liver, lungs, brain, heart, kidney, and testes at 24 h post-dose indicated maximum NP accumulation in the liver for both T and NT systems (Figure 7.15). BioD studies also indicated that the TPP-modified T-AuNPs demonstrated similar distribution profile as shown by $-NH_2$ midified NT-AuNPs.

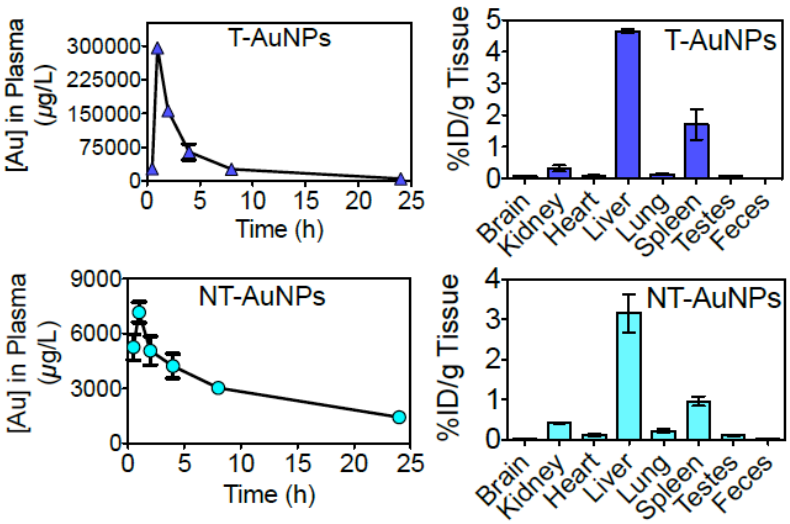


Figure 7.15. Variation of Au concentration in μg/L in plasma with time and tissue distribution following the administration of T-AuNPs and NT-AuNPs intravenously to male rats.

CONCLUSIONS

In conclusion, this study showed that 3-BP delivered by a mitochondria-targeted NP system has enormous potential in demonstrating increasing the therapeutic window of free 3-BP. To the best of our knowledge, this is the first demonstration of engineering of such a NP system for mitochondrial delivery of 3-BP with superior efficacy. Furthermore, we demonstrated that mitochondrial compartmentalization of 3-BP when delivered with a T-AuNP system is time-dependent which utilizes different targets of 3-BP present in the different mitochondrial compartments further enhancing 3-BP activity. 3-BP released from the T-AuNP in a protease mediated hydrolysis showed HK2 inhibition, anti-proliferative effects on highly glycolytic PC3 and DU145 cell lines, inhibited lactate production, complete inhibition of glycolysis, and blocked energy metabolism in these cells, finally triggered cell death and apoptosis. The efficiencies of all these activities were much higher compared to 3-BPs when delivered using a non-targeted NP system or the free formulation. Treatment-derived toxicity, cell-insensitivity to metabolic drugs such as free 3-BP, and lack of therapeutic selectivity are still the major issues in developing strategies leading to cancer cure. Given its ability to selectively deliver 3-BP inside mitochondria, T-3-BP-AuNPs could constitute a leading construct in the development of chemotherapeutics that target the unique neoplastic alterations of the cell glucose metabolism and up regulation of HK2. This study shows the potential that delivery of 3-BP using a mitochondria-targeted delivery system is an effective means of limiting systemic toxicity while enhancing efficacy thus providing new strategies for 3-BP therapy.

ACKNOWLEDGMENT

This work was supported by a start-up grant from the National Institutes of Health (P30 GM 092378) to UGA and by the Office of the Vice President for Research, UGA to S.D. We thank Prof. Rick Tarleton for Seahorse XF analyzer. We thank Dr. Nagesh Kolishetti for helpful discussions and critical reading of the manuscript.

REFERENCES

1. Vander Heiden, M. G.; Cantley, L. C.; Thompson, C. B., Understanding the Warburg effect: the metabolic requirements of cell proliferation. *Science* **2009,** *324*, 1029-1033.
2. Warburg, O., On the origin of cancer cells. *Science* **1956,** *123*, 309-314.
3. Hsu, P. P.; Sabatini, D. M., Cancer cell metabolism: Warburg and beyond. *Cell* **2008,** *134*, 703-707.
4. Wilson, J. E., Isozymes of mammalian hexokinase: structure, subcellular localization and metabolic function. *J. Exp. Biol.* **2003,** *206*, 2049-2057.
5. Mathupala, S. P.; Ko, Y. H.; Pedersen, P. L., Hexokinase II: cancer's double-edged sword acting as both facilitator and gatekeeper of malignancy when bound to mitochondria. *Oncogene* **2006,** *25*, 4777-4786.
6. Pedersen, P. L.; Mathupala, S.; Rempel, A.; Geschwind, J. F.; Ko, Y. H., Mitochondrial bound type II hexokinase: a key player in the growth and survival of many cancers and an ideal prospect for therapeutic intervention. *Biochim. Biophys. Acta* **2002,** *1555*, 14-20.

7. Pedersen, P. L., 3-Bromopyruvate (3BP) a fast acting, promising, powerful, specific, and effective "small molecule" anti-cancer agent taken from labside to bedside: introduction to a special issue. *J. Bioenerg. Biomembr.* **2012,** *44*, 1-6.

8. Chen, Z.; Zhang, H.; Lu, W.; Huang, P., Role of mitochondria-associated hexokinase II in cancer cell death induced by 3-bromopyruvate. *Biochim. Biophys. Acta* **2009,** *1787*, 553-560.

9. Birsoy, K.; Wang, T.; Possemato, R.; Yilmaz, O. H.; Koch, C. E.; Chen, W. W.; Hutchins, A. W.; Gultekin, Y.; Peterson, T. R.; Carette, J. E.; Brummelkamp, T. R.; Clish, C. B.; Sabatini, D. M., MCT1-mediated transport of a toxic molecule is an effective strategy for targeting glycolytic tumors. *Nat. Genet.* **2013,** *45*, 104-108.

10. Lee, H. B.; Blaufox, M. D., Blood Volume in the Rat. *J. Nucl. Med.* **1985,** *26*, 72-76.

11. Rosi, N. L.; Giljohann, D. A.; Thaxton, C. S.; Lytton-Jean, A. K.; Han, M. S.; Mirkin, C. A., Oligonucleotide-modified gold nanoparticles for intracellular gene regulation. *Science* **2006,** *312*, 1027-1030.

12. Seferos, D. S.; Prigodich, A. E.; Giljohann, D. A.; Patel, P. C.; Mirkin, C. A., Polyvalent DNA nanoparticle conjugates stabilize nucleic acids. *Nano Lett.* **2009,** *9*, 308-311.

13. Dhar, S.; Daniel, W. L.; Giljohann, D. A.; Mirkin, C. A.; Lippard, S. J., Polyvalent oligonucleotide gold nanoparticle conjugates as delivery vehicles for platinum(IV) warheads. *J. Am. Chem. Soc.* **2009,** *131*, 14652-14653.

14. Arvizo, R.; Bhattacharya, R.; Mukherjee, P., Gold nanoparticles: opportunities and challenges in nanomedicine. *Expert Opin. Drug Deliv.* **2010,** *7*, 753-763.

15. Arvizo, R. R.; Saha, S.; Wang, E.; Robertson, J. D.; Bhattacharya, R.; Mukherjee, P., Inhibition of tumor growth and metastasis by a self-therapeutic nanoparticle. *Proc. Natl. Acad. Sci. U. S. A.* **2013,** *110*, 6700-6705.

16. Kingshott, P.; Griesser, H. J., Surfaces that resist bioadhesion. *Curr. Opin. Solid State Mat. Sci.* **1999,** *4*, 403-412.

17. Marrache, S.; Dhar, S., Engineering of blended nanoparticle platform for delivery of mitochondria-acting therapeutics. *Proc. Natl. Acad. Sci. U. S. A.* **2012,** *109*, 16288-16293.

18. Marrache, S.; Tundup, S.; Harn, D. A.; Dhar, S., Ex vivo programming of dendritic cells by mitochondria-targeted nanoparticles to produce interferon-gamma for cancer immunotherapy. *ACS Nano* **2013,** *7*, 7392-7402.

19. Kim, J. S.; Ahn, K. J.; Kim, J. A.; Kim, H. M.; Lee, J. D.; Lee, J. M.; Kim, S. J.; Park, J. H., Role of reactive oxygen species-mediated mitochondrial dysregulation in 3-bromopyruvate induced cell death in hepatoma cells : ROS-mediated cell death by 3-BrPA. *J. Bioenerg. Biomembr.* **2008,** *40*, 607-618.

20. Kim, W.; Yoon, J. H.; Jeong, J. M.; Cheon, G. J.; Lee, T. S.; Yang, J. I.; Park, S. C.; Lee, H. S., Apoptosis-inducing antitumor efficacy of hexokinase II inhibitor in hepatocellular carcinoma. *Mol. Cancer Ther.* **2007,** *6*, 2554-2562.

CHAPTER 8

MITOCHONDRIA TARGETED MOLECULAR SCAFFOLD FOR EFFICACIOUS DELIVERY OF METABOLIC MODULATOR DICHLOROACETATE

Reprinted with the permission of Pathak, R.K.; Marrache, S.; Harn, D.A.; and Dhar, S. *ACS Chem. Biol.*, 9, 1178-1187. Copyright 2014, American Chemical Society

ABSTRACT

Tumor growth is fueled by the use of glycolysis, which normal cells use only in the scarcity of oxygen. Glycolysis makes tumor cells resistant to normal death process. Targeting this unique tumor metabolism can provide an alternative strategy to selectively destroy tumor leaving normal tissue unharmed. The orphan drug dichloroacetate (DCA) is a mitochondrial kinase inhibitor that has the ability to show such characteristics, however, its molecular form shows poor uptake, bioavailability, and limited ability to reach its target mitochondria. Here, we describe a targeted molecular scaffold for construction of a multiple DCA loaded compound, Mito-DCA, with two-orders of enhanced potency and cancer-cell specificity compared to DCA. Incorporation of a lipophilic triphenylphosphonium cation through a biodegradable linker in Mito-DCA allowed for mitochondria targeting. Mito-DCA did not show any significant metabolic effects towards normal cells but tumor cells lacking functional mitochondria were affected by Mito-DCA that caused reduction in glycolysis and subsequent cell death *via* apoptosis. Effective mitochondrial targeting of DCA resulted in thousand-time better activity compared to the generic drug DCA. Effective delivery of DCA to the mitochondria resulted in significant reduction in lactate levels and played important roles in modulating dendritic cell (DC) phenotype evidenced by secretion of interleukin-12 from DCs upon activation with tumor antigens from Mito-DCA treated cancer cells. Targeting mitochondrial metabolic inhibitors to the mitochondria could lead to the induction of an efficient anti-tumor immune response thus introducing the concept of combining glycolysis inhibition with immune system to destroy tumor.

Introduction

Stimulation of mitochondrial activity and alterations of cancer cell characteristic adenosine-5′ -triphosphate (ATP) generation pathways can be an efficient method in anticancer therapeutic strategy.[1-6] The small molecule mitochondrial kinase inhibitor, dichloroacetate (DCA) has the potential to become a major player in the field of cancer chemotherapy.[7-10] By utilizing the metabolic switch, DCA reverses cancer cell abnormal metabolism from aerobic glycolysis to glucose oxidation by reducing the activity of mitochondrial pyruvate dehydrogenase kinase 1 (PDK1),[11] which negatively regulates pyruvate dehydrogenase (PDH) causing pyruvate to convert to acetyl-CoA promoting oxidative phosphorylation (OXPHOS).[7] DCA reduces high mitochondrial membrane potential ($\Delta\psi_m$) and increases mitochondrial reactive oxygen species (ROS) in malignant, but not in normal cells.[7]

Therapeutically prohibitive high DCA doses are needed for tumor growth suppression due to the lack of effective cellular uptake[12] and its localization inside the target organelle, mitochondria of cells. There are limited efforts for direct use of DCA in cancer patients due to the fact that finding funding for clinical trials is a challenge since DCA is a generic drug for lactic acidosis.[10] In physiological conditions, orally or intravenously administered DCA is ionized and cannot pass through the plasma membrane by passive diffusion. We raised two questions: how to introduce physiologically relevant DCA doses into cancer cells and how to engineer the anionic form of DCA to cross the negatively charged inner mitochondrial membrane (IMM) to access PDK1 within the mitochondrial matrix? Like other mitochondria acting therapeutics; DCA encounters tremendous barriers in its navigation to enter the

mitochondria. Since the monocarboxylate transporters which are linked to DCA cellular entry are electroneutral in most cells including tumor,[13] we questioned the ability of these transporters to accumulate anionic DCA in tumor. Moreover, for mitochondrial uptake, DCA competes with pyruvate for its entry *via* the mitochondrial pyruvate transporter. Recent studies identified that sodium-coupled monocarboxylate transporter or solute carrier family-5 member-8 would accept DCA as a substrate.[14, 15] However, this transporter is expressed in normal cells, but expression is silenced in tumor cells.[16, 17] Lactate is the most abundant product of highly glycolytic tumor and high levels of extracellular lactate cause blocking of monocyte differentiation to dendritic cells (DCs), significant inhibition of cytokine release from DCs and cytotoxic T lymphocytes, inhibition of monocyte migration, and reduction of cytotoxic T-cell function.[18] Inhibition of cancer cell glycolysis using DCA has the potential to overcome immune suppressive nature of glycolytic tumor, however, it needs very high DCA doses. We hypothesized that DCA needs to be engineered for efficient cellular and mitochondrial uptake to show efficient glycolytic inhibition, to exhibit anticancer activity, and to enhance the effects of antitumor immunity at pharmacologically relevant doses.

Taking advantage of the fact that cancer cells frequently have more negatively charged mitochondrial membrane potential ($\Delta\psi_m$), we investigated a means to circumvent low efficacy of DCA by targeted delivery using a lipophilic triphenylphosphonium (TPP) cation, which equilibrates across the membranes in a Nernstian fashion and accumulates into the mitochondrial matrix in inverse proportion to $\Delta\psi_m$ (Figure 9.1).[19-24] Here, we report a technology for construction of a mitochondria targeted DCA analogue, Mito-

DCA by incorporating a TPP moiety and its ability to selectively alter cancer cell metabolism (Figure 8.1A).

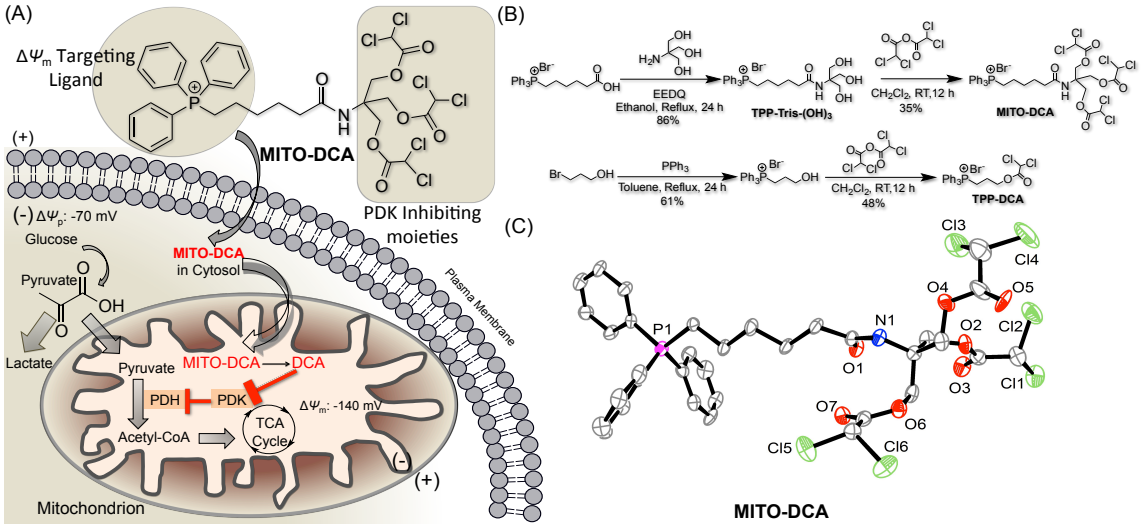


Figure 8.1. (A) Design of Mito-DCA and its possible mechanism of action; (B) synthesis of mitochondria-targeted DCA analogues; (C) ORTEP diagram of Mito-DCA with 50% thermal ellipsoids

Methods and Materials

Materials and instrumentations

All chemicals were received and used without further purification unless otherwise noted. Dichloroacetic (DCA) anhydride, tris(hydroxymethyl)aminomethane (Tris), triphenylphosphine (TPP), 6-bromohexanoic acid, N-ethoxycarbonyl-2-ethoxy-1,2-dihydroquinoline (EEDQ), 3-bromopropanol, 4-dimethylaminopyridine (DMAP), (3-(4,5-dimethylthiazol-2-yl)-2,5-diphenyltetrazolium bromide (MTT), and adenosine 5'-triphosphate (ATP) disodium salt hydrate were purchased from Sigma-Aldrich. Tetramethyl rhodamine methyl ester (TMRM) and 5,5',6,6'-tetrachloro-1,1',3,3'-tetraethylbenzimidazolylcarbocyanine iodide or JC-1 were procured from Invitrogen. Carbonyl cyanide 4-(trifluoromethoxy) phenylhydrazone (FCCP) was purchased from

Sigma-Aldrich. Alexa Fluor® 488 Annexin V/Dead cell apoptosis kit was purchased from Invitrogen. Lactate assay kit was obtained from BioVision, CA, USA. CellTiter-Glo® luminescent cell viability assay kit from Promega was used to quantify cellular ATP content. Granulocyte-macrophage colony-stimulating factor (GM-CSF) was purchased from R&D systems. Interleukin (IL)-6, IL-2, IL-10, interferon-gamma (IFN-γ), IL-12, IL-4, and tumor necrosis factor (TNF)-α cytokines were tested using BD OptEIA mouse enzyme-linked immunosorbent assay (ELISA) kits. IL-6, IL-2, IL-10, IFN-γ, IL-12, IL-4, and TNF-α cytokines on human cancer cell supernatants were tested using R&D systems human ELISA kits. Ultra-pure lipopolysaccharide (LPS) was purchased from Invivogen, CA, USA. CD11c microbeads for dendritic cell (DC) purification was purchased from Miltenyi Biotech, CA USA.

Distilled water was purified by passage through a Millipore Milli-Q Biocel water purification system (18.2 MΩ) containing a 0.22 μm filter. ^{1}H, ^{13}C spectra were recorded on a 400 MHz and ^{31}P NMR spectra recorded on a 500 MHz Varian NMR spectrometer, respectively. High-performance liquid chromatography (HPLC) analyses were made on an Agilent 1200 series instrument equipped with a multi-wavelength UV-visible and a fluorescence detector. Flow cytometry studies were performed on a BD LSRII flow cytometer equipped with digital acquisition using FACSDiva v6. Plate reader analysis was performed on a Bio-Tek Synergy HT microplate reader. Confocal images were recorded in a Nikon A1 confocal microscope. X-ray intensity data were collected at 100 K on a Bruker APEX CCD diffractometer. Electrospray ionization mass spectrometry (ESI-MS) and high-resolution mass spectrometry (HRMS)-ESI were recorded on Perkin Elmer SCIEX API 1 plus and Thermo scientific ORBITRAP ELITE instruments,

respectively. Bioenergetic assays were carried out using a Seahorse XF^e24 analyzer (Seahorse Biosciences, North Billerica, MA, USA).

JC-1 assay

PC3 cells were cultured on a live cell imaging glass bottom dish at a density of $1x10^6$ cells/mL and allowed to grow overnight at 37 °C. Cells were treated with 150 μM Na-DCA, 150 μM TPP-DCA, 50 μM TPP-Tris-$(OH)_3$, and 50 μM Mito-DCA for 6 h at 37 °C. A solution of JC-1 reagent (10 μg/mL in RPMI) was added and incubation was carried out at 37 °C for 20 min. The cells were washed 3 times with PBS, and live cell imaging was performed in phenol red free RPMI media. Quantification of fluorescence intensities and corrected total cell fluorescence (CTCF) values were carried out using ImageJ. Mitochondrial uncoupling by FCCP (50 μM, 1 h) was carried out as a control to cause mitochondrial depolarization and collapse of the mitochondrial membrane potential prior to JC1 assay.

TMRM assay

PC3 cells were cultured on a live cell imaging glass bottom dish at a density of $1x10^6$ cells/mL and allowed to grow overnight at 37 °C. Cells were treated with 50 μM TPP-Tris-$(OH)_3$, 150 μM Na-DCA, 150 μM TPP-DCA, and 50 μM Mito-DCA for 6 h at 37 °C. A solution of TMRM was added and incubation was carried out at 37 °C for 20 min. The cells were washed 3 times with PBS, and live cell imaging was performed in phenol red free RPMI media.

MTT assay and data analysis

The cytotoxic behaviors of Mito-DCA, TPP-DCA, Na-DCA, and TPP-Tris-$(OH)_3$ were evaluated using the MTT assay against PC3, DU145, LNCaP, and MSC cells. Cells

(2000 cells/well for PC3, DU145, and MSC cells; 5000 cells/well for LNCaP) were seeded on a 96-well plate in 100 μL of desired medium and incubated for 24 h. The cells were treated with different DCA compounds and TPP-Tris-$(OH)_3$ at varying concentrations and incubated for 72 h at 37 °C. The cells were then treated with 20 μL of MTT (5 mg/mL in PBS) for 5 h. The medium was removed, the cells were lysed with 100 μL of DMSO, and the absorbance of the purple formazan was recorded at 550 nm using a Bio-Tek Synergy HT microplate reader. Each well was performed in triplicate. All experiments were repeated three times. Cytotoxicity was expressed as mean percentage increase relative to the unexposed control ± SD. Control values were set at 0% cytotoxicity or 100% cell viability. Cytotoxicity data (where appropriate) was fitted to a sigmoidal curve and a three parameters logistic model used to calculate the IC_{50}, which is the concentration of chemotherapeutics causing 50% inhibition in comparison to untreated controls. The mean IC_{50} is the concentration of agent that reduces cell growth by 50% under the experimental conditions and is the average from at least three independent measurements that were reproducible and statistically significant. The IC_{50} values were reported at ±99% confidence intervals. This analysis was performed with GraphPad Prism (San Diego, U.S.A).

Apoptosis detection by flow cytometry

PC3 and MSC cells were seeded at a density of 1 x 10^6 cells/mL on each well of a six well plate and allowed to grow overnight. Cells were treated with 150 μM Na-DCA, 150 μM TPP-DCA, and 50 μM Mito-DCA for 12 h at 37 °C. As positive controls, etoposide (100 μM, incubation time: 12 h) for apoptosis and H_2O_2 (1 mM, incubation time: 45 min) for necrosis were used. The cells were trypsinized, repeatedly washed with

cold PBS, and centrifuged at 1,800 RPM for 3 min, and the supernatants were discarded. Cell density was determined and cells were resuspended in 1X annexin-binding buffer to ~1 × 10^6 cells/mL preparing a sufficient volume to have 100 μL per assay. To 100 μL of cell suspension, 5 μL Alexa Fluor® 488 annexin V and 1 μL (100 μg/mL) PI working solution were added, and incubated for 15 min at room temperature. After the incubation period, 400 μL 1X annexin-binding buffer was added to each sample, samples were gently mixed keeping the samples on ice and the samples were analyzed on the flow cytometer immediately.

Generation of Bone Marrow Derived Dendritic Cells (BMDCs)

BMDCS were isolated by Dr. Smanla Tundup and Mr. Joshua H. Choi. BMDCs were isolated from 6-8 weeks old C57BL/6 mice. After euthanization, bone marrows were isolated by flushing mouse femurs in RPMI. The harvested cells were centrifuged at 1250 rpm for 10 min and the pellet was resuspended in ice-cold 2 mL of buffer to lyse erythrocytes. The cells were counted, resuspended, and transferred to petri dishes at the final concentration of 1.5 × 10^6 cells/mL. To this culture, granulocyte-macrophage colony-stimulating factor (20 ng/mL) was added to generate BMDCs. Media was changed on days 2 and 4. On day 6 cells were processed further to obtain pure DC population by subjecting cells to MACS bead purification using anti-CD11c antibody as per manufacturer's instructions. DC purity was tested by incubating BMDCs with lipopolysaccharide (LPS) (100 ng/mL) and measuring the surface expression of CD11c.

Animals

Animals were obtained from Jackson Laboratory and handled in accordance with "The guide for the Care and Use of Laboratory Animals" of American Association for

Accreditation of Laboratory Animal Care (AAALAC), Animal Welfare Act (AWA), and other applicable federal and state guidelines. All animal work presented here was approved by Institutional Animal Care and Use Committee (IACUC) of University of Georgia.

Cell Line and Cell Culture

Human PCa LNCaP, PC3, and DU145 cells were procured from the American type culture collection (ATCC). Human bone marrow derived MSCs were purchased from Lonza. DU145 cells were grown at 37 °C in 5% CO_2 in Eagle's minimum essential medium (EMEM) supplemented with 10% fetal bovine serum (FBS) and 1% penicillin/streptomycin. LNCaP and PC3 cells were grown in Roswell Park Memorial Institute (RPMI) 1640 medium. MSC cells were grown in MSC basal medium supplemented with MSC growth kit-low serum components and 2% FBS. Cells were passed every 3 to 4 days and restarted from frozen stocks upon reaching pass number 20 for PC3, LNCaP, DU145, and 10 for MSC.

$C_{28}H_{35}NO_4P^+$, 480.2298; found, 480.2243.

Synthesis of Mito-DCA.

Mito-DCA was synthesized by Dr. Rakesh K. Pathak and the details of synthesis and characterization can be found in *ACS Chem. Biol.*, 9, 1178-1187.

Synthesis of TPP-$(CH_2)_3$-OH.

A mixture of 3-bromopropanol (1.0 g, 7.2 mmol) and TPP (2.1 g, 7.9 mmol) in toluene (25 mL) was heated to reflux for 24 h. The resulting white precipitate was filtered through fritted glass followed by the washing with diethyl ether (3 x 30 mL). The white solid was dried under vacuum to get the pure product of TPP-$(CH_2)_3$-OH. Yield, 61 %

(1.7 g). Melting point: 235-240 °C; ^{1}H NMR ($CDCl_3$): 7.65-7.80 (m, 15H), 4.94 (t, 1H), 3.70-3.83 (m, 4H), 1.81 (m, 2 H) ppm. ^{13}C NMR ($CDCl_3$): δ 135.09, 133.47, 130.51, 118.72, 60.40, 25.92, 20.43 ppm. ^{31}P NMR ($CDCl_3$) 24.77 ppm. HRMS-ESI (m/z): $[M-Br]^+$ calcd. for $C_{21}H_{22}OP^+$, 321.1403; found, 321.1403.

Synthesis of TPP-DCA.

TPP-DCA was synthesized by Dr. Rakesh K. Pathak and the details can be found in *ACS Chem. Biol.*, 9, 1178-1187.

Intra and Extracellular Lactate Determination.

PC3, LNCaP, and MSC cells were seeded at a density of 1 x 10^6 cells/mL on each well of a 12 well plate and allowed to grow overnight at 37 °C under 5% CO_2. Cells were treated with 50 μM TPP-Tris-$(OH)_3$, 150 μM Na-DCA, 150 μM TPP-DCA, and 50 μM Mito-DCA for 6 h at 37 °C. After 6 h, the media was removed and the cells were homogenized. The lysate and the media were separately added to the enzyme and substrate working reagent mixture and incubated for 30 min. Lactate concentrations in the cell lysates and media were measured using Bio-Tek Synergy HT microplate reader at 450 nm and lactate concentration were calculated using a standard curve.

CellTiter-Glo® Luminescent ATP Quantification.

PC3, LNCaP, and MSC cells were plated at a density of 10,000 cells per well in 96-well plates compatible with the luminometer used in 100 μL media. TPP-Tris-$(OH)_3$ (20 μM), Mito-DCA (20 μM), TPP-DCA (60 μM), and Na-DCA (60 μM) were added to experimental wells, and incubated for 3 h at 37 °C in 5% CO_2 atmosphere. Control wells containing medium without cells were prepared to obtain a value for background luminescence. Plates were then equilibrated at room temperature for ~30 min. A volume

of CellTiter-Glo reagent equal to the volume of cell culture medium present in each well was added, this mixtures were well mixed for 2 min using a shaker to induce cell lysis. The plates were allowed to incubate at room temperature for 10 min to stabilize luminescent signal. Luminescence was recorded using a plate reader. ATP quantification was carried out from a standard curve prepared in culture media using ATP disodium salt hydrate.

Seahorse XF24 Bioenergetics Assays.

The three key parameters of glycolytic function: glycolysis, glycolytic capacity, and glycolytic reserve were assessed using a Seahorse XF glycolysis stress kit. Prior to the assay, XF sensor cartridges were hydrated. To each well of an XF utility plate, 1 mL of Seahorse Bioscience calibrant was added and the XF sensor cartridge was placed on top of the utility plate, and kept at 37 °C without CO_2 for 14 h. PC3 cells were cultured in XF24-well cell culture microplates (Seahorse Bioscience) at a density of $5x10^4$ cells/well (0.32 cm^2) in 100 μL growth medium and incubated for 1 h at 37 °C in 5% CO_2 atmosphere. After the cells were attached, an additional 100 μL growth medium was added and the cells were incubated for 24 h at 37 °C in 5% CO_2 atmosphere. The cells were treated with TPP-DCA (30 μM), Na-DCA (30 μM), and Mito-DCA (10 μM) for 4 h at 37 °C in 5% CO_2 atmosphere. After 4 h, all but 50 μL of the culture medium was removed from each well and the cells were rinsed two times with 600 μL of XF stress test glycolysis optimization medium pre-warmed to 37 °C and finally 610 μL of optimization medium was added to each well and the plate was placed at 37 °C without CO_2 for 1 h prior to assay. The OCR, a measure of mitochondrial respiration and the ECAR, a marker for glycolysis, were measured simultaneously for 16 min to establish a baseline rate.

Glycolysis, glycolytic capacity, and glycolytic reserve were calculated by subtracting the average rates before and after the addition of glucose (10 mM), ATP synthase inhibitor oligomycin (1.0 μM), and 2-DG (100 mM). These three compounds were injected consecutively with specific time gap and ECAR values were measured after each injection.

Different parameters of respiration: basal respiration, coupling efficiency, and spare respiratory capacity were investigated by using Seahorse XF-24 cell Mito Stress Test Kit. PC3 cells were plated and treated with different constructs as mentioned above as mentioned above except the final volume was 500 μL. Different parameters of respiration were calculated by subtracting the average respiration rates before and after the addition of the electron transport inhibitors oligomycin (3.0 μM), FCCP (3.0 μM), an ionophore that is a mobile ion carrier, and a mixture of antimycin-A (3.0 μM) which is a complex III inhibitor, binds to the Qi site of cytochrome c reductase, thereby inhibiting the oxidation of ubiquinol in the electron transport chain of OXPHOS and rotenone (3.0 μM), a mitochondrial inhibitor that prevents the transfer of electrons from the Fe-S center in Complex I to ubiquinone. The parameters calculated included: basal respiration (baseline respiration minus antimycin-A post injection respiration), ATP turnover (baseline respiration minus oligomycin post injection respiration), maximal respiratory capacity (FCCP stimulated respiration minus antimycin-A post injection respiration) and reserve respiratory capacity (FCCP stimulated respiration minus baseline respiration). Test articles on each sample had five replicates.

Anti-tumor Immunity Study by ELISA.

PC3 cells were plated at a concentration of $0.5x10^6$ cells/mL in six well plates and allowed to grow for 12 h. The cells were incubated with 150 μM Na-DCA, 150 μM TPP-DCA, and 50 μM Mito-DCA for 24 h at 37 °C. PC3 cell supernatants were added to freshly prepared BMDCs ($0.5x10^6$ cells/mL) and incubated at 37 °C for 24 h. Additionally, lipopolysaccharides (LPS) alone (100 ng/mL) as a control was added to the DC cultures. The DCs were centrifuged at 1,800 RPM for 3 min and ELISA was performed on the supernatants against the cytokines IL-2, IL-4, IL-6, IL-10, IL-12, TNF-α, and IFN-γ according to the manufacturer's protocol. Briefly, antibody coated plates were blocked with 10% FBS in PBS for 1 h at room temperature followed by washings. BMDC supernatants were incubated on the plates for 1 h at room temperature. This was immediately followed by washings and sequential incubations with the cytokine-biotin conjugate and streptavidin working solution. Finally, the substrate reagent containing 3,3',5,5' tetramethylbenzidine (100 μL) was added to each well, incubated for 30 min, the reaction was stopped by adding 50 μL stop solution containing 0.1 M H_2SO_4. The absorbance was recorded at 450 nm using a BioTek Synergy HT well plate reader.

Statistics.

All data were expressed as mean ± standard deviation. Statistical analysis were performed using GraphPad Prism® software v. 5.00. Comparisons between two values were performed using an unpaired Student t test. A one-way ANOVA with a post-hoc Tukey test was used to identify significant differences among the groups.

RESULTS AND DISCUSSION

Mitochondrial Membrane Potential and Mito-DCA.

We next investigated the effect of Mito-DCA on cancer cell $\Delta\psi_m$ using a cationic dye, 5,5′,6,6′-tetrachloro-1,1′,3,3′-tetraethylbenzimidazolylcarbocyanine iodide or JC-1 that exhibits potential-dependent accumulation in the mitochondria accompanied by a fluorescence emission shift from green to red due to the concentration dependent formation of red fluorescent 'J aggregates'. Mitochondrial depolarization is indicated by an increase in the green/red fluorescence intensity ratio. Live cell imaging of PC3 cells treated with Na-DCA (150 μM), TPP-DCA (150 μM), or Mito-DCA (50 μM) for 6 h at 37 °C, followed by staining with JC-1, and a comparative analysis of JC-1 green/red fluorescence ratio from PC3 cells in response to these three DCA analogues are represented in Figure 8.2.

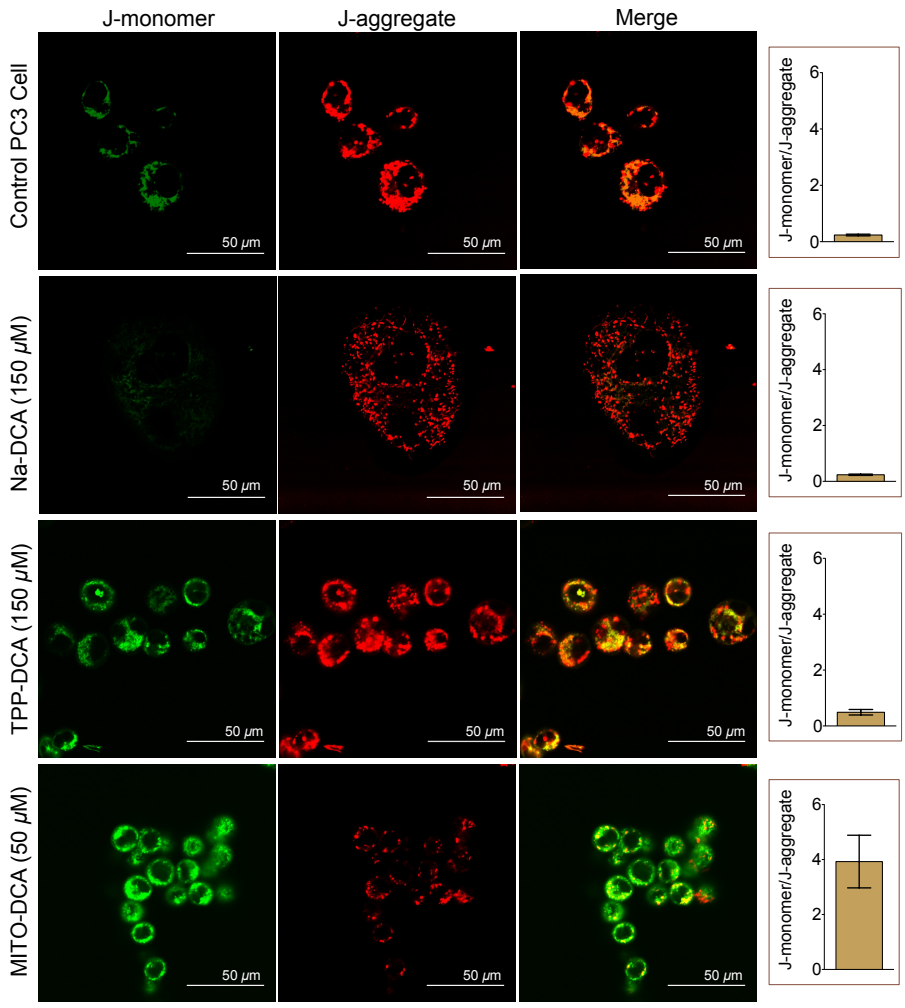


Figure 8.2. Changes in the $\Delta\psi_m$ by JC-1 assay. Treatment of PC3 cells with 50 μM Mito-DCA dramatically caused the collapse of $\Delta\psi_m$ in these cells compared to Na-DCA (150 μM) or TPP-DCA (150 μM). Cells were stained with JC-1 for 15 min. Green fluorescence, depolarized (J-monomer) mitochondria; red fluorescence, hyperpolarized (J-aggregates). The shift in $\Delta\psi_m$ observed by disappearance of red-orange-stained mitochondria (large negative $\Delta\psi_m$) and an increase in fluorescent green-stained mitochondria (loss of $\Delta\psi_m$) by Mito-DCA is higher compared that observed by TPP-DCA or Na-DCA. The JC-1 green/red ratio results from the mitochondria in all four groups are shown in the right.

Exposure of PC3 cells to Mito-DCA induced marked changes in $\Delta\psi_m$ as evident from the disappearance of red fluorescence and an increase of green fluorescence in most cells. In contrast, treatment with Na-DCA or TPP-DCA showed red fluorescence in most cells. Quantitative analysis of JC-1-stained PC3 cells revealed a significant decrease in the red (high $\Delta\psi_m$) to green (low $\Delta\psi_m$) ratio in Mito-DCA (Green:Red; 3.96±0.96) treated cells compared with control cells (Green:Red; 0.24±0.03), or the cells which were treated with Na-DCA (Green:Red; 0.24±0.02) at an equivalent DCA concentration. TPP-DCA showed a green:red ratio of 0.49±0.09 which was significantly lower than the ratio showed by Mito-DCA. Treatment of PC3 cells with TPP-Tris-$(OH)_3$ (50 μM) for 6 h at 37 °C did not show any changes in $\Delta\psi_m$ (Figure 8.3).

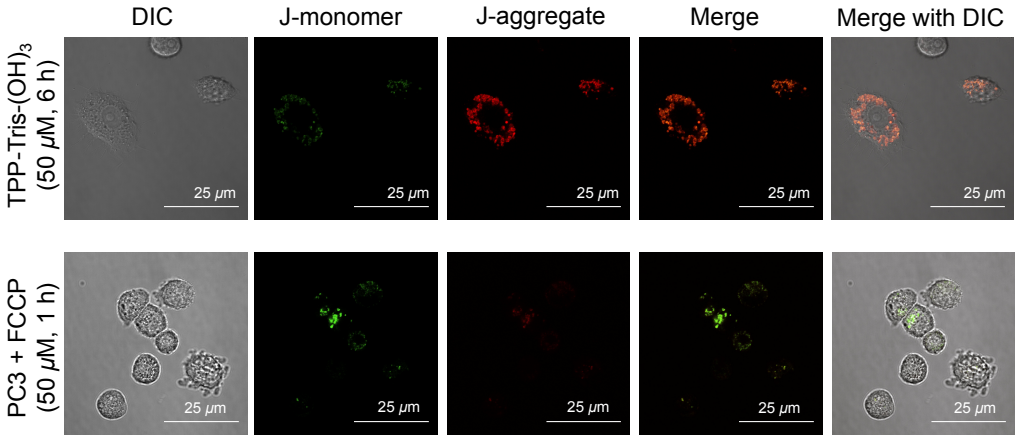


Figure 8.3. Changes in the $\Delta\psi_m$ by the JC-1 assay. Top: Treatment of PC3 cells with 50 μM TPP-Tris-$(OH)_3$ for 6 h. Bottom: Treatment of PC3 cells with 50 μM of FCCP for 1 h. Cells were stained with JC-1 for 15 min. Green fluorescence, depolarized (J-monomer) mitochondria; red fluorescence, hyperpolarized (J-aggregates). DIC: Differential Interference Contrast.

As a positive control of $\Delta\psi_m$ collapse, carbonyl cyanide 4-(trifluoromethoxy)phenylhydrazone (FCCP) was used which indicated mitochondrial depolarization in PC3 cells compared to untreated control cells (Figure 8.3). The ability of Mito-DCA to cause reduction in $\Delta\psi_m$ in a highly glycolytic PC3 cells at a low concentration of 50 μM indicated that incorporation of mitochondria targeting moiety and loading of multiple DCA units in a single molecule can help overcome the problems associated with high dosage required for Na-DCA. We investigated whether DCA released from Mito-DCA can restore the hyperpolarization of PC3 cells by carrying out tetramethyl rhodamine methyl ester (TMRM) assay. In general, cancer cells have significantly more hyperpolarized $\Delta\psi_m$ and therefore control PC3 cells exhibited increased fluorescence of the $\Delta\psi_m$-sensitive positive TMRM. Treatment of PC3 cells with Mito-DCA for 6 h reversed the hyperpolarization; in contrast, Na-DCA, TPP-DCA, and TPP-Tris-$(OH)_3$ did not alter the $\Delta\psi_m$ of the PC3 cells (Figure 8.4).

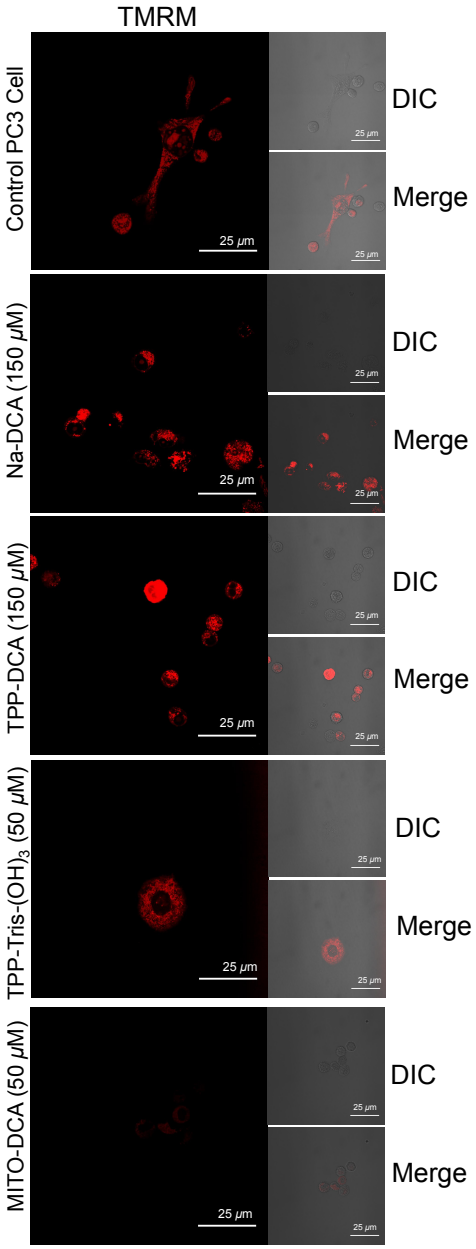


Figure 8.4. Reversal of mitochondrial membrane potential by TMRM live cell imaging assay. Mito-DCA significantly depolarized the PC3 cells at a concentration of 50 μM but Na-DCA (150 μM), TPP-DCA (150 μM), and TPP-Tris-$(OH)_3$ (50 μM) had no effect on these cells.

Mito-DCA is More Effective in Highly Glycolytic Cancer Cells.

Amplified glucose consumption and energy production from glycolysis are basic characteristics of most malignant cells, however, prostate cancer (PCa) cells have unique metabolic characteristics. Glycolytic profiles in androgen-dependent and androgen-independent PCa stages are not well understood.[27] The metabolic switching ability of Mito-DCA was studied on different PCa cell types. We used androgen-responsive LNCaP and androgen-nonresponsive PC3 and DU145 PCa cells. LNCaP cells have a significantly greater oxygen consumption and lower rate of lactate production compared to PC3 cells.[28] Mesenchymal precursor cells are believed to be the origin for various types of sarcoma and the transformation of these stem cells is a prerequisite for the development of most human malignancies.[29] We therefore used human mesenchymal stem cells (MSCs) as controls to examine the toxicity profile of Mito-DCA on normal cells. Representative cell viability profiles for PC3, DU145, LNCaP, and MSC cells after treatment with various concentrations of Mito-DCA, TPP-DCA, and Na-DCA for 72 h are shown in Figure 8.5A.

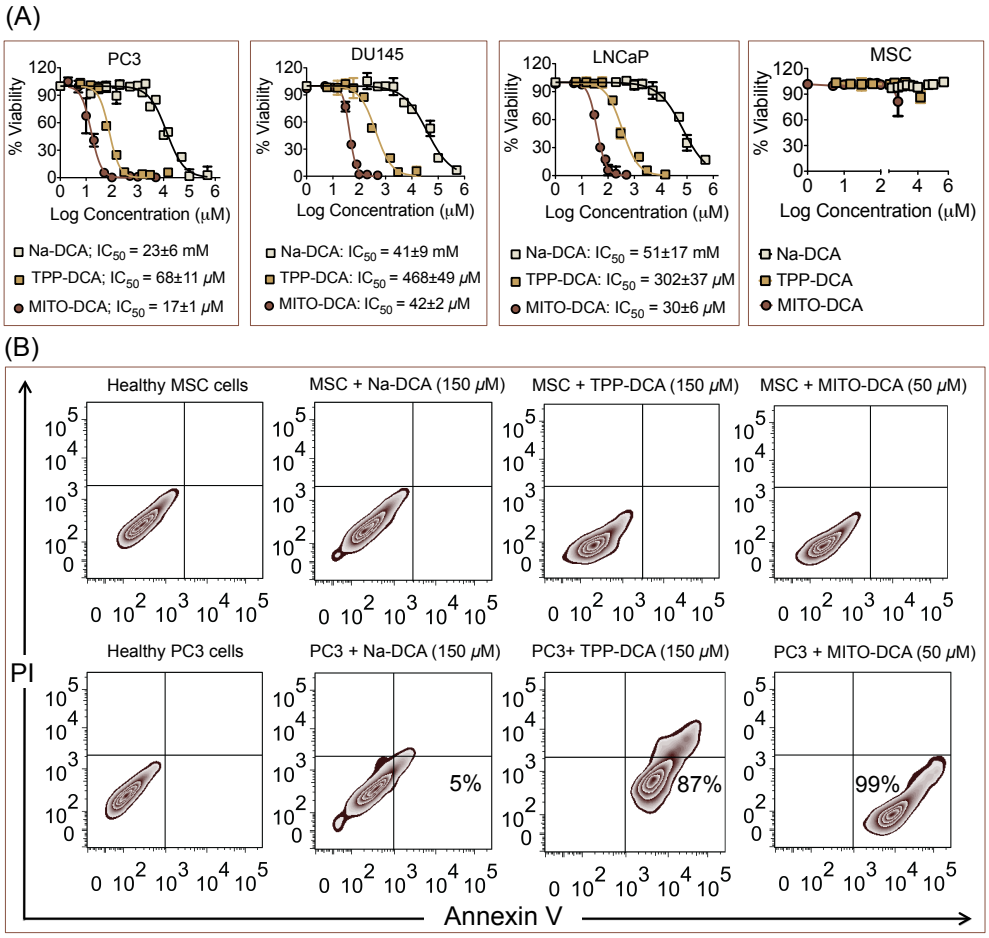


Figure 8.5. (A) Highly glycolytic PC3 and DU145 cells respond differently to Mito-DCA compared to less glycolytic LNCaP cells; Mito-DCA, TPP-DCA, and Na-DCA have no toxicity in MSC cells. Cells on 96-well plates were varied concentrations of Mito-DCA, TPP-DCA, and Na-DCA for 72 h and viability was assessed by the MTT assay. A representative experimental data are shown in the figure and the IC_{50} values were calculated from three independent experiments. (B) FACS analysis using annexin V-alexa fluor/PI staining for apoptosis detection in MSC and PC3 cells on treatment with Mito-DCA (50 μM), TPP-DCA (150 μM), and Na-DCA (150 μM) for 16 h. Cells in the lower right quadrant indicate annexin V-positive/PI negative, early apoptotic cells. The

cells in the upper right quadrant indicate annexin V-positive/PI positive, late apoptotic or necrotic cells.

The cytotoxicity profiles of TPP-Tris-$(OH)_3$, the carrier for targeted delivery of DCA to the mitochondria of cells shown in Figure 9.6 demonstrated nontoxic behavior of the carrier in PCa and MSC cells even at millimolar concentrations. Results indicated that Na-DCA is less active in all three PCa cell lines irrespective of their glycolytic states with IC_{50} values in the range of 20-40 mM in highly glycolytic PC3 and DU145 cells to >50 mM in less glycolytic LNCaP cells [IC_{50}(PC3): 23±6 mM; IC_{50}(DU145): 41±9 mM; IC_{50}(LNCaP): 51±17 mM], and no toxicity was observed in MSC cells. In contrast, when multiple DCA molecules were delivered directly to the mitochondria using a single TPP moiety in the form of Mito-DCA, a remarkable increase in cytotoxicity in all three PCa cell lines was observed. Mito-DCA with an IC_{50} value of 17±1 μM in highly glycolytic PC3 cells was found to be three orders of magnitude more active compared to Na-DCA. Similar trends were observed in DU145 (IC_{50}: 42±2 μM) and LNCaP (IC_{50}: 30±6 μM) cells; Mito-DCA showed three orders of magnitude more activity than Na-DCA. TPP-DCA [IC_{50}(PC3): 68±11μM; IC_{50}(DU145): 468±49 μM; IC_{50}(LNCaP): 302±37 μM] in PC3 cells was ~4 times and in LNCaP and DU145 cells ~10 times less active than Mito-DCA. In MSCs, both Mito-DCA and TPP-DCA did not show any toxic effects at these concentrations demonstrating their unique cancer cell selectivity.

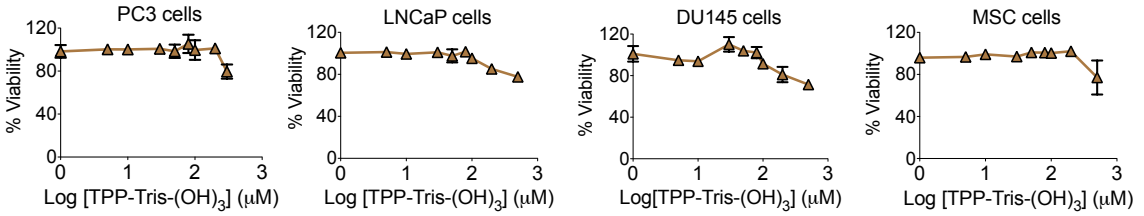


Figure 8.6. Cytotoxicity of TPP-Tris-$(OH)_3$ in PC3, LNCaP, DU145, and MSC cells as determined by the MTT assay.

In order to determine whether the enhanced activity of Mito-DCA was due to apoptosis or necrosis, we carried out an Alexa Fluor® 488-Annexin-V-propidium iodide (PI) cell staining in PC3 and MSC cells and analyzed using fluorescence-activated cell sorting (FACS) (Figure 8.5B). As controls, etoposide treated cells were used as early apoptosis population and H_2O_2 treated cells were marked as late apoptotic or necrotic population. MSC cells did not undergo apoptosis with Mito-DCA (50 μM), TPP-DCA (150 μM), and Na-DCA (150 μM) treatment for 12 h at 37 °C. However, at a low concentration of Mito-DCA (50 μM), complete early apoptosis was observed in PC3 cells; TPP-DCA showed similar behavior at 150 μM, no apoptosis was detected with Na-DCA at a concentration of 150 μM. There were no late apoptotic or necrotic populations observed with these compounds.

Selective Alteration of Cancer Cell Glucose Metabolism by Mito-DCA.

Cytosolic metabolism of glucose to pyruvate occurs before its entry into the mitochondria for OXPHOS. Glycolysis in the absence of OXPHOS in cancer causes an increase in lactate. To test the ability of Mito-DCA to inhibit glycolysis in cancer cells, we measured intracellular lactate levels in glycolytic PC3 cells and in the media and compared these values with those observed in less glycolytic LNCaP cells and normal MSCs (Figure 8.7, Figure 8.8). Treatment of PC3 cells with 50 μM Mito-DCA for 6 h

showed significant reduction in lactate levels both in the cells and in the media (Figure 8.7).

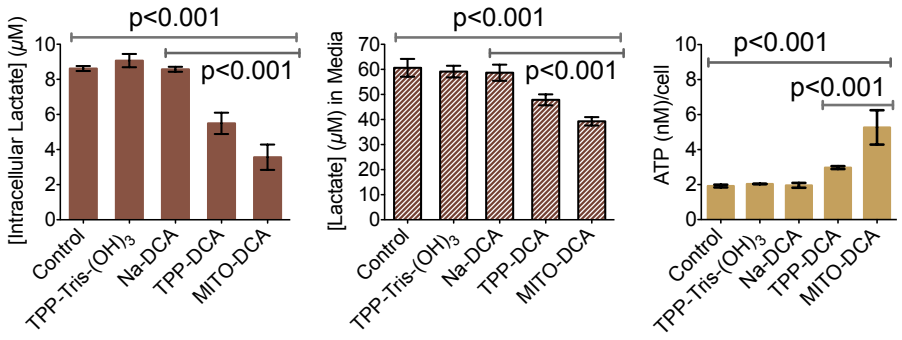


Figure 8.7. Lactate levels in PC3 cells (left), media (middle) after treatment with 150 μM Na-DCA, 150 μM TPP-DCA, and 50 μM Mito-DCA for 6 h at 37 °C. Changes in intracellular ATP content (right) associated with the lactate fluctuation in the PC3 cells after treatment with 60 μM Na-DCA, 60 μM TPP-DCA, and 20 μM Mito-DCA for 3 h at 37 °C.

Cells treated with the control delivery scaffold TPP-Tris-$(OH)_3$ did not show any effect. PC3 cells treated with 150 μM of Na-DCA showed no effect. TPP-DCA showed less efficiency in reducing both cellular lactate levels and in the media (Figure 8.7). Lactate levels in the less glycolytic LNCaP cells were significantly lower than those observed in PC3 cells. Pronounced lactate concentration differences were observed between healthy glycolytic PC3 and healthy MSC cells. The extent of relative decrease in glycolytic activity after treatment with Mito-DCA was similar in PC3 and LNCaP cells and the reduction was much more significant compared to cells treated with TPP-DCA or Na-DCA (Figure 8.8A). None of the DCA compounds showed any effect on the lactate levels of MSC cells (Figure 8.8A). These observations suggest that Mito-DCA is efficient in inhibiting glycolysis only in cancer cells.

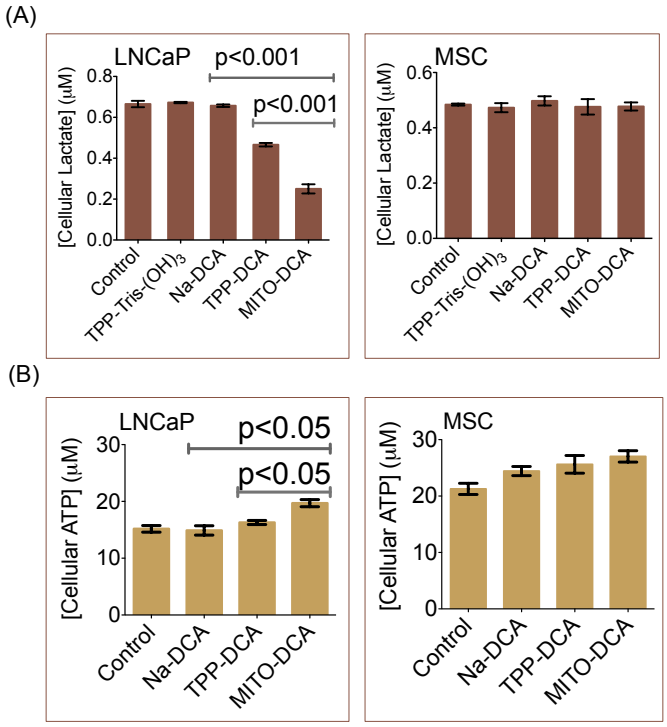


Figure 8.8. (A) Intracellular lactate levels in LNCaP and MSC cells after treatment with 50 μM TPP-Tris-$(OH)_3$, 150 μM Na-DCA, 150 μM TPP-DCA, and 50 μM Mito-DCA for 6 h at 37 °C. (B) Changes in intracellular ATP content associated with the lactate fluctuation in the LNCaP and MSC cells after treatment with 60 μM Na-DCA, 60 μM TPP-DCA, and 20 μM Mito-DCA for 3 h at 37 °C. Statistical analyses were performed using GraphPad Prism software 5.00. A one-way ANOVA with a post-hoc Tukey test was used to identify significant differences among the groups.

A decrease in cancer cell lactate levels is expected to be associated with an increase in ATP production. We next measured the intracellular ATP levels in PC3, LNCaP, and MSC cells treated with Mito-DCA (20 μM), TPP-DCA (60 μM), and Na-DCA (60 μM). After 3 h treatment with Mito-DCA, an increase in the intracellular ATP levels was observed in PC3 cells (Figure 8.7). Treatment with TPP-Tris-$(OH)_3$ or Na-DCA did not show any significant increase in the intracellular ATP levels. TPP-DCA at

three times higher concentrations showed less enhancement in intracellular ATP levels compared to Mito-DCA. Similar trends were observed in LNCaP cells upon treatment with Mito-DCA, TPP-DCA, and Na-DCA (Figure 8.8B). In contrast, normal MSC cells showed relatively high levels of ATP and upon treatment with all the three DCA compounds, there was marginal increase in the ATP levels (Figure 9.8B in the Supporting Information). At high concentrations of the DCA compounds (Mito-DCA: 50 μM; TPP-DCA; 150 μM; and Na-DCA: 150 μM) with longer incubation time of 6 h, PC3 cells showed ATP reduction and cell growth inhibition (Figure 8.9).

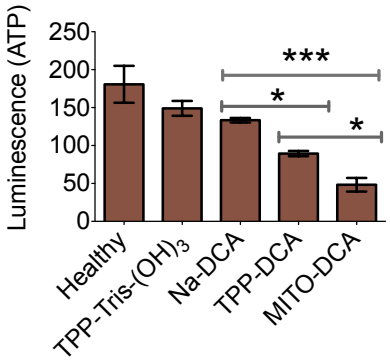


Figure 8.9. Intracellular ATP levels in PC3 cells after treatment with TPP-Tris-$(OH)_3$ (50 μM), Mito-DCA (50 μM), TPP-DCA (150 μM), and Na-DCA (150 μM) for 6 h. Statistical analyses were performed using GraphPad Prism software 5.00. A one-way ANOVA with a post-hoc Tukey test was used to identify significant differences among the groups.

Effects of Mito-DCA on Mitochondrial Bioenergetics Functions in PC3 Cells.

The selective ability of Mito-DCA in reducing lactate levels and early increase in intracellular ATP levels in cancer cells suggested that Mito-DCA has the potential in selectively altering the metabolism in cancer cells. To investigate this unique property of Mito-DCA in detail, we studied mitochondrial bioenergetics in PC3 cells using XF24

extracellular flux analyzer (Figures 8.10A and 8.10B). We examined the metabolic fluxes of both glycolysis and OXPHOS in PC3 cells. PC3 cells were treated with Mito-DCA (10 μM), TPP-DCA (30 μM), and Na-DCA (30 μM) for 4 h followed by washout and returned to fresh medium. As measures of glycolytic parameters, the changes in the extracellular acidification rate (ECAR) were monitored in response to the sequential administration of D-glucose, oligomycin, and 2-deoxy-D-glucose (2-DG) to assess glycolysis, maximal glycolytic capacity, and glycolytic reserve capacity, respectively (Figure 8.10A). Immediately after injecting 10 mM glucose to the treated PC3 cells in a glucose free medium, we observed an increase in the ECAR of control, Na-DCA, and TPP-DCA treated cells. In contrast, Mito-DCA treated cells did not show any increase in the ECAR (Figure 8.10A). An inhibitor of mitochondrial ATP synthase, oligomycin, triggered a further change in lactic acid production as evident from ECAR levels in control, TPP-DCA, and Na-DCA treated cells but no change was observed in Mito-DCA treated cells. Reduction of glycolysis flux by injecting a hexokinase inhibitor 2-DG into PC3 cells induced a rapid decline in the ECAR of control cells and those treated with either TPP-DCA or Na-DCA, however, Mito-DCA treated cells did not show any significant changes. These data documented greater inhibition of glycolysis and energetic collapse in PC3 cells treated with Mito-DCA.

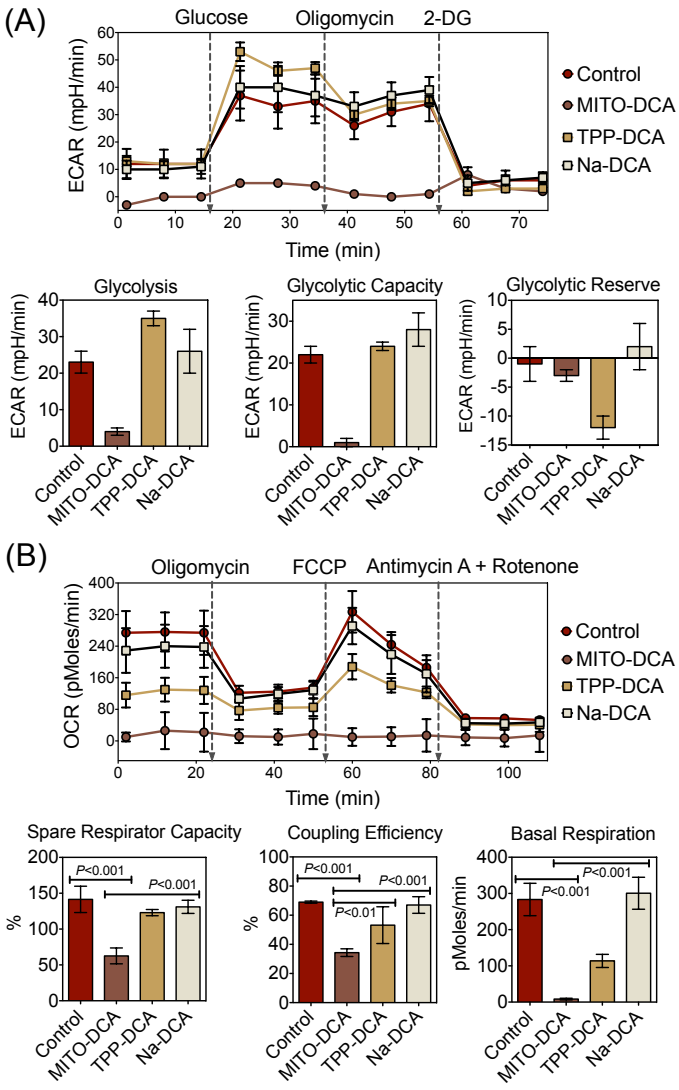


Figure 8.10. (A) Effect of Mito-DCA, TPP-DCA, and Na-DCA on PC3 cell glycolysis. PC3 cells were treated with 10 μM Mito-DCA, 30 μM TPP-DCA, 30 μM Na-DCA for 4 h. ECAR following the addition of glucose represents glycolysis; ECAR following oligomycin shows maximum glycolytic capacity, and ECAR following treatment with 2-DG represents acidification associated with non-glycolytic activity. PC3 cells were subsequently treated with glucose, oligomycin, and 2-DG.

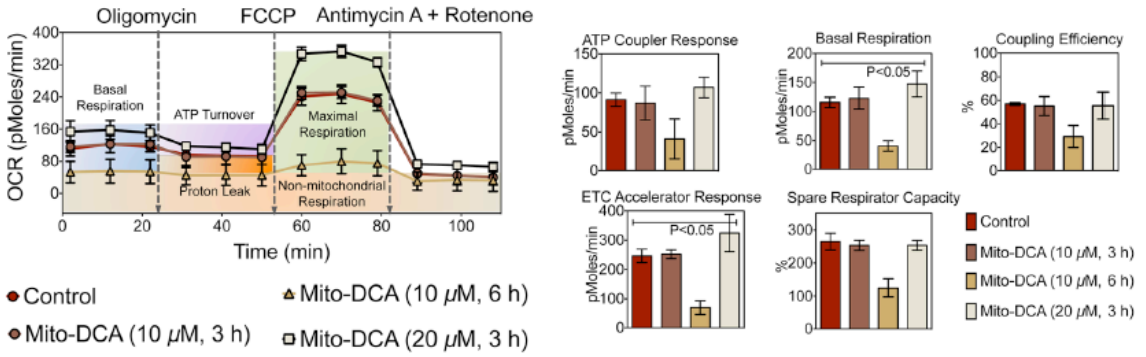


Figure 8.11. Effect of Mito-DCA on OCR in PC3 cells. PC3 cells were treated with 10 μM Mito-DCA, 30 μM TPP-DCA, 30 μM Na-DCA for 4 h. OCR traces were determined using a Seahorse mito stress kit and Seahorse XF24 analyzer. OCR prior to the addition of oligomycin and following the treatment of FCCP represent the basal mitochondrial respiration and maximal mitochondrial respiration capacity, respectively. OCR following rotenone plus antimycin treatment represents non-mitochondrial respiration.

We next investigated basal respiration, coupling efficiency, and spare respiratory capacity in response to DCA compounds using a XF24 mito stress assay kit (Figure 9.10B). To determine whether the above-described lost glycolysis and ATP production in presence of Mito-DCA in cancer cells also affected mitochondrial metabolism, we measured oxygen consumption rates (OCRs) in PC3 cells as a way of assessing OXPHOS. The basal OCR of Mito-DCA treated PC3 cells was less than control cells or cells treated with TPP-DCA or Na-DCA indicating a loss in total mitochondrial mass (Figure 8.10B). Subsequent addition of oligomycin showed that the levels of ATP-linked respiration were attenuated in control cells or cells treated with TPP-DCA or Na-DCA. However, cells treated with Mito-DCA did not show any changes in response to oligomycin addition. The cells treated with TPP-DCA or Na-DCA showed changes similar to control upon subsequent addition of mitochondrial uncoupler FCCP and a

combination of mitochondrial complex III inhibitor antimycin A and mitochondrial complex I inhibitor rotenone. However, in Mito-DCA treated cells, glycolysis is already adversely affected, and showed only a minor increase in response to FCCP and no significant changes were observed in response to antimycin A and rotenone (Figure 8.10B). Thus Mito-DCA caused reduction in both OXPHOS and glycolytic activity of cancer cells and mitochondria are the primary target of Mito-DCA, in particular as related to the significant inhibition of glycolysis.

Cancer Cell Lactate Reduction by Mito-DCA Results in Anti-tumor Immunity.

Cancer cells recruit multiple pathways to evade elimination by the immune system.[30] DCs, the major players for the initiation of a specific antitumor T-cell response, are the potential target to tumor-mediated immunosuppression.[31-33] Lactic acid secretion in highly proliferative glycolytic tumor induces alteration in antigen phenotype and functional activity of DCs, which contributes to the suppression of local immunity.[18] After observing significant and selective reduction in lactate levels in PCa cells by Mito-DCA, we investigated the impact of the reduced lactate producing PC3 cell antigens on DCs. Cancer cell supernatants were generated by treating PC3 cells with Mito-DCA (50 μM), Na-DCA (150 μM), and TPP-DCA (150 μM) for 24 h. First, we looked at the immune responses from the PC3 supernatants upon treatment with different DCA compounds by determining pro-inflammatory and anti-inflammatory cytokines interleukin (IL)-2, IL-4, IL-6, IL-10, IL-12, tumor necrosis factor-alpha (TNF-α), and interferon-gamma (IFN-γ) using enzyme-linked immunosorbent assay (ELISA) (Figure 8.12A).[34] Treatment of PC3 cells with DCA compounds resulted in up-regulation of IL-6, IL-10, and TNF-α. The levels of all these three cytokines were higher for Mito-DCA

treated cells compared to those, which were treated with TPP-DCA or Na-DCA. When DCs are activated appropriately, they take up tumor antigens and apoptotic bodies, initiate a series of actions for the selection of antigen-specific T cells, and the release of cytokines such as IFN-γ and IL-12. We therefore, added the PC3 supernatants containing the tumor antigens to mouse BMDCs and activation was studied using ELISA.[34] We observed that the BMDCs activated with cancer cell antigens generated from Mito-DCA showed significant increased secretion of IL-12 (Figure 8.12B). TPP-DCA mediated increase in IL-12 from BMDCs was lesser compared to Mito-DCA. Supernatants generated from Na-DCA treatment did not show any increase in IL-12 levels. An enhanced IL-12 secretion by Mito-DCA-treated tumor supernatant increases the potential of enhancing natural killer cell and cytotoxic T lymphocyte activities. Acidification by lactic acid results in the suppression of TNF-α secretion by human monocytes and mouse macrophage.[35] Our data showed that the cancer cell supernatant generated from the DCA compounds treatment stimulated BMDCs to secret TNF-α and the highest level of this cytokine was observed from the supernatants which was generated from Mito-DCA due to efficient alteration of glucose metabolism from glycolysis to glucose oxidation. These results support that Mito-DCA would be a better agent for the improvement of antitumor immunity compared to the parent drug DCA. Altered cytokine pattern in the cancer cells as a result of effective lactate reduction at a low concentration of Mito-DCA has the ability to modulate DC phenotype.

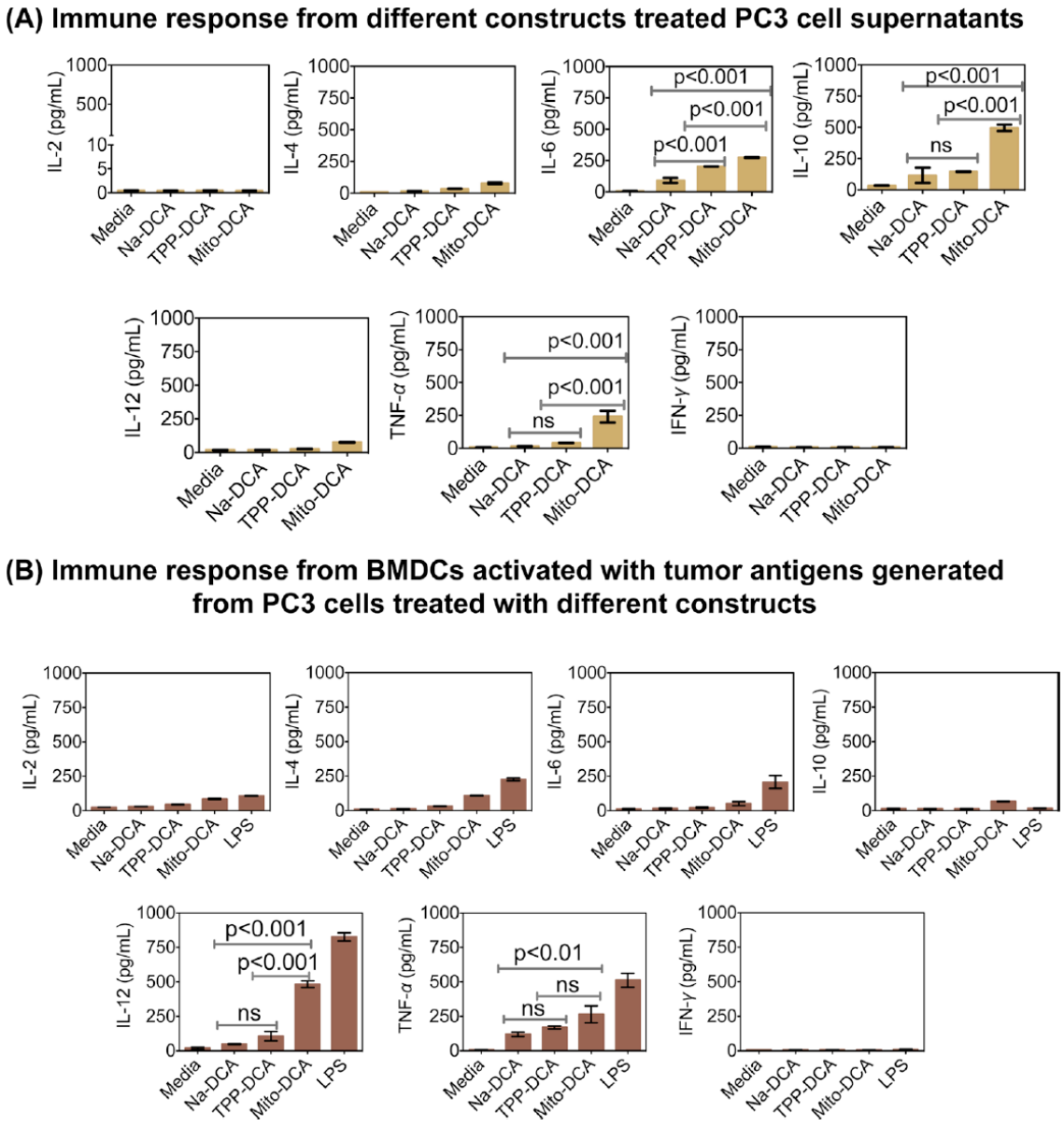


Figure 8.12. Lactate reduction by Mito-DCA stimulates anti-tumor immunity. (A) Cytokine production by PC3 cells on treatment with Mito-DCA, TPP-DCA, and Na-DCA for 24 h. (B) BMDCs activated with supernatants from PC3 cells treated with Mito-DCA, TPP-DCA, and Na-DCA show different cytokine secretion profile from the cancer cell supernatants. All data are expressed as mean ± S.D (standard deviation). Statistical analyses were performed using GraphPad Prism software 5.00. A one-way ANOVA with

a post-hoc Tukey test was used to identify significant differences among the groups. ns: non significant

Conclusion

In summary, the ability of Mito-DCA to reverse metabolism of PCa cells suggested enormous potential and warrants further investigation. TPP-based ligands represent an important class of non-peptidic mitochondrial targeting agents, however, prior to this work; this approach was never used for DCA intracellular compartmentalization. The molecular scaffold used in Mito-DCA provides opportunities to incorporate more copies of DCA keeping a single TPP targeting moiety. The lack of sensitivity of non-cancerous MSC cells to the pharmacologically relevant concentrations of Mito-DCA and two-orders of enhanced potency compared to DCA in cancer cells suggested that Mito-DCA has the potential to be non-toxic in normal tissue and highly efficacious in cancer cells. Mito-DCA showed reduced glycolytic functions, reduced basal cellular respiration, suppressed the calculated ATP synthesis, and attenuated the spare respiratory capacity in PCa cells. The effect of Mito-DCA treatments on glycolysis flux reflected its ability to reduce lactic acid production in cancer cells and that it simultaneously inhibited both OXPHOS and glycolysis. Effective lactate reduction in tumor cells by precise targeting of DCA to the mitochondria of cells in the form of Mito-DCA can not only change the tumor cell glycolysis efficiently, but also has the potential to alter the immunosuppressive environment modulated by lactic acid. These data suggest that targeting DCA to the mitochondria can stimulate cancer cell metabolism in unique ways, which can create new strategies for DCA therapy.

ACKNOWLEDGMENT

This work was supported by a start-up grant from the National Institutes of Health (P30GM092378) and Department of Defense Prostate Cancer Idea award (W81XWH-12-1-0406) to S.D. and a grant from the National Institutes of Health (NIH AI056484) to D.A.H. We thank Dr. Smanla Tundup and Joshua H. Choi for their help with BMDC isolation. We thank Prof. Rick Tarleton for Seahorse XF analyzer and Gretchen Cooley for assistance with XF analyzer. We thank Dr. Nagesh Kolishetti for valuable comments.

REFERENCES

1. Warburg, O. (1956) On the origin of cancer cells. *Science 123*, 309-314.
2. Zu, X. L.; Guppy, M. (2004) Cancer metabolism: facts, fantasy, and fiction. *Biochem. Biophys. Res. Commun. 313*, 459-465.
3. Samudio, I.; Fiegl, M.; Andreeff, M. (2009) Mitochondrial uncoupling and the Warburg effect: molecular basis for the reprogramming of cancer cell metabolism. *Cancer Res. 69*, 2163-2166.
4. Gatenby, R. A.; Gillies, R. J. (2004) Why do cancers have high aerobic glycolysis? *Nat. Rev. Cancer 4*, 891-899.
5. Kim, J. W.; Dang, C. V. (2006) Cancer's molecular sweet tooth and the Warburg effect. *Cancer Res. 66*, 8927-8930.
6. Cheong, H.; Lu, C.; Lindsten, T.; Thompson, C. B. (2012) Therapeutic targets in cancer cell metabolism and autophagy. *Nat. Biotechnol. 30*, 671-678.
7. Bonnet, S.; Archer, S. L.; Allalunis-Turner, J.; Haromy, A.; Beaulieu, C.; Thompson, R.; Lee, C. T.; Lopaschuk, G. D.; Puttagunta, L.; Bonnet, S.; Harry, G.; Hashimoto, K.; Porter, C. J.; Andrade, M. A.; Thebaud, B.; Michelakis, E. D.

(2007) A mitochondria-K+ channel axis is suppressed in cancer and its normalization promotes apoptosis and inhibits cancer growth. *Cancer Cell 11*, 37-51.

8. Dhar, S.; Lippard, S. J. (2009) Mitaplatin, a potent fusion of cisplatin and the orphan drug dichloroacetate. *Proc. Natl. Acad. Sci. U.S.A. 106*, 22199-22204.
9. Sun, R. C.; Fadia, M.; Dahlstrom, J. E.; Parish, C. R.; Board, P. G.; Blackburn, A. C. (2010) Reversal of the glycolytic phenotype by dichloroacetate inhibits metastatic breast cancer cell growth in vitro and in vivo. *Breast Cancer Res. Treat. 120*, 253-260.
10. Pearson, H. (2007) Cancer patients opt for unapproved drug. *Nature 446*, 474-475.
11. Christofk, H. R.; Vander Heiden, M. G.; Harris, M. H.; Ramanathan, A.; Gerszten, R. E.; Wei, R.; Fleming, M. D.; Schreiber, S. L.; Cantley, L. C. (2008) The M2 splice isoform of pyruvate kinase is important for cancer metabolism and tumour growth. *Nature 452*, 230-U274.
12. Stockwin, L. H.; Yu, S. X.; Borgel, S.; Hancock, C.; Wolfe, T. L.; Phillips, L. R.; Hollingshead, M. G.; Newton, D. L. (2010) Sodium dichloroacetate selectively targets cells with defects in the mitochondrial ETC. *Int. J. Cancer 127*, 2510-2519.
13. Jackson, V. N.; Halestrap, A. P. (1996) The kinetics, substrate, and inhibitor specificity of the monocarboxylate (lactate) transporter of rat liver cells determined using the fluorescent intracellular pH indicator, 2',7'-bis(carboxyethyl)-5(6)-carboxyfluorescein. *J. Biol. Chem. 271*, 861-868.

14. Coady, M. J.; Chang, M. H.; Charron, F. M.; Plata, C.; Wallendorff, B.; Sah, J. F.; Markowitz, S. D.; Romero, M. F.; Lapointe, J. Y. (2004) The human tumour suppressor gene SLC5A8 expresses a Na+-monocarboxylate cotransporter. *J. Physiol. 557*, 719-731.

15. Miyauchi, S.; Gopal, E.; Fei, Y. J.; Ganapathy, V. (2004) Functional identification of SLC5A8, a tumor suppressor down-regulated in colon cancer, as a Na(+)-coupled transporter for short-chain fatty acids. *J. Biol. Chem. 279*, 13293-13296.

16. Li, H.; Myeroff, L.; Smiraglia, D.; Romero, M. F.; Pretlow, T. P.; Kasturi, L.; Lutterbaugh, J.; Rerko, R. M.; Casey, G.; Issa, J. P.; Willis, J.; Willson, J. K.; Plass, C.; Markowitz, S. D. (2003) SLC5A8, a sodium transporter, is a tumor suppressor gene silenced by methylation in human colon aberrant crypt foci and cancers. *Proc. Natl. Acad. Sci. U.S.A. 100*, 8412-8417.

17. Babu, E.; Ramachandran, S.; CoothanKandaswamy, V.; Elangovan, S.; Prasad, P. D.; Ganapathy, V.; Thangaraju, M. (2011) Role of SLC5A8, a plasma membrane transporter and a tumor suppressor, in the antitumor activity of dichloroacetate. *Oncogene 30*, 4026-4037.

18. Gottfried, E.; Kunz-Schughart, L. A.; Ebner, S.; Mueller-Klieser, W.; Hoves, S.; Andreesen, R.; Mackensen, A.; Kreutz, M. (2006) Tumor-derived lactic acid modulates dendritic cell activation and antigen expression. *Blood 107*, 2013-2021.

19. Boddapati, S. V.; D'Souza, G. G. M.; Erdogan, S.; Torchilin, V. P.; Weissig, V. (2008) Organelle-targeted nanocarriers: Specific delivery of liposomal ceramide to mitochondria enhances its cytotoxicity in vitro and in vivo. *Nano Lett. 8*, 2559-2563.

20. Smith, R. A.; Porteous, C. M.; Gane, A. M.; Murphy, M. P. (2003) Delivery of bioactive molecules to mitochondria in vivo. *Proc. Natl. Acad. Sci. U.S.A. 100*, 5407-5412.

21. Ross, M. F.; Prime, T. A.; Abakumova, I.; James, A. M.; Porteous, C. M.; Smith, R. A.; Murphy, M. P. (2008) Rapid and extensive uptake and activation of hydrophobic triphenylphosphonium cations within cells. *Biochem. J. 411*, 633-645.

22. Marrache, S.; Dhar, S. (2012) Engineering of blended nanoparticle platform for delivery of mitochondria-acting therapeutics. *Proc. Natl. Acad. Sci. U.S.A. 109*, 16288-16293.

23. Marrache, S.; Dhar, S. (2013) Biodegradable synthetic high-density lipoprotein nanoparticles for atherosclerosis. *Proc. Natl. Acad. Sci. U.S.A. 110*, 9445-9450.

24. Marrache, S.; Tundup, S.; Harn, D. A.; Dhar, S. (2013) Ex vivo programming of dendritic cells by mitochondria-targeted nanoparticles to produce interferon-gamma for cancer immunotherapy. *ACS Nano 7*, 7392-7402.

25. Kato, M.; Li, J.; Chuang, J. L.; Chuang, D. T. (2007) Distinct structural mechanisms for inhibition of pyruvate dehydrogenase kinase isoforms by AZD7545, dichloroacetate, and radicicol. *Structure 15*, 992-1004.

26. Dhar, S.; Kodama, T.; Greenberg, M. M. (2007) Selective detection and quantification of oxidized abasic lesions in DNA. *J. Am. Chem. Soc. 129*, 8702-8703.

27. Benedettini, E.; Nguyen, P.; Loda, M. (2008) The pathogenesis of prostate cancer: from molecular to metabolic alterations. *Diagn. Histopathol. 14*, 195-201.

28. Higgins, L. H.; Withers, H. G.; Garbens, A.; Love, H. D.; Magnoni, L.; Hayward, S. W.; Moyes, C. D. (2009) Hypoxia and the metabolic phenotype of prostate cancer cells. *Biochim. Biophys. Acta. 1787*, 1433-1443.

29. Helman, L. J.; Meltzer, P. (2003) Mechanisms of sarcoma development. *Nat. Rev. Cancer 3*, 685-694.

30. Kim, R.; Emi, M.; Tanabe, K. (2007) Cancer immunoediting from immune surveillance to immune escape. *Immunology 121*, 1-14.

31. Gabrilovich, D. I.; Chen, H. L.; Girgis, K. R.; Cunningham, H. T.; Meny, G. M.; Nadaf, S.; Kavanaugh, D.; Carbone, D. P. (1996) Production of vascular endothelial growth factor by human tumors inhibits the functional maturation of dendritic cells. *Nat. Med. 2*, 1096-1103.

32. Radmayr, C.; Bock, G.; Hobisch, A.; Klocker, H.; Bartsch, G.; Thurnher, M. (1995) Dendritic antigen-presenting cells from the peripheral blood of renal-cell-carcinoma patients. *Int. J. Cancer 63*, 627-632.

33. Orsini, E.; Guarini, A.; Chiaretti, S.; Mauro, F. R.; Foa, R. (2003) The circulating dendritic cell compartment in patients with chronic lymphocytic leukemia is severely defective and unable to stimulate an effective T-cell response. *Cancer Res. 63*, 4497-4506.

34. Marrache, S.; Choi, J. H.; Tundup, S.; Zaver, D.; Harn, D. A.; Dhar, S. (2013) Immune stimulating photoactive hybrid nanoparticles for metastatic breast cancer. *Integr. Biol. 5*, 215-223.

35. Dietl, K.; Renner, K.; Dettmer, K.; Timischl, B.; Eberhart, K.; Dorn, C.; Hellerbrand, C.; Kastenberger, M.; Kunz-Schughart, L. A.; Oefner, P. J.;

Andreesen, R.; Gottfried, E.; Kreutz, M. P. (2010) Lactic acid and acidification inhibit TNF secretion and glycolysis of human monocytes. *J. Immunol. 184*, 1200-1209.

CHAPTER 9

CONCLUSIONS AND FUTURE DIRECTIONS

Conclusions

This thesis has introduced and described a fresh look on targeting NPs and small molecules to the mitochondria. These were developed in order to find new potential ways to treat cancer, obesity, Alzheimer's disease, cardiovascular disease, and traumatic brain injury. Chapter 1 provides an introduction on why mitochondria targeting is important and also a literature on what has been done in recent years. The majority of research is based on small molecules using lipophilic cations in order to pass into the matrix of the mitochondria. A few examples of nano-based delivery systems were also discussed.

Chapter 2 describes the development of a library of NPs with varying surface charge and sizes in order to optimize overall mitochondrial delivery. Once the optimum surface charge and size was found, the particles were loaded with a variety of different mitochondria acting therapeutics. Lonidamine and α-tocopherol succinate were encapsulated and tested *in vitro* for their efficacy in the reduction of cervical cancer cells. Curcumin was encapsulated to determine if the particles could limit the toxicity caused by β-amyloid peptide in neuroblastomas. Finally, 2,4-dinitrophenol was used to reduce lipid accumulation in 3T3-L1 adipocytes.

Chapter 3 demonstrates the use of the same NP system in mitochondria targeted photodynamic therapy. These NPs were able to stimulate dendritic cells to produce a

potent immune response, including the cytokine IFN-γ. When co-cultured with T-cells, cancer cell lysate treated dendritic cells were able to cause T-cell activation. This work is a promising step in the right direction for the development of anti-tumor immunity.

Chapter 4 describes a new strategy for overcoming cisplatin resistance by directing it to the mitochondria. A mitochondria targeted prodrug, Platin-M, in its free form and when encapsulated in a mitochondria targeted polymeric delivery vehicle, showed significant improvement over conventional cisplatin therapy *in vitro*. It was shown that the delivery vehicle has the potential to cross the blood-brain-barrier with high efficiency. In the future this nanoparticle formulation can be developed for potential use in brain cancer.

Chapter 5 shows the use of a mitochondria targeted NP platform for the treatment of the symptoms of traumatic brain injury. The NPs were able to deliver a combination of an anti-inflammatory and an antioxidant to neural stem cells. They were able to show protection against reactive oxygen species and inflammation. *In vivo*, the mitochondria targeted NPs were able to cross the blood-brain-barrier in healthy and traumatic brain injury induced pig models. This system has the potential to be an ideal delivery system for a combined neuroprotective-stem cell therapy for traumatic brain injury and other similar diseases of central nervous system.

Chapter 6 details the synthesis of mitochondria targeted, completely synthetic high-density lipoprotein mimicking NP for imaging and treatment of atherosclerosis. The NPs were able to not only sense apoptotic events of macrophages, but also bind to cholesterol making it an ideal theranostic delivery vehicle. *In vitro* results showed that the NPs were non-toxic and non-immunogenic. The NPs also showed favorable

biodistribution and pharmacokinetic properties and remarkable ability to reduce overall triglyceride and cholesterol content in rodent and pig models.

Chapter 7 describes the synthesis and biological activity of a mitochondria-targeted gold nanoparticle delivery vehicle for the mitochondria acting small molecule, 3-bromopyruvic acid. The delivery vehicle showed the ability to enter the mitochondria and release 3-bromopyruvate. The NPs were also able to exhibit enhanced cytotoxicity with laser irradiation.

Chapter 8 details the properties of a mitochondria targeted small molecule prodrug of dichloroacetate, Mito-DCA. The scaffold of Mito-DCA allows for the attachment of three dichloroacetates. While safe and non-toxic in normal mesenchymal stem cells, Mito-DCA displayed a significant improvement in the cytotoxic profiles in different prostate cancer cells. This is due to the high efficiency in which Mito-DCA was able to reduce lactate production, therefore inhibiting oxidative phosphorylation and glycolysis. It also has the ability, by limiting lactate production, to alter the immunosuppressive environment that highly glycolytic cancer cells produce.

Future Goals

This dissertation has shown numerous new methods to approach therapy of different diseases by targeting the mitochondria. Currently, work in our lab is directed towards determining the efficacy of these systems *in vivo*. With regards to the work in Chapter 3, the ability to generate IFN-γ, *in vivo* is currently underway. This would be a huge advance in the field of cancer immunotherapy. As a pilot study, the cancer cell lysates will be injected into mice and at a given time point, dendritic cells will be isolated and analyzed for intracellular IFN-γ.

The mitochondria-targeted cisplatin prodrug, Platin-M, and its nanoparticle formulation discussed in Chapter 5 has shown immense potential to overcome cisplatin resistance in prostate, brain, and ovarian cancer cells. Currently, there are *in vivo* studies underway to test the safety of this formulation in canine subjects. The next step will be to evaluate this system's potential to reduce brain tumors *in vivo*.

As illustrated in Chapter 4, PLGA-*b*-PEG-TPP NPs have the ability to efficiently cross the blood-brain-barrier. It was also demonstrated that the new mitochondria targeted cisplatin pro-drug was able to inhibit the growth of brain cancer cells. The next step of this would be to test the ability of these particles to reduce brain cancer in an animal model.

The high-density lipoprotein mimicking NPs discussed in Chapter 6 will be tested in an atherosclerotic mouse model. The studies done until now have all been performed in healthy rats. An atherosclerotic model would allow our lab to realize the true potential of these NPs at imaging and treating heart disease.

Chapter 7 describes a new AuNP formulation of 3-Bromopyruvate. While this has shown to be a vast improvement in the treatment of prostate cancer *in vitro*, there are many improvements that need to be done in order to ensure its success *in vivo*. The novelty of this system lies in its ease in further functionalization. In order to improve upon *in vivo* biodistribution, a tumor specific targeting ligand can be added to the formulation. This will increase the chance at selectively targeting the tumor. Moreover, more controlled synthetic methods during the AuNP synthesis can be done in order to have more control over the geometry. This could also open a wide array of opportunities in order to study *in vivo* and *in vitro* geometry based mitochondrial targeting.

Lastly, Chapter 8 was used to selectively inhibit glycolysis in prostate cancer. *In vivo* this system, however, could fail from the same typical drawbacks that many small molecules suffer from, premature cleavage and breakdown of the molecule before reaching its target location. To improve on this, encapsulation in a NP formulation could allow for protection from the body while also allowing for the advantages that NPs bring, such as the EPR effect.

APPENDIX I

IMMUNE STIMULATING PHOTOACTIVE HYBRID NANOPARTICLES FOR METASTATIC BREAST CANCER[1]

Reprinted with the permission of Marrache, S.; Choi, J.H.; Tundup, S.; Zaver, D.; Harn, D.A.; and Dhar, S. *Integr. Biol.,* 5, 215-223. Copyright 2013 Royal Society of Chemistry

Abstract

A therapeutic technology that combines the phototoxic and immune-stimulating ability of photodynamic therapy (PDT) with the widespread effectiveness of the immune system can be very promising to treat metastatic breast cancer. We speculated that the knowledge of molecular mechanisms of existing multi-component therapies could provide clues to aid the discovery of new combinations of an immunostimulant with a photosensitizer (PS) using a nanoparticle (NP) delivery platform. Therapeutic challenges when administering therapeutic combinations include the choice of dosages to reduce side effects, the definitive delivery of the correct drug ratio, and exposure to the targets of interest. These factors are very difficult to achieve when drugs are individually administered. By combining controlled release polymer-based NP drug delivery approaches, we were able to differentially deliver zinc phthalocyanine (ZnPc) based PS to metastatic breast cancer cells along with CpG-ODN, a single-stranded DNA that is a known immunostimulant to manage the distant tumors in a temporally regulated manner resulting in more effective management of deadly metastatic breast cancer. We encapsulated ZnPc which is a long-wavelength absorbing PS within a polymeric NP core made up of poly(D,L-lactic-*co*-glycolic acid)-*b*-poly(ethylene glycol) (PLGA-*b*-PEG). After coating the outside of the polymeric core with gold NPs (AuNPs), we further modified the AuNP surface with CpG-ODN. In vitro cytotoxicity using 4T1 metastatic mouse breast carcinoma cells shows significant photocytotoxicity of the hybrid NPs containing both ZnPc and CpG-ODN after irradiation with a 660 nm LASER light and this activity was remarkably better than either treatment alone. Treatment of mouse bone marrow derived dendritic cells with the PDT-killed 4T1 cell lysate shows that the

combination of PDT with a synergistic immunostimulant in a single NP system results in significant immune response, which can be used for the treatment of metastatic cancer.

Introduction

The management of metastatic breast cancer remains a therapeutic challenge.[1] An ideal cancer treatment should not only cause tumor regression and eradication but also induce a systemic antitumor immunity for control of metastatic tumors and long-term tumor resistance. This can be achieved by using the immune system as a weapon to recognize the tumor antigen so that once the primary tumor is eliminated, metastases will also be destroyed. Earlier success in applying the immune system to metastatic cancer, as well as the limited contributions from conventional chemo or radiation therapy makes metastatic cancer a focus for contemporary development of novel treatment options.[2] The main pillars of cancer treatment chemotherapy, surgery, and radiation therapy are known to suppress the immune system.[3] The only cancer treatment that stimulates anti-tumor immunity is photodynamic therapy (PDT).[3, 4] PDT involves administration of a photosensitizer (PS) followed by illumination of the tumor with a long wavelength (600-800 nm) light producing reactive oxygen species (ROS) resulting in vascular shutdown, cancer cell apoptosis, and the induction of a host immune response.[5] The exact mechanism involved in the PDT-mediated induction of anti-tumor immunity is not yet understood. Possible mechanisms include alterations in the tumor microenvironment by stimulating pro-inflammatory cytokines and direct effects of PDT on the tumor that increases immunogenicity.[3] PDT can increase dendritic cells (DC) maturation and differentiation, which leads to the generation of tumor specific cytotoxic CD8 T cells, that can destroy distant deposits of untreated tumor (Fig. A.1).[3, 6-8]

There are increasing number of studies showing that immunoadjuvants when injected intratumorally can produce a similar infiltration of leukocytes into the tumor.[3] Immunoadjuvants are frequently prepared from microbial cells and are thought to act via Toll-like receptors (TLRs)[9] present on macrophages and DCs. This indicates that a combination of PDT with a DC activating agent that can act as an agonist of TLR might be promising for the treatment of metastatic tumor. There are few reports of combinations of PDT with microbial derived products potentiating tumor response and leading to long-term anti-tumor immunity.[3, 10] However, thus far administrating the immunoadjuvants as separate constructs by intratumoral injection has only been explored to combine PDT with immunotherapy[11, 12], their use as a single construct should receive careful consideration. Nanotechnology-based differential combination therapy can be emphasized as a promising strategy for metastatic breast cancer. By combining controlled release nanoparticles (NPs), PDT, and immune activation**,** we aimed to differentially deliver PS with synergistic immunoadjuvants in a temporally regulated manner resulting in a safer and more effective management of the deadly form of metastatic breast cancer. Here we report a highly advanced biodegradable hybrid NP platform for proof-of-concept demonstration for such a technology (Fig. A.2). Polymeric NPs of poly(lactide-*co*-glycolide)-*b*-polyethyleneglycol (PLGA-*b*-PEG) block copolymers are especially promising as drug delivery vehicles.[13-18] The use of PLGA and PEG polymers in the Food and Drug Administration (FDA) approved products makes these biomaterials ideal for the development of new therapeutics. We used zinc(II) phthalocyanine (ZnPc)[19] as a PS because of its high optical absorption coefficient in the 600 to 800 nm phototherapeutic window, which is higher than the FDA approved PDT drug

photofrin®.[2] We encapsulated the PS inside PLGA-*b*-PEG polymeric NPs and modified the surface of the polymeric core with gold NPs (AuNPs) by using non-covalent interactions. For immune stimulation, the surface of the AuNPs was utilized to introduce 5'-purine-purine/T-CpG-pyrimidine-pyrimidine-3'-oligodeoxynucleotides (CpG-ODN) as a potent DC activating agent.[20, 21]

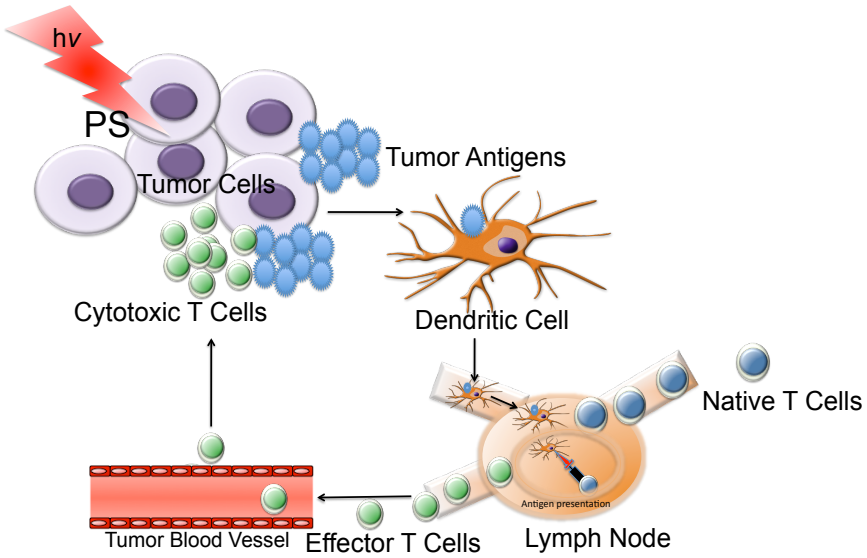


Fig. A.1. Phagocytosis of tumor antigens by DCs after PDT.

Materials and methods

All chemicals were used without further purification unless otherwise noted. PLGA-COOH of inherent viscosity of 0.18 dL/g was purchased from Lactel. NH_2-PEG-NH_2 (MW 2000) was obtained from JenKem USA. 4-dimethylaminopyridine (DMAP), N,N'-dicyclohexylcarbodiimide (DCC), and 3-(4,5-dimethylthiazol-2-yl)-2,5-diphenyltetrazolium bromide (MTT) were purchased from Sigma-Aldrich. AuNPs of size 5 nm (5 x 10^{13} particles/mL) were purchased from BBInternational. Phosphorothioate oligonucleotide CpG-ODN-1826 of sequence 5′-TCCATGACGTTCCTGACGTT-3′ was

purchased from Midland certified reagent company (Midland, Tex.). Granulocyte-macrophage colony-stimulating factor (GM-CSF) was purchased from R&D systems. Cytokines were tested using BD OptEIA mouse enzyme-linked immunosorbent assay (ELISA) kits. Distilled water was purified by passage through a Millipore Milli-Q Biocel water purification system (18.2 MΩ) containing a 0.22 μm filter. Dynamic light scattering (DLS) measurements for size, zeta potential, and polydispersity index (PDI) were carried out using a Malvern Zetasizer Nano ZS system. ^{1}H and ^{13}C NMR spectra were recorded on a 400 MHz Varian NMR spectrometer. Gel permeation chromatographic (GPC) analyses were performed on Shimadzu LC20-AD prominence liquid chromatographer equipped with a RI detector, molecular weights were calculated using a conventional calibration curve constructed from narrow polystyrene standards. Optical measurements were carried out on a NanoDrop 2000 spectrophotometer. HPLC analyses were made on an Agilent 1200 series instrument equipped with a multi-wavelength UV-visible detector. Transmission electron microscopy (TEM) images were taken in a FEI Tecnai 20 TEM microscope. LASER irradiation was performed using a Melles Griot 660 nm 56 ICS series diode laser equipped with a fiber optic cable in a dark environment.

Cell Line and Cell Culture

The BALB/c mammary adenocarcinoma 410.4 sub-line 4T1 cells from the American Type Culture Collection (ATCC) were grown in RPMI 1640 media containing HEPES, glutamine, sodium pyruvate, 10% fetal bovine serum (FBS), 100 U/mL penicillin, and 100 μg/mL streptomycin at 37 °C in 5% CO_2. Cells were passed every 3 days and restarted from the frozen stocks upon reaching pass number 20.

Animals

Animals were obtained from Jackson Laboratory and handled in accordance with "The guide for the Care and Use of Laboratory Animals" of American Association for Accreditation of Laboratory Animal Care (AALAC), Animal Welfare Act (AWA), and other applicable federal and state guidelines. All animal work presented here was approved by Institutional Animal Care and Use Committee (IACUC) of University of Georgia.

Synthesis of PLGA-*b*-PEG-NH_2

PLGA-b-PEG-NH2 was synthesized and characterized by Mr. Joshua Choi and Mr. Dhillon Zaver. Details can be found in *Integr. Biol.,* 5, 215-223.

Synthesis of ZnPc-Poly-NPs

ZnPc-encapsulated NPs (ZnPc-Poly-NPs) were prepared by using the nanoprecipitation method.[14] PLGA-*b*-PEG-NH_2 (50 mg/mL) and ZnPc, at varying percent weight with respect to the polymer weight, were dissolved in DMF. This mixture was slowly added to water over a period of 10 min. The NPs formed were stirred at room temperature for 2-3 h and washed 3 times with nanopure water using Amicon ultracentrifugation filtration membranes with a molecular weight cutoff of 100 kDa (3000 rpm, 4 ^{o}C). The NP size, PDI, and zeta potential were obtained by DLS measurements. Size and the morphology of the NPs were further confirmed by TEM. The ZnPc content in the NPs was measured by HPLC.

Synthesis of Au-ZnPc-Poly-NPs

An aqueous suspension of 1 mL ZnPc-Poly-NPs was added to a 2 mL aqueous solution of citrate coated AuNPs of size 5 nm and allowed to sit for 4 h at room temperature. The NPs were characterized by DLS, TEM, and UV-Vis spectroscopy.

Synthesis of CpG-ODN-Au-ZnPc-Poly-NPs

CpG-ODN of sequence 5′-TCCATGACGTTCCTGACGTT-3′ with a disulfide bond in the 5′ end was deprotected according to the manufacturer's protocol. Briefly, to a solution of CpG-ODN in 0.1 M triethylammonium acetate buffer (pH 6.5), an aqueous solution of 0.1 M DTT was added and incubated at room temperature for 30 min. The deprotected CpG-ODN was purified using a 50 mg C18 Sep-Pak cartridge (Waters, Milford, MA) equilibrated in and eluted with DNase/RNase-free distilled water. The concentration of the CpG-ODN was measured by UV-Vis spectroscopy. Au-ZnPc-Poly-NPs were added to an equivalent volume of 10% (v/v) Tween 20 at room temperature. Then CpG-ODN was added (210 μL, 105 μg/mL) and incubated at room temperature in a shaker for 20 h. CpG-ODN-Au-ZnPc-Poly-NPs were washed 3 times using Amicon ultracentrifugation filtration membranes with a molecular weight cutoff of 100 kDa (3000 rpm, 4 ^{o}C). Finally, NPs were resuspended in water and analyzed by DLS. NP solutions were analyzed by UV-Vis after dissolving the polymeric core using 1 M NaOH for determination of encapsulated ZnPc content or dissolving the gold core with 0.6 M KI for quantification of conjugated CpG-ODN.

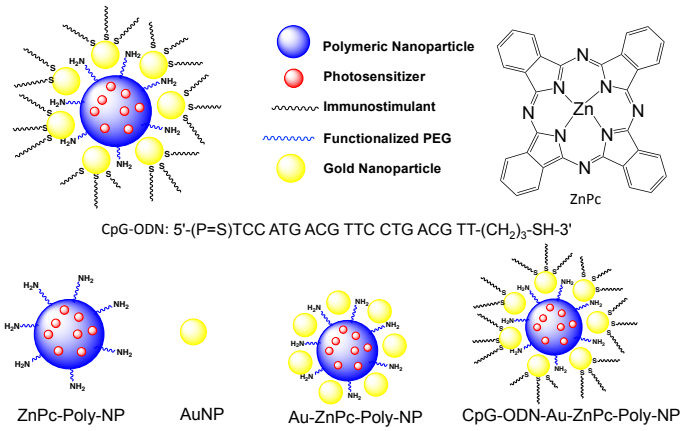


Fig. A.2. Schematic diagram of the NP platform for combination therapy of metastatic breast cancer.

Determination of ZnPc loading and encapsulation efficiency

ZnPc loading and encapsulation efficiency (EE) were calculated by dissolving the polymer core by mixing equal portions of the NP solution and 1 N NaOH, followed by dilution with a 50:50 water:acetonitrile mixture, and subsequent HPLC analysis (wavelength: 670 nm). ZnPc loading is defined as the mass fraction of PS in the NPs, whereas EE is the fraction of initial PS used for encapsulation by the NPs during nanoprecipitaion.[22]

MTT Assay

The phototoxic behavior of all the NPs was evaluated using the MTT assay against 4T1 cells. 4T1 cells (1500 cells/well) were seeded on a 96-well plate in 100 μL of RPMI medium and incubated for 24 h. The cells were treated with NPs at varying concentrations (with respect to ZnPc) and incubated for 2 h at 37 °C. The cells were then irradiated with a 660 nm LASER (power 20 mV) with a fiber optics for 5 min per well. Irradiated cells were incubated for 12 h at 37 °C, medium was changed after 12 h, and the cells were incubated for additional 60 h. The cells were then treated with 20 μL of MTT

(5 mg/mL in PBS) for 5 h. The medium was removed, the cells were lysed with 100 μL of DMSO, and the absorbance of the purple formazan was recorded at 550 nm using a Bio-Tek Synergy HT microplate reader. Each well was performed in triplicate. All experiments were repeated three times. Cytotoxicity was expressed as mean percentage increase relative to the unexposed control ± SD. Control values were set at 0% cytotoxicity or 100% cell viability. Cytotoxicity data (where appropriate) was fitted to a sigmoidal curve and a three parameters logistic model was used to calculate the IC_{50}, which is the concentration of the agent causing 50% inhibition in comparison to untreated controls. The mean IC_{50} is the concentration of agent that reduces cell growth by 50% under the experimental conditions and is the average from at least three independent measurements that were reproducible and statistically significant. The IC_{50} values are reported at ±95% confidence intervals (±95% CI). This analysis was performed with Graph Pad Prism (San Diego, U.S.A) software.

Generation of bone marrow derived dendritic cells

Bone marrow derived dendritic cells (BMDCs) were isolated and purified by Dr. Smanla Tundup from the Department of Infectious Diseases.

Preparation of PDT treated 4T1 cells

4T1 cells were plated at the concentration of 4 x 10^5 cells/well in six well plates and allowed to grow for 24 h. On the next day, the cells were incubated with 10 nM ZnPc, 6.16 nM CpG-ODN, a mixture of 10 nM ZnPc and 6.16 nM CpG-ODN, 10 nM ZnPc-Poly-NPs, 10 nM Au-ZnPc-Poly-NPs, 10 nM CpG-ODN-Au-ZnPc-Poly-NPs for 2 h, and irradiated with a 660 nm LASER light for 5 min. Cells were left in the culture for 12 h at 37 °C and PDT lysates were used for stimulation of the BMDCs.

Stimulation of BMDCs with supernatants from PDT treated tumor cells

The PDT–lysates obtained 24 h post PDT treatment of 4T1 cells were added to freshly prepared BMDCs. Additionally lipopolysaccharide (LPS) alone (100 ng/mL) or CpG-ODN alone (1 μg/mL or 10 μg/mL) was added to the DC cultures as controls. DCs were incubated with the supernatants for 12 h at 37 °C and the supernatants were harvested for further studies.

Immune response by ELISA

ELISA was performed using the supernatants harvested from BMDC culture to measure the levels of cytokines IL-2, IL-4, IL-6, IL-10, IL-12, TNF-α, and IFN-γ according to manufactures protocol. Briefly, the cell supernatants were incubated with antibody-coated plates for 2 h at room temperature. This was immediately followed by washings and sequential incubations with the biotin-conjugated detection antibody and streptavidin-horseradish peroxidase (HRP) solution. Finally, the ELISA was developed by adding the substrate (100 μL/well) to each well followed by a stop solution. The absorbance was recorded at 450 nm using a BioTek Synergy HT well plate reader.

Results and Discussions

Synthesis of the polymer and construction of the NPs

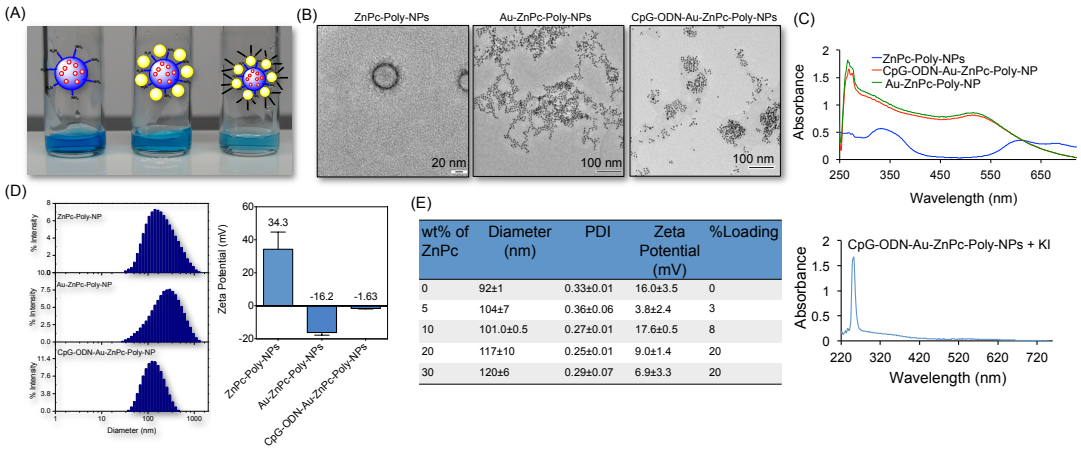
To co-deliver PS and an immunoadjuvant using a single NP construct and to obtain adequate control over encapsulation of the hydrophobic PS, ZnPc, we synthesized a biodegradable polymer with a terminal $–NH_2$ group (PLGA-*b*-PEG-NH_2) via an amide coupling of PLGA-COOH with NH_2-PEG-NH_2 using DCC/DMAP as coupling agents. This polymer was characterized by ^{1}H and ^{13}C NMR spectroscopy. Purity, molecular

weights, and PDI of the polymer were determined by GPC measurements using tetrahydrofuran mobile phase. These results are consistent with previously reported data for PLGA-*b*-PEG-COOH polymer.[23]

Synthesis of the NPs with PLGA-*b*-PEG-NH_2 was achieved by the nanoprecipitation method.[13, 14] PLGA-*b*-PEG-NH_2 was dissolved in a water miscible solvent DMF and then added drop wise into an aqueous solution, generating NPs. The properties of the encapsulated NPs were characterized by DLS to give the hydrodynamic diameter, zeta potential, and PDI of each preparation. To optimize the size and loading, a series of encapsulated NPs were prepared by varying the weight percentage of ZnPc to polymer (%w/w) and by using PEG of various molecular masses. When the DMF solution of the polymer and ZnPc was added to water, the mixture became turbid, indicating the formation of NPs. However, depending on the conditions, the final suspension contained a larger or smaller amount of larger polymeric aggregates either dispersed in the aqueous phase or adhering to the flask wall or to the magnetic stirring bar. In this way, we found that PLGA of inherent viscosity 0.18 dL/g in hexafluoroisopropanol affords the most suitable encapsulated NPs. It is worth noting that measurements of NP size made on three different batches produced under identical conditions fell within a range of 10% variation, indicating a good reproducibility. The loading efficiencies of ZnPc at various added weight percentage with respect to the polymer weight are given in Fig. 3. The size of the NPs increased with ZnPc loading (Fig. A.3). For all in vitro studies, we used encapsulated NPs containing 30% ZnPc added with respect to the polymer.

For the synthesis of the hybrid NPs, anionic ligand citrate stabilized AuNPs were used. This allowed an effective binding between the positively charged NH_2 groups of the polymeric ZnPc-Poly-NPs and the negatively charged citrate groups of the AuNPs. The formation of these hybrid Au-ZnPc-Poly-NPs was evident from the DLS measurement, which shows a change in the zeta potential of the polymeric NPs from positive to a negative value (Fig. A.3). The addition of ZnPc-Poly-NPs to AuNPs did not cause any aggregation (Fig. A.3).

We modified the AuNP surface with CpG-ODN with a 5′-modified –SH group.[24] We were able to load high concentration of CpG-ODN on the AuNP surface as evident from the UV-Vis study. CpG-ODN adsorption stabilizes the hybrid NPs and the steric repulsion of the NPs prevents flocculation as evident from the decrease in size and PDI (Fig. A.3). Negative zeta potential of Au-ZnPc-Poly-NPs decreased with the formation of CpG-ODN-Au-ZnPc-Poly-NPs.



wt% of ZnPc	Diameter (nm)	PDI	Zeta Potential (mV)	%Loading
0	92±1	0.33±0.01	16.0±3.5	0
5	104±7	0.36±0.06	3.8±2.4	3
10	101.0±0.5	0.27±0.01	17.6±0.5	8
20	117±10	0.25±0.01	9.0±1.4	20
30	120±6	0.29±0.07	6.9±3.3	20

Fig. A.3. Characterization of hybrid NP constructs. (A) Photographs of NP suspensions showing no visible aggregation. (B) TEM images of ZnPc-Poly-NPs, Au-ZnPc-Poly-NPs, and CpG-ODN-Au-ZnPc-Poly-NPs. (C) Characterization of hybrid NPs by UV-Vis spectroscopy. (D) Hydrodynamic diameter and zeta potential of the NPs by DLS

measurements. (E) Sizes, PDI, zeta potential, and loading of ZnPc in the PLGA-*b*-PEG-NH_2 with varied ZnPc percent weight.

In vitro stability of the hybrid NPs

In vitro stability of NPs can be defined relative to changes in hydrodynamic size and surface charge in response to changes in the sample environment. The key physicochemical properties, nanoparticle size, surface zeta potential, and morphology determine the in vivo stability profiles. We checked the short-term stability of an aqueous suspension of CpG-ODN-Au-ZnPc-Poly-NPs by storing at 4 °C for 30 days and evaluating the size distribution and zeta potential. The diameter of the hybrid NPs decreases day after day. The mean size decreased from 186 nm to ~90 nm after 30 days and the surface charge changes from ~ -10 mV to -20 mV.

In vitro phototoxicity on metastatic breast cancer cells

The photodynamic activities of ZnPc-Poly-NPs, Au-ZnPc-Poly-NPs, and CpG-ODN-Au-ZnPc-Poly-NPs were investigated against 4T1 cell line using a 660 nm laser. In parallel, cells were incubated with all the constructs without illumination to serve as dark controls (Fig. A.4). None of these constructs show any phototoxicity in the dark. The induction of cell death was both light and ZnPc-dose dependent. Two hours following the incubations, cells were illuminated with a 660 nm LASER light for 5 min per well. The mortality of post-PDT cultures was determined following the MTT assay. A higher phototoxic effect was observed with CpG-ODN-Au-ZnPc-Poly-NPs (IC_{50}; 2.8 nM) than the ZnPc-Poly-NPs (IC_{50}; 15 nM), Au-ZnPc-Poly-NPs (IC_{50}; 6 nM) or free ZnPc (IC_{50}; 317 nM) (Fig. A.4). Control cells incubated with unconjugated AuNPs did not display any significant cell death after illumination. Thus, under these in vitro conditions we can

exclude the possibility that any case of cell death is due to the photothermal activity of the AuNPs. Interestingly, the efficacy of free ZnPc was lower than that for hybrid NPs containing ZnPc in the polymeric core and CpG-ODN immobilized on the AuNP surface. This enhancement in photodynamic efficacy is likely to be a consequence of synergistic effect between ZnPc and CpG-ODN when delivered in a single construct.

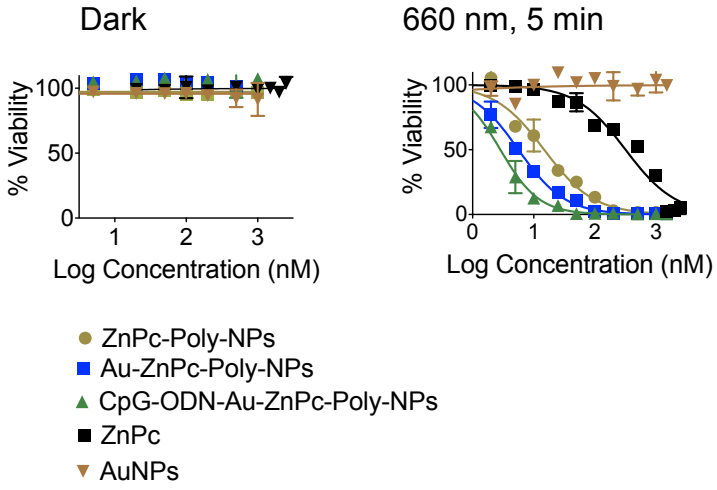


Fig. A.4. Cytotoxicity profiles of ZnPc-Poly-NPs, Au-ZnPc-Poly-NPs, and CpG-ODN-Au-ZnPc-Poly-NPs in 4T1 cells in the dark (left) and after 5 min exposure with a 660 nm LASER (right). Free ZnPc and AuNPs were used as controls.

In vitro antitumor immunity after PDT

We incubated bone marrow derived immature DCs isolated from C57BL/6 mice with CpG-ODN or with LPS, a TLR4 agonist generally employed as a positive factor to stimulate and activate DCs, as positive controls and with PDT killed 4T1 cell lysates. We used ELISA analysis to assess the immune response by measuring the levels of several proinflammatory cytokines (Fig. A.5). When CpG-ODN-Au-ZnPc-Poly-NP treated PDT killed 4T1 tumor cell lysate was incubated with DCs, there was a synergistic increase in the production of IL-2, IL-6, IL-12, and TNF-α and these levels were either comparable

or above the level of activation achieved with LPS (Fig. A.5). However when a combination of free CpG-ODN and ZnPc, or ZnPc-Poly-NP treated PDT killed 4T1 cell lysates were incubated with DCs, all the cytokine levels were below than the levels observed for CpG-ODN-Au-ZnPc-Poly-NPs. CpG-ODN alone had only a slight effect in secretion of these cytokines. These data suggest that a combination of CpG-ODN and a photosensitizer in a single NP construct can prime DC to recognize and phagocytosize PDT killed tumor cells, and that this phagocytosis can lead to DC maturation and activation. Our construct causes activation of a specific and systemic immune response after PDT, which may result in not only further destruction of remaining local tumor cells but also the prevention of possible recurrence. The antitumor efficacy of PDT was further enhanced through an effective immunoadjuvant CpG-ODN to expand its usefulness for a possible control of distant metastasis. The concentrations of other cytokines, IL-4, IL-10, and IFN-γ were not changed compared with those of dark controls. Control experiments with various NPs without encapsulated ZnPc showed no significant activation after PDT or in the dark except for empty-CpG-ODN-Au-Poly-NPs, which showed immune response comparable to free CpG-ODN.

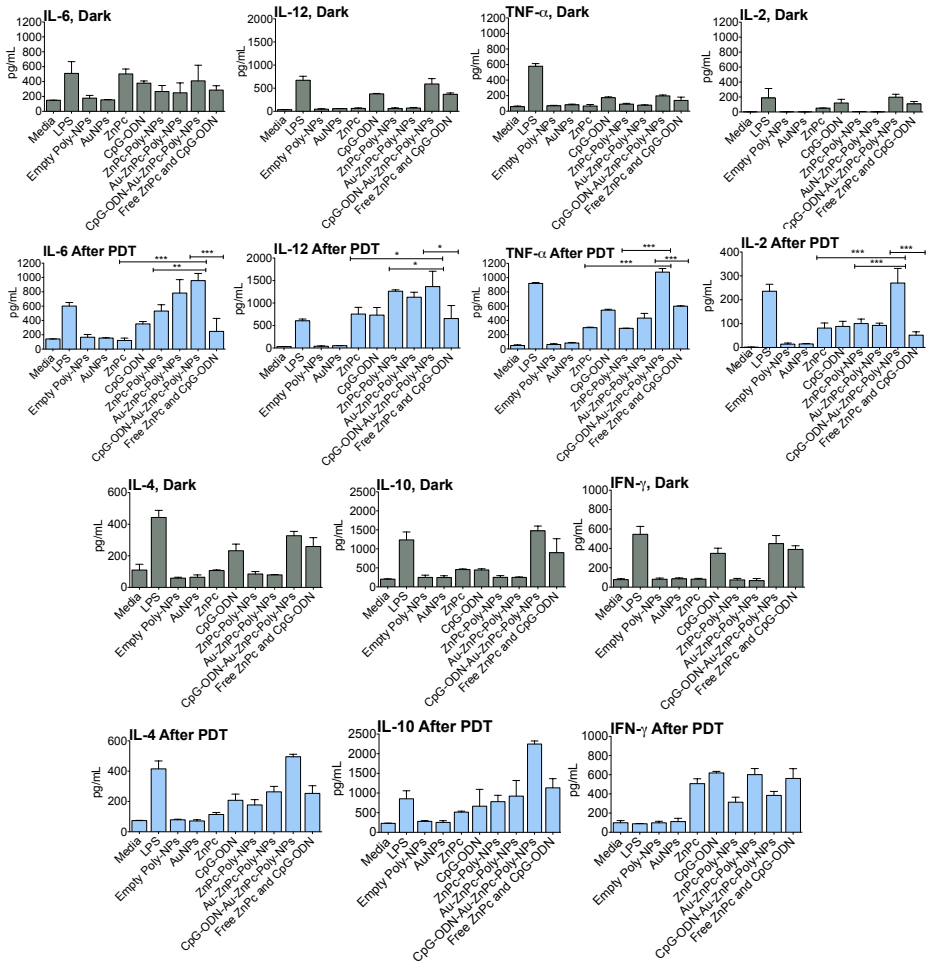


Fig. A.5. Combination of ZnPc and CpG-ODN in a single NP construct potentiate immune response after PDT. Asterisk represents significant differences between CpG-ODN-Au-ZnPc-Poly-NPs, ZnPc-Poly-NPs, free ZnPc, and a 1:1 combination of free ZnPc and CpG-ODN according to one-way ANOVA with Tukey post hoc test. Single, double, and triple asterisks indicate a P value < 0.05, < 0.004, and < 0.001, respectively.

Discussion

We designed a hybrid NP to load both PS and an immunoadjuvant. A hydrophobic photosensitizer is required to achieve high loading inside polymeric NPs. ZnPc, which is hydrophobic provided us with the required solubility needed for

encapsulation inside the hydrophobic core of biodegradable PLGA-*b*-PEG-NH_2 NPs. The terminal NH_2 groups were used as convenient handles for coupling of anionic citrate stabilized AuNPs through non-covalent electrostatic interaction. The formation of the AuNP coated NPs were evident from the changes in the zeta potential and appearance of the surface plasmon band at 520 nm in the absorption spectrum. Addition of ZnPc-Poly-NPs to AuNPs did not cause any visible aggregation (Fig. A.3A). This was followed photometrically by observing the decrease and/or red shift of the plasmon absorption band of AuNPs at ~520 nm. Absence of any change in the 520 nm band confirms that this hybrid NP system is stable (Fig. A.3C). Formation of the hybrid NPs were also evident from the TEM images (Fig. A.3B). We adopted this non-covalent attachment approach with the goal that ZnPc inside the polymeric core will be released inside the cancer cells, whereas CpG-ODN containing AuNPs will be detached from the polymeric NPs and can be engaged in activating tumor associated DCs after PDT. AuNP surface has many advantageous properties such as chemical stability, a highly electron dense core, and ease of conjugation to oligonucleotides.[24] CpG-ODNs are powerful stimulators of innate as well as adaptive immune responses; however, the immunopotency of CpG-ODN is less when given in the free form.[25] Our technology of mobilizing CpG-ODN on the AuNP surface for immediate release after PDT specifically targets CpG-ODN for uptake by the immune cells. Immobilization of CpG-ODN was confirmed by UV-vis spectroscopy (Fig. A.3C). In CpG-ODN-Au-ZnPc-Poly-NPs, the Au core masks DNA absorption band. The DNA band appears at 260 nm upon dissolution of the Au core by KI and confirms the presence of CpG-ODN in the hybrid NPs (Fig. A.3C). We have used a nuclease-resistant phosphorothioate backbone, which is known to improve the stability of an optimal CpG-

ODN and its ability to activate B cells and DCs, and to induce cytokine production.[26-29] However, it is important to note that the phosphorothioate backbone also reduces the ability to activate natural killer (NK) cells and thus may be less useful for tumor immunotherapy applications that depend on these effector cells.[30]

NP stability in aqueous solution is critical for their utility as a drug delivery vehicle in vivo. NP size is one of the most critical parameters that determine systemic circulation lifetime and NP ability to passively accumulate in tumor tissues and NPs with a size range of 10-150 nm are on demand for systemic drug delivery.[31, 32] Surface zeta potential is also a critical factor to determine both in vitro and in vivo stability of the NPs. An aqueous suspension of 5 mg/mL CpG-ODN-Au-ZnPc-Poly-NPs stored at 4 °C for 1 month did not show observable aggregation. Such excellent stability of these NPs renders them suitable for biomedical applications in vivo. However, when NP concentration is too high, there is always a chance of aggregation. Total volume fraction of NPs in the solution, PLGA length, PEG ratio, and PEG surface density can be varied to tune NP stability for possible in vivo applications.

We have used a mouse mammary tumor cell line 4T1, one of only a few breast cancer models with the capacity to metastasize, to test the in vitro photodynamic activity and PDT mediated anti tumor immunity with our construct.[33] It is poorly immunogenic, spontaneously metastatic, and highly malignant. We carried out a series of in vitro cytotoxicity assays to evaluate the potential of our engineered hybrid NP construct containing both ZnPc and CpG-ODN in metastatic breast cancer using 4T1 cells and directly comparing its efficacy to that of free ZnPc, AuNPs, ZnPc-Poly-NPs, and Au-ZnPc-Poly-NPs. As represented in Fig. A.4, CpG-ODN-Au-ZnPc-Poly-NPs are highly

phototoxic to 4T1 cells, having an IC_{50} value of 2.8 nM when irradiated with a 660 nm LASER for only 5 min. This construct has no toxicity in the dark. Under similar conditions, NPs containing the photosensitizer alone (ZnPc-Poly-NPs) have an IC_{50} value of 15 nM, and for free ZnPc the value with these cells is 317 nM, ~2 orders of magnitude less effective. Significant phototoxicity of our construct is indicative of the potential of a synergistic combination of a photosensitizer and an immuoadjuvant in a single delivery platform to treat metastatic breast cancer.

CpG-ODN stimulates B cells, NK cells, DCs, and macrophages, regardless of whether the DNA is in the form of genomic bacterial DNA or in the form of synthetic ODN. The production of high-affinity antibodies and the generation of cytotoxic T cells that provide long-lasting protection characterize the resultant antigen-specific immunity during PDT. The use of CpG-ODN in combination with ZnPc in a single NP construct had a significant immune response after PDT. TLR9 recognizes d(CpG) dinucleotides present in the synthetic CpG-ODN used in our construct. CpG-ODN has strong immunostimulatory activity on murine and human immune cells in vitro and in vivo, such as: induction of tumor specific Th17 response, triggering B cell proliferation, NK cell secretion of IFN-γ, increased lytic activity, and macrophage secretion of IFN-α/β, IL-6, IL-12, granulocyte-monocyte colony-stimulating factor, chemokines, and TNF-α. One important question to answer in designing any combinatory therapy is the order of administration of the respective component treatments, their local concentration, and the stoichiometric ratio. These parameters are very difficult to control when the components are administered separately. By designing a hybrid NP system, we aimed to provide PDT first followed by release of CpG-ODN for further enhancement of PDT-mediated

antitumor immunity. We assumed that the chief role of CpG-ODN is to potentiate phagocytosis of necrotic or apoptotic tumor cells by already present DCs and to induce DC maturation and migration to draining lymph nodes. CpG-ODN activation after PDT will be superior since the PDT induced damage will further enhance over all DC activity when stimulated with CpG-ODN conjugate. The results showed that our combination of ZnPc and CpG-ODN in a single NP construct was significantly better than either treatment alone. Treatment of DCs with PDT-cell lysates and CpG-ODN from a controlled release NP could produce better systemic immune responses due to the creation of potential tumor antigenic fragments before the immune stimulation, which facilitates uptake of antigen presenting cells. The immunosuppressive tumor environment is one of the key players of compromised anti-tumor immune responses. The dominant immunosuppressive cytokines in the tumor microenvironment are IL-10, transforming growth factor, and *vascular endothelial growth factor,* which inhibit DC maturation/activation.[34, 35] One of the most remarkable finding of our current study is the ability of the hybrid NP formulation to shift the balance at the tumor microenvironment towards immune stimulation, as evidenced by the increase in the level of proinflammatory/Th1-biased cytokines IL-2, IL-6, IL-12, TNF-α and minimal effect in the level of the immunosuppressant such as IL-10 (Fig. A.5). A hybrid NP-based delivery of PDT and CpG-ODN can produce effective synergistic response by activating innate and adaptive antitumor immunity, which can be used as a more effective adjuvant for tumor vaccines as well as immunotherapeutic adjuvant.

Conclusion

We synthesized a hybrid NP system that can be loaded with a photosensitizer and an immunoadjuvant for combination therapy. PLGA-*b*-PEG copolymer functionalized with a terminal -NH_2 group was used to provide a hydrophobic core for effective loading of a photosensitizer, ZnPc. The amine groups from the polymeric NPs, acting as anchors, were utilized to decorate the NP surface with anionic AuNPs and CpG-ODN-based immunoadjuvant was immobilized on the gold surface. Using 4T1 cells as a model for metastatic breast cancer, we demonstrated that the phototoxicity of this hybrid NP containing CpG-ODN and the photosensitizer, ZnPc, is significantly higher than the free PS, PS alone in a NP, or a combination of the PS and the immunoadjuvant in their free forms. We observed involvement of several cytokines in the PDT-induced immune response after treatment with CpG-ODN-Au-ZnPc-poly-NPs. When a mixture of CpG-ODN and ZnPc was used, no significant immune response was seen under similar conditions. These results indicate that the PDT-induced antitumor immune response and its further enhancement using synergistic immunoadjuvant in a suitably designed NP construct might play an important role in successful control of malignant diseases. These results support that a rational choice of an immunostimulant can be an ideal addition to PDT regimen if both the photosensitizer and the immunoadjuvant can be delivered using a single delivery vehicle. These results will play critical roles in building the knowledge required to design NPs to be used for photoimmunotherapy of metastatic cancers.

References

1. DeSantis, C.; Siegel, R.; Bandi, P.; Jemal, A., Breast cancer statistics, 2011. *Ca-Cancer J Clin* **2011,** *61* (6), 409-418.

2. Turcotte, S.; Rosenberg, S. A., Immunotherapy for metastatic solid cancers. *Adv Surg* **2011,** *45*, 341-360.

3. Castano, A. P.; Mroz, P.; Hamblin, M. R., Photodynamic therapy and anti-tumour immunity. *Nat Rev Cancer* **2006,** *6* (7), 535-545.

4. Gollnick, S. O.; Owczarczak, B.; Maier, P., Photodynamic therapy and anti-tumor immunity. *Laser Surg Med* **2006,** *38* (5), 509-515.

5. Dougherty, T. J.; Gomer, C. J.; Henderson, B. W.; Jori, G.; Kessel, D.; Korbelik, M.; Moan, J.; Peng, Q., Photodynamic therapy. *J Natl Cancer Inst* **1998,** *90* (12), 889-905.

6. Korbelik, M., Cancer vaccines generated by photodynamic therapy. *Photoch Photobio Sci* **2011,** *10* (5), 664-669.

7. van Duijnhoven, F. H.; Aalbers, R. I. J. M.; Rovers, J. P.; Terpstra, O. T.; Kuppen, P. J. K., Immunological aspects of photodynamic therapy of liver tumors in a rat model for colorectal cancer. *Photochem Photobiol* **2003,** *78* (3), 235-240.

8. Oseroff, A., PDT as a cytotoxic agent and biological response modifier: Implications for cancer prevention and treatment in immunosuppressed and immunocompetent patients. *J Invest Dermatol* **2006,** *126* (3), 542-544.

9. Werling, D.; Jungi, T. W., TOLL-like receptors linking innate and adaptive immune response. *Vet Immunol Immunopathol* **2003,** *91* (1), 1-12.

10. Gollnick, S. O.; Brackett, C. M., Enhancement of anti-tumor immunity by photodynamic therapy. *Immunol Res* **2010,** *46* (1-3), 216-226.

11. Qiang, Y. G.; Yow, C. M. N.; Huang, Z., Combination of photodynamic therapy and immunomodulation: Current status and future trends. *Med Res Rev* **2008,** *28* (4), 632-644.

12. St Denis, T. G.; Aziz, K.; Waheed, A. A.; Huang, Y. Y.; Sharma, S. K.; Mroz, P.; Hamblin, M. R., Combination approaches to potentiate immune response after photodynamic therapy for cancer. *Photoch Photobio Sci* **2011,** *10* (5), 792-801.

13. Dhar, S.; Gu, F. X.; Langer, R.; Farokhzad, O. C.; Lippard, S. J., Targeted delivery of cisplatin to prostate cancer cells by aptamer functionalized Pt(IV) prodrug-PLGA-PEG nanoparticles. *Proc Natl Acad Sci USA* **2008,** *105* (45), 17356-17361.

14. Dhar, S.; Kolishetti, N.; Lippard, S. J.; Farokhzad, O. C., Targeted delivery of a cisplatin prodrug for safer and more effective prostate cancer therapy in vivo. *Proc. Natl. Acad. Sci. USA* **2011,** *108* (5), 1850-5.

15. Farokhzad, O. C.; Jon, S. Y.; Khadelmhosseini, A.; Tran, T. N. T.; LaVan, D. A.; Langer, R., Nanopartide-aptamer bioconjugates: A new approach for targeting prostate cancer cells. *Cancer Res* **2004,** *64* (21), 7668-7672.

16. Kolishetti, N.; Dhar, S.; Valencia, P. M.; Lin, L. Q.; Karnik, R.; Lippard, S. J.; Langer, R.; Farokhzad, O. C., Engineering of self-assembled nanoparticle platform for precisely controlled combination drug therapy. *Proc. Natl. Acad. Sci. USA* **2010,** *107* (42), 17939-17944.

17. Soppimath, K. S.; Aminabhavi, T. M.; Kulkarni, A. R.; Rudzinski, W. E., Biodegradable polymeric nanoparticles as drug delivery devices. *J Controlled Rel* **2001,** *70* (1-2), 1-20.

18. Langer, R., Drug delivery. Drugs on target. *Science* **2001,** *293* (5527), 58-59.

19. Ochsner, M., Light scattering of human skin: a comparison between zinc (II)-phthalocyanine and photofrin II. *J Photochem Photobiol B.* **1996,** *32*, 3–9.

20. Yamamoto, S.; Yamamoto, T.; Nojima, Y.; Umemori, K.; Phalen, S.; McMurray, D. N.; Kuramoto, E.; Iho, S.; Takauji, R.; Sato, Y.; Yamada, T.; Ohara, N.; Matsumoto, S.; Goto, Y.; Matsuo, K.; Tokunaga, T., Discovery of immunostimulatory CpG-DNA and its application to tuberculosis vaccine development. *Jpn J Infect Dis* **2002,** *55* (2), 37-44.

21. Weeratna, R. D.; Makinen, S. R.; McCluskie, M. J.; Davis, H. L., TLR agonists as vaccine adjuvants: comparison of CpG ODN and Resiquimod (R-848). *Vaccine* **2005,** *23* (45), 5263-5270.

22. Karnik, R.; Gu, F.; Basto, P.; Cannizzaro, C.; Dean, L.; Kyei-Manu, W.; Langer, R.; Farokhzad, O. C., Microfluidic platform for controlled synthesis of polymeric nanoparticles. *Nano Lett* **2008,** *8* (9), 2906-2912.

23. Gu, F.; Zhang, L.; Teply, B. A.; Mann, N.; Wang, A.; Radovic-Moreno, A. F.; Langer, R.; Farokhzad, O. C., Precise engineering of targeted nanoparticles by using self-assembled biointegrated block copolymers. *Proc Natl Acad Sci USA* **2008,** *105* (7), 2586-2591.

24. Dhar, S.; Daniel, W. L.; Giljohann, D. A.; Mirkin, C. A.; Lippard, S. J., Polyvalent oligonucleotide gold nanoparticle conjugates as delivery vehicles for platinum(IV) warheads. *J Am Chem Soc* **2009,** *131* (41), 14652-14653.

25. de Jong, S.; Chikh, G.; Sekirov, L.; Raney, S.; Semple, S.; Klimuk, S.; Yuan, N.; Hope, M.; Cullis, P.; Tam, Y., Encapsulation in liposomal nanoparticles enhances

the immunostimulatory, adjuvant and anti-tumor activity of subcutaneously administered CpG ODN. *Cancer Immunol Immun* **2007,** *56* (8), 1251-1264.

26. Krieg, A. M.; Yi, A. K.; Matson, S.; Waldschmidt, T. J.; Bishop, G. A.; Teasdale, R.; Koretzky, G. A.; Klinman, D. M., CpG motifs in bacterial-DNA trigger direct B-cell activation. *Nature* **1995,** *374* (6522), 546-549.

27. Hartmann, G.; Weiner, G. J.; Krieg, A. M., CpG DNA: A potent signal for growth, activation, and maturation of human dendritic cells. *Proc Natl Acad Sci USA* **1999,** *96* (16), 9305-9310.

28. Krieg, A. M.; Matson, S.; Fisher, E., Oligodeoxynucleotide modifications determine the magnitude of B cell stimulation by CpG motifs. *Antisense Nucleic A* **1996,** *6* (2), 133-139.

29. Liang, H.; Nishioka, Y.; Reich, C. F.; Pisetsky, D. S.; Lipsky, P. E., Activation of human B cells by phosphorothioate oligodeoxynucleotides. *J Clin Invest* **1996,** *98* (5), 1119-1129.

30. Ballas, Z. K.; Rasmussen, W. L.; Krieg, A. M., Induction of NK activity in murine and human cells by CpG motifs in oligodeoxynucleotides and bacterial DNA. *J Immunol* **1996,** *157* (5), 1840-1845.

31. Alexis, F.; Pridgen, E.; Molnar, L. K.; Farokhzad, O. C., Factors affecting the clearance and biodistribution of polymeric nanoparticles. *Mol Pharmaceut* **2008,** *5* (4), 505-515.

32. Kolishetti, N.; Alexis, F.; Pridgen, E. M.; Farokhzad, O. C., Biodistribution and Pharmacokinetics of Nanoprobes. In *Nanoplatform-Based Molecular Imaging*, John Wiley & Sons, Inc.: 2011; pp 75-104.

33. Morecki, S.; Yacovlev, L.; Slavin, S., Effect of indomethacin on tumorigenicity and immunity induction in a murine model of mammary carcinoma. *Int J Cancer* **1998,** *75* (6), 894-899.

34. Mesa, C.; Fernandez, L. E., Challenges facing adjuvants for cancer immunotherapy. *Immunol Cell Biol* **2004,** *82* (6), 644-650.

35. Morisaki, T.; Katano, M.; Ikubo, A.; Anan, K.; Nakamura, M.; Nakamura, K.; Sato, H.; Tanaka, M.; Torisu, M., Immunosuppressive cytokines (IL-10, TGF-beta) genes expression in human gastric carcinoma tissues. *J Surg Oncol* **1996,** *63* (4), 234-239.

APPENDIX II

PHARMACOLOGICAL REVERSAL OF HISTONE METHYLATION PRESENSITIZES PANCREATIC CANCER CELLS TO NUCLEOSIDE DRUGS: *IN VITRO* OPTIMIZATION AND NOVEL NANOPARTICLE DELIVERY STUDIES

Reprinted with the permission of Hung, S.W.; Mody, H.; Marrache, S; Bhutia, Y.D.; Davis, F.; Cho, J.H.; Zastre, J.; Dhar, S.; Chu, C. K.; Govindarajan. *PLOS One,* 8, e71196. Copyright 2013 Public Library of Science

Abstract

We evaluated the potential of an investigational histone methylation reversal agent, 3-deazaneplanocin A (DZNep), in improving the chemosensitivity of pancreatic cancer to nucleoside analogs (i.e., gemcitabine). DZNep brought delayed but selective cytotoxicity to pancreatic cancer cells without affecting normal human pancreatic ductal epithelial (HPDE) cells. Co-exposure of DZNep and gemcitabine induced cytotoxic additivity or synergism in both well- and poorly-differentiated pancreatic cell lines by increased apoptosis. In contrast, DZNep exerted antagonism with gemcitabine against HPDE cells with significant reduction in cytotoxicity compared with the gemcitabine-alone regimen. DZNep marginally depended on purine nucleoside transporters for its cytotoxicity, but the transport dependence was circumvented by acyl derivatization. Drug exposure studies revealed that a short priming with DZNep followed by gemcitabine treatment rather than cotreatment of both agents to produce a maximal chemosensitization response in both gemcitabine-sensitive and gemcitabine-resistant pancreatic cancer cells. DZNep rapidly and reversibly decreased trimethylation of histone H3 lysine 27 but increased trimethylation of lysine 9 in an EZH2- and JMJD1A/2C-dependent manner, respectively. However, DZNep potentiation of nucleoside analog chemosensitization was found to be temporally coupled to trimethylation changes in lysine 27 and not lysine 9. Polymeric nanoparticles engineered to chronologically release DZNep followed by gemcitabine produced pronounced chemosensitization and dose-lowering effects. Together, our results identify that an optimized DZNep exposure can presensitize pancreatic cancer cells to anticancer nucleoside analogs through the reversal of histone methylation, emphasizing the promising clinical utilities of epigenetic reversal

agents in future pancreatic cancer combination therapies.

Introduction

Polycomb group proteins (PcGs) can remodel chromatin by influencing the degree of compaction, leading to epigenetic gene silencing. Polycomb Repressive Complex 2 (PRC2), one of the two classes of PcGs, induces histone methyltransferase activity primarily by trimethylating histone H3 at lysine 27 (H3K27me3), mediating silencing of tumor suppressor genes. The catalytic subunit of PRC2 is Enhancer of Zeste Homolog 2 (EZH2), in which the SET domain constitutes the active site for histone H3K27 methylation.[1] Studies support EZH2 as a key player in the development and progression of tumors due to its ability to alter gene expressions including those involved in cell cycle control, cell migration, and DNA repair.[2] EZH2 is crucial in the chromatin control of genetic reprogramming of cancer stem cell self-renewal and differentiation that have been implicated in chemoresistance. [3-6]

As a marker of advanced and metastatic disease in many solid tumors, EZH2 overexpression has been reported in pancreatic cancers, particularly those that are poorly differentiated.[6, 7] EZH2 was found to be upregulated by oncogenic RAS through MEK-ERK signaling, leading to the downregulation of tumor suppressors such as RUNX3 and p27(Kip1).[6, 8, 9] EZH2 depletion led to cell cycle arrest at the G1/S transition, suggesting the protein may repress the tumor suppressing p27 gene.[10] Similarly, knockdown of EZH2 resulted in a significant decrease in cellular proliferation and invasiveness[6, 7, 11] and sensitized pancreatic cancer cells to doxorubicin and gemcitabine, revealing the potential of an EZH2 inhibitor-chemotherapeutic combination therapy.[6, 7] In vivo, suppressing EZH2 diminished tumorigenicity and inhibited pancreatic cancer metastasis.[7] Clinically,

positive correlations have been observed between EZH2 expression and advanced pancreatic cancer stage and grade in patients.[11] In many cases, high levels of EZH2 in cancer were also significantly associated with decreased E-cadherin expression and highly aggressive disease. In gemcitabine-treated patients, significantly longer survival was observed in patients with low rather than high EZH2 expression.[12] Consequently, EZH2 may be a significant prognostic value for overall survival in pancreatic cancer patients.[13]

Recently, it has been shown that a potent chemical inhibitor of S-adenosylhomocysteine hydrolase, 3-deazaneplanocin A (DZNep), modulates chromatin through indirect (i.e., reducing methyl group availability) inhibition of histone methyltransferases including EZH2.[14, 15] DZNep, a carbocyclic analog of adenosine, depletes cellular levels of the PRC2 components while inhibiting the associated H3K27me3.[16] While the mechanisms and effects of DZNep have been studied in numerous solid tumors and leukemia,[2, 3, 14, 15, 17-21] less is known about the potential of this compound for pancreatic cancer treatment. Nevertheless, its current potential for reducing EZH2 levels, reverting epithelialtomesenchymal transition (EMT), and preventing tumor progression, makes it a highly promising antimetastatic agent.[5] The therapeutic potential of DZNep in combination with other agents, such as polyphenols and histone deacetylase inhibitors, has begun to emerge with encouraging results.[14, 15] Since increasing evidence suggests that future cancer therapies will take advantage of the synergistic effects achieved from different combinations of epigenetic reversal and conventional antitumor agents,[22] we investigated the potential of the DZNep-gemcitabine combination for improving anticancer activity in pancreatic cancer. Our results identified

that histone methylation reversal by DZNep presensitizes pancreatic cancer cells to gemcitabine. Optimization of the drug combination through dosage and delivery methods was further conducted.

This was carried out in collaboration with Prof. Rajgopal Govindarajan's group from UGA Pharmaceutical and Biomedical sciences. Our group was involved in the construct and evaluation of NPs for these studies. The work performed in our lab is included in this appendix chapter.

Materials and Methods

Reagents

All chemicals were purchased from Sigma Aldrich and used without further purification unless otherwise noted. PLGACOOH with an intrinsic viscosity of 0.18 dL/g was purchased from Lactel. The (5-carboxypentyl)triphenylphosphonium (TPP) cation was synthesized according to literature methods.[31] HO-PEG-OH with a MW of 3,350 g/mol was purchased from Sigma Aldrich. DSPE-PEG-COOH with a MW of 2,000 g/mol was purchased from Avanti Polar Lipids. Polyvinyl alcohol (PVA) with an average molecular weight of 10,000–26,000 was purchased from Alfa Aesar. Distilled water was purified by passage through a Millipore Milli-Q Biocel water purification system (18.2 MV) with a 0.22 mm filter. HPLC analyses were carried out using an Agilent 1200 series instrument. Size and zeta potential measurements were carried out on a Malvern Zetasizer Nanoseries instrument. Gel permeation chromatography (GPC) data was collected on a Shimadzu LC20-AD Prominence liquid chromatographer. All NMR spectra were recorded on a Varian 400 MHz NMR. TEM images were taken on a Tecnai 20 FEM microscope. Ultrasonication was performed on a Misonix S-4000 Ultrasonic

liquid processor.

Synthesis of PLGA-b-PEG-OH

Synthesis of PLGA-PEG-b-OH was performed as previously described.[32]

Synthesis of PLGA-b-PEG-TPP

Synthesis of PLGA-PEG-b-TPP was performed as previously described.[32]

Synthesis of Gemcitabine Encapsulated Nanoparticles (Gem-PLGA-b-PEG-OH-NPs)

Gemcitabine (10 mg/mL in nanopure H_2O) was emulsified with PLGA-b-PEG-OH (5 mg in CH_2Cl_2) using probe sonication for one minute (Amplitude: 40% of 600 W power, Pulse: 1 sec on, 1 sec off). The primary emulsion was emulsified again by adding the water-in-oil emulsion to 2 mL of nanopure water containing 0.5% polyvinyl alcohol followed by 8 mL of nanopure water containing 0.05% PVA and sonicated using the conditions mentioned above. Organic solvent was removed by washing three times using an Amicon filtration membrane with a 100 kDa cut-off. The NPs were resuspended in nanopure water and stored at 4uC until further use. Dynamic light scattering (DLS) measurements were carried to determine size, polydispersity index (PDI), and zeta potential of the NPs. NPs were characterized using TEM at an acceleration voltage of 200 kV. The TEM samples were prepared by depositing 8 mL of the NPs (5 mg/mL) onto a 200-mesh carbon-coated copper grid. Samples were blotted away after 15 min and grids were negatively stained with sterile 2% (w/v) uranyl acetate aqueous solution for 15 min.

Synthesis of DZNep Encapsulated Nanoparticles (DZNep-PLGA-b-PEG-OH-NPs)

DZNep (10 mg/mL in nanopure H2O) was emulsified with PLGA-b-PEG-OH (5 mg in CH_2Cl_2) using probe sonication for one minute (Amplitude 40% of 600 W power,

Pulse: 1 sec on, 1 sec off). The primary emulsion was emulsified again by adding the above formed water-in-oil emulsion to 2 mL of nanopure water containing 0.5% PVA and sonicated using similar conditions. Finally, this emulsion was re-emulsified using 8 mL of nanopure water containing 0.05% PVA under sonication using the similar conditions as before. Organic solvent was removed by washing three times using an Amicon filtration membrane with a 100 kDa cut-off. The NPs were resuspended in nanopure water and stored at 4uC until further use. DLS measurements were carried to determine size, PDI, and zeta potential of the NPs. NPs were characterized using TEM as mentioned above.

Synthesis of Gemcitabine and DZNep Encapsulated NPs (Gem-DZNep-PLGA-b -PEG-OH-NPs)

Gemcitabine and DZNep co-encapsulated PLGA-b-PEG-OH NPs were following the exact procedure mentioned above except the first step where DZNep (10 mg/mL in nanopure H_2O) and Gemcitabine (10 mg/mL in nanopure H_2O) was emulsified with PLGA-PEG-OH (5 mg in CH_2Cl_2). Organic solvent was removed by washing three times using an Amicon filtration membrane with a 100 kDa cut-off. The NPs were resuspended in nanopure water and stored at 4 °C until further use. DLS measurements were carried to determine size, PDI, and zeta potential of the NPs. NPs were characterized using TEM as mentioned above.

Synthesis of Controlled Release Gem-DZNep-DSPE-PEGOH-NPs

Gemcitabine (10 mg/mL in nanopure H_2O) was emulsified with PLGA-b-PEG-OH (5 mg in CH_2Cl_2) using probe sonication for one minute (Amplitude: 40% of 600 W power, Pulse: 1 sec on, 1 sec off). The primary emulsion was emulsified again by adding

the water-in-oil emulsion to 2 mL of nanopure water containing 0.5% PVA and sonicated using the conditions mentioned above. This emulsion was further emulsified using 8 mL of nanopure water containing 0.05% PVA, 0.1% DSPE-PEG-COOH, and DZNep (10 mg/mL in nanopure H_2O) under sonication using the same conditions as mentioned above. Organic solvent was removed by washing three times using an Amicon filtration membrane with a 100 kDa cut-off. The NPs were resuspended in nanopure water and stored at 4uC until further use. DLS measurements were carried to determine size, polydispersity index (PDI), and zeta potential of the NPs. NPs were characterized using TEM as mentioned above.

Loading and Encapsulation Efficiency of Gemcitabine and DZNep in NPs

Gemcitabine and DZNep loading and encapsulation efficiency (EE) were determined by dissolving the polymeric core in 0.1 M NaOH and quantifying the amount of therapeutic in the NPs using HPLC (Mobile phase: acetonitrile with 20% H_2O and 0.1% trifluoroacetic acid, Wavelength used: 270 nm).

Release Kinetic Studies of DZNep/Gemcitabine NPs

NPs were placed in Slide-A-Lyzer MINI dialysis units with a MW cutoff of 10,000 g/mol. Samples were dialyzed against 1X PBS (6.0 L) in a constant temperature shaker at 37uC and 35 RPM. At various pre-determined time points, samples were removed and the gemcitabine/DZNep content was determined by dissolving the polymeric core in 0.1 mMol NaOH and quantifying by HPLC analysis (Mobile phase: acetonitrile with 20% H2O and 0.1% trifluoroacetic acid, Wavelength used: 270 nm).

Results and discussion

To enhance tumor cell delivery of the drugs, we encapsulated DZNep and gemcitabine individually into biodegradable PLGA-b-PEG-NP formulations (Figs. AII-1A). TEM studies showed a uniform size distribution of both DZNep and gemcitabine NPs ranging between 100–200 nM (Fig. AII-1B). In vitro release kinetics suggested a similar release profile for both drugs with almost comparable physicochemical characteristics (Fig. AII-1C; Table AII-1). Cytotoxicity analyses with drug-encapsulated NPs indicated that DZNep entrapment within NPs can produce the same level of cytotoxicity as that of free DZNep although at a much lower (10-fold) concentration (Fig. AII-1D). A similar reduction in dose requirement was also obtained with gemcitabine when used in NP formulation (Fig. AII-1D).

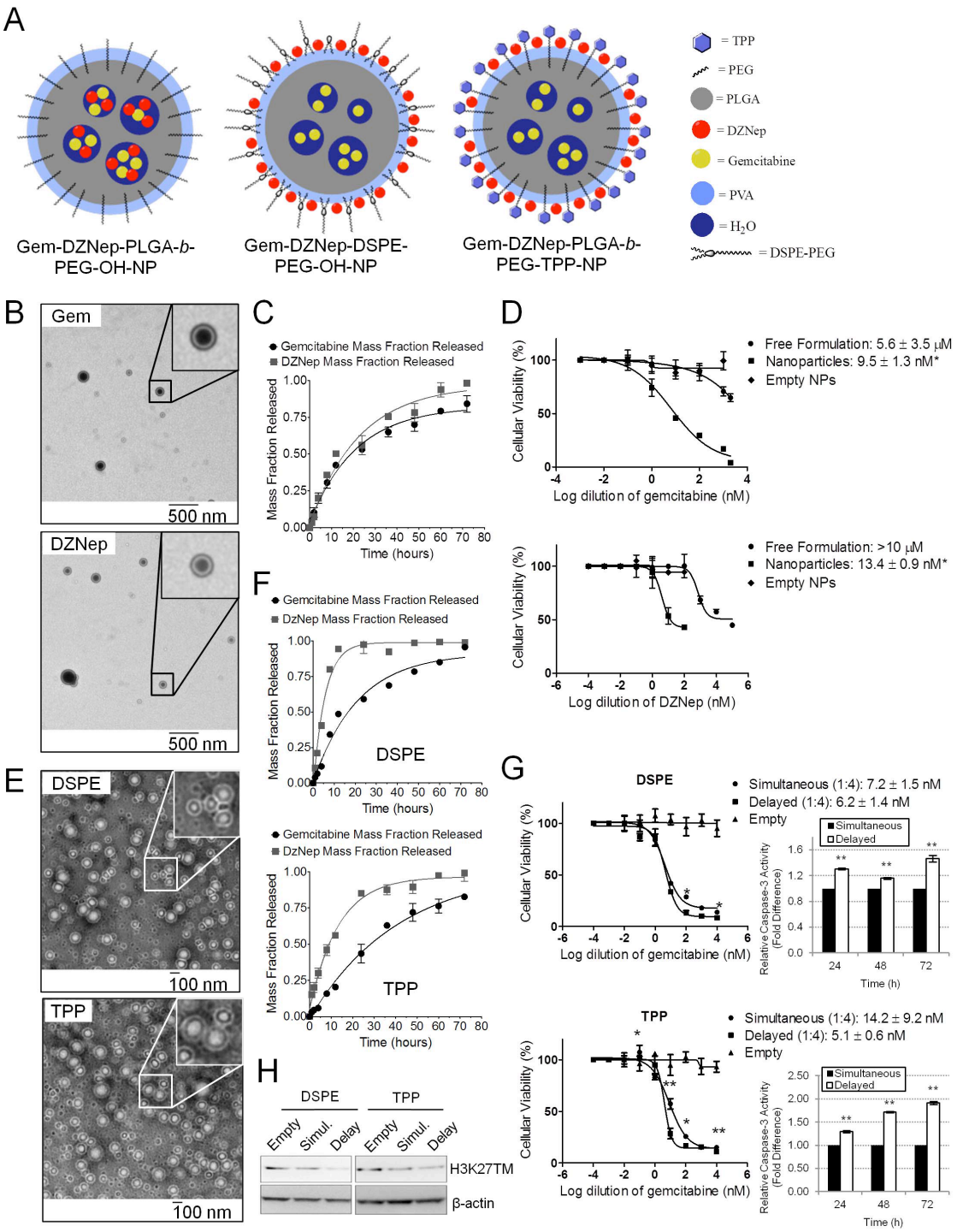


Figure AII-1. Spatiotemporal release of DZNep and gemcitabine using engineered nanoparticles reduced drug dose while potentiating chemosensitivity. A. Spatial distribution of DZNep and gemcitabine within NPs. Co-encapsulating double-emulsion

formulations were created using PLGA-b-PEG-OH (left), DSPE-PEG-OH (middle), and PLGA-b-PEG-TPP (right). B and E. TEM illustrates the inner core and outer shell of all the double-emulsion NPs created. Insets show the NPs at higher magnification. Bars, SD. n = 3. C. Release kinetics indicates the similarity between DZNep and gemcitabine release using the PLGA-b-PEG-OH formulation. D. Gemcitabine (top) and DZNep (bottom) in individual PLGA-b-PEG-OH formulations distinctly increased cytotoxicity in MIA PaCa-2. Significance between nanoparticles and free formulation is shown. F. HPLC analyses demonstrate the rapid and sequential release of DZNep compared with gemcitabine in both DSPE (top) and TPP (bottom) formulations.G. Both engineered DSPE (top) and TPP (bottom) delayed-release NPs increased the cytotoxicity of MIA PaCa-2 even further compared with PLGA-b-PEG-OH NPs. Twenty-four hours after 56103 cells/well were seeded in a 96-well plate, cells were treated for 72 h. Cellular viabilities were measured using MTT assays. Cytotoxic IC50 values are indicated. Significance between simultaneous and delayed NPs using the Student's t test is shown. Bar graphs to the right indicate the relative levels of caspase-3 activity as measured by fluorescence intensity. Values were background-subtracted and are indicated as fold-change from simultaneous NPs to delayed NPs. Bars, SD. n=3. *p,0.05, **p,0.01. H. H3K27 trimethylation decreases with simultaneous and delayed-release NPs. MIA PaCa-2 was treated with empty, simultaneous, or delayed NPs as above and total cell lysates were analyzed for H3K27 trimethylation using Western Blotting. A clear reduction in H3K27 trimethylation was noticed in both simultaneous and delayed NPs, with DSPE (left) and TPP (right) delayed NPs producing a slightly greater reduction compared with simultaneous NPs.

Since superior chemosensitization effects were seen when cells were initially primed with DZNep for a short period of time, we engineered two different NP formulations such that gemcitabine was encased in the core while DZNep was loaded within the outer layer (Figs. AII-9A). The first strategy used DSPE-PEG-OH to create a lipid layer to accommodate DZNep alone, and the second used a PLGA-b-PEG-TPP polymer to keep the two drugs separated by a cationic charge (Fig. AII-9A, S4). TEM studies once again showed a uniform size distribution of both NP formulations (Fig. AII-9E). However, comparison of gemcitabine and DZNep release kinetics showed a much more rapid release of DZNep (~80% within 8 h) than gemcitabine in the former and a slightly greater release of DZNep (~50% within 8 h) than gemcitabine in the latter (Fig. AII-9F). Treatment of MIA PaCa-2 with each controlled-release NP type showed a superior cytotoxicity response than gemcitabine and DZNep co-encapsulated NPs at the same ratios (IC50 reductions for DSPE formulation of 1.2–2.5-fold ($p = 0.48$) and TPP formulation of 1.5–4.9-fold ($p= 0.12$)) (Fig. AII-9G). In both cases, a significant induction of apoptosis consequent to inhibition of H3K27me3 was identified as key mechanism for the observed cytotoxicity (Figs. AII-9G,-H). The cytotoxicity studies with the NPs were performed by Sau Wai Hung.

Table AII-1. Physiochemical Characterization of NPs.

Nanoparticle	Size (nm)	PDI	Zeta Potential (mV)	Loading (%)		EE (%)	
				Gemcitabine	DZNep	Gemcitabine	DZNep
Empty-PLGA-*b*-PEG-OH-NPs	172±2	0.13	−23.5±1.3	–	–	–	–
Gem-PLGA-*b*-PEG-OH-NPs	200±4	0.16	−27.6±0.7	1.4±0.1	–	6.6±0.2	–
DZNep-PLGA-*b*-PEG-OH-NPs	206±2	0.16	−29.6±0.1	–	1.9±0.1	–	9.1±0.6
Gem-DZNep-PLGA-*b*-PEG-OH-NPs	200±2	0.17	−24.3±4.9	1.3±0.1	1.7±0.2	6.2±0.5	8.2±0.7
Gem-DZNep-PLGA-*b*-PEG-TPP-NPs	157±1	0.20	16.4±0.9	1.2±0.2	1.6±0.5	5.5±0.8	7.7±2.4
Gem-DZNep-DSPE-PEG-NPs	167±2	0.23	−17.9±2.8	1.3±0.2	1.9±1.0	6.3±0.8	8.9±4.9

References:

1. Simon, J. A.; Kingston, R. E., Mechanisms of polycomb gene silencing:knowns and unknowns. *Nat. Rev. Mol. Cell Bio.* **2009,** *10*, 607-708.
2. Crea, F.; Fornaro, L.; Bocci, G.; Sun, L.; Farrar, W. L.; Falcone, A.; Danesi, R., EZH2 inhibition: targeting the crossroad of tumor invasion and angiogenesis. *Cancer Metast. Rev.* **2012,** *3-4*, 753-761.
3. Suva, M. L.; Riggi, N.; Janiszewska, M.; Radovanovic, I.; Provero, P.; Stehle, J. C.; Baumer, K.; Bitoux, M. A. L.; Marino, D.; Cironi, L.; Marquez, V. E.; Clement, V.; Stamenkovic, I., EZH2 is essential for glioblastoma cancer stem cell maintenance. *Cancer Res.* **2009,** *69*, 9211-9218.
4. Bao, B.; Ali, S.; Banerjee, S.; Wang, Z.; Logna, F.; Azmi, A. S.; Kong, D.; Ahmad, A.; Li, Y.; Padhye, S.; Sarkar, F. H., Curcumin Analogue CDF Inhibits Pancreatic Tumor Growth by Switching on Suppressor microRNAs and Attenuating EZH2 Expression. *Cancer Res.* **2011,** *72*, 335-345.
5. Crea, F.; Paolicchi, E.; Marquez, V. E.; Danesi, R., Polycomb genes and cancer: Time for clinical application? *CRC Cr. Rev. Oncol-Hem* **2012,** *83*, 184-193.
6. Ougolkov, A. V.; Bilim, V. N.; Billadeau, D. D., Regulation of pancreatic tumor cell proliferation and chemoresistance by the histone methyltransferase enhancer of zeste homologue 2. *Clin. Cancer Res* **2008,** *14*, 6790-6796.
7. Chen, Y.; Xie, D.; Li, W. Y.; Cheung, C. M.; Yao, H.; Chan, C. Y.; Xu, F. P.; Liu, Y. H.; Sung, J. J.; Kung, H. F., RNAi targeting EZH2 inhibits tumor growth and liver metastasis of pancreatic cancer in vivo. *Cancer Lett* **2012,** *297*, 109-116.

8. Fujii, S.; Fukamachi, K.; Tsuda, H.; Ito, K.; Ito, Y.; Ochiai, A., RAS oncogenic signal upregulates EZH2 in pancreatic. *Biochem. Biophys. Res. Commun.* **2012,** *417*, 1074-1079.

9. Fujii, S.; Ito, K.; Ito, Y.; Ochiai, A., Enhancer of zeste homologue 2 (EZH2) down-regulates RUNX3 by increasing histone H3 methylation. *J. Biol. Chem.* **2008,** *283*, 17324-17332.

10. Fussbroich, B.; Wagener, N.; Macher-Goeppinger, S.; Benner, A.; Fälth, M.; Sültmann, H.; Holzer, A.; Hoppe-Seyler, K.; Hoppe-Seyler, F., EZH2 Depletion Blocks the Proliferation of Colon Cancer Cells. *PLoS ONE* **2011,** *6*, e21651.

11. Qazi, A.; Aggarwal, S.; Steffer, C.; Bouwman, D.; Weaver, D.; Gruber, S.; Batchu, R., Laser Capture Microdissection of Pancreatic Ductal Adeno-Carcinoma Cells to Analyze EzH2 by Western Blot Analysis. In *Laser Capture Microdissection*, Murray, G. I., Ed. Humana Press: **2011**;755, pp 245-256.

12. Toll, A. D.; Dasgupta, A.; Potoczek, M.; Yeo, C. J.; Kleer, C. G.; Brody, J. R.; Witkiewicz, A. K., Implications of enhancer of zeste homologue 2 expression in pancreatic ductal adenocarcinoma. *Human pathology* **2010,** *41*, 1205-1209.

13. Wei, Y.; Xia, W.; Zhang, Z.; Liu, J.; Wang, H.; Adsay, N. V.; Albarracin, C.; Yu, D.; Abbruzzese, J. L.; Mills, G. B.; Bast, R. C.; Hortobagyi, G. N.; Hung, M.-C., Loss of trimethylation at lysine 27 of histone H3 is a predictor of poor outcome in breast, ovarian, and pancreatic cancers. *Molecular Carcinogenesis* **2008,** *47*, 701-706.

14. Hayden, A.; Johnson, P. M.; Packham, G.; Crabb, S., S-adenosylhomocysteine hydrolase inhibition by 3-deazaneplanocin A analogues induces anti-cancer

effects in breast cancer cell lines and synergy with both histone deacetylase and HER2 inhibition. *Breast Cancer Res Treat* **2011,** *127*, 109-119.

15. Choudhury, S. R.; Balasubramanian, S.; Chew, Y. C.; Han, B.; Marquez, V. E.; Eckert, R. L., (-)-Epigallocatechin-3-gallate and DZNep reduce polycomb protein level via a proteasome-dependent mechanism in skin cancer cells. *Carcinogenesis* **2011,** *32*, 1525-1532.

16. Tan, J.; Yang, X.; Zhuang, L.; Jiang, X.; Chen, W.; Lee, P. L.; Karuturi, R. K. M.; Tan, P. B. O.; Liu, E. T.; Yu, Q., Pharmacologic disruption of Polycomb-repressive complex 2-mediated gene repression selectively induces apoptosis in cancer cells. *Genes & Development* **2007,** *21*, 1050-1063.

17. Cheng, L. L.; Itahana, Y.; Lei, Z. D.; Chia, N.-Y.; Wu, Y.; Yu, Y.; Li Zhang, S.; Thike, A. A.; Pandey, A.; Rozen, S.; Voorhoeve, P. M.; Yu, Q.; Tan, P. H.; Bay, B. H.; Itahana, K.; Tan, P., TP53 Genomic Status Regulates Sensitivity of Gastric Cancer Cells to the Histone Methylation Inhibitor 3-Deazaneplanocin A (DZNep). *Clinical Cancer Research* **2012,** *18*, 4201-4212.

18. Crea, F.; Hurt, E.; Mathews, L.; Cabarcas, S.; Sun, L.; Marquez, V.; Danesi, R.; Farrar, W., Pharmacologic disruption of Polycomb Repressive Complex 2 inhibits tumorigenicity and tumor progression in prostate cancer. *Molecular Cancer* **2011,** *10*, 40.

19. Chase, A.; Cross, N. C. P., Aberrations of EZH2 in Cancer. *Clinical Cancer Research* **2011,** *17*, 2613-2618.

20. *The histone methyltransferase inhibitor, DZNep, up-regulates TXNIP, increases ROS production, and targets leukemia cells in AML*. **2011**; 118, p 2830-2839.

21. Puppe, J.; Drost, R.; Liu, X.; Joosse, S.; Evers, B.; Cornelissen-Steijger, P.; Nederlof, P.; Yu, Q.; Jonkers, J.; van Lohuizen, M.; Pietersen, A., BRCA1-deficient mammary tumor cells are dependent on EZH2 expression and sensitive to Polycomb Repressive Complex 2-inhibitor 3-deazaneplanocin A. *Breast Cancer Research* **2009,** *11*, R63.

22. Yang, X.; Lay, F.; Han, H.; Jones, P. A., Targeting DNA methylation for epigenetic therapy. *Trends in Pharmacological Sciences 31*, 536-546.

23. Wong, A.; Soo, R. A.; Yong, W.-P.; Innocenti, F., Clinical pharmacology and pharmacogenetics of gemcitabine. *Drug Metabolism Reviews* **2009,** *41*, 77-88.

24. Bayraktar, S.; Bayraktar, U. D.; Rocha-Lima, C. M., Recent developments in palliative chemotherapy for locally advanced and metastatic pancreas cancer. *World J. Gastroenterol.* **2010,** *16*, 673-682.

25. Bhutia, Y. D.; Hung, S. W.; Patel, B.; Lovin, D.; Govindarajan, R., CNT1 Expression Influences Proliferation and Chemosensitivity in Drug-Resistant Pancreatic Cancer Cells. *Cancer Research* **2011,** *71*, 1825-1835.

26. Chou, T.-C.; Talalay, P., Quantitative analysis of dose-effect relationships: the combined effects of multiple drugs or enzyme inhibitors. *Advances in Enzyme Regulation* **1984,** *22*, 27-55.

27. Kang, N.; Jun, A. H.; Bhutia, Y. D.; Kannan, N.; Unadkat, J. D.; Govindarajan, R., Human Equilibrative Nucleoside Transporter-3 (hENT3) Spectrum Disorder Mutations Impair Nucleoside Transport, Protein Localization, and Stability. *Journal of Biological Chemistry* **2010,** *285*, 28343-28352.

28. Govindarajan, R.; Endres, C. J.; Whittington, D.; LeCluyse, E.; Pastor-Anglada, M.; Tse, C.-M.; Unadkat, J. D., *Expression and hepatobiliary transport characteristics of the concentrative and equilibrative nucleoside transporters in sandwich-cultured human hepatocytes*. 2008; Vol. 295, p G570-G580.

29. Adema, A. D.; Radi, M.; Daft, J.; Narayanasamy, J.; Hoebe, E. K.; Alexander, L. E.; Chu, C. K.; Peters, G. J., Troxacitabine Prodrugs for Pancreatic Cancer. *Nucleosides, Nucleotides and Nucleic Acids* **2007,** *26*, 1073-1077.

30. Radi, M.; Adema, A. D.; Daft, J. R.; Cho, J. H.; Hoebe, E. K.; Alexander, L.-E. M. M.; Peters, G. J.; Chu, C. K., In Vitro Optimization of Non-Small Cell Lung Cancer Activity with Troxacitabine, l-1,3-Dioxolane-cytidine, Prodrugs. *Journal of Medicinal Chemistry* **2007,** *50*, 2249-2253.

31. Deroose, F. D.; Clercq, P. J. D., Novel Enantioselective Syntheses of (+)-Biotin. *The Journal of Organic Chemistry* **1995,** *60*, 321-330.

32. Marrache, S.; Dhar, S., Engineering of blended nanoparticle platform for delivery of mitochondria-acting therapeutics. *Proceedings of the National Academy of Sciences* **2012,** *109*, 16288-16293.

33. Paproski, R. J.; Ng, A. M. L.; Yao, S. Y. M.; Graham, K.; Young, J. D.; Cass, C. E., The Role of Human Nucleoside Transporters in Uptake of 3′ -Deoxy-3′ -fluorothymidine. *Molecular Pharmacology* **2008,** *74*, 1372-1380.

34. Plunkett, W.; Huang, P.; Xu, Y. Z.; Heinemann, V.; Grunewald, R.; Gandhi, V., Gemcitabine: metabolism, mechanisms of action, and self-potentiation. *Semin. Oncol.* **1995,** *4 Suppl. 11*, 3-10.

35. Avan, A.; Crea, F.; Paolicchi, E.; Funel, N.; Galvani, E.; Marquez, V. E.; Honeywell, R. J.; Danesi, R.; Peters, G. J.; Giovannetti, E., Molecular Mechanisms Involved in the Synergistic Interaction of the EZH2 Inhibitor 3-Deazaneplanocin A with Gemcitabine in Pancreatic Cancer Cells. *Molecular Cancer Therapeutics* **2012,** *11*, 1735-1746.

36. Stathis, A.; Moore, M. J., Advanced pancreatic carcinoma: current treatment and future challenges. *Nat. Rev. Clin. Oncol.* **2010,** *7*, 163-172.

37. Coulombe, R. A.; Sharma, R. P.; Huggins, J. W., Pharmacokinetics of the antiviral agent 3-deazaneplanocin A. *European Journal of Drug Metabolism and Pharmacokinetics* **1995,** *20*, 197-202.

38. Glazer, R. I.; Hartman, K. D.; Knode, M. C.; Richard, M. M.; Chiang, P. K.; Tseng, C. K. H.; Marquez, V. E., 3-Deazaneplanocin: A new and potent inhibitor of S-adenosylhomocysteine hydrolase and its effects on human promyelocytic leukemia cell line HL-60. *Biochemical and Biophysical Research Communications* **1986,** *135*, 688-694.

39. Mallen-St. Clair, J.; Soydaner-Azeloglu, R.; Lee, K. E.; Taylor, L.; Livanos, A.; Pylayeva-Gupta, Y.; Miller, G.; Margueron, R.; Reinberg, D.; Bar-Sagi, D., EZH2 couples pancreatic regeneration to neoplastic progression. *Genes & Development* **2012,** *26*, 439-444.

40. ROGENHOFER, S.; KAHL, P.; HOLZAPFEL, S.; VON RUECKER, A.; MUELLER, S. C.; ELLINGER, J., Decreased Levels of Histone H3K9me1 Indicate Poor Prognosis in Patients with Renal Cell Carcinoma. *Anticancer Research* **2012,** *32*, 879-886.

41. Hou, J.; Wu, J.; Dombkowski, A.; Zhang, K.; Holowatyj, A.; Boerner, J. L.; Yang, Z. Q., Genomic amplification and a role in drug-resistance for the KDM5A histone demethylase in breast cancer. *Am. J. Transl. Res.* **2012,** *4*, 247-256.

42. Toth, M.; Boros, I. M.; Balint, E., Elevated level of lysine 9-acetylated histone H3 at the MDR1 promoter in multidrug-resistant cells. *Cancer Science* **2012,** *103*, 659-669.

43. Shi, L.; Sun, L.; Li, Q.; Liang, J.; Yu, W.; Yi, X.; Yang, X.; Li, Y.; Han, X.; Zhang, Y.; Xuan, C.; Yao, Z.; Shang, Y., Histone demethylase JMJD2B coordinates H3K4/H3K9 methylation and promotes hormonally responsive breast carcinogenesis. *Proceedings of the National Academy of Sciences* **2011,** *108*, 7541-7546.

44. Chang, C.-J.; Hung, M.-C., The role of EZH2 in tumour progression. *Brit. J. Cancer* **2012,** *106*, 243-247.

45. Abdel-Wahab, O.; Levine, R. L., EZH2 Mutations: Mutating the Epigenetic Machinery in Myeloid Malignancies. *Cancer Cell 18*, 105-107.

APPENDIX III

THE PRODRUG PLATIN-*A*: SIMULTANEOUS RELEASE OF CISPLATIN AND ASPIRIN

Reprinted with the permission of Pathak, R.K; Marrach, S.M.; Choi, J.H., Berding, T.B., and Dhar, S. *Angew. Chem. Int. Ed.,* 126, 1994-1998. Copyright 2014 Wiley-VCH

Abstract

The contribution of chronic inflammation to primary tumor formation and cancer-associated inflammation induce progression of tumor to metastatic stage indicate that a chemo-anti-inflammatory strategy will be of interest for management of aggressive cancers. Based on a simple methos, a prodrug Platin-*A* was fabricated to release cisplatin and aspirin to ameliorate the nephrotoxicity and ototoxicity cause by cisplatin. Platin-*A* exhibited excellent anticancer and anti-inflammatory properties better than combination of free formulation of cisplatin and aspirin. These findings highlight the advantages of combining anti-inflammatory treatment with chemotherapy when both the drugs are delivered in the form of a single prodrug.

Introduction

Chronic inflammation plays an important role in approximately 20% of human cancers.[1] Prostate cancer (PCa) is the most frequently diagnosed cancer and the second leading cause of cancer death in men in the United States.[2] Patients with PCa inevitably progress to hormone-independent disease. PCa that progresses in the presence of androgen blockade is defined as Castration-Resistant Prostate Cancer (CRPC).[3-6] A complex immune-mediated process and inflammation play roles in PCa progression in the castrate setting. Inflammatory responses triggered by the death of androgen-deprived primary cancer cells contribute to progression to CRPC.[3] Cancer-associated inflammation functionally plays an important role in the formation of metastasis.

Cis-diamminedichloroplatinum(II) or cisplatin is currently one of the most effective anticancer drugs available for treating a variety of solid tumors.[7] Resistance to apoptotic death is a characteristic feature of advanced PCa[8, 9] and is one of the reasons for

the failure of cisplatin-based therapeutic strategy of hormone refractory disease.[10, 11] Nonsteroidal anti-inflammatory drugs (NSAID) can be an attractive additive to chemotherapeutic approaches for PCa due to their ostensive potential in cancer chemoprevention.[12] The primary target of NSAIDs is cyclooxygenase isoforms, COX-1 and COX-2, enzymes that catalyze the rate-limiting step in the formation of prostaglandins (PGs).[13] PGs are the group of lipid molecules derived from arachidonic acid and play a key role to generate the inflammatory response during several chronic infections and drug related injuries. The inducible isoform COX-2 and its products, especially PGE2, are involved in the inflammatory responses, inhibition of apoptosis, and induction of resistance. Increased levels of PGE are found in PCa and COX-2 mRNA and protein are overexpressed in 83% of the human PCa samples.[14] The use of cisplatin is also limited for its side effects such as nephrotoxicity and ototoxicity.[15] Nephrotoxicity can be reduced using saline hydration; however, there are no protective modalities for cisplatin cytotoxicity. Recently, aspirin was shown to reduce severity of cisplatin-induced side effects related to hearing, balance, and kidney. Acetylsalicylic acid, or Aspirin, is known to inhibit COX-1 and COX-2 irreversibly through trans-esterification between acetylsalicylic acid and Ser-530 residue of COX,[16, 17] also has the potential to reduce the severity of cisplatin-induced side effects related to hearing, balance, and the kidneys.[15] Moreover, aspirin and its metabolite salicylates induce several anti-inflammatory cytokines to reduce inflammation.

A combination of cisplatin and aspirin can be an attractive strategy to manage highly aggressive PCa. Tremendous challenges exist in using drug combinations when drugs are individually administered. An alternative way for delivering a therapeutic

combination of cisplatin and aspirin is to fabricate a Pt(IV) prodrug that can be reduced to give cisplatin and aspirin. Pt(IV) prodrugs exhibit greater kinetic inertness compared to more labile cisplatin. With these issues in mind we constructed a Pt(IV) prodrug, Platin-*A*, with the ability to release cisplatin and aspirin for their respective biological actions. Herein, we discuss about the fabrication and biological activity of Platin-*A*.

Cell Line and Cell Culture.

Human prostate cancer LNCaP cells and RAW 264.7 macrophages were procured from the American type culture collection (ATCC). LNCaP, PC3 and RAW 264.7 cells were grown in Roswell Park Memorial Institute (RPMI) 1640 medium supplemented with 10% FBS and 1% penicillin/streptomycin. Cells were passed every 3 to 4 days and restarted from frozen stocks upon reaching pass number 20.

Synthesis of Platin-*A*.

Platin-A was synthesized and characterized by Dr. Rakesh K. Pathak and the details can be found in *Angew. Chem. Int. Ed.,* 126, 1994-1998

The (3-(4,5-dimethylthiazol-2-yl)-2,5-diphenyltetrazolium bromide or MTT Assay and Data Analysis.

The cytotoxic behaviors of cisplatin, aspirin, cisplatin+aspirin, and 'Platin-*A*' were evaluated using the MTT assay against LNCaP cells. LNCaP cells (10000 cells/well) were seeded on a 96-well plate in 200 μL of medium and incubated for 24 h. The cells were treated with different constructs at varying concentrations and incubated for 72 h at 37 °C. The cells were then treated with 20 μL of MTT (5 mg/mL in PBS) for 5 h. The medium was removed, the cells were lysed with 100 μL of DMSO, and the absorbance of the purple formazan was recorded at 550 nm using a Bio-Tek Synergy HT

microplate reader. Each well was performed in triplicate. All experiments were repeated three times. Cytotoxicity was expressed as mean percentage increase relative to the unexposed control ± SD. Control values were set at 0% cytotoxicity or 100% cell viability. Cytotoxicity data (where appropriate) was fitted to a sigmoidal curve and a three parameters logistic model used to calculate the IC_{50}, which is the concentration of chemotherapeutics causing 50% inhibition in comparison to untreated controls. The mean IC_{50} is the concentration of agent that reduces cell growth by 50% under the experimental conditions and is the average from at four independent measurements that were reproducible and statistically significant. The IC_{50} values were reported at ±99% confidence intervals. This analysis was performed with GraphPad Prism (San Diego, U.S.A).

Apoptosis Detection by Annexin V Assay.

PC3 cells were seeded at a density of 1 x 10^6 cells/mL on each well of a six well plate and allowed to grow overnight. Medium was changed and the cells were treated with 25 μM cisplatin, 25 μM aspirin, a mixture of cisplatin (25 μM) and aspirin (25 μM), and 25 μM of Platin-*A* for 8 h at 37 °C. As positive controls, etoposide (100 mM, incubation time: 12 h) for apoptosis and H_2O_2 (1 mM, incubation time: 45 min) for necrosis were used. The cells were trypsinized, repeatedly washed, and centrifuged at 1,800 RPM for 3 min, and the supernatants were discarded. Cell density was determined and cells were resuspended in 1X annexinV-binding buffer to 1x10^6 cells/mL preparing a sufficient volume to have 100 μL per assay. To 100 μL of cell suspension, 5 μL Alexa Fluor® 488 annexin V and 1 μL of 100 µg/mL propidium iodide (PI) working solution were added, incubated for 15 min at room temperature. After the incubation period, 400

μL of 1X annexin-binding buffer was added to each sample, samples were gently mixed keeping the samples on ice, and the samples were analyzed on the flow cytometer immediately.

Detarmination of Anti-inflammatory Properties of Platin-A by Enzyme-Linked Immunosorbent Assay (ELISA).

RAW 264.7 cells were plated at a concentration of 10,000 cells/mL in 96 well plates and allowed to grow for overnight. For preventative anti-inflammatory treatment, Platin-*A* (10 μM), aspirin (10 μM), cisplatin (10 μM) and an equimolar ratio of cisplatin and aspirin (10 μM each) was incubated with the RAW cells for 6 h. Lipopolysaccharide (LPS) (100 ng/mL) was added and the cells were further incubated for 12 h. For therapeutic anti-inflammatory treatment, LPS (100 ng/mL) was added to the RAW cells and incubated for 6 h. Platin-*A* (10 μM), aspirin (10 μM), cisplatin (μM) and an equimolar ratio of cisplatin and aspirin (10 μM each) was then added to the cells and incubated for 12 h. ELISA was performed on the supernatants against the cytokines interleukin (IL)-6, IL-10, and tumor necrosis factor alpha (TNF-α) according to the manufacturer's protocol. Briefly, antibody coated plates were blocked with 10% FBS in PBS for 1 h at room temperature followed by 3 washes. RAW cell supernatants were incubated on the plates for 2 h at room temperature. This was immediately followed by washings and sequential incubations with the cytokine-biotin conjugate and streptavidin working solution. Finally, the substrate reagent containing 3,3',5,5'-tetramethylbenzidine (100 μL) was added to each well, incubated for 15 min, the reaction was stopped by adding 50 μL H_2SO_4 (0.1 M). The absorbance was recorded at 450 nm using a BioTek Synergy HT well plate reader.

Induction of COX-2 using Human TNF-*α* in PC3 cells and Immunofluorescence Analysis of COX-2 Inhibiton by Platin-*A*.

PC3 cells were plated at a concentration of $1x10^6$ cells/mL on a glass coverslip and allowed to grow overnight. The cells were then grown in serum depleted media for 24 h. Human TNF-*α* (20 ng/mL) was then added to the cells and incubated for 2 h. Platin-*A* (1 μM), aspirin (1 μM), and an equimolar ratio of cisplatin and aspirin (1 μM each) was added to the cells and further incubated for another 2 h. The cells were then fixed with a 4% paraformaldehyde solution for 30 min at room temperature. The cells were then permeabilized using 1% Triton X-100 for 15 min at room temperature. The cells were blocked with a blocking buffer (1x PBS, 0.1% goat serum, 0.075% glycin) for 1 h at room temperature. The primary rabbit polyclonal antibody for COX-2 (2.5 μg/mL in blocking buffer) was added and incubation was carried out at 4 ºC for 12 h. The coverslips were washed 3 times with H_2O and 3 times with PBS. The cells were then incubated with the secondary AlexaFluor 488 goat anti-rabbit antibody for 1 h at 37 ºC. After 5 washes with blocking buffer, the cells were mounted on microscope slides with mounting media (20 mM Tris of pH 8.0, 0.5% N-propyl gallate, and 70% glycerol). Images were collected with 500 ms exposure using DAPI and FITC filters. RFUs were also analyzed by plate reader at an excitation wavelength of 488 nm and an emission of 519 nm.

RESULTS AND DISCUSSION

In LNCaP cells, Platin-*A* activity was better than an equimolar mixture of cisplatin and aspirin (IC_{50}: 18.65±1.2 μM). Aspirin did not show any significant toxicity in all PCa cells under these conditions. In general, Pt(IV) compounds are less cytotoxic

compared to their active Pt(II) form. The cytotoxic behavior of Platin-*A* was found to be very similar to cisplatin in all the three PCa cell lines. The comparable cytotoxicity of Platin-*A* with cisplatin even when it is a Pt(IV) prodrug demonstrated its unique anti-proliferative potency in PCa cells.

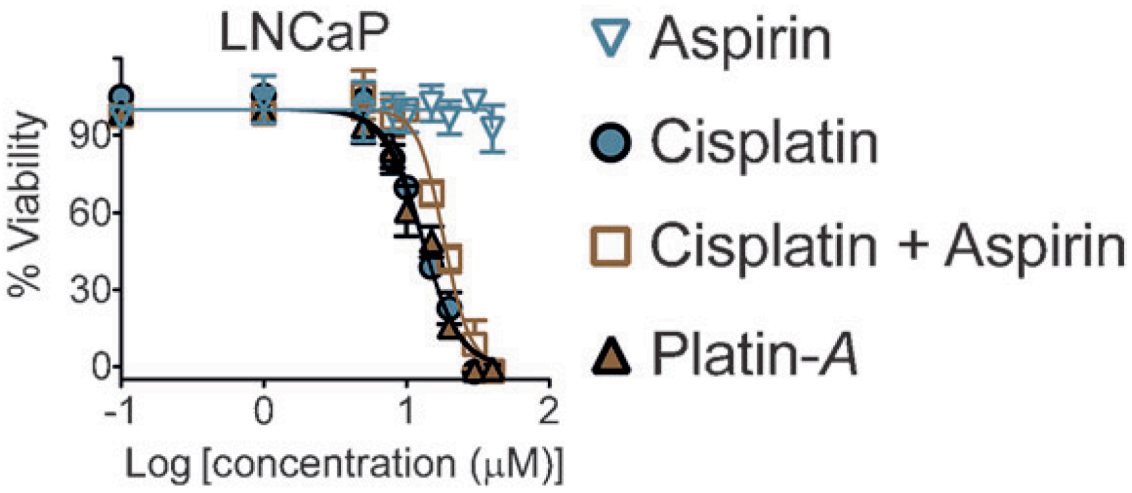


Figure AIII-1. Cytotoxic profiles of Platin-*A* in PCa cell lines by the MTT assay.

Apoptosis Inducing Properties of Platin-*A*.

To evaluate whether Platin-*A*-dependent inhibition of cancer cell proliferation is associated with apoptosis of these cells, we carried out Alexa Fluor® 488 annexinV/PI staining assay in PC3 cells and analyzed the data by FACS. Dot plots of green (Alexa Fluor® 488 annexinV) *vs* red (PI) fluorescence showed four separate clusters: viable cells (lower left quadrant); cells at early stage of apoptosis (lower right quadrant); cells at late stage of apoptosis or necrosis (upper right quadrant); debris (upper left quadrant) (Figure AIII-2). High level of apoptosis was induced by Platin-*A*. Apoptosis inducing property Platin-*A* was very similar to cisplatin and an equimolar mixture of cisplatin and aspirin.

Aspirin alone did not show any significant changes in healthy PC3 populations under these conditions. Not significant change in the levels of necrosis was observed.

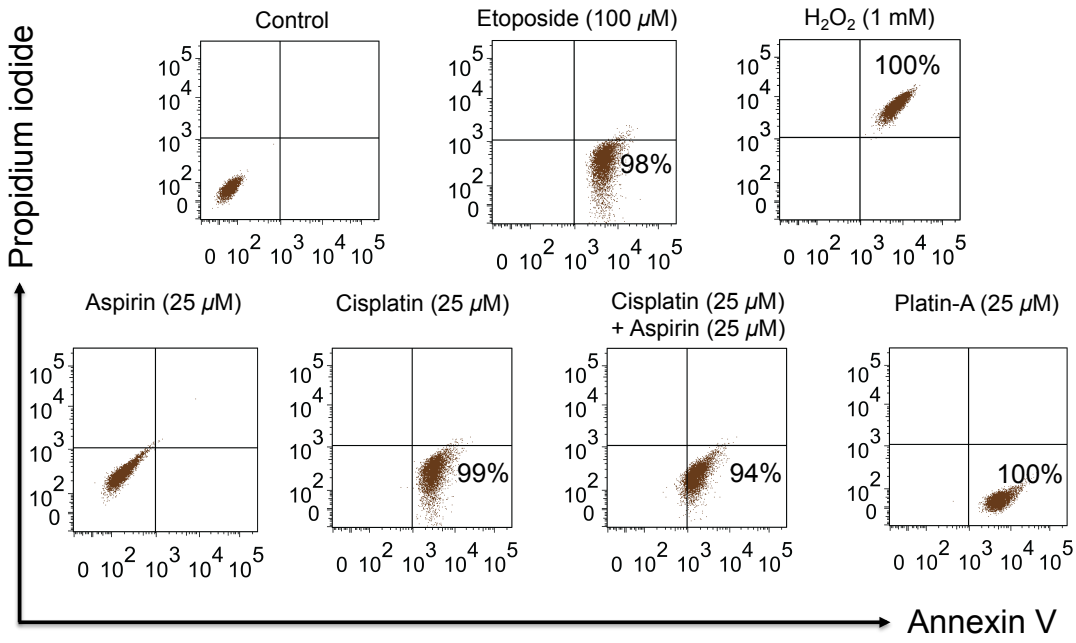


Figure AIII-2. Apoptosis inducing property of Platin-*A* by annexin V-FITC/PI staining of PC3 cells. PC3 cells ($1x10^6$ cells/mL) on day 2 were incubated with aspirin (25 μM), cisplatin (25 μM), an equimolar mixture of cisplatin and aspirin (25 μM), and Platin-*A* (25 μM) for 6 h. Additionally, etoposide (100 μM, 12 h) and H_2O_2 (1 mM, 45 min) treated cells were used as positive controls of apoptosis and necrosis, respectively. Four distinct phenotypes: viable cells (lower left quadrant); cells at early stage of apoptosis (lower right quadrant); cells at late stage of apoptosis or necrosis (upper right quadrant); debris (upper left quadrant).

COX-2 Inhibition by Platin-*A* in PCa Cells.

Many cancers show elevated levels of COX-2, however, COX-2 contributions to PCa and its regulation by inflammatory cytokines are controversial. We observed low

COX-2 levels in PC3 cells. We, therefore, investigated enhancement of COX-2 levels in response to COX-2 inducing cytokines. We used TNF-α because it is a strong inducer of COX-2 gene expression and TNF-α-induced expression may be driven by nuclear factor-κB (NF-κB)-binding motifs in the COX-2 promoter. We treated PC3 cells with TNF-α (20 ng/mL) for 2 h and examined the COX-2 expression pattern upon treatment with Platin-*A* (1 μM), cisplatin and aspirin (1 μM), aspirin (1 μM) for 2 h. Basal COX-2 levels were very low in PC3 cells and no effect was observed in the presence of all test articles. We found that the COX-2 level was increased in PC3 cells at 4 h after stimulation with TNF-α (Figure AIII-3B). Immunofluorescence studies showed that the COX-2 protein levels increased in PC3 cells after treatment with TNF-α indicating that COX-2 plays important roles in PCa progression in response to cytokines. COX-2 expression in TNF-α stimulated PC3 cells was reduced upon treatment with Platin-*A*, an equimolar mixture of cisplatin and aspirin did not show any effect on these activated cells, and the level of inhibition shown by aspirin was similar to that observed with Platin-*A* (Figure AIII-3). Significant inhibition of COX-2 in PC3 cells by Platin-*A* indicate that Platin-A has the ability to reduce tumor associated inflammation.

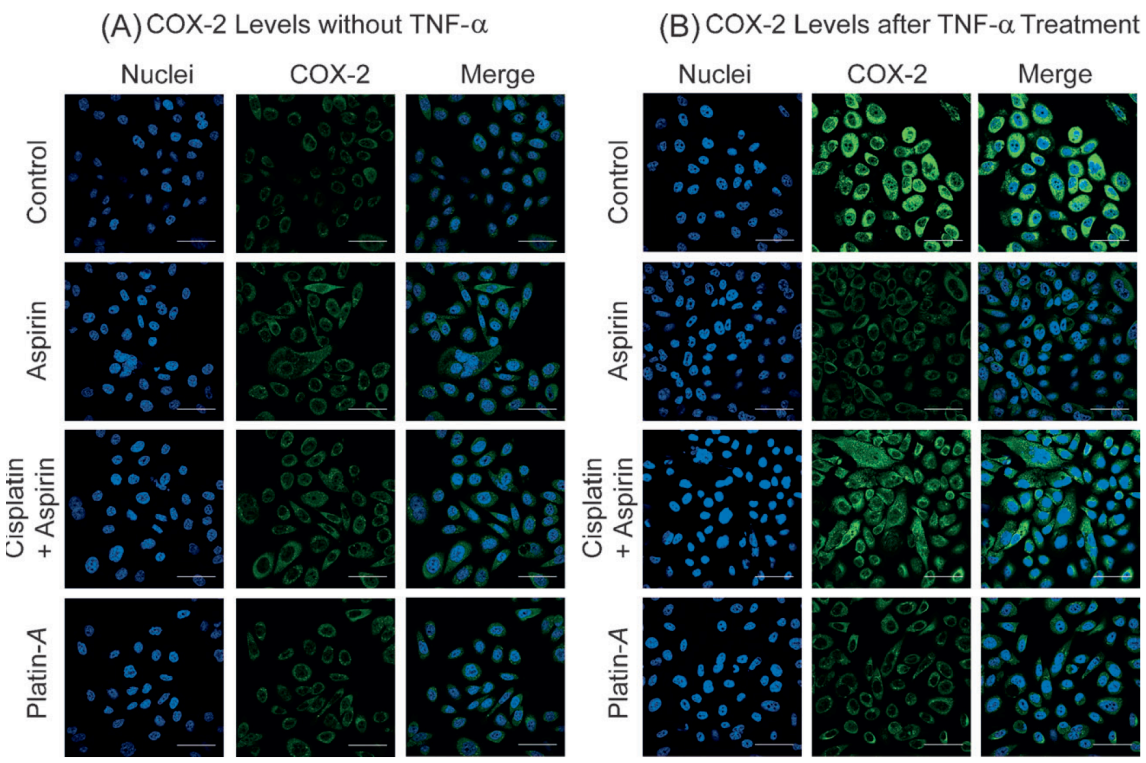


Figure AIII-3. Immunofluorescence analysis of COX-2 expression in PC3 cells. A) COX-2 expressions in PC3 cells and the effect of aspirin (1 μM), and an equimolar ration of cisplatin and aspirin (1 μM each), and Platin-A (1 μM) on TNF- stimulated cells. Cells were DAPI-stained in blue. COX-2 were labeled with a primary rabit polyclonal antibody and subsequently labed with a secondary AlexaFluor 488 goat anti-rabbit antibody. All scale bars are 25 μm.

Potential of Platin-*A* to Reduce Tumor Associated Inflammation.

Chronic inflammation is crucial to progression of human cancers, including PCa. Pro-inflammatory cytokines, tumor necrosis factor-alpha (TNF-α) and interleukin (IL)-6, are important for proliferation, survival, metastasis, and escape from immune surveillance of cancers.[23] Chronic inflammation by activation of toll like receptors

(TLRs) on cancer cells creates a tumor micro-environment which impairs the anti-tumor function of the immune system to allow to develop and survive.[24] The most important TLR-mediated cytokines involved in growth of tumors appear to be tumor-derived IL-10, TNF-α, and IL-6. The cytokines TNF-α and IL-6 are potent activators of NF-κB, a key modulator of inflammation-induced carcinogenesis. Enhanced TNF-α secretion mediates cisplatin nephrotoxicity.[25] The anti-inflammatory cytokine, IL-10 inhibits inflammatory and cytotoxic pathways in cisplatin-induced acute renal injury.[26] TLR-mediated pro-inflammatory cytokine production from tumor associated macrophages (TAMs) play a key role in tumor progression, metastasis, and TLR4 signaling is involved in the regulation of cancer cell metastasis.[27] We therefore investigated the effect of Platin-*A* on lipopolysaccharide (LPS), an exogenous ligand for TLR4, activated RAW 264.7 macrophages to mimic the inflammatory environment in cancer. [24]

First, we evaluated the effects of Platin-*A*, cisplatin, a combination of cisplatin and aspirin, and aspirin on pro-inflammatory cytokines IL-6, TNF-α and anti-inflammatory IL-10 production in LPS-stimulated RAW 264.7 macrophages. Macrophages were first stimulated with 100 ng/mL LPS for 6 h. Stimulation of RAW cells with LPS markedly increased IL-6 and TNF-α production, compared with that generated under control conditions (Figure AIII-4A). IL-10 is an anti-inflammatory cytokine that regulates excessive production of inflammatory cytokines such as IL-6, TNF-α during inflammation. Under our experimental conditions, we did not observe any secretion of IL-10 from RAW macrophages upon stimulation with LPS. We then tested whether Platin-*A* reduces the production of LPS-induced pro-inflammatory cytokines IL-6, TNF-α and possibility of induction of anti-inflammatory IL-10 using enzyme-linked

immunosorbent assay (ELISA).[28] Treatment of LPS activated macrophages with 10 μM of Platin-*A* for 12 h significantly reduced the levels of IL-6 and TNF-α; cisplatin under same conditions did not show any effect on the levels of these cytokines (Figure AIII-4A).

In general, macrophages need two stimuli to induce their anti-inflammatory activity. The first signal for example, such as a TLR ligand generally has little or no stimulatory function on its own. However, when combined with a second stimulus, immune complexes, prostaglandins, or apoptotic cells, the two signals reprogram macrophages to produce IL-10. Because IL-10 can inhibit the production and activity of various pro-inflammatory cytokines, these regulatory macrophages are potent inhibitors of inflammation, despite the fact that they retain the ability to produce many pro-inflammatory cytokines. Secretion of IL-10 by LPS activated macrophages in the presence of Platin-*A* indicates its anti-inflammatory properties.

We next assessed the effect of pretreatment of Platin-*A* on macrophages prior to LPS stimulation. As shown in Figure AIII-4B, stimulation of RAW macrophages with LPS (100 ng/mL) led to a significant increase in the levels of IL-6 and TNF-α in the cell conditioned media after 12 h. Pretreatment of these macrophages with Platin-*A* significantly inhibited the LPS-induced IL-6 and TNF-α production at a low concentration of 10 μM. A combination of pretreatment with Platin-*A* and LPS showed an enhanced levels of IL-10 (Figure AIII-4B). These results together indicated that Platin-*A* is efficient in curtailing inflammatory response. Pretreatment of macrophages

with cisplatin, aspirin, and an equimolar mixture of cisplatin and aspirin combination did not show any preventive action against LPS stimulation.

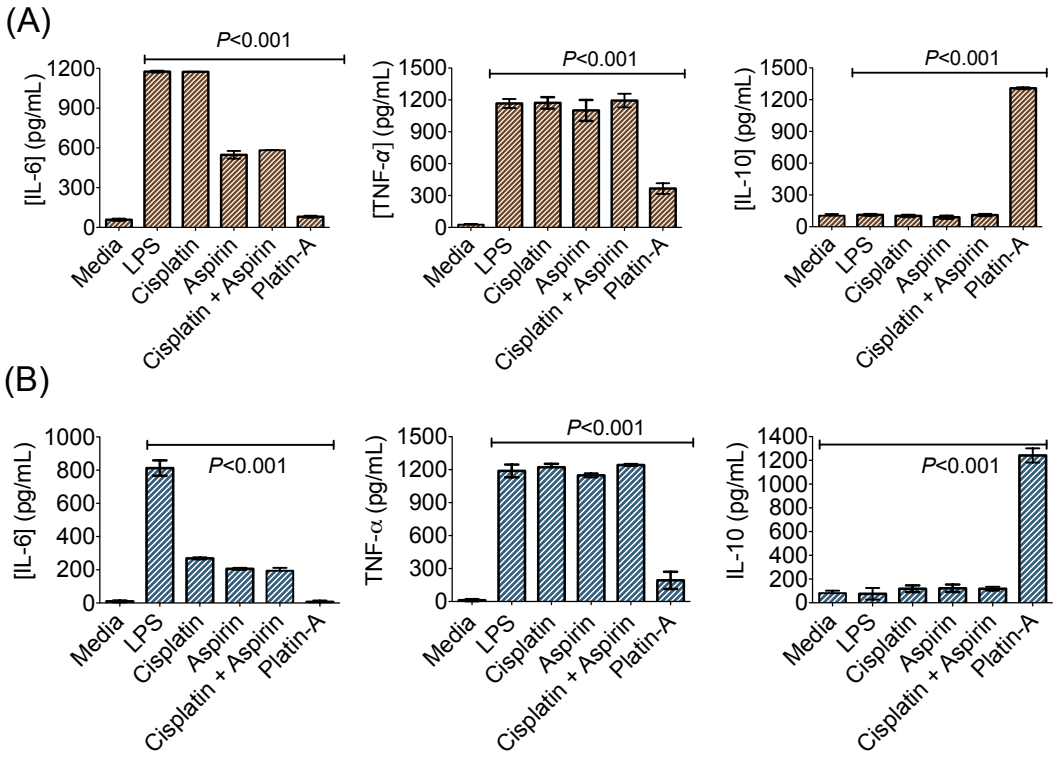


Figure AIII-4. Reduction of LPS-induced inflammation by Platin-*A* in RAW 264.6 macrophages. (A) RAW 264.6 macrophages were treated with LPS to induce inflammation and the effects of cisplatin, aspirin, an equimolar mixture of cisplatin and aspirin, and Platin-*A* on the levels of IL-6, TNF-α, and IL-10 were studied using ELISA. (B) RAW 264.6 macrophages were treated cisplatin, aspirin, an equimolar mixture of cisplatin and aspirin, and Platin-*A* followed by addition of LPS and preventive action of the test article on the levels of IL-6, TNF-α, and IL-10 were studied using ELISA.

References:

1. Marzo, A. M. D.; Platz, E. A.; Sutcliffe, S.; Xu, J.; Grönberg, H.; Drake, C. G.; Nakai, Y.; Isaacs, W. B.; Nelson, W. G., Inflammation in prostate carcinogenesis. *Nat. Rev. Cancer* **2007,** *7*, 256-269.
2. Jemal, A.; Siegel, R.; Xu, J.; Ward, E., Cancer Statistics, 2010. *CA: A Cancer Journal for Clinicians* **2010,** *60* (5), 277-300.
3. Sturge, J.; Caley, M. P.; Waxman, J., Bone metastasis in prostate cancer: emerging therapeutics. *Nat. Rev. Clin. Oncol.* **2011,** *8*, 357-368.
4. ROSENBERG, B.; VANCAMP, L.; TROSKO, J. E.; MANSOUR, V. H., Platinum Compounds: a New Class of Potent Antitumour Agents. *Nature* **1969,** *222*, 385-386.
5. Jamieson, E. R.; Lippard, S. J., Structure, Recognition, and Processing of Cisplatin−DNA Adducts. *Chemical Reviews* **1999,** *99* (9), 2467-2498.
6. Dhar, S.; Lippard, S. J., Current Status and Mechanism of Action of Platinum-Based Anticancer Drugs. In *Bioinorganic Medicinal Chemistry*, Wiley-VCH Verlag GmbH & Co. KGaA: 2011; pp 79-95.
7. Prestayko, A. W.; D'Aoust, J. C.; Issell, B. F.; Crooke, S. T., Cisplatin (cis-diamminedichloroplatinum II). *Cancer Treatment Reviews* **1979,** *6* (1), 17-39.
8. Denmeade, S. R.; Lin, X. S.; Isaacs, J. T., Role of programmed (apoptotic) cell death during the progression and therapy for prostate cancer. *The Prostate* **1996,** *28* (4), 251-265.
9. Oh, W. K.; Kantoff, P. W., Management of Hormone refractory prostate cancer: current standards and future prospects. *J. Urol.* **1998,** *160* (4), 1220-1229.

10. Borsellino, N.; Belldegrun, A.; Bonavida, B., Endogenous Interleukin 6 Is a Resistance Factor for cis-Diamminedichloroplatinum and Etoposide-mediated Cytotoxicity of Human Prostate Carcinoma Cell Lines. *Cancer Res.* **1995,** *55* (20), 4633-4639.

11. Dhar, S.; Gu, F. X.; Langer, R.; Farokhzad, O. C.; Lippard, S. J., Targeted delivery of cisplatin to prostate cancer cells by aptamer functionalized Pt(IV) prodrug-PLGA–PEG nanoparticles. *Proc. Natl. Acad. Sci. USA* **2008,** *105* (45), 17356-17361.

12. Thun, M. J.; Henley, S. J.; Patrono, C., Nonsteroidal Anti-inflammatory Drugs as Anticancer Agents: Mechanistic, Pharmacologic, and Clinical Issues. *J. Natl.Caner Inst.* **2002,** *94* (4), 252-266.

13. Ricciotti, E.; FitzGerald, G. A., Prostaglandins and Inflammation. *Arterioscler. Thromb. Vasc. Biol.* **2011,** *31* (5), 986-1000.

14. Hussain, T.; Gupta, S.; Mukhtar, H., Cyclooxygenase-2 and prostate carcinogenesis. *Cancer Letters* **2003,** *191* (2), 125-135.

15. Mukherjea, D.; Rybak, L. P.; Sheehan, K. E.; Kaur, T.; Ramkumar, V.; Jajoo, S.; Sheth, S., The design and screening of drugs to prevent acquired sensorineural hearing loss. *Exp. Opin. Drug Discovery.* **2011,** *6* (5), 491-505.

16. Tosco, P.; Lazzarato, L., Mechanistic Insights into Cyclooxygenase Irreversible Inactivation by Aspirin. *ChemMedChem* **2009,** *4* (6), 939-945.

17. Vane, J. R., Inhibition of prostaglandin synthesis as a mechanism of action for aspirin-like drugs. *Nature: New biology* **1971,** *231* (25), 232-5.

18. Graf, N.; Lippard, S. J., Redox activation of metal-based prodrugs as a strategy for drug delivery. *Adv. Drug Deliv. Rev.* **2012,** *64* (11), 993-1004.

19. Webb, B. A.; Chimenti, M.; Jacobson, M. P.; Barber, D. L., Dysregulated pH: a perfect storm for cancer progression. *Nat Rev. Cancer* **2011,** *11*, 671-677.

20. Gatenby, R. A.; Gawlinski, E. T.; Gmitro, A. F.; Kaylor, B.; Gillies, R. J., Acid-Mediated Tumor Invasion: a Multidisciplinary Study. *Cancer Res.* **2006,** *66* (10), 5216-5223.

21. Mehar, A.; Macanas-Pirard, P.; Mizokami, A.; Takahashi, Y.; Kass, G. E. N.; Coley, H. M., The Effects of Cyclooxygenase-2 Expression in Prostate Cancer Cells: Modulation of Response to Cytotoxic Agents. *J. Pharm. Exp. Ther.* **2008,** *324* (3), 1181-1187.

22. Mitchell, J. A.; Akarasereenont, P.; Thiemermann, C.; Flower, R. J.; Vane, J. R., Selectivity of nonsteroidal antiinflammatory drugs as inhibitors of constitutive and inducible cyclooxygenase. *Proc. Natl. Acad. Sci. USA.* **1993,** *90* (24), 11693-11697.

23. Lin, W.-W.; Karin, M., A cytokine-mediated link between innate immunity, inflammation, and cancer. *J. Clin. Invest.* **2007,** *117*, 1175-1183.

24. Sato, Y.; Goto, Y.; Narita, N.; Hoon, D. B., Cancer Cells Expressing Toll-like Receptors and the Tumor Microenvironment. *Cancer Microenvironment* **2009,** *2* (1), 205-214.

25. So, H.; Kim, H.; Lee, J.-H.; Park, C.; Kim, Y.; Kim, E.; Kim, J.-K.; Yun, K.-J.; Lee, K.-M.; Lee, H.-Y.; Moon, S.-K.; Lim, D.; Park, R., Cisplatin Cytotoxicity of

Auditory Cells Requires Secretions of Proinflammatory Cytokines via Activation of ERK and NF-κB. *JARO* **2007,** *8* (3), 338-355.

26. Deng, J.; Kohda, Y.; Chiao, H.; Wang, Y.; Hu, X.; Hewitt, S. M.; Miyaji, T.; Mcleroy, P.; Nibhanupudy, B.; Li, S.; Star, R. A., Interleukin-10 inhibits ischemic and cisplatin-induced acute renal injury. *Kidney Int.* **2001,** *60*, 2118-2128.

27. Mantovani, A.; Sica, A., Macrophages, innate immunity and cancer: balance, tolerance, and diversity. *Curr. Opin. Immunol.* **2010,** *22* (2), 231-237.

28. Marrache, S.; Tundup, S.; Harn, D. A.; Dhar, S., Ex Vivo Programming of Dendritic Cells by Mitochondria-Targeted Nanoparticles to Produce Interferon-Gamma for Cancer Immunotherapy. *ACS Nano* **2013,** *7* (8), 7392-7402.